Focused particle beam-induced processing

Edited by Michael Huth and Armin Gölzhäuser

Imprint

Focused particle beam-induced processing

Michael Huth[*1] and Armin Gölzhäuser[*2]

Editorial

Address:
[1]Goethe Universität, Physikalisches Institut, Max-von-Laue-Str. 1, D-60438 Frankfurt am Main, Germany and [2]Universität Bielefeld, Fakultät für Physik, Universitätsstr. 25, D-33615 Bielefeld, Germany

Email:
Michael Huth[*] - michael.huth@physik.uni-frankfurt.de;
Armin Gölzhäuser[*] - goelzhaeuser@physik.uni-bielefeld.de

* Corresponding author

In light of the success of 3D printing using fused-deposition modeling or higher-resolution variants with lasers applicable to polymers and metals, one may wonder whether an analogous approach exists on the nanometer scale. Indeed it does. With the aid of focused particle beam-induced deposition (FPBID) it is possible to create solid-state structures on the nanoscale. However, in contrast with large-scale 3D printing of plastic or metallic structures, FPBID provides nanomaterials with a wealth of interesting electronic, optical and magnetic properties. Due to this, focused electron beam-induced deposition (FEBID) has experienced a rapid expansion in the breadth of its application fields over the last 10 years.

In FEBID, a highly focused electron beam, in most cases provided by a scanning electron microscope, is raster-scanned over a substrate surface on which an adsorbed precursor layer is sustained by a precursor gas injection system. As the primary (as well as the secondary and backscattered) electrons of the focused beam dissociate the precursor adsorbate, a permanent deposit is formed. Depending on the precursor and other process parameters, amorphous, nanogranular, nanocrystalline or polycrystalline nanostructures are obtained. Their position

and shape (i.e., also in 3D) are fully controlled by the precise movements of the electron beam. Under optimized conditions, the intrinsic resolution limit of FEBID is below 5 nm.

In this Thematic Series, the FEBID process is considered from different perspectives. The current knowledge of the most relevant dissociation channels at play in FEBID are reviewed in the article by Rachel Thormann and coworkers [1]. FEBID-specific continuum modeling approaches are elucidated in a review article by Milos Toth and collaborators [2]. An aspect thus far not considered in electron beam-induced growth is the role of surface excitations, as pointed out in the article by Francesc Salvat-Pujol et al. [3]. Recently, in an effort towards obtaining pure metal nanostructures, the postprocessing of FEBID structures has become an active field of research. This is covered in this Thematic Series by Brett Lewis and coworkers with a focus on platinum [4]. The postprocessing of copper-based FEBID structures by vacuum annealing is presented by Aleksandra Szkudlarek and collaborators [5]. Additionally, high electric current densities can be used to induce structural changes in suspended nanowires, as is shown for cobalt deposits in the article by Gian Carlo Gazzadi and Stefano Frabboni [6]. This

leads into the important application field of magnetic nanostructures obtained by FEBID. Luis Rodríguez and coworkers present a detailed study on the influence of shape anisotropy and surface oxidation on the magnetization reversal of thin, iron nanowires [7]. In the article by Oleksandr Dobrovolskiy and colleagues [8], different postgrowth purification treatments for platinum and cobalt FEBID structures are employed to fine-tune the magnetic properties of heterostructures. A novel application of electron beam-induced deposition of amorphous carbon for the patterning of gold nanoparticle structures is introduced by Takahiro Noriki and coworkers [9]. The resolution limiting aspects are covered in the article by Roland Schmied and collaborators concerning fundamental edge-broadening effects in FEBID [10].

A more recent development that may help to alleviate the resolution-limiting issues in FEBID on solid substrates is the employment of helium ion microscopy (HIM). In its current development stage, HIM is mainly used for imaging applications, providing enhanced contrast for surface features as compared to scanning electron microscopy. Along this direction, Yuri Petrov and Oleg Vyvenko have exploited reflected helium ions for high-resolution imaging with "chemical contrast" [11]. Hongzhou Zhang and coworkers have utilized a focused helium ion beam to modify and mill thin silicon foils [12], which constitutes pioneering work in HIM towards nanofabrication. Along the same path, Gregor Hlawacek, Bene Poelsema and coworkers focused on the interaction of helium ions with metal surfaces (gold in particular) [13-15]. In a series of three distinct articles, they concentrate on ion channeling, crystal mapping, and finally, ion-induced modification of the gold surface. A novel route towards focused particle beam-induced processing (FPBIP) with HIM is paved by Xianghui Zhang and coworkers [16]. They used focused helium ions to perform the controlled modification of materials in monomolecular organic films. Here, ion exposure induced 2D polymerization that is a basis for the creation of ultrathin nanomembranes. Finally, André Beyer and coworkers show impressive HIM images of ultrathin carbon nanomembranes [17], which is a clear indication of the potential of the bourgeoning fields of helium ion microscopy and lithography towards nanofabrication with focused charged particles.

The idea for this Thematic Series arose in conjunction with the 5th International Workshop on Focused Electron Beam Induced Processing (FEBIP2014) held at the Physics Department of the Goethe University in Frankfurt am Main in July 2014, which brought together renowned experts in the field. A selection of the more than 80 contributions to the workshop are presented in this Thematic Series in the form of original research articles reflecting recent advances in FPBIP.

We would like to express our sincere gratitude to all the authors for contributing their excellent work to this Thematic Series. We would also like to give special thanks to all referees for their timely and highly valuable reports. This helped tremendously to keep the publication times short and thus attractive for all contributors. Last but not least, we thank the team at the Beilstein-Institut for their continuous support. In particular, we would like to acknowledge the open access policy of the Beilstein Journal of Nanotechnology, which guarantees that this Thematic Series, together with a wealth of other articles, is freely available to the community.

Michael Huth and Armin Gölzhäuser

Frankfurt am Main and Bielefeld, August 2015

References

1. Thorman, R. M.; Kumar, T. P. R.; Fairbrother, D. H.; Ingólfsson, O. *Beilstein J. Nanotechnol.* **2015,** *6,* in press.
2. Toth, M.; Lobo, C.; Friedli, V.; Szkudlarek, A.; Utke, I. *Beilstein J. Nanotechnol.* **2015,** *6,* 1518–1540. doi:10.3762/bjnano.6.157
3. Salvat-Pujol, F.; Valentí, R.; Werner, W. S. *Beilstein J. Nanotechnol.* **2015,** *6,* 1260–1267. doi:10.3762/bjnano.6.129
4. Lewis, B. B.; Stanford, M. G.; Fowlkes, J. D.; Lester, K.; Plank, H.; Rack, P. D. *Beilstein J. Nanotechnol.* **2015,** *6,* 907–918. doi:10.3762/bjnano.6.94
5. Szkudlarek, A.; Rodrigues Vaz, A.; Zhang, Y.; Rudkowski, A.; Kapusta, C.; Erni, R.; Moshkalev, S.; Utke, I. *Beilstein J. Nanotechnol.* **2015,** *6,* 1508–1517. doi:10.3762/bjnano.6.156
6. Gazzadi, G. C.; Frabboni, S. *Beilstein J. Nanotechnol.* **2015,** *6,* 1298–1305. doi:10.3762/bjnano.6.134
7. Rodríguez, L. A.; Deen, L.; Córdoba, R.; Magén, C.; Snoeck, E.; Koopmans, B.; De Teresa, J. M. *Beilstein J. Nanotechnol.* **2015,** *6,* 1319–1331. doi:10.3762/bjnano.6.136
8. Dobrovolskiy, O. V.; Kompaniiets, M.; Sachser, R.; Porrati, F.; Gspan, C.; Plank, H.; Huth, M. *Beilstein J. Nanotechnol.* **2015,** *6,* 1082–1090. doi:10.3762/bjnano.6.109
9. Noriki, T.; Abe, S.; Kajikawa, K.; Shimojo, M. *Beilstein J. Nanotechnol.* **2015,** *6,* 1010–1015. doi:10.3762/bjnano.6.104
10. Schmied, R.; Fowlkes, J. D.; Winkler, R.; Rack, P. D.; Plank, H. *Beilstein J. Nanotechnol.* **2015,** *6,* 462–471. doi:10.3762/bjnano.6.47
11. Petrov, Y. V.; Vyvenko, O. F. *Beilstein J. Nanotechnol.* **2015,** *6,* 1125–1137. doi:10.3762/bjnano.6.114
12. Fox, D.; Chen, Y.; Faulkner, C. C.; Zhang, H. *Beilstein J. Nanotechnol.* **2012,** *3,* 579–585. doi:10.3762/bjnano.3.67
13. Veligura, V.; Hlawacek, G.; Berkelaar, R. P.; van Gastel, R.; Zandvliet, H. J. W.; Poelsema, B. *Beilstein J. Nanotechnol.* **2013,** *4,* 453–460. doi:10.3762/bjnano.4.53
14. Hlawacek, G.; Veligura, V.; Lorbek, S.; Mocking, T. F.; George, A.; van Gastel, R.; Zandvliet, H. J. W.; Poelsema, B. *Beilstein J. Nanotechnol.* **2012,** *3,* 507–512. doi:10.3762/bjnano.3.58
15. Veligura, V.; Hlawacek, G.; van Gastel, R.; Zandvliet, H. J. W.; Poelsema, B. *Beilstein J. Nanotechnol.* **2012,** *3,* 501–506. doi:10.3762/bjnano.3.57
16. Zhang, X.; Vieker, H.; Beyer, A.; Gölzhäuser, A. *Beilstein J. Nanotechnol.* **2014,** *5,* 188–194. doi:10.3762/bjnano.5.20

17. Beyer, A.; Vieker, H.; Klett, R.; Meyer zu Theenhausen, H.;
Angelova, P.; Gölzhäuser, A. *Beilstein J. Nanotechnol.* **2015,** *6,*
1712–1720. doi:10.3762/bjnano.6.175

Channeling in helium ion microscopy: Mapping of crystal orientation

Vasilisa Veligura, Gregor Hlawacek[*], Raoul van Gastel,
Harold J. W. Zandvliet and Bene Poelsema

Abstract

Background: The unique surface sensitivity and the high resolution that can be achieved with helium ion microscopy make it a competitive technique for modern materials characterization. As in other techniques that make use of a charged particle beam, channeling through the crystal structure of the bulk of the material can occur.

Results: Here, we demonstrate how this bulk phenomenon affects secondary electron images that predominantly contain surface information. In addition, we will show how it can be used to obtain crystallographic information. We will discuss the origin of channeling contrast in secondary electron images, illustrate this with experiments, and develop a simple geometric model to predict channeling maxima.

Conclusion: Channeling plays an important role in helium ion microscopy and has to be taken into account when trying to achieve maximum image quality in backscattered helium images as well as secondary electron images. Secondary electron images can be used to extract crystallographic information from bulk samples as well as from thin surface layers, in a straightforward manner.

Introduction

The superior resolution of the helium ion microscope (HIM) and its outstanding performance on insulating samples [1,2] make it an interesting tool for materials research. Whilst images based on secondary electrons (SE) can yield an edge resolution down to 0.29 nm [2], backscattered helium (BSHe) images reveal the elemental composition of the specimen. A measurement of the energy of the backscattered helium atoms provides quantitative information on composition [3], and ionolumines-

cence gives access to electronic properties such as the band structure and the nature of color centers. Unfortunately, to date no experimental procedure has been developed to obtain texture data or crystallographic information systematically in HIM. Especially the latter is an important issue in materials characterization. An important phenomenon that can be exploited in HIM for this purpose is channeling. This well-known process has been studied extensively in the past in the context of ion scattering methods, such as Rutherford backscattering (RBS) and medium- and low-energy ion scattering. Many ion scattering phenomena are well understood for the very high energies of several hundred keV up to MeV that are used in RBS. Although energies in HIM are different and typically range between 5 keV and 40 keV, the existing theories can in fact describe the channeling phenomena with sufficient precision.

Here, we highlight the importance of channeling in the formation of images in HIM. Using gold as an example, we show how the SE yield can be increased by a factor of two. Judicious use of this knowledge allows for an efficient optimization of signal and contrast in HIM images. In the second part of this manuscript we provide an experimental procedure to accurately obtain crystallographic information in HIM. The strong dependence of channeling on the angle of incidence of the beam is used to perform crystal orientation mapping. This procedure provides information that is comparable to electron backscatter diffraction (EBSD). We also show that a fully fledged scattering calculation is not necessary to access this information. Simple geometric considerations are in fact sufficient.

Experimental

All images were recorded on an ultrahigh vacuum (UHV) Orion Plus helium ion microscope from Carl Zeiss [4]. The microscope is equipped with an Everhardt–Thornley (ET) detector to record SE images. A micro channel plate, which is placed in the beam path below the last lens, is used to record BSHe images. A silicon drift detector measures the energy of backscattered helium atoms and a Gatan MonoCL4 Elite detector measures ionoluminescence. The base pressure of 2×10^{-9} mbar allows for extended exposure of the same sample area to the He$^+$ ion beam. The near absence of hydrocarbons in the sample chamber effectively reduces carbon build-up in the investigated sample area. High-resolution images were recorded by using the ET detector and a typical primary energy (PE) of 33 keV. To enhance the channeling contrast, some of the data has been recorded with a lower PE of 15 keV. This increases the scattering probability and results in a better signal-to-noise ratio for ion-channeling contrast images. Commercially available polycrystalline gold{111} films on glass, with a chromium interlayer, were flame annealed in a hydrogen flame before the samples were loaded into the vacuum chamber. In addition the

samples were cleaned for 15 min in the load lock by using a 10 W air plasma. SRIM-2011 [5] was used to assess the damage caused by the swift helium atoms. The Monte Carlo code was setup to track the full damage cascade and 1×10^6 ions were used. To obtain a measure for the backscattering probability, angle-dependent projections of the crystal lattice were calculated by using a simple geometric model of the crystal slab. The atomic radius of gold was fixed to 0.68 Å and the lattice parameter was 4.078 Å (density 6×10^{22} cm^{-3}). To speed up the calculations, the thickness of the crystal slab was restricted to 14 layers. This corresponds to a thickness of 3.06 nm and is greater or equal to the information depth in SE images. This in turn depends on the escape depth of SEs in HIM [6]. The crystal slab was tilted and rotated with respect to the (111) surface plane and the [1$\bar{1}$0] direction, and the blocked area fraction (opacity) of the projection was calculated. To avoid lateral finite size errors, an area of 14 nm^2 was used for averaging, and border atoms were included with their corresponding area fraction.

Results and Discussion
### Channeling in helium ion microscopy

In Figure 1 SE images of a polycrystalline gold film with a {111} texture are shown. The images with a field of view (FoV) of 10 μm were recorded by using a sample tilt (polar angle) of 35°, a PE of 15 keV and an ion dose of 4.9×10^{14} cm^{-2}. In Figure 1a individual grains with an average size of 1 μm^2 can easily be distinguished, not only by their distinct shape, but also through the different gray levels. In Figure 1b and Figure 1c, HIM images are presented that show the same area but for different stage rotation angles (sample rotation is about the [111] surface normal). The gray level of the highlighted grain changes from dark gray to a brighter shade and finally back to a medium shade of gray. The gray level of the other grains changes in an identical sequence, but with different starting points. As we will show below, this allows us to identify the orientation of the individual grains.

A BSHe channeling contrast image recorded with the MCP detector is presented in Figure 2. Although, there is excellent contrast at the selected acceleration voltage of 20 keV and the mild dose of 1.11×10^{15} cm^{-2}, the signal-to-noise ratio is considerably worse compared to the SE images presented above. The reason for this is rooted in the low number of ions used per pixel. In the present case only 2375 ions are used per pixel, of which roughly 20% are backscattered, according to SRIM calculations. However, not all of these 500 ions will be counted by the detector. Different to the SE images, BSHe images contain information on the bulk crystallography. The achievable information depth will depend on acceleration voltage and elemental composition of the specimen. However,
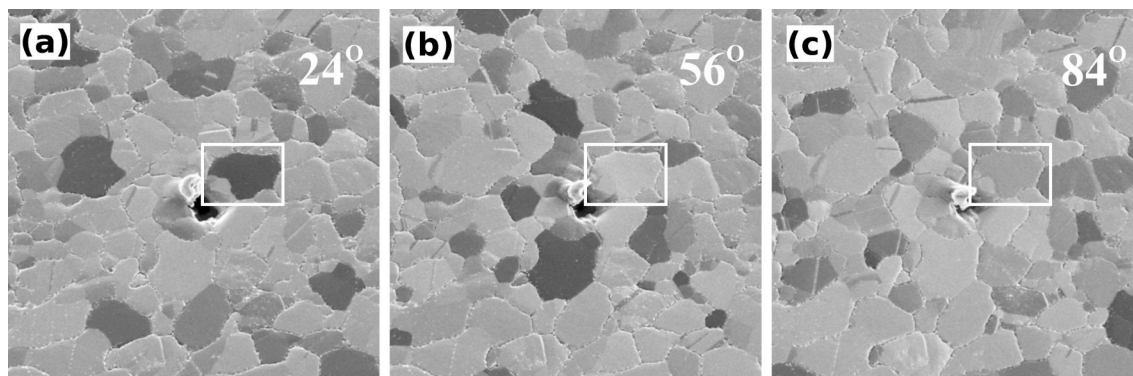
Figure 1: HIM SE images of the hydrogen-flame-annealed polycrystalline Au{111} film taken with a PE of 15 keV and an ion dose of 4.9×10^{14} cm^{-2}. Relative sample rotation angles around the surface normal are 24°, 56° and 84°. The polar angle is fixed at 35°. FOV: 10 μm.

for gold at 20 keV it is of the order of a few tens of nanometers, and consequently higher than the SE information depth of 2 nm to 3 nm [6].
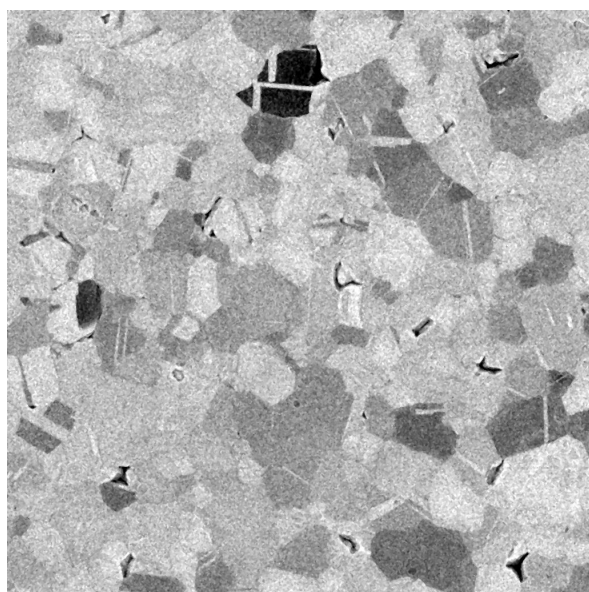
Figure 2: HIM BSHe images of the hydrogen-flame-annealed polycrystalline Au{111} film. A PE of 20 keV and an ion dose of 1.11×10^{15} cm^{-2} has been used. The stage tilt was 0°. FOV: 15 μm.

The stability of the contrast is quite remarkable. With the selected ion dose up to a 100 images can be recorded in the same area. After this, the accumulated dose will have induced an unacceptable number of defects and amorphization will start [7]. In this study, roughly 30 images were recorded, resulting in an ion dose well below the critical threshold. In addition, SE ion-channeling contrast images were used to obtain the data. The information depth in SE images is restricted to the first two

or three nanometers below the sample surface. However, ion-induced damage will occur mostly in deeper sample areas and therefore not affect the SE images directly. Using SRIM [5] and a PE of 15 keV into gold, we calculate that 49 vacancies are generated per ion. After a fluence of 4.9×10^{14} cm^{-2}, necessary to record one image, the defect density at a depth of 3 nm is 4% for the 0 K SRIM simulation. If we assume that about 99% of the defects will heal at a more realistic temperature of 300 K, we obtain a defect density of approximately 1% at a depth of 3 nm after 30 images have been recordeds (fluence: 1.5×10^{16} cm^{-2}).

The use of an UHV HIM also suppresses the formation of carbon residues on the surface due to hydrocarbon cracking by the energetic helium beam. This is illustrated by a measurement of the SE yields as a function of ion dose presented in Figure 3. A PE of ≈30 keV and an ion dose of 1×10^{14} cm^{-2} per image was used to record the data. After a fluence of 4.0×10^{15} cm^{-2} the SE yield in a well-maintained standard HV HIM decreased by 10%. However, under identical imaging conditions and for the same total dose, a small 5% increase in SE yield is observed in a UHV HIM. We attribute this slight increase to a mild surface sputtering under the prolonged beam exposure. In general a rougher surface will have a smaller work function, which allows a higher number of SE to escape.

In Figure 4a the average SE yield of several grains is plotted versus the azimuthal angle for two different primary energies. The SE yield of individual grains has been normalized with respect to the maximum intensity and data for the individual grains has been aligned by using the position of the strongest peak. We can understand the angular dependence of the SE yield if we view it as a direct result of the fcc structure of the crystallites in the Au{111} film. The insets in Figure 4a are models of the Au crystal structure. For a given thickness of the

sample slab, different fractions of the projected view of the crystal will be occupied by Au atoms. As a result, helium atoms traveling in a direction perpendicular to the projected plane will experience a different channeling probability. If a {111} oriented fcc crystal is tilted by 35° with respect to the incoming beam, for a specific azimuthal orientation, the {110} planes will be parallel to the trajectory of the incoming helium. For symmetry reasons, this configuration can be found every 120°. Particles traveling along the low index <110> directions will undergo a series of small-angle collisions with the atoms of the crystal. This results in a focusing action that allows the particles to travel along the channel [8]. However, to excite electrons in the inner shells of the lattice atoms, hard collisions are necessary. Subsequently, a low number of SE is generated under these conditions [9]. For the images presented in Figure 1 all grains have a {111} plane parallel to the substrate surface. However, the in-plane orientation is random. Consequently, only some grains will be oriented in a channeling direction, while others are not. As a result, a strong grain contrast can be achieved [10,11], in which dark grains are viewed along a channeling direction, while bright crystallites have a blocking orientation. For the marked grain in Figure 1 the stage rotation angles correspond to the azimuthal angle around [111] measured with respect to the [1$\bar{1}$0] surface direction.

Figure 4b is the result of a simple channeling simulation. A gold fcc crystal slab was tilted by 35° with respect to the (111) plane and rotated around [111] with respect to the [1$\bar{1}$0] direction. The opacity was then calculated for different azimuthal angles. When compared to the experimental data in Figure 4a it is obvious that the peak positions are reproduced correctly. The shoulders at 75° and 105° are artifacts from the limited crystal slab thickness. In our calculation the fraction of the opaque projected area is directly related to the SE yield measured in the experiment in a qualitative way. In accordance with the experimental results, the calculation predicts minima in the opaque area fraction for the [$\bar{1}$41] and [$\bar{1}$10] crystal directions.

The depth and width of the minima will depend on the diameter of the simulated atoms. This diameter corresponds to the cross section for scattering and will in turn depend on the actual collision parameters, in particular the primary energy of the incoming particles. The effect of the energy can be seen from Figure 4a: the channeling minima is wider and deeper for the lower energy. The maximum critical angle is determined by the maximum transverse energy [8]. Thus, in the case of lower ion energies the opening angle is bigger, and as a result, more incident ions can be trapped in the channel. In addition, the smaller transverse energy leads to a decrease in the dechanneling probability. Therefore, the lower energies will result in a higher contrast in the SE images.
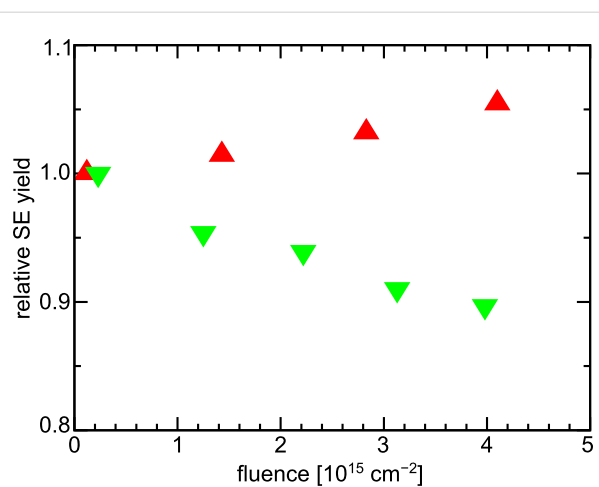
Figure 3: Comparison of contrast evolution in a standard HV and the used UHV HIM. The SE yield, which is proportional to the gray level in SE images, is plotted against the total dose for a HV system (green pointing down triangles) and the used UHV HIM (red pointing up triangles).
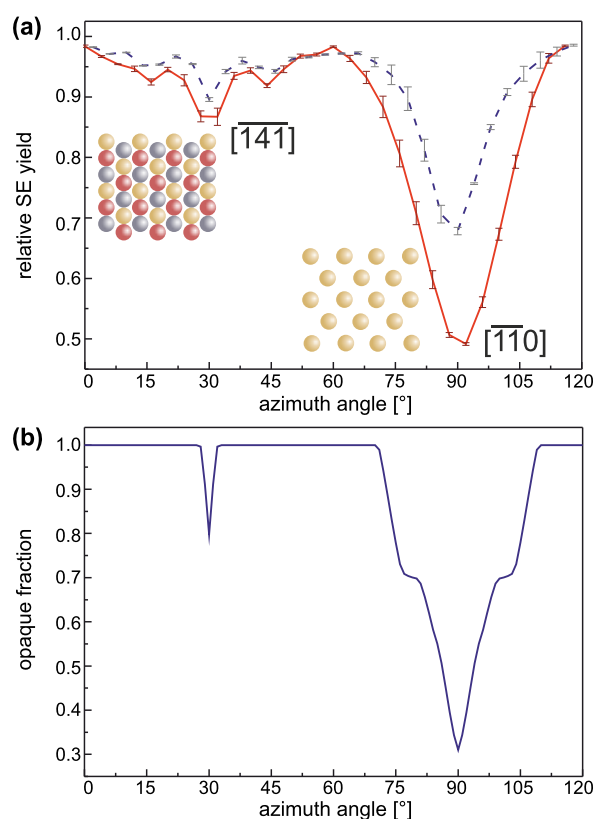
Figure 4: SE yield and opaque fraction for a polar angle of 35° with respect to the (111) plane. The azimuthal angle around the [111] direction is measured with respect to the [1$\bar{1}$0] direction. (a) Experimentally obtained dependence of the SE yield on the azimuthal angle. He$^+$ PEs are 15 keV (red, solid line) and 33.6 keV (blue, dashed line). The insets present the view of the crystal along the two indicated directions. The color code is as follows: gold: 1st layer, silver: 2nd layer, and red: 3rd layer. (b) Calculated opacity of a gold crystal lattice (14 atomic layers). The used effective atomic diameter is 0.68 Å.

Orientation mapping with channeling

The results that we have presented demonstrate that it is possible to obtain crystallographic information directly from SE images in HIM. This information is also accessible from BSHe images; however, the usage of SE has several advantages. First, the required ion dose for a high-quality image with a good signal-to-noise ratio is significantly lower. This is particularly important for light materials. The gold sample that has been used here has a comparatively large backscattering probability for helium atoms. The situation changes, however, for many technologically relevant materials, such as aluminum, iron and silicon. Second, the small information depth of the SEs enables the probing of adlayers and coatings with a thickness in the nanometer range.

In Figure 5 we show the calculated positions of the channeling minima of a fcc crystal for imaging with SEs. No exhaustive channeling calculation is necessary to obtain this plot. A simple geometric projection of the first few layers along the beam direction suffices. Despite the fact that the orientation map in Figure 5 resembles a typical stereographic projection of channeling minima [12] or a Laue map [13] for crystal orientations, we briefly highlight the differences. Low-index orientations, such as the <110> directions, are located in the nodes visible in the map. In contrast to a typical stereographic projection of channeling directions, the nodes are connected by a continuous minimum with only small depth undulation. The presence of these shallow lines is directly related to the limited slab thickness used in the calculation. An increase of slab thickness reduces the width and depth of the channeling minima. While stereographic projections give measures for the depth of channeling minima, this information has to be carefully reviewed in the present projection of the opaque crystal fraction map. The width and depth of the minima also depends on the ratio of the nearest-neighbor distance and effective atom radius. In this case we have simply used the ionic radius of gold. However, the parameters that were used create an excellent match between the experimental and simulated data (see Figure 4). In particular, the presence of the zone lines allows for an easy alignment of experimental maps to the calculated data, and the successive identification of crystal orientation.

The map presented in Figure 5 was used to index several grains. A color code representing the different orientations was used to illustrate the different in-plane orientations of the grains. Such a color-coded map is shown in Figure 6. Figure 6 shows the orientation for the grains imaged in Figure 1. The grain that is highlighted in Figure 1 is darkest for a 24° rotation angle. This corresponds to a yellow-green color in Figure 6. The color scale ranges from a 0° to 120° azimuthal rotation around [111]. Consequently, the color of an individual grain corresponds to
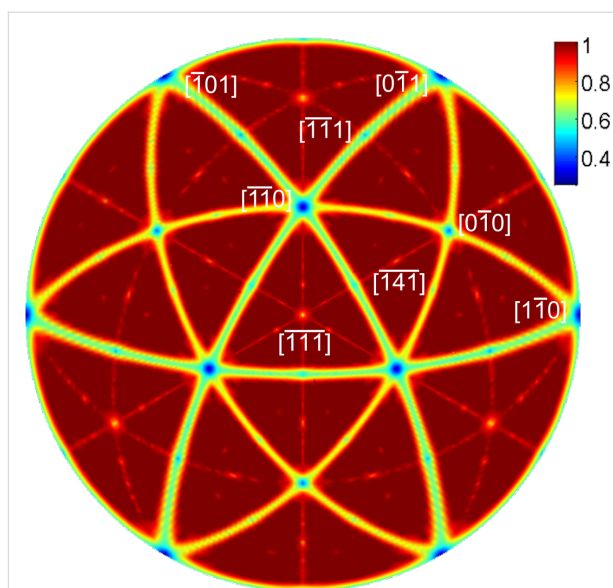
Figure 5: Calculated map of channeling directions for an fcc crystal. The lines connecting the nodes at low-index directions in the polar plot represent channeling directions in the used thin slab of an fcc crystal. The color coding (opaque fraction) allows a qualitative interpretation of the width and depth of the scattering minima.
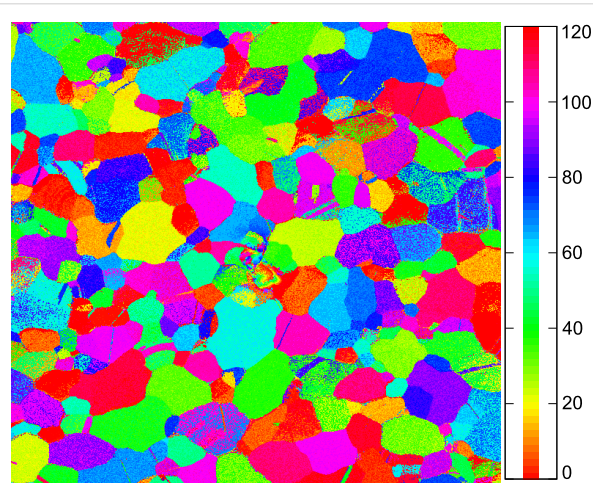
Figure 6: Color-coded orientation map of a polycrystalline gold film. The colors indicate the azimuthal angle around the [111] surface normal for a 35° sample tilt at which a <110> direction is aligned with the incoming helium ion beam. Parts of the data set used are presented in Figure 1.

the azimuthal angle for which a <110> direction in this gold grain is parallel to the beam. For the marked grain the stage rotation angle for this condition is 24°.

Conclusion

We have demonstrated the importance of channeling in HIM using polycrystalline gold films with a <111> texture. To quantitatively explain the orientation-dependent changes in

contrast it is not necessary to perform a full calculation of the scattering process. A straightforward projection of the crystal lattice is sufficient to identify low-index channeling directions. Such a map was calculated for an fcc lattice and used to determine the orientation of all gold crystallites in the FoV. The effect is observed in both types of HIM images. It is, however, particularly useful with SE images. Because of the limited information depth of SE ion-channeling contrast images, crystallographic data from thin adlayers can be obtained. BSHe ion-channeling contrast images, on the other hand, yield similar bulk crystallographic information. This adds a new capability to helium ion microscopy. The possibility to obtain crystallographic information on a per pixel basis strengthens the applicability of HIM for materials characterization.

Acknowledgements

References

1. Ward, B. W.; Notte, J. A.; Economou, N. P. *J. Vac. Sci. Technol., B* **2006,** *24,* 2871–2874. doi:10.1116/1.2357967
2. Hill, R.; Faridur Rahman, F. H. M. *Nucl. Instrum. Methods Phys. Res., Sect. A* **2011,** *645,* 96–101. doi:10.1016/j.nima.2010.12.123
3. Sijbrandij, S.; Notte, J.; Scipioni, L.; Huynh, C.; Sanford, C. *J. Vac. Sci. Technol., B* **2010,** *28,* 73–77. doi:10.1116/1.3271254
4. van Gastel, R.; Barriss, L.; Sanford, C.; Hlawacek, G.; Scipioni, L.; Merkle, A.; Voci, D.; Fenner, C.; Zandvliet, H.; Poelsema, B. *Microsc. Microanal.* **2011,** *17* (Suppl. S2), 928–929. doi:10.1017/S1431927611005514
5. Ziegler, J. F.; Biersack, J. P.; Ziegler, M. D. *SRIM–The stopping and range of ions in matter;* Lulu Press: Morrisville, NC, USA, 2008.
6. Ramachandra, R.; Griffin, B.; Joy, D. *Ultramicroscopy* **2009,** *109,* 748–757. doi:10.1016/j.ultramic.2009.01.013
7. Livengood, R.; Tan, S.; Greenzweig, Y.; Notte, J.; McVey, S. *J. Vac. Sci. Technol., B* **2009,** *27,* 3244. doi:10.1116/1.3237101
8. Lindhard, J. *Mat.-Fys. Medd.–K. Dan. Vidensk. Selsk.* **1965,** *34,* 1–64.
9. Feijen, H. H. W.; Verhey, L. K.; Boers, A. L.; Suurmeijer, E. P. T. M. *J. Phys. E: Sci. Instrum.* **1973,** *6,* 1174. doi:10.1088/0022-3735/6/12/005
10. Franklin, R. E.; Kirk, E. C. G.; Cleaver, J. R. A.; Ahmed, H. *J. Mater. Sci. Lett.* **1988,** *7,* 39–41. doi:10.1007/BF01729909
11. Levi-Setti, R. *Scanning Electron Microsc.* **1983,** *1,* 1–15.
12. MEIS - fcc(111) stereographic projection. http://www.dl.ac.uk/MEIS/stereographs/sp.fcc.111.html (accessed April 19, 2012).
13. Preuss, E.; Krahl-Urban, B.; Butz, R. *Laue-Atlas: plotted Laue back-reflection patterns of the elements, the compounds RX and RX2;* Bertelsmann-Universitätsverlag: Düsseldorf, 1974.

Imaging ultra thin layers with helium ion microscopy: Utilizing the channeling contrast mechanism

Gregor Hlawacek[*1], Vasilisa Veligura[1], Stefan Lorbek[2], Tijs F. Mocking[1], Antony George[3], Raoul van Gastel[1], Harold J. W. Zandvliet[1] and Bene Poelsema[1]

Address:
[1]Physics of Interfaces and Nanomaterials, MESA+ Institute for Nanotechnology, University of Twente, PO Box 217, 7500AE Enschede, The Netherlands, [2]Institute for Physics, Montanuniversitaet Leoben, Franz Josef Straße 18, 8700 Leoben, Austria and [3]Inorganic Material Science, MESA+ Institute for Nanotechnology, University of Twente, PO Box 217, 7500AE Enschede, The Netherlands

Email:
Gregor Hlawacek[*] - g.hlawacek@utwente.nl

* Corresponding author

Abstract

Background: Helium ion microscopy is a new high-performance alternative to classical scanning electron microscopy. It provides superior resolution and high surface sensitivity by using secondary electrons.

Results: We report on a new contrast mechanism that extends the high surface sensitivity that is usually achieved in secondary electron images, to backscattered helium images. We demonstrate how thin organic and inorganic layers as well as self-assembled monolayers can be visualized on heavier element substrates by changes in the backscatter yield. Thin layers of light elements on heavy substrates should have a negligible direct influence on backscatter yields. However, using simple geometric calculations of the opaque crystal fraction, the contrast that is observed in the images can be interpreted in terms of changes in the channeling probability.

Conclusion: The suppression of ion channeling into crystalline matter by adsorbed thin films provides a new contrast mechanism for HIM. This dechanneling contrast is particularly well suited for the visualization of ultrathin layers of light elements on heavier substrates. Our results also highlight the importance of proper vacuum conditions for channeling-based experimental methods.

Introduction

The helium ion microscope (HIM) has established itself as a high-performance alternative to the classic scanning electron microscope (SEM). The superior resolution and the outstanding performance on insulating samples are well-known facts [1,2]. While images based on secondary electrons (SE) allow a resolution as good as 0.29 nm [2], backscattered helium (BSHe) images reveal the elemental composition of the specimen. The contrast ratio that can be achieved in both types of images is determined by the chemical composition as well as the crystal orientation. Channeling along low index directions affects SE as well as BSHe images [3,4].

Here, we discuss how channeling can be utilized to gain unexpected contrast in BSHe images on ultrathin surface layers. HIM already provides superior surface sensitivity in SE-based images. The described contrast mechanism for BSHe images extends this capability to backscatter images. We demonstrate how hard-to-visualize thin layers of light elements on top of heavier element substrates can be detected in BSHe mode by clever utilization of channeling into the substrate.

Experimental

All data presented were recorded on an ultrahigh vacuum (UHV) Orion Plus helium ion microscope from Zeiss [5]. The microscope is equipped with an Everhardt–Thornley (ET) detector to record SE images, and a microchannel plate situated in the beam path below the final lens to record BSHe images. A silicon drift detector to measure the energy of backscattered ions and a Gatan MonoCL4 Elite detector for ionoluminescence complete the setup. The base pressure of 2×10^{-9} mbar allows the extended exposure of the same sample area to the He^+ ion beam. The near absence of hydrocarbons in the sample chamber effectively reduces carbon build-up in the irradiated sample area [5]. Contrast in SE images is primarily based on differences in work function and the yield of SE generation in the region near the surface [6]. As a consequence, HIM has an unprecedented surface sensitivity in SE mode. Together with the high lateral resolution, this permits the routine visualization of thin surface layers [7]. Contrast in BSHe images on the other hand is formed by differences in the backscattering probability of the impinging helium ions. As a rule of thumb these images therefore contain information on the elemental composition of the first 20 nm to 300 nm of the specimen. The backscattering yield has a roughly quadratic dependence on the atomic number (Z) of the target atom. Consequently these images are considered to contain complementary information, namely from the bulk, compared to SE images. However, the obtainable signal intensities will depend on the detector sensitivity. High-resolution images, using the ET detector and a primary energy (PE) of 35 keV, have been recorded for all samples. Since the backscat-

tering yield depends on the scattering cross section, it increases strongly with decreasing primary energy. Therefore, the BSHe data presented here was recorded with lower PEs between 10 keV and 20 keV. This results in a better signal-to-noise ratio for the BSHe images. Patterns of self-assembled monolayers (SAM) were created by using a PDMS stamp and gas-phase silanization. Orthogonal stripes with an identical width of 4 μm of (3-mercaptopropyl)trimethoxysilane (MS, $C_6H_{16}O_3SSi$) and triethoxy($1H,1H,2H,2H$-tridecafluoro-*n*-octyl)silane (PFS, $C_{14}H_{19}F_{13}O_3Si$) were formed on the native oxide present on Si{001} wafers [7]. The thickness of the layers corresponds to the length of the molecules, which are 7 Å and 11 Å for MS and PFS, respectively. *para*-Sexiphenyl (6P) thin films were grown on Si{001} wafers covered by a native oxide in an UHV system with a base pressure of 1×10^{-10} mbar. Prior to thin-film growth the substrate was flashed to 500 °C. 6P was deposited at room temperature from a Knudsen cell [8,9]. For the formation of cobalt nanoclusters, an atomically clean Ge{001} substrate was obtained by prolonged 800 eV Ar^+ ion sputtering followed by annealing of the sample through resistive heating at 1100 K. Several monolayers of Co were evaporated by resistively heating a tungsten wire wrapped with a pure Co (99.995%) wire. During evaporation the sample was kept at room temperature. Afterwards it was annealed at 600 K for 8 min and for a shorter period of 4 min at 700 K. Before insertion into the HIM the sample was briefly exposed to air during which time a thin oxide layer most likely formed [10].

Angle-dependent projections of the silicon crystal lattice, to obtain measures for the backscattering probability, were calculated by using a simple geometric model of the crystal slab. For some of these calculations a graphene-like carbon overlayer was added to the silicon slab. Atom radii were fixed to 0.42 Å and 0.30 Å for silicon and carbon, respectively. Lattice constants of 5.43 Å and 2.46 Å were used for silicon and carbon, respectively. To speed up the calculations the thickness of the crystal slab was restricted to 24 layers or six unit cells. This thickness equals 3.3 nm, which corresponds roughly to the escape depth of the SE in the HIM [6]. The crystal slab was rotated and tilted with respect to the [001] direction and the projected blocked area fraction (opacity) was calculated [3] for the area of one unit cell, or in other words eight neighboring channels. Due to the mismatch in unit-cell size, the positions of the carbon adatoms were different in these eight channels. To average over many possible configurations for the overlayer atoms, the adlayer was shifted across 25 different positions relative to the bulk. SRIM [11] calculations to obtain measures for the backscatter probability and the range of the helium particles were performed with SRIM-2008 and the quick Kinchin–Pease formalism [11,12]. To ensure a sound statistical result 1×10^5

He ions of the selected energy were traced in appropriately thick slabs of the bulk material.

Results
Thin organic layers

In Figure 1 HIM images of a network of two SAMs, namely MS and PFS, are presented. The images were recorded with a PE of 15 keV and an ion dose of 2.46×10^{16} cm^{-2} under normal beam incidence. Figure 1a was obtained by using the ET detector. SEs in HIM originate from near surface regions. The characteristic escape depth of SEs in carbon is 1 nm [6]. The high contrast between the different patches, and the high lateral resolution, are a result of this characteristic of the SEs in HIM. All the SEs contributing to the different contrast patches are generated under identical conditions, nearly exclusively within a thin surface layer of the relevant material (SiO$_2$, PFS, or MS). As a consequence of the identical strip width for PFS and MS strips, we do not know a priori which stripe is which. However, we assign the bright structureless areas to the uncovered SiO$_2$/Si substrate. It is understood that because of the relatively low work function of SiO$_2$, these areas are brightest. The work functions of PFS and MS are 6.6 eV and 5.3 eV [13], respectively. The value for PFS was extrapolated from a shorter fluorinated alkanethiol [14], and should be treated as an estimate. We can therefore identify the medium light-gray areas below and above the Si patches as being MS-covered. The medium dark areas to the left and the right of the Si patches are covered by the higher-work-function PFS layer. The remaining square is covered by an unknown mixture of both, MS and PFS. A clear statement on the work function or the contrast mechanism for this remaining patch is therefore difficult. Figure 1b shows the simultaneously recorded BSHe image. Interestingly, the SAMs are not only discernible but can also be distinguished. In addition, small details at the edge of the vertical SAM stripes are clearly visible. The relative average backscattered He yields with respect to SiO$_2$/Si (BSHe yield: 1) are 1.58 and 1.45 for PFS and MS, respectively. We will discuss the underlying contrast mechanisms below; however, we first highlight two more examples of ultrathin surface structures that are made visible in BSHe images.

In Figure 2 HIM images of single-layer high ($\approx$2.6 nm) 6P islands on native-oxide-covered Si{001} wafers are shown [8,9]. Figure 2a is an ET image of such an island. The FoV is 11 µm, the PE was 20 keV and an ion dose of 3.21×10^{15} cm^{-2} was used. The ramified shape of the island (dark) is clearly visible against the bright silicon substrate. Figure 2b is the simultaneously recorded BSHe image. The shape of the island (bright) can easily be distinguished against the darker background of the silicon substrate. Figure 2c shows a different island recorded with a sample tilt of 10°, but otherwise under
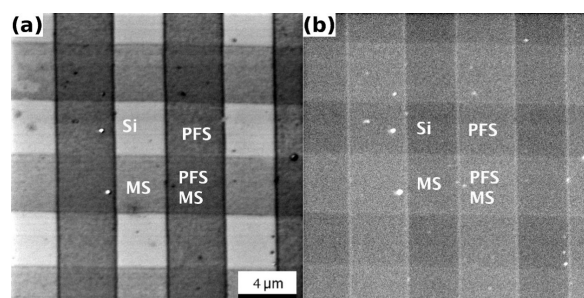
Figure 1: HIM images with a FoV of 20 µm of thin organic layers on Si{001}. Data was recorded with a PE of 15 keV, and an ion dose of 2.46×10^{16} cm^{-2}. (a) ET image of stripes of PFS (vertical) and MS (horizontal). The different areas and their termination are indicated. (b) BSHe image recorded simultaneously with (a). The different surface terminations can be distinguished.
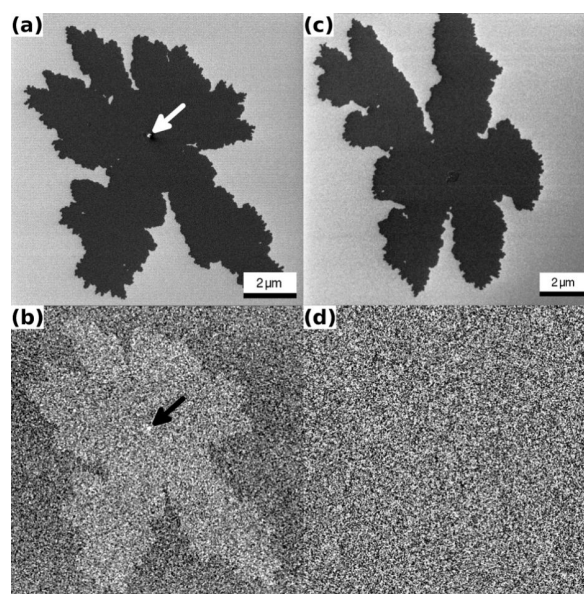
Figure 2: HIM images of single-layer 6P islands on Si{001}, recorded with PE of 20 keV and an ion dose of 3.21×10^{15} cm^{-2}. (a) ET image with a FoV of 11 µm recorded under normal incidence. The island and a small second-layer island (bright spot in the center, marked by an arrow) can be seen. (b) Corresponding BSHe image. The island and the second-layer island (marked by an arrow) can be seen. (c) ET image with a FoV of 12 µm recorded under identical conditions as in (a,b) but with an incidence angle of 10°. The island can be seen clearly. (d) In the corresponding BSHe image the island is invisible.

unchanged conditions. The corresponding BSHe image presented in Figure 2d does not, however, show a signature of the island. We note that the overall gray level in Figure 2d is found to be higher than for the bare silicon in Figure 2b and close to the one of the 6P island in Figure 2b.

Inorganic nanocrystals

As a third example of the same contrast mechanism, we present selected results of a study dealing with the growth of Co islands on Ge{001} [10]. Figure 3a shows epitaxially aligned Co islands with average sizes between 10 nm and 60 nm. The aspect ratio varies from 1 up to approximately 3 with 1.54 and 1.20 being the mean and the mode of the distribution, respectively. The height of the nanocrystals was found to vary between 4 nm and 7 nm [10]. Figure 3b is a 1 µm FoV BSHe image recorded with a PE of 10 keV and an ion dose of 1.05×10^{16} cm^{-2}. The islands and the different lateral shapes are clearly visible. In contrast, in Figure 3c, which was recorded under identical conditions but with a sample tilt of 10°, the islands are hardly discernible.

Discussion

As we have seen above, BSHe images can be used to obtain information on ultrathin surface structures on crystalline substrates. In this context, the last part of the previous sentence is important. We now discuss the role of channeling in the underlying crystalline substrate for obtaining the BSHe images presented above. In all three experiments a thin layer of a lighter element(s) was deposited on top of a heavier substrate. Different to the ET images, in which SEs are generated in regions near the surface, the backscattering of He is a bulk effect. For a layer of heavy elements on a lighter substrate one expects an increased BSHe yield for the following two reasons: (1) The heavier element has a larger cross section and will therefore add to the BSHe yield; (2) the adlayer decreases the energy of the primary beam, thereby increasing the backscatter probability and reducing the range of helium in the material. The increased scattering will lead earlier, in terms of energy and depth, to hard collisions with large scattering angles and result

in a larger deviation from the initial particle trajectory. We will discuss this in more depth in the next paragraph. For the present case in which a light adlayer (either carbon or cobalt) covers a heavier substrate (silicon or germanium), (1) does not play a significant role and (2) will be weak in general.

To underline the above statement, SRIM calculations were used to obtain a generic view of the expected processes. Artificial silicon samples with a thickness of 1 µm and a 10 nm adlayer of either heavy (Pb) or light (Li) elements, and without an adlayer were compared. 1×10^5 He$^+$ ions with a PE of 35 keV under normal incidence were used to perform the calculation. The results are summarized in Table 1. As expected, the backscattering yield for Pb/Si (1.9%) is higher by a factor of two compared to the other two combinations (0.9% for both cases). While the light adlayer does not affect the lateral range and straggle of the He, the heavy adlayer induces an 8% larger lateral range and a 10% increased lateral straggle. Here, straggle is defined in accordance with the SRIM software to be the

Table 1: Scattering process dependence on adlayer material as obtained by SRIM. For each adlayer/sample combination the number of backscattered helium atoms and the longitudinal and radial ion ranges (in Å) are given. 1×10^5 He ions with a PE of 35 keV under normal incidence were used in the calculation.

sample	BSHe	direction	range [Å]	straggle [Å]
Pb/Si	1863	long.	3095	952
		rad.	1567	782
Li/Si	881	long.	3261	918
		rad.	1443	712
Si	979	long.	3190	917
		rad.	1446	714
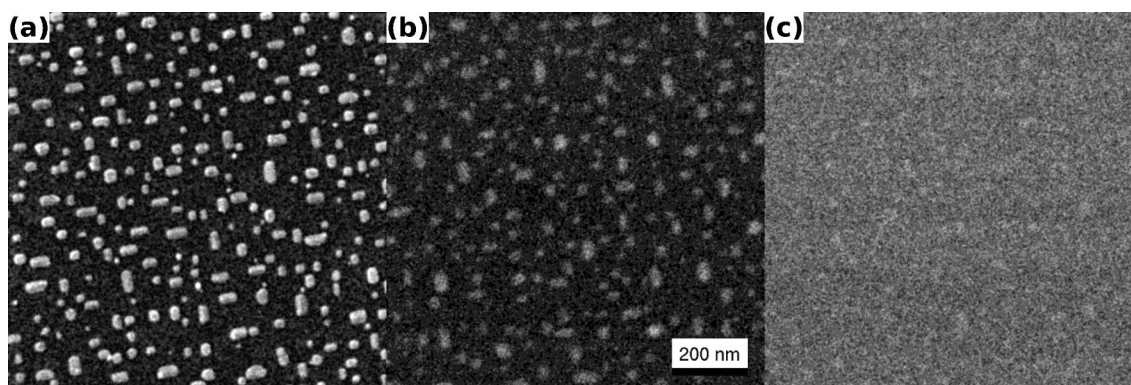
Figure 3: Co-containing nanocrystals on Ge{001} (FoV: 1 µm) (a) High-resolution ET image obtained with a PE of 34.6 keV and an ion dose of 1.05×10^{16} cm^{-2}. Aligned Co-containing nanocrystals are visible. The average extent of the crystals is between 10 nm and 60 nm laterally with a height of around 5 nm. (b) BSHe image obtained under normal incident with a PE of 10 keV and an ion dose of 1.05×10^{16} cm^{-2}. The Co-containing nanocrystals are clearly visible. (c) BSHe image recorded under identical conditions as used in (b) but with an incident angle of 10°. Reprinted from [10], copyright (2012) with permission from Elsevier.

square root of the second moment of the range distribution [11]. Although these values represent averages that are dominated by the ions stopped deep in the sample, a comparable relative change will occur closer to the surface for the helium particles that will eventually be backscattered. This will have a negative influence on the lateral resolution that can be achieved in BSHe images. SE images will not be affected since the SEs are generated in the first few nanometers of the sample where the beam is still sharply focused.

For the case of the SAMs on SiO_2 (Figure 1), SRIM calculations were performed to estimate the backscatter probability from the different layers. Bulk samples of SiO_2, MS, and PFS were created and exposed to 5×10^5 He^+ ions with an energy of 15 keV. The backscattering probabilities obtained are 1.73, 0.69, and 0.71% for SiO_2, MS, and PFS, respectively. In this model calculation SiO_2 has the highest backscattering probability and should appear brightest in BSHe images. Keeping in mind the considerations mentioned in the previous paragraph and the calculated backscatter probabilities, no additional contribution is to be expected from the BS- or PFS-covered areas. However, a detailed analysis of the image data reveals that, relative to SiO_2/Si, the backscatter probabilities are higher by a factor of 1.45 and 1.58 for MS and PFS, respectively.

As we have demonstrated in Figure 2 and Figure 3, the polar angle of the incident He^+ beam is critical for the contrast in BSHe images. In Figure 4 we show the result of calculations of the opaque area fraction for a silicon {001} crystal. The graphs show the opaque fraction of the crystal, which is proportional to the backscattering yield. For normal beam incidence (Figure 4a) 15% of the area is blocked (blue dashed line). Adding a single carbon overlayer increases the opaque fraction to 29% (dark solid line). At normal incidence, this corresponds to an increase in the blocked fraction by 66%, independent of the azimuthal angle. Tilting the incident beam with respect to the surface normal increases the overall backscattering probability, but reduces the expected contrast ratio between a clean Si crystal and one that is covered by a single adlayer. The increased yield of backscattered He is evident by comparing Figure 2b and Figure 2d. The BSHe yield has increased substantially for the uncovered surface areas. The expected contrast depends on the azimuthal angle and varies between 26% and 4% with a mean value of 8% for a 10° beam tilt. The insets in Figure 4 show the model crystal slabs with carbon adlayer that were used, illustrating the reduced transparency for the tilted cases. Despite the simplicity of this model it nicely confirms the physics involved in the decrease in contrast between areas with and without an adlayer when the sample is tilted. For thicker adlayers this effect is going to be more pronounced because the channels in the underlying crystal are more effectively blocked. In fact, the

amount of backscattered He due to the thin 6P adlayer in Figure 2b is comparable to the amount for the uncovered, but tilted, area in Figure 2d.

The results presented in Figure 1, Figure 2, and Figure 3 are based on the angle-dependent channeling probability described above. In all three cases the surface is covered by a native oxide. The thickness and nature of this oxide layer is unknown. We assume that it is of the order of 2 nm and amorphous. This will cause a partial blocking of the underlying channels in Si{001} or Ge{001}. However, the effectiveness of the dechanneling will depend on the thickness of the overlayer. A local increase in thickness of the amorphous overlayer will increase the contrast, because more He is backscattered. This can be seen in the organic overlayer, in particular for the rims of the vertical stripes of PFS in Figure 1(b). The edges of the stripes are thicker [7], and this leads to an increased chance for an ion to be deviated from the initial trajectory. Consequently, this results in
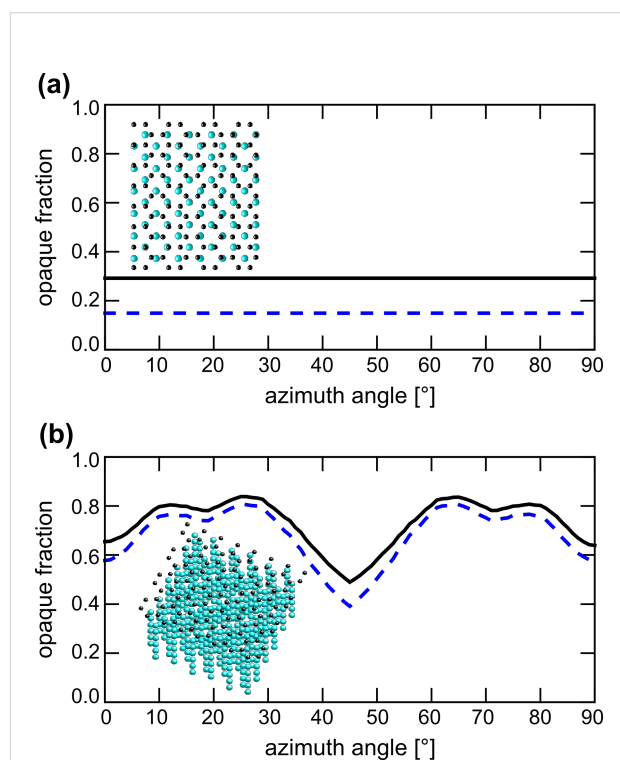
Figure 4: Simulation of dechanneling contrast for clean and carbon-covered Si. The graphs show the opaque fraction of the projected crystal lattice. Blue dashed lines are obtained for a clean Si(001) crystal, whereas the black lines are obtained with a thin carbon layer added. (a) Normal incidence. The opaque projected area fraction is 15 and 29% for the clean and carbon-covered surface, respectively. There is no azimuthal dependence for this incident angle. (b) The same calculation but for a 10° sample tilt. The average opaque projected area fractions are 68 and 73% for the clean and carbon covered surface, respectively. A clear dependence on the azimuthal angle exists.

more backscattering of He due to the enhanced dechanneling. A similar effect can be observed for the small second-layer island on top of the 6P island in Figure 2a and Figure 2b.

Conclusion

Besides the possibility to obtain crystallographic information, channeling can also be used to obtain information on ultrathin organic and inorganic layers. We demonstrated that even a thin layer of submonolayer coverage can be detected in BSHe images. The enhanced backscattering is a result of changes in the channeling probability and does not depend on the mass of the participating film or bulk atoms. As an unanticipated result, light adlayers on heavy substrates can be imaged. We emphasize that this contrast mechanism is purely based on changes in the crystallography of the sample. Apart from the detection of ultrathin adlayers, this mechanism therefore also has the potential to reveal crystal defects, such as dislocations or clusters of interstitial atoms. In fact the contrast mechanism has been successfully applied to the Co on Ge system. In this case the new contrast mechanism reveals the different structural nature of the Co-containing nanocrystals on top of the Ge{001} substrate. The fact that the crystallites can only be seen under incident beam angles that allow channeling into Ge{001} is a sign of their different structural properties. The Co in the crystallites influences the position of the atoms sufficiently to block the channels in the covered part of the Ge{001} surface. This independently supports the scanning tunneling spectroscopy results, which show that the crystals are cobaltgermanides [10]. Due to the small size of these crystallites, this information is difficult to obtain by other techniques such as diffraction methods or transmission electron microscopy.

Finally, we wish to stress the point that this is a clear hint for the importance of good vacuum conditions during HIM measurements. From our geometrical-projection-based calculation, we conclude that just a single monolayer of carbon can result in a 66% contrast loss. This not only affects the general performance of the imaging technique but will in particular affect channeling-based contrast mechanisms.

Acknowledgement

References

1. Ward, B. W.; Notte, J. A.; Economou, N. P. *J. Vac. Sci. Technol., B* **2006,** *24,* 2871–2874. doi:10.1116/1.2357967
2. Hill, R.; Faridur Rahman, F. H. M. *Nucl. Instrum. Methods Phys. Res., Sect. A* **2011,** *645,* 96–101. doi:10.1016/j.nima.2010.12.123
3. Veligura, V.; Hlawacek, G.; van Gastel, R.; Poelsema, B.; Zandvliet, H. J. W. *Beilstein J. Nanotechnol.* **2012,** *3,* 501–506. doi:10.3762/bjnano.3.57
4. Petrov, Y. V.; Vyvenko, O. F.; Bondarenko, A. S. *J. Surf. Invest.: X-Ray, Synchrotron Neutron Tech.* **2010,** *4,* 792–795. doi:10.1134/S1027451010050186
5. van Gastel, R.; Barriss, L.; Sanford, C.; Hlawacek, G.; Scipioni, L.; Merkle, A.; Voci, D.; Fenner, C.; Zandvliet, H.; Poelsema, B. *Microsc. Microanal.* **2011,** *17* (Suppl. S2), 928–929. doi:10.1017/S1431927611005514
6. Ramachandra, R.; Griffin, B.; Joy, D. *Ultramicroscopy* **2009,** *109,* 748–757. doi:10.1016/j.ultramic.2009.01.013
7. George, A.; Knez, M.; Hlawacek, G.; Hagedoorn, D.; Verputten, H. H. J.; van Gastel, R.; ten Elshof, J. E. *Langmuir* **2012,** *28,* 3045–3052. doi:10.1021/la204437r
8. Hlawacek, G.; Puschnig, P.; Frank, P.; Winkler, A.; Ambrosch-Draxl, C.; Teichert, C. *Science* **2008,** *321,* 108–111. doi:10.1126/science.1159455
9. Lorbek, S.; Hlawacek, G.; Teichert, C. *Eur. Phys. J.: Appl. Phys.* **2011,** *55,* 23902. doi:10.1051/epjap/2011100428
10. Mocking, T. F.; Hlawacek, G.; Zandvliet, H. J. W. *Surf. Sci.* **2012,** *606,* 924–927. doi:10.1016/j.susc.2012.02.007
11. Ziegler, J. F.; Biersack, J. P.; Ziegler, M. D. *SRIM, the stopping and range of ions in matter;* Lulu Press: Morrisville, NC; USA, 2008.
12. Kinchin, G. H.; Pease, R. S. *Rep. Prog. Phys.* **1955,** *18,* 1–51. doi:10.1088/0034-4885/18/1/301
13. Singh, J.; Whitten, J. E. *J. Phys. Chem. C* **2008,** *112,* 19088–19096. doi:10.1021/jp807536z
14. Wu, K.-Y.; Yu, S.-Y.; Tao, Y.-T. *Langmuir* **2009,** *25,* 6232–6238. doi:10.1021/la900046b

Nano-structuring, surface and bulk modification with a focused helium ion beam

Daniel Fox[1], Yanhui Chen[1], Colm C. Faulkner[2] and Hongzhou Zhang[*1]

Full Research Paper

Open Access

Address:
[1]School of Physics and CRANN, Trinity College Dublin, Dublin 2, Republic of Ireland and [2]CRANN Advanced Microscopy Laboratory, Trinity College Dublin, Dublin 2, Republic of Ireland

Email:
Hongzhou Zhang[*] - hongzhou.zhang@tcd.ie

* Corresponding author

Abstract

We investigate the ability of a focused helium ion beam to selectively modify and mill materials. The sub nanometer probe size of the helium ion microscope used provides lateral control not previously available for helium ion irradiation experiments. At high incidence angles the helium ions were found to remove surface material from a silicon lamella leaving the subsurface structure intact for further analysis. Surface roughness and contaminants were both reduced by the irradiation process. Fabrication is also realized with a high level of patterning acuity. Implantation of helium beneath the surface of the sample is visualized in cross section allowing direct observation of the extended effects of high dose irradiation. The effect of the irradiation on the crystal structure of the material is presented. Applications of the sample modification process are presented and further prospects discussed.

Introduction

Ion beams are widely used to modify the physical and chemical properties of the surface of materials with a high degree of control. Ion beam irradiation can be used to modify and control a material's optical [1], electrical [2], magnetic [3] and mechanical [4] properties. The gallium focused ion beam (FIB) microscope has been commercially available for twenty years. FIB microscopes have proven themselves as versatile tools with applications in a range of fields including biology [5], geology [6], materials science [7,8] and the semiconductor industry [9]. While the FIB has been adopted for many uses it is not without

its limitations. The FIB uses gallium ions, a metallic element which is often considered a contaminant. The large momentum of the gallium ions in the FIB can have a very destructive effect on materials, greatly altering their crystal structure. The resolution of the FIB is limited by the energy spread of the gallium ions generated from the liquid metal ion source (LMIS). The sputter yield is also too large for acute patterning control over very short lateral distances. The recently developed Carl Zeiss Orion Plus helium ion microscope (HIM) is a new type of focused ion beam microscope. The HIM uses helium ions

instead of gallium ions. Helium ions have a lower mass and therefore are less destructive than gallium ions. Helium ions are effectively non-contaminating. The source is a gas field ion source which does not suffer the energy spread and subsequent chromatic aberration which limits the resolution of the FIB [10]. Our HIM is capable of sub-nm resolution imaging with its <0.75 nm probe size. This makes it ideally suited to both high resolution imaging and also modification of materials with a higher level of control and precision than can be offered by other ion beam tools. The HIM has the unique ability to directly mill arbitrary patterns with sub 10 nm feature sizes. To date most of this work has been done on graphene [11-13]. The HIM can also directly write sub 10 nm features via precursor gas decomposition [14,15]. The depth of implantation of helium ions in a material can be varied by adjusting the beam energy [16]. Subsurface voids can be produced in such a fashion. Further exposure and subsequent growth of the void can be used to separate a thin film of material from a substrate [17], or to modify the optical properties of the surface [18]. Some other applications to date include imaging of chemical variations at high resolution [19], quantitative dopant contrast mapping [20] and imaging of uncoated biological materials [21]. In this work we further investigate the ability of the HIM to modify a material's surface and structure using advanced transmission electron microscopy (TEM) techniques such as energy filtered TEM (EFTEM) and electron energy loss spectroscopy (EELS). We also present the limitations of this surface modification technique.

Results and Discussion

Sample 1 is a silicon lamella shown after FIB lift-out and thinning in the SEM image in Figure 1a. Figure 1b shows the TEM high angle annular dark field (HAADF) image of the lamella after HIM modification. The three dark vertical grooves indicate the areas modified in the HIM. In Figure 1b one effect of the helium ion modification process is clear; material is selectively removed from the sample sidewalls. The thickness map of the modified area is shown in Figure 1c. From this map we can calculate quantitative thickness values based on the mean free path of a 300 keV electron in silicon (180 nm) [22]. The arrows on the image indicate the regions from which the integrated intensity profiles were plotted in Figure 1d. The dashed red line is from a region prepared by gallium ions only. The solid blue line is from the helium ion modified area. The profiles both show an increase in thickness with increasing distance from the top of the lamella, indicating that the sample has a wedge shape. This increase is more gradual and noticeably smoother after helium ion modification. The modified area was observed to be consistently thinner than the unmodified region when compared at the same distance from the top of the lamella. The suitable area for TEM extends further from the top

of the sample in the modified region, this results in a larger area useable for TEM in samples modified by the HIM. Figure 1e shows the EFTEM gallium map of the region. The areas of higher intensity in this map have a greater concentration of gallium contamination. The solid red arrow indicates the region from which the integrated intensity profile in Figure 1f was plotted. The solid white line is below the FIB prepared areas, while the dashed green line is beneath the areas further modified by helium ions. In Figure 1f the intensity profile from Figure 1e is plotted with the corresponding ion beam used to modify the area indicated below. This graph clearly shows a significant reduction in gallium contamination implanted by the FIB lift-out process. Typically around a 32% reduction in gallium concentration is achieved by HIM modification.
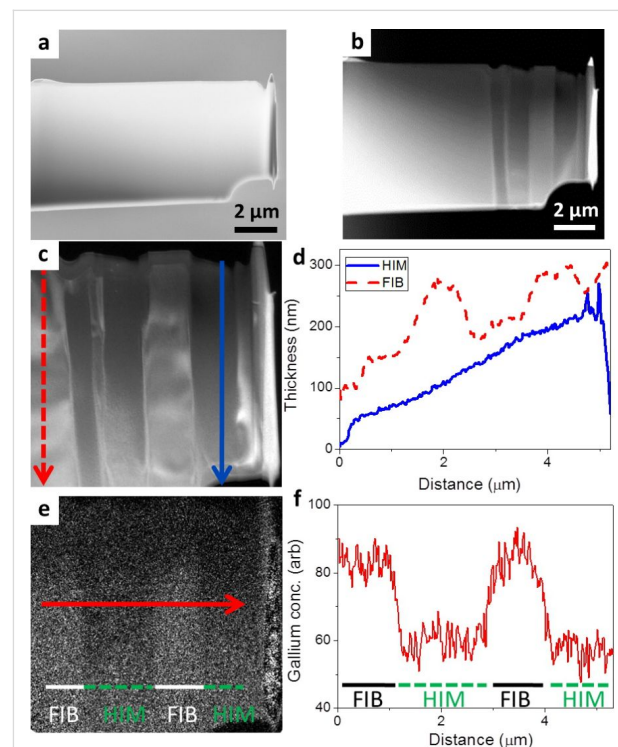
Figure 1: (a) SEM image of the silicon lamella (sample 1) after FIB preparation. (b) HAADF TEM image of the sample after three separate areas (observed as three vertical dark streaks) were modified by helium ions. (c) Thickness map of the modified area. The dashed red arrow is on an unmodified area of silicon. The solid blue arrow is on a HIM modified area. (d) The intensity profiles of the arrows from (c) are plotted, with the thickness calibrated. (e) EFTEM map indicating the distribution and concentration of gallium. The solid red line indicates the area from which (f) is plotted. The areas above the solid lines marked FIB have not been modified with helium ions, the areas above the dashed line marked HIM have been modified with helium ions. The integrated intensity profile from the arrow in (e) is plotted with the ion beam used to modify the region indicated below.

High resolution TEM (HRTEM) was performed on the HIM modified grooves and the unmodified sidewalls to afford further insight into the material modification. Figure 2a is the HRTEM

image of the unmodified region of silicon; Figure 2b is the corresponding selected area diffraction (SAED) pattern from the region. Figure 2c is the HRTEM image of the HIM modified region of the sample, Figure 2d is the corresponding SAED pattern. Figure 2a displays a noisy HRTEM image when compared with that of Figure 2c from the HIM modified region of the sample. The inset FFT of the images also show the increase in high frequency information attained from the modified region. The uniform background contrast of the modified area indicates that it has a more uniform thickness. These images indicate that the amorphous layer of material on the sample, which contributes to background noise only, is reduced by HIM modification. Similarly, the SAED pattern in Figure 2b shows less information than that in Figure 2d. The extended high frequency information in the diffraction pattern recorded from the HIM modified region in Figure 2d indicates that this area of the sample is thinner, while still retaining its high quality crystalline structure. The diffraction patterns show that the sample was measured along the [110] direction.

Figure 2: HRTEM (a) and diffraction (b) information from gallium finished region. HRTEM (c) and diffraction information (d) from helium modified region.
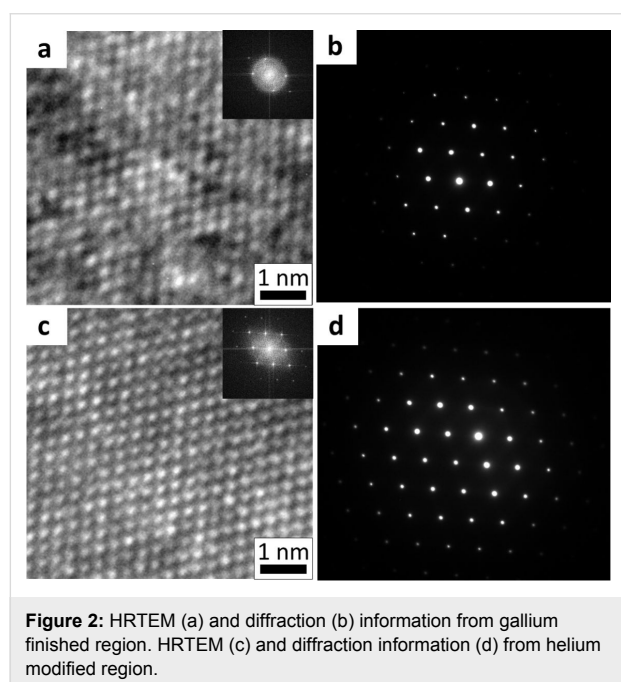
This analysis of sample 1 clearly shows us that HIM modification of a FIB prepared TEM lamella can be used to further reduce sample thickness while removing contamination and also retaining the crystallinity of the material. In order to investigate this polishing effect further we used the HIM to modify a TiO_2 TEM lamella prepared by FIB lift-out. We called this sample 2. Figure 3a is a HAADF image of the sample after FIB lift-out, gallium contamination is observed as the small white spots on the image, the background noise is also large. The same sample was analyzed again after modification with

35 keV helium ions. The HAADF image of the modified region in Figure 3b shows a striking improvement as the surface agglomerations were removed and the contrast in the image was greatly improved.

Figure 3: (a) HAADF image of the TiO_2 sample (sample 2) after FIB lift-out. (b) HAADF image of the sample after HIM modification.
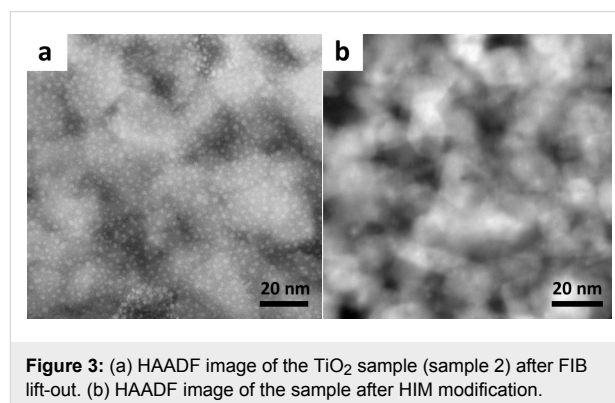
In samples 1 and 2 we have used lamellae finished only with 30 keV gallium ions in the FIB. A lower energy gallium ion beam can be used to produce lamellas with significantly less FIB induced damage [23]. FIBs with low energy capability have become more widely available over the past few years. We prepared the silicon lamella in sample 3 with a 5 keV gallium ion beam final polish in order to reduce FIB induced artifacts which would obscure our analysis of the patterning and subsurface modification effects of the HIM modification. Sample 3 is shown after FIB lift-out in the SEM image in Figure 4a. Figure 4b is an illustration of the beam–sample geometry used to modify the sample in the HIM. The sample sidewall was inclined 15° to the beam. This geometry was used in order to mill a wedge shape within the lamella in order to observe the minimum thickness dimensions which can be fabricated by HIM. This geometry also allows us to observe the extended effects of the modification process. Figure 4c is a bright field TEM image of the area of the sample after controlled sidewall modification by helium ion irradiation. Figure 4d is a HAADF image of the same area. A rectangular hole is observed at the center of the image, this was fabricated due to the high dose used. Below this hole is a circular region with rapid variations in contrast. This circular area has been heavily modified by the HIM. Figure 5 is a thickness map of the area. Below this map is the integrated intensity profile of the area indicated by the solid red arrow on the thickness map. This profile shows the sloping thickness of the wedge fabricated by helium ion irradiation, followed by the hole where the beam penetrated the lamella. Finally, the circular feature is observed to have rapidly varying thickness. The hole has a non-zero thickness due to the limitations of the thickness mapping process, such as its tendency to overestimate the thickness of very thin areas [24]. It is well known that helium ion irradiation, with an appropriate beam

energy, can produce helium bubbles beneath the surface of a sample [25]. In this case the center of the circular feature is approximately at the implantation depth of 35 keV helium ions in silicon, about 318 nm (SRIM) [26]. This is made clear by the SRIM simulation image inset in Figure 4d showing the distribution of 35 keV helium ions in silicon; this simulation has the same scale as the image and correlates well with our experimental data. What we observe in this region is the implantation of helium ions, where the incident helium ions have been scattered by the silicon and have come to rest within the sample. These implanted ions then lead to the formation of bubbles beneath the surface which stretch and distort the silicon. The contrast observed corresponds to regions where helium bubbles have formed and silicon has been displaced.
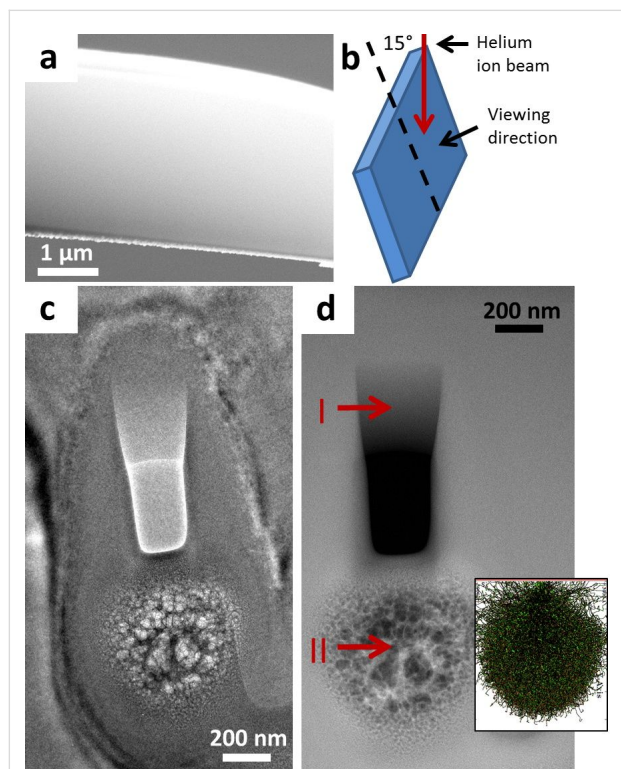
Figure 4: (a) SEM image of the silicon lamella (sample 3) after FIB lift-out and a 5 keV gallium ion polish. (b) Illustration of the geometry of the helium ion beam irradiation. The red arrow represents the helium ions which are incident on the face of the sample at an angle of 15°. (c) Bright field TEM image of the area modified by helium ions. (d) HAADF image of the modified area. "I" shows the location of the wedge shape and "II" shows the circular area with bubbles. Inset is a SRIM simulation of 35 keV helium ions in silicon with the same scale as the image.

At this point we have described the morphological changes induced by a high dose of HIM irradiation on sample 3. We then investigated the effect of the HIM modification on the structure of the silicon. Figure 6a is a graph of the EELS spectra recorded from three different locations on the sample. The black
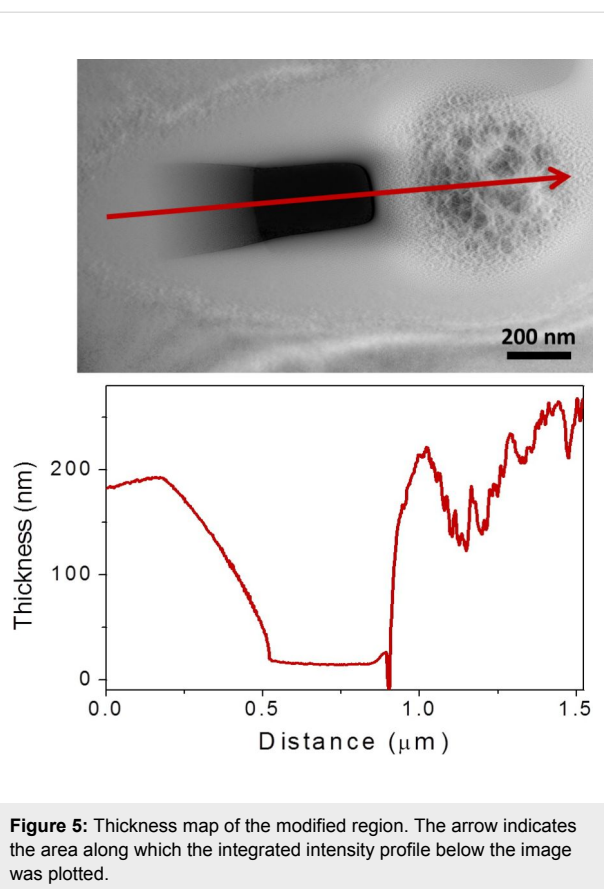
Figure 5: Thickness map of the modified region. The arrow indicates the area along which the integrated intensity profile below the image was plotted.

solid line at the top was recorded at a region which was not modified by helium ion irradiation. The red dashed line in the middle was recorded from the wedge shape region fabricated by helium ion irradiation (marked "I" in Figure 4d). And finally the blue dotted line at the bottom was recorded at the circular feature (marked "II" in Figure 4d). When we analyzed our three EELS spectra in Figure 6a (spectra are offset for clarity) we found that the intensity of the first peak in the spectra at ≈99 eV was observed to degrade from the top spectrum to the bottom. We compared our data to the spectra for crystalline and amorphous silicon from an online database [27]. The intensity of the peak at ≈99 eV is used as an indication of the crystallinity of the silicon. A higher intensity indicates more crystallinity in that area, a lower intensity corresponds to an area which is more amorphous [28]. The top spectrum in our data corresponds to an area of high crystallinity, as indicated by the presence of a peak in this region of the spectrum. This result was to be expected as the spectrum was recorded from an unmodified region of the sample. However, the spectrum from the wedge shape area fabricated by the HIM (marked "I" in Figure 4d) shows a high degree of amorphization as the intensity of the first peak at ≈99 eV is greatly reduced. The spectrum from the area of the sample containing the bubbles (marked "II" in Figure 4d) shows an area which is even more amorphous again.

Figure 6: (a) EELS spectra of an unmodified area of silicon (solid black line), the HIM fabricated wedge marked I in Figure 4(d) (dashed red line) and the circular featured marked II in Figure 4(d) (dotted blue line). The spectra are offset for clarity. (b) HRTEM image of the wedge shaped area (I in Figure 4(d)) and FFT inset. (c) HRTEM of the circular feature (II in Figure 4(d)).
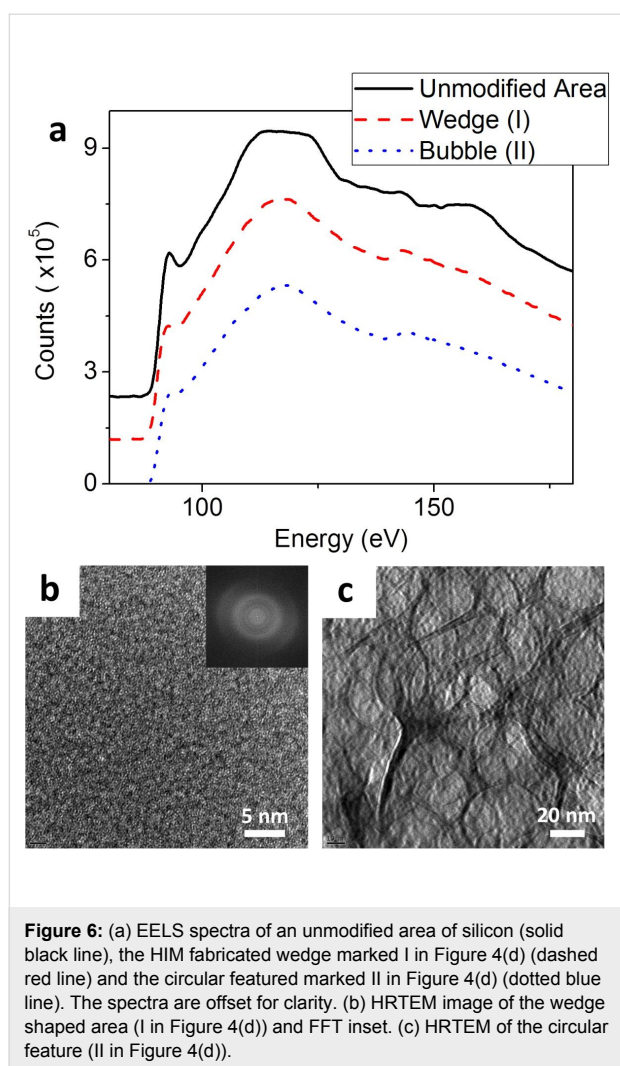
Figure 6b is a HRTEM image from the wedge area (marked "I" in Figure 4d) with an inset FFT of the image. This image shows only amorphous material is present at this location. Figure 6c is a HRTEM image of the area with the circular feature (marked "II" in Figure 4d). This image shows the presence of circles created by the growth of helium bubbles. No crystal structure was observed in this region either. We have observed that a high dose of HIM irradiation on sample 3 was used to fabricate a smooth wedge of material on a TEM lamella with minimum thickness dimensions of just a few tens of nanometers. This thickness may even be less than our thickness map indicates as significant errors may be present in the mapping process for very thin samples due to surface excitations, which can lead to overestimation of the thickness in this region [24]. The lateral dimensions of the pattern can also be tailored with a high degree of precision; the HIM can fabricate 4 nm nanopores quickly and reliably [29]. The EELS spectra and HRTEM from the HIM modified areas show that the wedge fabrication process caused significant amorphization of the sample in that

region. The beam particles were also observed to implant in the sample below the wedge causing bubbles to form in the material, again resulting in significant amorphization of the silicon, as observed by EELS and HRTEM.

Conclusion

We have demonstrated that a focused helium ion beam can modify a surface's physical properties, such as crystallinity, roughness and thickness, in a controlled manner. 35 keV helium ions were used to produce a surface which was smoother than could be achieved by 30 keV FIB. Low energy FIB polishing can also improve the lamella quality; however the HIM polishing step has many benefits over the relatively broad beam of low energy FIB due to the its small probe size and the ion species used. The helium ion beam is non-contaminating and can even be used to selectively remove surface contaminants, such as the gallium contamination removal demonstrated here. Thickness dimensions can also be reduced to just a few tens of nanometers. This is critical for techniques in aberration corrected TEM such as atomically resolved EELS [30]. The higher imaging resolution of the HIM than the conventional SEM beam used in dual-beam FIB systems means that smaller features of interest can be located during sample preparation, prior to TEM. Clearly one application of this technique is as a highly useful step in the production of high quality TEM lamellae of silicon based devices, as well as a broader range of materials as demonstrated by our dramatic TiO_2 sample quality improvement. Beyond TEM sample modification, it has been shown that a finely focused beam of helium ions can sputter material from a sample with a high level of control, allowing sub 10 nm features to be patterned. This high dose irradiation can also be used to modify the structure of a material, as demonstrated by our EELS and HRTEM results. The new models of the HIM feature variable acceleration voltage operation, our microscope is in the process of receiving this upgrade and further work will need to be done to assess the effect of reduced beam energies on sample modification. Helium ion irradiation is a widely studied field in nuclear physics. Helium ion irradiation has been used to modify mechanical [31], optical [25] and magnetic [32] properties of surfaces. The highly focused probe of the helium ion microscope provides a greater level of spatial control than previously available for such experiments.

Experimental

An intrinsic silicon substrate was used as a base material for our experiments. The silicon was mounted on a lift-out sample holder and inserted into a Carl Zeiss Auriga CrossBeam FIB-SEM. A 12 µm long, 0.6 µm wide and 6 µm deep section of silicon was removed from the sample and transferred to an Omniprobe TEM lift-out grid by the in situ lift-out technique

[33]. 30keV gallium ions were used to thin the silicon lamella to approximately 200 nm. The final thinning, to ≈100 nm, was done with a 20 pA beam of 30 keV gallium ions until the sample became almost transparent to a 5 keV electron beam, this is an indication that the sample is of sufficient thinness for TEM analysis. This is a common technique for TEM sample preparation. This process was then repeated to produce a second sample. Sample 2 is composed of TiO_2 and was subjected to the same process as sample 1. Sample 3 is a silicon sample; it was treated with an extra final step. The sample face was tilted 2° into the beam and scanned with reduced energy gallium beam of 5 keV for one minute on each side, the beam current was 20 pA. A short dwell time and a large number of scan repeats were used for this step. This step is known to produce high quality TEM lamellae with a FIB induced amorphization and implant layer as thin as ≈2 nm, roughly ten times less than the damage layer produced by 30 keV gallium ions [23]. Sample 1 was then inserted into our HIM. The HIM beam energy was fixed at approximately 35 keV for all experiments. The lamella was loaded with the normal of the sidewall surface perpendicular to the ion beam, the sample was then tilted 1° into the beam. This geometry has been shown to produce surfaces with minimal damage and implantation layer thickness and reduced surface roughness in the FIB. A focused beam of helium ions was then scanned over a 500 nm wide region of the lamella sidewall. This step was conducted a number of times in adjacent regions in order to optimize the dose. The area used in our analysis was exposed to a dose of 3.4×10^{16} ions/cm^2. The beam current used was 1.2 pA. The beam was rastered in a single scan over the area with a pixel spacing of 1 nm and a dwell time at each point of 1.3×10^{-3} s. The sample was rotated through 180° and the process was repeated on the opposite sidewall. The scanning time per sidewall was 68 s. This section of the sample was observed to have a reduced thickness after modification with helium ions. To investigate controlled modification for different materials sample 2 was treated with the same process. Sample 3 was then loaded into the HIM in the same upright manner. This sample was tilted 15° to the beam and a 300×200 nm area was exposed to a dose of 6.2×10^{18} ions/cm^2. The beam current used was 3.4 pA. The beam was rastered in a single scan over the area with a pixel spacing of 0.7 nm and a dwell time at each point of 5×10^{-3} s. The total scanning time was 612 s. This process produced a hole straight through the lamella. The purpose of this exposure geometry was to produce a wedge shape of silicon within the lamella so that we could observe the minimum thickness dimensions which can be fabricated by HIM. It also allows us to analyze the subsurface modification effects due to helium ion implantation. All helium ion patterning was performed with the integrated pattern generator on the tool. For detailed analysis of the effects of our HIM modification these samples were analyzed in an FEI Titan 80-300 (S)TEM operating at 300 kV. High angle annular dark field (HAADF) images were recorded. HAADF images contain contrast due to sample thickness and composition. Thickness maps of samples 1 and 3 were recorded, these maps use energy filtering of electrons to provide quantitative thickness information. Energy filtered TEM (EFTEM) mapping of the gallium concentration and distribution in sample 1 was recorded. EELS spectra were recorded from sample 3. High resolution TEM (HRTEM) images and selected area electron diffraction (SAED) patterns were also recorded.

Supporting Information

A full size HRTEM image of an unmodified region of sample 1 is available in Figure S1. A JEMS[34] software simulation of the HRTEM images is available in Figure S2. The simulated images illustrate the effect of crystal thickness on image contrast.

Supporting Information File 1
High resolution TEM imaging and simulation. [http://www.beilstein-journals.org/bjnano/content/supplementary/2190-4286-3-67-S1.pdf]

References

1. Na, H.-J.; Lee, J.-W.; Lee, W.-K.; Lim, J.-H.; Park, H.-G.; Kim, B.-Y.; Hwang, J.-Y.; Han, J.-M.; Seo, D.-S. *Opt. Lett.* **2010,** *35,* 1151–1153. doi:10.1364/OL.35.001151
2. Colli, A.; Fasoli, A.; Ronning, C.; Pisana, S.; Piscanec, S.; Ferrari, A. C. *Nano Lett.* **2008,** *8,* 2188–2193. doi:10.1021/nl080610d
3. Panigrahy, B.; Aslam, M.; Bahadur, D. *Appl. Phys. Lett.* **2011,** *98,* 183109. doi:10.1063/1.3574772
4. Wong, K. K. H.; Hutter, J. L.; Zinke-Allmang, M.; Wan, W. *Eur. Polym. J.* **2009,** *45,* 1349–1358. doi:10.1016/j.eurpolymj.2009.02.002
5. Raffa, V.; Vittorio, O.; Pensabene, V.; Menciassi, A.; Dario, P. *IEEE Trans. NanoBiosci.* **2008,** *7,* 1–10. doi:10.1109/TNB.2008.2000143
6. Wirth, R. *Chem. Geol.* **2009,** *261,* 217–229. doi:10.1016/j.chemgeo.2008.05.019

7. Kiener, D.; Motz, C.; Rester, M.; Jenko, M.; Dehm, G. *Mater. Sci. Eng., A* **2007,** *459,* 262–272. doi:10.1016/j.msea.2007.01.046

8. Genet, C.; Ebbesen, T. W. *Nature* **2007,** *445,* 39–46. doi:10.1038/nature05350

9. Yuan, C.; Xiaowen, Z. Focused ion beam technology and application in failure analysis. In *Proceedings of 11th International Conference on Electronic Packaging Technology & High Density Packaging (ICEPT-HDP 2010),* Xi'an, China, Aug 16–19, 2010; IEEE: New York, 2010; pp 957–960.

10. Ward, B. W.; Notte, J. A.; Economou, N. P. *J. Vac. Sci. Technol., B* **2006,** *24,* 2871–2874. doi:10.1116/1.2357967

11. Lemme, M. C.; Bell, D. C.; Williams, J. R.; Stern, L. A.; Baugher, B. W. H.; Jarillo-Herrero, P.; Marcus, C. M. *ACS Nano* **2009,** *3,* 2674–2676. doi:10.1021/nn900744z

12. Bell, D. C.; Lemme, M. C.; Stern, L. A.; Williams, J. R.; Marcus, C. M. *Nanotechnology* **2009,** *20,* 455301. doi:10.1088/0957-4484/20/45/455301

13. Annamalai, M.; Mathew, S.; Viswanathan, V.; Fang, C.; Pickard, D. S.; Palaniapan, M. Design, fabrication and Helium Ion Microscope patterning of suspended nanomechanical graphene structures for NEMS applications. In *16th International Conference on Solid-State Sensors, Actuators and Microsystems Conference (TRANSDUCERS 2011),* Beijing, China, June 5–9, 2011; IEEE: New York, 2011; pp 2578–2581. doi:10.1109/TRANSDUCERS.2011.5969824

14. Chen, P.; van Veldhoven, E.; Sanford, C. A.; Salemink, H. W. M.; Maas, D. J.; Smith, D. A.; Rack, P. D.; Alkemade, P. F. A. *Nanotechnology* **2010,** *21,* 455302. doi:10.1088/0957-4484/21/45/455302

15. van Veldhoven, E.; Sidorkin, V.; Chen, P.; Alkemade, P.; van der Drift, E.; Salemink, H.; Zandbergen, H. W.; Maas, D. *Microsc. Microanal.* **2010,** *16* (Suppl. S2), 202–203. doi:10.1017/S1431927610063270

16. Alkemade, P. F. A.; van Veldhoven, E. Deposition, Milling, and Etching with a Focused Helium Ion Beam. In *Nanofabrication: Techniques and Principles;* Stepanova, M.; Dew, S., Eds.; Springer: Vienna, 2011; pp 275–300.

17. Livengood, R.; Tan, S.; Greenzweig, Y.; Notte, J.; McVey, S. *J. Vac. Sci. Technol., B* **2009,** *27,* 3244–3249. doi:10.1116/1.3237101

18. Ebihara, A.; Tokitani, M.; Tokunaga, K.; Fujiwara, T.; Sagara, A.; Yoshida, N. *J. Nucl. Mater.* **2007,** *363–365,* 1195–1200. doi:10.1016/j.jnucmat.2007.01.153

19. Pearson, A. J.; Boden, S. A.; Bagnall, D. M.; Lidzey, D. G.; Rodenburg, C. *Nano Lett.* **2011,** *11,* 4275–4281. doi:10.1021/nl202269n

20. Jepson, M. A. E.; Inkson, B. J.; Liu, X.; Scipioni, L.; Rodenburg, C. *EPL* **2009,** *86,* 26005. doi:10.1209/0295-5075/86/26005

21. Bazou, D.; Behan, G.; Reid, C.; Boland, J. J.; Zhang, H. Z. *J. Microsc. (Oxford, U. K.)* **2011,** *242,* 290–294. doi:10.1111/j.1365-2818.2010.03467.x

22. Lee, C. W.; Ikematsu, Y.; Shindo, D. *J. Electron Microsc.* **2002,** *51,* 143–148. doi:10.1093/jmicro/51.3.143

23. Giannuzzi, L. A.; Geurts, R.; Ringnalda, J. *Microsc. Microanal.* **2005,** *11* (Suppl. S2), 828–829. doi:10.1017/S1431927605507797

24. Egerton, R. F. *Electron Energy-Loss Spectroscopy in the Electron Microscope;* Plenum Publishing Corporation: New York, 1996.

25. Siegele, R.; Weatherly, G. C.; Haugen, H. K.; Lockwood, D. J.; Howe, L. M. *Appl. Phys. Lett.* **1995,** *66,* 1319–1321. doi:10.1063/1.113228

26. Ziegler, J. F.; Biersack, J. P.; Ziegler, M. D. *Stopping and range of ions in matter;* Lulu Press: Morrisville, NC, USA, 2008.

27. Crystalline & Amorphous Silicon (Si) Spectrum. http://people.ccmr.cornell.edu/~davidm/WEELS/View/Si_c-Si_a-Si.html (accessed Jan 24, 2012).

28. Yan, Y.; Page, M.; Wang, T. H.; Al-Jassim, M. M.; Branz, H. M.; Wang, Q. *Appl. Phys. Lett.* **2006,** *88,* 121925. doi:10.1063/1.2189670

29. Yang, J.; Ferranti, D. C.; Stern, L. A.; Sanford, C. A.; Huang, J.; Ren, Z.; Qin, L.-C.; Hall, A. R. *Nanotechnology* **2011,** *22,* 285310. doi:10.1088/0957-4484/22/28/285310

30. Schaffer, M.; Schaffer, B.; Ramasse, Q.; Falke, M.; Abou-Ras, D.; Schmidt, S.; Caballero, R.; Marquardt, K. *Microsc. Microanal.* **2011,** *17* (Suppl. S2), 630–631. doi:10.1017/S1431927611004028

31. Li, N.; Fu, E. G.; Wang, H.; Carter, J. J.; Shao, L.; Maloy, S. A.; Misra, A.; Zhang, X. *J. Nucl. Mater.* **2009,** *389,* 233–238. doi:10.1016/j.jnucmat.2009.02.007

32. Sundararajan, J. A.; Zhang, D. T.; Qiang, Y.; Jiang, W.; McCloy, J. S. *J. Appl. Phys.* **2011,** *109,* 07E324. doi:10.1063/1.3560119

33. Langford, R. M.; Clinton, C. *Micron* **2004,** *35,* 607–611. doi:10.1016/j.micron.2004.03.002

34. jems opening page sept 21 2004. http://cimewww.epfl.ch/people/stadelmann/jemsWebSite/jems.html (accessed March 5, 2012).

Digging gold: keV He$^+$ ion interaction with Au

Vasilisa Veligura, Gregor Hlawacek, Robin P. Berkelaar, Raoul van Gastel[*],
Harold J. W. Zandvliet and Bene Poelsema

Full Research Paper

Address:
Physics of Interfaces and Nanomaterials, MESA+ Institute for
Nanotechnology, University of Twente, P.O. Box 217, 7500 AE
Enschede, The Netherlands

Email:
Raoul van Gastel[*] - r.vangastel@utwente.nl

* Corresponding author

Abstract

Helium ion microscopy (HIM) was used to investigate the interaction of a focused He$^+$ ion beam with energies of several tens of kiloelectronvolts with metals. HIM is usually applied for the visualization of materials with extreme surface sensitivity and resolution. However, the use of high ion fluences can lead to significant sample modifications. We have characterized the changes caused by a focused He$^+$ ion beam at normal incidence to the Au{111} surface as a function of ion fluence and energy. Under the influence of the beam a periodic surface nanopattern develops. The periodicity of the pattern shows a power-law dependence on the ion fluence. Simultaneously, helium implantation occurs. Depending on the fluence and primary energy, porous nanostructures or large blisters form on the sample surface. The growth of the helium bubbles responsible for this effect is discussed.

Introduction

The helium ion microscope allows the projection of a He$^+$ beam of several tens of kiloelectronvolts with a diameter of 0.4 nm [1] onto a sample. This makes HIM an attractive tool for surface patterning and nanofabrication [2-6]. In addition to ultrahigh-resolution imaging, HIM can be utilized for the compositional analysis and crystallographic characterization of samples [7,8]. Since it is a relatively new technique, many questions concerning the interaction of the focused He$^+$ beam with matter remain open. As helium ions are light particles, sputtering processes are much less effective with HIM as compared to other focused ion beam (FIB) techniques that typically use gallium ions. Never-

theless, helium ion beam imaging can lead to considerable sample and, in particular surface, modifications. The implantation of He, and the associated possible structural and chemical changes, can create substantial problems in experiments where prolonged imaging or high ion doses are required.

The effect of the He$^+$ ions on the target depends as much on the ion beam characteristics as on the properties of the imaged material itself. Existing publications on damage by a focused He$^+$ beam mostly concentrate on the interaction of ions with semiconductor materials such as silicon [9-12]. In this paper we

investigate the interaction of a He^{+} beam with metals. Previously, the effect of a low-energy He^{+} ion beam on an atomically flat gold surface was observed by scanning tunneling microscopy (STM) [13,14]. Mounds with spacing of a few nanometers were formed. In the current work we have studied the He^{+}-ion-induced modifications of crystalline gold samples due to sputtering, helium implantation and defect formation, as a function of ion fluence and energy.

Experimental

The experiments were performed with an ultrahigh vacuum (UHV) Orion® Plus Helium Ion Microscope from Carl Zeiss NTS [15] at room temperature. As a result of the interaction of the He^{+} beam with the target, secondary electrons (SE), backscattered He (BSHe), and sometimes photons are created. Image acquisition is done by collecting SEs with an Everhardt–Thornley (ET) detector. Due to the nature of the interaction of low-energy ions with matter, the lateral size of the interaction volume in the immediate vicinity of the surface remains extremely small [16,17]. This makes the microscope highly suited for obtaining high-resolution images of the surface topography. An image can further be recorded by simultaneous collection of the backscattered He with a microchannel plate [18]. The microscope is also equipped with a silicon drift detector for the measurement of the backscattered ion energy and a Gatan MonoCL4 Elite detector for the detection of ionoluminescence.

The images were recorded using the ET detector. During the measurements the ion current was kept at 0.7 pA. Brightness and contrast settings were kept constant, and the beam was oriented perpendicular to the surface. Three primary ion energies were used in the experiments: 15, 25 and 35 keV. The images were recorded with 0.68 nm pixel spacing, 2 µs dwell time and 32-line averaging, giving an ion dose per image of 6×10^{16} cm^{-2}. The chamber base pressure during imaging was in the low 10^{-9} mbar range.

The samples were polycrystalline gold specimens, which are commercially available 200 nm thick Au{111} films on a glass substrate with a Cr interlayer. The textured samples were prepared by hydrogen-flame annealing for 5 min. As a result of the annealing process, grains with an average size of a few micrometers were formed. X-ray diffraction measurements confirmed the primarily {111} textured surface orientation of the grains with a 3.5° wide angular distribution. The grains have random azimuthal orientations. In order to remove carbon contamination, all samples were exposed to a 10 W air plasma for 15 min immediately before loading the samples into the main chamber. After ion implantation the topography of the samples was measured with an Agilent 5100 atomic force microscope

(AFM) in intermittent mode. The cantilever was a Mikromasch NSC silicon probe, with a guaranteed tip radius of less than 10 nm, and a typical resonance frequency of 150 kHz. The scan size was 2×2 µm^2.

Results and Discussion
Au{111} surface modification

We have recorded sequences of images of submicron size to study the evolution of the Au{111} surface under the impact of a focused He^{+} beam as a function of fluence. Ion energies of 15, 25 and 35 keV were used to gauge the influence of the beam energy. The same sample area was exposed to the beam several times with a constant ion dose per scan. The final state of the surface after a fluence of 8.4×10^{17} cm^{-2} is shown in Figure 1a and Figure 1c: at 15 keV primary energy a porous structure is formed on the surface (Figure 1a), while in the case of a 35 keV beam a subsurface helium blister is formed (Figure 1c).

We emphasize that due to the low background pressure, the present setup does not suffer from the problem of carbon deposition in the imaged area. This is a common problem in conventional non-UHV HIM and scanning electron microscopes (SEM) [15,17,19]. The absence of the carbon layer that is normally present, allows us to obtain detailed information on the surface structure and how it evolves during repeated imaging of the same area. Figure 2 shows several images of the gold surface after exposure to identical ion fluences, but with different primary energies.

Under the influence of the 15 keV beam a regular nanopattern develops. The topographic contrast increases and the surface pattern becomes more pronounced with each subsequent scan of the same area, which indicates an increase of the corrugation of the pattern. Although the feature spacing increases with increasing ion fluence, the shape of the features remains almost unchanged and the features do not coalesce. After a fluence of 3×10^{17} cm^{-2} a uniform distribution of holes starts to appear on the surface (see Figure 2a). With a further increase of the fluence the porous structure gets more pronounced (Figure 2b and Figure 2c).

In the case of 25 keV primary ion energy the surface modification initially looks similar to the one at 15 keV (Figure 2d), but at a fluence of 4.8×10^{17} cm^{-2} a blister forms, which is shown in Figure 2e. For larger fluences pores start to appear on the surface of the blister (see Figure 2f). A beam with a primary energy of 35 keV initially induces a comparable nanopattern formation (Figure 2g). Higher fluences result in blister formation (Figure 2h) and eventually the formation of a large subsurface helium blister at a fluence of 6×10^{17} cm^{-2} (Figure 2i). We also observe some pores on the surface of the blister.
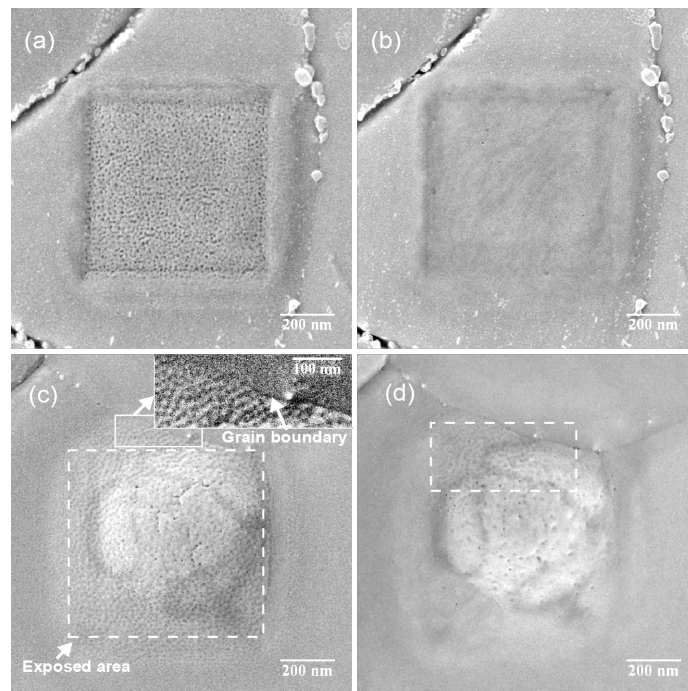
Figure 1: HIM SE image of a Au{111} surface, exposed to a He$^+$ beam with a fluence of 8.4×10^{17} cm^{-2} at different energies. The field of view (FOV) is 1.25 μm, pixel spacing is 1.5 nm. (a) Porous structure formed by a 15 keV He$^+$ beam. (b) The same area as in image (a) after 1.5 months storage under dry atmospheric conditions. The surface has partly self-annealed. (c) Blister formed by a 35 keV beam. The area exposed to the beam is marked by a dashed line. The surface has developed a periodic pattern. The influence of the beam is easily visible outside the marked area as well, but does not extend on the neighboring grain (see inset). (d) The same area as in (c), imaged after 4 months storage under dry atmospheric conditions. The surface of the blister has partly self-annealed, except the marked area in the vicinity of the grain boundary.
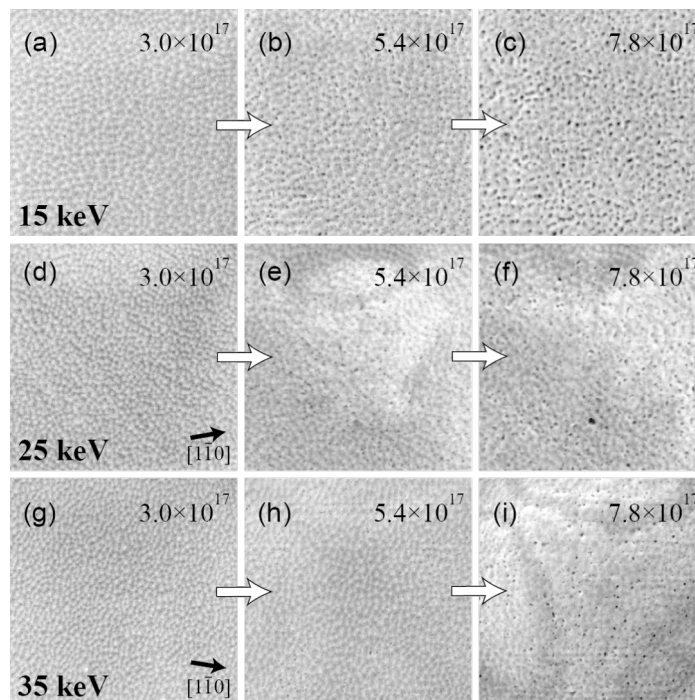
Figure 2: HIM SE images of the pattern that develops on the Au{111} surface as a function of ion fluence. Numbers indicate the ion fluence in helium ions per cm^2. Arrows in (d) and (g) indicate the azimuthal directions of the grains. The He$^+$ beam energies are 15, 25 and 35 keV. FOV is 500 nm, pixel spacing is 0.68 nm.
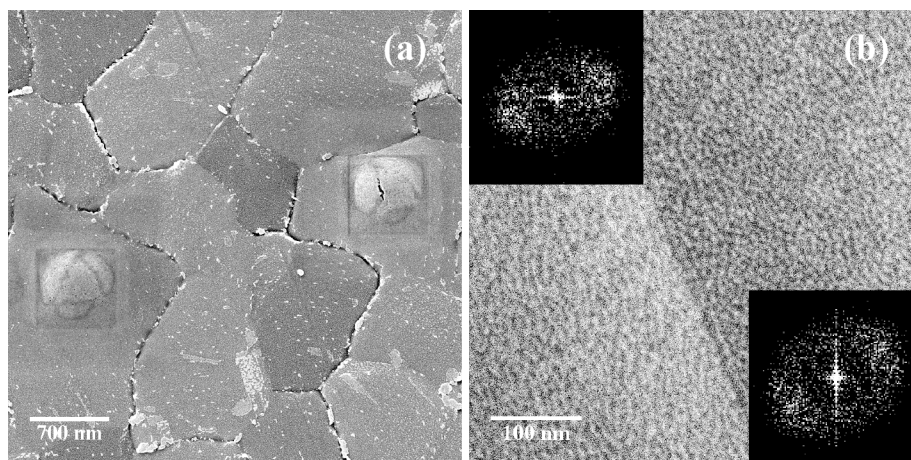
Figure 3: (a) Two blisters created by the 35 keV He$^+$ beam on grains with different azimuthal orientation. FOV is 4 µm. (b) HIM SE image of a Au{111} textured polycrystalline film. The insets are 2D FFTs to demonstrate the relation of the patterns to the orientation of the two grains. He$^+$ beam energy is 35 keV. FOV is 500 nm.

In Figure 3a two blisters on grains with different azimuthal orientation are shown. Although severe damage has been done to the surface and bulk of the gold grains, their crystalline nature is still evident. The blisters have equilateral triangles on top. The same triangles are also observed in the BSHe images, hinting at the channeling nature of the contrast. We attribute these dark triangles and rings to channeling along the {11$\bar{1}$} planes of the FCC crystal. The crystalline shell of the blister is bent (see Figure 1c) due to the high internal gas pressure. As a consequence the ⟨111⟩ surface vector locally tilts. This leads to a local channeling condition with the {11$\bar{1}$} planes along sections of the blister, resulting in the dark bands on the blister surface. The contrast changes with variation of the beam incidence angle, the channeling condition is no longer fulfilled and the dark stripes move or even vanish entirely [8]. The orientations of the sides of the triangles in Figure 2e and Figure 2i help to determine the azimuthal orientations of the grains. Since we used a [111] oriented FCC crystal, the ions are expected to channel along {11$\bar{1}$} planes [8], which cross the (111) surface along ⟨1$\bar{1}$0⟩ directions. Hence, the sides of the triangles are oriented along ⟨1$\bar{1}$0⟩, which is indicated with arrows in Figure 2d and Figure 2g.

The polycrystalline nature of the samples influences the pattern formation as well. First, the pattern propagation is stopped by grain boundaries as can be seen in the inset in Figure 1c: no pattern or rising of the surface level is observed on the neighboring grain. Second, the pattern orientation depends on the underlying crystal and thus on the orientation of the grain. Figure 3b displays patterns on two neighboring grains. The patterns are rotated relative to each other on the two different grains, as is also visible from the 2D FFT, shown in the insets.

The average pattern periodicity was extracted from the images by analyzing 2D autocorrelation functions (ACF). The dependence of the nanopattern periodicity on the He$^+$ fluence for different primary energies is shown in Figure 4.
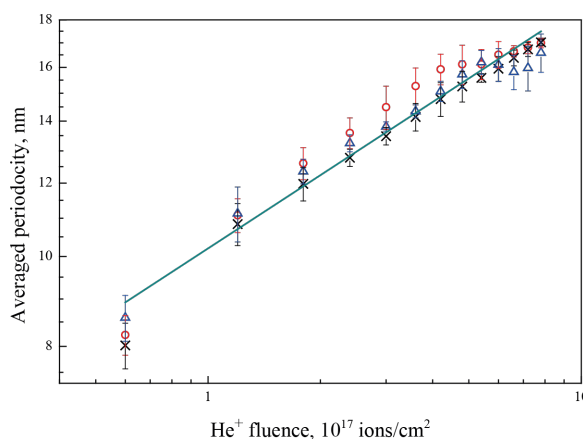
Figure 4: Dependence of the Au{111} average pattern periodicity on helium fluence for 15 keV (red circles), 25 keV (black crosses) and 35 keV (blue triangles) He$^+$ beams.

The periodicity does not show a significant energy dependence and increases from 8.3 ± 0.3 nm to a maximum of 16.9 ± 0.4 nm, showing a power-law dependence on the ion fluence with a coarsening exponent of 0.26 ± 0.01. The same scaling with a time factor of 0.27 ± 0.02 was obtained by Ramana Murty et al. [14]. The authors studied the surface morphology of Au{111} during sputtering with 500 eV Ar$^+$ ions incident at 45° by real-time X-ray scattering. At temperatures of 20–60 °C they observed the formation of mounds with

a characteristic spacing. A similar pattern was also observed on Cu{110}, sputtered by 1 keV Ar$^+$ ions at 320 K and normal incidence [20]. The corresponding scaling factor was 0.26 ± 0.02. To a certain extent, sputter erosion and atom deposition are similar processes. A continuum model for the mound formation in molecular beam epitaxy (MBE) predicts a coarsening exponent of 0.25 [21], which is very close to the measured values.

The pattern exhibits a preferential orientation along the $\langle 1\bar{1}0\rangle$ direction (Figure 2d and Figure 2g), as well as the 2D FFTs in Figure 3b). This suggests that the pattern formation is governed by diffusion processes of gold adatoms and surface vacancies. Together with the sputtering processes it leads to surface roughening and the development of a periodic pattern. Although the sputtering rate is low, it cannot be completely neglected. As He$^+$ ions impinge on the surface at normal incidence, the sputtering of gold atoms by the direct energy transfer from incoming helium is unlikely. Furthermore, the energy transfer from light helium ions to gold atoms in general is limited because of the unfavorable mass ratio. The sputtering is mainly caused by short-range gold recoils and backscattered helium [22,23]. The presence of the pattern outside of the irradiated area (Figure 1c) is additional evidence of the sputtering by gold recoils. Additionally, the gold interstitials themselves are a source of adatoms on the surface. Gold interstitials are able to travel a few tens of nanometers outside the exposed area, but they cannot cross grain boundaries.

The pattern orientation along a specific crystallographic direction can be explained by considering its formation as a result of the suppression of interlayer diffusion by the step edge or Ehrlich–Schwoebel barrier [14,20,24-28]. The activation energy for vacancy diffusion on Au{111} is much higher than the one for adatoms [29], hence we can suppose that at room temperature adatoms are dominantly responsible for the pattern formation. The presence of a step edge barrier along $\langle 1\bar{1}0\rangle$ does not allow the adatoms to descend the $\langle 1\bar{1}0\rangle$ step, and produces a net uphill flow. As a result, mounds are formed along a $\langle 1\bar{1}0\rangle$ direction. However, one would expect a homogeneous distribution of all three possible pattern orientations due to the symmetry of the {111} surface [28]. The out-of-plane orientation of the grains has some angular distribution. Hence, the surfaces are not atomically flat and have a local miscut. The step edges run in one of the three high-symmetry directions that become preferential for the pattern orientation on any one grain.

The exposed areas were imaged again after several weeks. Samples were stored under dry ambient conditions between the experiments. As can be seen in Figure 1, the surface has a tendency to self-anneal over time. In Figure 1b the same area as in

Figure 1a, which was initially exposed to a 15 keV He$^+$ beam, is presented, but after six weeks. The blister, formed by the 35 keV beam and presented in Figure 1c, was imaged again after 16 weeks. The image is shown in Figure 1d. In both cases the pattern has almost completely vanished, except in areas close to the grain boundary (inset in Figure 1c), which apparently acts as an efficient sink for adatoms and interstitials. Thus it hinders the smoothing of the surface in the vicinity. The surface is smoothed, but after a few repetitive scans, the pores, hidden deeper in the substrate, open again. The blister shell self-anneals over time, indicating a possibility to heal the defects. That process can be enhanced by in situ heating of a sample during ion bombardment.
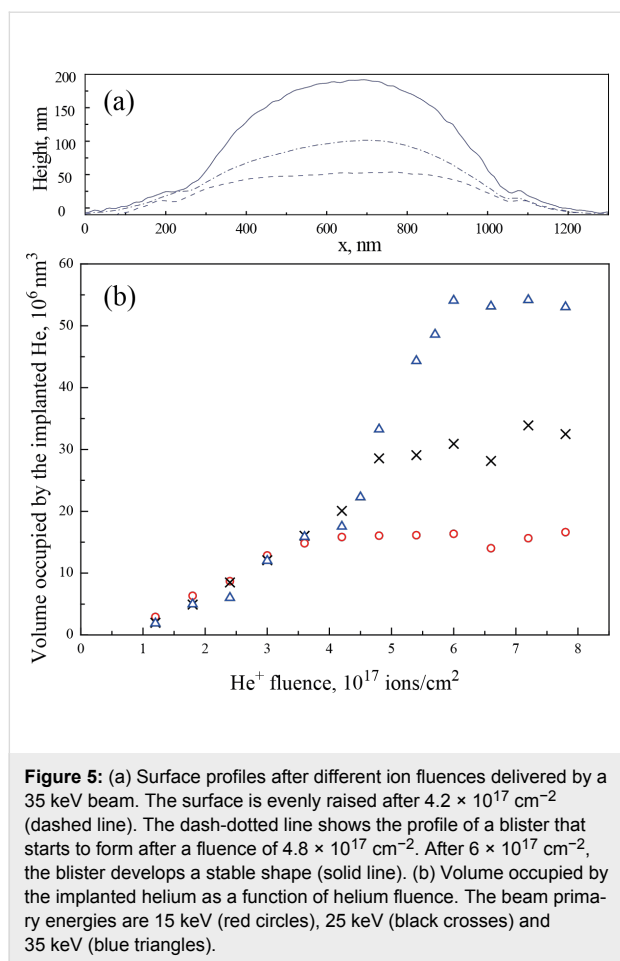
We mention, that the surface modification depends not only on the final fluence, but also on the speed at which it was generated. With an increase of the dose per scan, the modifications occur more swiftly and are more severe.

Helium implantation

Helium implantation occurs during sample irradiation. Since HIM SE images do not contain height information, we have used AFM to directly measure the volume that is occupied by the implanted helium. As a result of the low background pressure of hydrocarbons in the UHV HIM we can exclude false volume estimations due to carbon contamination.

The change of the surface profile with ion fluence for a primary energy of 35 keV is shown in Figure 5a. After a fluence of 4.2×10^{17} cm^{-2}, the surface is still comparatively flat (dashed line), but already for a slightly larger fluence a subsurface blister develops. The profile of a growing blister at 4.8×10^{17} cm^{-2} is shown by the dash–dotted line. At 6×10^{17} cm^{-2} a blister with a stable shape has developed (solid line).

After an initial dose of 6×10^{16} cm^{-2} the exposed area is eroded by 1.0–1.5 nm with respect to the nonirradiated surface. This is the result of sputtering of a few gold layers. The signature of this sputtering-related indentation remains discernible in all subsequent images. After doubling the dose to 1.2×10^{17} cm^{-2}, helium implantation has a noticeable effect: the surface of the exposed square and also the unexposed area adjacent to it, starts to rise with increasing ion fluence. The influence of the helium implantation extends as far as 144 ± 12 nm (15 keV), 162 ± 6 nm (25 keV) and 181 ± 7 nm (35 keV) away from the exposed area. In Figure 5b the increase of blister volume due to helium implantation is presented as a function of ion fluence. The volume depends linearly on the fluence up to 4.2×10^{17} cm^{-2}. After this total dose, the volume occupied by ions implanted at 15 keV stagnates at

Figure 5: (a) Surface profiles after different ion fluences delivered by a 35 keV beam. The surface is evenly raised after 4.2×10^{17} cm^{-2} (dashed line). The dash-dotted line shows the profile of a blister that starts to form after a fluence of 4.8×10^{17} cm^{-2}. After 6×10^{17} cm^{-2}, the blister develops a stable shape (solid line). (b) Volume occupied by the implanted helium as a function of helium fluence. The beam primary energies are 15 keV (red circles), 25 keV (black crosses) and 35 keV (blue triangles).

$(15.8 \pm 0.3) \times 10^{6}$ nm^{3}. In the case of 35 keV ions, after a fluence of 4.2×10^{17} cm^{-2} a more rapid expansion begins. Later, when the fluence reaches 6×10^{17} cm^{-2}, the volume saturates at $(54.2 \pm 0.4) \times 10^{6}$ nm^{3}. For the energy of 25 keV the rapid expansion sets in at the same fluence, but saturates at an intermediate level of $(30.5 \pm 0.9) \times 10^{6}$ nm^{3}.

In the review by Donnelly [30], surface swelling of several materials (Er, Nb and Ni) under helium irradiation is compared. The general trend of the expansion is similar to the one described in this work. The initial linear expansion was found to be energy-independent as well. In the work of Terreault et al. [31], the authors studied helium trapping in Cu, which has similar physical properties to Au. In this case blistering was observed after a fluence of 4.0×10^{17} cm^{-2}.

As is seen from the Figure 5b, there is a negative volume offset, which is attributed to two effects. First, sputtering of the surface will result in material loss. Secondly, at low ion fluences helium ions can occupy existing crystal defects and interatomic positions without causing a substantial volume increase. The subsequent fluence increase leads to the creation of helium nanobub-

bles in the bulk gold. The formation of voids in metals due to He$^+$ ion bombardment is a well-known phenomenon [32-34]. After entering the crystal, an energetic He$^+$ ion creates vacancy–interstitial pairs. These vacancies can aggregate into bigger voids. Since helium is hardly solvable in metals, it is effectively trapped at open-volume defects and has a tendency to agglomerate into nanosized bubbles [35,36]. That leads to deformations, which cause the initial linear volume increase in the graph in Figure 5b. At these fluences (up to 4.2×10^{17} cm^{-2}) the volume change does not depend on the primary energy of the implanted ions.

As more helium ions are implanted, the cavities expand. The helium nanobubbles are highly over-pressurized. Up to a certain bubble size the excess pressure is relieved by loop punching. This bubble growth mechanism was first suggested by Greenwood et al. [37] and later on discussed by Evans [38]. As bubbles grow, several neighboring bubbles eventually create enough local stress to create a crack in the crystal and coalesce. At higher fluences the different stopping powers of gold and (high pressure) helium become relevant. At low energies helium is implanted in a near-surface region. This near-surface helium volume is an effective stopping material for more helium. As a result, a rapid expansion sets in until the bubble reaches the surface. The above described porous structure develops (Figure 1a). At higher energies these processes occur deeper in the material and more helium is incorporated, and as a result a blister develops. The blister formation mechanism by interbubble fracture, has been suggested by Evans [39]. However, also at these high energies helium will start to leak to the surface and the blister growth saturates. The steep part of the graph at 35 keV in Figure 5a corresponds to the blister formation and growth process. At 25 keV this stage of the damage development was not resolved and only the volume of the already formed blister was measured.

We have made rough estimations of the pressure in the nanobubbles, and the pressure in the final blister at 35 keV. Not all of the incident helium is trapped in the bubbles: a part of it is backscattered, and some diffuses into the bulk or out of the material. SRIM-2011 [40] has been used to assess the percentage of backscattered helium. A gold slab with a thickness of 200 nm and 10^5 ions have been used in the calculations. According to these simulations 16% of the incident helium is backscattered at 35 keV. Attributing 4% to other loss mechanisms we used 80% of the fluence for our further calculations. Two approaches were used for the pressure estimation. In the first approach, the pressure was calculated using the virial equation of state:

$$PV_{\mathrm{m}}/RT = 1 + B/V_{\mathrm{m}} + C/V_{\mathrm{m}}^2 , \qquad (1)$$

where P and T are the helium pressure and temperature respectively, V_m is the helium molar volume, R is the universal gas constant, B and C are the second and third virial coefficients. The values of B and C for He at room temperature were taken from [41] and [42]. This gives a lower estimate of 2.1 GPa for the pressure in the nanobubbles just before the start of the rapid expansion. Another assessment was done by applying a relation used by Evans [38], which is based on the work of Rowlinson [43]:

$$P[\text{Pa}] = 4.83 \times 10^7 \exp(5.15 \times 10^{-2} \times \rho), \qquad (2)$$

where ρ is the helium density in units of atoms/nm^3. In this case the calculated pressure is 6.1 GPa. Please note that these two estimates only give an idea of the order of magnitude of the He pressure inside the nanobubbles. As the bubbles grow in size the material cannot support such high pressures, and the bubbles merge. In the case of the final blister grown with a primary energy of 35 keV, both models yield similar values of 437 MPa and 442 MPa, respectively.

Conclusion

Exposure to high He$^+$ ion fluences has a dramatic influence on a crystalline sample, which strongly depends on the energy of the incident beam. Sample modifications are mainly caused by helium implantation producing surface deformations. After the initial formation of nanobubbles filled with helium in the gigapascal pressure range, different scenarios evolve. At low energies the bubbles quickly reach the surface and release the helium, and a sponge-like surface develops. At high energies, the initial nanobubbles form deeper in the material due to the greater range of the helium ions. Consequently, bubble coalescence leads to the formation of a large blister that continues to grow. The final size before the shell leaks depends on the primary energy and thus the implantation depth.

During irradiation with He$^+$ ions at normal beam incidence also a periodic nanopattern develops on the surface at room temperature. The pattern is oriented along the $\langle 1\bar{1}0 \rangle$ direction and its periodicity scales with the ion fluence with a coarsening exponent of 0.26 ± 0.01. The observed features do not coalesce and preserve their shape. An important observation is that the beam influences not only those areas that are directly irradiated by the beam, but also the neighboring regions.

Acknowledgements

References

1. Hill, R.; Faridur Rahman, F. H. M.
   Nucl. Instrum. Methods Phys. Res., Sect. A **2011,** *645,* 96–101.
   doi:10.1016/j.nima.2010.12.123
2. Bell, D. C.; Lemme, M. C.; Stern, L. A.; Williams, J. R.; Marcus, C. M.
   Nanotechnology **2009,** *20,* 455301.
   doi:10.1088/0957-4484/20/45/455301
3. Maas, D.; van Veldhoven, E.; Ping, C.; Sidorkin, V.; Salemink, H.; van der Drift, E.; Alkemade, P. Nanofabrication with a Helium Ion Microscope. In *Proceedings of the SPIE - The International Society for Optical Engineering,* 2010; pp 763814 ff.
4. Scipioni, L.; Ferranti, D. C.; Smentkowski, V. S.; Potyrailo, R. A.
   J. Vac. Sci. Technol., B **2010,** *28,* C6P18. doi:10.1116/1.3517514
5. Annamalai, M.; Mathew, S.; Viswanathan, V.; Fang, C.; Pickard, D. S.; Palaniapan, M. Design, fabrication and Helium Ion Microscope patterning of suspended nanomechanical graphene structures for NEMS applications. In *2011 16th International Solid-State Sensors, Actuators and Microsystems Conference,* IEEE, 2011; pp 2578–2581.
6. Boden, S. A.; Moktadir, Z.; Bagnall, D. M.; Mizuta, H.; Rutt, H. N.
   Microelectron. Eng. **2011,** *88,* 2452–2455.
   doi:10.1016/j.mee.2010.11.041
7. Sijbrandij, S.; Notte, J.; Scipioni, L.; Huynh, C.; Sanford, C.
   J. Vac. Sci. Technol., B **2010,** *28,* 73–77. doi:10.1116/1.3271254
8. Veligura, V.; Hlawacek, G.; van Gastel, R.; Zandvliet, H. J. W.; Poelsema, B. *Beilstein J. Nanotechnol.* **2012,** *3,* 501–506.
   doi:10.3762/bjnano.3.57
9. Livengood, R.; Tan, S.; Greenzweig, Y.; Notte, J.; McVey, S.
   J. Vac. Sci. Technol., B **2009,** *27,* 3244–3249. doi:10.1116/1.3237101
10. Tan, S.; Livengood, R.; Shima, D.; Notte, J.; McVey, S.
    J. Vac. Sci. Technol., B **2010,** *28,* C6F15–C6F21.
    doi:10.1116/1.3511509
11. Cohen-Tanugi, D.; Nan, Y. *J. Appl. Phys.* **2008,** *104,* 063504.
    doi:10.1063/1.2976299
12. Fox, D.; Chen, Y.; Faulkner, C. C.; Zhang, H. *Beilstein J. Nanotechnol.* **2012,** *3,* 579–585. doi:10.3762/bjnano.3.67
13. Donnelly, S. E.; Vishnyakov, V.; Taylor, D.; Valizadeh, R.; Ballard, I. M.; Goddard, D. T. *Appl. Surf. Sci.* **1994,** *74,* 81–90.
    doi:10.1016/0169-4332(94)90102-3
14. Ramana Murty, M. V.; Curcic, T.; Judy, A.; Cooper, B. H.; Woll, A. R.; Brock, J. D.; Kycia, S.; Headrick, R. L. *Phys. Rev. Lett.* **1998,** *80,* 4713–4716. doi:10.1103/PhysRevLett.80.4713
15. van Gastel, R.; Barriss, L.; Sanford, C.; Hlawacek, G.; Scipioni, L.; Merkle, A.; Voci, D.; Fenner, C.; Zandvliet, H. J. W.; Poelsema, B.
    Microsc. Microanal. **2011,** *17,* 928–929.
    doi:10.1017/S1431927611005514
16. Ramachandra, R.; Griffin, B.; Joy, D. *Ultramicroscopy* **2009,** *109,* 748–757. doi:10.1016/j.ultramic.2009.01.013
17. Hlawacek, G.; Veligura, V.; Lorbek, S.; Mocking, T. F.; George, A.; van Gastel, R.; Zandvliet, H. J. W.; Poelsema, B.
    Beilstein J. Nanotechnol. **2012,** *3,* 507–512. doi:10.3762/bjnano.3.58
18. Morgan, J.; Notte, J.; Hill, R.; Ward, B. *Microsc. Today* **2006,** *14* (4), 24–31.
19. Lau, D.; Hughes, A. E.; Muster, T. H.; Davis, T. J.; Glenn, A. M.
    Microsc. Microanal. **2010,** *16,* 13–20.
    doi:10.1017/S1431927609991206
20. Rusponi, S.; Costantini, G.; Boragno, C.; Valbusa, U.
    Phys. Low-Dimens. Struct. **1999,** *5–6,* 95–103.
21. Siegert, M.; Plischke, M. *Phys. Rev. Lett.* **1994,** *73,* 1517–1520.
    doi:10.1103/PhysRevLett.73.1517

22. Littmark, U.; Fedder, S. *Nucl. Instrum. Methods Phys. Res.* **1982,** *194,* 607–610. doi:10.1016/0029-554X(82)90590-0
23. Vicanek, M.; Urbassek, H. M. *Nucl. Instrum. Methods Phys. Res., Sect. B* **1990,** *48,* 549–552. doi:10.1016/0168-583X(90)90180-3
24. Michely, T.; Kalff, M.; Comsa, G.; Strobel, M.; Heinig, K.-H. *J. Phys.: Condens. Matter* **2002,** *14,* 4177–4185. doi:10.1088/0953-8984/14/16/309
25. Valbusa, U.; Boragno, C.; Buatier de Mongeot, F. *J. Phys.: Condens. Matter* **2002,** *14,* 8153–8175. doi:10.1088/0953-8984/14/35/301
26. Everts, F.; Wormeester, H.; Poelsema, B. *Phys. Rev. B* **2010,** *82,* 081415. doi:10.1103/PhysRevB.82.081415
27. Rabbering, F.; Wormeester, H.; Everts, F.; Poelsema, B. *Phys. Rev. B* **2009,** *79,* 075402. doi:10.1103/PhysRevB.79.075402
28. Jorritsma, L.; Bijnagte, M.; Rosenfeld, G.; Poelsema, B. *Phys. Rev. Lett.* **1997,** *78,* 911–914. doi:10.1103/PhysRevLett.78.911
29. Stoltze, P. *J. Phys.: Condens. Matter* **1994,** *6,* 9495–9517. doi:10.1088/0953-8984/6/45/004
30. Donnelly, S. E. *Radiat. Eff.* **1985,** *90,* 1–47. doi:10.1080/00337578508222514
31. Terreault, B.; Ross, G.; St.-Jacques, R. G.; Veilleux, G. *J. Appl. Phys.* **1980,** *51,* 1491. doi:10.1063/1.327797
32. Primak, W.; Luthra, J. *J. Appl. Phys.* **1966,** *37,* 2287–2294. doi:10.1063/1.1708805
33. Yadava, R. D. S. *J. Nucl. Mater.* **1981,** *98,* 47–62. doi:10.1016/0022-3115(81)90386-X
34. Jäger, W.; Manzke, R.; Trinkaus, H.; Crecelius, G.; Zeller, R.; Fink, J.; Bay, H. L. *J. Nucl. Mater.* **1982,** *111–112,* 674–680. doi:10.1016/0022-3115(82)90288-4
35. Laakmann, J.; Jung, P.; Uelhoff, W. *Acta Metall.* **1987,** *35,* 2063–2069. doi:10.1016/0001-6160(87)90034-4
36. Rajainmaki, H.; Linderoth, S.; Hansen, H. E.; Nieminen, R. M.; Bentzon, M. D. *Phys. Rev. B* **1988,** *38,* 1087–1094. doi:10.1103/PhysRevB.38.1087
37. Greenwood, G. W.; Foreman, A. J. E.; Rimmer, D. E. *J. Nucl. Mater.* **1959,** *4,* 305–324. doi:10.1016/0022-3115(59)90030-3
38. Evans, J. H. *J. Nucl. Mater.* **1978,** *76–77,* 228–234. doi:10.1016/0022-3115(78)90145-9
39. Evans, J. H. *J. Nucl. Mater.* **1977,** *68,* 129–140. doi:10.1016/0022-3115(77)90232-X
40. Ziegler, J. F.; Ziegler, M. D.; Biersack, J. P. *Nucl. Instrum. Methods Phys. Res., Sect. B* **2010,** *268,* 1818–1823. doi:10.1016/j.nimb.2010.02.091
41. Hurly, J. J.; Mehl, J. B. *J. Res. Natl. Inst. Stand. Technol.* **2007,** *112,* 75–94. doi:10.6028/jres.112.006
42. Garberoglio, G.; Moldover, M. R.; Harvey, A. H. *J. Res. Natl. Inst. Stand. Technol.* **2011,** *116,* 729–742. doi:10.6028/jres.116.016
43. Rowlinson, J. S. *Mol. Phys.* **1964,** *7,* 349–361. doi:10.1080/00268976300101121

Fabrication of carbon nanomembranes by helium ion beam lithography

Xianghui Zhang[*], Henning Vieker, André Beyer and Armin Gölzhäuser

Abstract

The irradiation-induced cross-linking of aromatic self-assembled monolayers (SAMs) is a universal method for the fabrication of ultrathin carbon nanomembranes (CNMs). Here we demonstrate the cross-linking of aromatic SAMs due to exposure to helium ions. The distinction of cross-linked from non-cross-linked regions in the SAM was facilitated by transferring the irradiated SAM to a new substrate, which allowed for an ex situ observation of the cross-linking process by helium ion microscopy (HIM). In this way, three growth regimes of cross-linked areas were identified: formation of nuclei, one-dimensional (1D) and two-dimensional (2D) growth. The evaluation of the corresponding HIM images revealed the dose-dependent coverage, i.e., the relative monolayer area, whose density of cross-links surpassed a certain threshold value, as a function of the exposure dose. A complete cross-linking of aromatic SAMs by He$^+$ ion irradiation requires an exposure dose of about 850 µC/cm^2, which is roughly 60 times smaller than the corresponding electron irradiation dose. Most likely, this is due to the energy distribution of secondary electrons shifted to lower energies, which results in a more efficient dissociative electron attachment (DEA) process.

Introduction

Carbon nanomembranes (CNMs) with monomolecular thickness and macroscopic lateral size represent a new type of functional two-dimensional (2D) materials [1]. A universal scheme to fabricate CNMs is the irradiation-induced cross-linking of aromatic self-assembled monolayers (SAMs), which allows for creating a variety of functional nanomembranes by using different molecular precursors as building blocks [2]. The properties of CNMs, such as stiffness, chemical functionality and

porosity, can be tailored through a prudent choice of the molecular precursors and the fabrication conditions. CNMs are capable of being released from the substrate and transferred onto arbitrary substrates, e.g., solid supports and holey substrates [3]. Mechanical properties of freestanding CNMs were characterized by bulge test in an atomic force microscope (AFM): biphenyl-based CNMs possess a Young's modulus of ca. 10 GPa and a remarkable tensile strength of ca. 600 MPa

[4]. The possibility of transferring CNMs and their high mechanical strength make them suitable candidates for nano-electromechanical systems (NEMS). Postsynthetic modifications, e.g., multilayer stacking [5], thermal annealing [6], chemical functionalization [7], and perforation [8,9], lead to a further tailoring of the performance of the CNMs and enable various investigations and applications.

The cross-linking of SAMs is so far conducted by exposure to electrons [10] and photons [11]. Electron irradiation induces the dissociation of C–H bonds at the phenyl rings. The consequent cross-linking between adjacent aromatic moieties is a critical step in the formation of CNMs. Both electron beam lithography and extreme ultraviolet (EUV) lithography have been utilized to fabricate CNMs from SAMs [11,12]. The EUV photon induced cross-linking is, for that matter, related to secondary electrons generated by the photoemission process [11]. Turchanin et al. investigated the electron induced cross-linking of biphenylthiol (BPT) SAMs on gold with complementary spectroscopic techniques and they suggested a dissociative electron attachment (DEA) as the dominating process to which both primary electrons and secondary electrons contribute [13]. However, a detailed picture of how the spatial distribution of cross-links evolves until a complete CNM has been formed is still missing.

Further modification and patterning of SAMs have been achieved by using ion irradiation (e.g. Ar^+, Ga^+, Si^+, etc.), which leads to the desorption and the fragmentation of molecules [14,15]. High energy helium ions passing through polymer films modify the macroscopic properties of these films, too. This is related to changes in the chemical structures of the polymers [16,17]. Recently, the helium ion microscope (HIM) has been employed as an imaging and measurement tool for nanotechnology, for which the sub-nanometer sized ion probe and its resulting high brightness lead to a higher resolution and the small convergence angle of the ion beam leads to a larger depth of field. As an imaging tool, this instrument has a high surface sensitivity and is particularly advantageous to distinguish monolayers from the supporting substrate [18,19]. As a tool for nanofabrication, the low proximity effect that arises from the finite excited volume, in which the ion–material interaction takes place, extending deeply into the material, and the confinement of ion scattering to the secondary electron escape depth promise an outstanding performance of HIM [20]. So far, various approaches have been used to exploit the capabilities of HIM, such as ion milling [21], scanning helium ion beam lithography (SHIBL) [22], and helium ion beam induced deposition (HIBID) [20].

Here we used 4'-nitro-1,1'-biphenyl-4-thiol (NBPT) as a molecular precursor to form SAMs on a Au substrate and employed HIM both as a nanofabrication tool to cross-link SAMs and as an imaging tool for the ex situ observation of the crosslinking process. As regards the nanofabrication, both supported and freestanding CNMs were fabricated by transferring them onto a silicon substrate and a transmission electron microscopy (TEM) grid, respectively. As regards the investigation of the cross-linking process, the helium ion beam was programmed to irradiate NBPT SAMs with a series of different doses. The separation of cross-linked and non-cross-linked SAMs was conducted by transferring them onto a Si substrate with an oxide layer. The observation was done by using HIM in doing so taking advantage of the high surface sensitivity of the instrument.

Results and Discussion

Figure 1 shows a schematic representation of the cross-linking and transfer process. Firstly, the SAM that consists of closely packed NBPT molecules is formed on a gold substrate; secondly, the SAM is irradiated locally with He^+ ions; thirdly, the transfer is assisted by a layer of poly(methyl methacrylate) (PMMA) for mechanical stabilization, which allows the dissolu-
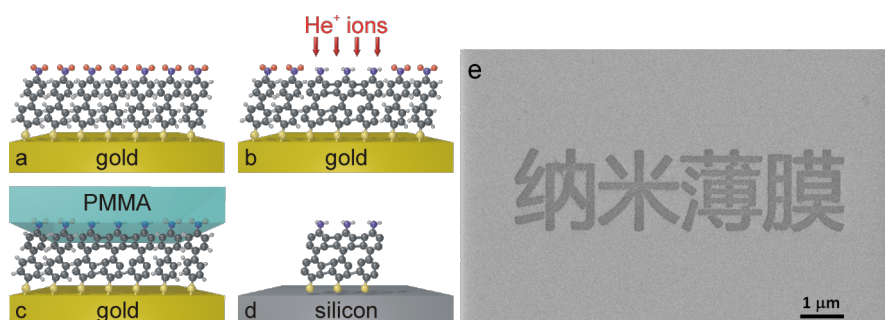
**Figure 1:** (a–d) A schematic representation of the NBPT SAM cross-linked with He$^+$ ions and the transfer onto a Si substrate: (a) Formation of SAM on Au; (b) Local exposure to He$^+$ ions; (c) Transfer of CNM with a polymeric film; (d) Separation of cross-linked from non-cross-linked regions. (e) A demonstration of lithographic CNMs in Chinese characters *nanomembranes* transferred on a silicon substrate.

tion of underlying Au layer; lastly, the PMMA layer is dissolved and only the cross-linked SAM is transferred onto another substrate, e.g., SiO_2/Si. Figure 1e demonstrates a successful transfer of structured CNMs in Chinese characters which means *nanomembranes*: the grey background is SiO_2/Si substrate and the darker features are transferred CNMs.

For the fabrication of freestanding CNMs, NBPT SAMs were irradiated in square patterns by helium ions at 35 keV and holey carbon-coated TEM grids were used as supporting substrates. Figure 2a shows the HIM image of a CNM with a size of 50×50 μm^2 on a TEM grid and the corresponding irradiation dose is approximately 500 $\mu C/cm^2$. The CNM is supported by a holey carbon film on a grid. The holey carbon film appears brighter and the CNM slightly darker due to the charging effect. To identify the CNM, its three corners are marked with arrows. Figure 2b shows the higher magnification HIM micrograph of the CNM in Figure 2a. It is noticeable that the CNM has many tiny holes, indicating that the crosslinking is not complete at this dose. Figure 2c and Figure 2d show the HIM micrographs of a CNM with an irradiation dose of ca. 1000 $\mu C/cm^2$. The CNM shows homogeneous features and no pores are visible here, which indicates a complete crosslinking. The CNM in the upper–left corner is damaged and the dark features arise from the sample stage beneath the TEM grid (see Figure 2d). Notice that imaging doses are at least one order of magnitude smaller than the irradiation dose, no further modification of CNMs is expected during imaging.

In order to observe the development of the crosslinking of the SAM, the NBPT SAM was irradiated in circular regions by helium ion beam with a series of different doses. The variations of the irradiation dose are achieved by controlling the dwell time of the beam. Provided that the fabrication conditions are the same for the whole series, the irradiation dose is proportional to the total irradiation time. Therefore, the dynamics of cross-linking and growth regimes can be studied by making ex situ observations of the development of cross-linked SAMs. To this end, the distinction of cross-linked from non-cross-linked regions in the SAM was facilitated by transferring the irradiated SAM to a new substrate. Strictly speaking, there exists a threshold value, which is given by the density of cross-links that is required for a successful transfer of a monolayer. Below this threshold, the formed supramolecular network is not dense enough to sustain a lift-off from its initial substrate. Therefore, the transfer distinguishes the irradiated SAMs whose density of cross-links surpasses the threshold value from those below the threshold. Figure 3 shows a series of HIM images of a cross-linked SAM that have been transferred onto a SiO_2/Si substrate. Interestingly, the first step is the formation of circular shaped nuclei, which is analogous to the nucleation for thin films or
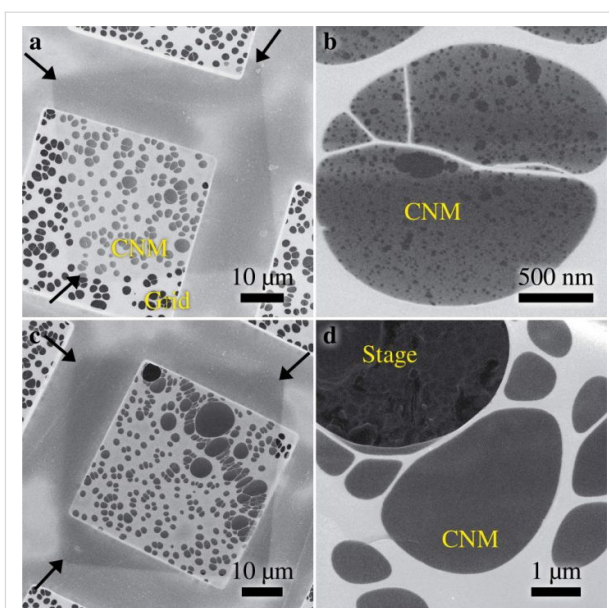
Figure 2: Freestanding CNMs with a dimension of 50×50 μm^2 supported by a TEM grid with a holey carbon film: (a) the HIM micrograph of a CNM with an irradiation dose of 500 $\mu C/cm^2$, where three arrows mark its corners; (b) the high magnification HIM micrograph shows that the CNM contains tiny holes; (c) the HIM image of a CNM with an irradiation dose of 1000 $\mu C/cm^2$; (d) the high magnification HIM image shows that the CNM contains no microscopic defects. (Imaging doses: a) 0.27 $\mu C/cm^2$, b) 55.9 $\mu C/cm^2$, c) 3.36 $\mu C/cm^2$ and d) 33.6 $\mu C/cm^2$).

polymer crystallization [23]. After a dose of 176 $\mu C/cm^2$ (Figure 3a), the average diameter of the nuclei is 9.0 ± 1.7 nm, which means that each nucleus consists of ca. 300 molecules, and the nucleus density is approximately 450 μm^{-2}. When the dose is 225 $\mu C/cm^2$, the nucleus density increases to approximately 930 μm^{-2} (see Figure 3b). The above mentioned threshold is related to the density of the cross-links of these smallest patches (nuclei) that are able to be transferred. After the early stage, the nuclei start to grow in one dimension and chainlike structures with a typical length of about 100 nm become the dominant features, as shown in Figure 3c. Figure 3d shows a marked change of structures, i.e., chain thickening, which indicates that a two dimensional (2D) growth (or lateral growth) begins to take place. Figure 3g and Figure 3h show an incomplete CNM with tiny holes and a complete CNM without holes, respectively. In order to make sure that all these structures are indeed CNMs and to exclude the possibility that some features (especially the small nuclei) might be due to contaminations from the transfer process, the sample (irradiated SAM on SiO_2) was annealed up to 300 °C in ultra-high vacuum (UHV). The subsequent imaging with HIM confirms that no change of the structures occurs. It is also worth mentioning that an excessive exposure to He^{+} ions (>4000 $\mu C/cm^2$) leads to a damage of the CNMs, which is attributed to the swelling of the Au substrate from ion implantation [24].
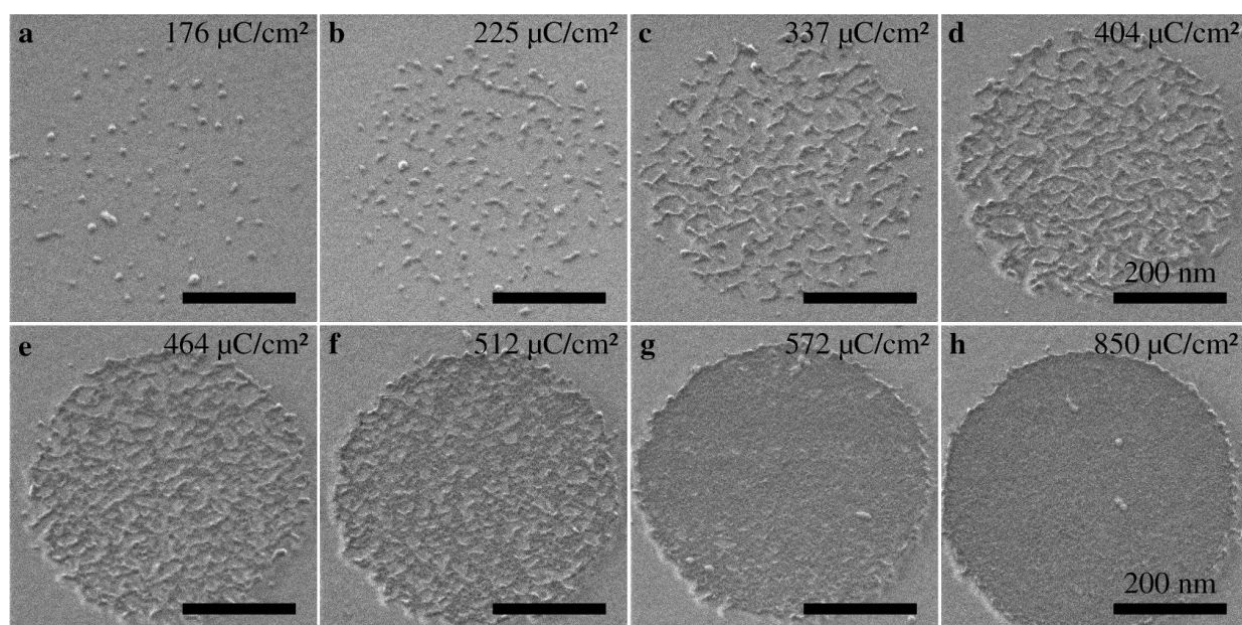
Figure 3: A series of HIM images showing the cross-linking of a NBPT SAM induced by helium ion irradiation, where the cross-linked SAM was transferred onto a SiO$_2$/Si substrate after being cross-linked within a circular region with the dose given in the upper right corner of each image: (a) formation of circular shaped nuclei which are widely separated and randomly distributed. (b) more nuclei come into being and some of them start to grow one dimensionally; (c) chainlike structures with a typical length of ca. 100 nm become the majority; (d) chain thickening indicates a two-dimensional (2D) growth beginning to take place; (e–f) 2D growth plays a dominating role; (g) the CNM contains tiny holes; (h) the CNM forms completely and no defects are observed, indicating the status of a complete cross-linking. The scale bars are 200 nm.

A complete cross-linking of NBPT SAMs by He$^+$ ion irradiation requires an exposure dose of approximately 850 μC/cm^2, which is roughly 60 times smaller than the corresponding electron irradiation dose (ca. 50,000 μC/cm^2, 100 eV) [13]. The energy loss of helium ions in alkanethiol SAMs on Au were investigated by neutral impact collision ion scattering spectroscopy (NICISS) and the stopping power was determined to be about 3.7 eV/Å for the ion energy of 4 keV [25]. Though the total scattering cross–section of He$^+$ ions by the SAM is very small, the energy transfer could induce molecular excitation and bond scissions, which may contribute to the cross-link formation to a certain extent. However, the tremendous dose difference can be associated with distinctive characteristics of secondary electrons that are excited by the helium ions. Firstly, the secondary electron yield for 35 keV He$^+$ ions impinging perpendicularly on a Au substrate is calculated by the software package IONiSE to be about 2.7 [26]. And this is approximately three times higher than the experimentally determined secondary electron yield (approximately 0.85) for 100 eV electrons [27]. Secondly, the energy spectrum of secondary electrons excited by 35 keV He$^+$ ions on Au showed a peak around 2 eV, with a small shoulder in the range of 5–6 eV [28]. For the excitation by electrons at 100 eV, the energy distribution of secondary electrons shows a peak at about 5 eV [27]. It is known that secondary electrons at energies well below the ionization threshold could produce single strand and double strand breaks in DNA and thus induce genotoxic effects in living cells [29]. These breaks are attributed to the DEA process, in which the attachment of incident electrons leads to the formation of a transient molecular anion (TMA) state and this TMA decays by electron autodetachment or by dissociation of a specific bond. The probability of forming a TMA, i.e., the electron capture cross section, varies inversely with the energy of the TMA state with respect to the ground state. In addition, the life time of TMAs increases with decreasing their energies [30]. This indicates that in the case of electron irradiation in NBPT SAMs, by analogy with strand-breaks in DNA, the DEA process is more efficient for secondary electrons with lower energies around 2 eV.

The DEA process is endothermic, as the electron affinity of a biphenyl molecule (3–7 kJ/mol) is much smaller than the bond energy of C–H (ca. 430 kJ/mol) [31,32]. The characteristic energy barriers for cross-linking arise from the activation energy for the DEA process and the entropic barrier to form a covalent bond among adjacent molecules. The activation energy and the above mentioned energy-dependent DEA cross section determine the rate coefficient of the DEA process [33]. The entropic barrier can be associated with a conformational entropy reduction of a molecule after being cross-linked, as a single molecule is more flexible and thus possesses higher degrees of freedom compared to a molecule being cross-linked and

constrained by covalent bonds. The sequence of cross-linking depends on the characteristic energy barriers, as the entire region is irradiated homogeneously. A formation of nuclei would be associated with minimum activation energies in the SAMs. Further crosslinking prefers to occur around those already cross-linked nuclei, instead of regions that are not cross-linked. This implies that activation energies in cross-linked regions are relatively smaller, as π-electrons are laterally delocalized due to the cross-links and the electron mobility in cross-linked regions increases as well. The formation of interfaces between cross-linked and non-cross-linked region could result in entropic barriers due to steric hindrance. Note that the orientation of the 1D structures appears to be closer to the horizontal (scan) direction than to the vertical direction, which implies that the activation energy could be slightly brought down by the helium ion beam scanning due to the local electronic field around the growth front. Therefore, the growth direction of the nuclei is determined by the growth front that exhibits the lowest activation energies as well as the lowest entropic barriers. Lastly, the fact that a 2D growth follows the 1D growth could be attributed to a higher entropic barrier encountered at the sides of 1D structures. As regards the entropic barrier, an extreme example would be that for the insurmountable entropic barriers the crosslinking does not occur and vacancies that contain isolated molecules are formed. XPS spectra showed that the maximum degree of crosslinking of the BPT SAM was approximately 90% and further crosslinking was sterically hindered [13].

As mentioned above, three stages of the crosslinking process were designated: the formation of nuclei, 1D growth, and 2D growth of cross-linked regions. Figure 4 shows the percentage of the cross-linked area as a function of the irradiation doses: (1) the initial formation of nuclei occurs up to a surface coverage of 6–10%; (2) the 1D growth dominates for a coverage up to about 35%; (3) the 2D growth dominates for a coverage above about 35%. We employed Gaussian distributions to describe the probability of surpassing the threshold cross-linking density at a given dose. As shown in Figure 4, the cross-linked area coverage in dependence on the exposure dose can be described by two superimposed sigmoid functions represented by the following cumulative Gaussian distribution functions

$$\theta(D) = \frac{I_1}{I_1 + I_2} \frac{1}{2} \left[1 + \mathrm{erf}\left(\frac{D - D_1}{\sigma_1 \sqrt{2}} \right) \right]$$
$$+ \frac{I_2}{I_1 + I_2} \frac{1}{2} \left[1 + \mathrm{erf}\left(\frac{D - D_2}{\sigma_2 \sqrt{2}} \right) \right] \quad (1)$$

where θ is the cross-linked area coverage, D is the irradiation dose, $D_1 = (204 \pm 18)$ μC/cm^2 is the mean dose of the first Gaussian distribution, $\sigma_1 = (42 \pm 24)$ μC/cm^2 is the corresponding standard deviation, and $I_1 = 0.22 \pm 0.04$ is the magnitude of the first cumulative Gaussian distribution. The corresponding quantities of the second Gaussian distribution are $D_2 = (476 \pm 8)$ μC/cm^2, $\sigma_2 = (56 \pm 7)$ μC/cm^2 and $I_2 = 0.78 \pm 0.04$. The existence of two distinct Gaussian distributions indicates that two types of monolayer regions for 1D and 2D growth regimes are involved, which require different doses for cross-linking with mean values of approximately 200 μC/cm^2 and approximately 480 μC/cm^2, respectively.

Figure 4: Percentage of the cross-linked area plotted as a function of the irradiation dose: (1) no CNM forms below the threshold dose of approximately 160 μC/cm^2; (2) the formation of nuclei occurs up to a surface coverage of 6–10%; (3) the 1D growth dominates for a coverage of up to about 35% and the required mean dose is approximately 200 μC/cm^2; (4) the 2D growth dominates for a coverage above about 35% and the required mean dose is approximately 480 μC/cm^2.

A possible explanation for this behaviour can be found by considering the in-plane tension of cross-linked SAMs. It is known that free-standing CNMs from fully cross-linked NBPT SAMs exhibit an in-plane tensile residual strain of about 1% [4]. This strain is expected to be introduced during the cross-linking process, as new bonds are created between neighbouring molecules. Figure 3a shows the formation of small nuclei in the initial phase of the cross-linking process. Such island-like structures are known to partially relax compressive as well as tensile strain by slight expansion or shrinkage, respectively [34]. A 10 nm sized nucleus may shrink up to 1 Å by relaxing a tensile strain of 1%. Consequently, the distance between neighbouring molecules adjacent to such cross-linked nuclei should increase, which will reduce the probability of a new cross-link formation. This increases the mean dose for the non-cross-linked monolayer areas near cross-linked patches to reach the threshold cross-linking density. The two distinct Gaussian distributions in Figure 4 can be understood to reflect

the cross-linking of unstrained and strained regions with mean doses of approximately 200 $\mu C/cm^2$ and approximately 480 $\mu C/cm^2$, respectively. A consequence of this interpretation is that the formation of nuclei as well as the formation of 1D structures is assigned to the cross-linking process with the lower mean dose, i.e., to the unstrained monolayer regions. This is obvious by Figure 3c and Figure 4. The HIM image of Figure 3c shows the occurrence of 1D structures while the second sigmoidal function in Figure 4 possesses a negligible value at this dose. Therefore, cross-linked patches are not isotropically surrounded by strained regions but in certain directions the adjacent monolayer is unstrained, which results in the observed formation of 1D cross-linked structures with the lower mean dose. The 2D growth of cross-linked areas is then assigned to the higher mean dose due to the strain in these monolayer regions.

Conclusion

Freestanding carbon nanomembranes were successfully fabricated from aromatic self-assembled monolayers by using helium ion beam lithography. Three distinct stages of the cross-linking process, i.e., the initial nucleation, 1D growth and 2D growth, were observed ex situ by helium ion microscopy. Such a sequence could be related to different activation energies of dissociative electron attachment process as well as different entropic barriers encountered by the growth fronts. The irradiation dose for a complete cross-linking with helium ions is roughly 60 times smaller than that with electrons. Most likely, this is due to the energy distribution of helium ion excited secondary electrons being shifted to lower energies.

Experimental
Preparation of self-assembled monolayers

For the preparation of 4'-nitro-1,1'-biphenyl-4-thiol (NBPT) SAMs we used a 300 nm polycrystalline Au layer with (111) crystal planes epitaxially grown on a mica substrate (Georg Albert Physical Vapor Deposition, Germany). The substrate was cleaned with a UV/ozone cleaner (UVOH 150 LAB FHR) for 5 min, rinsed with ethanol, and then blown dry under a nitrogen stream. Afterwards the substrates were immersed into 10 mL of a solution of dry and degassed dimethylformamide (DMF) with ca. 10 mmol NBPT molecules for 72 h in a sealed flask under nitrogen atmosphere.

Helium ion lithography and helium ion microscopy

The experiments were conducted with a Carl Zeiss Orion Plus® helium ion microscope at room temperature. The irradiation of NBPT SAMs was performed by using the built-in software. The ion beam is programmed to irradiate an array of circular features by using a bitmap file and the dose variations are achieved by controlling the dwell time per pixel. The helium ion beam was operated at an acceleration voltage of 34.8 kV and a current of 3.5 pA. Due to the discreteness of bitmap files, the helium ion beam is intentionally slightly defocused in order to minimize any inhomogeneities in crosslinking. One circular feature consists of 2160 write points at a pixel distance of 10 nm. The fabrication of freestanding square CNMs was carried out by irradiating NBPT SAMs by HIM in a repeated scanning mode. The sizes of CNMs are the same to the field of view (FOV) and dose variations are achieved by controlling the total scanning time. For imaging, the helium ion beam was operated at acceleration voltages of 36.5–37.9 kV and currents of 0.3–0.6 pA. Images on SiO_2 were acquired at a working distance of 9 mm and a tilt angle of 35° with 30 μs dwell time per pixel. Images on grid were acquired at a working distance of 30 mm with 0.5 μs dwell time and 128 frames averaged.

Transfer of carbon nanomembranes

After helium ion irradiation, the whole NBPT CNMs were transferred onto another substrate for further investigations again with the HIM. For the transfer of NBPT CNMs onto a SiO_2/Si substrate the samples were spin-coated with a layer of poly(methyl methacrylate) (PMMA) for stabilization and baked on a hotplate at 90 °C for 5 min. The separation of the PMMA/CNM/Au layer from the mica substrate was achieved by carefully dipping the sample into water. Subsequently, the Au layer was completely etched by a gold etchant (5 wt % I_2 and 10 wt % KI in water). Afterwards, the PMMA/CNM layer was transferred to a Si substrate with an oxide layer with the thickness of 300 nm and the sample was immersed into acetone for 40 min for the dissolution of the PMMA layer. For the fabrication of freestanding NBPT CNMs on a TEM grid the same process was carried out, except for the drying process being conducted in a critical-point dryer (CPD, Autosamdri-815B, Tousimis, USA) to yield intact and suspended CNMs.

References

1. Turchanin, A.; Gölzhäuser, A. *Prog. Surf. Sci.* **2012,** *87,* 108–162. doi:10.1016/j.progsurf.2012.05.001
2. Angelova, P.; Vieker, H.; Weber, N.-E.; Matei, D.; Reimer, O.; Meier, I.; Kurasch, S.; Biskupek, J.; Lorbach, D.; Wunderlich, K.; Chen, L.; Terfort, A.; Klapper, M.; Müllen, K.; Kaiser, U.; Gölzhäuser, A.; Turchanin, A. *ACS Nano* **2013,** *7,* 6489–6497. doi:10.1021/nn402652f

3. Nottbohm, C. T.; Beyer, A.; Sologubenko, A. S.; Ennen, I.; Hütten, A.; Rösner, H.; Eck, W.; Mayer, J.; Gölzhäuser, A. *Ultramicroscopy* **2009,** *108,* 885–892. doi:10.1016/j.ultramic.2008.02.008
4. Zhang, X.; Beyer, A.; Gölzhäuser, A. *Beilstein J. Nanotechnol.* **2011,** *2,* 826–833. doi:10.3762/bjnano.2.92
5. Nottbohm, C. T.; Turchanin, A.; Beyer, A.; Stosch, R.; Gölzhäuser, A. *Small* **2011,** *7,* 874–883. doi:10.1002/smll.201001993
6. Turchanin, A.; Beyer, A.; Nottbohm, C. T.; Zhang, X.; Stosch, R.; Sologubenko, A.; Mayer, J.; Hinze, P.; Weimann, T.; Gölzhäuser, A. *Adv. Mater.* **2009,** *21,* 1233–1237. doi:10.1002/adma.200803078
7. Zheng, Z.; Nottbohm, C. T.; Turchanin, A.; Muzik, H.; Muzik, A.; Heilemann, M.; Sauer, M.; Gölzhäuser, A. *Angew. Chem.* **2010,** *122,* 8671–8675. doi:10.1002/ange.201004053
   Angew. Chem., Int. Edit. **2010,** *49,* 8493–8497. doi:10.1002/anie.201004053
8. Ritter, R.; Wilhelm, R. A.; Stöger-Pollach, M.; Heller, R.; Mücklich, A.; Werner, U.; Vieker, H.; Beyer, A.; Facsko, S.; Gölzhäuser, A.; Aumayr, F. *Appl. Phys. Lett.* **2013,** *102,* 063112. doi:10.1063/1.4792511
9. Schnietz, M.; Turchanin, A.; Nottbohm, C. T.; Beyer, A.; Solak, H. H.; Hinze, P.; Weimann, T.; Gölzhäuser, A. *Small* **2009,** *5,* 2651–2655. doi:10.1002/smll.200901283
10. Gölzhäuser, A.; Eck, W.; Geyer, W.; Stadler, V.; Weimann, T.; Hinze, P.; Grunze, M. *Adv. Mater.* **2001,** *13,* 806–809. doi:10.1002/1521-4095(200106)13:11%3C803::AID-ADMA806%3E3.0. CO;2-W
11. Turchanin, A.; Schnietz, M.; El-Desawy, M.; Solak, H. H.; David, C.; Gölzhäuser, A. *Small* **2007,** *3,* 2114–2119. doi:10.1002/smll.200700516
12. Nottbohm, C. T.; Turchanin, A.; Beyer, A.; Gölzhäuser, A. *J. Vac. Sci. Technol., B* **2009,** *27,* 3059–3062. doi:10.1116/1.3253536
13. Turchanin, A.; Käfer, D.; El-Desawy, M.; Wöll, C.; Witte, G.; Gölzhäuser, A. *Langmuir* **2009,** *25,* 7342–7352. doi:10.1021/la803538z
14. Ada, E. T.; Hanley, L.; Etchin, S.; Melngailis, J.; Dressick, W. J.; Chen, M.-S.; Calvert, J. M. *J. Vac. Sci. Technol., B* **1995,** *13,* 2189–2196. doi:10.1116/1.588102
15. Cyganik, P.; Vandeweert, E.; Postawa, Z.; Bastiaansen, J.; Vervaecke, F.; Lievens, P.; Silverans, R. E.; Winograd, N. *J. Phys. Chem. B* **2005,** *109,* 5085–5094. doi:10.1021/jp0478209
16. Evelyn, A. L.; Ila, D.; Zimmerman, R. L.; Bhat, K.; Poker, D. B.; Hensley, D. K.; Klatt, C.; Kalbitzer, S.; Just, N.; Drevet, C. *Nucl. Instrum. Methods Phys. Res., Sect. B* **1999,** *148,* 1141–1145. doi:10.1016/S0168-583X(98)00858-1
17. Rangel, E. C.; Cruz, N. C.; Lepienski, C. M. *Nucl. Instrum. Methods Phys. Res., Sect. B* **2002,** *191,* 704–707. doi:10.1016/S0168-583X(02)00637-7
18. Postek, M. T.; Vladár, A.; Archie, C.; Ming, B. *Meas. Sci. Technol.* **2011,** *22,* 024004. doi:10.1088/0957-0233/22/2/024004
19. Bell, D. C. *Microsc. Microanal.* **2009,** *15,* 147–153. doi:10.1017/S1431927609090138
20. Maas, D.; van Veldhoven, E.; Chen, P.; Sidorkin, V.; Salemink, H.; van der Drift, E.; Alkemade, P. *Proc. SPIE* **2010,** *7638,* 763814. doi:10.1117/12.862438
21. Bell, D. C.; Lemme, M. C.; Stern, L. A.; Williams, J. R.; Marcus, C. M. *Nanotechnology* **2009,** *20,* 455301. doi:10.1088/0957-4484/20/45/455301
22. Sidorkin, V.; van Veldhoven, E.; van der Drift, E.; Alkemade, P.; Salemink, H.; Maas, D. *J. Vac. Sci. Technol., B* **2009,** *27,* L18–L20. doi:10.1116/1.3182742

23. Muthukumar, M. *Adv. Chem. Phys.* **2004,** *128,* 1–63. doi:10.1002/0471484237.ch1
24. Veligura, V.; Hlawacek, G.; Berkelaar, R. P.; van Gastel, R.; Zandvliet, H. J. W.; Poelsema, B. *Beilstein J. Nanotechnol.* **2013,** *4,* 453–460. doi:10.3762/bjnano.4.53
25. Andersson, G.; Morgner, H. *Nucl. Instrum. Methods Phys. Res., Sect. B* **1999,** *155,* 357–368. doi:10.1016/S0168-583X(99)00475-9
26. Ramachandra, R.; Griffin, B.; Joy, D. *Ultramicroscopy* **2009,** *109,* 748–757. doi:10.1016/j.ultramic.2009.01.013
27. Völkel, B.; Gölzhäuser, A.; Müller, H. U.; David, C.; Grunze, M. *J. Vac. Sci. Technol., B* **1997,** *15,* 2877–2881. doi:10.1116/1.589748
28. Petrov, Yu. V.; Vyvenko, O. F.; Bondarenko, A. S. *J. Surf. Invest.: X-Ray, Synchrotron Neutron Tech.* **2010,** *4,* 792–795. doi:10.1134/S1027451010050186
29. Boudaiffa, B.; Cloutier, P.; Hunting, D.; Huels, M. A.; Sanche, L. *Science* **2000,** *287,* 1658–1660. doi:10.1126/science.287.5458.1658
30. Martin, F.; Burrow, P. D.; Cai, Z.; Cloutier, P.; Hunting, D.; Sanche, L. *Phys. Rev. Lett.* **2004,** *93,* 068101. doi:10.1103/PhysRevLett.93.068101
31. Fielding, W.; Pritchard, H. O. *J. Phys. Chem.* **1962,** *66,* 821–823. doi:10.1021/j100811a011
32. Arulmozhiraja, S.; Fujii, T. *J. Chem. Phys.* **2001,** *115,* 10589–10594. doi:10.1063/1.1418438
33. Fabrikant, I. I.; Hotop, H. *J. Chem. Phys.* **2008,** *128,* 124308. doi:10.1063/1.2841079
34. Voigtländer, B. *Surf. Sci. Rep.* **2001,** *43,* 127–254. doi:10.1016/S0167-5729(01)00012-7

Fundamental edge broadening effects during focused electron beam induced nanosynthesis

Roland Schmied[1], Jason D. Fowlkes[2,3], Robert Winkler[1], Phillip D. Rack[2,3] and Harald Plank[*1,4,§]

Address:
[1]Graz Centre for Electron Microscopy, 8010 Graz, Austria, [2]Center for Nanophase Materials Sciences, Oak Ridge National Laboratory, Oak Ridge, Tennessee 37831, USA, [3]Department of Materials Science and Engineering, University of Tennessee, Knoxville, Tennessee 37996, USA and [4]Institute for Electron Microscopy and Nanoanalysis, Graz University of Technology, 8010 Graz, Austria

Email:
Harald Plank[*] - harald.plank@felmi-zfe.at

* Corresponding author
§ Tel: +43 316 873 8821

Keywords:
focused electron beam induced deposition; nanofabrication; platinum; simulation

Abstract

The present study explores lateral broadening effects of 3D structures fabricated through focused electron beam induced deposition using MeCpPt(IV)Me$_3$ precursor. In particular, the scaling behavior of proximity effects as a function of the primary electron energy and the deposit height is investigated through experiments and validated through simulations. Correlated Kelvin force microscopy and conductive atomic force microscopy measurements identified conductive and non-conductive proximity regions. It was determined that the highest primary electron energies enable the highest edge sharpness while lower energies contain a complex convolution of broadening effects. Moreover, it is demonstrated that intermediate energies lead to even more complex proximity effects that significantly reduce lateral edge sharpness and thus should be avoided if desiring high lateral resolution.

Introduction

Focused electron beam induced deposition (FEBID) has attracted increasing attention due to capability to directly write functional (3D) structures with nanometer resolution [1-3]. Compared to lithography-based methods, FEBID does not require pre- or post-growth treatments and can be used on non-flat surfaces. This makes this technique a potential candidate for an enabling nanofabrication technology. The technique relies on the local nano-synthesis of precursor molecules by a focused electron beam and its subsequent electron emission from the substrate and the deposit itself [1,3-6]. Typically, a gaseous precursor is brought into the chamber via a dedicated gas injection system where it adsorbs at the surface, undergoes random diffusion and desorbs again after a system-dependent residence time [1,3,4,7-19]. A major problem of FEBID, however, is the

large amount of carbon impurities that often stem from incompletely dissociated precursor molecules or non-volatile fragments [10]. As these contents can reduce or even mask the intended functionality [4,6] strong efforts have been made to optimize the purification processes [6,20-33]. Recently, Geier et al. demonstrated an approach that finally allows a full purification at high rates without elevated temperatures and/or highly reactive gases after initial fabrication [32]. While this approach is ideal for small structures, Sachser et al. demonstrated a catalytic purification approach without the need of a scanning e-beam that is, hence, highly suited for the purification of large areas [33]. Despite these purity issues, a variety of applications have been demonstrated for different precursors such as nano-optics [34,35], magnetic storage, sensing and logic applications [36-40], and nanoscale stress/strain or gas sensors [28,41,42]. While highly accurate and reproducible surface morphologies are essential for some of these applications, e.g., nano-optics, all of these applications require predictable and reproducible shape control in the context of high integration densities due to the ongoing downscaling trends. While Hari et al. recently demonstrated the fabrication of sub-20 nm structures by a careful experimental setup [43], Arnold et al. described the role of backscattered electrons (BSEs) generated by the growing deposit itself and its consequences on lateral broadening effects [44]. Both studies, however, used highly defined quasi-1D or quasi-2D structures as ideal test models and/or with the aim of unique lithography alternatives. For many applications, however, 3D deposits are required and thus more complex proximity effects emerge due to the extensive electron trajectories, which have been basically demonstrated in experiments and simulations [18]. In order to push this technique further towards the intrinsic limits, a detailed knowledge of broadening effects, their origins and the scaling behavior for edge-effects of 3D structures needs to be acquired.

In this study, we focus on such broadening effects for 1×1 µm deposits with heights below 140 nm. We analyze the morphology, the chemistry and the electric properties of the proximity effects by a multi-technique approach and complement the experimental data with Monte Carlo electron–solid simulations. Furthermore, we focus on the qualitative scaling behavior of proximity effects as a function of primary electron energy and deposit height or thicknesses. Beside the discussion of fundamental broadening effects, we derive ideal and non-ideal parameter ranges from the scaling behavior as a practical output of this study.

Experimental

FEBID was performed with a FEI Nova200™ dual beam microscope (DBM) equipped with a FEI gas-injection-system (GIS) for Pt deposition, arranged at an angle of 52° and a vertical dis-

tance of 120 µm to the substrate with an exact alignment of the GIS main axis with respect to the deposition area as described in detail by Winkler et al. [45]. For the deposition of PtC (MeCpPt(IV)Me$_3$) precursor was used at a reservoir temperature of 45 °C (heated for at least 45 min prior to any experiment). Two types of substrates have been used: 1) bare B-doped Si substrates with a 500 nm SiO$_2$ top-layer providing a root mean square (RMS) surface roughness values of less than 0.1 nm, and 2) the same substrates with 60 nm Au electrodes, fabricated through electron-beam lithography using a 3 nm Cr interfacial adhesion layer. While the former were used for atomic force microscopy (AFM) and Kelvin force microscopy (KFM) investigations, the latter have been used for conductive-AFM (C-AFM) measurements. All substrates were taken from sealed wafer boxes and were immediately transferred to the dual beam microscope followed by overnight pumping towards a target chamber pressure of $(2–3) \cdot 10^{-6}$ mbar. Prior to patterning, the GIS was opened for about 2 min to establish stable precursor conditions at the surface at a chamber pressure of $(1–2) \cdot 10^{-5}$ mbar. All structures have been fabricated by using stream-files that were generated through a patterning algorithm custom-written in C++ [46]. Unless otherwise noted, 1×1 µm^2 squares with variable heights have been used for investigations. Primary electron energies and beam currents were 5 keV/98 pA, 10 keV/130 pA, 15 keV/140 pA, 20 keV/150 pA, 25 keV/ 150 pA and 30 keV/150 pA (in contrast to the finely adjustable beam energies, the beam current can only be chosen in steps due to technical reasons). All patterns used a serpentine scanning strategy, constant pixel dwell times (DTs) of 100 µs and pixel point pitches (PoPs) of 50% beam overlap resulting in distances of 14.9 down to 7.1 nm. Different thicknesses have been realized by varying the number of patterning loops. Beam currents, DTs and PoPs were based on previous studies, suggesting a widely balanced working regime without strong excess of electrons or molecules [10,44,45,47]. Preliminary experiments were performed without precursor gas by using the same patterns at the highest exposure times revealing low carbon contamination in the sub-nanometer range. After successful fabrication the deposits were not e-beam inspected but immediately transferred to the AFM system. AFM and KFM experiments have been performed with a Dimension 3100 System (Bruker Nano), equipped with a Hybrid scan head and operated with a Nanoscope IV controller together with the C-AFM application module for the respective measurements. OMCL-C240-TS and ASYELEC-01 (TiIr surface coating) cantilevers have been used for AFM/KFM (2-pass tapping mode) and C-AFM (contact mode) measurements, respectively. The latter experiments have been carried out at voltages between −12 and +12 V depending on the individual purpose. All AFM-based experiments have been performed in a glove box under inert nitrogen atmosphere, which reduces the H$_2$O

wetting layer on the surface, particularly beneficial for high-resolution KFM measurements.

Monte Carlo simulations for radial BSE distributions have been performed by using the software package CASINO v2.42 [48] assuming the AFM-measured deposit values and a typical PtC_5 chemistry for such FEBID deposition conditions. All emission profiles were subsequently re-normalized to areal values to access the real radial distributions.

Results
Morphology

At first, a full set of FEBID structures have been deposited with different primary electron energies (5–30 keV), similar beam currents (98–150 pA) and varying deposit thicknesses between 5 and 132 nm. The upper part of Figure 1b (left Y axis) shows a comparison of normalized AFM height cross sections for similarly thick deposits (65 ± 6 nm) to reveal the energy dependent evolution of proximity deposition. Although different in their dimensions the proximal shapes can be classified by three distinct features as schematically shown on the right hand side in Figure 1a: 1) small edge-broadening (EB), which is always found in the range of 20–60 nm per side in agreement with single line broadening effects recently described by Arnold et al. [44]; 2) a large outer halo (OH), which is extremely thin (less than 5% of the deposit height, see Figure S1, Supporting Information File 1); and 3) an inner halo (IH), which changes its shape depending on the primary energy. As can be seen, the inner halo reveals a distinct plateau for intermediate electron energies around 20 keV, which strongly reduces the achievable lateral deposit edge sharpness (magenta line in Figure 1b). For decreasing primary energies the plateau gets higher but more narrow (e.g., blue line in Figure 1b for 15 keV). In contrast, higher primary energies lead to flatter plateaus with increasing radius finally resulting in a broadening that is dominated by the outer halo (green line in Figure 1b for 30 keV). Figure 2 shows the thickness-dependent radius of the outer halo (AFM-based) for 30 keV deposits (a) together with the simulated backscattered electron (BSE) radius (b) derived from the used Si–SiO$_2$ substrate (simulated by the Monte Carlo package CASINO [48]). As evident in Figure 2, the experimentally measured outer halo radius approaches the simulated value (indicated by the dashed red line), which reveals substrate-related BSEs (BSE-S) to be involved in the formation of the outer halo. Considering the cross-section of MeCpPt(IV)Me$_3$ precursor molecules [3,17,49,50] with its maximum clearly below 1 keV, it is very likely that secondary electrons type II (SE-II) are mainly responsible for the dissociation although a direct dissociation through BSE-S is also likely to contribute. Hence, it can be concluded that the outer-halo can predominantly be assigned to substrate-related BSE-S and SE-II, further denoted as SE-II-S

(see also the left hand scheme in Figure 1a). A detailed discussion for the edge broadening, EB, and in particular for the inner halos, IH, is given later as more experimental data and simulations are needed for a comprehensive explanation.
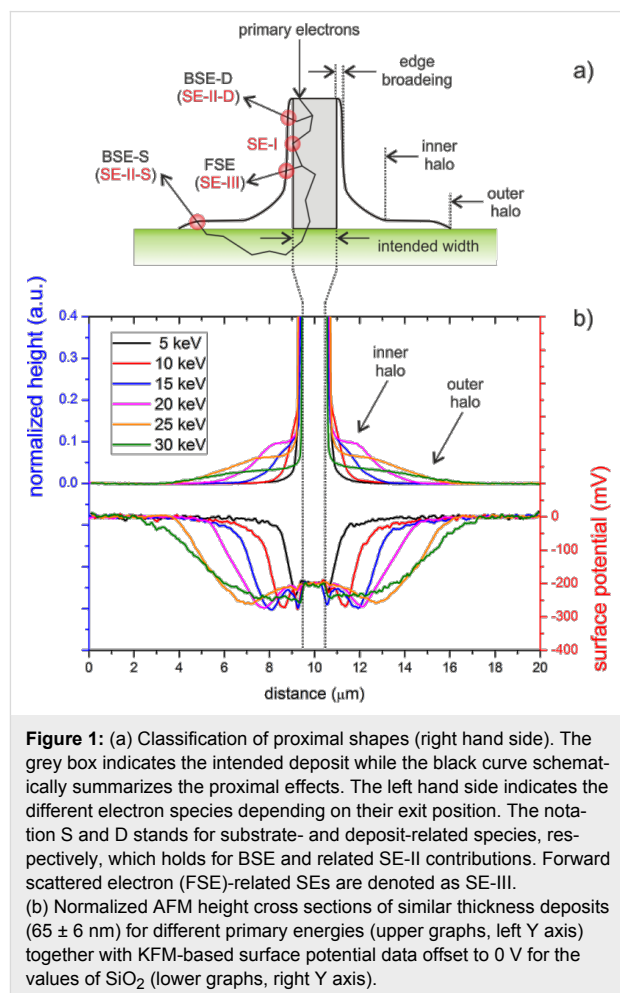
Figure 1: (a) Classification of proximal shapes (right hand side). The grey box indicates the intended deposit while the black curve schematically summarizes the proximal effects. The left hand side indicates the different electron species depending on their exit position. The notation S and D stands for substrate- and deposit-related species, respectively, which holds for BSE and related SE-II contributions. Forward scattered electron (FSE)-related SEs are denoted as SE-III. (b) Normalized AFM height cross sections of similar thickness deposits (65 ± 6 nm) for different primary energies (upper graphs, left Y axis) together with KFM-based surface potential data offset to 0 V for the values of SiO$_2$ (lower graphs, right Y axis).
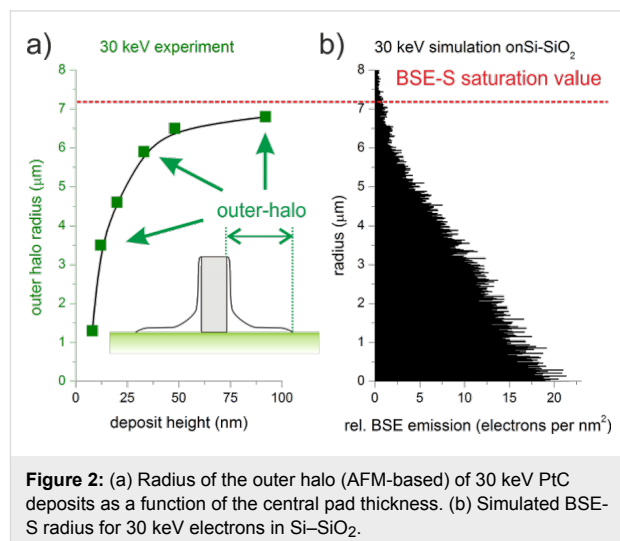
Figure 2: (a) Radius of the outer halo (AFM-based) of 30 keV PtC deposits as a function of the central pad thickness. (b) Simulated BSE-S radius for 30 keV electrons in Si–SiO$_2$.

Functionality

In the following a two-step approach is followed: First, the surface potential, which reflects the chemical composition and its electronic properties, and, subsequently, the electric conductivity are mapped. The combination of both measurements allows one then to derive the scaling behavior of functional (electrically conductive) and non-functional (electrically insulating) proximity regions in dependence on the primary electron energy and the deposit thickness.
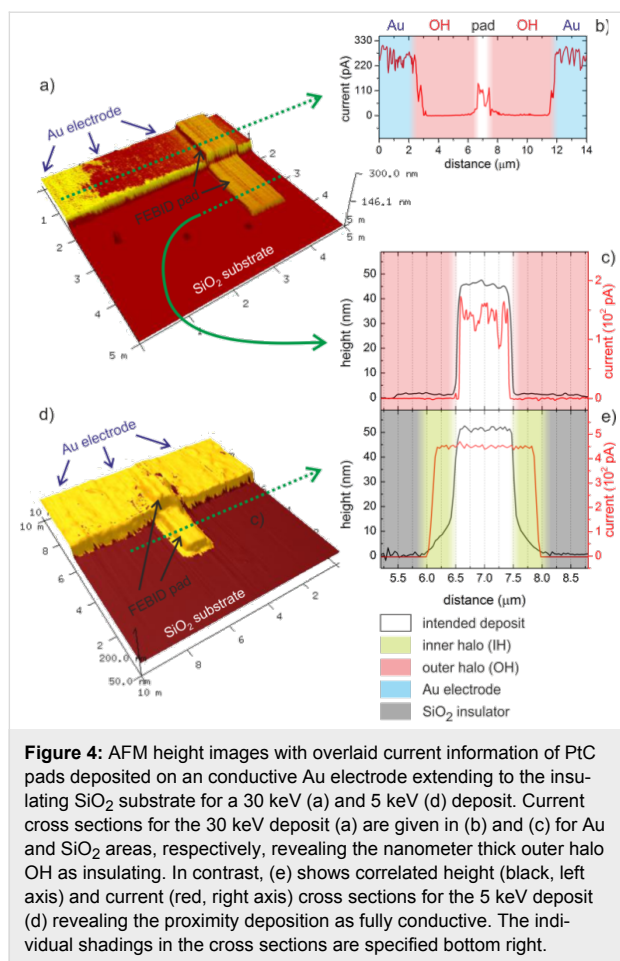
To access the chemical properties of the deposits, Kelvin force microscopy (KFM) was conducted as it provides a laterally resolved measurement of the variations in surface potential. Figure 3 gives a representative AFM height image (a) together with the corresponding surface potential (b) of a ca. 9 nm thick deposit fabricated at 25 keV. Correlated cross sections are shown in Figure 3c for the height (top), the tapping phase (center, green), and the surface potential (bottom, blue). As can be seen the surface potential reveals three different levels: 1) the SiO_2 substrate (offset to zero); 2) the deposit with a potential difference of about −150 mV; and 3) another level for the outer halo at −300 mV.

The essential information is the fact that the surface potential of the outer halo level is *below* those of both the PtC pad and the SiO_2. This excludes the idea that the formation of this intermediate level is a simple convolution of substrate and central deposit. Once the outer halo gets thinner at increasing radii, the associated surface potential gets increasingly dominated by the SiO_2 substrate underneath and finally approaches the same

value. As KFM gives insight into the electronic band structure, the distinct potential of the outer halo indicates different chemistries and/or functional properties compared to the central PtC deposit. This is further supported by the tapping phase signal (central plot in Figure 3c) that suggests different mechanical properties for the outer halo. As KFM is not able to reveal the electric conductivity, conductive-AFM (C-AFM) measurements were carried out. For that, FEBID structures were deposited across the edge between a grounded Au electrode and the highly insulating SiO_2 substrate as shown in Figure 4a for a 40 nm thick 30 keV deposit. The color scale corresponds to the correlated current signals through sample/deposit/AFM tip and brighter colors indicate higher conductivities. Figure 4b gives a current cross section along the upper dotted green line in Figure 4a revealing three different levels: 1) highest currents for the conductive Au electrode as expected (blue region); 2) reduced currents at the central deposit area due to the lower conductivity of as-deposited PtC structures (white regions) [28,31,41]; and 3) zero current in between according to the darkest areas in Figure 4a (red zones). The latter can be assigned to the very thin outer halo (less than 2 nm thickness), which corresponds well with the observation of different surface potentials for the same regions. To confirm the finding of a non-conductive outer halo, another current cross section on the insulating SiO_2 substrate is shown in Figure 4c (along the lower dotted line in Figure 4a) also revealing electrical conductivity only for the central deposit (white area). From this data we can conclude that lower surface potentials (KFM) indicate lower electric conductivities (C-AFM), further denoted as "functionality".
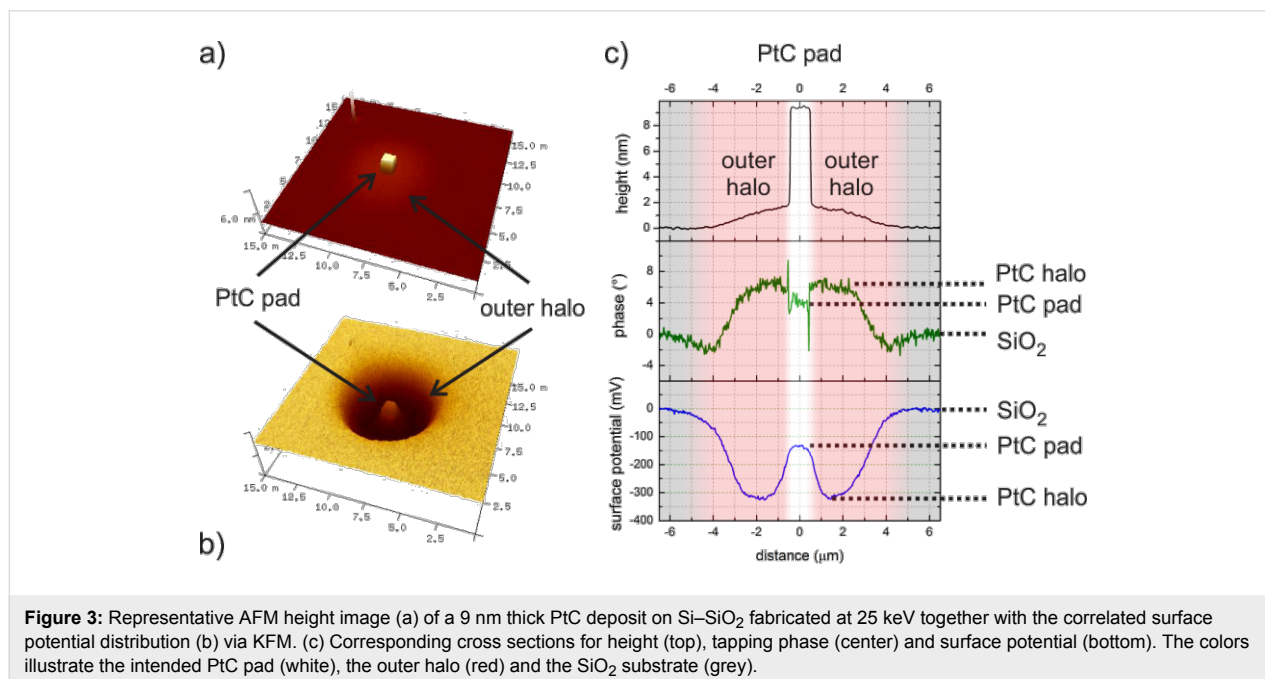
Figure 3: Representative AFM height image (a) of a 9 nm thick PtC deposit on Si–SiO₂ fabricated at 25 keV together with the correlated surface potential distribution (b) via KFM. (c) Corresponding cross sections for height (top), tapping phase (center) and surface potential (bottom). The colors illustrate the intended PtC pad (white), the outer halo (red) and the SiO₂ substrate (grey).

Figure 4: AFM height images with overlaid current information of PtC pads deposited on an conductive Au electrode extending to the insulating SiO$_2$ substrate for a 30 keV (a) and 5 keV (d) deposit. Current cross sections for the 30 keV deposit (a) are given in (b) and (c) for Au and SiO$_2$ areas, respectively, revealing the nanometer thick outer halo OH as insulating. In contrast, (e) shows correlated height (black, left axis) and current (red, right axis) cross sections for the 5 keV deposit (d) revealing the proximity deposition as fully conductive. The individual shadings in the cross sections are specified bottom right.

Figure 5: (a) Functional classification of proximity deposition based on KFM measurements. (b) and (c) show the energy- and thickness-dependent radii of the non-functional and the fully-functional radius, respectively. A detailed explanation is given in the main text.

Following this correlation approach we can classify the lateral functionalities based on KFM data as summarized in Figure 5a: 1) a fully-functional range for potential values very similar to the central deposit (white area); 2) a non-functional radius starting from lowest potential values to highest detectable deviation from the substrates (red zone); and 3) a transition area between (1) and (2) (green range). Figure 5b summarizes the non-functional radii as a function of the primary energy for different thicknesses (see bottom legend). Associated simulations of substrate-related BSE-S radii (green spheres) are in good agreement with the experimentally observed radii of the outer halo, which further confirms their strong correlation. The decaying behavior for thinnest pads at highest energies (encircled on the right hand side) can be explained by the decreasing number of primary electrons together with the low BSE yield at such high primary energies. This leads to very low areal BSE emission at the highest radial positions which can (partly) dissociate precursor molecules, however, below the KFM detection sensitivity. On the other hand, the increasing non-functional radius for thicker deposits at lower energies (encircled on the left hand side) is a result of increasing FSE contributions as will be discussed in the following section.
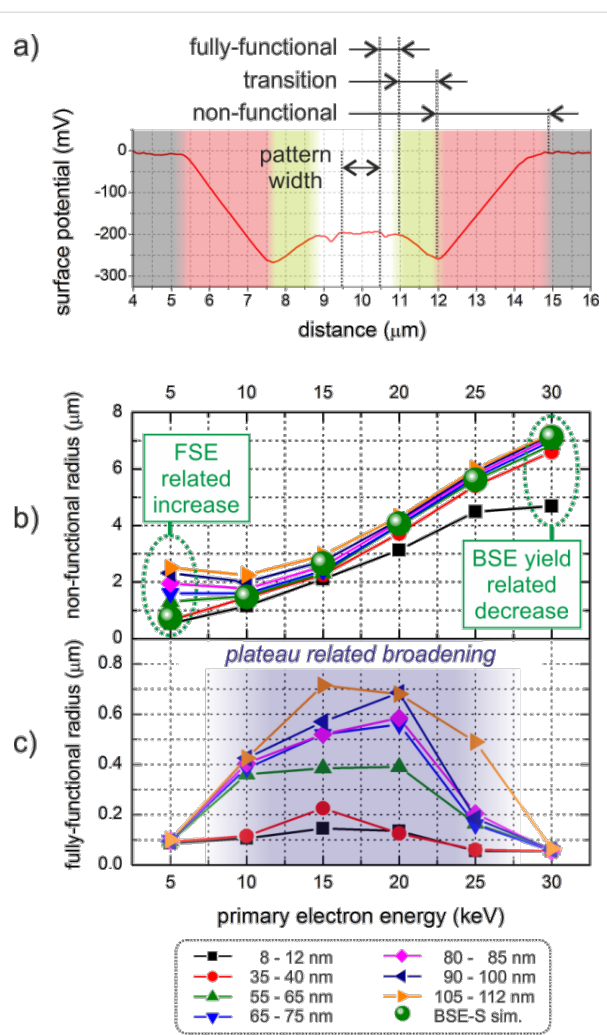
Interestingly, the fully-functional radius (Figure 5c) shows the smallest values at high and low primary energies while considerable broadening is observed for intermediate energies. Correlation with the morphological data reveals the distinct proximity plateaus (see Figure 1b and supplement Figure S2) as partly electrically functional areas as indicated by the blue shading in Figure 5c. The origin of the plateaus is discussed in the following section.

Discussion

At this point it is important to note that the present study primarily focuses on the qualitative description of energy- and height-dependent proximity effects with respect to morphology and functionality. The latter describes the electrical conductivity and is derived from combined C-AFM and KFM measurements. The absolute values for halo heights and func-

tional radii might slightly change for different precursor regime conditions but show the same qualitative scaling behavior. The discussion starts with highest primary energies due to simplicity further expanded by the more complex situation for low primary energies. Finally, intermediate energies are discussed, which show distinct morphological proximity plateaus as evident in Figure 1.

High primary energies

First, we focus on the non-functional outer halo (C-AFM, Figure 4) revealing distinctly different surface potentials compared to the central deposit (KFM, Figure 3). It is well-known that the dissociation of the $MeCpPt(IV)Me_3$ precursor molecules is not a single step process [2,3,16,17]. Thus, we suggest the low areal flux of substrate related BSE-S/SE-II-S at high primary energies results in a partial dissociation, e.g., single methyl dissociation [51], which hinders the formation of Pt nanograins. This is further supported by the very low thickness of the OH [44]. This can explain both, the distinctly different surface potential as well as the insulating characteristic of the outer halo observed via KFM and C-AFM, respectively. To understand the edge-broadening effect a closer look at the edge morphology is required as shown in Figure 6a, which is a normalized plot of 30 keV deposits with different thicknesses. The dotted vertical line gives the last patterning point at the edge (intended patterning edge) revealing the final slope to be symmetrically distributed at half maximum. Previous studies by Arnold et al. [44] revealed that the achievable width of single lines is determined by BSE/SE-II contributions from the deposit itself (BSE-D/SE-II-D). Analogous to that work, Figure 6b shows the simulated radial BSE-D distribution for the outermost patterning point (30 keV in 30 nm PtC_5 on Si–SiO_2 (500 nm)). The direct comparison (highlighted by the red shading) shows good agreement between the lateral BSE-D spread and the symmetric slope determined via simulations and experiments, respectively. This strongly suggests that the edge-broadening (EB) outside of the intended deposit is influenced by SE-II contributions, which are triggered by BSE originating from the deposit. Detailed KFM analyses of EB areas reveal the same surface potential as the central deposit suggesting a fully-functional character (same electric properties as the central deposit).

The observation of an increasing slope inside the intended footprint is described in detail by Winkler et al. [52] and can be mainly attributed to the patterning itself: While volume growth rates at the very central patterning points are supported by deposit related BSE/SE-II contributions in X and Y, patterning points at the edges and corners show a reduced number of neighboring patterning points [18]. The resulting decrease of deposit-related BSE/SE-II contributions then leads to decreased
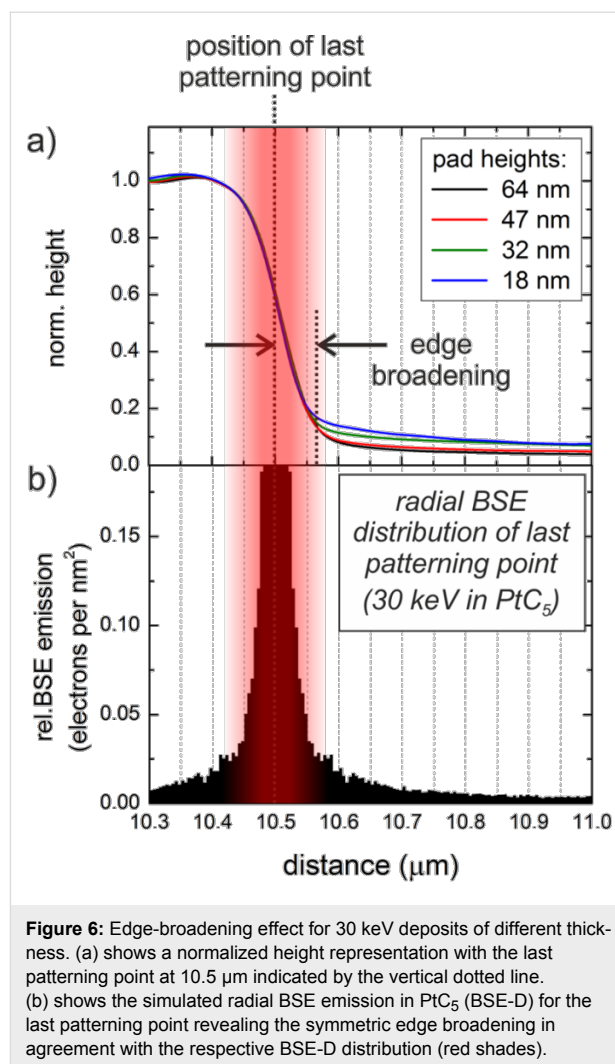
Figure 6: Edge-broadening effect for 30 keV deposits of different thickness. (a) shows a normalized height representation with the last patterning point at 10.5 μm indicated by the vertical dotted line. (b) shows the simulated radial BSE emission in PtC_5 (BSE-D) for the last patterning point revealing the symmetric edge broadening in agreement with the respective BSE-D distribution (red shades).

net volume growth rates at the outermost patterning edges and corners [18,52].

In summary, the observed edge-broadening for high primary electron energy is an unavoidable effect ultimately contributing to the finally achievable, fully-functional edge sharpness. It is important to mention that absolute values of the proximity radii strongly depend on the experimental setup as impressively demonstrated by van Oven et al. and Hari et al. [15,43].

Low primary energies

Next, the broadening effects for lowest energies and increasing deposit thicknesses are discussed. Figure 7 shows a normalized set of AFM height cross-sections of 5 keV deposits of different thickness (b) with the last patterning point at the edge being indicated by the dashed line. Evidently, a symmetric slope around the pattern edge can be identified (red shading) followed by a strong decay (blue shading). The symmetric slope can again be explained by the radial BSE distribution origi-
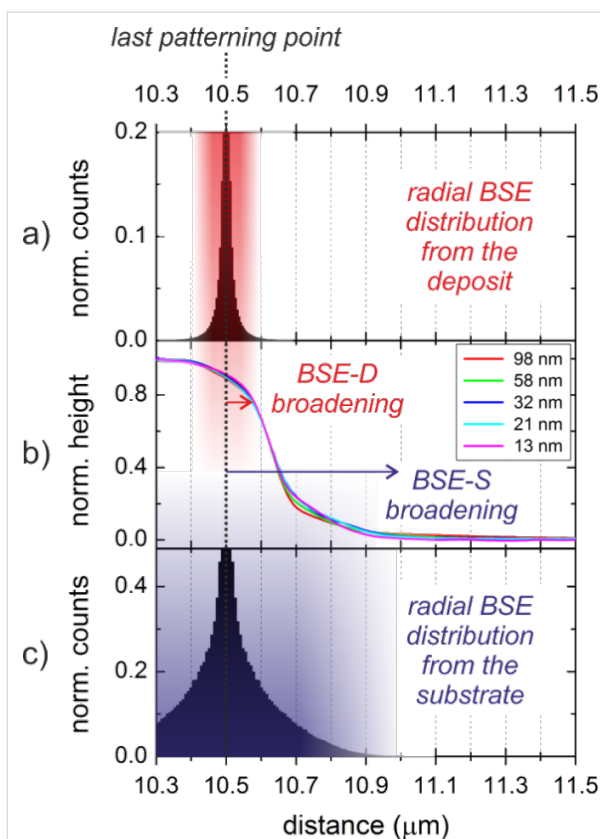
Figure 7: Broadening effects for 5 keV deposits of different thickness. (b) shows the normalized height representation (absolute pad thicknesses are specified in the legend) with the last patterning point at 10.5 µm (dotted vertical line). (a) shows the simulated BSE-D distribution of 5 keV electrons in PtC$_5$ for the last patterning point which again is in good agreement with the symmetric edge broadening (red shades). (c) gives the simulated BSE-S distribution of 5 keV electrons in the substrate which can explain the outer proximity deposition (blue shades).
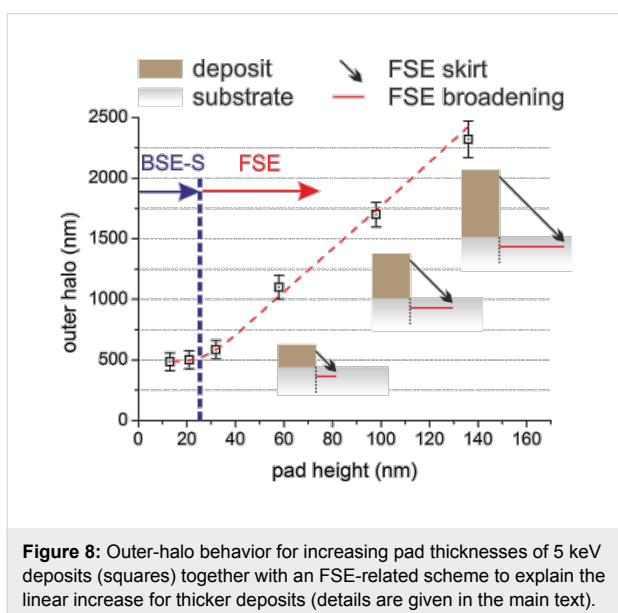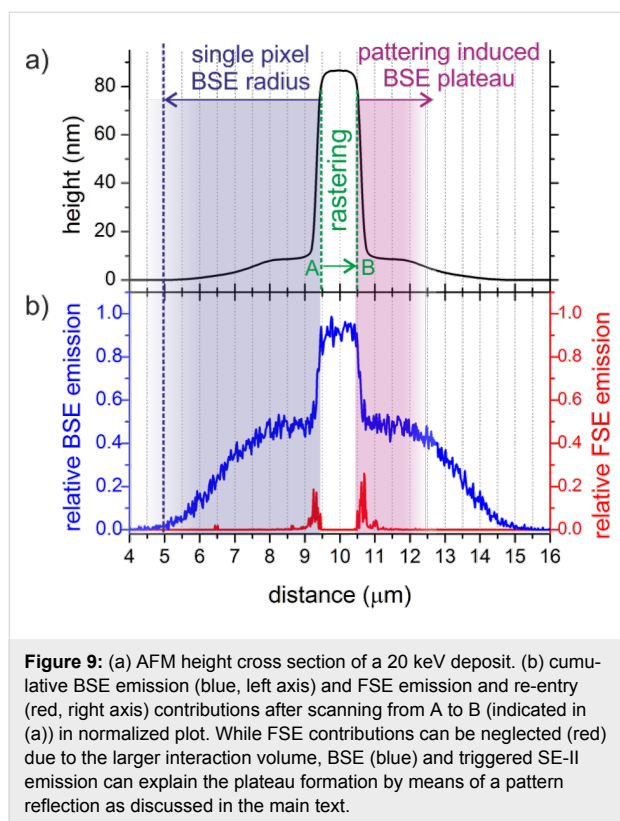

Figure 8: Outer-halo behavior for increasing pad thicknesses of 5 keV deposits (squares) together with an FSE-related scheme to explain the linear increase for thicker deposits (details are given in the main text).

nating from the deposit (BSE-D and entailed SE-II-D) as shown for the last patterning point in Figure 7a (correlated red shading). The large scale proximity deposition can clearly be attributed to substrate-related BSE/SE-II electrons (BSE-S/SE-II-S) as shown by correlated simulations in Figure 7c (correlated blue shades). Very careful KFM analyses with respect to largest detectable outer-halo radii revealed a behavior which is shown in Figure 8 by the squares. For deposit thicknesses below 30 nm, outer-halo radii of around 450 nm are found, which are in good agreement with the BSE-S radius shown in Figure 7c (schematically indicated by the vertical dashed line in Figure 8). Thicker deposits, however, led to an almost linear increase of the outer halo (dashed red line). To explain this proximity deposition the small interaction volume for low energy electrons in the growing deposit has to be considered, which leads to forward scattered electrons (FSE) at the sidewalls followed by re-entry in the surrounding areas [18,53]. Please note that similar to the SE-II emission we expect FSE triggered type-III secondary electrons (SE-III) as the predominantly dissociating species. As indicated by the inset schematic in Figure 8, the growing deposits (brown boxes) lead to an almost linearly scaling FSE radius (red lines), which corroborates the experimentally observed scaling of the outer halo. This strong height-dependent broadening also explains why the non-functional radius increases as shown in Figure 5b (encircled green).

In summary, we conclude from this section that for low energy deposits, the highest lateral sharpness can only be achieved for thin deposits for which the FSE contributions are negligible. In such a situation the deposit-related BSE-D/SE-II-D broaden the edges (Figure 7a). This broadening is overlaid by a substrate-related broadening due to BSE-S/SE-II-S contributions (Figure 7c). Thicker deposits lead to increasing FSE/SE-III contributions that further broaden the deposit although the related halo thickness is very thin (less than 2 nm for highest deposits of 136 nm). The non-conductive character is attributed to the low FSE/SE-III re-entry yield and thus to a low dissociation rate. As a general rule deduced here, low primary energies should only be used for very thin deposits in order to achieve sharp deposit edges.

Intermediate primary energies

Finally, the distinct plateaus for intermediate primary energies (Figure 1b) and the corresponding strongly varying functionalities (Figure 5d) need to be explained. As evident in Figure 9a, 20 keV deposits reveal a distinct morphological plateau outside the intended deposit. To explain this feature, the cumulative BSE and FSE emission during a patterning line from point A to B (indicated in green) has to be considered. This is shown in Figure 9b by a normalized representation in which the FSE simulation takes exiting and re-entering electrons into account

Figure 9: (a) AFM height cross section of a 20 keV deposit. (b) cumulative BSE emission (blue, left axis) and FSE emission and re-entry (red, right axis) contributions after scanning from A to B (indicated in (a)) in normalized plot. While FSE contributions can be neglected (red) due to the larger interaction volume, BSE (blue) and triggered SE-II emission can explain the plateau formation by means of a pattern reflection as discussed in the main text.

as well. As is evident, FSE contributions (red) are irrelevant for the plateau formation due to the low scattering of 20 keV electrons in sub-100 nm PtC deposits. The cumulative BSE distribution (blue), however, shows two different features. As indicated by the blue shading on the left side of the intended deposit, the substrate-related BSE-S radius is in the range of about 5 μm in agreement with the outer-halo radius. The more important features are the plateau-like shapes outside the intended deposit as highlighted by the right hand red shade in Figure 9. These shapes evolve as a consequence of the patterning process itself: When rastering from A to B, the lateral BSE-S distribution from the substrate is a superposition of each single point along the patterning line leading to the blue BSE emission curve. As evident the profile shape is in very good agreement with the experimentally observed plateau (black curve) and can be understood as pattern reflection outside the intended structure (red shade). Once, point B is reached a continuous decay follows with a total radius of about 5 μm in agreement with simulated BSE radius stemming from the substrate (blue shades). Please note, the very distinct plateau formation at 20 keV is a complex interplay between primary electron energy, the substrate material used and the patterning footprint geometry and by that complicated to predict. As general rule, however, it can be deduced that intermediate primary electron energies should be avoided when aiming for highest lateral resolution (see also Figure 5c).

Conclusion

In conclusion, we have qualitatively studied side-wall broadening effects for three-dimensional FEBID deposits using MeCpPt(IV)Me$_3$ precursor on Si–SiO$_2$ substrates. It is found that highest primary electron energies lead to sharpest deposit edges widely independent of the thickness in a sub-140 nm regime. If samples are not compatible with high energies, low primary energies are an alternative, however, with a strong thickness dependency due to increasing contributions from forward scattered electrons (see Figure S3, Supporting Information File 1). The important finding of this study, however, is the fact that intermediate primary energies can lead to significant edge broadening as a consequence of substrate-related backscattered electrons resulting in distinct plateaus around the intended deposit. Finally, as previously observed for quasi-1D single lines [44], an unavoidable edge broadening occurs as the result of deposit-related backscattered electrons. It is important to note that absolute values for the observed broadening effects strongly depend on the deposit chemistry (different precursors), the working regime (beam current, dwell times, point pitches) as well as on the substrate type as spatial electron trajectories change with these properties. Nevertheless, the findings of this study give a general qualitative insight into the behavior and scaling of proximity deposition that ultimately limits the achievable edge sharpness and by that lateral resolution (see Figure S4, Supporting Information File 1).

Supporting Information

Supporting Information File 1
Additional experimental data.
[http://www.beilstein-journals.org/bjnano/content/supplementary/2190-4286-6-47-S1.pdf]

Acknowledgements

References

1. Randolph, S. J.; Fowlkes, J. D.; Rack, P. D.
   Crit. Rev. Solid State Mater. Sci. **2006,** *31,* 55–89.
   doi:10.1080/10408430600930438

2. Utke, I.; Hoffmann, P.; Melngailis, J. *J. Vac. Sci. Technol., B* **2008,** *26,* 1197. doi:10.1116/1.2955728

3. Van Dorp, W. F.; Hagen, C. W. *J. Appl. Phys.* **2008,** *104,* 81301–81342. doi:10.1063/1.2977587

4. Utke, I.; Russell, P. E. *Nanofabrication using focused ion and electron beams: principles and applications;* Oxford University Press: New York, NY, USA, 2012.

5. Van Dorp, W. F.; Hansen, T. W.; Wagner, J. B.; De Hosson, J. T. M. *Beilstein J. Nanotechnol.* **2013,** *4,* 474–480. doi:10.3762/bjnano.4.56

6. Botman, A.; Mulders, J. J. L.; Hagen, C. W. *Nanotechnology* **2009,** *20,* 372001. doi:10.1088/0957-4484/20/37/372001

7. Bret, T.; Utke, I.; Bachmann, A.; Hoffmann, P. *Appl. Phys. Lett.* **2003,** *83,* 4005–4007. doi:10.1063/1.1626261

8. Utke, I.; Gölzhäuser, A. *Angew. Chem., Int. Ed.* **2010,** *49,* 9328–9330. doi:10.1002/anie.201002677

9. Plank, H.; Gspan, C.; Dienstleder, M.; Kothleitner, G.; Hofer, F. *Nanotechnology* **2008,** *19,* 485302–485309. doi:10.1088/0957-4484/19/48/485302

10. Plank, H.; Haber, T.; Gspan, C.; Kothleitner, G.; Hofer, F. *Nanotechnology* **2013,** *24,* 175305. doi:10.1088/0957-4484/24/17/175305

11. Utke, I.; Friedli, V.; Purrucker, M.; Michler, J. *J. Vac. Sci. Technol., B* **2007,** *25,* 2219–2223. doi:10.1116/1.2789441

12. Fowlkes, J. D.; Rack, P. D. *ACS Nano* **2010,** *4,* 1619–1629. doi:10.1021/nn901363a

13. Smith, D. A.; Fowlkes, J. D.; Rack, P. D. *Small* **2008,** *4,* 1382–1389. doi:10.1002/smll.200701133

14. Fowlkes, J. D.; Randolph, S. J.; Rack, P. D. *J. Vac. Sci. Technol., B* **2005,** *23,* 2825–2832. doi:10.1116/1.2101732

15. Van Oven, J. C.; Berwald, F.; Berggren, K. K.; Kruit, P.; Hagen, C. W. *J. Vac. Sci. Technol., B* **2011,** *29,* 06F305. doi:10.1116/1.3640743

16. Van Dorp, W. F.; Wnuk, J. D.; Gorham, J. M.; Fairbrother, D. H.; Madey, T. E.; Hagen, C. W. *J. Appl. Phys.* **2009,** *106,* 074903. doi:10.1063/1.3225091

17. Wnuk, J. D.; Gorham, J. M.; Fairbrother, D. H. *J. Phys. Chem. C* **2009,** *113,* 12345–12354. doi:10.1021/jp900966m

18. Plank, H.; Smith, D. A.; Haber, T.; Rack, P. D.; Hofer, F. *ACS Nano* **2012,** *6,* 286–294. doi:10.1021/nn204237h

19. Smith, D. A.; Fowlkes, J. D.; Rack, P. D. *Nanotechnology* **2008,** *19,* 415704–415711. doi:10.1088/0957-4484/19/41/415704

20. Mulders, J. J. L.; Belova, L. M.; Riazanova, A. *Nanotechnology* **2011,** *22,* 055302. doi:10.1088/0957-4484/22/5/055302

21. Córdoba, R.; Sesé, J.; De Teresa, J. M.; Ibarra, M. R. *Microelectron. Eng.* **2010,** *87,* 1550–1553. doi:10.1016/j.mee.2009.11.027

22. Roberts, N. A.; Fowlkes, J. D.; Magel, G. A.; Rack, P. D. *Nanoscale* **2013,** *5,* 408–415. doi:10.1039/c2nr33014h

23. Roberts, N. A.; Magel, G. A.; Hartfield, C. D.; Moore, T. M.; Fowlkes, J. D.; Rack, P. D. *J. Vac. Sci. Technol., A* **2012,** *30,* 041404. doi:10.1116/1.4731254

24. Langford, R. M.; Ozkaya, D.; Sheridan, J.; Chater, R. *Microsc. Microanal.* **2004,** *10* (Suppl. 2), 1122–1123. doi:10.1017/S1431927604883417

25. Gopal, V.; Stach, E. A.; Radmilovic, V. R.; Mowat, I. A. *Appl. Phys. Lett.* **2004,** *85,* 49–51. doi:10.1063/1.1765736

26. Botman, A.; Mulders, J. J. L.; Weemaes, R.; Mentink, S. *Nanotechnology* **2006,** *17,* 3779–3785. doi:10.1088/0957-4484/17/15/028

27. Langford, R. M.; Wang, T.-X.; Ozkaya, D. *Microelectron. Eng.* **2007,** *84,* 784–788. doi:10.1016/j.mee.2007.01.055

28. Huth, M.; Porrati, F.; Schwalb, C.; Winhold, M.; Sachser, R.; Dukic, M.; Adams, J.; Fantner, G. *Beilstein J. Nanotechnol.* **2012,** *3,* 597–619. doi:10.3762/bjnano.3.70

29. Schwalb, C. H.; Grimm, C.; Baranowski, M.; Sachser, R.; Porrati, F.; Reith, H.; Das, P.; Müller, J.; Völklein, F.; Kaya, A.; Huth, M. *Sensors* **2010,** *10,* 9847–9856. doi:10.3390/s101109847

30. Frabboni, S.; Gazzadi, G. C.; Felisari, L.; Spessot, A. *Appl. Phys. Lett.* **2006,** *88,* 213116. doi:10.1063/1.2206996

31. Plank, H.; Kothleitner, G.; Hofer, F.; Michelitsch, S. G.; Gspan, C.; Hohenau, A.; Krenn, J. *J. Vac. Sci. Technol., B* **2011,** *29,* 51801–51807. doi:10.1116/1.3622314

32. Geier, B.; Gspan, C.; Winkler, R.; Schmied, R.; Fowlkes, J. D.; Fitzek, H.; Rauch, S.; Rattenberger, J.; Rack, P. D.; Plank, H. *J. Phys. Chem. C* **2014,** *118,* 14009–14016. doi:10.1021/jp503442b

33. Sachser, R.; Reith, H.; Huzel, D.; Winhold, M.; Huth, M. *ACS Appl. Mater. Interfaces* **2014,** *6,* 15868–15874. doi:10.1021/am503407y

34. Perentes, A.; Bachmann, A.; Leutenegger, M.; Utke, I.; Sandu, C.; Hoffmann, P. *Microelectron. Eng.* **2004,** *73–74,* 412–416. doi:10.1016/S0167-9317(04)00146-7

35. Utke, I.; Jenke, M. G.; Röling, C.; Thiesen, P. H.; Iakovlev, V.; Sirbu, A.; Mereuta, A.; Caliman, A.; Kapon, E. *Nanoscale* **2011,** *3,* 2718–2722. doi:10.1039/c1nr10047e

36. Gavagnin, M.; Wanzenboeck, H. D.; Belić, D.; Bertagnolli, E. *ACS Nano* **2013,** *7,* 777–784. doi:10.1021/nn305079a

37. Gabureac, M. S.; Bernau, L.; Boero, G.; Utke, I. *IEEE Trans. Nanotechnol.* **2013,** *12,* 668–673. doi:10.1109/TNANO.2013.2266733

38. Serrano-Ramón, L.; Córdoba, R.; Rodríguez, L. A.; Magén, C.; Snoeck, E.; Gatel, C.; Serrano, I.; Ibarra, M. R.; De Teresa, J. M. *ACS Nano* **2011,** *5,* 7781–7787. doi:10.1021/nn201517r

39. Fernández-Pacheco, A.; De Teresa, J. M.; Córdoba, R.; Ibarra, M. R. *J. Phys. D: Appl. Phys.* **2009,** *42,* 055005. doi:10.1088/0022-3727/42/5/055005

40. Gabureac, M.; Bernau, L.; Utke, I.; Boero, G. *Nanotechnology* **2010,** *21,* 115503. doi:10.1088/0957-4484/21/11/115503

41. Porrati, F.; Sachser, R.; Schwalb, C. H.; Frangakis, A. S.; Huth, M. *J. Appl. Phys.* **2011,** *109,* 063715. doi:10.1063/1.3559773

42. Kolb, F.; Schmoltner, K.; Huth, M.; Hohenau, A.; Krenn, J.; Klug, A.; List, E. J. W.; Plank, H. *Nanotechnology* **2013,** *24,* 305501. doi:10.1088/0957-4484/24/30/305501

43. Hari, S.; Hagen, C. W.; Verduin, T.; Kruit, P. *J. Micro/Nanolithogr., MEMS, MOEMS* **2014,** *13,* 033002. doi:10.1117/1.JMM.13.3.033002

44. Arnold, G.; Timilsina, R.; Fowlkes, J.; Orthacker, A.; Kothleitner, G.; Rack, P. D.; Plank, H. *ACS Appl. Mater. Interfaces* **2014,** *6,* 7380–7387. doi:10.1021/am5008003

45. Winkler, R.; Fowlkes, J.; Szkudlarek, A.; Utke, I.; Rack, P. D.; Plank, H. *ACS Appl. Mater. Interfaces* **2014,** *6,* 2987–2995. doi:10.1021/am405591d

46. Code::Blocks. http://www.codeblocks.org (accessed Oct 19, 2014).

47. Winkler, R.; Geier, B.; Plank, H. *Appl. Phys. A* **2014,** *117,* 1675–1688. doi:10.1007/s00339-014-8496-y

48. Drouin, D.; Couture, A. R.; Joly, D.; Tastet, X.; Aimez, V.; Gauvin, R. *Scanning* **2007,** *29,* 92–101. doi:10.1002/sca.20000

49. Botman, A.; de Winter, D. A. M.; Mulders, J. J. L. *J. Vac. Sci. Technol., B* **2008,** *26,* 2460–2463. doi:10.1116/1.2976576

50. Van Dorp, W. F. *Phys. Chem. Chem. Phys.* **2012,** *14,* 16753–16759. doi:10.1039/c2cp42275a

51. Spencer, J. A.; Rosenberg, S. G.; Barclay, M.; Wu, Y.-C.;
McElwee-White, L.; Howard Fairbrother, D. *Appl. Phys. A* **2014,** *117,*
1631–1644. doi:10.1007/s00339-014-8570-5

52. Winkler, R.; Szkudlarek, A.; Fowlkes, J. D.; Rack, P. D.; Utke, I.;
Plank, H. *ACS Appl. Mater. Interfaces* **2015,** *7,* 3289–3297.
doi:10.1021/am508052k

53. Bret, T.; Utke, I.; Hoffmann, P.; Abourida, M.; Doppelt, P. Electron
range effects in focused electron beam induced deposition of 3D
nanostructures. In *Microelectronic Engineering,* Micro- and
Nano-Engineering MNE 2005, Vienna, Austria, Sept 19–22, 2005;
Loeschner, H., Ed.; Elsevier: Doordrecht, Netherlands, 2006;
pp 1482–1486. doi:10.1016/j.mee.2006.01.146

Electron-stimulated purification of platinum nanostructures grown via focused electron beam induced deposition

Brett B. Lewis[1], Michael G. Stanford[1], Jason D. Fowlkes[1,2], Kevin Lester[2], Harald Plank[3] and Philip D. Rack[*1,2]

Address:
[1]Materials Science and Engineering Department, University of Tennessee, Knoxville, TN 37996, USA, [2]Nanofabrication Research Laboratory, Center for Nanophase Materials Sciences, Oak Ridge National Laboratory, Oak Ridge, TN 37381, USA and [3]Institute for Electron Microscopy and Nanoanalysis, Graz University of Technology, Steyrergasse 17, 8010 Graz, Austria

Email:
Philip D. Rack[*] - prack@utk.edu

* Corresponding author

Abstract

Platinum–carbon nanostructures deposited via electron beam induced deposition from MeCpPt(IV)Me$_3$ are purified during a post-deposition electron exposure treatment in a localized oxygen ambient at room temperature. Time-dependent studies demonstrate that the process occurs from the top–down. Electron beam energy and current studies demonstrate that the process is controlled by a confluence of the electron energy loss and oxygen concentration. Furthermore, the experimental results are modeled as a 2nd order reaction which is dependent on both the electron energy loss density and the oxygen concentration. In addition to purification, the post-deposition electron stimulated oxygen purification process enhances the resolution of the EBID process due to the isotropic carbon removal from the as-deposited materials which produces high-fidelity shape retention.

Introduction

Focused electron beam induced deposition (FEBID) is an attractive nanotechnology application because of its unique processing latitude and high precision resolution. FEBID uses an electron beam scanned in a specific pattern to dissociate and condense precursor material onto a substrate with high shape fidelity and a high degree of flexibility in the final form of the structure [1-3]. Additionally, FEBID is a more gentle technique as compared to similar techniques (e.g., ion beam induced deposition (IBID)) which is beneficial for many applications. The major drawback to FEBID is the purity of the final deposits which results from unwanted precursor fragments left after dissociation. The immediate potential for high impact applications makes the purification strategies for FEBID an important area of study. Several strategies have been investigated for puri-

fying EBID deposits (see Botman et al. [1] for a review). In situ purification strategies include: 1) precursors which easily decompose, for instance: WF_6 [4], $Co_2(CO)_8$ [5], and $AuClPF_3$ [6]; 2) mixed gas chemistries which react with the typically organic fragments [7,8] and 3) in situ substrate [9,10] or pulsed laser heating [11-13]. Several ex situ strategies have also been explored. Post annealing treatments in various ambients have been shown to improve the purity in PtC_x deposits from the $MeCpPt(IV)Me_3$ precursor and AuC_x deposits from the $Me_2Au(acac)$ precursor [14]. Recently, pulsed laser annealing of PtC_x deposits in O_2 was also successful in fully photo-thermally inducing a C–O reaction to remove the carbon matrix and densify the platinum [15]. Electron stimulated carbon reduction in vacuum was also demonstrated for PtC_x deposits [16,17]. Recently, Huth et al. explored a pulsed heating process in O_2 which accelerates the carbon removal relative to a constant heat source and is suggested to be facilitated via a catalytic Pt–O reaction [18]. Finally, Mackus et al. have demonstrated that EBID deposited seed layers can be used as catalyst sites for selective area atomic layer deposition growth of Pt layers [19].

To this end, we have recently studied the post-deposition purification of platinum–carbon nanostructures deposited from $MeCpPt(IV)Me_3$ via an electron stimulated reaction with oxygen gas [16] and water vapor [20]. Additionally we have investigated the purification of ruthenium–carbon nanostructures deposited from the bis(ethylcyclopentyldienyl) ruthenium(II) precursor via electron stimulated reaction with O_2 [21]. The electron-stimulated H_2O study was performed in a variable pressure scanning electron microscope (SEM) with a much higher pressure range of (10–100 Pa). In this regime, the purification appears to be reaction-rate-limited as various processing conditions could be reduced to a linear change in carbon content versus electron dose. Interestingly cross-sectional TEM studies revealed that the process occurred bottom-up where the purification rate is fastest at the end of the electron-beam range in the PtC_x deposit and eventually propagates to the surface. Our previous electron-stimulated purification study in O_2 was performed in a standard high-vacuum SEM and the O_2 was injected with a localized gas injection system. In the previous study we examined the purification rate as a function of deposit thickness, localized oxygen pressure and oxygen temperature. The results suggested that the rate-limiting mechanism is the electron stimulated reaction of oxygen molecules adsorbed/permeated into the PtC_x matrix. In this contribution we have expanded our initial study of the electron-stimulated purification in O_2, namely we have: 1) extended our temperature study to room temperature; 2) demonstrated that the process propagates top–down; 3) studied variable current and scanning parameters; 4) compared the purification rate as a function of beam energy; 5) compared the purification of pseudo-1-dimensional

wires; and 6) introduced an adsorption/permeation and reaction model, which can mimic the purification rates observed in the different regimes studied.

# Results and Discussion
Purification rates
In our previous work [16] we demonstrated that both the purification rate and final purity increased with decreasing temperature as the oxygen gas temperature decreased between 78 and 50 °C. It was speculated that this trend could be extended to room temperature due to the increased residence time of O_2 on the surface of the deposit, however, at temperatures below 50 °C, competitive $MeCpPt(IV)Me_3$ adsorption arrested the purification process. For this study, the GIS was cleaned of all trace $MeCpPt(IV)Me_3$ to mitigate the precursor contamination.

Thus, extending the study to room temperature, we re-examined the temperature dependence of the purification. Figure 1a,b illustrates in situ EDS spectra as a function of the purification time for the 25 and 78 °C studies, respectively. The initial deposit thickness before purification was ca. 100 nm. Figure 1c shows the integrated Pt/C ratios as a function of purification time and Figure 1d compares the ex situ EDS spectra for the purified deposits to the as-deposited spectra. Figure 1 clearly illustrates that the purification extent and rate is increased down to room temperature. This is consistent with our proposed mass-transport limited regime where the O_2 residence time increases the available O_2 on the surface (and ultimately diffused to the PtC_x matrix) so subsequent electron stimulated reactions and CO_x removal can proceed.

While the initial purification rates appear to be comparable, non-intuitively, the reaction rate at longer purification times and ultimately the final purity are both higher using a lower temperature reactive gas. Since higher temperature is expected to enhance oxygen diffusion, we speculate that the observed purification enhancement is due to an enhanced residence time for O_2 at lower temperature; subsequently setting up a larger concentration gradient to enhance the diffusive transport necessary for the reaction front to propagate. It is also worth commenting on the slight peak that appears in the EDS spectra of the fully purified deposit. This peak is present because the Pt-N peak overlaps with the C-K peak. For pure platinum, the N peak to M peak ratio is about 0.09 and thus is always present even in the absence of carbon.

Top–down reaction process
Figure 2 shows a series of relatively thick PtC_x pads that were originally grown to a thickness of ca. 400 nm and subsequently purified at 25 °C at various times from 1 to 12 min. After curing, the pads were sectioned using gallium focused ion beam
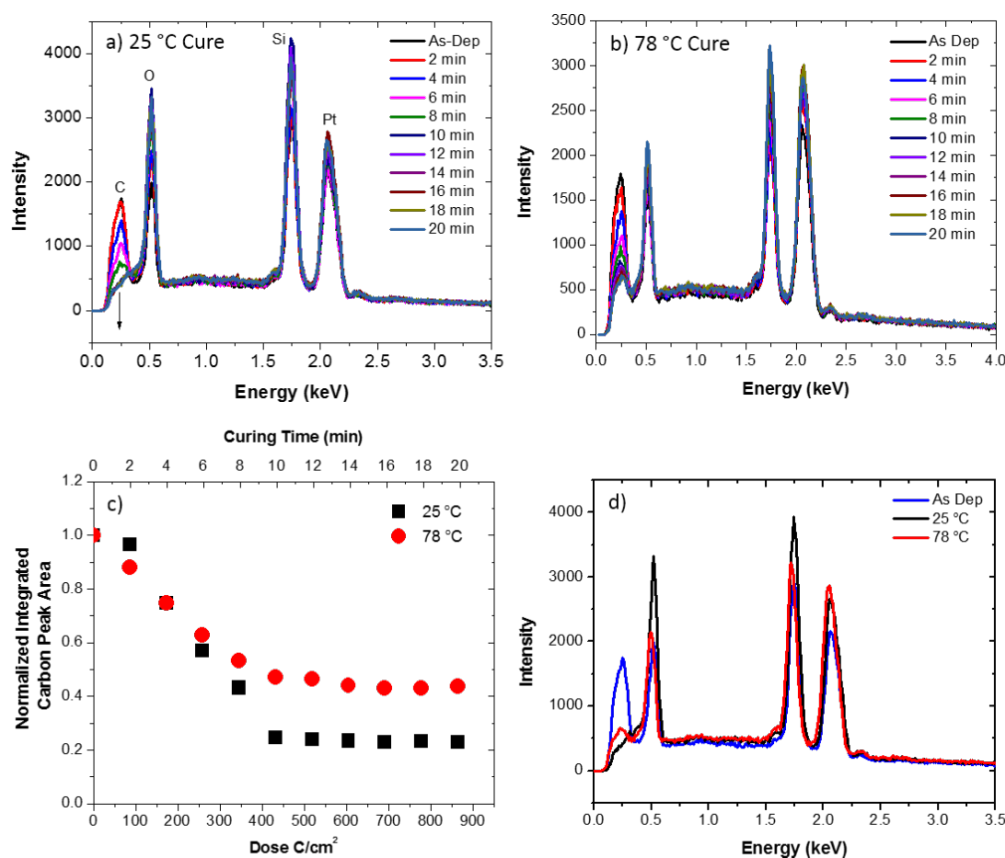
Figure 1: In situ EDS spectra of deposits purified using an electron beam with an energy of 5 keV, a current of 1.6 nA, a dwell time of 100 ns, and a pixel spacing of roughly 0.65 nm plotted for different purification times for the (a) 25 and (b) 78 °C O_2 flow studies. (c) Shows the normalized integrated Pt/C ratios as a function of purification time (top axis) and estimated received dose (bottom axis). (d) Shows the final EDS spectra after 20 min of purification.

milling to reveal the Pt layer thickness as a function of purification time. The SEM micrographs in Figure 2 depict the bright purified platinum on top of the darker un-purified PtC_x at the various purification time increments. As demonstrated, the electron stimulated O_2 purification process appears to be occurring in a top–down manner which is distinctly different from what is observed for higher pressure H_2O purification [20]. Consistent with the energy dispersive X-ray spectroscopy (EDS) measurements, the measured thickness versus time (Figure 2b) reveals an approximately linear purification rate (R^2 value of 0.97). The thickness of the pad after 2 and 4 min of purification shown on the plot is included for completeness, but the error bars based on multiple measurements are quite large because the the purified layer is very thin. This suggests the O_2 reactant surface concentration is relatively constant at the growth front. Based on amorphous carbon O_2 etching studies by Hopf et al. [22] we previously suggested that two types of O_2 species could be contributing to the process – namely: 1) O_2 adsorbing simultaneous with the electron flux and 2) O_2 adsorbed to high-binding energy carbon sites which result from electron irradiation. As

the process is now revealed to occur top–down, we suggest that the process is likely facilitated via a catalytic O_2-Pt dissociative adsorption process [18,23]; specifically, whereas O_2 has a very low adsorption energy (and thus short residence time) on amorphous carbon the Pt surface promotes a dissociative adsorption process with a higher binding energy with consequently higher equilibrium surface coverage.

Beam parameter studies

To explore this growth mechanism further we performed two additional studies: 1) increased pixel spacing on the live scan imaging during purification by a factor of 1.85, and 2) reduced the current to about 0.5 nA (ca. 3.6× reduction). Figure 3a compares the integrated carbon peak as a function of exposure time for the different scanning conditions. Clearly, changing the pixel spacing does not affect the purification process. The effect of increasing the pixel spacing has the effect of reducing the loop or frame time by a factor of about 3.5 (from 79 to 22 ms) and thus increasing the total number of loops by the same factor for a constant purification time. Therefore, if the process is
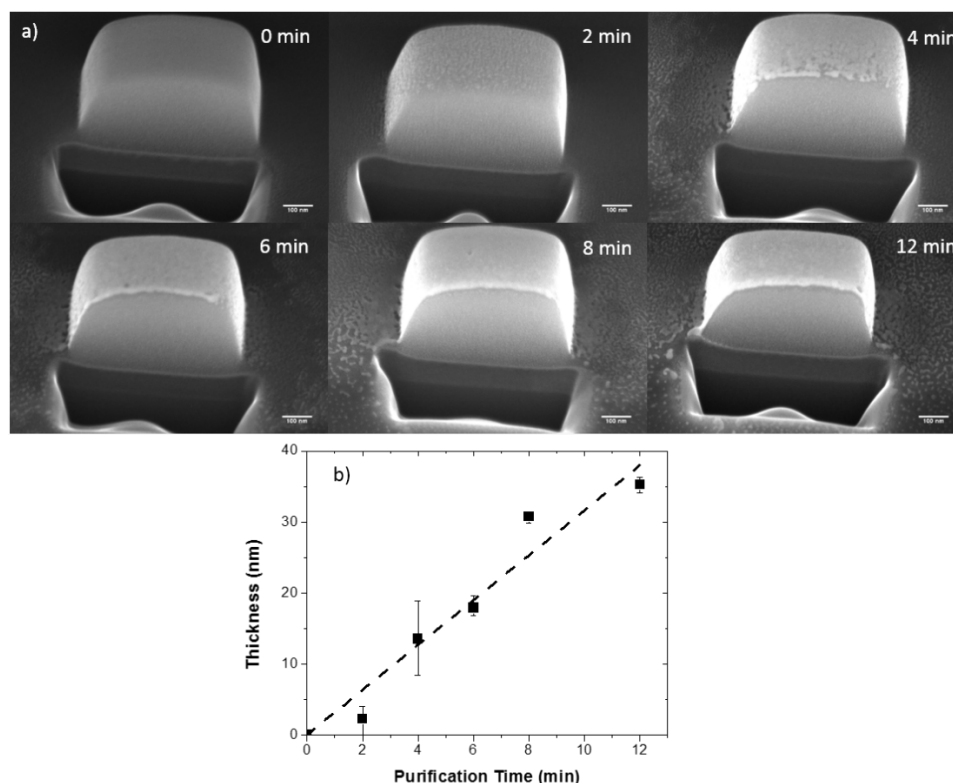
Figure 2: a) Cross-section SEM images of 400 nm thick PtC$_x$ deposits that were purified for 1, 2, 4, 6, 8, and 12 min (reading from left to right) demonstrating the linear, top–down nature of the purification process and b) is a plot of the purified layer thickness on the top of the pad against the total purification time.
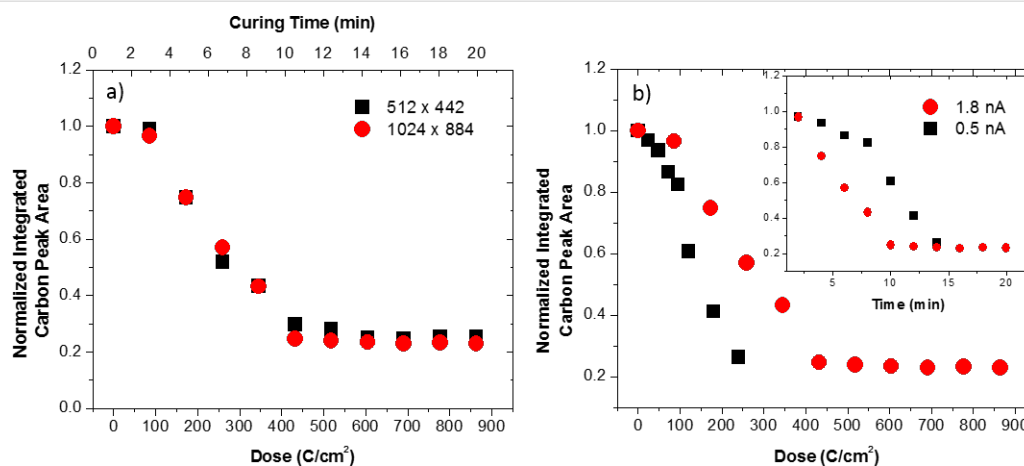
Figure 3: Normalized carbon peak area plotted as a function of a) curing time for the indicated pixel resolutions (note higher pixel resolution resulted in longer frame time) and b) dose for indicated beam currents. The inset depicts the same normalized carbon peak area as a function of time. The 1024 × 884 pixel resolution corresponds to ca. 0.65 nm point pitch while the 512 × 442 resolution corresponds to a point pitch of about 1.2 nm.

limited by the oxygen concentration as we suspect, the local oxygen concentration in the reaction zone appears to scale with the loop time and is not saturating. This is consistent with the estimated O$_2$ flux [16] of ca. 1×10^{16} O$_2$/(cm^2·s) and sticking probability of 0.05 approximating a monolayer coverage time

on the order of 100 ms. In the second study the current was decreased with the other scanning parameters held constant. Figure 3b is a plot of the integrated carbon peak as a function of effective dose (with an inset plotted versus time). Interestingly, while the current was decreased a factor of about 3.6, the purifi-

cation rate only decreased a factor of approximately two (see inset). This result implies that, at lower current, purification is more efficient (note that low current purifies at lower dose). This is consistent with a 2nd order reaction in which the reaction is a function of the electron flux (or as we will demonstrate the electron energy loss density) and the concentration of the O_2 reactant. At the beginning of the beam dwell the per-electron purification reaction probability is highest since the O_2 interfacial concentration is the highest. As the dwell time persists, O_2 is consumed and the reaction probability dynamically decreases. The lower current study indicates that the integrated efficiency during the entire pixel dwell time is approximately twice as high at low current as at high current due to the dynamic consumption of the O_2.

To investigate the effect of the purification rate with beam energy, twenty one identical 500 × 500 nm, ca. 80 nm thick pads were grown. The beam energies studied (and associated beam current as measured in a Faraday cup) were: 5 (1.8 nA), 7.5 (2.7 nA), 10 (3.1 nA), 15 (3.1 nA) and 20 keV (2.7 nA). The temporal evolution of the purification process was investigated with purification exposure times of 5, 7, 10 and 15 min for each beam energy. Figure 4a is a plot of the integrated EDS carbon intensity as a function of exposure dose (time × current / cross-sectional area) for the different beam energies. Consistent with electron stimulated reactions, the apparent reaction cross-section decreases with increasing beam energy [24]. Because the reaction cross section is envisioned to scale with the electron energy loss in the PtC_x layer, the electron energy loss was simulated at the various beam energies in 100 nm PtC_5 films on a 100 nm SiO_2 layer on a silicon substrate (Figure 4b). As shown, the Monte Carlo energy loss simulations in the PtC_5 layer decreases with increasing beam energy. Since the O_2 concentration is believed to be localized near the Pt–PtC_x interface due to limited diffusion and trapping at Pt nanoparticles and the purification front, we compare in Figure 4c the normalized purification rate (normalized to 5 keV and adjusted for different currents) from Figure 4a and the near surface energy loss in the PtC_5 layer in Figure 4b as a function of beam energy. Also shown is the normalized purification rate from our adsorption/permeation and electron stimulated reaction model as will be overviewed below. As demonstrated, good agreement between the experimental and simulated plots is observed, supporting the top–down purification model.

Enhanced resolution

The volumetric reduction in the PtC_x deposits is proportional to the removal of carbonaceous byproduct and as demonstrated previously, purification of PtC_5 to pure Pt results in an approx. 70% volumetric reduction [16]. Volumetric reduction in a typical 3-dimensional deposit varies in magnitude depending on
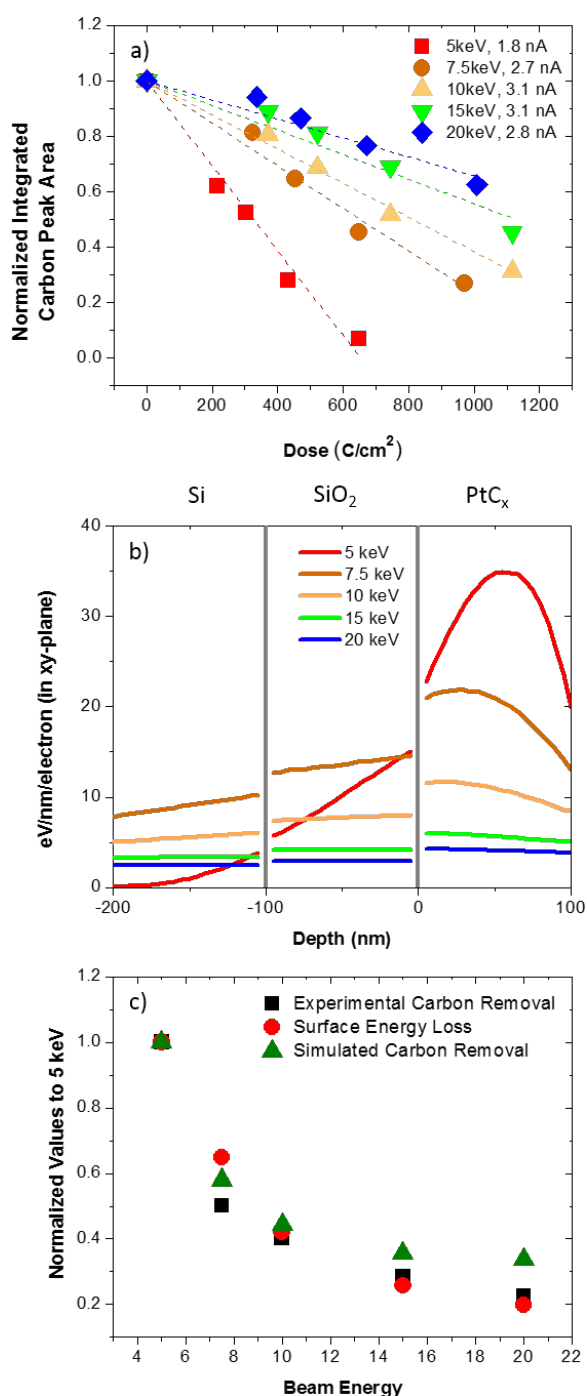
Figure 4: a) Normalized carbon peak area plotted as a function of dose for the beam energies shown. b) Monte Carlo simulation data depicting the electron energy loss over a 100 nm PtC_5 film on top of 100 nm SiO_2 as a function of *z* height (thickness) at different beam energies. The gray vertical lines represent the Si–SiO_2 and SiO_2–PtC_5 interfaces. c) Comparison of the empirical purification rate to the simulated surface electron energy loss as normalized to the values at 5 keV.

the length scale in each direction. For instance, the pseudo 2-dimensional pads have asymmetric length scales as the height (ca. 100 nm) is much smaller than the lateral dimensions (500 nm); so the volume loss is dominated in the *z*-dimension with very little lateral contraction. To compare, we deposited wire patterns that were grown with progressively higher number of electron passes to investigate the purification direction and volumetric contraction of wires that are nearly symmetric in height and width. Figure 5a illustrates the purification progression of the deposits as a function of purification time; for convenience and easy comparison, we only purified half of the wires. Figure 5b summarizes the reduction in wire-width as a function of purification time for the wires grown with progressively more passes and result in different initial thicknesses (ca. 55, 90, 110, and 160 nm) and due to proximity effects [25] also increased widths (ca. 60, 75, 100, and 115 nm), respectively. Once fully purified, the wire-width reduction ceases with further irradiation time. For the wire purification of the smallest two wires one can envision an almost semi-circular cross section where each wire has a similar purification rate (slope of the wire-width versus time). The tilted image reveals that the purification is occurring in a nearly isotropic manner (both

lateral and vertical contraction) and thus the complete purification time is dependent on the initial wire thickness/width. For the first and second wires there is greater than 50% wire-width reduction after a short purification time. Assuming a semi-circular cross-sectional shape and negligible relative shrinkage along the long axis, the volumetric reduction was found to be ca. 75% for wires one and two. For the thicker wires (three and four) the wire symmetry was different and thus the volumetric contraction was distributed differently across the width of the wires and the thickness of the wires. For these, volumetric reduction can be approximated more accurately by assuming a rectangular cross-section. Assuming this geometry and the final wire-widths, the volumetric reduction for both wires three and four was estimated to be 71%. This result indicates that the final shape of the deposition after purification can be predicted analytically. The overall contraction is proportional to the volumetric reduction resulting from the carbon removal from the deposit (ca. 70%) and therefore the final shape will shrink in proportion to the original dimensions.

Finally, it is worth noting the slight asymmetry or shift in the wire center for the purified wires and the residual deposition
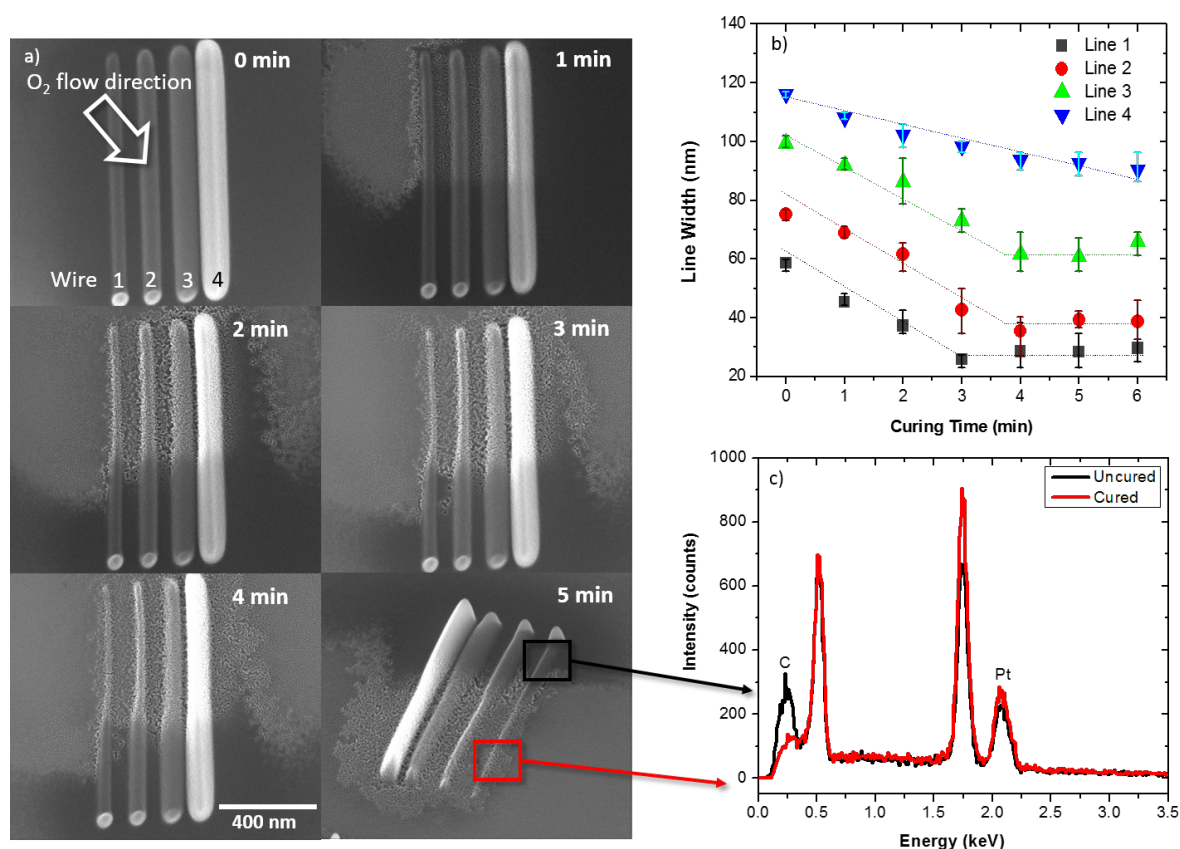
Figure 5: a) Images of wire deposits with different initial thicknesses (wires 1–4) purified at 1 min intervals for 6 min (inset on image). b) Estimated wire-width as a function of purification time for wires. c) EDS measurements of the purified and as-deposited part of the wire pattern.

that is visible after purification. This shift is attributed to the directionality of the O_2 gas flux; the position of the gas nozzle relative to the SEM image is noted in Figure 5a. The preferential purification is due to a slightly higher gas flux on the left side of the wires as discussed in detail elsewhere [26]. Importantly, because the O_2-assisted electron beam purification is isotropic, one can predict the shape change due to the volumetric contraction and which fortuitously can increase the EBID spatial resolution while simultaneously purifying the deposit. The residue that becomes visible near the purified wires is a result of peripheral or proximal deposition from the electron beam tail and backscattered, type II secondary electrons and in some cases forward scattered electrons during the initial

deposition [27]. This proximal deposition can be avoided with careful selection of the beam parameters during deposition. As the layer is extremely thin (a few monolayers) it can also be easily removed ex situ by with a brief focused ion beam etch.

Microstructure

Transmission electron microscopy (TEM) images of the as-deposited and cured PtC_x EBID patterns were taken to compare the microstructure with progressive carbon reduction. Figure 6a illustrates initial EDS measurements of ca. 30 nm thick PtC_5 samples that were grown on SiN_x membranes confirming the decrease in carbon with increasing purification time. Interestingly, the carbon reduction is not as severe as
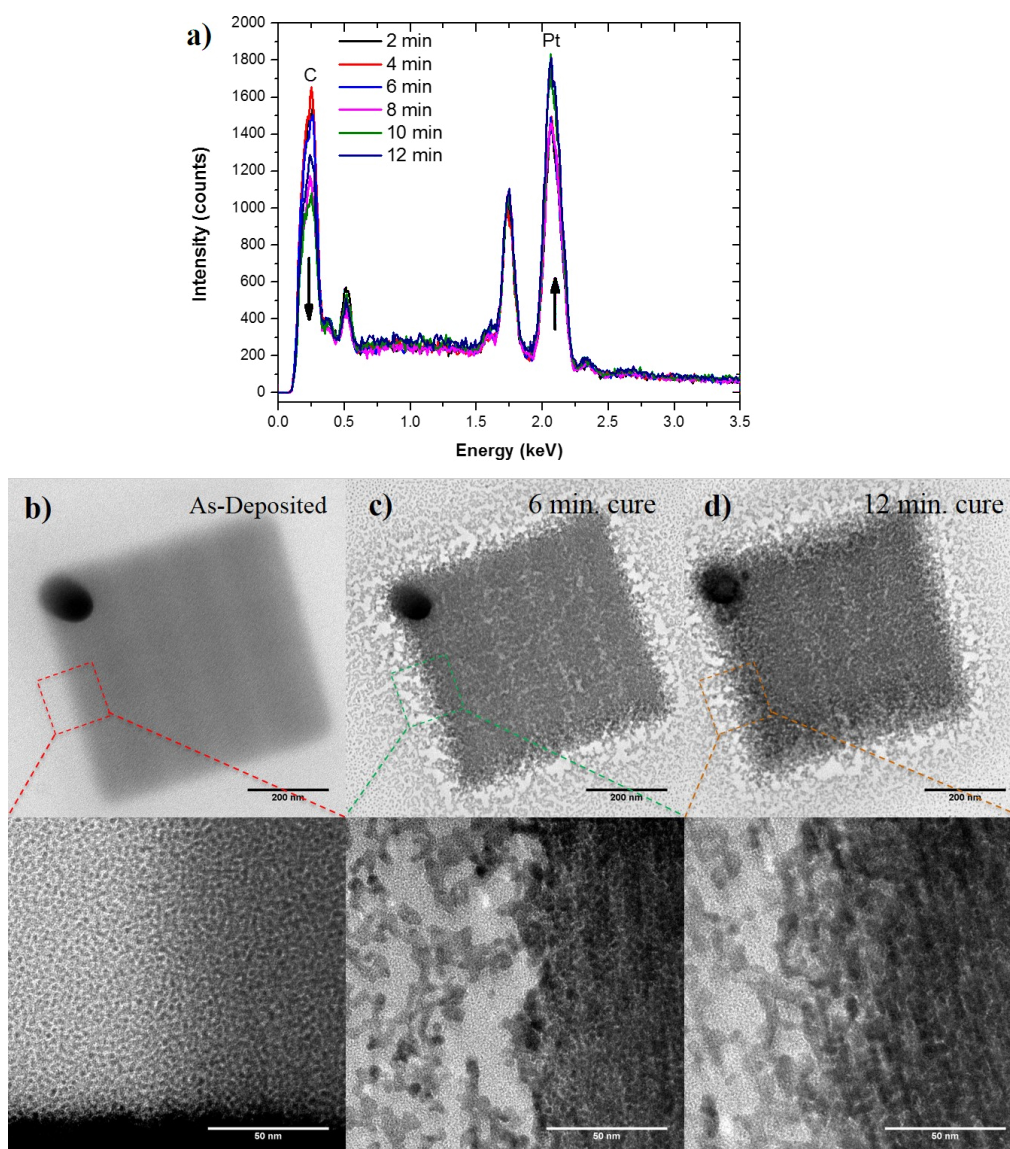
Figure 6: a) EDS measurements of the samples deposited and purified on the TEM membranes. TEM images of an b) as-deposited, and samples purified for c) 6 min and d) 12 min. The images reveal an increase in Pt grain size that occurs with increasing purification time.

compared to samples done on bulk substrates. While not conclusive, this could be due to two reasons: 1) an overall decrease in the energy loss in the deposits during purification due to limited backscattering from the thin membrane; 2) possible carbon deposition on the backside of the membrane due to slight outgassing from the copper tape adhesive. Figure 6b–d shows plane-view TEM images of the EBID structures at different purification times. A comparison of the TEM images reveals that the platinum grains coarsen and densify with increasing purification time. The estimated grain sizes were 1.97 nm (±0.34 nm), 3.36 nm (±0.69 nm), and 5.06 nm (±0.80 nm) for as-deposited, 6 min, and 12 min purification patterns, respectively. In order to further characterize the microstructure development during purification, selected area electron diffraction patterns (SAED) were taken for an as-deposited and purified PtC_x deposit as shown in Figure 7a. Figure 7b compares the radially averaged diffraction patterns which clearly illustrates that the electron-beam assisted O_2 purification successfully causes Pt grain densification and coarsening as indicated by the increased diffraction peak intensity and narrowing of the peak widths. The as-deposited diffraction pattern exhibits broad diffraction rings characteristic of small grain size and possibly disorder due to high carbon content. The diffraction peaks narrow as grain size increases

Figure 7: Selected area electron diffraction (SAED) patterns for O_2 E-beam uncured (left) and cured (right) deposit. Diffraction peaks become more pronounced after curing.

after curing. Grain coarsening is commonly associated with an increase in electrical conductivity of the PtC_x deposit as the tunnel coupling strengths increase for percolating networks [17]. For fully purified materials, our previous work [16] demonstrated a purely metallic material and thus low resistivity only one order of magnitude higher than bulk Pt. Future work will correlate purification time to the resultant percolating network and ultimately their temperature dependent electrical behavior which can reveal the granular properties of the evolving nanostructure as well as the insulator to metal transition.

Modeling

Finally, to emulate the purification reaction we have developed a model which incorporates the O_2 1) surface adsorption, 2) permeation/diffusion, 3) preferential O_2–Pt adsorption, 4) electron stimulated reaction, and 5) subsequent CO_x out-diffusion. Purification experiments were simulated using a hybrid numerical approximation consisting of (1) a Monte Carlo electron scattering simulation coupled with (2) an explicit finite difference treatment of oxygen diffusion and the (3) Huen–Euler method to approximate the dissociative chemisorption of atomic oxygen on metal nanoparticle surfaces internal to the deposited solid. Electron energy loss converts bound oxygen into an activated form that is assumed to instantaneously oxidize amorphous carbon. The resulting CO_x liberated from the deposit via subsequent diffusion to the surface. The details of the simulation will be provided in a future publication and only a brief summary is provided here.

The Monte Carlo simulation is executed in order to accumulate the 3D spatial profile of the inelastic energy deposited in a semi–infinite thin film stack consisting of a $PtC_{x(z)}$ deposit of thickness (h_{film}) resting on a substrate. The 3D inelastic energy profile is then scanned across the deposit surface (to mimic the experimental beam scanning procedure) and the energy is accumulated at the center of the scanning pattern ($x = 0$, $y = 0$) in order to emulate the transiently evolving inelastic energy profile with depth (z-coordinate) during real experiments at the pad center. Thus, the critical parameter in the Monte Carlo simulation is the rate of electron energy loss, per unit length scattering, to the film [1-3];

$$\frac{dE(z)}{dS} = -78,500\frac{\rho(z)Z(z)}{A(z)}\frac{1}{E(z)}\log\left(\frac{1.166\cdot E(z)}{J(z)}+1\right) \text{ (1)}$$

where E is the electron energy, S is the spatial path length for the scattering electron in the current voxel, ρ is the material density, Z is the atomic number, A is the atomic weight and J is the mean ionization potential. This value is converted into a
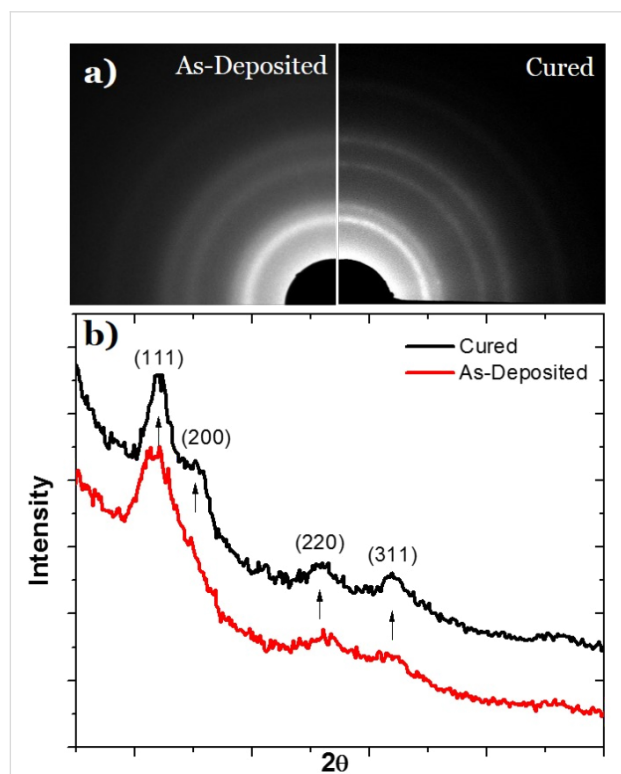
deposited energy "concentration" with units of, e.g., [eV/nm^3·s] for input into the transport simulation. Lastly, the semi–infinite deposit composition in the depth dimension is updated based on the transport calculations (described below) in order to account for the experimentally observed deposit densification – $\rho(z)$, $Z(z)$ and $A(z)$ are recalculated by volume averaging based on $PtC_{x(z)}$ for the next Monte Carlo simulation iteration.

In the transport simulation, O_2 is introduced into the deposit based on a surface impingement rate derived from the input pressure P. Dissolution at the surface is treated according to Henry's law $S = K_{eq}P$ where S is the solubility of oxygen and K_{eq} is the solubility constant. The use of this approximation requires a description of the deposit composition model. The model deposit consists of metal nanoparticles with a defined density ρ_{np} and a radius r_{np} distributed in an amorphous carbon matrix (aC) which was constructed based on TEM images of real structures. Further, the aC was modeled as "polymer-like" in the simulation. O_2 dissolved and diffused within a partitioned pixel fraction based on the mean pixel composition $PtC_{x(z)}$.

The transport equation treating the diffusion of the mobile O_2 concentration ($C_{O2}{}^{m}$) is shown in Equation 2 as the first term on the right hand side with the remaining terms describing the interaction of mobile oxygen gas with Pt nanoparticles. An explicit finite differencing scheme is used to calculate the diffusion term in Equation 2. Importantly, the numerical approximation was derived including a variable pixel size which made it possible to "contract" the deposit based on the amount of carbon lost.

The second term in Equation 2 describes the chemisorption of mobile oxygen gas as adsorbed atomic oxygen at nanoparticle surfaces. Φ_{O2} is the impingement rate of mobile O_2 on the nanoparticle surface (this parameter is derived from Monte Carlo simulations of a diffusing test particle impinging on a spherical nanoparticle and will be discussed in detail in the future publication) and depends on the concentration of mobile oxygen, the nanoparticle radius, depth into the deposit and time. Also important to the adsorption interaction is the sticking para-

meter (δ), the number of binding sites per unit nanoparticle area (s_d) and the mean residence time of atomic oxygen on the nanoparticles (τ). The later appears in the third term which describes the associative desorption of atomic oxygen to form dissolved, mobile molecular oxygen. Terms 2 and 3 are combined and solved by using the improved Euler, or Heun–Euler method, applicable for a first-order differential equation which is a predictor–corrector method and is second order accurate with a cubed truncation error.

Adsorbed, immobile atomic oxygen $C_O{}^{im}$ is available for electron-induced dissociation as represented by Equation 3 and provides the coupling between the Monte Carlo electron scattering simulation and the transport calculations. Specifically, term 1 on the right hand side of the equation treats the electron-driven activation of atomic oxygen using the law of mass action and treats the reaction as 2nd order (1st order in each concentration) where the units of the reaction constant are, e.g., [nm^3/eV·s], and C_{eV} is the "concentration" of electron energy loss.

Importantly, once the oxygen is chemically "activated" the assumption is made that this species (O*) instantly reacts with aC yielding $CO_{1.5}$ (without actual knowledge of the ratio of CO and CO_2 byproduct yields, parity was assumed);

$$\frac{2}{3}a\mathrm{C} + \mathrm{O}^{*} \rightarrow \frac{2}{3}\mathrm{CO}_{1.5} \qquad (4)$$
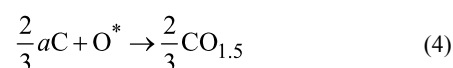
$$\frac{\partial \mathrm{CO}_{1.5}}{\partial t} = -\frac{\partial a\mathrm{C}(z,t)}{\partial t} = \frac{2}{3}kC_{\mathrm{eV}}(z,t)C_{\mathrm{O}}^{im}(z,t) \qquad (5)$$

Subsequently, the liberated $CO_{1.5}$ diffuses within the aC matrix and is vaporized at the deposit surface. Pixels shrink according to the amount of aC liberated. Conversely, the flow of both O_2 and $CO_{1.5}$ are prohibited at the buried deposit–substrate interface under a no–flow boundary condition. It is important to note that the spontaneous oxidation of carbon by chemisorbed atomic oxygen is neglected in the current model. As a result, the

$$\frac{\partial C_{\mathrm{O}_2}^{m}(z,t)}{\partial t} = D_{\mathrm{O}_2}\frac{\partial^2 C_{\mathrm{O}_2}^{m}(z,t)}{\partial z^2} - \delta\Phi_{\mathrm{O}_2}\left(C_{\mathrm{O}_2}^{m},r_{\mathrm{np}},z,t\right)\left[4\pi r_{\mathrm{np}}^2(z,t)\rho_{\mathrm{np}}(z) - \frac{C_{\mathrm{O}}^{im}(z,t)}{s_{\mathrm{d}}}\right] + \frac{C_{\mathrm{O}}^{im}(z,t)}{2\tau} \qquad (2)$$

$$\frac{\partial C_{\mathrm{O}}^{im}(z,t)}{\partial t} = -kC_{\mathrm{eV}}(z,t)C_{\mathrm{O}}^{im}(z,t) + 2\delta\Phi_{\mathrm{O}_2}\left(C_{\mathrm{O}_2}^{m},r_{\mathrm{np}},z,t\right)\left[4\pi r_{\mathrm{np}}^2(z,t)\rho_{\mathrm{np}}(z) - \frac{C_{\mathrm{O}}^{im}(z,t)}{s_{\mathrm{d}}}\right] - \frac{C_{\mathrm{O}}^{im}(z,t)}{\tau} \qquad (3)$$

simulation results reported are expected to overestimate the rate of beam induced oxidation.

The summarized simulation flow above represents one loop of purification. Following the completion of a single loop, the $PtC_{x(z)}$ composition for each xy-planar slice in the 3D spatial domain for the Monte Carlo simulation is updated based on the contraction of the spatial nodes in the transport simulation due to the loss of aC. This procedure accounts for both (1) the motion of the deposit surface as well as (2) the deposit densification.

Table 1 summarizes of the relevant variables derived to match the 5 keV purification rate illustrated in Figure 2. Based on these variables, the different beam parameter studies were simulated. Figure 8 is a normalized (to 5 keV) bar graph of the experimental and simulated purification rates for the different

Table 1: The relevant derived variables used in the simulation to obtain the correct experimentally determined purification rates.

O₂ purification	
Electron beam energy	5 keV
Electron beam current	1800 pA
Beam scanning pixel size	0.65 nm
Beam scanning region	620 nm
Beam dwell time per pixel	100 ns
Pad thickness	100 nm
Initial pad composition (PtC_x)	5 [ ]
Rate constant	4000 nm³/(eV·s)
Diffusion coefficient	4 μm²/s
Solid dissolution constant	0.03 atoms/(nm³·Torr)
Mean residence time (reactant on metal np)	12.5 ms
Sticking probability	0.05 [%]
Pressure (reactant gas)	2 mTorr
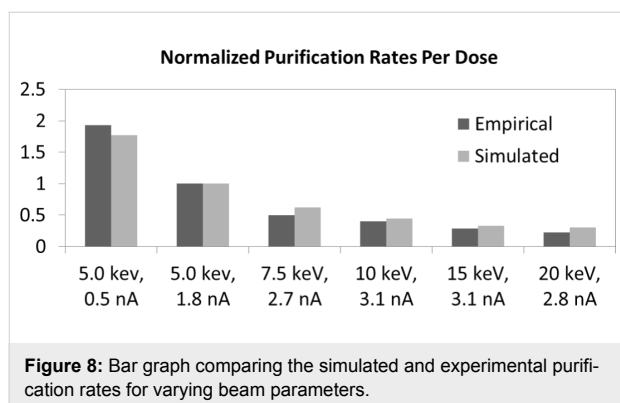
Figure 8: Bar graph comparing the simulated and experimental purification rates for varying beam parameters.

beam parameters. As can be seen the purification model accurately mimics the experimental trends presented here. We will elaborate on the model and compare the O_2 and H_2O purification mechanisms in a near future publication.

Experimental

Platinum boxes were deposited onto a pre-cleaned 100 nm thermal SiO_2 on Si substrate and then purified. The deposition and subsequent purification was performed using a FEI NOVA 600 dual-beam system equipped with FEI and Omniprobe gas injection systems. Prior to deposition, the substrate was sonicated in isopropanol for 5 min and annealed at 900 °C in an Ar-H_2 atmosphere. The sample was then transferred to the SEM chamber and cleaned using a XEI Scientic plasma cleaner for 30 min at a pressure of 5.34×10^{-1} mbar. Subsequent to cleaning, the system was pumped to a base pressure of less than 3×10^{-6} mbar. Platinum deposition was performed using the FEI GIS and MeCpPt(IV)Me₃ precursor which raised the chamber pressure to ≈1.5×10^{-5} mbar. 500×500 nm boxes were synthesized at this elevated pressure using the NOVA patterning software with a beam energy of 5 keV, beam current of 120 pA, point pitch of 13.55 nm, a pixel dwell time of 10 μs, and 1000 loops in order to create a pad with a thickness of about 100 nm. After deposition and pumpdown back to <3×10^{-6} mbar, the pads were purified using an O_2 flow during electron beam irradiation. The oxygen flow and temperature were controlled using the Omni GIS system which was inserted to the same position as our previous work: an angle 52° with respect to the substrate surface and the lower end of the GIS nozzle at a straight line distance of 120 μm from the substrate surface. The oxygen gas line was heated to 78 °C and 25 °C though some cooling likely occurs before delivery from the nozzle. After the target oxygen temperature was reached, the oxygen was injected into the SEM chamber at a pressure of ≈1.4×10^{-5} mbar which was determined by controlling the valve sequence in the OmniGIS. At this point, the electron beam was used to irradiate the deposit with the simultaneous flow of O_2. Typical purification parameters were: a beam energy and current of 5 keV and 1.8 nA, respectively, a ≈0.65 nm point pitch with a field of view of 1024×884 pixels (665×575 nm), a dwell time of 100 ns, and a typical curing time of 20 min.

To characterize the reduction in PtC_x deposit size with purification, four EBID wires were deposited on a SiO_2 substrate and purified using the same parameters as with the pads. The wire patterns were deposited with 5 keV, 28 pA beam conditions and a varying number (10,000, 15,000, 20,000 and 50,000) of EBID passes to achieve heights of 48, 70, 95, and 150 nm and widths of approximately 55 nm, 75 nm, 95 nm, and 115 nm, respectively. Half of the wire pattern's length was purified and the

other half was left in as-deposited conditions to provide a dimensional comparison to reveal shrinkage associated with purification.

To compare the resultant microstructure and grain size of progressively purified material, six samples were prepared on 30 nm thick SiN_x substrates for transmission electron microscopy (TEM) imaging. The samples were deposited and purified using similar parameters reported above. The samples were purified to different times (and doses) of 2 min (51.2 C/cm^2), 4 min (102.3 C/cm^2), 6 min (153.5 C/cm^2), 8 min (204.7 C/cm^2), 10 min (255.8 C/cm^2), and 12 min (307.0 C/cm^2). Selected area electron diffraction was also performed to obtain diffraction patterns. These experiments were conducted in a Zeiss Libra 200 HT FE MC at 120 keV and minimal beam current to prevent morphological changes.

Conclusion

We have studied the electron-stimulated O_2 purification of PtC EBID deposits and have shown that the process can be extended to room temperature. Electron beam current and energy studies suggest the process is governed by a dynamic process which is a function of both the electron energy loss and oxygen concentration. Importantly, the purification front propagates from the top–down which suggests a preferential trapping or limited permeation of the O_2 reactive gas. A model based on a 2nd order reaction rate was also demonstrated, which accurately reproduces the experimental trends. Finally, purification of pseudo-1-dimensional wires illustrate that the purification process is isotropic and conveniently the carbon reduction leads to higher resolution wires.

Acknowledgements

References

1. Botman, A.; Mulders, J. J. L.; Hagen, C. W. *Nanotechnology* **2009,** *20,* 372001. doi:10.1088/0957-4484/20/37/372001

2. Huth, M.; Porrati, F.; Schwalb, C.; Winhold, M.; Sachser, R.; Dukic, M.; Adams, J.; Fantner, G. *Beilstein J. Nanotechnol.* **2012,** *3,* 597–619. doi:10.3762/bjnano.3.70

3. Utke, I.; Moshkalev, S.; Russell, P., Eds. *Nanofabrication Using Focused Ion and Electron Beams: Principles and Applications;* Oxford University Press: Oxford, United Kingdom, 2012.

4. Klein, K. L.; Randolph, S. J.; Fowlkes, J. D.; Allard, L. F.; Meyer, H. M., III; Simpson, M. L.; Rack, P. D. *Nanotechnology* **2008,** *19,* 345705. doi:10.1088/0957-4484/19/34/345705

5. Fernández-Pacheco, A.; De Teresa, J. M.; Córdoba, R.; Ibarra, M. R. *J. Phys. D: Appl. Phys.* **2009,** *42,* 055005. doi:10.1088/0022-3727/42/5/055005

6. Brintlinger, T.; Fuhrer, M. S.; Melngailis, J.; Utke, I.; Bret, T.; Perentes, A.; Hoffmann, P.; Abourida, M.; Doppelt, P. *J. Vac. Sci. Technol., B* **2005,** *23,* 3174. doi:10.1116/1.2130355

7. Rykaczewski, K.; White, W. B.; Fedorov, A. G. *J. Appl. Phys.* **2007,** *101,* 054307. doi:10.1063/1.2437065

8. Riazanova, A. V.; Costanzi, B. N.; Aristov, A.; Rikers, Y. G. M.; Ström, V.; Mulders, J. J. L.; Kabashin, A. V.; Dan Dahlberg, E.; Belova, L. M. *Nanotechnology* **2014,** *25,* 155301. doi:10.1088/0957-4484/25/15/155301

9. Mehendale, S.; Mulders, J. J. L.; Trompenaars, P. H. F. *Nanotechnology* **2013,** *24,* 145303. doi:10.1088/0957-4484/24/14/145303

10. Toth, M.; Lobo, C. J.; Hartigan, G.; Ralph Knowles, W. *J. Appl. Phys.* **2007,** *101,* 054309. doi:10.1063/1.2437667

11. Roberts, N. A.; Magel, G. A.; Hartfield, C. D.; Moore, T. M.; Fowlkes, J. D.; Rack, P. D. *J. Vac. Sci. Technol., A* **2012,** *30,* 041404. doi:10.1116/1.4731254

12. Roberts, N. A.; Fowlkes, J. D.; Magel, G. A.; Rack, P. D. *Nanoscale* **2013,** *5,* 408–415. doi:10.1039/C2NR33014H

13. Nicholas, A. R.; Carlos, M. G.; Jason, D. F.; Philip, D. R. *Nanotechnology* **2013,** *24,* 415301. doi:10.1088/0957-4484/24/41/415301

14. Graells, S.; Alcubilla, R.; Badenes, G.; Quidant, R. *Appl. Phys. Lett.* **2007,** *91,* 121112. doi:10.1063/1.2786600

15. Stanford, M. G.; Lewis, B. B.; Noh, J. H.; Fowlkes, J. D.; Roberts, N. A.; Plank, H.; Rack, P. D. *ACS Appl. Mater. Interfaces* **2014,** *6,* 21256–21263. doi:10.1021/am506246z

16. Plank, H.; Noh, J. H.; Fowlkes, J. D.; Lester, K.; Lewis, B. B.; Rack, P. D. *ACS Appl. Mater. Interfaces* **2014,** *6,* 1018–1024. doi:10.1021/am4045458

17. Porrati, F.; Sachser, R.; Schwalb, C. H.; Frangakis, A. S.; Huth, M. *J. Appl. Phys.* **2011,** *109,* 063715. doi:10.1063/1.3559773

18. Sachser, R.; Reith, H.; Huzel, D.; Winhold, M.; Huth, M. *ACS Appl. Mater. Interfaces* **2014,** *6,* 15868–15874. doi:10.1021/am503407y

19. Mackus, A. J. M.; Thissen, N. F. W.; Mulders, J. J. L.; Trompenaars, P. H. F.; Verheijen, M. A.; Bol, A. A.; Kessels, W. M. M. *J. Phys. Chem. C* **2013,** *117,* 10788–10798. doi:10.1021/jp402260j

20. Geier, B.; Gspan, C.; Winkler, R.; Schmied, R.; Fowlkes, J. D.; Fitzek, H.; Rauch, S.; Rattenberger, J.; Rack, P. D.; Plank, H. *J. Phys. Chem. C* **2014,** *118,* 14009–14016. doi:10.1021/jp503442b

21. Noh, J. H.; Stanford, M. G.; Lewis, B. B.; Fowlkes, J. D.; Plank, H.; Rack, P. D. *Appl. Phys. A* **2014,** *117,* 1705–1713. doi:10.1007/s00339-014-8745-0

22. Hopf, C.; Schlüter, M.; Schwarz-Selinger, T.; von Toussaint, U.; Jacob, W. *New J. Phys.* **2008,** *10,* 093022. doi:10.1088/1367-2630/10/9/093022

23. Mackus, A. J. M.; Leick, N.; Baker, L.; Kessels, W. M. M. *Chem. Mater.* **2012,** *24,* 1752–1761. doi:10.1021/cm203812v

24. van Dorp, W. F.; Wnuk, J. D.; Gorham, J. M.; Fairbrother, D. H.; Madey, T. E.; Hagen, C. W. *J. Appl. Phys.* **2009,** *106,* 074903. doi:10.1063/1.3225091

25. Arnold, G.; Timilsina, R.; Fowlkes, J.; Orthacker, A.; Kothleitner, G.; Rack, P. D.; Plank, H. *ACS Appl. Mater. Interfaces* **2014,** *6,* 7380–7387. doi:10.1021/am5008003

26. Winkler, R.; Fowlkes, J.; Szkudlarek, A.; Utke, I.; Rack, P. D.; Plank, H. *ACS Appl. Mater. Interfaces* **2014,** *6,* 2987–2995. doi:10.1021/am405591d

27. Smith, D. A.; Fowlkes, J. D.; Rack, P. D. *Nanotechnology* **2008,** *19,* 415704. doi:10.1088/0957-4484/19/41/415704

Patterning technique for gold nanoparticles on substrates using a focused electron beam

Takahiro Noriki[1], Shogo Abe[1], Kotaro Kajikawa[2] and Masayuki Shimojo[*1]

Abstract

We propose a novel patterning technique for gold nanoparticles on substrates that combines a chemical reaction with electron beam irradiation. First, gold nanoparticles are placed in a two-dimensional arrangement on the substrate. Then, particular nanoparticles are fixed on the substrate by irradiation with a focused electron beam to produce a desired pattern. Finally, the unfixed nanoparticles are removed. Using this technique, an array of gold nanoparticles, for example, in the form of a line or patterned over an area, are prepared on the substrate. This technique could contribute to the fabrication of plasmonic devices and other applications that require the controlled placement of gold nanoparticles on substrates.

Introduction

Plasmonic waveguides and circuits utilizing localized surface plasmon resonance (LSPR) are attracting attention for future optical transmission, sensor, and data processing devices. The development of these LSPR-based structures would lead to a reduction in the size of optical circuits and devices [1,2]. Light energy can be propagated through nanometer-sized wires or through rows of particles due to the LSPR effect. Gold and silver nanowires or particles can be used for such waveguides, as these materials interact with visible light.

Plasmon propagation through nanowires has been experimentally investigated. Sanders et al. [3] showed the propagation of

plasmons in silver nanowires and the emission of photons at the end of the nanowires. Branching is considered necessary to make integrated photonic/plasmonic circuits. The plasmon propagation on branched silver nanowires was also experimentally demonstrated [4]. However, most of these experiments were performed using nanowires placed on substrates without regard to their position. It is difficult to produce a branched nanowire with a designed shape and to place the nanowire at a desired position at the nanoscale.

It has been theoretically demonstrated that a plasmon can propagate through a chain of spherical metal nanoparticles [5].

According to these results, the nanoparticles should be placed at designated positions and close enough to neighboring particles for transmission at the nanoscale. Gwo et al. [6] fabricated nanoparticles in a line as well as in the form of other two- and three-dimensional structures with gold and silver nanoparticles using a nanomanipulator. This technique is fascinating, but it may be a time-consuming process for production of relatively large circuits.

Nanostructures have also been fabricated using focused ion beam- or focused electron beam-induced deposition [1,7]. However, nanostructures made by these techniques generally have low purity as they contain a large amount of carbon, and thus, the structures need to be coated with gold or silver for use in plasmonic devices. Therefore, a manageable, practical, and not too complicated technique for fabricating nanoparticle arrays of a designed shape is needed.

In this paper, we propose a new patterning technique for gold nanoparticles on substrates. The nanoparticles are first placed in a two-dimensional arrangement on a substrate by chemical methods. Thereafter, the desired nanoparticles are immobilized by focused electron beam irradiation, and finally, the unfixed nanoparticles are removed.
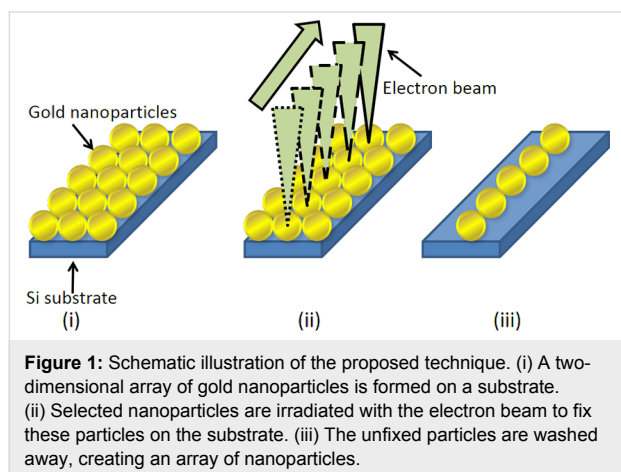
Results and Discussion

In this technique, the sample was made by implementing the following steps:

Step (i): Au nanoparticles are placed on a substrate.

Step (ii): Selected nanoparticles are immobilized on the substrate by electron beam irradiation.

Step (iii): The unfixed nanoparticles are removed from the substrate.

A schematic illustration of this process is shown in Figure 1. Two methods were employed for step (i), the amine-epoxy method and the amino-undecanethiol method.

Figure 2 shows a scanning electron microscope (SEM) image of gold nanoparticles arranged on the substrate after step (i) using the amine-epoxy method. A similar arrangement technique has been previously published [8]. The length of the molecules attached to the gold particles controlled the distance between neighboring particles. In this method, a two-dimensional close packing of Au particles was partially obtained; however, particles were missing in some areas.

Figure 3 shows a SEM image of the sample after step (iii) where a line of gold nanoparticles remains on the substrate.

Figure 2: SEM image of the substrate after step (i) using the amine-epoxy method.

Figure 1: Schematic illustration of the proposed technique. (i) A two-dimensional array of gold nanoparticles is formed on a substrate. (ii) Selected nanoparticles are irradiated with the electron beam to fix these particles on the substrate. (iii) The unfixed particles are washed away, creating an array of nanoparticles.

Figure 3: SEM image of the sample demonstrating that a row of nanoparticles was formed after step (iii), wherein the sample was irradiated and washed.

Since the observation process using SEM immobilizes the nanoparticles in the observation area due to electron beam irradiation, it was necessary to scan the electron beam without prior observation of the substrate. Thus, the area of the sample shown in Figure 3 is different from that of Figure 2. As the position of the focused electron beam can be controlled using a computer, we were able to control and adjust the arrangement of gold nanoparticles, for example, in the form a line.

Figure 4 shows a SEM image of the sample that was irradiated over a relatively large, L-shaped area and processed after step (iii). Some close packed regions were left in the irradiated L-shaped area. Although the original distribution was not perfect and many particles were missing in the L-shaped area, it is demonstrated that the electron beam irradiation can immobilize the nanoparticles over a large area on the substrate.
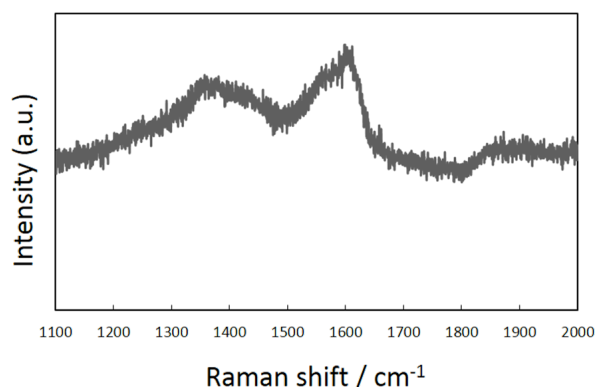

Figure 5: Raman shift measured for the sample, providing evidence of the existence of amorphous carbon.

Figure 4: SEM image of the sample irradiated over a relatively large, L-shaped area.

To reveal the mechanism of nanoparticle immobilization, Raman spectroscopy was carried out after all process steps of the sample had been performed; however, the electron beam irradiated a large area. Figure 5 shows the Raman shift measured in the area of electron beam irradiation where the G-band (1580 cm^{-1}) and D-band (1360 cm^{-1}) of carbon are observed. The presence of these bands suggests that amorphous carbon or diamond-like carbon exists on the specimen. It should be noted that no such peaks were observed for the sample without electron beam irradiation (after the steps (i) and (iii)). Figure 6 shows a transmission electron microscope (TEM) image of a nanoparticle on an edge of the widely irradiated specimen, which was tilted in the microscope. An amorphous substance is observed in the gap between the substrate and the particle. A thin amorphous layer is also observed covering the particle. These results suggest that electron beam irradiation

Figure 6: TEM image of the amorphous deposit formed around/ between the particle and the substrate (a), and schematic illustration of the immobilization mechanism (b).

decomposes organic molecules formed on the surfaces of the substrate and the nanoparticles, and that the amorphous carbon was formed during step (ii). This amorphous carbon is considered to fix the particles onto the substrate.

The immobilization of the nanoparticle on the substrate surface is considered to occur due to the deposition of amorphous carbon. This amorphous carbon most likely originates from organic molecules around the nanoparticles, as similar mechanisms of decomposition and deposition occur in electron beam-induced deposition (EBID) [9-11]. Fujita et al. reported that amorphous carbon was formed after the irradiation of phenanthrene molecules adsorbed on a substrate by an electron beam [12]. Amorphous carbon was also formed by electron beam-induced deposition using a ferrocene precursor [13]. In our experiment, no precursor gas was introduced into the SEM chamber, however, the nanoparticles were covered with organic molecules and hydrocarbon molecules may have been present in the SEM chamber. Thus, the deposition of amorphous carbon was considered to occur around the particles during the irradiation process, due to the decomposition of organic substances by the high-energy electron beam.

In Figure 3, the spacing between neighboring particles is not uniform. This is probably because the original two-dimensional arrangement was not perfect, as shown in Figure 2. The result of the sample which underwent large area irradiation, as shown in Figure 4, further supports this reason. Thus, another method, the amino-undecanethiol method, was used for step (i).

Figure 7 shows a SEM image of the substrate after step (i) using the amino-undecanethiol method. Using this method, the distribution of nanoparticles becomes relatively uniform, as compared with the amine-epoxy method, though the two-dimensional close packing is not obtained. The electron beam was used to irradiate a rectangular area on the substrate prepared using the amino-undecanethiol method. A SEM image of this substrate after step (iii) is shown in Figure 8. Almost all particles remained in the irradiated area on the substrate, while most particles were washed away outside of the irradiated area.

This patterning process for nanoparticles, which combines both chemical and electron beam techniques, could contribute to the fabrication of single electron transistors [14], Fano resonance devices [15] and plasmonic waveguides, as the placement of gold nanoparticles on a substrate could be precisely controlled.

Conclusion

A novel technique for patterning by controlling the placement of gold nanoparticles on substrates was proposed. The technique combines a chemical reaction with electron beam irradi-
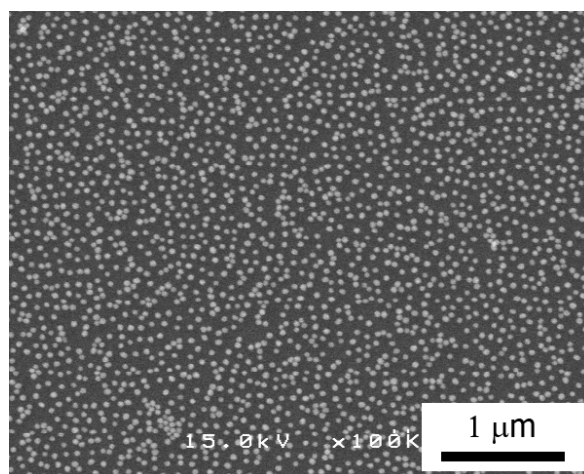
Figure 7: SEM image of the sample after step (i) using the amino-undecanethiol method.
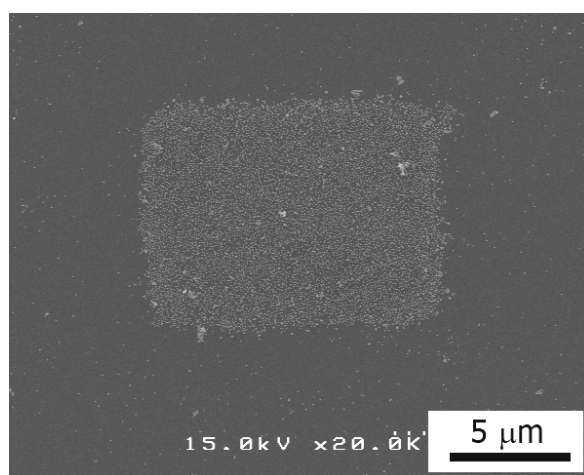
Figure 8: SEM image of the specimen using the amino-undecanethiol method after step (iii), illustrating that the nanoparticles remained in the rectangular area of electron irradiation.

ation. This technique could contribute to the fabrication of nanodevices such as plasmonic waveguides.

Experimental
Step (i): amino-epoxy method

A polished Si wafer, with dimensions of about 3×1 mm, was used as the substrate. The substrate was immersed in a mixture (1:3 by volume) of hydrogen peroxide (30%) and concentrated sulfuric acid (98%) for 10 h to create a hydrophilic surface [16,17]. The substrate was then immersed in 3-glycidoxypropyltrimethoxysilane for 16 h. During this process, a self-assembled monolayer of molecules with an epoxy group was formed on the Si surface [18].

An ethanol solution (3 mL) of 2-aminoethanethiol (8 mmol/L) was added to a commercially available colloidal gold particle solution (3 mL) and stirred for 1 min. During this process, a monolayer of molecules with an amino group was formed on the gold surface [19].

The substrate was then immersed for 12 h in the colloidal gold solution described above in order to attach the amino group on the gold particles with the epoxy group on the substrate. Afterwards, the substrate was dried in air at room temperature. As a result of these process steps, a two-dimensional array of gold nanoparticles formed on the substrate, as shown schematically in Figure 9.

Figure 9: Schematic illustration of the formation of a two-dimensional, dense array of gold nanoparticles on a silicon substrate: step (i).
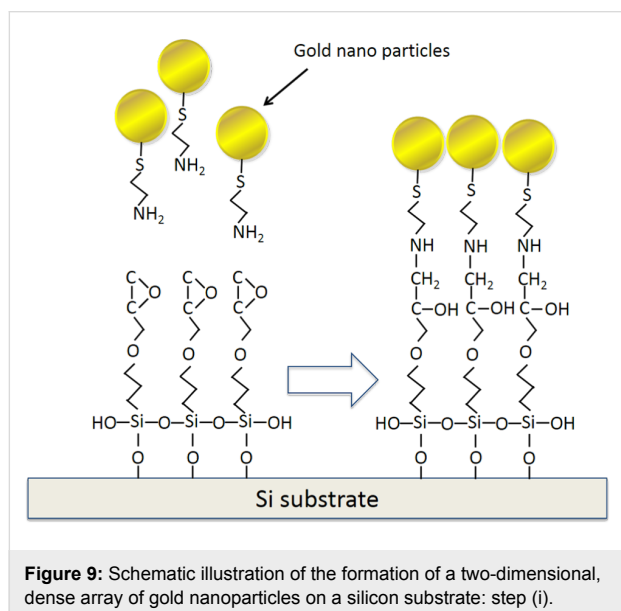
Step (i): the amino-undecanethiol method

A thin gold film of 25 nm thickness was formed by sputtering on a Si plate sample. The sample was immersed in amino-1-undecanethiol in an ethanolic solution at a concentration of 1 mM for 3 h. In this process, a self-assembled monolayer was formed [20]. Then, the sample was immersed for 3 h in a colloidal gold solution containing gold particles of 50 nm diameter.

Although this method will not produce a two-dimensional close packing of Au nanoparticles, it will result in the relatively uniform distribution of Au nanoparticles.

Step (ii): electron beam irradiation

Focused electron beam irradiation on the gold particle-covered substrate was carried out using a SEM equipped with a field emission gun. The accelerating voltage of the electron beam was 15 kV. For a line scan, the irradiation time was about 2 s

for each particle. For the L-shaped and rectangular patterns, the electron dose was about 0.07 nC/μm^2.

This process immobilized the irradiated particles on the substrate by changing the structure of the organic molecules that surrounded the irradiated particles. The detailed mechanism of this step was discussed above.

Step (iii): removal of unfixed particles

Finally, the irradiated substrate was rinsed in water during ultrasonication with a commercially available surface-active agent for the amine-epoxy method. For the amino-undecanethiol method, an amino-1-undecanethiol in an ethanolic solution was used instead of water. This step removed the unfixed particles on the substrate. Then, the sample, which consisted of the final substrate with immobilized particles, was observed using SEM.

The TEM observation and the Raman spectroscopy measurement were carried out on the specimen to reveal the mechanism of immobilization.

Acknowledgements

References

1. Nomura, W.; Ohtsu, M.; Yatsui, T. *Appl. Phys. Lett.* **2005,** *86,* 181108. doi:10.1063/1.1920419
2. Ozbay, E. *Science* **2006,** *311,* 189–193. doi:10.1126/science.1114849
3. Sanders, A. W.; Routenberg, D. A.; Wiley, B. J.; Xia, Y.; Dufresne, E. R.; Reed, M. A. *Nano Lett.* **2006,** *6,* 1822–1826. doi:10.1021/nl052471v
4. Fang, Y.; Li, Z.; Huang, Y.; Zhang, S.; Nordlander, P.; Halas, N. J.; Xu, H. *Nano Lett.* **2010,** *10,* 1950. doi:10.1021/nl101168u
5. Quinten, M.; Leitner, A.; Krenn, J. R.; Aussenegg, F. R. *Opt. Lett.* **1998,** *23,* 1331–1333. doi:10.1364/OL.23.001331
6. Gwo, S.; Lin, M.-H.; He, C.-L.; Chen, H.-Y.; Teranishi, T. *Langmuir* **2012,** *28,* 8902. doi:10.1021/la300226r
7. Höflich, K.; Becker, M.; Leuchs, G.; Christiansen, S. *Nanotechnology* **2012,** *23,* 185303. doi:10.1088/0957-4484/23/18/185303
8. Andres, R. P.; Bielefeld, J. D.; Henderson, J. I.; Janes, D. B.; Kolagunta, V. R.; Kubiak, C. P.; Mahoney, W. J.; Osifchin, R. G. *Science* **1996,** *273,* 1690. doi:10.1126/science.273.5282.1690
9. Shimojo, M.; Mitsuishi, K.; Tameike, A.; Furuya, K. *J. Vac. Sci. Technol., B* **2004,** *22,* 742–746. doi:10.1116/1.1688349
10. Han, M.; Mitsuishi, K.; Shimojo, M.; Furuya, K. *Philos. Mag.* **2004,** *84,* 1281–1289. doi:10.1080/14786430310001646772
11. Che, R.; Takeguchi, M.; Shimojo, M.; Furuya, K. *J. Phys.: Conf. Ser.* **2007,** *61,* 200–204. doi:10.1088/1742-6596/61/1/040
12. Fujita, J.; Ishida, M.; Ichihashi, T.; Ochiai, Y.; Kaito, T.; Matsui, S. *J. Vac. Sci. Technol., B* **2003,** *21,* 2990–2993. doi:10.1116/1.1624259
13. Che, R.; Takeguchi, M.; Shimojo, M.; Zhang, W.; Furuya, K. *Jpn. J. Appl. Phys.* **2006,** *45,* 5582–5585. doi:10.1143/JJAP.45.5582
14. Dutta, A.; Oda, S.; Fu, Y.; Willander, M. *Jpn. J. Appl. Phys.* **2000,** *39,* 4647–4650. doi:10.1143/JJAP.39.4647

15. Wen, F.; Ye, J.; Liu, N.; Van Dorpe, P.; Norlander, P.; Halas, N. J. *Nano Lett.* **2012,** *12,* 5020–5026. doi:10.1021/nl302799h
16. Jia, X.; Jiang, X.; Liu, R.; Yin, J. *Macromol. Chem. Phys.* **2009,** *210,* 1876–1882. doi:10.1002/macp.200900291
17. Okamoto, T.; Yamaguchi, I.; Kobayashi, T. *Opt. Lett.* **2000,** *25,* 372–374. doi:10.1364/OL.25.000372
18. Zhao, J.; Chen, M.; Liu, J.; Yan, F. *Thin Solid Films* **2009,** *517,* 3752–3759. doi:10.1016/j.tsf.2009.02.031
19. Weisbecker, C. S.; Merritt, M. V.; Whitesides, G. M. *Langmuir* **1996,** *12,* 3763–3772. doi:10.1021/la950776r
20. Yamaguchi, T.; Okawa, H.; Hashimoto, K.; Shimojo, M.; Kajikawa, K. *Phys. Rev. B* **2011,** *83,* 085425. doi:10.1103/PhysRevB.83.085425

Tunable magnetism on the lateral mesoscale by post-processing of Co/Pt heterostructures

Oleksandr V. Dobrovolskiy[*1,2], Maksym Kompaniiets[1], Roland Sachser[1], Fabrizio Porrati[1], Christian Gspan[3], Harald Plank[3,4] and Michael Huth[1]

Full Research Paper

Address:
[1]Physikalisches Institut, Goethe University, 60438 Frankfurt am Main, Germany, [2]Physics Department, V. Karazin Kharkiv National University, 61077 Kharkiv, Ukraine, [3]Graz Centre for Electron Microscopy, 8010 Graz, Austria and [4]Institute for Electron Microscopy and Nanoanalysis, TU Graz, 8010 Graz, Austria

Email:
Oleksandr V. Dobrovolskiy[*] - Dobrovolskiy@Physik.uni-frankfurt.de

* Corresponding author

Keywords:
cobalt; focused electron beam induced deposition; heterostructures; in situ processing; platinum

Abstract

Controlling magnetic properties on the nanometer-scale is essential for basic research in micro-magnetism and spin-dependent transport, as well as for various applications such as magnetic recording, imaging and sensing. This has been accomplished to a very high degree by means of layered heterostructures in the vertical dimension. Here we present a complementary approach that allows for a controlled tuning of the magnetic properties of Co/Pt heterostructures on the lateral mesoscale. By means of in situ post-processing of Pt- and Co-based nano-stripes prepared by focused electron beam induced deposition (FEBID) we are able to locally tune their coercive field and remanent magnetization. Whereas single Co-FEBID nano-stripes show no hysteresis, we find hard-magnetic behavior for post-processed Co/Pt nano-stripes with coercive fields up to 850 Oe. We attribute the observed effects to the locally controlled formation of the CoPt $L1_0$ phase, whose presence has been revealed by transmission electron microscopy.

Introduction

Controlling magneto-transport properties on the nanometer-scale is essential for basic research in micro-magnetism [1] and spin-dependent transport [2] as well as for various applications, such as magnetic domain-wall logic [3] and memory [4], fabrication of Hall sensors [5] and cantilever tips [6] for magnetic force microscopy (MFM). In particular, the ability to tune the magnetization is the basic property needed for the realization of stacked nanomagnets [7], pinning of magnetic domain walls [8] and Abrikosov vortices [9-11], magnetic sensing [5,12] and storage [3,4], and spin-triplet proximity-induced superconductivity [13-17]. This magnetization tuning has been accomplished to a very high degree by means of layered heterostructures in the vertical dimension, which can be prepared by thin film techniques or by an alternative approach, as used by us, namely the direct writing of metal-based layers by focused electron beam induced deposition (FEBID) [18,19]. The resolution

of FEBID is better than 10 nm laterally and 1 nm vertically [18,19] and, thus, its proven applications range from photomask repair [20] to fabrication of nanowires [17,21], nanopores [22], magnetic [5,12] and strain sensors [23] as well as direct-write superconductors [24].

The precursors $Co_2(CO)_8$ and $(CH_3)_3CH_3PtC_5H_4$ from which Pt- an Co-based structures can be fabricated in the FEBID process, like most metal-organic precursors, do not dissociate into the respective pure materials, unless FEBID of Co is done at elevated substrate temperatures [25]. By contrast, when decomposed in the focus of the electron beam into volatile components and the permanent deposit on the processed surface, these form granular metals, whose grains are embedded in a carbon-rich, poorly conducting matrix. In consequence, the electrical conductivity of as-deposited Pt-based FEBID structures usually is in the high-ohmic or even the insulating regime while that of as-deposited Co-FEBID structures is at least one order of magnitude lower than that of pure Co, typically. In addition, though the magnetic properties of as-deposited Co-FEBID structures are sufficient for application in Co MFM tips [6] and studying the effects of topological structures on the magnetization reversal process [26], these properties differ from those of pure Co. Still, owing to the sensitivity of the matrix to post-processing treatments, the compositional, structural, and, hence, electrical [27,28] and magnetic [29,30] properties of metal-based layers fabricated by FEBID can be substantially modified either in situ or ex situ. Exemplary purification treatments of samples include annealing in reactive gases [31], electron irradiation [27,28], or a combination of both [30,32-34].

Several approaches have already been proposed for the preparation of magnetic nanoparticles and their alloying, in particular, with the purpose of eventually using them for ultrahigh-density data-storage media. Thus, driven by the need to accomplish the above demand, FePt magnetic nanoparticles were prepared using colloidal chemistry [35] and micellar methods [36]. The latter method was also extended to the preparation of CoPt nanoparticles [37]. Later on, it turned out easier to deposit self-assembled Co nanoparticles on top of Pt thin films [38] and thereby fabricate surface alloys formed at step edges of Pt single crystalline substrates. In that work [38], an increase of the coercive field and of the Co orbital magnetic momentum was observed and attributed to the formation of the CoPt L1$_0$ phase with strongly increased magnetic anisotropy compared to pure Co.

Here, we employ direct writing of Pt and Co layers by FEBID and demonstrate by means of in situ post-processing how to locally tune the coercive field and the remanent magnetization of layered Co/Pt FEBID nano-stripes. This is achieved by a combination of in situ heating in a local reactive gas atmosphere (H_2 and O_2) and electron-beam irradiation of as-deposited layers, as is sketched in Figure 1. We show that the magnetic response of the nano-stripes can be tuned on the lateral mesoscale, from the magnetic properties of Co to the hard ferromagnetic response of the CoPt L1$_0$ phase, whose presence has been revealed by transmission electron microscopy.

Experimental
Preparations and geometry
Co and Pt growth, processing and imaging experiments were carried out in a dual-beam high-resolution scanning electron microscope (SEM: FEI, Nova NanoLab 600). The SEM was equipped with a multi-channel gas injection system for FEBID. As substrates we used epi-polished c-cut (0001) Al_2O_3 with Cr/Au contacts of 3/50 nm thickness prepared by photolithography in conjunction with lift-off. The samples are one Co-FEBID structure and three Co/Pt-FEBID nano-stripes labeled as sample A, B, C, and D, respectively. The Co/Pt deposits B and C bridging a 12 μm gap between the Au contacts were deposited in a 6-point geometry, while samples A and D were deposited in a cross-shaped fashion, see Figure 2 for an overview. The only reason for the different geometry of
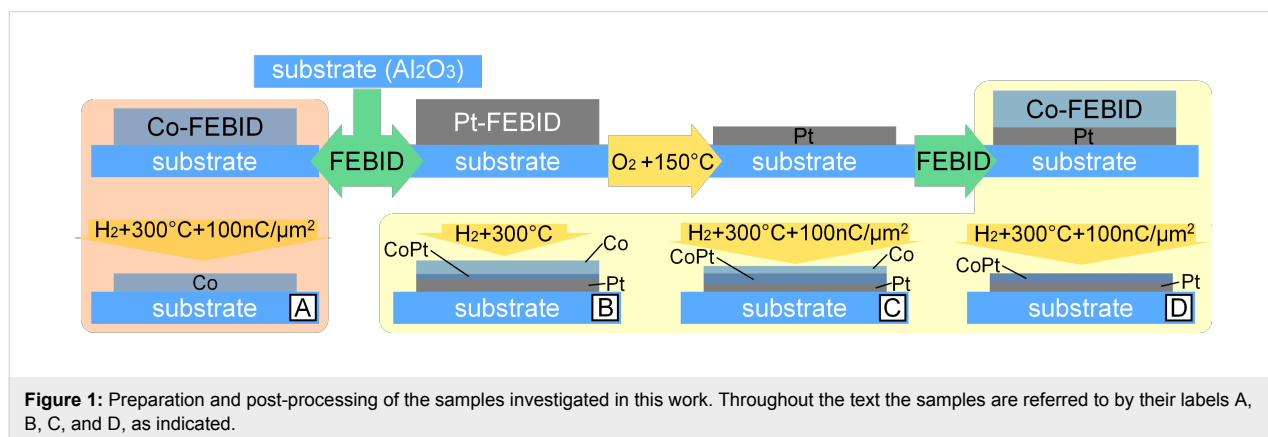
Figure 1: Preparation and post-processing of the samples investigated in this work. Throughout the text the samples are referred to by their labels A, B, C, and D, as indicated.
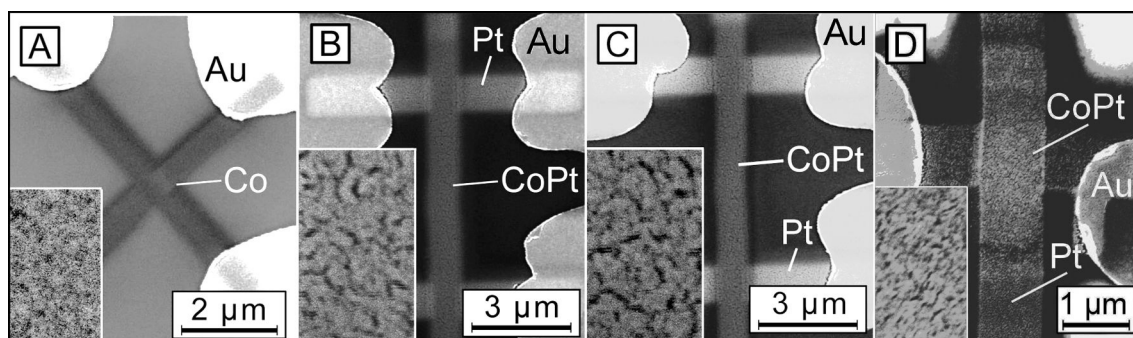
Figure 2: SEM images of the samples. The 500 × 860 nm^2 insets show the morphology of the post-processed Co/Pt FEBID nano-stripes in the middle of the overlap of the nano-stripes.

samples B and C lies in that they were originally designed for other measurements in addition to those reported here.

FEBID of Pt

FEBID of Pt was used for the fabrication of the bottom layers of all samples, with exception of sample A. In the FEBID process the precursor gas was $(CH_3)_3Pt(CpCH_3)$, the beam parameters were 5 kV/1 nA, the pitch was 20 nm, the dwell time was 1 μs, the precursor temperature was 44 °C, and the process pressure was 9.5×10^{-6} mbar for a needle position of the gas injector at 100 μm height and 100 μm lateral shift from the writing field position. After the Pt deposition, the samples were heated up to 150 °C in the same SEM without breaking the vacuum. For the design of the heatable stage adapter and the sample holder we refer to [39]. Once heated, the Pt-based deposits were subjected to an oxygen flux fed into the vacuum chamber up to a pressure of 1.5×10^{-5} mbar through a home-made gas injection system. The samples were subjected to 12 cycles of oxygen flux switched on for 5 min interrupted by 5-minute turn-offs. The resistivity of the as-deposited Pt-based layers was 0.4 Ω·cm, decreased to about 90 mΩ·cm as the temperature rose to 150 °C, and dropped to 70–90 μΩ·cm after 10 oxygen pulses. Figure 3 depicts the time-dependent normalized conductance of the Pt layer of sample C during the purification process. The post-processed Pt layers exhibited a nano-porous structure and a reduction of height from 50 ± 1.5 nm to 11 ± 1.5 nm, as inferred from atomic force microscopy, due to the removal of the carbonaceous matrix [39]. The void volume fraction of the very thin purified Pt layer was estimated from a grey scale threshold analysis of the SEM image which yields a value of 0.31 ± 0.07.

FEBID of Co

FEBID of Co was used for the preparation of the top layers of the structures. In the FEBID process the precursor gas was $Co_2(CO)_8$, the beam parameters were 5 kV/1 nA, the pitch was 20 nm, the dwell time was 50 μs, the precursor temperature was 27 °C, and the process pressure was 8.85×10^{-6} mbar.
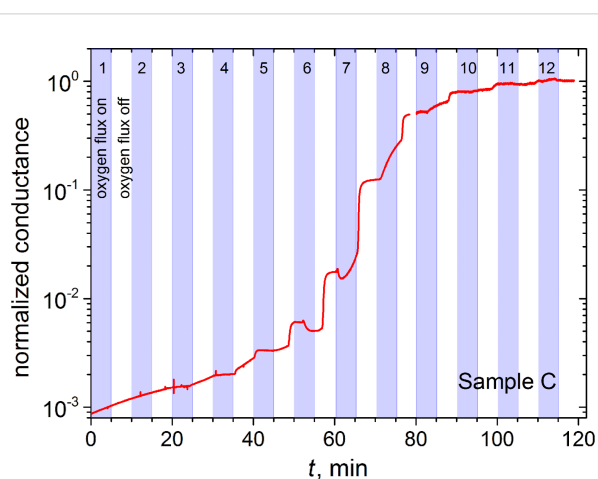
Figure 3: Time-dependent conductance of the Pt layer of sample C normalized to its saturation value after the purification process at 150 °C consisting of 12 cycles with a total duration of 120 min. The filled areas under the curve show the time intervals with the oxygen flux switched on.

Before the deposition, the chamber was evacuated down to 4.12×10^{-6} mbar. For removing the residual water from the SEM chamber a custom-made liquid-nitrogen trap filled with zeolite powder was employed. After the deposition all samples were heated up to 300 °C in the SEM without breaking the vacuum and subjected to a H_2 flux fed into the SEM chamber up to a pressure of 1.5×10^{-5} mbar. While kept at 300 °C, samples A and C, and D were additionally irradiated with the electron beam (5 kV/1 nA, 20 nm pitch, 50 μs dwell time), whereas sample B was left non-irradiated. The irradiation dose was 100 nC/μm^2 for all irradiated samples. After this purification step, the thickness of the Co layers reduced by a factor of 1.55, in agreement with previous work [30].

Thickness-integrated EDX

The thickness-integrated material composition of the samples was inferred from energy-dispersive X-ray (EDX) spectrosco-

py, in the same SEM without exposure of the deposits to air. The EDX parameters were 5 kV and 1.6 nA. The elemental composition was calculated considering ZAF (atomic number, absorbtion and fluorescence) and background corrections. The software we used to analyze the material composition in the deposits was EDAX's Genesis Spectrum v. 5.11. The elemental composition was quantified without thickness correction, so that the reported data are a qualitative indicator only.

Electrical resistance measurements

The electrical and magneto-resistance measurements were carried out in a helium-flow cryostat equipped with a superconducting solenoid. The measurements were done in the current-drive mode, with a current density of the order of 10 kA/cm^2. For the Hall voltage measurements a lock-in amplifier in conjunction with a differential preamplifier and a ratio transformer to null the signal at $H = 0$ were used [40]. The measurements were done with the magnetic field directed normally to the stripe plane and immediately after transferring the samples from the SEM after the Co purification step.

Transmission electron microscopy

For an inspection of the selected sample C by scanning transmission electron microscopy (STEM) a Titan G2 microscope from FEI with a CS probe corrector (DCOR) was used. The TEM was equipped with a X-FEG high-brightness electron gun, the high-end post-column electron energy filter Quantum ERSTM from Gatan, and four high sensitivity SDD X-ray detectors from Bruker (Super-X). The measurements were performed at an accelerating voltage of 300 kV with an electron probe diameter smaller than 1 Å. Before the TEM measurements, sample C was covered with a 300 nm thick protective Pt–C layer deposited by FEBID. The pixel time for the energy-dispersive X-ray cross-sectional line scan (cross-sectional EDX) was 8 seconds per spectrum and the step size was 0.8 nm.

Nano-diffraction and simulations

A convergence angle of 1.0 mrad was used to generate electron nanodiffraction patterns in the STEM mode. These diffraction patterns were recorded energy-filtered on a 16-bit CCD. To collect the nanodiffraction images over the complete layer the

"diffraction spectrum image" technique was used as part of the software package Digital Micrograph (Gatan). The lateral step size from pixel to pixel was 3.7 nm. Therefore, an individual selection of the diffraction patterns from the upper and the lower layer was possible. For a comparison with the experimental nanodiffraction data from the upper and lower layer, electron diffraction simulations for the CoPt fcc- and fct-phase assuming bulk lattice constants were made with the software JEMS [41]. The simulations were done in the kinematic mode. For the generation of the elemental signal profile the intensity from the Pt M edge (2.05 keV) and the Co K edge (6.92 keV) was used.

Results and Discussion
Structural and electrical resistance properties

SEM images of the samples investigated in this work are shown in Figure 2, while their geometrical dimensions, elemental composition, and magnetic properties are compiled in Table 1.

The EDX data were acquired at the overlaps of the nano-stripes and normalized to 100 atom % after exclusion of the oxygen-based signal whose bulk part unavoidably stems from the substrate (Al_2O_3), due to the small thickness of the investigated samples. At the same time, from previous work [30] in which we reported, in particular, a reduction of the oxygen content in individual Co stripes at different stages of the same purification treatment, we aware of the remaining O content at a level of about 10 atom % in the processed stripes. For these reasons, though acquired with a statistical error of 3%, the EDX data in Table 1 only serve as an indicator of the Co/Pt ratio being crucial for the different Co/Pt alloy phase formation — an issue to which we return in what follows.

The temperature dependence of the electrical resistance of all samples is metallic. The resistivities of the samples at 10 K are about 40 μΩ·cm and the room temperature-to-10-K resistance ratios are about 1.3. The room temperature resistivity values are an order of magnitude larger than the literature values for bulk Co and Pt [42] and are in agreement with the recently reported values for purified individual Co [30] and Pt [39] FEBID structures.

Table 1: Geometrical dimensions, thickness-integrated composition, and magnetic properties of the samples. *l*: length; *w*: width; d_{Co}: thickness of the Co layer; d_{Pt}: thickness of the Pt layer; H_c: coercive field; H_s: saturation field; M_r/M_s: remanent-to-saturation magnetization ratio (squareness).

sample	*l* [μm]	*w* [μm]	d_{Co} [nm]	d_{Pt} [nm]	Co [atom %]	Pt [atom %]	C [atom %]	H_c [Oe]	H_s [T]	M_r/M_s	Co/Pt
A	0.49	0.5	11	0	92	0	8	—	1.7	—	∞
B	5.45	1	10	11	54	27	19	770	1.5	0.15	2
C	5.35	1	11	11	49	22	29	850	1.3	0.25	2.23
D	1	1	5	11	35	35	30	420	0.5	0.18	1

Magneto-transport properties

The central finding of this work lies in the modification of the field dependences of the Hall voltage $U(H)$ measured at 10 K for all samples, see Figure 4. The magnetic field was directed perpendicular to the sample plane and, hence, the out-of-plane magnetization was probed by the measurements. This means that first the shape anisotropy of the stripe had to be overcome and all recorded loops relate to the hard-axis magnetization behavior.

The reference Co-based sample A shows no hysteresis, whereby $U(H)$ is nearly linear from −1.5 T to 1.5 T and saturates at $H_s = \pm 1.7$ T. The $U(H)$ curve of the Co/Pt-based sample B demonstrates two distinctive features compared to sample A: Sample B shows a noticeable hysteresis loop and its saturation field H_s is by about 30% smaller than H_s for sample A. The behavior of sample B is that of ferromagnet, with a coercive field H_c of 770 Oe and a remanent-to-saturation magnetization ratio (squareness) M_r/M_s of 0.15. The irradiated Co/Pt-based sample C exhibits an even broader hysteresis loop with $H_c = 850$ Oe and $M_r/M_s = 0.25$, respectively, and its saturation field H_s amounts to 1.3 T. Even though samples B and C demonstrate a hysteresis loop, we note that it is not completely open and the overall behavior of the Hall voltage curves is suggestive of a superposition of a soft and hard ferromagnetic response. We attribute these contributions to different phases formed at different depths within the layered nano-stripe, as will be corroborated by a TEM inspection in the section devoted to the microstructure analysis.

Summarizing this part, the following two effects are observed in the post-processed Co/Pt samples, namely (i) the development of hysteresis and (ii) a reduction of the saturation field. To explain both effects, we next discuss the processes which take place in the deposits in the course of purification treatments.

Purification mechanisms

The as-deposited reference sample A has a nanogranular Co microstructure with inclusions of carbon and oxygen. The employed purification procedure of heating at 300 °C in H_2 atmosphere in conjunction with electron irradiation relies upon the Fischer–Tropsch reaction [30,43]. In this chemical process, cobalt serves as a catalyst, while volatile hydrocarbons and water are produced, effectively oxidizing the carbon. Thus, in the course of the reaction, carbon is partially removed from the deposit causing a reduction of the deposit thickness. The magnetic behavior of the thin polycrystalline Co stripe A is dominated not by the magnetocrystalline anisotropy, but rather by the shape anisotropy causing the magnetization to lie preferentially along the stripe axis. Given the demagnetizing factor for the created geometry, $N \approx 1$ [44], we arrive at a saturation magnetization of $M_s = H_s/N = 1.7$ T $\times 10^4/4\pi \cong 1353$ emu/cm^3, corresponding to 98% of the bulk value [45]. Allowing for an up to 5% error in the determination of the saturation magnetization value and a concurrence of the presence of carbon and oxygen in sample A, this value is likely slightly overestimated and, hence, should be regarded as an upper bound only.

The as-deposited Pt-FEBID layers for samples B and C are also nanogranular metals. The purification mechanism for Pt-FEBID structures relies upon the catalytic activity of Pt [39,46] in oxygen atmosphere. Namely, when delivered close to the deposit surface, molecular oxygen is dissociatively chemisorbed on the surface of the metallic Pt particles. Since the process takes place at 150 °C, a thermally activated oxidation of carbon at the Pt/C interface occurs, leading to the formation of CO and a reorganization and coalescence of Pt nanocrystallites by surface diffusion. The latter, in turn, results in a nanoporous morphology, which is clearly seen in the SEM images of samples B and C in the insets to Figure 2. As will be shown below by TEM, it is this nanoporosity which allows Co to pene-
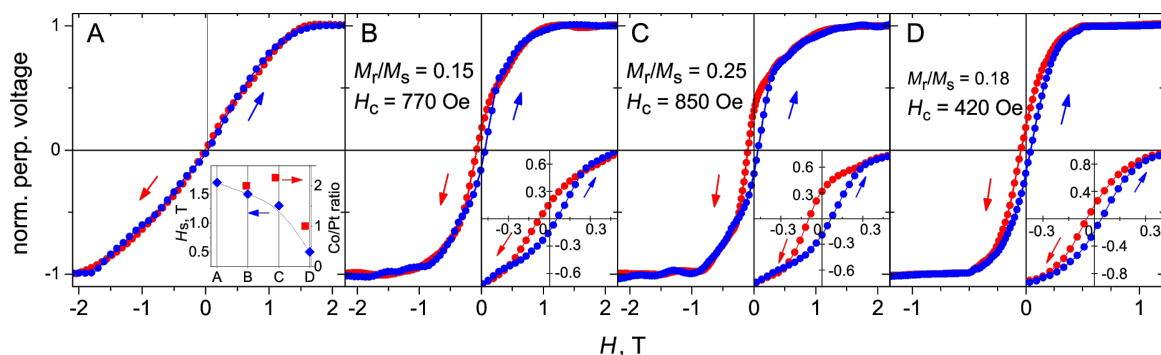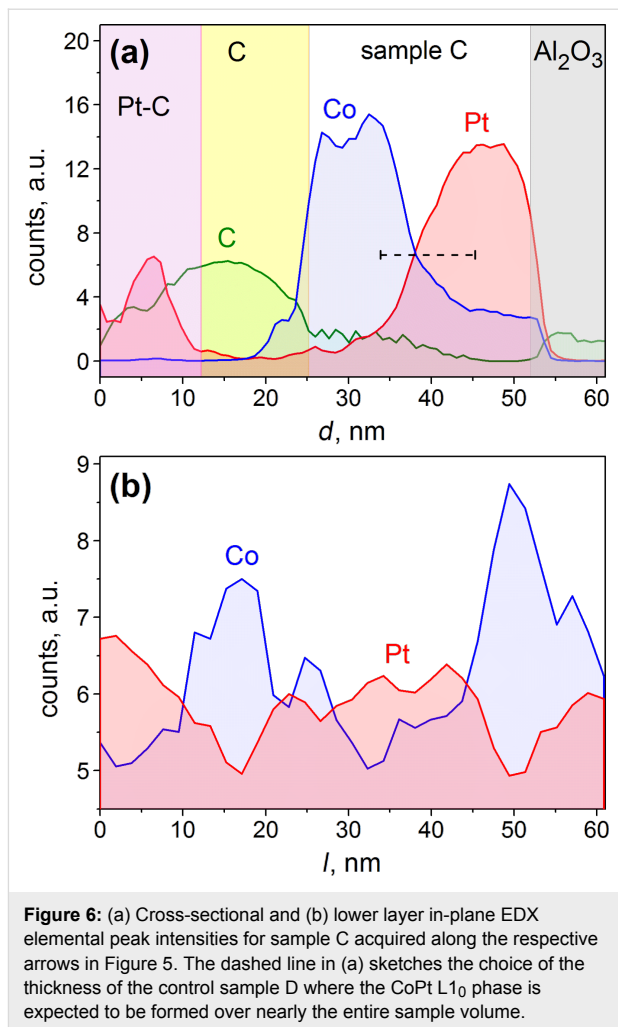

Figure 4: Hall voltage cycling at 10 K for all samples. Before measurements, all samples were saturated at 3 T. Note the different field range and scale for sample D. Inset in A: The magnetization saturation fields H_s and the Co/Pt ratios for all samples.

trate into the Pt layer during the Co deposition and to form a Co/Pt alloy phase. Considering the Co–Pt binary phase diagram [47], for a Co/Pt-ratio of 1:1, the CoPt $L1_0$ phase can form. This phase is a hard ferromagnet whose presence can explain both, the reduction of the saturation field as well as the appearance of a hysteresis loop in samples B and C.
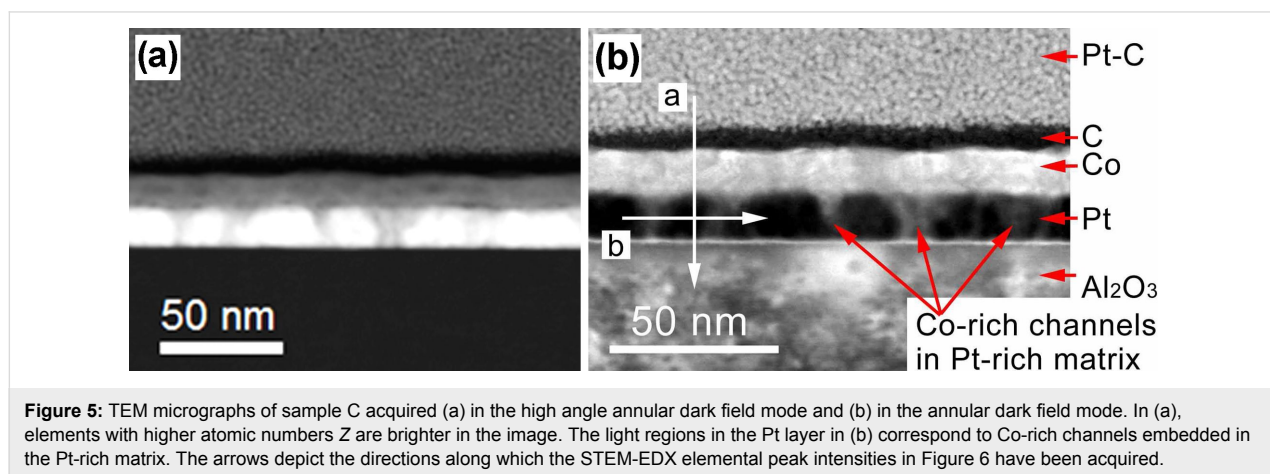
Microstructure analysis

To get insight into the microstructure of the purified samples and to examine, whether the assumed CoPt $L1_0$ phase is indeed present in sample C, once its magneto-resistance measurements had been completed, we inspected sample C by STEM. Figure 5 presents cross-sectional TEM images of sample C in the high angle annular dark field mode (a) and in the annular dark field mode (b). The respective elemental peak intensities obtained by STEM-EDX along the direction depicted by the arrows in Figure 5b are shown in Figure 6.

We now consider the TEM and EDX data in detail. From the cross-sectional STEM-EDX elemental peak intensities in Figure 6a it follows that the top layer of sample C predominantly consists of Co with a very minor content of Pt and C, whereby the Pt content gradually increases upon reaching the Co/Pt interface. The bottom layer largely consists of Pt with a notable content of Co down to the Al_2O_3 substrate, see the "step" in the Co signal profile in Figure 6a. The black region above the Co layer in Figure 5b is a carbon-rich layer peculiar to the TEM lamella preparation. When taking a closer look at the TEM micrograph in Figure 5b, one recognizes a series of light channels running through the entire thickness of the bottom layer. The in-plane scan, acquired within the bottom layer and shown in Figure 6b, reveals that these light channels correspond to Co-rich areas in the Pt-rich layer. The substantial variation of the Co and Pt signals in the in-plane scan further corroborates the hypothesis that the pores emerged in the course of purification of the Pt layer have been filled with Co.

Figure 6: (a) Cross-sectional and (b) lower layer in-plane EDX elemental peak intensities for sample C acquired along the respective arrows in Figure 5. The dashed line in (a) sketches the choice of the thickness of the control sample D where the CoPt $L1_0$ phase is expected to be formed over nearly the entire sample volume.

The individual nanodiffraction images for the upper and the lower layer are shown in Figure 7. The diffractograms are accompanied by the respective simulated diffraction patterns. Among the reflections in the upper layer in Figure 7b one recognizes the intensive (100)+(101) rings and clearly visible

Figure 5: TEM micrographs of sample C acquired (a) in the high angle annular dark field mode and (b) in the annular dark field mode. In (a), elements with higher atomic numbers *Z* are brighter in the image. The light regions in the Pt layer in (b) correspond to Co-rich channels embedded in the Pt-rich matrix. The arrows depict the directions along which the STEM-EDX elemental peak intensities in Figure 6 have been acquired.

Figure 7: The location of the probed layers is shown in panel (a). Nano-diffractograms of the upper (b) and the lower (c,d) layer of sample C alongside with the simulated diffraction patterns for a Co hcp phase (b), a Pt fcc lattice (c) and a CoPt fct phase (d).

(110) and (200) rings, which are the fingerprint for a Co hcp lattice. The rings (102), (103), and (114) may also be recognized, though these have a much lower intensity. As for the reflections for lower layer, we compare these with a Pt fcc lattice in Figure 7c and a CoPt fct phase in Figure 7d. As the simulation patterns depict, the bright rings (111), (200), (220) and (311) are expected for both lattices while the main reflections are dominated by Pt. At the same time, a weak additional diffraction intensity within the innermost Pt (111) ring suggests the presence of some smaller contribution from a CoPt fct phase, thereby supporting our hypotheses that the CoPt $L1_0$ phase is formed in the lower layer. For comparison, no such intensity is visible for Co in the upper layer. At the same time,

we believe that no full transformation to the $L1_0$ phase took place in the lower layer, but a partial transformation on the large inner surface of the nanoporous Pt layer in which the Co deposit (and then purified Co) is located. Accordingly, the diffraction pattern of the lower layer most likely shows an overlay of the Pt and the CoPt $L1_0$ phases.

Hard-magnetic response at a Co/Pt ratio of 1:1

As the presence of the CoPt $L1_0$ phase is confirmed by TEM inspection, we next examine the assumption that the hysteresis development and the rectangularity enhancement are indeed due to the presence of the CoPt $L1_0$ phase in the processed samples.

For this reason a control sample D was prepared, with the entire thickness chosen as shown by the dashed line in Figure 6a. The thickness of the Co layer in sample D was chosen such that, given the nano-porosity of the processed platinum, its atomic content per volume was set to be nearly equal to that in the processed Pt layer. In consequence of this, sample D is a nano-stripe where the formation of the CoPt $L1_0$ phase is most favorable (the Co/Pt ratio is very close to 1:1) and this phase is expected to be formed over nearly the entire sample volume. This is in contrast to samples B and C, where the CoPt $L1_0$ phase is likely formed within an interface layer only.

The Hall voltage cycling for sample D is shown in Figure 4D. It demonstrates a mostly hard-magnetic behavior. The $U(H)$ curve exhibits the most open, rectangular hysteresis loop among all measured samples, with $H_c = 0.5$ T and a squareness M_r/M_s of 0.18. This provides strong evidence that magnetic response hardening in the processed CoPt-FEBID nano-stripes is indeed due to the CoPt $L1_0$ phase, that is, in turn, in agreement with the correlation between the magnetization saturation field and the Co/Pt ratio depicted in the inset to Figure 4A. Indeed, the reduction of the saturation field H_s with reduction of the Co/Pt ratio can be explained by the increasing perpendicular magnetocrystalline anisotropy.

The Hall voltage cycling $U(H)$ for sample D was repeated at different temperatures up to room temperature, see Figure 8. The temperature-induced reduction of the coercive field and the remanent magnetization is presented in the inset to Figure 8. A linear extrapolation of the $H_c(T)$ data suggests that above 400 K sample D will exhibit paramagnetic behavior, attesting to the robustness of the ferromagnetism in this sample at room temperature.
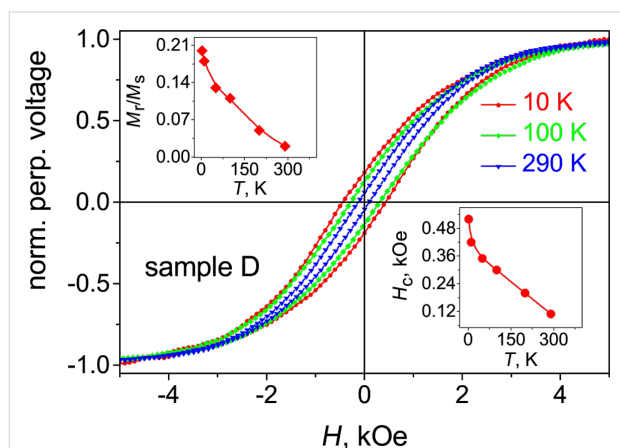
Figure 8: Isothermal Hall voltage cycling for sample D at a series of temperatures, as indicated. Insets: Temperature dependencies of the squareness M_r/M_s and the coercive field H_c for sample D. The lines are guides for the eye.

Conclusion

To summarize, we present an approach allowing for a controllable tuning of the magnetic properties of nano-stripe layered Co/Pt heterostructures with high resolution on the lateral mesoscale. We have demonstrated that by means of post-growth irradiation and heating of samples as well as by pre-defining the layer thicknesses, the magnetic response of the nano-stripes can be locally tuned from the soft-magnetic properties of Co to the hard ferromagnetic response of the CoPt $L1_0$ phase. The reported approach is relevant for basic research in micromagnetism and spin-dependent transport, as well as for various applications.

Acknowledgements

References

1. Kronmüller, H.; Fähnle, M. *Micromagnetism and the Microstructure of Ferromagnetic Solids (Cambridge Studies in Magnetism;* Cambridge University Press: Cambridge, United Kingdom, 2003.
2. Keizer, R. S.; Goennenwein, S. T. B.; Klapwijk, T. M.; Miao, G.; Xiao, G.; Gupta, A. *Nature* **2006,** *439,* 825–827. doi:10.1038/nature04499
3. Allwood, D. A.; Xiong, G.; Faulkner, C. C.; Atkinson, D.; Petit, D.; Cowburn, R. P. *Science* **2005,** *309,* 1688–1692. doi:10.1126/science.1108813
4. Parkin, S. S. P.; Hayashi, M.; Thomas, L. *Science* **2008,** *320,* 190–194. doi:10.1126/science.1145799
5. Gabureac, M.; Bernau, L.; Utke, I.; Boero, G. *Nanotechnology* **2010,** *21,* 115503. doi:10.1088/0957-4484/21/11/115503
6. Belova, L. M.; Hellwig, O.; Dobisz, E.; Dan Dahlberg, E. *Rev. Sci. Instrum.* **2012,** *83,* 093711. doi:10.1063/1.4752225
7. Takahashi, Y. K.; Hono, K.; Okamoto, S.; Kitakami, O. *J. Appl. Phys.* **2006,** *100,* 074305. doi:10.1063/1.2355442
8. O'Brien, L.; Petit, D.; Lewis, E. R.; Cowburn, R. P.; Read, D. E.; Sampaio, J.; Zeng, H. T.; Jausovec, A.-V. *Phys. Rev. Lett.* **2011,** *106,* 087204. doi:10.1103/PhysRevLett.106.087204
9. Vélez, M.; Martín, J. I.; Villegas, J. E.; Hoffmann, A.; González, E. M.; Vicent, J. L.; Schuller, I. K. *J. Magn. Magn. Mater.* **2008,** *320,* 2547. doi:10.1016/j.jmmm.2008.06.013
10. Dobrovolskiy, O. V.; Huth, M.; Shklovskij, V. A. *Supercond. Sci. Technol.* **2010,** *23,* 125014. doi:10.1088/0953-2048/23/12/125014
11. Dobrovolskiy, O. V.; Begun, E.; Huth, M.; Shklovskij, V. A.; Tsindlekht, M. I. *Physica C* **2011,** *471,* 449–452. doi:10.1016/j.physc.2011.05.245

12. Fernández-Pacheco, A.; De Teresa, J. M.; Córdoba, R.; Ibarra, M. R.; Petit, D.; Read, D. E.; O'Brien, L.; Lewis, E. R.; Zeng, H. T.; Cowburn, R. P. *Appl. Phys. Lett.* **2009,** *94,* 192509. doi:10.1063/1.3139068

13. Buzdin, A. I. *Rev. Mod. Phys.* **2005,** *77,* 935–976. doi:10.1103/RevModPhys.77.935

14. Bergeret, F. S.; Volkov, A. F.; Efetov, K. B. *Rev. Mod. Phys.* **2005,** *77,* 1321–1373. doi:10.1103/RevModPhys.77.1321

15. Wang, J.; Singh, M.; Tian, M.; Kumar, N.; Liu, B.; Shi, C.; Jain, J. K.; Samarth, N.; Mallouk, T. E.; Chan, M. H. W. *Nat. Phys.* **2010,** *6,* 389–394. doi:10.1038/nphys1621

16. Kompaniiets, M.; Dobrovolskiy, O. V.; Neetzel, C.; Porrati, F.; Brötz, J.; Ensinger, W.; Huth, M. *Appl. Phys. Lett.* **2014,** *104,* 052603. doi:10.1063/1.4863980

17. Kompaniiets, M.; Dobrovolskiy, O. V.; Neetzel, C.; Begun, E.; Porrati, F.; Ensinger, W.; Huth, M. *J. Appl. Phys.* **2014,** *116,* 073906. doi:10.1063/1.4893549

18. Utke, I.; Hoffmann, P.; Melngailis, J. *J. Vac. Sci. Technol., B* **2008,** *26,* 1197. doi:10.1116/1.2955728

19. Huth, M.; Porrati, F.; Schwalb, C.; Winhold, M.; Sachser, R.; Dukic, M.; Adams, J.; Fantner, G. *Beilstein J. Nanotechnol.* **2012,** *3,* 597–619. doi:10.3762/bjnano.3.70

20. Liang, T.; Frendberg, E.; Lieberman, B.; Stivers, A. *J. Vac. Sci. Technol., B* **2005,** *23,* 3101–3105. doi:10.1116/1.2062428

21. Fernández-Pacheco, A.; Serrano-Ramón, L.; Michalik, J. M.; Ibarra, M. R.; De Teresa, J. M.; O'Brien, L.; Petit, D.; Lee, J.; Cowburn, R. P. *Sci. Rep.* **2013,** *2,* No. 1492. doi:10.1038/srep01492

22. Danelon, C.; Santschi, C.; Brugger, J.; Vogel, H. *Langmuir* **2006,** *22,* 10711–10715. doi:10.1021/la061321c

23. Schwalb, C. H.; Grimm, C.; Baranowski, M.; Sachser, R.; Porrati, F.; Reith, H.; Das, P.; Müller, J.; Völklein, F.; Kaya, A.; Huth, M. *Sensors* **2010,** *10,* 9847–9856. doi:10.3390/s101109847

24. Winhold, M.; Weirich, P. M.; Schwalb, C. H.; Huth, M. *Appl. Phys. Lett.* **2014,** *105,* 162603. doi:10.1063/1.4898819

25. Belova, L. M.; Dahlberg, E. D.; Riazanova, A.; Mulders, J. J. L.; Christophersen, C.; Eckert, J. *Nanotechnology* **2011,** *22,* 145305. doi:10.1088/0957-4484/22/14/145305

26. Lara, A.; Dobrovolskiy, O. V.; Prieto, J. L.; Huth, M.; Aliev, F. G. *Appl. Phys. Lett.* **2014,** *105,* 182402. doi:10.1063/1.4900789

27. Sachser, R.; Porrati, F.; Schwalb, C. H.; Huth, M. *Phys. Rev. Lett.* **2011,** *107,* 206803. doi:10.1103/PhysRevLett.107.206803

28. Porrati, F.; Sachser, R.; Schwalb, C. H.; Frangakis, A. S.; Huth, M. *J. Appl. Phys.* **2011,** *109,* 063715. doi:10.1063/1.3559773

29. Bernau, L.; Gabureac, M.; Erni, R.; Utke, I. *Angew. Chem., Int. Ed.* **2010,** *49,* 8880–8884. doi:10.1002/anie.201004220

30. Begun, E.; Dobrovolskiy, O. V.; Kompaniiets, M.; Gspan, C.; Plank, H.; Huth, M. *Nanotechnology* **2015,** *26,* 075301. doi:10.1088/0957-4484/26/7/075301

31. Botman, A.; Mulders, J. J. L.; Hagen, C. W. *Nanotechnology* **2009,** *20,* 372001. doi:10.1088/0957-4484/20/37/372001

32. Mehendale, S.; Mulders, J. J. L.; Trompenaars, P. H. F. *Nanotechnology* **2013,** *24,* 145303. doi:10.1088/0957-4484/24/14/145303

33. Plank, H.; Noh, J. H.; Fowlkes, J. D.; Lester, K.; Lewis, B. B.; Rack, P. D. *ACS Appl. Mater. Interfaces* **2014,** *6,* 1018–1024. doi:10.1021/am4045458

34. Geier, B.; Gspan, C.; Winkler, R.; Schmied, R.; Fowlkes, J. D.; Fitzek, H.; Rauch, S.; Rattenberger, J.; Rack, P. D.; Plank, H. *J. Phys. Chem. C* **2014,** *118,* 14009–14016. doi:10.1021/jp503442b

35. Sun, S.; Murray, C. B.; Weller, D.; Folks, L.; Moser, A. *Science* **2000,** *287,* 1989–1992. doi:10.1126/science.287.5460.1989

36. Ethirajan, A.; Wiedwald, U.; Boyen, H.-G.; Kern, B.; Han, L.; Klimmer, A.; Weigl, F.; Kästle, G.; Ziemann, P.; Fauth, K.; Cai, J.; Behm, R. J.; Romanyuk, A.; Oelhafen, P.; Walther, P.; Biskupek, J.; Kaiser, U. *Adv. Mater.* **2007,** *19,* 406–410. doi:10.1002/adma.200601759

37. Wiedwald, U.; Han, L.; Biskupek, J.; Kaiser, U.; Ziemann, P. *Beilstein J. Nanotechnol.* **2010,** *1,* 24–47. doi:10.3762/bjnano.1.5

38. Han, L.; Wiedwald, U.; Biskupek, J.; Fauth, K.; Kaiser, U.; Ziemann, P. *Beilstein J. Nanotechnol.* **2011,** *2,* 473–485. doi:10.3762/bjnano.2.51

39. Sachser, R.; Reith, H.; Huzel, D.; Winhold, M.; Huth, M. *ACS Appl. Mater. Interfaces* **2014,** *6,* 15868–15874. doi:10.1021/am503407y

40. Beyer, A. D.; Koesters, M.; Libbrecht, K. G.; Black, E. D. *Am. J. Phys.* **2005,** *73,* 1014–1019. doi:10.1119/1.2049284

41. *Electron Microscopy Software Java Version,* 3.7824U2012; Dr. P. Stadelmann, 2012, http://cimewww.epfl.ch/people/stadelmann/jemsWebSite/jems.html.

42. Kittel, C. *Introduction to Solid State Physics;* Wiley-VCH: Weinheim, Germany, 2004.

43. Anderson, R. B. *The Fischer-Tropsch Synthesis;* Academic Press: Waltham, MA, United States, 1984.

44. Hubert, A.; Schäfer, R. *Magnetic Domains: The Analysis of Magnetic Microstructures;* Springer: Berlin, Germany, 2008.

45. Chappert, C.; Bernas, H.; Ferré, J.; Kottler, V.; Jamet, J.-P.; Chen, Y.; Cambril, E.; Devolder, T.; Rousseaux, F.; Mathet, V.; Launois, H. *Science* **1998,** *280,* 1919–1922. doi:10.1126/science.280.5371.1919

46. Wintterlin, J.; Zambelli, T.; Barth, J. V.; Ertl, G. *Nature* **1997,** *390,* 495–497. doi:10.1038/37329

47. Massalski, T. B. *Binary Alloy Phase Diagrams;* ASM Intl.: Russel Township, Ohio, United States, 1990.

Scanning reflection ion microscopy in a helium ion microscope

Yuri V. Petrov[*1] and Oleg F. Vyvenko[2]

Abstract

Reflection ion microscopy (RIM) is a technique that uses a low angle of incidence and scattered ions to form an image of the specimen surface. This paper reports on the development of the instrumentation and the analysis of the capabilities and limitations of the scanning RIM in a helium ion microscope (HIM). The reflected ions were detected by their "conversion" to secondary electrons on a platinum surface. An angle of incidence in the range 5–10° was used in the experimental setup. It was shown that the RIM image contrast was determined mostly by surface morphology but not by the atomic composition. A simple geometrical analysis of the reflection process was performed together with a Monte Carlo simulation of the angular dependence of the reflected ion yield. An interpretation of the RIM image formation and a quantification of the height of the surface steps were performed. The minimum detectable step height was found to be approximately 5 nm. RIM imaging of an insulator surface without the need for charge compensation was successfully demonstrated.

Introduction

Reflection ion microscopy (RIM) is a technique that uses low-angle, scattered ions to form an image of the specimen surface. This technique is similar to reflection electron microscopy (REM) proposed by Ruska in 1933 [1] who realized REM using an angle of 90° between the incident and reflected beams. Later, in the 1950s, a REM technique employing lower incidence angles [2-4] was developed to increase the sensitivity to vertical surface irregularities. A vertical resolution of tens of nanome-

ters was obtained and it was shown that the negative effect of chromatic aberration was also reduced at low incidence angles, yet was still more pronounced in REM as compared to TEM [2,4]. The further development of REM in ultrahigh vacuum conditions allowed imaging of the single atomic steps [5-8] and monitoring of atomic layer-by-layer crystal growth by means of reflection high energy electron diffraction (RHEED) [9]. In the late 1960s, scanning reflection electron microscopy (SREM)

was developed [10,11] for the scanning electron microscope (SEM). Chromatic aberration does not appear in SEM because the sample is placed outside of the electron optics. Both REM and SREM require a sufficiently long depth of focus for high quality imaging because of the glancing angle of incidence geometry.
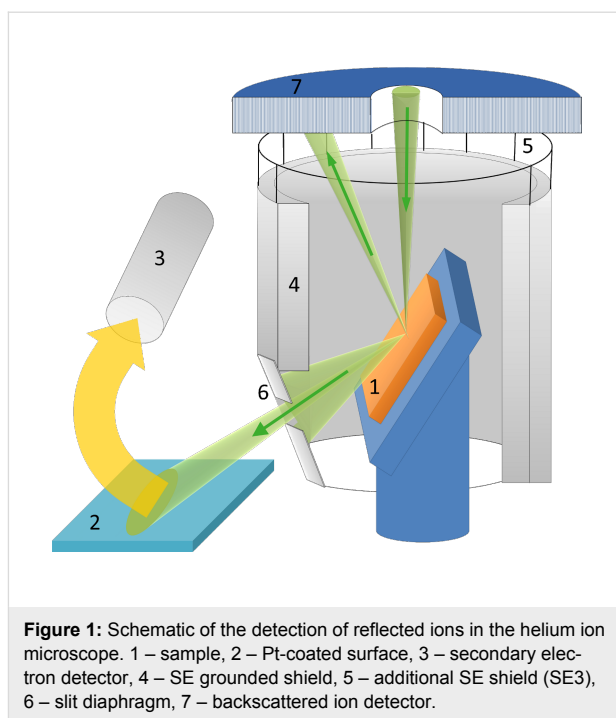
The helium ion microscope is a new scanning microscope with a single atom ion source that was developed in 2006 [12-15]. One of the main features of this device is a large depth of focus provided by a narrow beam divergence angle of about 0.5 mrad [15,16], which is ten times less than the best beam divergence angle possible in SEM. The large depth of focus makes helium ion microscopy (HIM) a very promising tool for scanning reflection microscopy. During the last decade the imaging capabilities of HIM were examined in the field of material science [15,17-23] as well as in biology [15,16,24-26]. Different techniques such as secondary electron energy filtering [27], helium ion channeling contrast [28-30], helium ion transmission microscopy [31], secondary ion mass spectrometry [32,33], and ionoluminescence [34,35] were developed.

In this paper we report on the development of the instrumentation and the analysis of the capabilities and limitations of scanning reflection ion microscopy (RIM) in a helium ion microscope. In the experimental part of our work we describe a configuration of a sample holder developed for RIM and demonstrate first results obtained for standard test samples. In the discussion part a simple theoretical treatment of the image contrast formation in RIM is provided, which is necessary to obtain quantitative information from RIM images.

Experimental

All investigations were performed in a Zeiss Orion scanning helium ion microscope. The detection of reflected ions (RIs) requires an additional detector installed below the specimen. One of the easiest ways to detect the reflected ions is by their "conversion" to secondary electrons (SEs). Previously, such a RI-to-SE conversion was used for the detection of backscattered electrons in SEM [36] and for scanning transmission mode in HIM [37]. A schematic of the originally developed RI detection system is shown in Figure 1.

The sample (1) was mounted on a stage at a grazing angle relative to the focused helium ion beam. The reflected helium ions were directed to the Pt-coated plate (2) which served as the main RI-to-SE converter. Platinum was chosen because of its high SE yield under He-ion excitation [12]. The SE signal was measured by a conventional Everhart–Thornley (ET) detector (3). The sample was surrounded by grounded metal shields (4 and 5) and was kept under a positive bias of 100 V to exclude

Figure 1: Schematic of the detection of reflected ions in the helium ion microscope. 1 – sample, 2 – Pt-coated surface, 3 – secondary electron detector, 4 – SE grounded shield, 5 – additional SE shield (SE3), 6 – slit diaphragm, 7 – backscattered ion detector.

the detection of SEs coming from the sample and SEs excited by backscattered ions from the chamber walls and objective lens (by the so-called SE3). The shield (5) is shown as transparent in Figure 1 in order to make the ion beam paths visible. The detection of SEs excited from the conductive sample occurred when the bias was switched off, as the SEs excited from the conductive sample exceeded the signal of the RI-to-SE converter. For insulating samples, the SE signal from the sample could not be detected because of positive charging as will be described further in detail below.

The angular aperture of detected reflected ions was limited by the slit (6) installed under specular reflection conditions. The slit, with the width of about 1 mm, was mounted parallel to the tilt axis of the sample stage at a distance of about 14 mm, which corresponds to an RI detection angular aperture of 4°. Backscattered ions (BSI) were detected by the microchannel plate detector (7). The width of the scanned area was less than tens of micrometers, corresponding to the variation of the detection angle of less than 0.1°. The incidence angle of the RIs was also practically unchanged during the scan over the small sample area, which assured the proportionality between the number of SEs excited from the Pt plate and the number of RIs.

All measurements were performed in the chamber with a base pressure in the range of 10^{-7} Torr. The energy of the He ions was 35 keV with a beam current of 0.5 pA. The compensation of the sample charge by the electron flood gun was not possible due to the configuration of the sample holder.

The following model test samples were investigated: (1) a Au on carbon SEM test sample from Agar scientific, (2) an AFM standard TGQ-1 from NT-MDT: a grid of SiO_2 square bars of 22 nm thickness on a silicon substrate, and (3) a mica (phlogopite) sample prepared by mechanical cleavage.

Results

Comparison of RI, SE and BSI imaging modes: Au on carbon test sample

Figure 2 represents the RI and BSI images of Au on a carbon sample taken at the grazing angle of incidence of 5° and the same angle for RI detection.

In Figure 2, one can easily recognize that only the central part of the images is in focus, which is due to the tilt of the sample with respect to the incident beam. This allows the independent estimation of the divergence angle of the He-ion beam from the pixel size and the depth of focus. The depth of focus is defined as the distance between the edges of the in-focused part of the image plane divided by the tangent of the grazing angle. From the image in Figure 2, the depth of focus can be estimated to be approximately 10 μm. Using digital signal processing in HIM, the image remains sharp unless the diameter of the beam is larger than the pixel size in the image. From the width of the image field of view (2.5 μm) and the number of acquisition points 1000 × 1000, the pixel size was calculated to be 2.5 nm. These values gave the angle of the beam divergence of approximately 0.5 mrad, which is in a good agreement with the manufacturer's data.

Figure 2 represents the images of a Au on carbon sample that is partially covered by Au nanoparticles in the central part only.

As expected, the Au particles exhibit a bright contrast in the BSI image on the dark background of the carbon substrate due to its significantly larger atomic number. On the contrary, the RI image does not show any noticeable signal difference between two different materials, giving information about surface morphology only. Additionally, the ratio of the signals from the top and side surface of the Au particles in the BSI and RI images are inverted. The top surface of the particles is brighter than the side wall in the RI image, whereas in BSI image, the situation is reversed.

Figure 3a,b represents a comparison of the SE and RI imaging modes of Au on carbon. One can see that in both imaging modes there is no noticeable signal level difference between the Au nanoparticles in the central part of the image and the carbon substrate in the upper and the lower parts of the image. This implies that the RI yield at low ion incidence angles does not depend on the element properties and the RI contrast in the images originates from the surface morphology only in contrast to the case of normal incidence. One should also note that SE and RI images focusing on the same structural peculiarities differ from each other. A more detailed description of the difference will be treated in the next section.

Reflection ion microscopy of silicon dioxide steps on silicon

Figure 4 shows images of SiO_2 bars on silicon obtained by the detection of SEs (Figure 4a) or RIs (Figure 4b) under the grazing and detection angles of 10°. One can easily recognize two main differences between the RI and SE images. Firstly, the contrast between silicon and silicon dioxide is clearly distinguishable in SE image, but not in the RI image. Note that the
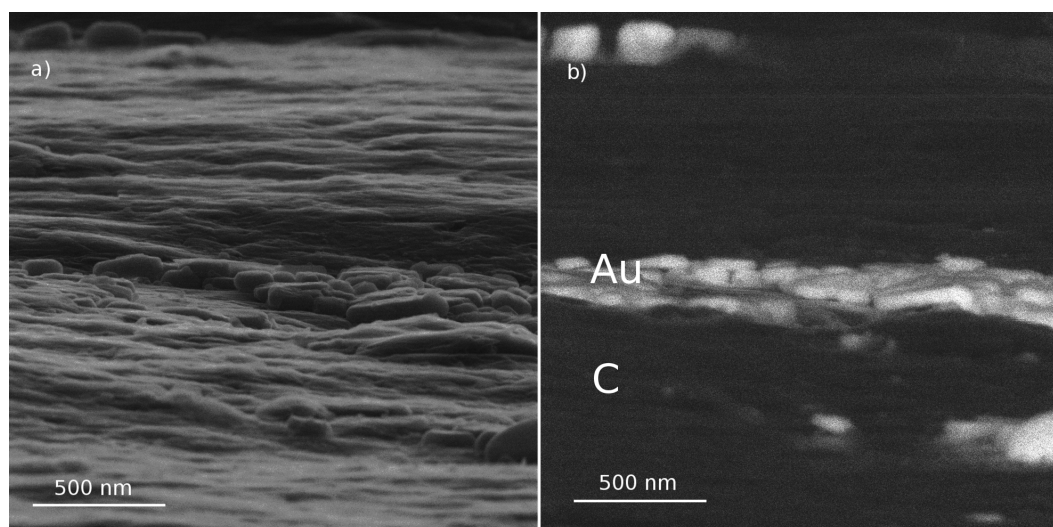
Figure 2: Images of Au on carbon by detection of reflected He ions (a) and backscattered ions (b).
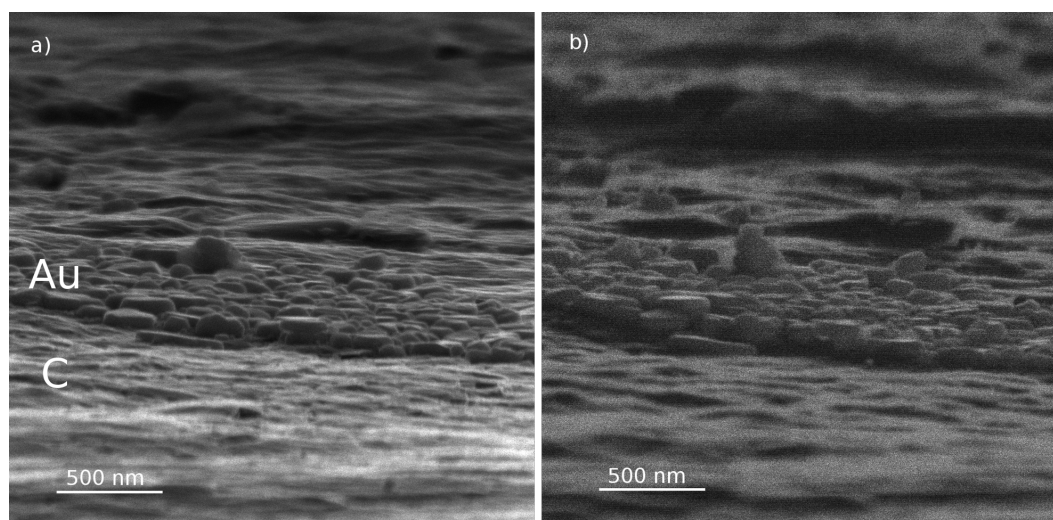
Figure 3: Images of Au on carbon obtained by detection of secondary electrons (a) and reflected He ions (b).
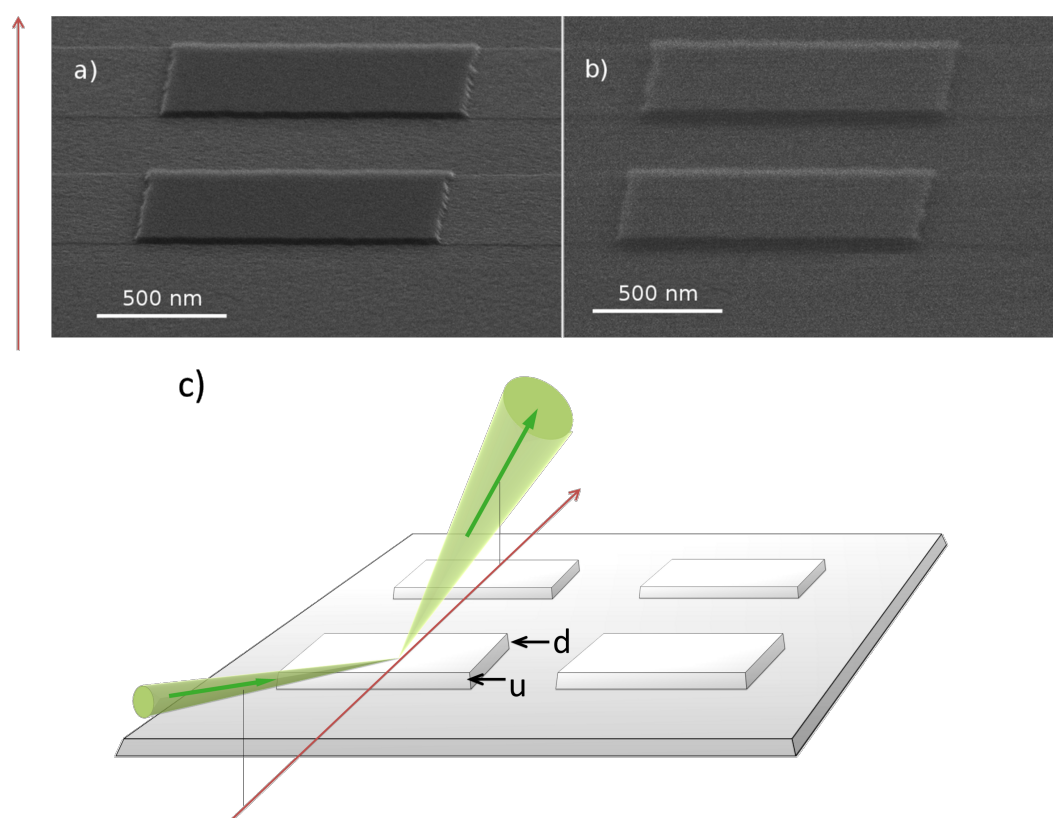
Figure 4: Images of silicon dioxide bars on silicon (TGQ-1 sample) obtained by detection of (a) secondary electrons, (b) reflected ions. (c) Sketch of ion beam path: green arrows correspond to the direction of the primary beam and reflected beam, the red axis corresponds to the vertical axis of the images in (a) and (b). "Upward" and "downward" steps are marked with "u" and "d", respectively.

silicon dioxide bars are darker than the silicon substrate in the SE image (see Figure 4a), while there was no noticeable SE signal difference between Au and carbon (see Figure 3a). Addi- tionally, the dark contrast of the upward steps (marked "u" in Figure 4c) seems to be broader in the RI image than in the SE image.

The profiles of the SE signal and RI signal measured across the silicon dioxide bar are presented in Figure 5a. The profiles are measured along the beam projection, and the profiling path is shown by the red line in Figure 5b. The edge of upward step and the edge of downward step are marked with "u" and "d", respectively. The comparison of the SE profile (dashed line in Figure 5a) and RI profile (solid line in Figure 5a) revealed that the dark area in the RI image of the upward step was broader than the dark area in the SE image for the same step. The width of the bright area in the RI image of the downward step was found to be equal to the width of this area in the SE image.

Reflection ion microscopy of cleaved mica

Figure 6 shows an RI image of a cleaved mica surface obtained at a magnification of 100,000× under the grazing angle of 5° without charge compensation or conductive coatings. One can see that all details of the step-like surface are well reproduced without any noticeable image distortion that might be expected due to surface charging. Some distortion of the image caused by the charging appeared only at significantly higher magnification. It should be noted that the overall detector signal of registered electrons was not changed by the variation of the sample bias, indicating that SEs excited immediately near the sample could not reach the detector because of sample surface charging.

The step of a minimum height in the field of view of the image in Figure 6 is marked with arrows. The value of the height, as retrieved from the image processing, was found to be 7 ± 2 nm. The details of the calculation procedure will be described in the next section.
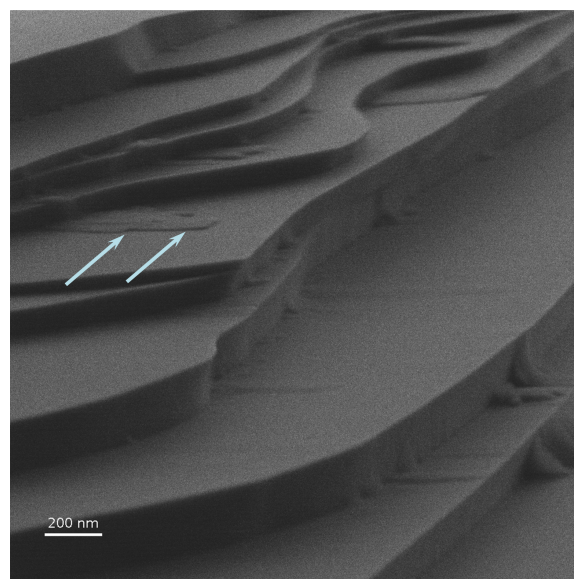
Figure 6: RIM image of cleaved mica. White arrows shows mark the smallest step in this image. Accelerating voltage: 30 keV, beam current: 0.3 pA.

Discussion
Contrast formation in scanning reflection ion microscopy

The results presented in the previous sections showed that imaging using an incident ion beam at low grazing angles exhibits following properties:

- RI detection is insensitive to the atomic number or density of the material;
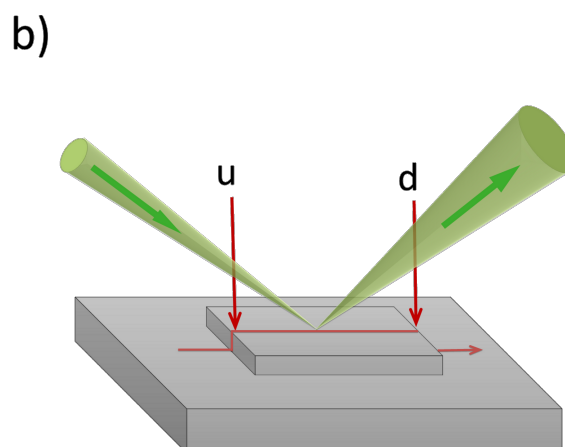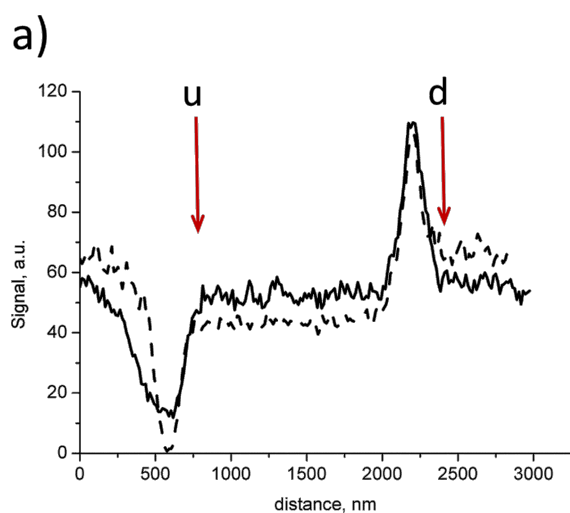
Figure 5: (a) Signal profiles: secondary electrons (dashed line) and reflected ions (solid line), red arrows shows the position of upward (u) and downward (d) steps. (b) Schematic view of ion reflection, green arrows correspond to the direction of the primary beam and reflected beam, the red line corresponds to the profile path, and the red arrows show the position of upward (u) and downward (d) steps.

- there is a difference between SE and RI imaging of upward steps but not for the downward case;
- no distortion caused by charging effects is observed in an RI image for insulators.

An explanation for these RIM properties and an analysis of the advantages and limitations of RIM require a theoretical description of the ion reflection and detection processes. In this part of the paper such a description will be provided combining a simple geometrical modeling and ion–matter interaction simulations.

The following designations are used to describe the incident and reflection paths as shown in Figure 7: Θ_0 - grazing angle between the incident beam and the specimen plane, Θ_1 - angle between the incident beam and a local detail of the specimen surface, Θ_2 - angle between the reflected beam and the specimen plane, $\Delta\Theta$ - angular aperture of RI detection, $\delta\Theta$ - halfwidth of the angular divergence of RI, φ_1, φ_2 - polar angles of the incident and of the reflected beams, respectively, in the specimen plane (not shown in Figure 7). To describe the surface morphology we will use the angle α between the specimen plane and the detail of the specimen surface roughness under consideration. From this geometry, $\Theta_1 = \Theta_0 + \alpha$. We will neglect the incident beam divergence angle since it is much smaller than both the angular aperture of the RI detector diaphragm and the halfwidth of the angular distribution of the RIs. Thus, we will further consider the incident beam as being infinitely narrow.
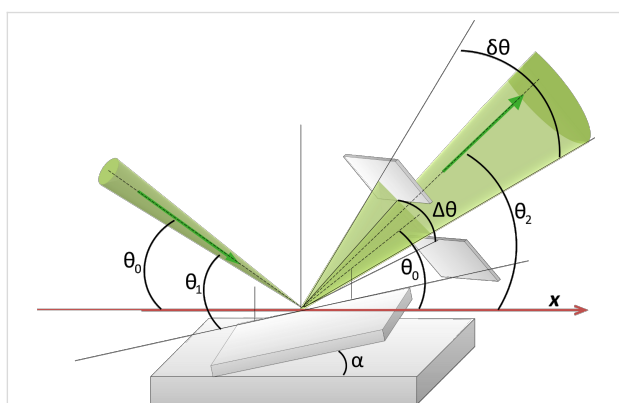

Figure 7: A schematic diagram of the incident and reflected ion paths with designations given in the text.

The number of reflected ions per incident ion is called the reflection coefficient or reflected ion yield. In the simple geometrical model, the reflection coefficient, η, depends on the angle of incidence and the reflection only, that is, $\eta = \eta(\Theta_1, \varphi_1, \Theta_2, \varphi_2)$.

Firstly, we assume that the reflection coefficient is independent of the polar incident angle, φ_1, that is, $\eta = \eta(\Theta_1, \varphi_1, \Theta_2, \varphi_2) = \eta(\Theta_1, \Theta_2, \varphi_2)$. This assumption is valid for amorphous materials and in the absence of ion channeling in crystalline materials. Ion channeling can cause the reflection coefficient to become strongly dependent on the angle in the vicinity of the channeling critical angles [28,30] and can be eliminated by a proper choice of the angle between the incident beam and crystal atomic planes [38].

The RI signal is the number of SEs per second measured by the ET detector as the flux of SEs from the Pt RI–SE converter (see (2) in Figure 1). The total number of reflected ions is proportional to the number of primary ions, N_I, and the proportionality constant is the reflection coefficient, $\eta(\Theta_1, \Theta_2, \varphi_2)$. In fact, only those reflected ions that are transmitted through the slit aperture can reach the Pt-coated surface and excite the SEs. The portion of the RIs that reach the Pt converter is a function of the ion reflection angles $f(\Theta_2, \varphi_2)$. The number of SEs excited from th Pt surface is proportional to the number of ions reflected within the aperture, and the proportionality constant is the secondary electron yield for the Pt-coated surface, γ_0. The SE yield depends on the angle of incidence and is determined by Θ_2, thus, $\gamma_0 = \gamma_0(\Theta_2)$. Thus, the detected RI signal should be calculated as the product of the number of reflected ions and the efficiency of SE detection, while integrating over all angles as shown in Equation 1.

In the case of the slit-like aperture installed at a fixed angle, Θ_2, one can assume that the portion of RIs that reaches the Pt converter is independent of the polar angle, that is, $f(\Theta_2, \varphi_2) = f(\Theta_2)$. This assumption gives rise to the explicit form of the $f(\Theta_2)$ dependence: $f(\Theta_2) = 1$ if $\Theta_0 - \Delta\Theta/2 < \Theta_2 < \Theta_0 + \Delta\Theta/2$, otherwise $f(\Theta_2) = 0$.

The SE yield from the Pt surface depends on the ion angle of incidence with this surface, β, and can be approximated by the inverse cosine law [19]: $\gamma(\beta) = \gamma_0/\cos\beta$. The typical ion grazing angle of incidence in our work was 5° and the slit angular aperture was 4°. In this case, β can vary between 6° and 14°. The cosine function varies only within 2% for this angular range and we can neglect dependence of the SE yield on the ion reflection angle, thus, $\gamma_0(\Theta_2) = \gamma_0$. We factor out the integral sign for the number of primary ions and SE yield and integrate Equation 1 over Θ_1 and φ_2 to arrive at the expression:

$$S = \frac{1}{8\pi} \int\int\int N_I \eta(\Theta_1, \Theta_2, \varphi_2) f(\Theta_2, \varphi_2) \gamma_0(\Theta_2) \sin\Theta_2 \sin\Theta_1 d\Theta_2 d\varphi_2 d\Theta_1. \qquad (1)$$

$$S(\alpha) = \frac{N_I \gamma_0}{2} \int_{\Theta_0 - \Delta\Theta/2}^{\Theta_0 + \Delta\Theta/2} \eta(\Theta_0 + \alpha, \Theta_2) \sin\Theta_2 \, d\Theta_2. \quad (2)$$

According to this expression, the RI signal is determined by the ion reflection coefficient and its angular dependence, the angular distribution of the reflected ions and the angular aperture of the slit diaphragm. We will now consider the effect of all these factors separately.

Angular dependence of the ion reflection coefficient

The dependence of the reflection coefficient for singly charged He ions on the grazing angle as obtained by a Monte Carlo simulation with SRIM software [39] for different materials is depicted in Figure 8. Note that the SRIM Monte Carlo simulation assumes that the ions are reflected from an amorphous target and all of them are collected by a detector.
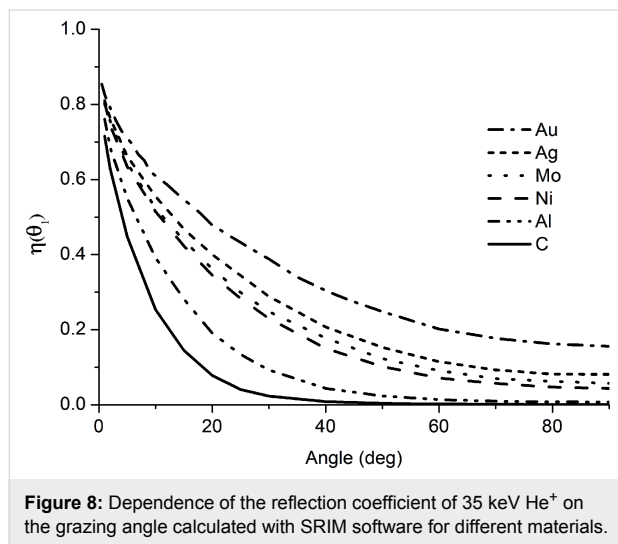
Figure 8: Dependence of the reflection coefficient of 35 keV He$^+$ on the grazing angle calculated with SRIM software for different materials.

As it can be seen in Figure 8, the ion reflection coefficient is a monotonically decreasing function that tends to the yield of backscattered ions when the grazing angle is greater than 90°. As Θ_1 approaches zero, the reflection coefficient tends towards unity, implying that for reflection at very low angles nearly all ions will pass over the specimen surface. The highest relative difference in the reflection coefficient for the different materials (i.e., material contrast) is observed at normal incidence, whereas this difference reduces for low grazing angles and the material contrast vanishes. At the same time, the slope of angular dependence on the reflection coefficient is high at low grazing angles and low for normal incidence. This explains why the morphology contrast in the RI images is determined mostly by the surface morphology but not by the surface composition in our experiments.

In fact, the RI contrast is determined by the angular dependence of the reflection coefficient only when all of the reflected ions are detected. In turn, this assumption is valid when the halfwidth of the angular aperture is larger than the halfwidth of the RI angular distribution, that is, $\Delta\Theta > \delta\Theta$, and the sample surface is sufficiently smooth so that $|\Theta_1 - \Theta_0| = \alpha < \Delta\Theta$. Under these conditions the expression for the RI signal given by Equation 2 can be simplified as:

$$\eta_0(\Theta_1) = \frac{1}{2} \int_0^\pi \eta(\Theta_1, \Theta_2) \sin\Theta_2 \, d\Theta_2 \quad (3)$$

$$S(\Theta_1) = N_I \gamma_0 \eta_0(\Theta_1), \quad (4)$$

where $\eta_0(\Theta_1)$ is the RI reflection coefficient as a function of the grazing angle.

Effect of angular distribution of reflected ions

As indicated above, the signal of the reflected ions is determined by the angle between surface and primary ion beam if all reflected ions are detected. In practice, some part of the reflected ions may be stopped by the diaphragm or by the elements of the specimen surface (shadowing effect). Firstly, we suppose that the angular distribution of the reflected ions $\eta(\Theta_1, \Theta_2)$ has a maximum at an angle of Θ_2^0 that corresponds to specular reflection: $\Theta_2^0 = \Theta_2^0 + 2\alpha$ and the shape of the angular distribution of reflected ions is independent of the Θ_1 angle.

The reflection coefficient can be presented as two multiplicands: $\eta(\Theta_1, \Theta_2) = \eta_0(\Theta_1) g(\Theta_2 - \Theta_2^0)$, where $\eta(\Theta_1)$ is described by Equation 3 and $g(\Theta_2 - \Theta_2^0)$ is the normalized angular distribution of the reflected ions, centered at Θ_2^0. Substituting this reflection coefficient into Equation 2:

$$S(\alpha) = \frac{N_I \gamma_0}{2} \eta_0(\Theta_0 + \alpha) \int_{\Theta_0 - \Delta\Theta/2}^{\Theta_0 + \Delta\Theta/2} g(\Theta_2 - \Theta_2^0) \sin\Theta_2 \, d\Theta_2. \quad (5)$$

Using the notation $t = \Theta_2 - \Theta_2^0$ we obtain:

$$S(\alpha) = \frac{N_I \gamma_0}{2} \eta_0(\Theta_0 + \alpha) \int_{2\alpha - \Delta\Theta/2}^{2\alpha + \Delta\Theta/2} g(t) \sin(t + \Theta_2^0) \, dt \quad (6)$$

and variations of α can be described now as a shift of the integrating window. In particular, the comparison of Equation 4 and Equation 6 shows that the RI signal will decrease when $\alpha > \Delta\Theta$.

Further, a suggestion for an explicit analytical shape of $g(t)$ is required for the calculation of the RI signal profile with the help

of Equation 6. If $\alpha > \delta\Theta/2 + \Delta\Theta/4$, then we can assume that the signal tends to zero because we integrate Equation 6 far from a maximum of $g(t)$, that is, all ions are stopped by the diaphragm. Hence, such regions of the sample will appear in dark contrast in the RI image. Additionally, double (or multiple) reflections can take place giving rise to a "shadow effect". This so-called shadow effect means that after the first reflection from the surface with low α, the ions are iteratively reflected from some pronounced details of the specimen and do not contribute to the signal. The simplest example of the shadow effect is the rectangular upward step that was investigated for the SiO_2 sample bars on silicon (Figure 4).

To further simplify the description, we assume that the surface between the steps is flat and parallel to the specimen plane (i.e., $\alpha = 0$) and the step sidewall is perpendicular to the surface (i.e., $\alpha = 90°$). The area at the step can be then divided into three regions, as shown in Figure 9.

Figure 9: Designation of the regions of the upward step (a), and their projection onto the image plane (b): 1 – sidewall region, 2 – shadow region, 3 – penumbra region.
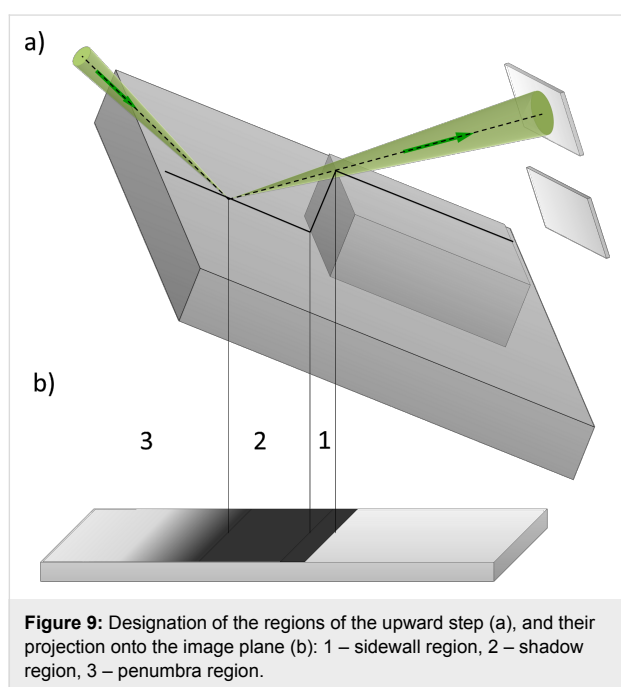
In region 1 in Figure 9 all ions are reflected by the step sidewall away from the aperture and do not contribute to the detected signal, $S(\alpha) = 0$. In this case, a dark area of width $d_1 = h\cos\Theta_0$ appears in the image, where h is the step height.

In region 2, all ions reflected from a plane bottom sample surface will be scattered by the sidewall, and an additional dark area (shadow) appears in the image (see Figure 9). If we denote the distance from step along the substrate as x, then the ions can pass through aperture when: $\Theta_2 = \arctan(h/x)$. In this case, the detected signal is described as follows:

$$S(\Theta_0, x) = 0, \text{when } \Theta_0 + \Delta\Theta \leq \arctan(h/x) \qquad (7)$$

The width of the shadowed region 2, as calculated from simple geometry, is given by $d_2 = h\cdot\sin\Theta_0/\tan(\Theta_0 + \Delta\Theta)$.

In region 3 a smooth transition (penumbra) from zero RI signal to a constant RI signal from the substrate takes place. The form of the transition curve is determined by the RI angular distribution according to:

$$S(\Theta_0, x) = \frac{N_{\mathrm{I}}\gamma_0}{2} \int_{\arctan(h/x)}^{\Theta_0+\Delta\Theta} \eta(\Theta_0, \Theta_2)\sin\Theta_2 d\Theta_2, \qquad (8)$$

$$\text{when } \Theta_0 + \Delta\Theta > \arctan(h/x).$$

The total width of the dark area in the image of the step will then be a sum of the widths of regions 1 and 2:

$$d = h\left(\cos\Theta_0 + \frac{\sin\Theta_0}{\tan(\Theta_0 + \Delta\Theta)}\right). \qquad (9)$$

Thus, the step height can be calculated from the dark contrast width in the RI image and the halfwidth of the slit aperture as follows:

$$h = \frac{d}{\cos\Theta_0 + \dfrac{\sin\Theta_0}{\tan(\Theta_0 + \Delta\Theta)}}. \qquad (10)$$

Using Equation 10 we calculated the step height from the experimental data presented in Figure 4 ($\Theta_0 = 10°$, $\Delta\Theta = 2°$, $d = 40 \pm 10$ nm), where a value of $h = 22 \pm 6$ nm was obtained, in good agreement with the AFM results.

In conclusion, the shadow effect and a finite aperture size result in dark areas in the image. These dark areas appears in the regions of a sample where $\alpha > \delta\Theta/2 + \Delta\Theta/4$. If a surface feature can be described with the rectangular step model, then Equation 10 can be used for the calculation of the step height.

Effect of ion transmission

The contrast formation mechanisms presented above describe the RI signal from the parts of the sample surface facing the incident ion beam. On the opposite side, the primary beam does not reach the surface and, accordingly, no RI signal can be obtained. In the vicinity of a sharp edge of a feature the ion transmission may contribute to the image contrast formation. As was demonstrated in Figure 4a, a bright contrast was observed in the downward step region. The peak position of the RI contrast coincided with one of the SE bright contrasts and with

the sharp edge of the step. The bright RI contrast originates from the transmission of ions through the step edge and their subsequent reflection [40]. This divides the sample surface into two regions of reflection: the upper surface of the bar and the substrate surface beyond the step edge (see Figure 10a). To quantify the bright contrast profile we will use following simplified model.
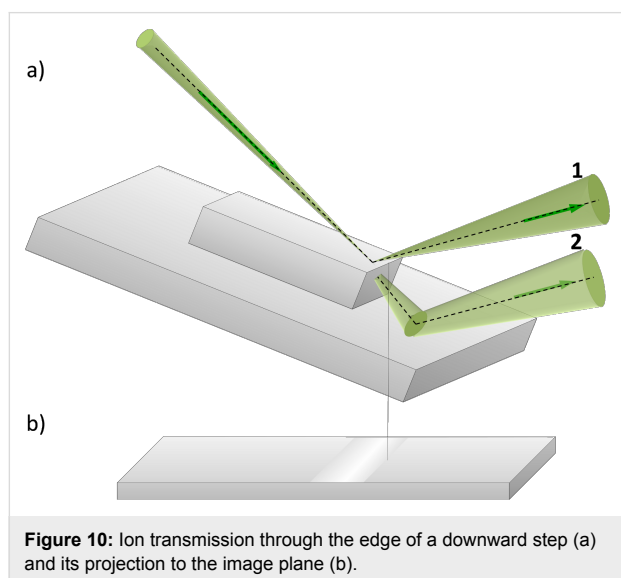
Figure 10: Ion transmission through the edge of a downward step (a) and its projection to the image plane (b).

The reflection coefficient of the primary beam from the upper surface (beam 1 in Figure 10a) is denoted as $\eta^*(\Theta_1,\Theta_2)$. The asterisk is used to emphasize that the reflection coefficient near the step edge differs from the reflection coefficient of the bulk sample surface when the distance to the step edge is comparable with the ion penetration depth. Near the step edge some part of the incident beam penetrates through it with the probability $\rho(\Theta_1,\Theta_3)$ and hits the substrate at an angle Θ_3, which we assume to be close to the angle of incidence, that is, $\Theta_3 \approx \Theta_1$. The transmitted ions are reflected from the substrate with the reflection coefficient $\eta(\Theta_3,\Theta_2)$ (beam 2 in Figure 10a). Using these designations the total reflection coefficient can be written as:

$$\eta_{edge}(\Theta_1,\Theta_2) = \eta^*(\Theta_1,\Theta_2) + \rho(\Theta_1,\Theta_3)\eta(\Theta_3,\Theta_2) \quad (11)$$

Figure 11 shows the dependence of the reflection and transmission coefficients on the distance from rectangular step edge along the top surface. All values were calculated with SRIM Monte Carlo simulation software for a silicon dioxide step on silicon and 35 keV He ions. The ion transmission probability (dotted line in Figure 11) decreases from unity when the ion beam moves away from the step edge. On the other hand, the number of ions reflected from the upper surface (dashed line in

Figure 11) increases with the distance from the step edge. The total reflection coefficient calculated using the Equation 11 (solid line in Figure 11) exhibits a maximum at a distance of about 50 nm from the edge of the step, which is related to the bright line in the RI image.
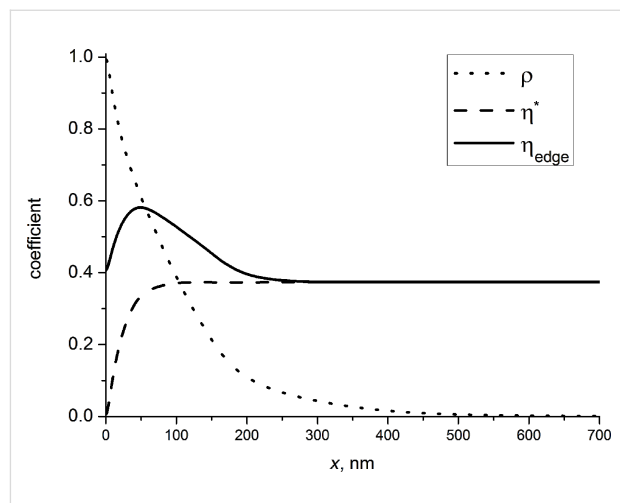
Figure 11: Dependence of the coefficients on the distance from the edge of the step: reflection coefficient from upper surface (dashed line), ion transmission probability (dotted line) and the total reflection coefficient calculated with Equation 11 (solid line) (angle of incidence was 10°).

The solid line in Figure 12 represents the profile of the RIM contrast calculated according to Equation 8 at a rectangular downward step of a SiO_2 bar on Si. Far away from the step edge the reflection coefficient tends towards the constant value of the bulk material. The contrast is presented in Figure 12 with respect to the reflection coefficient value for a SiO_2 bar.
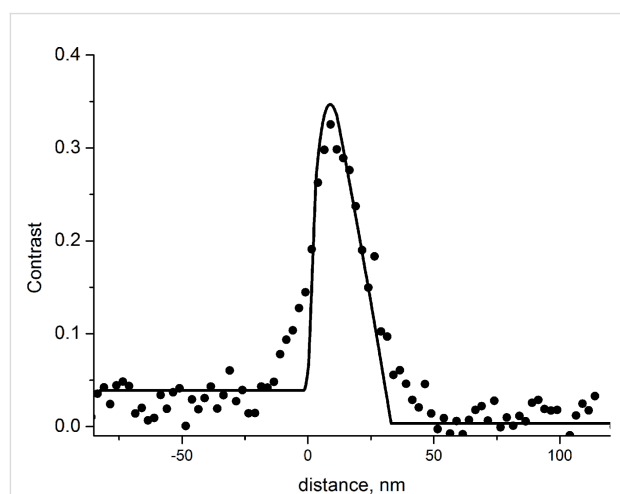
Figure 12: Profile of the relative contrast of a downward step: dots – experimental data, solid line – data calculated with SRIM software. Zero corresponds to the reflection from bulk SiO_2.

From Figure 12 one can see that the simulated curve is in good agreement with experimental data, confirming the validity of the suggested simple theoretical model. A difference between the experimental points and the calculated results can be seen in the tails of the profile, which is caused by the finite size of the ion beam and the angular distribution of transmitted ions (assumed to be zero in the calculations).

From the point of view of applications of this technique, it is interesting to know the minimum value of the step height that can be distinguished in RIM contrast. Figure 11 shows that the edge contrast becomes negligible when the distance from the step edge is less than $x_{min} = 10$ nm. At the same time, the edge contrast can appear only when the primary beam projection passes above the bottom boundary between the step and the substrate. Consequently, the step height must be greater than $h > x_{min}\tan\Theta_1$ to observe edge contrast. In our case $\Theta \approx 10°$, and the edge contrast can be observed if the step height is greater than 2 nm.

In summary, the ion transmission through small features on the surface and their subsequent reflection can result in bright contrast in the RIM image. One should note that despite of the similarity of the bright contrasts in the SE and in RI images, the origin of their mechanisms are quite different.

Effect of a surface charge

The RI image formation mechanisms described above originate from the ion scattering by the geometrical specimen relief and do not take into account the possible impact of surface charging produced by the positively charged ions. Our experiments with the mica surface demonstrated very sharp RI images without any noticeable effect of charging on the image quality, despite a strong positive surface charging that was revealed as the absence of the SE in the detected signal due to their attraction to the sample. Although the charging makes SE detection for imaging both at the normal and glancing ion incidence impossible to use, RI detection can still be successfully implemented.

Despite the fact that the energy of the SEs is three orders of magnitude less than the energy of the primary ions, the influence of surface charge on their trajectories might not be negligible, and the question regarding possible image distortion arises.

Under the action of the electric field of the positively charged sample surface, the trajectories of the primary ions become curved as schematically shown in Figure 13. The primary ion beam is decelerated before the reflection from the surface, but the reflected beam is accelerated back to its initial energy since the electric field is almost uniform.
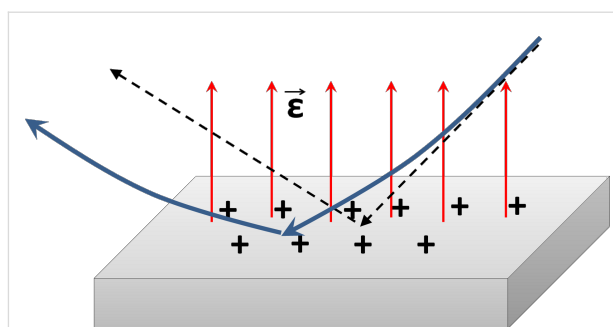
Figure 13: Reflection of ions from the charged surface. Trajectories of ions reflected from a charged surface (solid blue line) and trajectories of ions reflected from a neutral surface (dashed black line).

In general, the grazing angle changes due to surface charging should be taken into account for the metrology of the surface relief. Theoretically, the changes of the angle can proceed until the beam is no longer parallel to the surface. Since that potential increases inversely proportionally to the size of the scan area with the same charge, the model predicts an increase of the charging effect on the beam trajectory with the increasing in the magnification. Accordingly, the simplest test to check for the presence of the effect of beam charge bending is a comparison of results of two scans preformed with different magnifications. Similar results will provide evidence of the accuracy of the lateral size definition. As for the accurate calculation of the step height from the shadow contrasts, it should be noted that the dependence of the width of the shadow on the angle of incidence (according to Equation 10) is rather weak for the experimental parameters used in RIM. In fact, a variation of the angle of incidence from 0° to 10° results in the relative variation of the shadow width of a few percent and does not affect the accuracy of the measurements.

In summary, reflection ion microscopy is useful for imaging of the surface of dielectric materials without the need for charge compensation, and the accumulated surface charge plays te role of positive sample bias. The impact of the charging on the height of the surface steps is negligible.

Conclusion

In summary, we investigated the capabilities of a scanning reflection helium ion microscopy technique that was realized in a helium ion microscope for the first time. No additional RI detector was installed in the He IM chamber. Instead, reflected ions were detected with a conventional SE detector by using RI conversion to secondary electrons on a Pt-coated surface.

It was demonstrated that in contrast to the case of a backscattered geometry, the reflection coefficient of the ions, which are incident and reflected at low grazing angles, is not sensitive to

the atomic number of the sample material, and the contrast in RI images is determined mostly by the surface morphology. This experimental fact is in agreement with the results of the Monte Carlo simulations of the angular dependence of the ion reflection coefficient. Accordingly, RIM can be used for the imaging of surface morphology but not for the imaging of surface composition.

The obtained experimental results show that there are some quantitative differences in the surface morphology imaging between SE and RI imaging modes. The quantitative calculation of the shadow contrast at a rectangular step was performed based on a simple geometrical model. The calculation results show that the width of the dark contrast area in the RI image of an upward step is approximately twice broader than the same step width in the SE image. At the same time, the width of a bright area is practically the same in the RI and SE image of a downwards step. It should be also noted that in contrast to RIM, the width of the dark contrast in the SE image can vary depending on the SE detector collector grid voltage. Accordingly, the precision of the RIM definition of the height of an individual surface rectangular step is noticeably better than with the SE detector. With regards to the subject of surface morphology, we should compare RIM with other methods of surface investigation such as REM and AFM.

Conventional REM demonstrates the capability of imaging of a single atomic step, and it is used mostly for this purpose. Single atomic steps were not observed by means of RIM yet, but there are several features of the developed detection system that limit the imaging capabilities of RIM. The REM imaging of surface steps exploits the specific diffraction conditions, and the obtained contrast is a superposition of phase contrast and diffraction contrast [9]. All described mechanisms of RIM contrast formation neglect the dependence of a reflection coefficient on the polar angle because a slit diaphragm was used in the experiment. In reality, this dependence contains additional information on the surface details [41], and the channeling effect and the deviation from channeling conditions can be used for RIM contrast formation analogous to diffraction conditions in REM. A 2D aperture instead of slit is required to limit both angles of the reflected beam. Another distinction of the REM setup is a high vacuum specimen chamber that is required for the observation of the surface steps. The high vacuum chamber is also required to reduce the effect of contamination as noted below. Thus, observation of atomic steps in RIM seems to be possible, but requires modification of the specimen chamber and detection conditions.

Atomic force microscopy as well as RIM allows for precise, quantitative measurements of the height of surface details;

however, the scanning process is very slow. From this point of view, RIM has the same advantage as SEM: fast scanning and a large maximum field of view. On the other hand, scanning and measurements in AFM can be performed for all sides of the sample features, whereas in RIM (as well as in REM) only the side facing the beam is suited for investigation.

In this work, RIM was demonstrated to obtain sharp images of an insulator surface without the need for charge compensation or a conductive coating. A positive surface charge produced by ions attracts SEs but does not significantly change the RI trajectory and their detection. The changes in trajectory caused by the electric field of the charged surface can reduce the ion incident and reflection angles, but our calculation shows that their influence on the step height determination is negligible and can be monitored by changing the imaging magnification. The alternative method of the imaging of an insulating surface in HIM is charge compensation by an electron flood gun. Imaging with a flood gun requires accurate adjustment of the flood gun parameters and ion beam parameters to neutralize the surface charge. The scan speed decreases when line-by-line charge compensation is used. The reflected ions are less sensitive to surface charge than SEs, thus RIM of insulating surfaces is more straightforward. At the same time, RIM requires a special sample holder. One of the main disadvantages of RIM is the inability to image the whole surface of a sample. Part of a sample is always hidden by sample features. Thus, the potential advantage of RIM over the use of a flood gun is determined by the sample surface details. Unfortunately, the construction of the RIM specimen holder does not allow for charge compensation, and a direct comparison of these methods is impossible.

Beside the factors mentioned above, the sensitivity and the precision of the RIM measurements are obviously defined by the signal-to-noise ratio that increases with the image acquisition duration. There are two factors that limit measurement time in RIM: the ion beam induced deposition (IBID) of hydrocarbons and the sputtering of the surface material.

The first problem exists both in a case of RIM and in conventional HIM. Fortunately, IBID that is mainly stimulated by secondary electrons [21] can be eliminated in RIM by applying a positive bias to the sample and reducing the contamination growth rate, and it can be completely avoided by usage of high vacuum conditions.

Ion beam-induced sputtering always takes place and, unfortunately, the sputtering yield increases at low angles, and even for ions as light as He this can exceed one atom per ion. Thus, this effect is the main factor limiting the acquisition time. Most of the images were obtained with a dose of about 10^{14} cm^{-2}, and

the largest ion dose used for the acquisition of RI images of Au on carbon was about 10^{15} cm^{-2}. In this case we expect the sputtering of a single atomic layer of the sample. The resolution of the obtained images was insufficient to observe such a sputtering effect, but it can be a limiting factor for the observation of the atomic steps. Thus, the further enhancement of the detection system is desirable to reduce the measurement time and to avoid sputtering of a sample.

In conclusion, reflection helium ion microscopy is a promising tool for the investigation of surface morphology and is especially useful when applied to non-conductive materials. Further development of this technique would require a special, more sensitive RI detector, higher vacuum conditions, and a polar angle limiting aperture.

Acknowledgements

References
1. Ruska, E. *Z. Phys.* **1933,** *83,* 492–497. doi:10.1007/BF01338960
2. Haine, M. E.; Hirs, W. *Br. J. Appl. Phys.* **1953,** *4,* 239–244. doi:10.1088/0508-3443/4/8/303
3. Cosslett, V. E.; Jones, D. J. *J. Sci. Instrum.* **1955,** *32,* 86–91. doi:10.1088/0950-7671/32/3/302
4. Page, D. H. *Br. J. Appl. Phys.* **1958,** *9,* 60–67. doi:10.1088/0508-3443/9/2/303
5. Yagi, K. *Surf. Sci. Rep.* **1993,** *17,* 307–362. doi:10.1016/0167-5729(93)90002-7
6. Hsu, T. *Ultramicroscopy* **1987,** *22,* 217–224. doi:10.1016/0304-3991(87)90065-9
7. Latyshev, A. V.; Aseev, A. L.; Krasilnikov, A. B.; Stenin, S. I. *Surf. Sci.* **1989,** *213,* 157–169. doi:10.1016/0039-6028(89)90256-2
8. Banzhof, H.; Herrmann, K. H. *Ultramicroscopy* **1990,** *33,* 23–26. doi:10.1016/0304-3991(90)90101-Q
9. Wang, Z. L. *Rep. Prog. Phys.* **1993,** *56,* 997–1065. doi:10.1088/0034-4885/56/8/002
10. Oatley, C. W.; Nixon, W. C.; Pease, R. F. W. *Adv. Electron. Electron Phys.* **1966,** *21,* 181–247. doi:10.1016/S0065-2539(08)61010-0
11. Broers, A. N. *Rev. Sci. Instrum.* **1969,** *40,* 1040–1045. doi:10.1063/1.1684146
12. Notte, J.; Hill, R.; McVey, S.; Farkas, L.; Percival, R.; Ward, B. *Microsc. Microanal.* **2006,** *12,* 126–127. doi:10.1017/S1431927606069820
13. Ward, B. W.; Notte, J. A.; Economou, N. P. *J. Vac. Sci. Technol., B* **2006,** *24,* 2871–2874. doi:10.1116/1.2357967
14. Economou, N. P.; Notte, J. A.; Thompson, W. B. *Scanning* **2012,** *34,* 83–89. doi:10.1002/sca.20239
15. Hill, R.; Notte, J. A.; Scipioni, L. *Adv. Imaging Electron Phys.* **2012,** *170,* 65–148. doi:10.1016/B978-0-12-394396-5.00002-6
16. Boden, S. A.; Asadollahbaik, A.; Rutt, H. N.; Bagnall, D. M. *Scanning* **2012,** *34,* 107–120. doi:10.1002/sca.20267
17. Rodenburg, C.; Jepson, M. A. E.; Inkson, B. J.; Liu, X. *J. Phys.: Conf. Ser.* **2010,** *241,* No. 012076. doi:10.1088/1742-6596/241/1/012076
18. Ramachandra, R.; Griffin, B.; Joy, D. *Ultramicroscopy* **2009,** *109,* 748–757. doi:10.1016/j.ultramic.2009.01.013
19. Bell, D. C. *Microsc. Microanal.* **2009,** *15,* 147–153. doi:10.1017/S1431927609090138
20. Hill, R.; Faridur Rahman, F. H. M. *Nucl. Instrum. Methods Phys. Res., Sect. A* **2011,** *645,* 96–101. doi:10.1016/j.nima.2010.12.123
21. Alkemade, P. F. A.; Koster, E. M.; Van Veldhoven, E.; Maas, D. J. *Scanning* **2012,** *34,* 90–100. doi:10.1002/sca.21009
22. Fox, D.; Zhou, Y. B.; O'Neill, A.; Kumar, S.; Wang, J. J.; Coleman, J. N.; Duesberg, G. S.; Donegan, J. F.; Zhang, H. Z. *Nanotechnology* **2013,** *24,* No. 335702. doi:10.1088/0957-4484/24/33/335702
23. Zhang, X.; Vieker, H.; Beyer, A.; Gölzhäuser, A. *Beilstein J. Nanotechnol.* **2014,** *5,* 188–194. doi:10.3762/bjnano.5.20
24. Joens, M. S.; Huynh, C.; Kasuboski, J. M.; Ferranti, D.; Sigal, Y. J.; Zeitvogel, F.; Obst, M.; Burkhardt, C. J.; Curran, K. P.; Chalasani, S. H.; Stern, L. A.; Goetze, B.; Fitzpatrick, J. A. J. *Sci. Rep.* **2013,** *3,* No. 3514. doi:10.1038/srep03514
25. Bazou, D.; Behan, G.; Reid, C.; Boland, J. J.; Zhang, H. Z. *J. Microsc. (Oxford, U. K.)* **2011,** *242,* 290–294. doi:10.1111/j.1365-2818.2010.03467.x
26. Vanden Berg-Foels, W. S.; Scipioni, L.; Huynh, C.; Wen, X. *J. Microsc. (Oxford, U. K.)* **2012,** *246,* 168–176. doi:10.1111/j.1365-2818.2012.03606.x
27. Petrov, Yu.; Vyvenko, O. *Proc. SPIE* **2011,** *8036,* No. 80360. doi:10.1117/12.886347
28. Petrov, Y. V.; Vyvenko, O. F.; Bondarenko, A. S. *J. Surf. Invest.: X-Ray, Synchrotron Neutron Tech.* **2010,** *4,* 792–795. doi:10.1134/S1027451010050186
29. Hlawacek, G.; Veligura, V.; Lorbek, S.; Mocking, T. F.; George, A.; van Gastel, R.; Zandvliet, H. J. W.; Poelsema, B. *Beilstein J. Nanotechnol.* **2012,** *3,* 507–512. doi:10.3762/bjnano.3.58
30. Veligura, V.; Hlawacek, G.; van Gastel, R.; Zandvliet, H. J. W.; Poelsema, B. *Beilstein J. Nanotechnol.* **2012,** *3,* 501–506. doi:10.3762/bjnano.3.57
31. Notte, J., IV; Hill, R.; McVey, S. M.; Ramachandra, R.; Griffin, B.; Joy, D. *Microsc. Microanal.* **2010,** *16,* 599–603. doi:10.1017/S1431927610093682
32. Wirtz, T.; Vanhove, N.; Pillatsch, L.; Dowsett, D.; Sijbrandij, S.; Notte, J. *Appl. Phys. Lett.* **2012,** *101,* 041601. doi:10.1063/1.4739240
33. Pillatsch, L.; Vanhove, N.; Dowsett, D.; Sijbrandij, S.; Notte, J.; Wirtz, T. *Appl. Surf. Sci.* **2013,** *282,* 908–913. doi:10.1016/j.apsusc.2013.06.088
34. Boden, S. A.; Franklin, T. M. W.; Scipioni, L.; Bagnall, D. M.; Rutt, H. N. *Microsc. Microanal.* **2012,** *18,* 1253–1262. doi:10.1017/S1431927612013463
35. Hlawacek, G.; Veligura, V.; van Gastel, R.; Poelsema, B. *J. Vac. Sci. Technol., B* **2014,** *32,* 020801. doi:10.1116/1.4863676
36. Reimer, L.; Volbert, B. *Scanning* **1979,** *2,* 238–248. doi:10.1002/sca.4950020406
37. Hall, A. R. *Microsc. Microanal.* **2013,** *19,* 740–744. doi:10.1017/S1431927613000500
38. Gemmell, D. S. *Rev. Mod. Phys.* **1974,** *46,* 129–227. doi:10.1103/RevModPhys.46.129
39. Ziegler, J. F.; Ziegler, M. D.; Biersack, J. P. *Nucl. Instrum. Methods Phys. Res., Sect. B* **2010,** *268,* 1818–1823. doi:10.1016/j.nimb.2010.02.091

40. Baba-Kishi, K. Z. *Scanning* **1996,** *18,* 315–321.
doi:10.1002/sca.1996.4950180408
41. Pfandzelter, R. *Phys. Rev. B* **1998,** *57,* 15496–15506.
doi:10.1103/PhysRevB.57.15496

Surface excitations in the modelling of electron transport for electron-beam-induced deposition experiments

Francesc Salvat-Pujol[*1], Roser Valentí[1] and Wolfgang S. Werner[2]

Address:
[1]Institut für Theoretische Physik, Goethe-Universität Frankfurt, Max-von-Laue-Straße 1, 60438 Frankfurt am Main, Germany and [2]Institut für Angewandte Physik, Technische Universität Wien, Wiedner Hauptstraße 8-10/134, 1040 Wien, Austria

Email:
Francesc Salvat-Pujol[*] - salvat-pujol@itp.uni-frankfurt.de

* Corresponding author

Abstract

The aim of the present overview article is to raise awareness of an essential aspect that is usually not accounted for in the modelling of electron transport for focused-electron-beam-induced deposition (FEBID) of nanostructures: Surface excitations are on the one hand responsible for a sizeable fraction of the intensity in reflection-electron-energy-loss spectra for primary electron energies of up to a few kiloelectronvolts and, on the other hand, they play a key role in the emission of secondary electrons from solids, regardless of the primary energy. In this overview work we present a general perspective of recent works on the subject of surface excitations and on low-energy electron transport, highlighting the most relevant aspects for the modelling of electron transport in FEBID simulations.

Introduction

An accurate modelling of the energy losses of electrons traversing a solid surface is instrumental for a quantitative understanding of a series of techniques exploiting transmitted, reflected, or emitted electrons, including a number of spectroscopies (electron-energy-loss spectroscopy, X-ray photoelectron spectroscopy, and Auger-electron spectroscopy), electron microscopy, and the focused-electron-beam-induced deposition (FEBID) of nanostructures, on which we focus here. This technique employs beams of focussed kiloelectronvolts-electrons to trigger and steer the growth of nanostructures with tunable elec-

tronic and magnetic properties from molecules of organometallic precursor gases [1] adsorbed on a substrate [2]. It has been shown that, for irradiation with electrons of 1–5 keV, both the incoming primary electrons and the emitted secondary electrons influence the growth of the nanostructures, the latter electrons being responsible for the lateral resolution [3].

In the modelling of electron transport for FEBID [2-7], electron stopping is described on the basis of properties that are applicable in the bulk of the material. However, electrons traversing a

solid interface additionally excite surface modes, an energy-loss channel that amounts to a sizeable fraction of the energy-loss spectrum for electrons of up to a few kiloelectronvolts. The existence of surface excitations was predicted in the late 1950s [8]; experimental evidence was obtained shortly thereafter [9,10]. In order to model surface excitations in electron spectroscopies, several models have been developed to date [11-31]. Various approaches are considered, often with underlying simplifications, evoked on physical or technical grounds, in the interest of making calculations feasible in a finite time. In order to derive a distribution of energy losses of charged projectiles moving in the vicinity of the surface, some of the models cited above rely on the semiclassical dielectric formalism, whereas others adopt a many-body formalism. Both approaches have been shown to yield results in equivalently good agreement [32] with experimental data.

In what follows we briefly review the stopping of charged projectiles in the vicinity of a solid surface, along the lines of [31], which will be referenced for further details. We summarize a series of rules which characterize the behavior of the probability for surface excitations and we briefly review a practical model for the emission of secondary electrons. Relevant aspects to FEBID modelling will be highlighted.

Review
Inelastic collisions in the bulk of the material
Energy losses of a charged projectile moving in a solid can be described accurately within the semiclassical dielectric formalism. In this approach, one assumes that the presence of the charged projectile disturbs the equilibrium charge density of the solid, which becomes polarized and, thus, an electric field is induced at all points of space. The force acting on the charged projectile due to the induced electric field is assumed to be the agent responsible for its (electronic) stopping. In order to derive physical quantities that describe the stopping, it is now a matter of calculating first the induced electric field and, from it, the so-called stopping power, defined as the variation of the kinetic energy of the projectile per unit path length. Once an expression for the stopping power is derived, one can identify from it an expression for the distribution of energy losses per unit path length, the basic quantity that is needed to describe energy losses in a detailed Monte-Carlo simulation of electron transport. In this section we briefly outline the basic steps of these calculations and highlight the underlying assumptions. Further details can be found in the cited works.

The starting point of the calculation is the dielectric function $\varepsilon(q,\omega)$ of the material, where q and ω are the respective Fourier-conjugate variables of the position, $\mathbf{r}$, and the time, t. In practice one typically has data available for $\varepsilon(\omega)$, be it from optical

data obtained experimentally [33] or from theoretical calculations, e.g., via density-functional theory calculations [33-35]. An ω-dependent dielectric function is sufficient to describe the response of the medium to a spatially homogeneous perturbation, such as that of an incoming photon. However, for incoming charged projectiles the perturbation is strongly dependent on the spatial coordinates, so that a q-dependent dielectric functions is required. Physically reliable models are built on the basis of the (q,ω)-dependent dielectric function for the homogeneous electron gas [36-38] or on the basis of a simple superposition of Drude–Lindhard oscillators [33].

Assuming a projectile that moves with a velocity $\mathbf{v}$ along a trajectory $\mathbf{r} = \mathbf{v}t$, one can conveniently solve the Maxwell equations in Fourier space to obtain the following expression for the induced electric field [31]

$$\mathbf{E}_{\text{ind}}\left(\mathbf{q},\omega\right) = -\mathrm{i}4\pi\frac{\mathbf{q}}{q^2}\rho\left(\mathbf{q},\omega\right)\left[\frac{1}{\varepsilon\left(\mathbf{q},\omega\right)}-1\right], \qquad (1)$$

where $\rho(\mathbf{q},\omega)$ is the Fourier transform of the projectile charge density $\rho(\mathbf{r},t) = Z_0 e\delta(\mathbf{r}-\mathbf{v}t)$, where Z_0 is the projectile charge in units of the modulus of the electron charge, e, and $\mathbf{v}$ is the velocity of the projectile. To obtain this expression, the following approximations were considered: (1) The Coulomb gauge was adopted and the contribution from the vector potential was neglected. (2) The dielectric displacement field was assumed to be proportional to the electric field in Fourier space (linear response). The first approximation restricts the validity of the calculation to non-relativistic projectiles (the calculation with the full electric field for relativistic projectiles is also feasible [39]), whereas the second approximation can be seen to be formally equivalent to a first-order Born approximation in perturbation theory, imposing a lower bound to the domain of validity of the calculation [22,40], which for practical purposes is above 100 eV.

The stopping power S is obtained as the variation of the kinetic energy per unit path length,

$$S = -\frac{\mathrm{d}\mathcal{E}}{\mathrm{d}s} = \hat{\mathbf{v}}\cdot\mathbf{E}_{\text{ind}}\left(\mathbf{r},t\right)\Big|_{\mathbf{r}=\mathbf{v}t}, \qquad (2)$$

where $\mathcal{E}$ is the kinetic energy of the projectile and $s = vt$ is the path length. Combining Equation 1 and Equation 2 one obtains

$$S = \frac{2\left(Z_0\right)^2}{\pi}\frac{1}{v^2}\int\limits_0^\infty \mathrm{d}q\,\frac{1}{q}\int\limits_0^{qv}\mathrm{d}\omega\,\omega\,\mathrm{Im}\left[-\frac{1}{\varepsilon\left(q,\omega\right)}\right]. \qquad (3)$$

Up to this point the stopping of the projectile is treated as a continuous phenomenon, whereas in reality charged projectiles lose energy and are deflected in the course of individual inelastic collisions. The so-called semiclassical approximation consists in assigning to $\hbar\mathbf{v}$ and $\hbar\omega$ the meaning of a momentum transfer from the projectile to the medium and of an energy loss of the projectile, respectively. Atomic units ($\hbar = m_e = e = 1$) will be used below. Now that these variables have a well-defined physical meaning, the corresponding integrals must be restricted to the kinematically allowed domain,

$$S(\mathcal{E}) = \frac{2(Z_0)^2}{\pi} \frac{1}{v^2} \int_0^{\mathcal{E}} d\omega \, \omega \int_{q_-}^{q_+} dq \, \frac{1}{q} \mathrm{Im}\left[-\frac{1}{\varepsilon(q,\omega)}\right], \quad (4)$$

where

$$q_\pm = \sqrt{2\mathcal{E}} \pm \sqrt{2(\mathcal{E}-\omega)} \quad (5)$$

are the minimum (−) and maximum (+) momentum transfers allowed by the energy and momentum conservation laws.

Equation 4 can be understood as the average energy loss per unit path length dictated by a distribution of energy losses per unit path length, $d\mu/d\omega$:

$$S(\mathcal{E}) = \int_0^{\mathcal{E}} d\omega \, \omega \, \frac{d\mu}{d\omega}. \quad (6)$$

The quantity $d\mu/d\omega$ is known as the differential inelastic inverse mean free path (DIIMFP), explicitly given by

$$\frac{d\mu}{d\omega} = \frac{2Z_0^2}{\pi} \frac{1}{v^2} \int_{q_-}^{q_+} dq \, \frac{1}{q} \mathrm{Im}\left[-\frac{1}{\varepsilon(q,\omega)}\right]. \quad (7)$$

Note that the DIIMFP is a function of the energy loss for the given velocity of the projectile. The integral of the DIIMFP over all allowed energy losses gives the inelastic inverse mean free path

$$\lambda_i^{-1} = \int_0^{\mathcal{E}} d\omega \, \frac{d\mu}{d\omega}. \quad (8)$$

The latter two quantities are the necessary quantities for a detailed Monte-Carlo simulation of electron transport (see section "Monte-Carlo simulation of electron energy-loss

spectra"), a method that has been successfully used in the last decades.

Inelastic collisions in the vicinity of a planar surface

The scheme outlined in the previous section to describe inelastic interactions of charged projectiles in solids gives a good account of inelastic collisions in the bulk of the solid. However, projectiles impinging and emerging from a solid additionally cross a planar interface to vacuum (or another solid) that is not explicitly accounted for. The existence of a planar surface imposes additional boundary conditions on the electric field [41,42].

Several approaches exist in the literature to solve the Maxwell equations with these boundary conditions for the stopping problem: Some consider the dielectric function of a semi-infinite medium [43], and others (preferred in the electron-spectroscopy community) rely on a method that allows one to work with bulk dielectric functions, the method of image charges, also known as the method of extended pseudomedia. The method consists in rephrasing the semi-infinite-geometry problem as the sum of two infinite-geometry problems, supplied with a series of fictitious charges that are determined in terms of known quantities by imposing the boundary conditions at the interface.

The resulting induced electric field has a more complex expression than in the bulk case. Nevertheless, it can be expressed as the sum of one contribution arising from a charge density induced in the bulk of the material and another one arising from a charge density induced at the surface of the material.

The DIIMFP resulting from the induced electric field becomes more complicated, with two additional parametric dependencies: (1) on the depth coordinate with respect to the surface and (2) on the surface crossing angle with respect to the surface normal. Several models exist with varying approximations [23,24,30,31], the effects of which were scrutinized [31]. Regardless of the details of the models, they all yield a number of consistent general features and trends of the surface excitation probability:

- Surface energy losses can be undergone by the charged projectile on either side of the interface, at the solid side or at the vacuum side. Indeed, a surface charge can be induced regardless of the side at which the projectile is moving on and, thus, a charged projectile moving on the vacuum side of the interface can also undergo energy losses. It has been recently shown that, in reflection-electron-energy-loss spectra, surface losses on the vacuum

side of the interface account for a large fraction of the surface-excitation intensity, often more than half of it [44].

- The probability for an electron that crosses a surface to undergo a surface excitation is, to a first approximation [45], proportional to the surface dwell time $t \sim 1/\left(\sqrt{\mathcal{E}}\cos\theta\right)$, where $\mathcal{E}$ is the projectile energy and θ is the surface crossing angle with respect to the surface normal. The energy dependency implies that, in practice, surface excitations are relevant for electron energies up to a few kiloelectronvolts. Additional structure to the aforementioned angular behavior is predicted for scattering geometries coinciding with deep minima of the differential elastic scattering cross section: minor deflections in the course of an inelastic collision lead to an effective scattering geometry with enhanced elastic scattering and therefore higher detection probability [44].

- The DIIMFP for energy losses of charged projectiles impinging on a surface differs from the DIIMFP for the conjugate emerging direction. This effect, known as in-out asymmetry in surface energy-losses, has been long predicted but only recently observed experimentally [46]. In-out differences are most accentuated for surface-crossing directions close to the surface normal and for high kinetic energies (about 1 keV).

## Monte-Carlo simulation of electron energy-loss spectra

The electron-transport problem in a solid is described in terms of a Boltzmann-type transport equation. A practical method for solving the problem is provided by Monte-Carlo simulation, which consists in sampling an ensemble of trajectories undergoing collisions of the relevant types as dictated by a given set of interaction cross sections. A statistical average of the desired observable is performed over the sampled trajectories to the selected precision [47].

In the energy range between 100 eV and a few keV the relevant interaction mechanisms of electrons with the solid are elastic collisions with the atoms and inelastic collisions with typically weakly bound electrons in the solid. Elastic scattering can be accurately described by means of a differential cross section for elastic scattering (DCES), which can be systematically calculated by means of partial-wave calculations [48,49]. Inelastic scattering is accounted for by the DIIMFPs described above. Monte-Carlo simulations of electron transport (bulk losses only) for typical geometries in FEBID experiments have been previously considered [2,7]. The inclusion of surface excitations implies a modification of the sampling algorithm in the vicinity of the surface (typically 15 Å above and below the surface), as schematically shown in Figure 1. Technical details on the

implementation of the algorithm for the simulation of surface energy losses can be found elsewhere in great detail [30,31,50]. Here the focus is on the effect of surface excitations on the reflection-electron-energy-loss spectrum (REELS). To this effect, Figure 2 compares the REELS of Si (left) and Cu (right) under bombardment with 1 keV electrons impinging perpendicularly on the sample; all reflected electrons are collected. The simulation geometry is depicted in Figure 3. The materials are chosen as representative substrate (Si) and deposit (Cu) materials. The solid red curves (dashed blue curves) in Figure 2 correspond to REELS simulated without (with) the inclusion of surface excitations. We observe that even for a primary energy of 1 keV surface excitations account for (1) additional features, i.e. the excitation of surface plasmons, in the low-energy-loss part of the REELS that are not accounted for by a bulk-only description of the energy losses of charged projectiles in the material and (2) a sizeable fraction of the intensity in the first few tens of eV of energy losses, about 20% of the intensity in the case of Si and 15% of the intensity in the case of Cu. Although the relative importance of surface excitations is enhanced for lower energies, their effect is noticeable even in the 1 keV domain. Thus, the inclusion of surface excitations in the modelling of electron-transport is expected to give a yet more quantitative description of FEBID processes at and below the 1 keV primary-energy domain.

Secondary-electron emission

Energy losses of the charged projectile can lead to the ejection of loosely bound electrons of the solid, which emerge as secondary electrons (SE). The majority of these SE are of relatively low energies (≤50 eV). These energies are well below the domain of validity of the elastic and inelastic interaction cross sections available in the literature, which has been a limitation for progress in the field. Electron coincidence measurements [51-54] have supplied a wealth of valuable information.
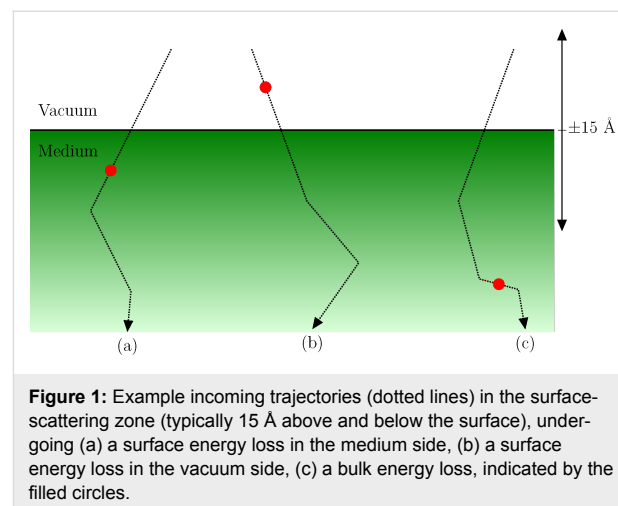
Figure 1: Example incoming trajectories (dotted lines) in the surface-scattering zone (typically 15 Å above and below the surface), undergoing (a) a surface energy loss in the medium side, (b) a surface energy loss in the vacuum side, (c) a bulk energy loss, indicated by the filled circles.
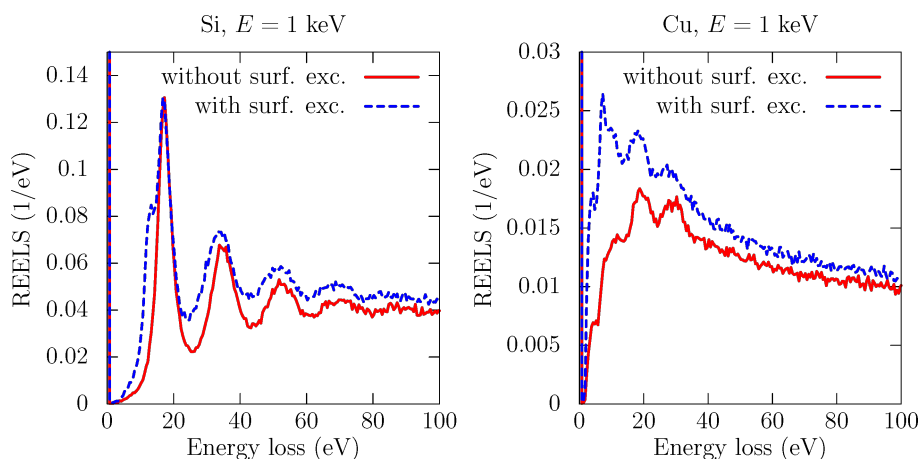
Figure 2: Comparison of reflection-electron-energy-loss spectra (REELS) of Si (left) and Cu (right) under bombardment with 1-keV electrons at normal incidence, without (red solid curves) and with (blue dashed curves) an account of surface excitations. All backscattered electrons are collected.
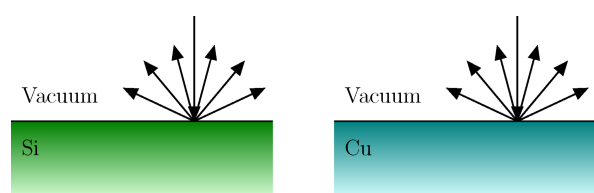
Figure 3: Simulation geometry: 1 keV electrons impinge normally onto the material (Si or Cu); all backscattered electrons are collected.

Recently, coincidence measurements of correlated electron pairs emitted from solids (Al, Si, Ag) under electron bombardment have been measured, providing a double-differential SE yield, differential with respect to the energy loss of the primary electron and with respect to the energy (or the time of flight) of the emitted secondary electron [55]. These experimental data are displayed for Si under 100 eV electron bombardment in the lower panel of Figure 4 as a bird's-eye-view plot (only the shape and relative intensities of the spectrum are of relevance here, hence the missing units in the linear color scale, where black is the null point and white is the maximum attained value). The horizontal white lines indicate the corresponding times of flight for electrons with 0 eV (accelerating grids were used), 50 eV, and 100 eV. See [55] for the experimental details. The plot can be read as the (time-of-flight) spectrum of secondary electrons emitted as a result of different energy losses of the impinging electron (to be read at the abscissae). The upper panel of Figure 4 displays the REELS of 100 eV from Si, where the energy-loss peaks corresponding to the excitation of one surface plasmon, one bulk plasmon, and two surface plasmons are indicated by vertical red dashed lines and labeled, respectively, 1s, 1b, 2s as a guideline for the abscissae scale in the other plots of the figure.
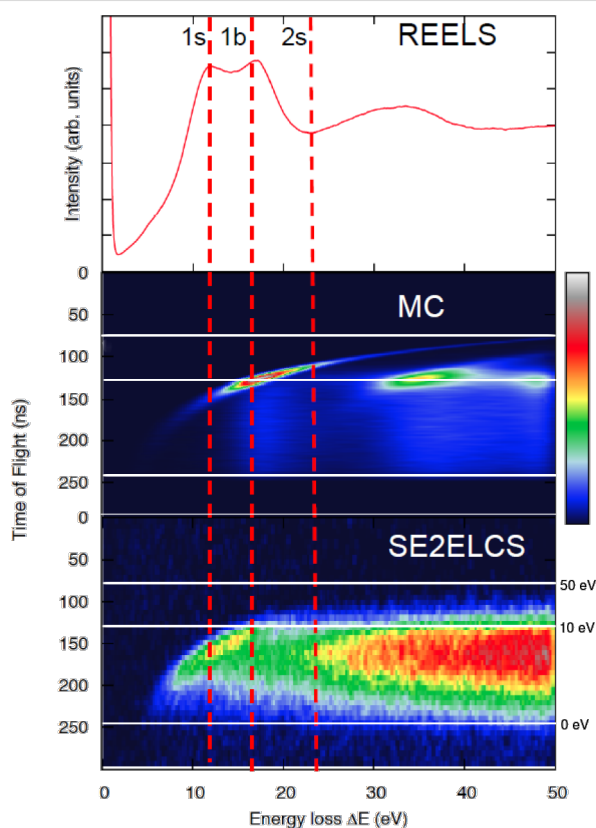
Figure 4: (Upper panel) Reflection-electron-energy-loss spectrum (REELS) of Si under 100 eV bombardment (see [55] for experimental details). (Lower panel) (e,2e)-coincidence spectrum of secondary electrons emitted in coincidence with energy losses (SE2ELCS) of 100-eV electrons backscattered from Si. (Middle panel) Monte-Carlo simulation of the SE2ELCS measurement without accounting for surface energy losses. The vertical dashed lines in red indicate energy losses corresponding to the excitation of one surface, one bulk, and two surface plasmons. The horizontal solid white lines indicate the times of flight corresponding to electrons with 0 eV (accelerating grids were used), 10 eV, and 50 eV.

The coincidence data (e.g., lower panel of Figure 4) provide on the one hand very detailed insight into the mechanisms responsible for SE emission and, on the other hand, provide a benchmark against which models for SE emission and low-energy electron transport in general can be tested. The transport models, in turn, aid in the interpretation of the data, as discussed below. The Monte-Carlo simulation briefly outlined above was extended to include the generation and the transport of the secondary electrons and to simulate the electron-coincidence measurement on the basis of a simple model for SE emission: every time that the primary electron undergoes an energy loss, a SE trajectory is started with the energy loss as an initial energy (see [55] for the simulation details). Having the experimental data as a guideline, the interaction cross sections described above were used down to 1 eV (knowing that this is well below the domain where they are formally applicable) as a first approximation. Simulations were first carried out using bulk energy-loss DIIMFPs exclusively. The resulting spectrum is displayed in the middle panel of Figure 4. It is clear that these simulated peaks do not reproduce the onset of the experimentally observed peaks. Only after the inclusion of surface excitations, both for the incoming primary electrons, for the backscattered electrons, and for the emitted secondary electrons, is good agreement between simulations and measurements found, as shown in Figure 5. The Monte Carlo simulations further allow one to discern the processes that give rise to the different regions of the coincidence spectrum [55].

Thus, it was found that any realistic model of SE emission and low-energy electron transport near solid surfaces must account for surface excitations. This conclusion has strong implications on the emission depth from which SE are emitted: if secondary electrons undergo additional energy losses on their way out of the solid, the average SE-emission depth becomes much shallower than one would assume on the basis of a model based only on bulk properties. The predicted number of emitted SE can also differ appreciably with respect to a bulk-only simulation. Furthermore, the energies of the SE are also modified by the presence of additional surface energy-loss channels.

Conclusion

In light of the presented richness in the behavior of surface excitations and their effect on both the energy losses of the impinging electrons and on the emission of secondary electrons, it is to be expected that their inclusion in the modelling of electron transport for FEBID will yield a more detailed description of the role played by both the primary electrons and the emitted secondary electrons in the growth process. It should be noted that, while surface excitations are relevant for primary electrons with energies up to 1–2 keV, they are essential ingredients for the modelling of slow secondary electrons regardless of
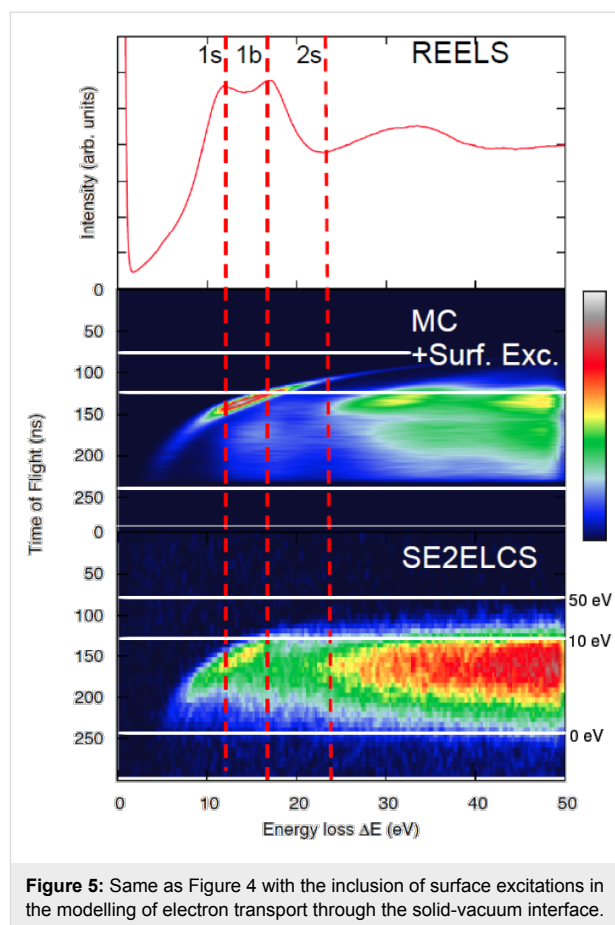
Figure 5: Same as Figure 4 with the inclusion of surface excitations in the modelling of electron transport through the solid–vacuum interface.

the energy of the primary electron responsible for their emission.

The previous considerations suggest that the inclusion of surface excitations in the electron-transport model employed to investigate FEBID experiments might lead to noticeable effects. On the one hand, more primary electrons are backscattered compared to the case without surface excitations (see Figure 2), so that an increase in the simulated deposition rate might be expected (at least for primary energies in the 1–2 keV regime and below). On the other hand, more slow (≤50 eV) secondary electrons will be available from the decay of surface plasmons [56] excited by either the incoming electrons or the outgoing electrons (backscattered electrons or emitted secondary electrons). This should also contribute to an increase of the simulated deposition rate and additionally lead to an enhancement of the FEBID proximity effect.

Acknowledgements

References

1. Huth, M.; Porrati, F.; Schwalb, C.; Winhold, M.; Sachser, R.; Dukic, M.; Adams, J.; Fantner, G. *Beilstein J. Nanotechnol.* **2012,** *3,* 597–619. doi:10.3762/bjnano.3.70

2. Utke, I.; Hoffmann, P.; Melngailis, J. *J. Vac. Sci. Technol., B* **2008,** *26,* 1197. doi:10.1116/1.2955728

3. Smith, D. A.; Fowlkes, J. D.; Rack, P. D. *Nanotechnology* **2007,** *18,* 265308. doi:10.1088/0957-4484/18/26/265308

4. Silvis-Cividjian, N.; Hagen, C. W.; Kruit, P. *J. Appl. Phys.* **2005,** *98,* 084905. doi:10.1063/1.2085307

5. Liu, Z.-Q.; Mitsuishi, K.; Furuya, K. *Nanotechnology* **2006,** *17,* 3832–3837. doi:10.1088/0957-4484/17/15/038

6. Smith, D. A.; Fowlkes, J. D.; Rack, P. D. *Small* **2008,** *4,* 1382–1389. doi:10.1002/smll.200701133

7. Salvat-Pujol, F.; Jeschke, H. O.; Valentí, R. *Beilstein J. Nanotechnol.* **2013,** *4,* 781–792. doi:10.3762/bjnano.4.89

8. Ritchie, R. H. *Phys. Rev.* **1957,** *106,* 874–881. doi:10.1103/PhysRev.106.874

9. Powell, C. J.; Swan, J. B. *Phys. Rev.* **1959,** *115,* 869–875. doi:10.1103/PhysRev.115.869

10. Powell, C. J.; Swan, J. B. *Phys. Rev.* **1959,** *116,* 81–83. doi:10.1103/PhysRev.116.81

11. Ritchie, R. H.; Marusak, A. L. *Surf. Sci.* **1966,** *4,* 234–240. doi:10.1016/0039-6028(66)90003-3

12. Geiger, J. *Phys. Status Solidi* **1967,** *24,* 457–459. doi:10.1002/pssb.19670240207

13. Otto, A. *Phys. Status Solidi* **1967,** *22,* 401–406. doi:10.1002/pssb.19670220211

14. Kröger, E. *Z. Phys.* **1968,** *216,* 115–135. doi:10.1007/BF01390952

15. Kröger, E. *Z. Phys.* **1970,** *235,* 403–421. doi:10.1007/BF01394931

16. Chan, D.; Richmond, P. *Surf. Sci.* **1973,** *39,* 437–440. doi:10.1016/0039-6028(73)90014-9

17. Jacob, J. H. *Phys. Rev. A* **1973,** *8,* 226–235. doi:10.1103/PhysRevA.8.226

18. Chan, D.; Richmond, P. *J. Phys. C* **1975,** *8,* 2509–2521. doi:10.1088/0022-3719/8/15/025

19. Chan, D.; Richmond, P. *J. Phys. C* **1975,** *8,* 3221–3231. doi:10.1088/0022-3719/8/19/021

20. Chan, D.; Richmond, P. *J. Phys. C* **1976,** *9,* 163–168. doi:10.1088/0022-3719/9/1/023

21. Arista, N. R. *Phys. Rev. A* **1994,** *49,* 1885–1896. doi:10.1103/PhysRevA.49.1885

22. Tung, C. J.; Chen, Y. F.; Kwei, C. M.; Chou, T. L. *Phys. Rev. B* **1994,** *49,* 16684–16692. doi:10.1103/PhysRevB.49.16684

23. Chen, Y. F.; Kwei, C. M. *Surf. Sci.* **1996,** *364,* 131–140. doi:10.1016/0039-6028(96)00616-4

24. Yubero, F.; Sanz, J. M.; Ramskov, B.; Tougaard, S. *Phys. Rev. B* **1996,** *53,* 9719–9727. doi:10.1103/PhysRevB.53.9719

25. Denton, C.; Gervasoni, J. L.; Barrachina, R. O.; Arista, N. R. *Phys. Rev. A* **1998,** *57,* 4498–4511. doi:10.1103/PhysRevA.57.4498

26. Ding, Z.-J. *J. Phys.: Condens. Matter* **1998,** *10,* 1733–1751. doi:10.1088/0953-8984/10/8/009

27. Ding, Z.-J. *J. Phys.: Condens. Matter* **1998,** *10,* 1753–1765. doi:10.1088/0953-8984/10/8/010

28. Kwei, C. M.; Wang, C. Y.; Tung, C. J. *Surf. Interface Anal.* **1998,** *26,* 682–688. doi:10.1002/(SICI)1096-9918(199808)26:9<682::AID-SIA415>3.0.CO;2-7

29. Vicanek, M. *Surf. Sci.* **1999,** *440,* 1–40. doi:10.1016/S0039-6028(99)00784-0

30. Li, Y. C.; Tu, Y. H.; Kwei, C. M.; Tung, C. J. *Surf. Sci.* **2005,** *589,* 67–76. doi:10.1016/j.susc.2005.05.050

31. Salvat-Pujol, F.; Werner, W. S. M. *Surf. Interface Anal.* **2013,** *45,* 873–894. doi:10.1002/sia.5175

32. Da, B.; Mao, S. F.; Ding, Z. J. *J. Phys.: Condens. Matter* **2011,** *23,* 395003. doi:10.1088/0953-8984/23/39/395003

33. Werner, W. S. M.; Glantschnig, K.; Ambrosch-Draxl, C. *J. Phys. Chem. Ref. Data* **2009,** *38,* 1013–1092. doi:10.1063/1.3243762

34. Koepernik, K.; Eschrig, H. *Phys. Rev. B* **1999,** *59,* 1743–1757. doi:10.1103/PhysRevB.59.1743

35. Ambrosch-Draxl, C.; Sofo, J. O. *Comput. Phys. Commun.* **2006,** *175,* 1–14. doi:10.1016/j.cpc.2006.03.005

36. Lindhard, J. *Mat.-Fys. Medd. - K. Dan. Vidensk. Selsk.* **1954,** *28,* 1–57.

37. Mermin, N. D. *Phys. Rev. B* **1970,** *1,* 2362–2363. doi:10.1103/PhysRevB.1.2362

38. Denton, C. D.; Abril, I.; Garcia-Molina, R.; Moreno-Marín, J. C.; Heredia-Avalos, S. *Surf. Interface Anal.* **2008,** *40,* 1481–1487. doi:10.1002/sia.2936

39. Schattschneider, P.; Hébert, C.; Franco, H.; Jouffrey, B. *Phys. Rev. B* **2005,** *72,* 045142. doi:10.1103/PhysRevB.72.045142

40. Bote, D.; Salvat, F. *Phys. Rev. A* **2008,** *77,* 042701. doi:10.1103/PhysRevA.77.042701

41. Jackson, J. D. *Classical Electrodynamics,* 2nd ed.; John Wiley & Sons, Inc.: Hoboken, NJ, U.S.A., 1975.

42. Griffiths, D. J. *Introduction to Electrodynamics,* 3rd ed.; Prentice Hall: Upper Saddle River, NJ, U.S.A., 1999.

43. Nazarov, V. U. *Surf. Sci.* **1995,** *331–333,* 1157–1162. doi:10.1016/0039-6028(95)00090-9

44. Werner, W. S. M.; Novák, M.; Salvat-Pujol, F.; Zemek, J.; Jiricek, P. *Phys. Rev. Lett.* **2013,** *110,* 086110. doi:10.1103/PhysRevLett.110.086110

45. Werner, W. S. M.; Tratnik, H.; Brenner, J.; Störi, H. *Surf. Sci.* **2001,** *495,* 107–119. doi:10.1016/S0039-6028(01)01516-3

46. Salvat-Pujol, F.; Werner, W. S. M.; Novák, M.; Jiricek, P.; Zemek, J. *Phys. Rev. B* **2014,** *89,* 205435. doi:10.1103/PhysRevB.89.205435

47. Werner, W. S. M. *Surf. Interface Anal.* **2001,** *31,* 141–176. doi:10.1002/sia.973

48. Salvat, F.; Jablonski, A.; Powell, C. J. *Comput. Phys. Commun.* **2005,** *165,* 157–190. doi:10.1016/j.cpc.2004.09.006

49. Bote, D.; Salvat, F.; Jablonski, A.; Powell, C. J. *J. Electron Spectrosc. Relat. Phenom.* **2009,** *175,* 41–54. doi:10.1016/j.elspec.2009.07.003

50. Novák, M. *Surf. Sci.* **2008,** *602,* 1458–1465. doi:10.1016/j.susc.2008.02.008

51. Voreades, D. *Surf. Sci.* **1976,** *60,* 325–348. doi:10.1016/0039-6028(76)90320-4

52. Pijper, F. J.; Kruit, P. *Phys. Rev. B* **1991,** *44,* 9192–9200. doi:10.1103/PhysRevB.44.9192

53. Müllejans, H.; Bleloch, A. L. *Phys. Rev. B* **1992,** *46,* 8597–8599. doi:10.1103/PhysRevB.46.8597

54. Müllejans, H.; Bleloch, A. L.; Howie, A.; Tomita, M. *Ultramicroscopy* **1993,** *52,* 360–368. doi:10.1016/0304-3991(93)90047-2

55. Werner, W. S. M.; Salvat-Pujol, F.; Bellissimo, A.; Khalid, R.; Smekal, W.; Novák, M.; Ruocco, A.; Stefani, G. *Phys. Rev. B* **2013,** *88,* 201407. doi:10.1103/PhysRevB.88.201407
56. Chung, M. S.; Everhart, T. E. *Phys. Rev. B* **1977,** *15,* 4699–4715. doi:10.1103/PhysRevB.15.4699

Structural transitions in electron beam deposited Co–carbonyl suspended nanowires at high electrical current densities

Gian Carlo Gazzadi[*1] and Stefano Frabboni[1,2]

Abstract

Suspended nanowires (SNWs) have been deposited from Co–carbonyl precursor ($Co_2(CO)_8$) by focused electron beam induced deposition (FEBID). The SNWs dimensions are about 30–50 nm in diameter and 600–850 nm in length. The as-deposited material has a nanogranular structure of mixed face-centered cubic (FCC) and hexagonal close-packed (HCP) Co phases, and a composition of 80 atom % Co, 15 atom % O and 5 atom % C, as revealed by transmission electron microscopy (TEM) analysis and by energy-dispersive X-ray (EDX) spectroscopy, respectively. Current (I)–voltage (V) measurements with current densities up to 10^7 A/cm^2 determine different structural transitions in the SNWs, depending on the I–V history. A single measurement with a sudden current burst leads to a polycrystalline FCC Co structure extended over the whole wire. Repeated measurements at increasing currents produce wires with a split structure: one half is polycrystalline FCC Co and the other half is graphitized C. The breakdown current density is found at 2.1×10^7 A/cm^2. The role played by resistive heating and electromigration in these transitions is discussed.

Introduction

The growing importance of nanotechnology and nanoscience in advanced applications and fundamental research requires nanofabrication techniques that are highly resolved but at the same time flexible and feasible with research laboratory equipment. A promising approach is represented by focused electron beam induced deposition (FEBID), a direct-write nanolithography based on the decomposition of gas precursors molecules with electron beams [1]. This technology, in fact, allows for the

deposition of various materials on planar and non-planar substrates with nanoscale resolution [2], and it can be easily implemented on scanning electron microscopes (SEM) by installing a gas injection system (GIS).

FEBID flexibility has been exploited in applications that are critical for traditional lithography techniques, such as the deposition of electrical connections to isolated nanostructures [3,4]

or the fabrication of scanning probe nanotips [5,6], but it has been also employed successfully in the realization of different types of nanosensors [7-10] and nanodevices [11,12]. Among the FEBID capabilities, the deposition of nanowires with nanoscale site specificity [10,13] becomes appealing for the development of future nanoscale devices which need scaled interconnects, and the deposition of magnetic nanostructures opens interesting perspectives in the field of magnetic nanodevices [14,15].

To keep up with such challenging tasks, FEBID has to face a deposit purity issue [16], the C and O contamination of metal deposits coming from incomplete fragmentation of the metalorganic molecules, typically employed as precursors. Several methods have been investigated, mainly consisting in the deposit treatment by thermal annealing [17,18] or e-beam irradiation [19], but also the design and synthesis of new precursors is considered [20].

Another important aspect, often not considered in the literature, is to investigate the electrical behavior and stability of FEBID nanodeposits under critical conditions that may occur in real devices, such as extended voltage and current ranges and high current density, where Joule heating and electromigration effects [21,22] come into play and are a major cause of failures.

In this work, we deposit free-standing suspended nanowires (SNWs) using Co–carbonyl precursor ($Co_2(CO)_8$), and study their behavior under high electrical current density, following the same approach used for Pt–metallorganic SNWs [23]. While FEBID deposits are usually grown on a substrate, suspended deposition is obtained by moving the electron beam away from an elevated edge under gas flow. If the scanning speed (beam stepsize/beam dwell time) is properly tuned, a self-standing nanowire can be deposited along the beam path [24]. This approach offers the possibility to deposit and analyze the material free from any substrate contribution, but above all it enables 3D nanofabrication [25]. The SNWs are characterized electrically at high current densities and analyzed structurally by transmission electron microscopy (TEM). The Co–carbonyl precursor has been chosen because it is one of the most commonly used for the deposition of magnetic nanostructures, and also because it yields one of the highest metal concentrations among metalorganics [26].

Experimental

FEBID was performed in a dual beam system (FEI Strata DB235M) combining a Ga-ion focused ion beam (FIB) with a thermal field emission SEM, equipped with a Co–carbonyl ($Co_2(CO)_8$) GIS operated at room temperature (RT). The GIS is mounted at a polar angle of 52° and an azimuthal angle of 115°
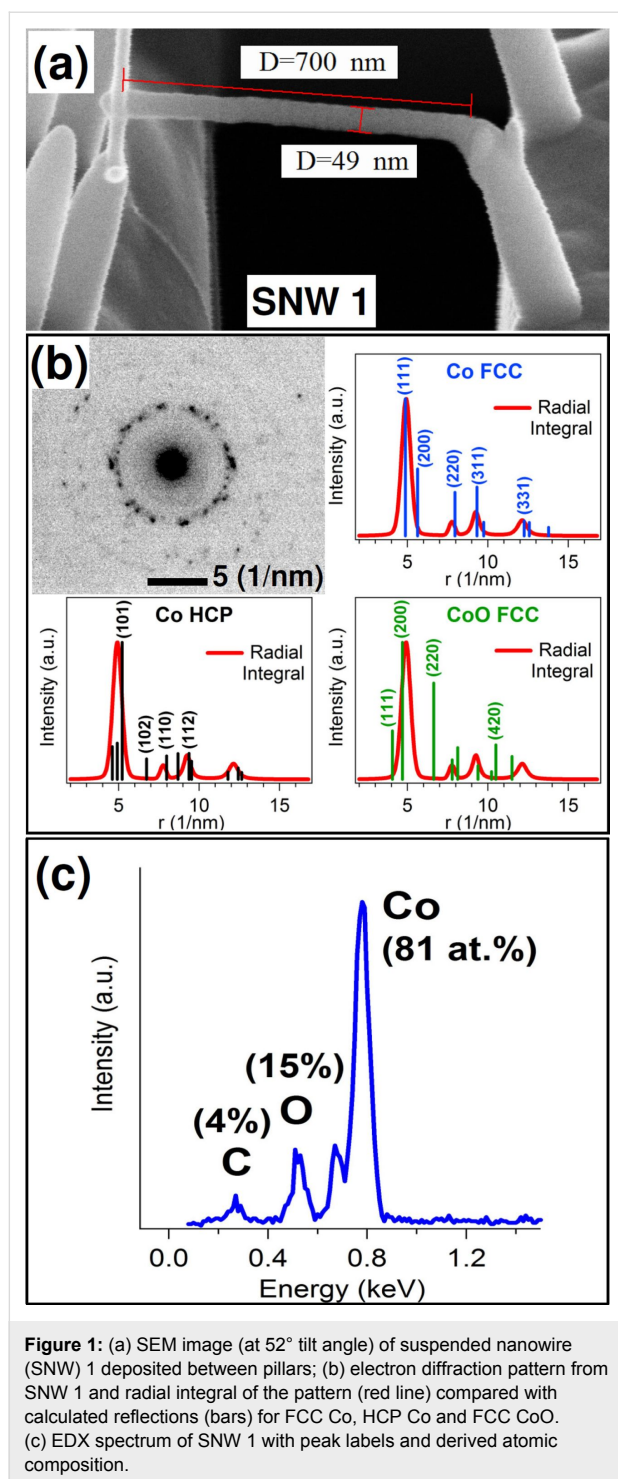
with respect to the sample surface. An injection nozzle with a reduced diameter of 160 μm was installed in order to limit the pressure bursts that typically occur for this kind of precursor at the first openings, and to reach a gas pressure into the chamber of the order of 3×10^{-6} mbar (with respect to a base pressure of 6×10^{-7} mbar), a value that allowed for a fine control of the deposition process. The nozzle-to-sample distance during deposition was about 200 μm.

The samples are Au-coated (100 nm thickness) silicon nitride membranes (500 nm thick). Pairs of contact pads were patterned on gold by FIB milling, and, at the gap between the pads, a slit (500 nm wide and 6 μm long) was opened through the membrane to enable TEM observation and obtain substrate-less suspended growth. SNWs were deposited across the slit by focusing a 15 keV, 67 pA electron beam (probe size about 5 nm) either on Co nanopillars, grown by FEBID, or directly on the gold pads, and moving it towards the opposite side with 5 nm steps and dwell times varying between 10 and 35 ms in order to obtain the desired horizontal growth.

Electrical characterization was done in situ using two nanomanipulated probes (Kleindiek MM3A-EM) connected to a Keithley 6487 source meter. The current (*I*)–voltage (*V*) measurements were performed by applying voltage to the left Au pad and sweeping it over a (0, +*V*, −*V*, 0) loop with the right pad grounded (GND) while measuring the current. After each *I–V* curve an SEM image of the SNW was taken to check for morphological modifications. TEM analysis was performed with a JEOL 2010 microscope, equipped with energy dispersive X-ray spectroscopy (EDX) system (Oxford INCA 100) for composition analysis.

Results and Discussion

In Figure 1a, an example of Co–carbonyl SNW deposited by FEBID is shown. The suspended wire is deposited across the slit and connects two Co–carbonyl nanopillars facing on the opposite sides. Deposition of the SNW is performed by focusing the beam, normal to the sample, on the right pillar and moving it toward the left with the scan parameters specified before. The obtained SNW (SNW 1) is about 700 nm long, 50 nm thick and 30 nm wide, and because it is slightly sloped upward another deposition (30 nm wide and 65 nm long) was necessary to connect to the left pillar. The deposited material shows a uniform bright contrast under the SEM, and TEM imaging (not shown) reveals a nanogranular structure typical of metallorganic deposits, where metal grains with a size of few nanometers are embedded in an amorphous, carbonaceous matrix [27]. The structure is confirmed by TEM selected area electron diffraction (SAED) measured at the center of the wire and presented in Figure 1b. The pattern shows an innermost

Figure 1: (a) SEM image (at 52° tilt angle) of suspended nanowire (SNW) 1 deposited between pillars; (b) electron diffraction pattern from SNW 1 and radial integral of the pattern (red line) compared with calculated reflections (bars) for FCC Co, HCP Co and FCC CoO. (c) EDX spectrum of SNW 1 with peak labels and derived atomic composition.

CoO, displayed as bars proportional to the intensities of the reflections. The experimental curve shows the main peak at $r = 4.9$ 1/nm and three smaller structures at $r = 7.7, 9.2$ and 12.1 1/nm. The best agreement is found with the Co FCC pattern, which can fit all the four peaks with (111), (220), (311) and (331) reflections, respectively. A lower degree of agreement also exists with the Co HCP pattern. On the contrary, the absence of any structure at $r = 6.6$ and 4.0 1/nm, corresponding to the second (220) and third (111) most intense reflections of CoO FCC, suggests that such a phase is not present. This comparison indicates that the deposited material is a mixture of FCC (a larger fraction) and HCP cobalt nanograins. EDX analysis was also performed by TEM. The measured spectrum, in Figure 1c, shows the peaks of the precursor components, C, O and Co, with atomic concentrations of 4, 15 and 81 atom %, respectively. This high Co concentration is in line with the best values reported in the literature for this precursor [25], though concentrations above 90 atom % have also been obtained [10,26,28].

Electrical characterization of SNW 1, shown in Figure 2a, was carried out inside the dual beam system. The bias range in this

Figure 2: (a) Current(*I*)–voltage(*V*) measurements on SNW 1. In the inset, the first *I–V* measurement taken on the wire as shown in Figure 1a is magnified; (b) SEM image (at 52° tilt angle) of SNW 1 after *I–V* 1.

high-intensity ring with many single spots, and outer, fainter rings with spots apparently randomly arranged. This kind of pattern is typical of nanocrystalline materials with randomly oriented nanograins. To establish the structure of these nanograins the radial integral of the pattern (red curve) was compared to the main reflections calculated for face-centered cubic (FCC) Co, hexagonal close-packed (HCP) Co and FCC
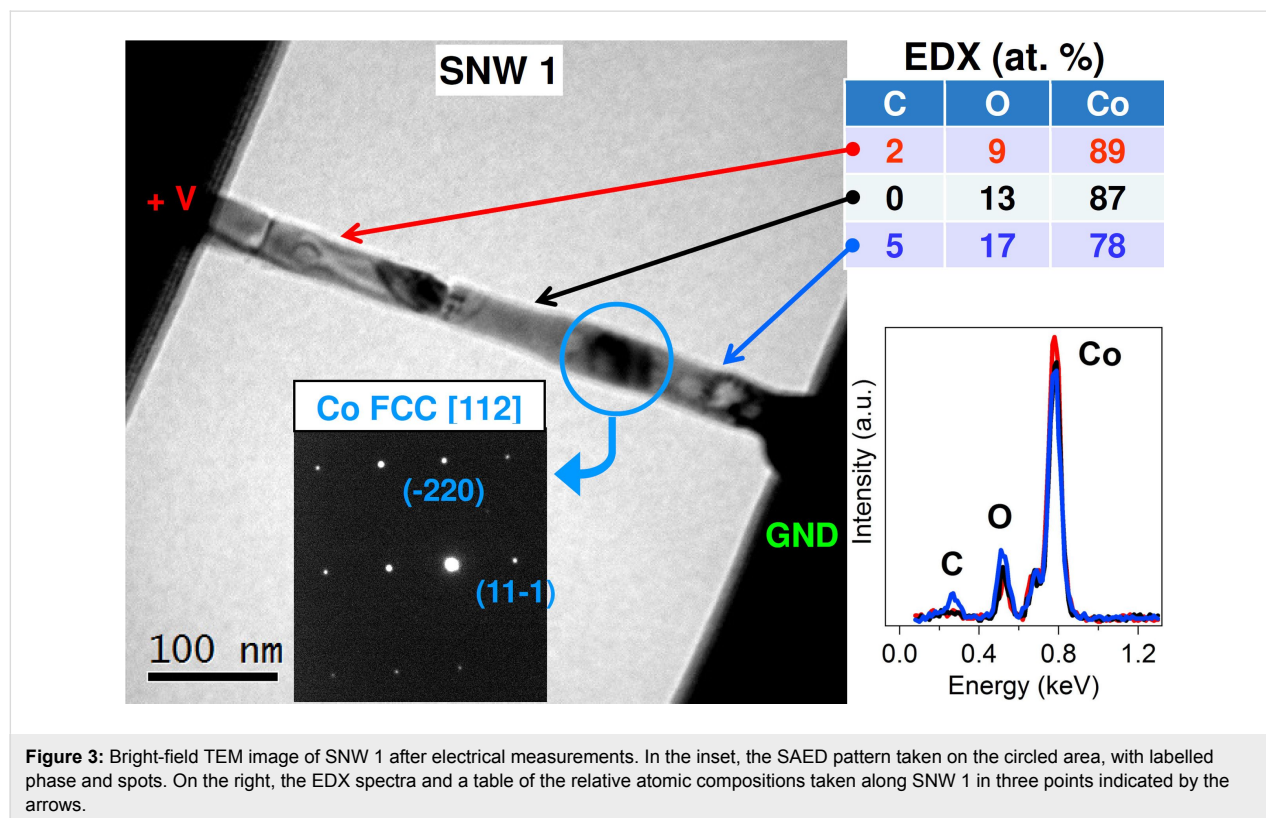
case was $V = 0.1$ V. In the first measurement, shown in the inset of Figure 2a (squares), the current starts increasing linearly with voltage, but around $V = 0.07$ V, a big spike from $I = 0.7$ to 2.7 µA is recorded, followed by a return to values on the original linear trend. The measurement was stopped before finishing the loop to observe SNW 1. The SEM image is shown in Figure 2b. It is clear that a structural transformation has occurred due to the current spike, because the nanowire shows a completely changed morphology, with dark bumps and spots on the surface and inside, and a reduced thickness in the middle. The connection to the left pillar is heavily bent and deformed as if a mechanical stress was applied. The supporting pillars do not show such modifications and maintain the same uniform bright contrast. A second *I–V* measurement was taken on the same bias range, completing the cycle, and data are shown in Figure 2a (circles). The *I–V* trend is strictly linear, and current values are increased dramatically from the previous run, reaching almost $I = 200$ µA at $V = 0.1$ V. The resistivity obtained considering SNW 1 alone drops from 1.6×10^4 µΩ·cm, before the transition, to about 110 µΩ·cm, a value to be compared to 6 µΩ·cm for bulk cobalt. SEM inspection after this measurement shows no further difference from the picture in Figure 2b.

TEM structural analysis after these electrical measurements is reported in Figure 3. The bright-field image of SNW 1 is completely changed from the grainy structure observed after deposition. Now it has the typical appearance of a polycrystalline material, with regions of well-defined contrast extending for tens of nanometers along the wire, and separated by sharp contrast lines. This suggests the presence of big metal grains inside the nanowire. The SAED pattern taken on the central dark region (blue circled), 35 nm wide and 55 nm long, shows single spots arranged in a rectangular lattice that correspond to the FCC structure of Cobalt, oriented along the [112] zone axis. This type of pattern indicates that a highly ordered, essentially monocrystalline, structure is present within this region. Other orientations of the same Co FCC phase were found along the wire, while the bright circles on the right turn out to be hollow graphite cages, as will be shown for the second SNW. EDX analysis performed along the wire reveals a small gradient in Co concentration on going from right to left: 78 atom % on the right, 87 atom % on the center and 89 atom % on the left.

Interestingly, this distribution follows the electron current direction, from cathode (right) to anode (left), suggesting that an electromigration effect is involved in the structural transition. This effect occurs in metallic micro- and nanowires under high current densities (10^6 to 10^7 A/cm^2) and consists in the dragging of metal ions along the electron current direction due to momentum transfer by the flowing electrons [21]. From EDX spectra, shown in the right-bottom panel of Figure 3, it is also

C	O	Co
2	9	89
0	13	87
5	17	78

Figure 3: Bright-field TEM image of SNW 1 after electrical measurements. In the inset, the SAED pattern taken on the circled area, with labelled phase and spots. On the right, the EDX spectra and a table of the relative atomic compositions taken along SNW 1 in three points indicated by the arrows.

evident that a true carbon peak, above background level, remains only on the right part of SNW 1, where the graphite circles were observed.

A second SNW (SNW 2), shown in Figure 4a, was deposited directly between the Au contacts without pillars. It is about 600 nm long, 45 nm thick and 30 nm wide. To ensure good connection to the left pad, an additional deposition was performed on a square area around SNW end. EDX analysis, not shown, returned concentrations similar to SNW 1: 5 atom % C, 17 atom % O and 78 atom % Co. SNW 2 was tested with five subsequent I–V measurements, shown in Figure 4b, extending the voltage range from 0.1 to 2 V, and after each one
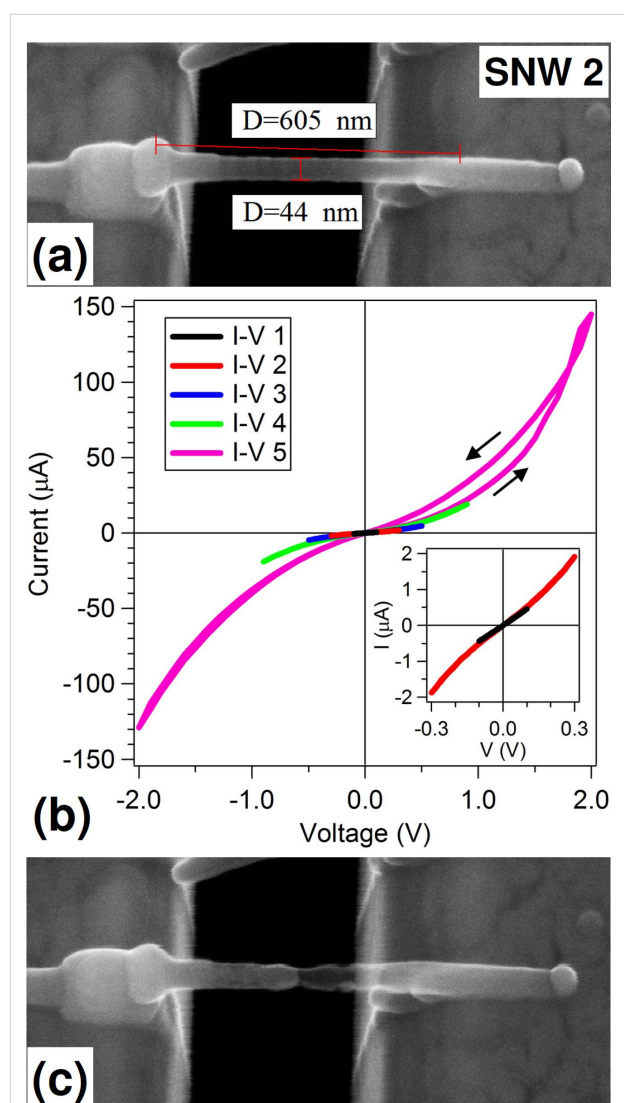
Figure 4: (a) SEM image (at 20° tilt angle) of SNW 2 deposited between the Au pads across the slit. (b) Five subsequent I–V measurements taken on SNW 2 at increasing bias range. In the inset, the first two I–V curves are shown; (c) SEM image (at 20° tilt angle) of SNW 2 after the last I–V measurement.

of them a check for morphology changes was done by SEM. The first measurement, shown in the inset of Figure 4b (black line), has a linear behavior with a resistance of 223 kΩ and resistivity of 5×10^4 μΩ·cm, while the second I–V curve (red line) shows a slight upward bending as the voltage increases above 0.1 V. All subsequent I–V curves show an increasing bending for increasing voltage. These semiconductor-like trends are typical of potential-barrier conduction systems, such are the nanogranular FEBID deposits, but they might also include an Au/SNW contact barrier that the two probe setup is not able to cancel. SEM observation after the first four cycles did not reveal any modification in SNW 2. In the last I–V curve (pink line), a different behavior appears: an hysteresis between [0,2 V] and [2,0 V] data is present, the return curve having higher currents with respect to the first leg. The negative bias portions reflect the return curve trend and do not show any hysteresis. The observed effect might be linked to some structural transformation that was indeed confirmed by SEM analysis, in Figure 4c. The left-hand half of the wire looks brighter while the right-hand one has become transparent.

To deeper investigate the nature of this transition we turned to TEM analysis. As shown by the bright-field image in Figure 5, the opaque portion on the left is polycrystalline cobalt while the transparent region on the right is graphitized carbon. The SAED pattern taken on the big central grain (55 nm wide and 65 nm long, blue circled), after a tilt of the sample, is shown in the upper panel. The spots arranged in a diamond lattice reveal that the grain has an FCC structure oriented along the [110] zone axis.

The extra spots around the main lattice arise from nearby grains entering the diffraction volume due to the sample tilt. A high-resolution image of the transparent region (orange squared) is reported in the lower panel, and shows graphite planes arranged in a rounded cage structure with a hollow/amorphous-like interior. This carbon structure, strongly resembling the one of carbon-encapsulated metal nanoparticles [29], was probably hosting a Co grain before its migration. From this analysis, the effect of electromigration is even more evident than before: the metallic part has all migrated toward the anode, leaving a graphitic skeleton behind.

Finally, a third SNW (SNW 3) was deposited between the Au pads and stressed electrically until breakdown. As shown in Figure 6a, SNW 3 is 850 nm long, 30–35 nm thick and 25–30 nm wide. A square deposition on SNW end was applied as for SNW 2. EDX analysis, not shown, gave concentrations of 6 atom % C, 13 atom % O and 81 atom % Co. The first I–V measurement, shown in the inset of Figure 6b, was taken with a bias of $V = 0.4$ V and displays a linear behavior, slightly devi-
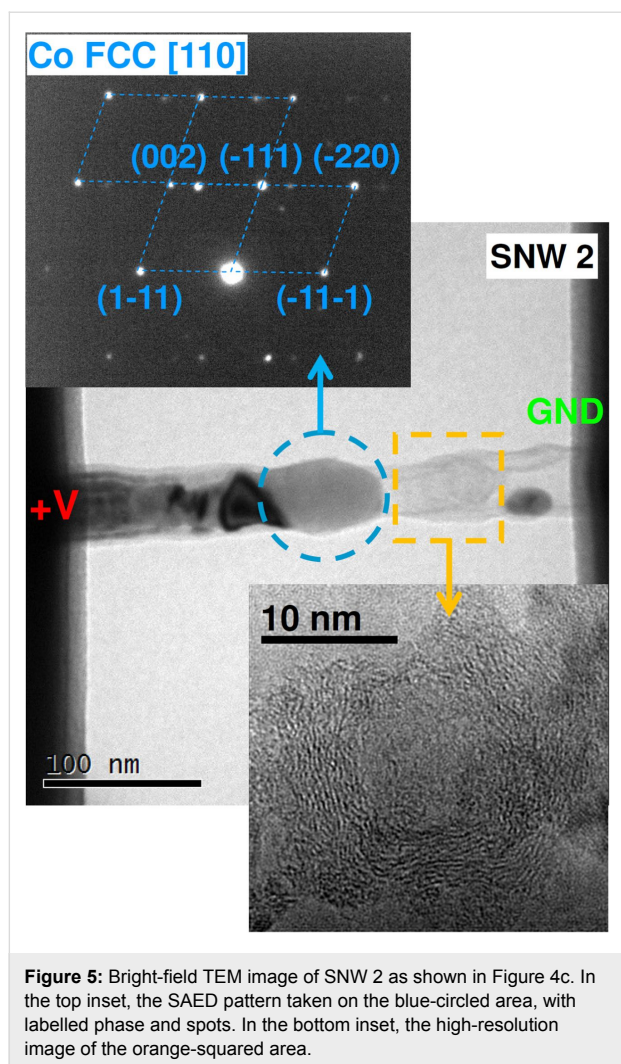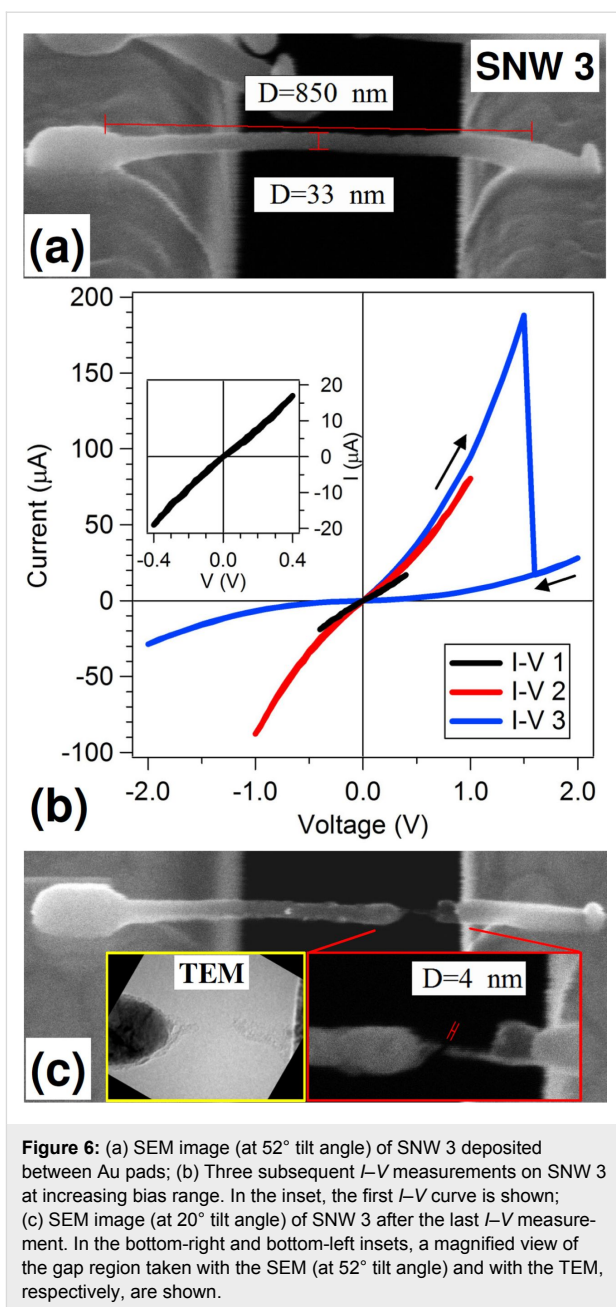
Figure 5: Bright-field TEM image of SNW 2 as shown in Figure 4c. In the top inset, the SAED pattern taken on the blue-circled area, with labelled phase and spots. In the bottom inset, the high-resolution image of the orange-squared area.

Figure 6: (a) SEM image (at 52° tilt angle) of SNW 3 deposited between Au pads; (b) Three subsequent *I–V* measurements on SNW 3 at increasing bias range. In the inset, the first *I–V* curve is shown; (c) SEM image (at 20° tilt angle) of SNW 3 after the last *I–V* measurement. In the bottom-right and bottom-left insets, a magnified view of the gap region taken with the SEM (at 52° tilt angle) and with the TEM, respectively, are shown.

ating at the extreme points of the negative interval. The measured resistance is 23 kΩ, corresponding to a resistivity of 2.5×10^3 μΩ·cm. The second measurement (red line) starts exhibiting the bent-up characteristic, less pronounced than for SNW 2, and also an asymmetry between positive and negative branches. At $V = -1$ V, in fact, a 10% increase in the absolute current is recorded, possibly indicating that structural modifications are going on during measurement. The third and last *I–V* curve (blue line) rises up steeper and at $V = 1.5$ V, $I = 190$ μA, corresponding to a current density of 2.1×10^7 A/cm^2, it drops down not to zero but to $I = 17$ μA, where it keeps following a bent-up trend to 2 V and finishes the cycle drawing a symmetric negative branch. The SEM image taken at the end of the measurement (Figure 6c) clearly shows a gap in the SNW with Co depletion in the terminal of the right section, which appears transparent.

By zooming in the gap region (bottom-right inset) we can distinguish a very narrow gap (4 nm) separating the left part,

ending with a dark tip on a bright grain, and the right part, ending with a 9 nm thick, 45 nm long dark, i.e., transparent tip. TEM analysis (bottom-left inset) confirms that the right section is polycrystalline Co ending with a tiny tip of graphitized C, and the tip on the right is also graphitized C. A question arises whether the current measured after the drop is flowing through a still-continuous C bridge or it is tunneling across the gap. The second case seems to be excluded because the current values are too high and the curve does not fit a Fowler–Nordheim model. The first option is favored because the cross section reduction from 35 to 9 nm diameter, observed at the bridge, can roughly account for a current drop of a factor of 13. If this is the case,

then the gap probably formed after measurement by some vibration during nanoprobes lift-up.

At the basis of the structural evolution observed in the three SNWs there is an interplay of several factors. Primarily the physical effects related to high current density (Joule heating and electromigration), but also geometrical factors represented by the suspended geometry and nanosize dimension of the conductor, and the highly-resistive nanogranular material. Let us first consider the materials obtained at the end of the electrical measurements: polycrystalline FCC cobalt and graphitized carbon. The equilibrium phase of bulk cobalt at RT is HCP, and at 430 °C there is a transition to the FCC phase. Co is known to stabilize FCC at RT as a consequence of either rapid quenching from annealing above the transition temperature or of the grain size confinement to submicron range [30]. The transition temperature is easily surpassed during the electrical measurements, where current densities up to 10^7 A/cm^2 are injected into the SWNs. As already shown in our previous study on Pt SNWs [23], and in W nanowires either suspended [31] or deposited on ultrathin membranes [32], the temperature reached in such conditions can be as high as or exceed 1000 °C. The fact that cobalt does not stabilizes back into the HCP phase at the end of the measurement, when the SNWs return to RT, is a consequence of the nanosize cross-section of the wire: FCC structure at RT is often reported for both Co nanoparticles and nanowires in the diameter range of tens of nanometers [33]. Concerning graphitized carbon, this material is formed around the Co grains, acting as catalyzers, under the combined action of high temperature and nanograin motion, as reported in similar amorphous C nanowires loaded with Fe nanoparticles [34].

A second consideration regards the distribution of cobalt along the wires and its connection to *I–V* measurement history and electromigration. In SNW 1, the Joule heating during the current burst is making the wire fully metallic and polycrystalline. The current density associated to the burst (1.8×10^5 A/cm^2) is relatively low for electromigration to be effective, and during the second measurement, though a much higher current density is reached (1.3×10^7 A/cm^2), the electromigration effect is only minor (a small Co concentration gradient) because Co ions are strongly bound in large monocrystalline grains. In SNW 2, the current density increases progressively, reaching 10^7 A/cm^2 in the last cycle, where the SNW structure is still apparently unchanged from the as-deposited one. So this high electron current is flowing through a nanogranular material and can more easily displace and accumulate the Co ions toward the anode side. The gap morphology observed in SNW 3 may have a twofold interpretation. It could be considered as an evolution of the final SNW 2

structure, where, at the boundary between Co grain and graphitized C, a neck forms as the current density is increased, and the C portion thins down to form a bridge of a few nanometers. Alternatively, looking at the shape of SNW 3 at the bridge (bottom-right inset of Figure 6c), the sharp SNW truncation on the right could suggest that a big Co grain was present above the bridge and has moved left, leaving a void.

Conclusion

In conclusion, we have deposited Co (80 atom % concentration) SNWs from Co–carbonyl precursor by FEBID, and characterized them electrically at increasing bias range to reach high current density (10^7 A/cm^2). Starting from a nanogranular material of mixed FCC and HCP Co grains, Joule heating leads to the formation of polycrystalline FCC Co already at low voltages and current densities. Different structural morphologies are observed in the SNWs depending on the *I–V* history. With a short current burst the wire becomes fully polycrystalline Co and shows ohmic behaviour. When repeated *I–V* measurements at increasing voltage are performed, an electromigration effect becomes dominant dividing the wire in two halves: a metallic portion, on the anode side, and a graphitic carbon portion on the cathode side. The highest current density reached before breakdown is 2×10^7 A/cm^2.

Acknowledgements

References

1. Utke, I.; Moshkalev, S.; Russel, P., Eds. *Nanofabrication Using Focused Ion and Electron Beams;* Oxford University Press: New York, NY, U.S.A., 2012.
2. van Dorp, W. F.; Zhang, X.; Feringa, B. L.; Hansen, T. W.; Wagner, J. B.; De Hosson, J. T. M. *ACS Nano* **2012**, *6*, 10076–10081. doi:10.1021/nn303793w
3. Brintlinger, T.; Fuhrer, M. S.; Melngailis, J.; Utke, I.; Bret, T.; Perentes, A.; Hoffmann, P.; Abourida, M.; Doppelt, P. *J. Vac. Sci. Technol., B* **2005**, *23*, 3174–3177. doi:10.1116/1.2130355
4. Hernàndez-Ramìrez, F.; Rodrìguez, J.; Casals, O.; Russinyol, E.; Vilà, A.; Romano-Rodrìguez, A.; Morante, J. R.; Abid, M. *Sens. Actuators, B* **2006**, *118*, 198–203. doi:10.1016/j.snb.2006.04.022
5. Utke, I.; Hoffmann, P.; Berger, R.; Scandella, L. *Appl. Phys. Lett.* **2002**, *80*, 4792–4794. doi:10.1063/1.1489097
6. Belova, L. M.; Hellwig, O.; Dobisz, E.; Dan Dahlberg, E. *Rev. Sci. Instrum.* **2012**, *83*, 093711. doi:10.1063/1.4752225
7. Schwalb, C. H.; Grimm, C.; Baranowski, M.; Sachser, R.; Porrati, F.; Reith, H.; Das, P.; Muller, J.; Völklein, F.; Kaya, A.; Huth, M. *Sensors* **2010**, *10*, 9847–9856. doi:10.3390/s101109847
8. Gabureac, M.; Bernau, L.; Utke, I.; Boero, G. *Nanotechnology* **2010**, *21*, 115503. doi:10.1088/0957-4484/21/11/115503

9. Kolb, F.; Schmoltner, K.; Huth, M.; Hohenau, A.; Krenn, J. R.; Klug, A.;
    List, E. J. W.; Plank, H. *Nanotechnology* **2013,** *24,* 305501.
    doi:10.1088/0957-4484/24/30/305501
10. Serrano-Ramón, L.; Córdoba, R.; Rodríguez, L. A.; Magén, C.;
    Snoeck, E.; Gatel, C.; Serrano, I.; Ibarra, M. R.; De Teresa, J. M.
    ACS Nano **2011,** *5,* 7781–7787. doi:10.1021/nn201517r
11. Koops, H. W. P.; Hoinkis, O. E.; Honsberg, M. E. W.; Schmidt, R.;
    Blum, R.; Bottger, G.; Kuligk, A.; Liguda, C.; Eich, M.
    Microelectron. Eng. **2001,** *57–58,* 995–1001.
    doi:10.1016/S0167-9317(01)00565-2
12. De Angelis, F.; Liberale, C.; Coluccio, M. L.; Cojoc, G.; Di Fabrizio, E.
    Nanoscale **2011,** *3,* 2689–2696. doi:10.1039/c1nr10124b
13. Frabboni, S.; Gazzadi, G. C.; Felisari, L.; Spessot, A. *Appl. Phys. Lett.*
    2006, *88,* 213116. doi:10.1063/1.2206996
14. Gavagnin, M.; Wanzenboeck, H. D.; Belić, D.; Bertagnolli, E.
    ACS Nano **2013,** *7,* 777–784. doi:10.1021/nn305079a
15. Costanzi, B. N.; Riazanova, A. V.; Dan Dahlberg, E.; Belova, L. M.
    Appl. Phys. Lett. **2014,** *104,* 222401. doi:10.1063/1.4880728
16. Botman, A.; Mulders, J. J. L.; Hagen, C. W. *Nanotechnology* **2009,** *20,*
    372001. doi:10.1088/0957-4484/20/37/372001
17. Frabboni, S.; Gazzadi, G. C.; Spessot, A. *Physica E* **2007,** *37,*
    265–269. doi:10.1016/j.physe.2006.06.018
18. Córdoba, R.; Sesé, J.; De Teresa, J. M.; Ibarra, M. R.
    Microelectron. Eng. **2010,** *87,* 1550. doi:10.1016/j.mee.2009.11.027
19. Porrati, F.; Sachser, R.; Schwalb, C. H.; Frangakis, A. S.; Huth, M.
    J. Appl. Phys. **2011,** *109,* 063715. doi:10.1063/1.3559773
20. See website of COST Action CM1301, Chemistry for ELectron-Induced
    NAnofabrication (CELINA): http://celina.uni-bremen.de/celina/
21. Ho, P. S.; Kwok, T. *Rep. Prog. Phys.* **1989,** *52,* 301–348.
    doi:10.1088/0034-4885/52/3/002
22. Jeong, W.; Kim, K.; Kim, Y.; Lee, W.; Reddy, P. *Sci. Rep.* **2014,** *4,*
    No. 4975. doi:10.1038/srep04975
23. Gazzadi, G. C.; Frabboni, S. *Appl. Phys. Lett.* **2009,** *94,* 173112.
    doi:10.1063/1.3119582
24. Gazzadi, G. C.; Frabboni, S.; Menozzi, C. *Nanotechnology* **2007,** *18,*
    445709. doi:10.1088/0957-4484/18/44/445709
25. Fernández-Pacheco, A.; Serrano-Ramón, L.; Michalik, J. M.;
    Ibarra, M. R.; de Teresa, J. M.; O'Brien, L.; Petit, D.; Lee, J.;
    Cowburn, R. P. *Sci. Rep.* **2013,** *3,* No. 1492. doi:10.1038/srep01492
26. Fernández-Pacheco, A.; De Teresa, J. M.; Córdoba, R.; Ibarra, M. R.
    J. Phys. D: Appl. Phys. **2009,** *42,* 055005.
    doi:10.1088/0022-3727/42/5/055005
27. Córdoba, R.; Fernández-Pacheco, R.; Fernández-Pacheco, A.;
    Gloter, A.; Magén, C.; Stéphan, O.; Ibarra, M. R.; De Teresa, J. M.
    Nanoscale Res. Lett. **2011,** *6,* 592. doi:10.1186/1556-276X-6-592
28. Belova, L. M.; Dahlberg, E. D.; Riazanova, A.; Mulders, J. J. L.;
    Christophersen, C.; Eckert, J. *Nanotechnology* **2011,** *22,* 145305.
    doi:10.1088/0957-4484/22/14/145305
29. Lukanov, P.; Anuganti, V. K.; Krupskaya, Y.; Galibert, A.-M.; Soula, B.;
    Tilmaciu, C.; Velders, A. H.; Klingeler, R.; Büchner, B.; Flahaut, E.
    Adv. Funct. Mater. **2011,** *21,* 3583–3588. doi:10.1002/adfm.201100364
30. Owen, E. A.; Madoc Jones, D. *Proc. Phys. Soc., London, Sect. B* **1954,**
    67, 456–466. doi:10.1088/0370-1301/67/6/302
31. You, G. F.; Gong, H.; Thong, J. T. L. *Nanotechnology* **2010,** *21,*
    195701. doi:10.1088/0957-4484/21/19/195701
32. Reguer, A.; Bedu, F.; Nitsche, S.; Chaudanson, D.; Detailleur, B.;
    Dallaporta, H. *Ultramicroscopy* **2009,** *110,* 61–66.
    doi:10.1016/j.ultramic.2009.09.006

33. Athanassiou, E. K.; Grossmann, P.; Grass, R. N.; Stark, W. J.
    Nanotechnology **2007,** *18,* 165606.
    doi:10.1088/0957-4484/18/16/165606
34. Jin, C. H.; Wang, J. Y.; Chen, Q.; Peng, L.-M. *J. Phys. Chem. B* **2006,**
    110, 5423–5428. doi:10.1021/jp057240r

Influence of the shape and surface oxidation in the magnetization reversal of thin iron nanowires grown by focused electron beam induced deposition

Luis A. Rodríguez[‡1,2,3], Lorenz Deen[‡1,4], Rosa Córdoba[1,4], César Magén[1,2,5], Etienne Snoeck[3], Bert Koopmans[4] and José M. De Teresa[*1,2,6]

Address:
[1]Laboratorio de Microscopias Avanzadas (LMA) - Instituto de Nanociencia de Aragón (INA), Universidad de Zaragoza, 50018 Zaragoza, Spain, [2]Departamento de Física de la Materia Condensada, Universidad de Zaragoza, 50009 Zaragoza, Spain, [3]CEMES-CNRS 29, rue Jeanne Marvig, B.P. 94347, F-31055 Toulouse Cedex, France, [4]Department of Applied Physics, Eindhoven University of Technology, PO Box 513, 5600 MB Eindhoven, Netherlands, [5]Fundación ARAID, 50018 Zaragoza, Spain and [6]Instituto de Ciencia de Materiales de Aragón (ICMA), Universidad de Zaragoza-CSIC, 50009 Zaragoza, Spain

Email:
José M. De Teresa[*] - deteresa@unizar.es

* Corresponding author   ‡ Equal contributors

Keywords:
coercive field; focused electron beam induced deposition; iron nanowires; magnetization reversal; magneto-optical Kerr effect; transmission electron microscopy

Abstract

Iron nanostructures grown by focused electron beam induced deposition (FEBID) are promising for applications in magnetic sensing, storage and logic. Such applications require a precise design and determination of the coercive field (H_C), which depends on the shape of the nanostructure. In the present work, we have used the $Fe_2(CO)_9$ precursor to grow iron nanowires by FEBID in the thickness range from 10 to 45 nm and width range from 50 to 500 nm. These nanowires exhibit an Fe content between 80 and 85%, thus giving a high ferromagnetic signal. Magneto-optical Kerr characterization indicates that H_C decreases for increasing thickness and width, providing a route to control the magnetization reversal field through the modification of the nanowire dimensions. Transmission electron microscopy experiments indicate that these wires have a bell-type shape with a surface oxide layer of about 5 nm. Such features are decisive in the actual value of H_C as micromagnetic simulations demonstrate. These results will help to make appropriate designs of magnetic nanowires grown by FEBID.

Introduction

The fabrication of magnetic nanostructures in a single lithographic step by focused electron beam induced deposition (FEBID) is currently an exciting research topic [1,2]. In this technique, a scanning electron microscope (SEM) dissociates the precursor molecules delivered into the area of interest by a gas-injection system, producing a deposit [3-6]. The use of precursor molecules containing cobalt [7-10] or iron [11-14] allows for the growth of magnetic nanostructures with tailored dimensions. Some of the most recent advances in this topic are: the achievement of resolution in single magnetic structures below 30 nm [15-17], the fabrication of nanomagnets for logic [18], the production of highly-dense isolated magnetic structures [19], the growth of three-dimensional nanowires [20,21] and the fabrication of nanospheres on scanning probe tips [22,23].

One of the crucial parameters to be controlled in such magnetic nanostructures grown by FEBID is the coercive field, H_C, which corresponds to the magnetic field producing the magnetization reversal. Most of magnetic devices work by producing a voltage output when the magnetization reversal occurs. In the case of cobalt deposits, it was previously found that the coercive field is governed by shape anisotropy [24] due to the polycrystalline microstructure [25], and is thus a function of the deposit dimensions [26]. However, more detailed studies subsequently emphasized the role played by the halo and the effective magnetic shape in the coercive field of cobalt nanowires [27-29]. In brief, the halo structure around the main deposit (caused by proximity effects in FEBID [30]) is an easy place for nucleation of domain walls (DWs) [31] starting the magnetization reversal of the nanowire, which gives rise to low coercive fields. This can be a source of troubles if one naively aims to control the coercive field of magnetic nanostructures by means of the shape of the main deposit without taking into account the effect of the halo.

Regarding the case of iron nanostructures grown by FEBID, the work by Gavagnin et al. has highlighted that the coercive field could be controllable by means of the deposit thickness [18]. These authors found that nanomagnets with thicknesses of 25 and 35 nm (but equal length and width) produced different coercive fields [18]. However, a detailed explanation for such phenomenology was not provided. The same group later found that, similar to the case of cobalt nanowires grown by FEBID, a magnetic halo in iron nanowires is an easy nucleation center for domain walls, decreasing the observed coercive field [31].

At this point, further research towards a deeper understanding of the processes that determine the coercive field in magnetic nanostructures grown by FEBID is required. A true control over

coercivity is the only way to design and fabricate appropriate magnetic devices based on FEBID materials. In the present work, we focus our attention on iron nanowires with fixed length (4 μm) and varying width (50–500 nm) and nominal thickness (t_{Nom}) between 10 and 45 nm. We have chosen this geometry given our previous experience with cobalt nanowires grown by FEBID [24,27]. In these experiments mono-domain magnetic structures in remanence, as required in most applications, were obtained for nanowire widths around 400 nm or smaller and length/width aspect ratios of the order of 10. By performing systematic studies of the coercive field as a function of dimensions and carrying out micromagnetic simulations, we are able to conclude that the specific shape of the nanowire as well as the surface oxidation are key to explain the observed behavior. These will determine the effective magnetic shape of the nanowires, which will control the coercivity. This will be still more relevant as the dimensions of the nanowires become smaller, as it is desired in some applications where high integration of magnetic nanostructures is needed.

Results and Discussion
Growth of the nanowires

The iron nanowires have been grown on B-doped Si substrates inside an FEI Helios 600 apparatus, using $Fe_2(CO)_9$ as precursor and the scanning electron microscope (SEM) to produce magnetic deposits in a single step, as sketched in Figure 1a. The precursor is delivered to the area of interest through a single gas-injection-system (GIS) with inner diameter of 160 μm, whose tip is located approximately 150 μm above (*z* direction) and 50 μm off (*x* direction) the central irradiation point of the electron beam. The base pressure inside the chamber (before the flow of the precursor gas) is about 1×10^{-6} mbar. The precursor flux can be controlled through a leak valve in the GIS and had to be optimized in order to obtain deposits exhibiting ferromagnetic properties with suitable shape anisotropy. In these experiments, the nominal turbopump speed is 260 L/s for nitrogen gas. When the leak valve is opened, the chamber pressure increases. The chamber pressure is monitored through a Penning vacuum gauge, which serves to perform systematic quantitative studies (we cannot provide direct values of precursor flux on the substrate because the pumping efficiency of the vacuum pump for $Fe_2(CO)_9$ molecules in our apparatus is unknown). The beam current and voltage used for the growth were, respectively, 1.4 nA and 3 kV. The first experiments under relatively high precursor flux (process pressure approx. 6×10^{-6} mbar) indicated that the microstructure of the deposits consisted of grains with a typical size of about 100 nm, as can be observed in Figure S1 of Supporting Information File 1. In those wires, there was no significant modification of the coercive field as a function of
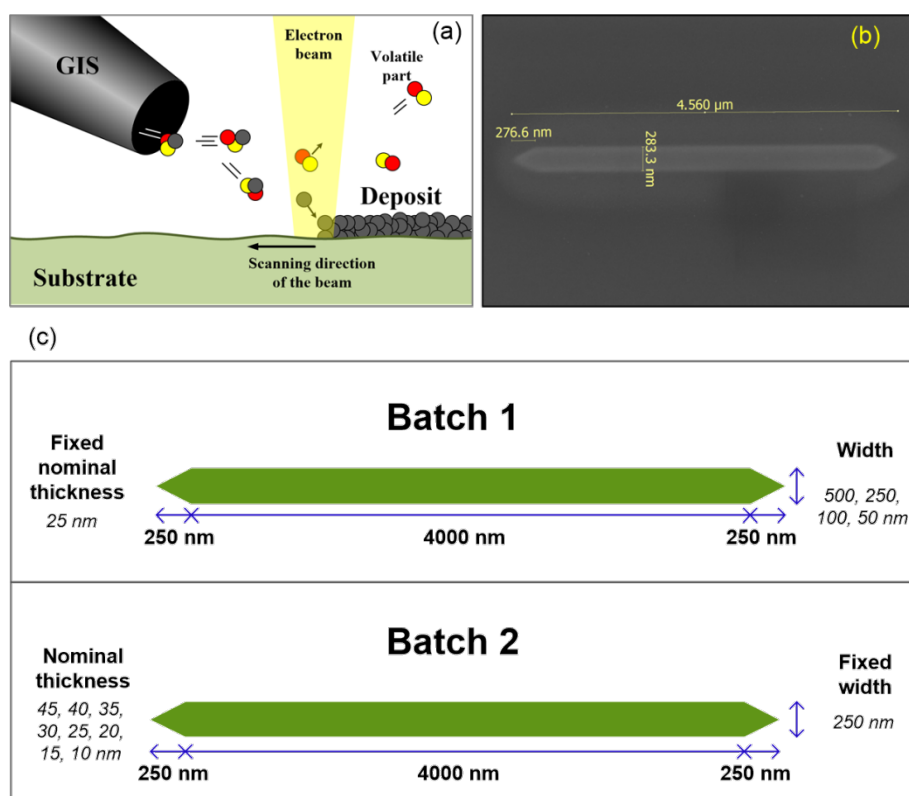
Figure 1: (a) A sketch of the FEBID process. (b) A SEM image of the nanowire with targeted width of 250 nm and nominal thickness of 15 nm. (c) Sketch of the two batches of nanowires: Batch 1 has got 25 nm nominal thickness and varying width whereas batch 2 has got 250 nm width and varying thickness.

the deposit dimensions, indicating that the magnetization reversal was governed by the individual grains, somehow magnetically decoupled one from each other. However, when the process pressure was decreased to the range from 3×10^{-6} to 4×10^{-6} mbar, the deposits did not show the granular structure and the magnetization reversal was found to be dominated by shape anisotropy (see next section). In situ compositional analysis by energy dispersive X-ray spectroscopy (EDS) indicated that the Fe content in these optimized deposits were always in the range of 80–85%, the rest being C and O. These values are similar to those found by Gavagnin et al. with the precursor $Fe(CO)_5$ [18]. In Figure S2 of Supporting Information File 1, we show one of the typical EDS spectra of these deposits.

In the following, we will describe the results obtained in two batches of samples corresponding to optimized nanowires. In both batches, the length is fixed to 4.5 μm and the ends are triangular (see Figure 1c), as frequently used in this type of nanowires to avoid easy nucleation of domain walls at the end of the nanowire and thus the appearance of low coercive fields. In the first batch, t_{Nom} is fixed to 25 nm and the width is varied from 50 to 500 nm (4 samples). In the second batch, the width

is fixed to 250 nm and t_{Nom} is varied from 10 to 45 nm (8 samples). This will allow for a systematic study of the effect of varying width and thickness in these nanowires.

MOKE experiments: coercive field

Magneto-optical Kerr effect (MOKE) experiments have been carried out using the Nano-MOKE-3 apparatus by Durham Magnetooptics. This device uses a 2 μm diameter infrared laser beam that scans the area of interest in raster mode to detect MOKE contrasts via the variation of the signal amplitude or the change in the rotation angle of the light. The positioning of the beam permits the localization of the nanostructure to be measured and to position the beam in a targeted place. For measurements as a function of the magnetic field, the laser beam is fixed on the centre of the nanowire and quadrupole coils are used to apply a magnetic field in the plane of the sample, which allows for tracing the MOKE changes versus the magnetic field. The MOKE signal is proportional to the total magnetization, allowing one to study magnetization reversal processes and precise determination of the coercive field of the nanowires. In our experiments, we have measured the longitudinal MOKE signal with the magnetic field being applied parallel to the nanowire length (easy axis) [32].

As an example of the type of magnetization loops measured, we show in Figure 2a and Figure 2b the results for two nanowires from the second batch with t_{Nom} of 10 and 35 nm. The signal-to-noise ratio is ten, certainly enough to determine the coercive field, which is given by the measured MOKE field at the mid-point between the two saturation values at high positive and high negative fields. The observed noise, about 10% of the signal, is small given that the nanowire width is only 1/8 of the laser diameter (thus having significant signal originated from the non-magnetic substrate). The values of H_C for both batches are represented in Figure 2c and Figure 2d. All results shown in Figure 2 correspond to the average of more than 100 hysteresis loops. Given the sharp switching transitions observed, a high level of reproducibility can be inferred.

The observed decrease of H_C with the width was also observed in polycrystalline cobalt nanowires grown by FEBID with widths above 250 nm [26,27] and previously in permalloy [33] and cobalt [34-36] nanowires patterned by electron beam lithography. Such dependence was explained by a model in which a small volume in the wire reverses magnetization coherently, propagating across the entire wire. In such a model, the coer-

cive field is proportional to the ratio thickness (*t*)/width (*w*) due to demagnetizing effects:

$$H_C = H_\infty + a(t/w),\qquad(1)$$

where H_∞ is the coercive field for a wire with infinite width (thin film) and *a* is constant parameter that depends of the finite-length shape anisotropy factor and saturation magnetization [37]. Applying this model to the Fe wires of the batch 1, we obtain that H_∞ is 7 Oe, indicating that the material is soft magnetic, as expected for Fe.

We note, however, that the model is not able to explain the thickness dependence of H_C in the 250 nm wide Fe nanowires of the batch 2. In fact, we observe that H_C decreases with increasing thickness, contrary to the model. Similar behavior has also been observed theoretically in permalloy nanowires [38] and experimentally in permalloy nanowires arrays [39] and in cobalt nanowires grown by FEBID [40]. In all cases, the occurrence of the failure of the model is caused by a transition in the type of magnetization reversal process, which led us to
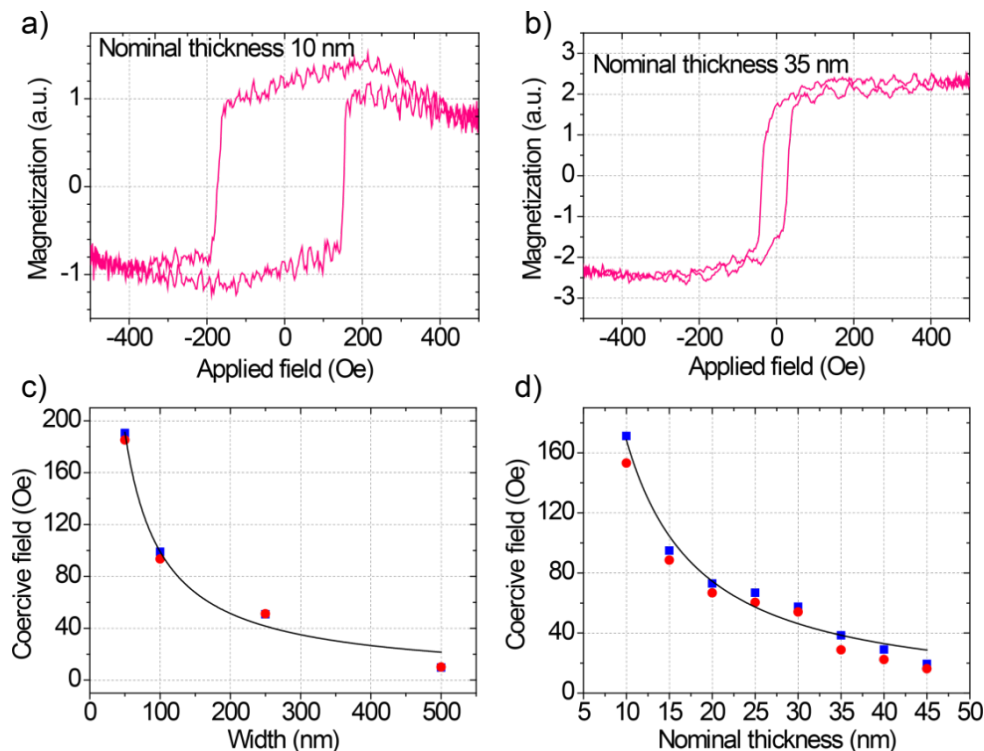
Figure 2: MOKE results. (a) Average magnetic hysteresis loop of the sample with width/nominal thickness of 250 nm/10 nm. (b) Average magnetic hysteresis loop of the sample with width/nominal thickness of 250 nm/35 nm. (c) Coercive field as a function of width for batch 1 (t_{Nom} = 25 nm) with positive and negative applied magnetic field (blue squares and red circles respectively). Please, be aware that the red circles partially hide the blue squares. The line is a fit to Equation 1. (d) Coercive field as a function of t_{Nom} for batch 2 (width = 250 nm) with positive and negative applied magnetic field (blue squares and red circles respectively). The line is a visual guide.

perform micromagnetic simulations to investigate this possibility. Given the previous knowledge regarding the influence of the halo [31] and the effective magnetic shape [27] in the coercive field of FEBID magnetic nanostructures, it is convenient to know these properties in the studied nanowires. This is why we first carried out transmission electron microscopy (TEM) experiments to investigate the exact shape and composition of the nanowires, so that the subsequent micromagnetic calculations could reliably reproduce the observed dependence of the coercive field.

## TEM experiments: deposit shape, halo extension, surface oxidation

TEM characterization of the microstructure and composition of Fe nanowires was carried out in a probe-corrected FEI Titan 60-300 operated at 300 kV. Two TEM lamellae of Fe nanowires with a width of 250 nm and nominal thicknesses of 10 and 45 nm were fabricated using a focused Ga$^+$ ion beam and standard lift-out procedures in an FEI Helios 600 Nanolab. The slices were cut perpendicular to the nanowire length to analyze their cross-sectional width profile. The morphology and microstructure were determined by bright field (BF) TEM and high

resolution TEM (HRTEM) imaging, and chemical composition of the sections was determined by combining high angle annular dark field (HAADF) imaging and electron energy loss spectroscopy (EELS) in scanning transmission electron microscopy (STEM) mode. The beam current in the STEM-EELS experiments was 250 pA. Focused beam induced annealing effects were not observed in the experiments. These are easily observable because the images change with time, which was not the case in the experiments presented here.

Low-magnification BF-TEM images of the cross-sections of Fe nanowires are shown in Figure 3a and Figure 3b. These wires have been chosen for the TEM study because they are respectively the thinnest and the thickest ones for the fixed width of 250 nm. Both wires presented irregular bell-shaped profiles, which are fitted using the following empirical formula:

$$z = A \tanh\left[C\left(|y - y_c| - y_0\right)\right] + z_0 , \qquad (2)$$

where A and C are fitting parameters while y_c corresponds to the peak position in the lateral y direction (in this case manu-
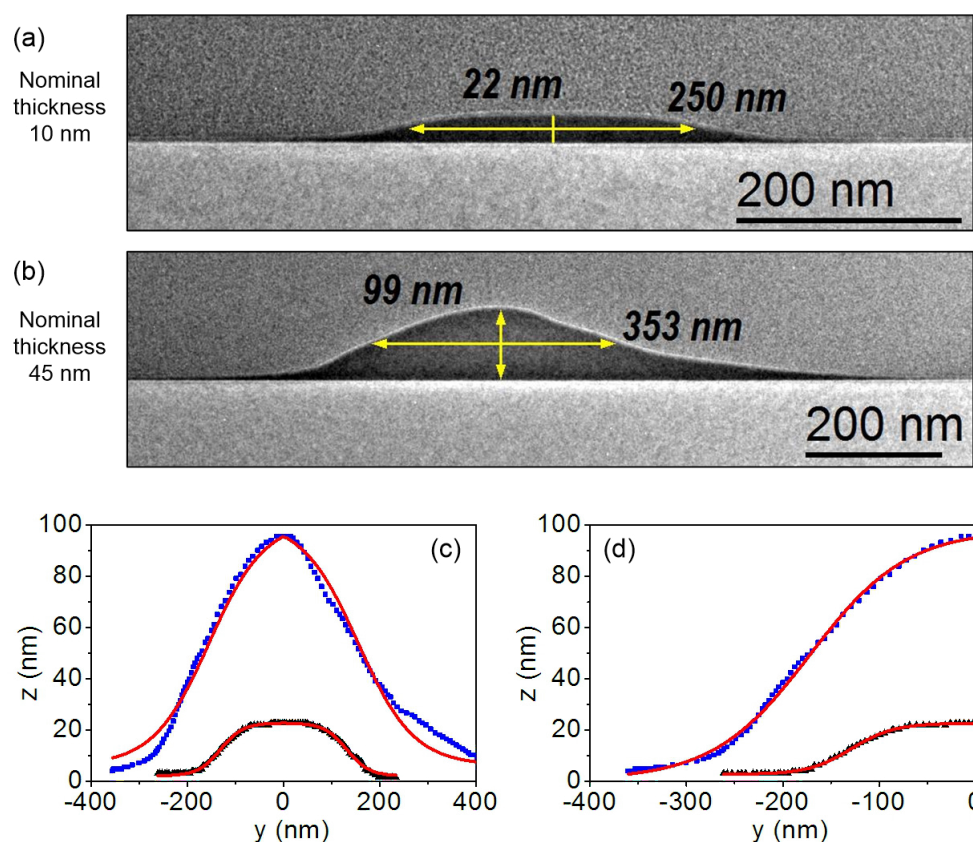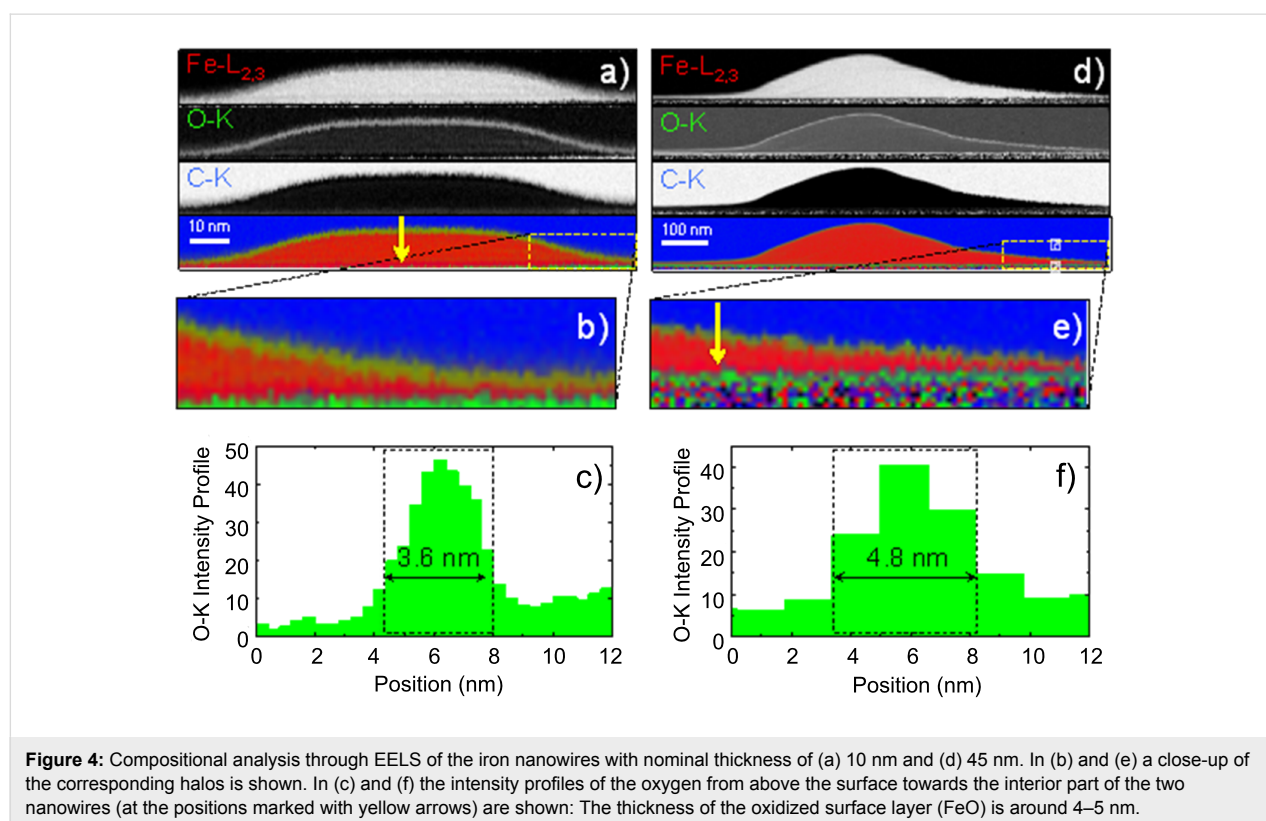

Figure 3: Low-magnification TEM images of the iron nanowires with width of 250 nm and nominal thickness of (a) 10 and (b) 45 nm. Fitting of the (c) full and (d) half profiles of both nanowires using Equation 2.

ally centered, $y_c = 0$) and $2y_0$ corresponds to the full width of the profile measured along the y direction at a height of z_0. Mathematically speaking, z_0 will correspond to the height where the bell profile changes its concavity (inflexion point). As one can notice in Figure 3c and Figure 3d, Equation 2 fits well the profiles of the nanowires extracted from TEM images of Figure 3a and Figure 3b. A better fit is obtained if we only take into account a half part of the profiles. All fitted parameters of both cases are reported in Table S3 (Supporting Information File 2). Comparing the values obtained from the fit for $2y_0$ and z_0, one can note that both correlate, respectively, with the nominal values of the width and thickness of these two nanowires, being more similar for the thinnest one. In addition, the TEM images clearly reveal that the bell-shaped profile of the nanowires makes that the t_{Nom} is almost half of the maximum thickness (t_{Max}), corresponding to the peak height. Taking this fact into account and given that we have experimentally measured the profiles of the thinnest and the thickest nanowires, a linear extrapolation of the fitting parameters of Equation 2 permits to estimate the profile parameters of the intermediate thicknesses. The values of this extrapolation are reported in Table S2 (Supporting Information File 2), considering the fitted parameters obtained from Figure 3d (half profile) and establishing z_0 as the t_{Nom} of the nanowires. The HRTEM images of the nanowires, shown in Figure S3 (Supporting Information File 1), indicate that the Fe is

nanocrystalline, as previously reported [14,18]. This microstructure will produce negligible magnetocrystalline anisotropy effects and, as a consequence, shape anisotropy will determine the magnetic anisotropy of the wires. The Fe content determined by EELS inside the wires is around 85%, in good agreement with the EDS performed inside the FIB-SEM equipment. According to previous studies, the saturation magnetization in Fe deposits grown by FEBID corresponds well with the Fe content [14,41]. Then, one would expect a saturation magnetization about 80–85% of that of bulk Fe.

From the STEM-EELS experiments shown in Figure 4, where the oxygen intensity is probed from above the surface towards the interior part of the nanowires, it can be concluded that the top surface of the nanowires exhibits an oxidized layer of 4–5 nm thickness. The stoichiometry of this oxidized layer is found to be Fe/O = 1:1 (49.4 ± 2% of Fe and 50.6 ± 2% of O), which corresponds to a paramagnetic material at room temperature. Such an oxidized surface is not ferromagnetic, which affects the overall magnetization reversal of the wires. The oxidized layer will have a strong impact on the thinner part of the wires, i.e., the tails and halo, which will be prone to lose the ferromagnetism. As a consequence, the effective ferromagnetic volume of the wire will be more localized towards the centre of the nanowire, thus modifying its functional ferromagnetic shape.

Figure 4: Compositional analysis through EELS of the iron nanowires with nominal thickness of (a) 10 nm and (d) 45 nm. In (b) and (e) a close-up of the corresponding halos is shown. In (c) and (f) the intensity profiles of the oxygen from above the surface towards the interior part of the two nanowires (at the positions marked with yellow arrows) are shown: The thickness of the oxidized surface layer (FeO) is around 4–5 nm.
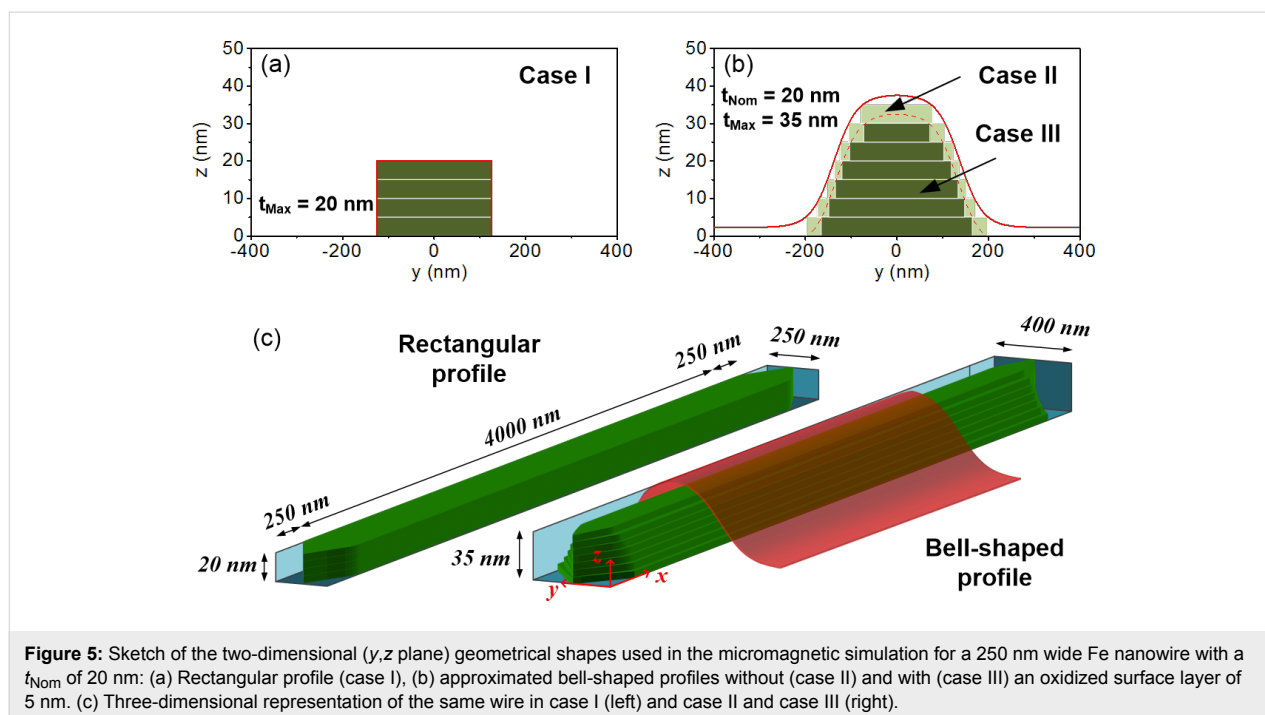
Micromagnetic simulations

Quasi-static micromagnetic simulations were carried out to study the influence of the shape profile of the Fe nanowires and oxidized surface layer on the magnetization reversal process. We have focused our attention on the dependence of H_C on the thickness, which deviates from the model of magnetization reversal for nanowires described by Equation 1. In particular, we have studied the variation of H_C with the thickness for 250 nm wide Fe nanowires considering the actual geometry of the Fe nanowires of batch 2. The GPMagnet software package [42] was used to perform the simulations employing the following magnetic parameters for polycrystalline pure iron [43]: saturation magnetization = 1.7×10^6 A/m, exchange constant = 2.1×10^{-11} J/m, anisotropy constant = 0 (we assume that in nanocrystalline iron the magnetocrystalline anisotropy is averaged out). For the simulation, we have adopted the same in-plane geometry used for the MOKE measurements shown before. In order to decrease the simulation time, different cell sizes have been used depending on the thickness (see Table S1 in Supporting Information File 2). H_C has been calculated for three different cases, which allows us to investigate in a more general way the influence of the shape of the nanowires in the behavior of the coercive field:

case I: a rectangular profile where constant width (250 nm) is considered, **case II:** the actual bell-shaped profile determined from the TEM measurements, and **case III:** a reduced bell-shaped profile considering a surface oxidation layer of 5 nm along the whole deposit.

The three different cases are schematically shown in Figure 5 for the Fe nanowire with a t_{Nom} of 20 nm. As one can notice in Figure 5, in case I a single value of thickness can be considered, corresponding to the maximum height of the rectangular profile (i.e., $t = t_{Nom} = t_{Max}$). However, in the nanowires of cases II and III we defined $t_{Nom} = z_0$ and $t_{Max} = z_{Max}$ (peak height). The three-dimensional (3D) shape of the nanowires was designed by stacking several layers of equal thickness and either using the same area in the x,y plane (for case I) or progressively reducing their widths in order to approach the bell-shape of the profile (for case II and III). The sketch shown in Figure 5c provides a visual understanding of the 3D structure of the simulated Fe nanowires. To simulate the oxidized bell-shaped profile, the structural bell-shaped profile has been reduced 5 nm from the surface in order to keep only the magnetic volume. It should be pointed out that temperature is not taken into account in the simulations. This is why the absolute value of H_C in the simulations is expected to be twice or more the experimental value at room temperature [27].

Plots of the simulated H_C values as a function of the nominal thickness for the three cases considered are presented in Figure 6. For case I (rectangular profile), in the range of thickness 5 nm < t_{Nom} < 30 nm, one notices that H_C increases with the thickness, as expected from Equation 1, until reaching a critical thickness (t_c) of 30 nm. At that point, H_C exhibits a maximum. Above t_c, H_C decreases with thickness. A similar behavior is observed in the nanowires with bell-shaped profiles, with and without the oxidized top layer of 5 nm (cases II and

Figure 5: Sketch of the two-dimensional (*y,z* plane) geometrical shapes used in the micromagnetic simulation for a 250 nm wide Fe nanowire with a t_{Nom} of 20 nm: (a) Rectangular profile (case I), (b) approximated bell-shaped profiles without (case II) and with (case III) an oxidized surface layer of 5 nm. (c) Three-dimensional representation of the same wire in case I (left) and case II and case III (right).
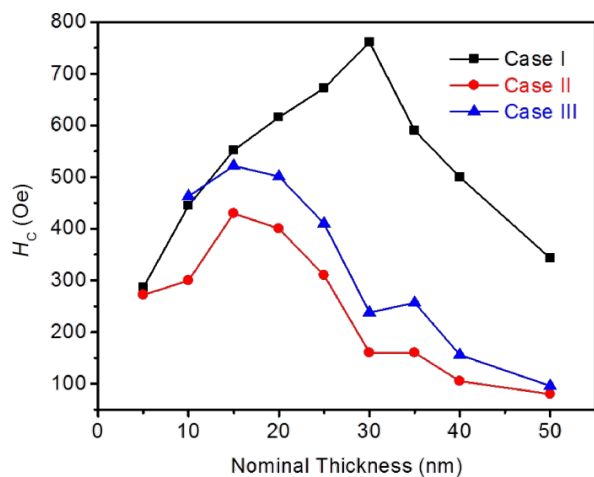
III, respectively). However, one can notice that the bell-shaped profile favors the occurrence of the maximum value of H_C at a lower t_{Nom} ($t_c = 15$ nm, for both cases II and III), also reducing the values of H_C for the same t_{Nom} compared to case I. Above t_C, we note that the decreasing of H_C with the thickness observed in the nanowires of cases II and III resembles the experimental result (shown in Figure 2d). The full behavior of the simulated H_C as a function of the thickness in the bell-shaped Fe nanowires resembles the one that is reported for 500 nm wide L-shaped Co-FEBID nanowires [40]. In [40], a maximum value of H_C is obtained at the crossover between two types of DWs nucleated in the corner of the "L". The transition is from transversal DWs (at low thicknesses) to vortex DWs (at high thicknesses). In principle, a change in the magnetization
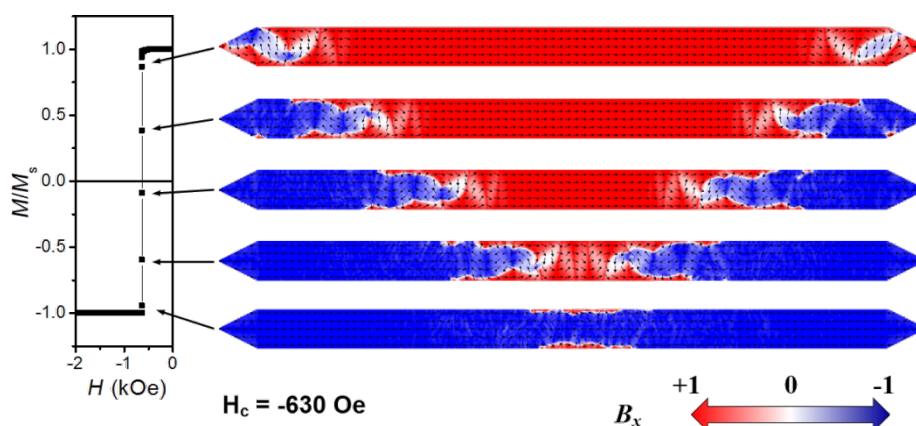
reversal mode is a good candidate to produce a dependence of H_C with thickness presenting a maximum. The micromagnetic simulations in the Fe nanowires permit a direct visualization of the magnetic configuration during magnetization reversal, which allows us to explore the changes in the reversal magnetization mechanism between nanowires with low and high thickness.

In Fe nanowires with rectangular profile (case I), for values of thickness $t_{Nom} < t_c$ ($t_c = 30$ nm), we find that the reversal magnetization process occurs through the propagation of two extended domain walls (EDWs). These relatively complex head-to-head and tail-to-tail EDWs are first nucleated at the ends of the nanowire and then propagate along the nanowire until they meet at the nanowire center and annihilate. Figure 7 shows five snapshots of the magnetization reversal process in the sample with width of 250 nm, thickness of 20 nm and profile defined as case I. This magnetization reversal mechanism is not via the formation of a multi-domain structure but monodomain-type, with EDW nucleation at the pointed ends of the nanowires and propagation towards the center.

Figure 6: Coercive field (H_C) obtained from the simulations of iron nanowires with nominal width of 250 nm and varying nominal thickness (from 5 to 50 nm) for the three cases discussed in the text.

Interestingly, the simulations performed give access to image the *x,y* plane-view magnetization states along the full depth of the nanowires. One example is the top and bottom layers of the 20 nm thick nanowire with rectangular profile, shown in Figure 8a. The EDWs observed in this nanowire consist of small (extending only locally) 180° and 90° DWs, where the local magnetization rotates coherently in the plane of the nanowire (*x,y* plane) without out-of-plane magnetization rotations. This is in agreement with the observed magnetization reversal through coherent rotation modes that occurs at low thickness of magnetic nanowires [39,44]. This behavior can also


Figure 7: Simulated magnetization reversal with five snapshots of the magnetization state in the nanowire with width of 250 nm, thickness of 20 nm and profile defined as case I.

be observed in cross-sectional images of the magnetization extracted along an EDW (y,z plane), where the local magnetization rotation across the whole thickness of the DWs occurs in the x,y plane (see the y,z plane view included in Figure 8a). Thus, the magnetic structure of the EDW is composed by small DWs covering the whole thickness and propagating to produce the magnetization reversal. This magnetization reversal mechanism, corresponding to a coherent rotation mode, is theoretically well described by Equation 1 [37]. Therefore, an increasing value of H_C with the thickness is expected in that nanowire thickness range. For $t_c < t_{Nom} < 50$ nm simulations also indicate a monodomain-type reversal magnetization, through nucleation and propagation of EDWs, even though their small constituent DWs present local non-coherent rotation modes. This effect can be noticed in the cross-sectional images of the magnetization extracted across the EDWs for the 35 nm thick Fe nanowire of rectangular profile depicted in Figure 8b. Both, the pseudo-vortex wall formed in the inner part of EDW structure and the extended transversal 180° DW formed in the

external part of the EDW structure, reveal local out-of-plane magnetization rotations of either Neél-type or C-shape magnetization distributions. In thicker films (above t_c) the formation of DWs with non-coherent magnetization rotation is energetically more favorable than having coherent magnetization rotation [44,45]. The crossover to non-coherent magnetization reversal modes will be accompanied by a decrease of the DWs energy with the thickness. A direct consequence of this fact is that H_C will decrease with the thickness, as experimentally observed in Figure 2d.

The same reversal magnetization mechanisms previously observed in the rectangular profile nanowires have been found in the bell-shaped profile nanowires (case II and III). Thus, for $t_{Nom} < t_c$, with $t_c = 15$ nm, a monodomain-type reversal magnetization of EDWs with coherent rotation occurs, as shown in Figure 9a for a bell-shaped profile nanowire (case II) with $t_{Nom} = 10$ nm. For $t_c < t_{Nom} \leq 25$ nm, a monodomain-type reversal magnetization of EDWs with non-coherent rotation
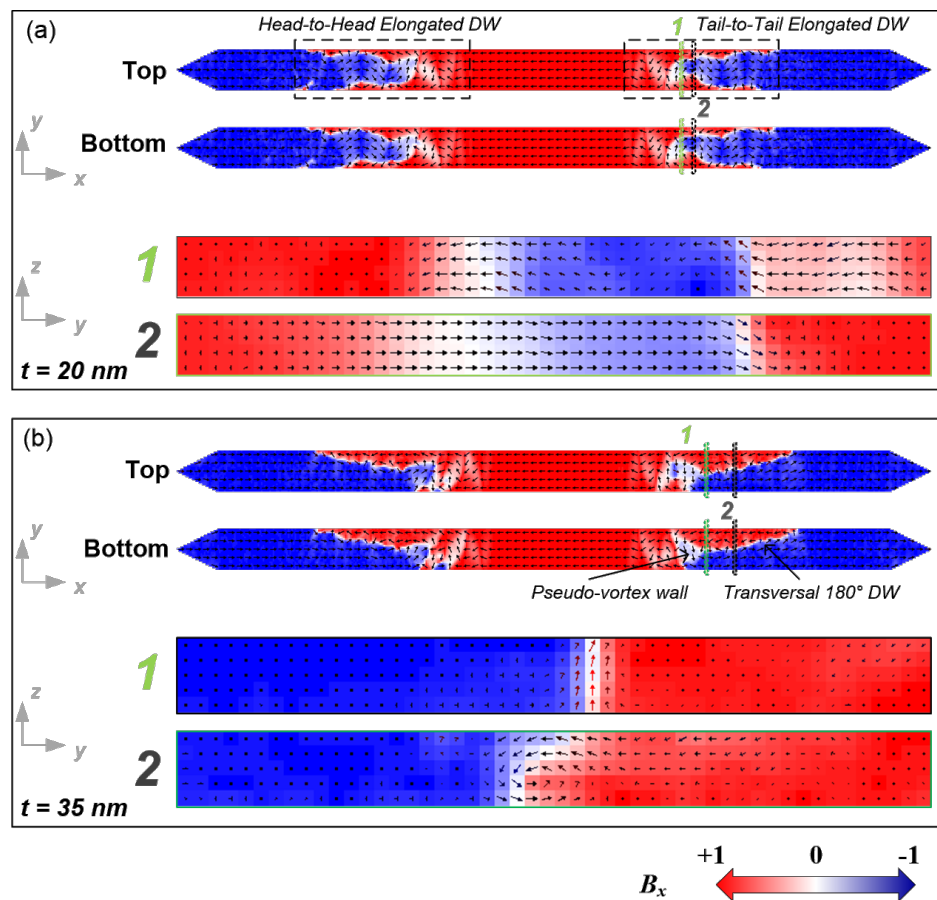
Figure 8: Magnetization vector-color maps extracted from the simulations for 250 nm wide Fe nanowires with rectangular profile (case I) and thickness of (a) 20 nm and (b) 35 nm. The areas named "1" (green lines) and "2" (black lines) in the x,y plane representations have been chosen for the representation in the y,z plane.
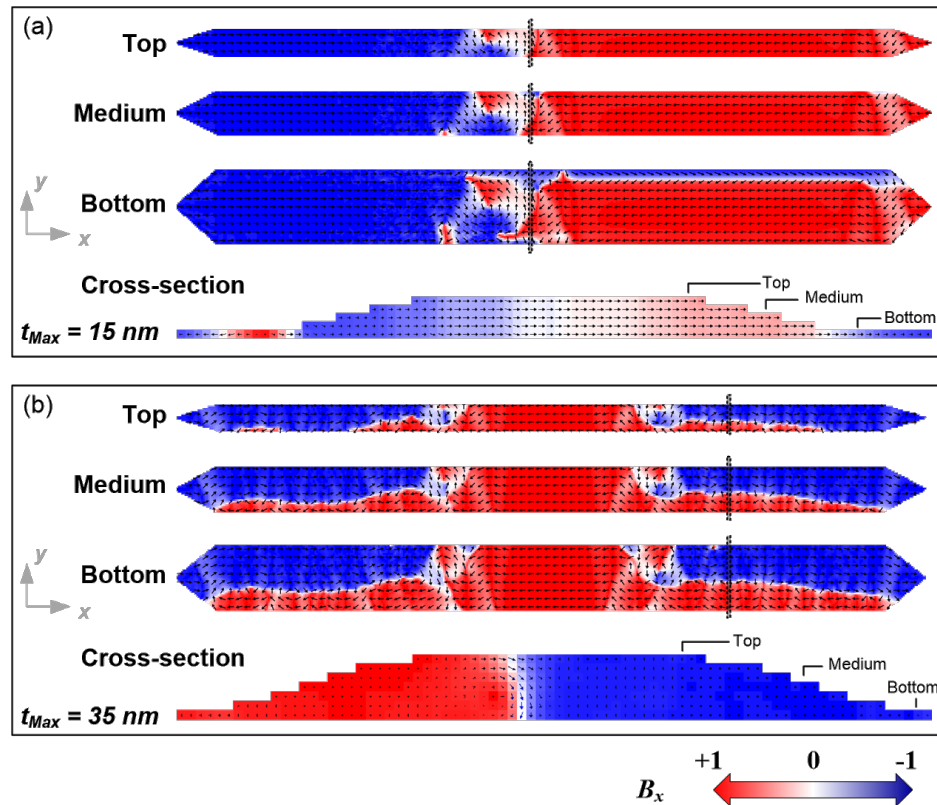
Figure 9: Magnetization vector-color maps extracted from the simulations for 250 nm wide Fe nanowires with bell-shaped profile (case II) and nominal thickness of (a) 10 nm and (b) 20 nm. The areas marked with black lines in the *x,y* plane representations have been chosen for the representation in the *y,z* plane (cross-section).

occurs, as shown in Figure 9b for a bell-shaped profile nanowire (case II) with $t_{\text{Nom}} = 20$ nm.

Interestingly, for 30 nm $\leq t_{\text{Nom}} \leq 50$ nm, the reversal magnetization process is already multidomain-type, as shown in Figure 10. Indeed, for nominal thicknesses of 30 and 35 nm, the switching is produced through the formation and displacement of several magnetic domains along the nanowire length. The example of the 30 nm nanowire is shown in Figure 10a. For $t_{\text{Nom}} = 40$ and 50 nm, the magnetization reversal is given by the displacement of two transversal 180° DWs, each of them initiated at one of the pointed ends of the nanowires. In this displacement, while one extreme of the transversal 180° DW is pinned at the apex of the nanowire, the other extreme moves towards the center of the nanowire. When both DW meet at the center, they form a single DW spanning along the full length of the nanowire, forming a Landau–Liftshitz domain pattern, as displayed in Figure 10b.

An interesting behavior is observed if we plot the values of H_C as a function of t_{Max}. This new representation, shown in Figure 11, indicates that the different reversal magnetization

mechanisms are directly linked to the maximum thickness, independently of the shape of the profiles. The shape of the profile, however, allows for the tuning of the value of H_C, being higher in the rectangular profile nanowires. The surface oxidation in the bell-shaped profile (giving rise to a reduction of the magnetic volume) produces an increase in the values of H_C. In Figure 11, two additional values of H_C for rectangular profile nanowires with $t_{\text{Max}} = t_{\text{Nom}} = 70$ and 90 nm are reported. The simulations show a non-coherent multidomain magnetization reversal in such nanowires, similar to that observed in the bell-shaped profile nanowires in the same t_{Max} range.

From the information obtained in the micromagnetic simulations, one can safely infer that the dependence of H_C on the thickness in Fe nanowires is directly related to the specific magnetization reversal mode taking place at that thickness range. While reversal modes via coherent magnetization rotation produce an increasing value of H_C with the thickness, reversal modes via non-coherent magnetization rotation make H_C decrease with the thickness. Extrapolating this analysis to the experimental results obtained, we conclude that the decreasing value of H_C with thickness observed in Figure 2d is
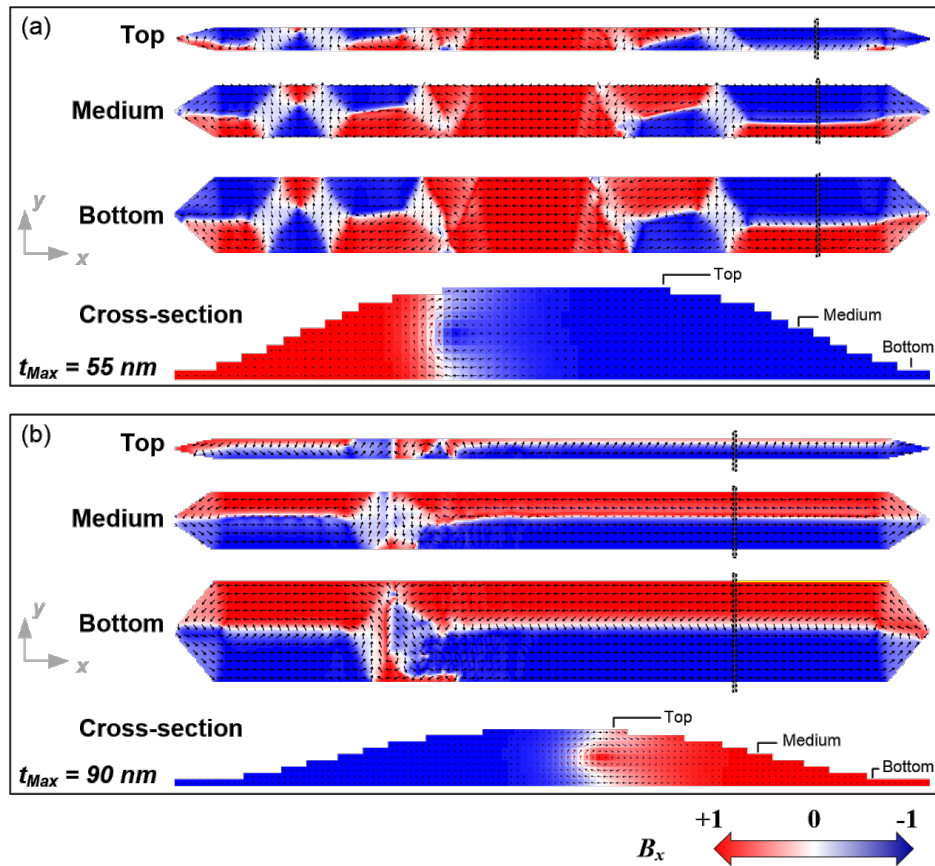
Figure 10: Magnetization vector-color maps extracted from the simulations for 250 nm wide Fe nanowires with bell-shaped profile (case II) and nominal thicknesses of (a) 30 nm and (b) 50 nm. The areas marked with black lines in the *x,y* plane representations have been chosen for the representation in the *y,z* plane (cross-section).
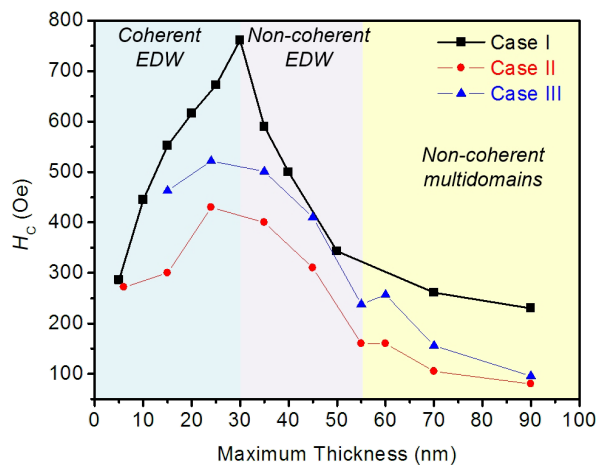
Figure 11: Coercive field (H_C) obtained from the simulations of nanowires as a function of t_{Max} for the three cases.

caused by magnetization reversal modes with non-coherent magnetization rotation.

Having established the reason for the dependence of H_C on the thickness over the thickness range studied, a number of interesting features need to be discussed.

i) Effects produced by the bell shape and the halo of the nanowires. As shown in Figure 6, the bell-shaped nanowires present a lower H_C compared to the ones with a rectangular profile. This was already found in the simulations of FEBID Co nanowires performed by Fernández-Pacheco et al. [27]. The reason is that the nucleation of DWs is favored at the thinnest parts of the nanowire, which facilitates the magnetization reversal. Previous simulations in Fe nanowires considering an extended halo also highlighted its influence on the magnetization reversal [31]. Moreover, experiments where the halo was eliminated by means of ion irradiation already indicated its relevant role played in the magnetization reversal [28,29].

ii) Effects produced by the oxidized top layer of 5 nm. The oxidized top layer of 5 nm is expected to play some role in thin nanowires due to the modification of the magnetic properties of a substantial part of the nanowire. Assuming that this oxidized layer is paramagnetic at room temperature (as the Fe/O 1:1 stoichiometry suggests), this surface layer will lose its ferromagnetic behavior. According to the simulations shown in Figure 6, the main effect of such oxidized layer is therefore to increase H_C. This is explained by the change in the ferromagnetic shape of the nanowire caused by the oxidation, which degrades or annihilates the ferromagnetism in the halo. The halo is a source for easy DW nucleation and its oxidation will weaken such mechanism for the initiation of the magnetization reversal.

iii) Behavior of H_C at low thickness. The simulations predict that for the thinnest bell-shaped nanowires (t_{Nom} < 15 nm), a regime of increasing H_C with thickness could be observed. This thickness regime was not experimentally addressed by us in a systematic way as it was beyond the scope of the present work. In fact, only one sample in our study falls in that thickness range, which does not permit to extract any reliable conclusion. However, it seems an interesting focus for future work. Such challenging work should consider, for example, a systematic characterization of the iron oxides formed at the surface, the continuity of the magnetic layer at such low thicknesses, and the nanowire roughness.

Conclusion

A systematic magneto-optical Kerr effect study of the coercive field as a function of thickness and width in Fe nanowires grown by focused electron beam induced deposition (FEBID) has been carried out. It has been found that the coercive field decreases for increasing thickness and width in the range of dimensions studied. In the particular case of H_C vs thickness for nanowires with constant width (250 nm), micromagnetic simulations have demonstrated that the decrease of H_C with thickness is due to the prevalent magnetization reversal mechanism, namely non-coherent magnetization reversal. In addition, micromagnetic simulations also show that the actual bell shape of the FEBID nanowires is important for the exact value of H_C. The formation of a 5 nm surface oxidation layer on top of the nanowires has been observed experimentally. Micromagnetic simulations show that such surface oxidation produces a slight increase in H_C. The results shown in this work demonstrate that H_C can be tailored in Fe nanowires grown by FEBID with appropriate control over their dimensions and shape, which is a crucial step towards the fabrication of functional devices based on these deposits such as magnetic memories, logic circuits and magnetic sensors. The reported micromagnetic simulations provide a detailed understanding of the magnetization reversal mechanisms in these Fe nanowires.

Supporting Information

Supporting Information File 1
Structural and compositional characterization of the iron nanowires.
[http://www.beilstein-journals.org/bjnano/content/supplementary/2190-4286-6-136-S1.pdf]

Supporting Information File 2
Additional information about the profile shape of the nanowires and micromagnetic simulations.
[http://www.beilstein-journals.org/bjnano/content/supplementary/2190-4286-6-136-S2.pdf]

References

1. De Teresa, J. M.; Fernández-Pacheco, A. *Appl. Phys. A* **2014,** *117,* 1645–1658. doi:10.1007/s00339-014-8617-7
2. Idigoras, O.; Nikulina, E.; Porro, J. M.; Vavassori, P.; Chuvilin, A.; Berger, A. *Nanofabrication* **2014,** *1,* 23–34. doi:10.2478/nanofab-2014-0003
3. Randolph, S. J.; Fowlkes, J. D.; Rack, P. D. *Crit. Rev. Solid State Mater. Sci.* **2006,** *31,* 55–89. doi:10.1080/10408430600930438
4. Utke, I.; Hoffmann, P.; Melngailis, J. *J. Vac. Sci. Technol., B* **2008,** *26,* 1197–1276. doi:10.1116/1.2955728
5. van Dorp, W. F.; Hagen, C. W. *J. Appl. Phys.* **2008,** *104,* 081301. doi:10.1063/1.2977587
6. Huth, M.; Porrati, F.; Schwalb, C.; Winhold, M.; Sachser, R.; Dukic, M.; Adams, J.; Fantner, G. *Beilstein J. Nanotechnol.* **2012,** *3,* 597–619. doi:10.3762/bjnano.3.70
7. Utke, I.; Hoffmann, P.; Berger, R.; Scandella, L. *Appl. Phys. Lett.* **2002,** *80,* 4792–4794. doi:10.1063/1.1489097
8. Boero, G.; Utke, I.; Bret, T.; Quack, N.; Todorova, M.; Mouaziz, S.; Kejik, P.; Brugger, J.; Popovic, R. S.; Hoffmann, P. *Appl. Phys. Lett.* **2005,** *86,* 042503. doi:10.1063/1.1856134
9. Fernández-Pacheco, A.; De Teresa, J. M.; Córdoba, R.; Ibarra, M. R. *J. Phys. D: Appl. Phys.* **2009,** *42,* 055005. doi:10.1088/0022-3727/42/5/055005
10. Belova, L. M.; Dahlberg, E. D.; Riazanova, A.; Mulders, J. J. L.; Christoferson, C.; Eckert, J. *Nanotechnology* **2011,** *22,* 145305. doi:10.1088/0957-4484/22/14/145305
11. Kunz, R. R.; Mayer, T. M. *J. Vac. Sci. Technol., B* **1988,** *6,* 1557–1564. doi:10.1116/1.584214
12. Takeguchi, M.; Shimojo, M.; Furuya, K. *Nanotechnology* **2005,** *16,* 1321–1325. doi:10.1088/0957-4484/16/8/057

13. Lukasczyk, T.; Schirmer, M.; Steinrück, H. P.; Marbach, H. *Langmuir* **2009,** *25,* 11930–11939. doi:10.1021/la901612u

14. Lavrijsen, R.; Córdoba, R.; Schoenaker, F. J.; Ellis, T. H.; Barcones-Campo, B.; Kohlhepp, T. J.; Swagten, H. J. M.; Koopmans, B.; De Teresa, J. M.; Magén, C.; Ibarra, M. R.; Trompenaars, P.; Mulders, J. J. L. *Nanotechnology* **2011,** *22,* 025302. doi:10.1088/0957-4484/22/2/025302

15. Serrano-Ramón, L.; Córdoba, R.; Rodríguez, L. A.; Magén, C.; Snoeck, E.; Gatel, C.; Serrano, I.; Ibarra, M. R.; De Teresa, J. M. *ACS Nano* **2011,** *5,* 7781–7787. doi:10.1021/nn201517r

16. Nikulina, E.; Idigoras, O.; Vavassori, P.; Chuvilin, A.; Berger, A. *Appl. Phys. Lett.* **2012,** *100,* 142401. doi:10.1063/1.3701153

17. Belova, L. M.; Hellwig, O.; Dobisz, E.; Dahlberg, E. D. *Rev. Sci. Instrum.* **2012,** *83,* 093711. doi:10.1063/1.4752225

18. Gavagnin, M.; Wanzenboeck, H. D.; Belić, D.; Bertagnolli, E. *ACS Nano* **2013,** *7,* 777–784. doi:10.1021/nn305079a

19. De Teresa, J. M.; Córdoba, R. *ACS Nano* **2014,** *8,* 3788–3795. doi:10.1021/nn500525k

20. Fernández-Pacheco, A.; Serrano-Ramón, L.; Michalik, J. M.; Ibarra, M. R.; De Teresa, J. M.; O' Brien, L.; Petit, D.; Lee, J.; Cowburn, R. P. *Sci. Rep.* **2013,** *3,* 1492. doi:10.1038/srep01492

21. Franken, J. H.; van der Heijden, M. A. J.; Ellis, T. H.; Lavrijsen, R.; Daniels, C.; McGrouther, D.; Swagten, H. J. M.; Koopmans, B. *Adv. Funct. Mater.* **2014,** *24,* 3508–3514. doi:10.1002/adfm.201303540

22. Chia, H.-J.; Guo, F.; Belova, L. M.; McMichael, R. D. *Appl. Phys. Lett.* **2012,** *101,* 042408. doi:10.1063/1.4738789

23. Lavenant, H.; Naletov, V.; Klein, O.; de Loubens, G.; Casado, L.; De Teresa, J. M. *Nanofabrication* **2014,** *1,* 65–73. doi:10.2478/nanofab-2014-0006

24. Jaafar, M.; Serrano-Ramón, L.; Iglesias-Freire, O.; Fernández-Pacheco, A.; Ibarra, M. R.; De Teresa, J. M.; Asenjo, A. *Nanoscale Res. Lett.* **2011,** *6,* 407. doi:10.1186/1556-276X-6-407

25. Córdoba, R.; Fernández-Pacheco, R.; Fernández-Pacheco, A.; Gloter, A.; Magén, C.; Stéphan, O.; Ibarra, M. R.; De Teresa, J. M. *Nanoscale Res. Lett.* **2011,** *6,* 592. doi:10.1186/1556-276X-6-592

26. Fernández-Pacheco, A.; De Teresa, J. M.; Córdoba, R.; Ibarra, M. R.; Petit, D.; Read, D. E.; O'Brien, L.; Lewis, E. R.; Zeng, H. T.; Cowburn, R. P. *Appl. Phys. Lett.* **2009,** *94,* 192509. doi:10.1063/1.3139068

27. Fernández-Pacheco, A.; De Teresa, J. M.; Szkudlarek, A.; Córdoba, R.; Ibarra, M. R.; Petit, D.; O'Brien, L.; Zeng, H. T.; Lewis, E. R.; Read, D. E.; Cowburn, R. P. *Nanotechnology* **2009,** *20,* 475704. doi:10.1088/0957-4484/20/47/475704

28. Serrano-Ramón, L.; Fernández-Pacheco, A.; Córdoba, R.; Magén, C.; Rodríguez, L. A.; Petit, D.; Cowburn, R. P.; Ibarra, M. R.; De Teresa, J. M. *Nanotechnology* **2013,** *24,* 345703. doi:10.1088/0957-4484/24/34/345703

29. Nikulina, E.; Idigoras, O.; Porro, J. M.; Vavassori, P.; Chuvilin, A.; Berger, A. *Appl. Phys. Lett.* **2013,** *103,* 123112. doi:10.1063/1.4821034

30. Plank, H.; Smith, D. A.; Haber, T.; Rack, P.; Hofer, F. *ACS Nano* **2012,** *6,* 286–294. doi:10.1021/nn204237h

31. Gavagnin, M.; Wanzenboeck, H. D.; Belic, D.; Shawraw, M. M.; Persson, A.; Gunnarsson, K.; Svedlindh, P.; Bertagnolli, E. *Phys. Status Solidi A* **2014,** *211,* 368–374. doi:10.1002/pssa.201330114

32. Cowburn, R. P. *J. Phys. D: Appl. Phys.* **2000,** *33,* R1–R16. doi:10.1088/0022-3727/33/1/201

33. Casey Uhlig, W.; Shi, J. *Appl. Phys. Lett.* **2004,** *84,* 759–761. doi:10.1063/1.1645332

34. Leven, B.; Dumpich, G. *Phys. Rev. B* **2005,** *71,* 064411. doi:10.1103/PhysRevB.71.064411

35. Dumpich, G.; Krome, T. P.; Hausmanns, B. *J. Magn. Magn. Mater.* **2002,** *248,* 241–247. doi:10.1016/S0304-8853(02)00347-5

36. Brands, M.; Leven, B.; Dumpich, G. *J. Appl. Phys.* **2005,** *97,* 114311. doi:10.1063/1.1921343

37. Yuan, S. W.; Bertram, H. N.; Smyth, J. F.; Schultz, S. *IEEE Trans. Magn.* **1992,** *28,* 3171–3173. doi:10.1109/20.179748

38. Koehler, T. R.; Fredkin, D. R. *IEEE Trans. Magn.* **1991,** *27,* 4763–4765. doi:10.1109/20.278939

39. Goolaup, S.; Singh, N.; Adeyeye, A. O.; Ng, V.; Jalil, M. B. A. *Eur. Phys. J. B* **2005,** *44,* 259–264. doi:10.1140/epjb/e2005-00122-7

40. Rodríguez, L. A.; Magén, C.; Snoeck, E.; Serrano-Ramón, L.; Gatel, C.; Córdoba, R.; Martínez-Vecino, E.; Torres, L.; De Teresa, J. M.; Ibarra, M. R. *Appl. Phys. Lett.* **2013,** *102,* 022418. doi:10.1063/1.4776709

41. Córdoba, R.; Lavrijsen, R.; Fernández-Pacheco, A.; Ibarra, M. R.; Schoenaker, F. J.; Ellis, T. J.; Barcones-Campo, B.; Kohlhepp, T. J.; Swagten, H. J. M.; Koopmans, B.; Mulders, J. J. L.; De Teresa, J. M. *J. Phys. D: Appl. Phys.* **2012,** *45,* 035001. doi:10.1088/0022-3727/45/3/035001

42. Lopez-Diaz, L.; Aurelio, D.; Torres, L.; Martinez, E.; Hernandez-Lopez, M. A.; Gomez, J.; Alejos, O.; Carpentieri, M.; Finocchio, G.; Consolo, G. *J. Phys. D: Appl. Phys.* **2012,** *45,* 323001. doi:10.1088/0022-3727/45/32/323001

43. Donahue, M. J.; Porter, D. G. *OOMMF User's Guide Version 1.0;* 1999.

44. Skomski, R.; Zeng, H.; Sellmyer, D. J. *J. Magn. Magn. Mater.* **2002,** *249,* 175–180. doi:10.1016/S0304-8853(02)00527-9

45. Huo, S.; Bishop, J. E. L.; Tucker, J. W. *J. Appl. Phys.* **1997,** *81,* 5239–5241. doi:10.1063/1.364906

BEILSTEIN JOURNAL OF NANOTECHNOLOGY

Formation of pure Cu nanocrystals upon post-growth annealing of Cu–C material obtained from focused electron beam induced deposition: comparison of different methods

Aleksandra Szkudlarek[1,2], Alfredo Rodrigues Vaz[1,3], Yucheng Zhang[4],
Andrzej Rudkowski[5], Czesław Kapusta[5], Rolf Erni[4], Stanislav Moshkalev[3] and Ivo Utke[*1]

Full Research Paper

Address:
[1]Empa, Swiss Federal Laboratories for Materials Science and Technology, Laboratory for Mechanics of Materials and Nanostructures, Feuerwerkerstrasse 39, 3602 Thun, Switzerland, [2]AGH University of Science and Technology, Academic Centre for Materials and Nanotechnology, al. A. Mickiewicza 30, 30-059 Krakow, Poland, [3]Center for Semiconductor Components, State University of Campinas, 13083-870, Campinas, SP, Brazil, [4]Empa, Swiss Federal Laboratories for Materials Science and Technology, Electron Microscopy Center, Überlandstrasse 129, 8600 Dübendorf, Switzerland and [5]AGH University of Science and Technology, Faculty of Physics and Applied Computer Science, Department of Solid State Physics, al. A. Mickiewicza 30, 30-059 Krakow, Poland

Email:
Ivo Utke[*] - ivo.utke@empa.ch

* Corresponding author

Abstract

In this paper we study in detail the post-growth annealing of a copper-containing material deposited with focused electron beam induced deposition (FEBID). The organometallic precursor Cu(II)(hfac)$_2$ was used for deposition and the results were compared to that of compared to earlier experiments with (hfac)Cu(I)(VTMS) and (hfac)Cu(I)(DMB). Transmission electron microscopy revealed the deposition of amorphous material from Cu(II)(hfac)$_2$. In contrast, as-deposited material from (hfac)Cu(I)(VTMS) and (hfac)Cu(I)(DMB) was nano-composite with Cu nanocrystals dispersed in a carbonaceous matrix. After annealing at around 150–200 °C all deposits showed the formation of pure Cu nanocrystals at the outer surface of the initial deposit due to the migration of Cu atoms from the carbonaceous matrix containing the elements carbon, oxygen, and fluorine. Post-irradiation of deposits with 200 keV electrons in a transmission electron microscope favored the formation of Cu nanocrystals within the carbonaceous matrix of freestanding rods and suppressed the formation on their surface. Electrical four-point measurements on FEBID lines from Cu(hfac)$_2$ showed five orders of magnitude improvement in conductivity when being annealed conventionally and by laser-induced heating in the scanning electron microscope chamber.

Introduction

Focused electron beam induced deposition (FEBID) is a direct maskless nanolithography technique, based on the local dissociation of adsorbates upon the irradiation with electrons [1]. The molecules are delivered into the microscope chamber by a gas injection system (GIS) where they reversibly physisorb onto the substrate surface. Part of the energy from the primary electron beam or from the secondary electrons generated in the vicinity of the impinging primary beam is transferred to the adsorbates and breaks their chemical bonds. The non-volatile fragments stick to the substrate surface whereas the volatile fragments are removed from the chamber by the pumping system. By controlling the beam scanning three dimensional structures of a complex shape can be created in a single direct-write deposition step onto planar or non-planar surfaces [2].

Nanodevices with various functionalities have been deposited comprising gas sensors [3,4], magnetic sensors [5,6] strain sensors [7], thermal sensors [8], photodetectors [9], and mode stabilizers for vertical surface emitting lasers [10]. Other deposits were used as ferromagnetic wires [11,12], superconducting wires [13], plasmonic structures [14], or as electrode nanocontacts [15,16]. The feasibility of obtaining 3D nanostructures with a high aspect ratio makes FEBID suitable for fabrication of high resolution probes to scanning magnetic force microscopy (MFM) [17-19].

Purification methods of FEBID structures

For FEBID direct-write nanostructures lateral resolution can be well-controlled by adjusting the beam and gas flow settings [20] as well as by optimizing scanning strategies [21]. However, the purity of FEBID materials obtained with organic precursors still remains an issue. Recently, post-growth purification methods using electron beam irradiation in combination with thermal annealing and co-injection of reactive gases/ions were developed. In the case of Pt–C deposits, the catalytic properties of Pt nanoparticles facilitate the process of molecular oxygen dissociation, thereby increasing the efficiency of removing the carbonaceous matrix [22]. Pure Pt material was obtained with a post deposition treatment using O_2 gas and a) laser pulsing [23] or b) low-temperature substrate annealing (up to 50 °C) [24]. The presence of H_2O during electron irradiation performed at rt allowed for a total elimination of carbon from Pt–C deposits without affecting the shape [25]. The combination of thermal heating to 300 °C, injection of H_2 gas and simultaneous electron irradiation led to pure Co deposits [26]. Microstructural changes were observed upon simple 5 keV electron beam curing of FEBID structures. The Pt–C deposits exhibited an increased conductivity by three to four orders of magnitude [27,28]. For W–C deposits an improvement of one order of magnitude was found [29].

Conventional post-growth annealing of FEBID material in vacuum was summarized in a review by Botman et al. [30]: The thermal energy which is delivered to the sample can cause a desorption of carbonaceous fragments increasing the metal concentration from 15 atom % of Au (rt) to 24 atom % of Au (at 100 °C). Increasing the substrate temperature during FEBID also favors the desorption of non-metallic dissociation by-products as it was observed by Mulders et al. [31] for various precursors: TEOS (tetraethylorthosilicate), $Co(CO)_3NO$, $Co_2(CO)_8$, and $Me_2Au(acac)$ with the best purity enhancement for $W(CO)_6$ (from 37 atom % at 25 °C to 59 atom % of W at 280 °C). However, the temperature rise during the deposition may not be favorable as it also decreases the residence time of adsorbates, significantly lowering the growth rate. Furthermore, the high temperature may also cause the diffusion of deposit atoms into or from the substrate.

A compromise approach is based on pulsed heating with an IR laser as a heat source which can generate abrupt temperature peaks in the microseconds range only (sufficient for desorption), allowing the substrate surface to equilibrate quickly and to replenish with new adsorbates before the next electron-beam scan frame. FEBID together with synchronized pulsed IR laser heating helped to increase the metal concentration of Au, W, Pt in FEBID deposits, however, did not fully remove the carbon. For deposits obtained from $Me_2Au(acac)$ the initial atomic ratio of C to Au decreased from 4 to 0.5 with the laser assistance [32]. For $W(CO)_6$ FEBID the atomic ratio of W to C was improved from 1:4 to 2:1 [33]. For $MePtCpMe_3$ FEBID the Pt concentration increased from about 15 atom % to 35 atom % [34]. Such an improvement was not observed when using a conventional heating stage during the deposition process with $MePtCpMe_3$. The deposit obtained at 350 °C did not exhibit a different Pt/C ratio than the deposit obtained at room temperature, where 15 atom % Pt were measured [31].

Copper purification

The very high conductivity of copper makes the localized deposition of this metal very attractive for applications in nano-electronics. The organometallic hexafluoroacetylacetonate (hfac)-based Cu(I) and Cu(II) precursors are widely used in chemical vapor deposition (CVD) methods due to their stability and high vapor pressure. They allow to obtain pure metal CVD films with the same resistivity as in a bulk material at deposition temperatures below 300 °C [35-37].

Recently, it was shown for condensed monolayers of $Cu(hfac)_2$ (also $Pt(hfac)_2$ and $Pd(hfac)_2$) that electron-beam irradiation results in about 80 atom % of carbon content [38]. The metal content could be then increased by two sequential purification

steps: 1) deposit bombardment with atomic oxygen 2) deposit bombardment with atomic hydrogen. In the first step the carbonaceous material was fully removed from the material and in the next step the metal oxide was reduced to the metal. Although this method was successfully applied to obtain a deposit with high metal purity, the total exposure time was rather long: 40 h for oxygen and 2 h for hydrogen. The efficiency of atomic hydrogen only for purification of Cu–C material obtained by an ion-induced deposition process at room temperature was shown by Chiang et al. [36]. It led to 99 atom % pure Cu films. H_2/Ar microplasma-assisted FEBID increased the Cu content from 12 atom % to 41 atom % but also caused extended halo deposits [39]. Ga^+ ion beam deposition showed that heating the substrate surface has a crucial influence on the properties of the deposit structure, from small isolated nanocrystals of Cu (ca. 20 nm) at 25 °C towards continuous thin films of pure copper at 100 °C, using (hfac)CuVTMS [40].

In this paper we will show results obtained by SEM, TEM, and electrical resistance monitoring during post-growth annealing of Cu–C FEBID material from Cu(II) and Cu(I) precursors with respect to nanostructural changes and conductivity showing the potential of fabricating pure copper nanodots, from the as-grown amorphous Cu–C deposit. The thermal energy input favors the migration of Cu atoms to coalesce to pure Cu nanocrystals being dispersed inside and on top of the carbonaceous matrix.
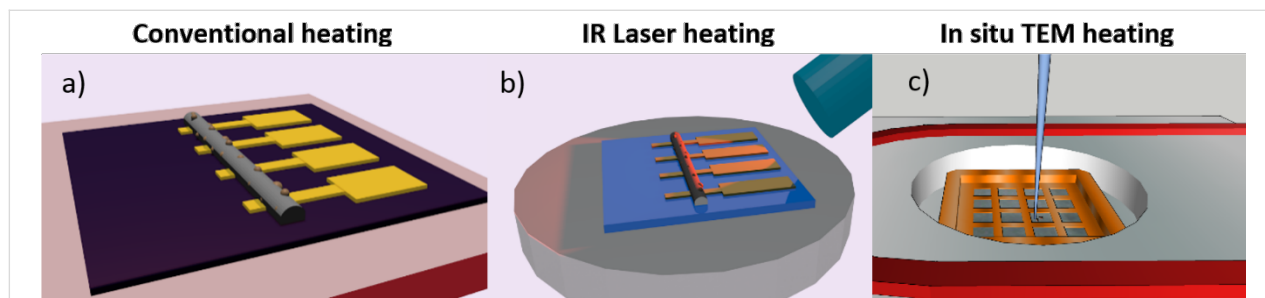
Experimental
FEBID
The experiments were performed using a Hitachi 3600 scanning electron microscope (SEM) with a tungsten filament. The precursors were filled into their reservoirs inside a glove box in argon or dry nitrogen atmosphere. The deposition process has been carried out at room temperature on two types of substrates: Si with a 200 nm top layer of SiO_2 and copper TEM grids with holey carbon films. The beam energy was fixed to 25 keV.

In this study bis(hexafluoroacetylacetonato)copper(II) [$Cu(hfac)_2$, $Cu(HC_5O_2F_6)_2$] was used as a precursor and compared to earlier experiments with the precursors vinyltrimethylsilane copper(I) hexafluoroacetylacetonate, [(hfac)CuVTMS, $(C_6H_{12}Si)Cu(HC_5O_2F_6)$], and dimethylbutene copper(I) hexafluoroacetylacetonate [(hfac)CuDMB, $(C_5H_{12})Cu(HC_5O_2F_6)$] [41].

The precursor flux was estimated to be about 10 monolayers per second for $Cu(hfac)_2$. The exposure parameters for $Cu(hfac)_2$ for 1 µm × 1 µm square deposits were: dwell time of 1 µs, pixel distance of 0.4 nm, and frame repetitions varying from 100 to 1000 with refreshment times of 0.625 s. The beam current was 0.4 nA. This corresponds to doses of 0.25 nC/µm² (100 repetitions) and 2.5 nC/µm² (1000 repetitions). For the 15 µm long lines we used 100 µs dwell time per pixel, 0.5 nm pixel distance, and 300 line repetitions with a refreshment time of 3 s. The beam current was 1 nA, which corresponds to the dose of 9 nC/µm² and exposure time of 900 s. Tip deposits were obtained by the stationary dot exposure mode exposing a pixel for two minutes. Line and freestanding-rod deposits with (hfac)CuDMB and (hfac)CuVTMS from earlier FEBID experiments [39,40] were performed with a single scan at around 30 nm/s with 600 pA.

Annealing
Post-growth annealing in vacuum was achieved by various setups shown in Figure 1. The conventional heating using a hot plate was performed without breaking the vacuum after the deposition process. The experiments were performed inside the SEM for a temperature range from room temperature up to 220 °C. The sample was supported in a custom-made massive copper block on a resistive heater (Boraelectric). The control of temperature was done with a thermocouple directly coupled to the base of the substrate. During the heating we observed an increase of the pressure inside the SEM chamber from 5×10^{-6} to 5×10^{-5} mbar. We cannot exclude possible reactions of the deposits with the residual gas (most likely water and residual

Figure 1: Sketch of post-growth annealing experiments: a) conventional heating using a hot plate in an SEM, b) SEM integrated laser heating; the substrate is heated by the IR laser pulses, c) post-growth thermal annealing during in situ TEM analysis. Conventional and IR laser annealing experiments were combined with in situ four-point probe resistance measurements.

hydrocarbons) but we judge the influence as negligible as TEM annealing experiments at pressures better than 1×10^{-6} mbar also resulted in nanocrystal formation (see below in Figure 6).

An infrared laser system was integrated into the SEM chamber for in situ post-growth annealing directly after the deposition. The system was composed of a SvetWheel's MU40-960-01 laser diode module and a fast diode current modulator VFM 20-25s (Messtec Power Converter GmbH) triggered by a signal function generator. The wavelength of emitted photons was equal to 960 nm (corresponding to an energy of 1.29 eV) with a total maximum laser power of 29 W. The tip of the laser optical fiber was placed in close vicinity of the FEBID deposit. The laser power, pulse duration and its frequency were adjustable by the signal generator. The size of the laser spot on the substrate was estimated to 65 μm × 130 μm, based on the molten area in SiO_2 using the maximum laser power and a high pulse frequency.

The substrate surface temperatures generated by the laser during post-deposition annealing were determined experimentally and theoretically. Numerical finite element simulations with the annealing conditions (peak laser power of 13.6 W, pulse duration of 10 μs and frequency of 10 kHz) gave a stationary substrate surface temperature at the center of the laser beam of 158 °C which was reached after approximately 30 s. This was in good agreement with the value of 150 °C deduced from in situ four-point-probe resistance measurements of a gold wire deposited by e-beam lithography and PVD metal lift-off together with the pre-structure of the four-point electrodes.

TEM in situ annealing of FEBID deposits from $Cu(hfac)_2$ was performed with a Gatan double tilt heating holder (Model 652) in a JEOL-2200FS microscope. The samples were heated up to 220 °C with a ramp rate of 20 K/min.

Characterization

For SEM observation we used a Hitachi S4800 electron microscope and for the EDX measurements a Brooker/Oxford device mounted on a TESCAN LYRA microscope. EDX measurements were performed at 5 kV and 2 nA over 30 s with a 300 nm × 300 nm scan area on the squares to account for inhomogeneities in the lateral copper nanocrystal precipitation. Standard EDX software was used to calculate the composition from the spectra.

High-resolution TEM (HR-TEM) images were taken at 200 keV. Selected area diffraction (SAD) was taken using the second smallest selected area aperture corresponding to an area of 400 nm in diameter on the sample. Chemical mapping was obtained using electron energy loss spectroscopy (EELS) operated in the scanning TEM (STEM) mode. The Cu K edge (928 eV) and a signal energy window of 40 eV (920–960 eV) after background subtraction were used to map the composition distribution of Cu, see Figure S1 in Supporting Information File 1.

The changes of resistance during the annealing were monitored by four-point probe measurements using an SEM-integrated 15-stage nanomanipulator from SmarAct. Conductive microprobes were connected via an SEM feedthrough to a Keithley 2400 Sourcemeter, with a source current of 100 μA and a voltage compliance level of 500 mV.

Results and Discussion
As-deposited material

Energy dispersive X-ray (EDX) analysis showed that at room temperature deposited Cu–C lines and squares obtained from $Cu(II)(hfac)_2$ had an atomic ratio of approximately Cu/C/O/F = 10:64:25:1 with standard deviations of ±1 atom % for Cu, ±2 atom % for C, ±1 atom % for O, and ±0.3 atom % for F on eight deposits. This amounts to 10 ± 2 atom % of Cu. With respect to the stoichiometric copper content in the $Cu(hfac)_2$ precursor of 3.7 atom % (disregarding the hydrogen) this was 2.7 times more copper in the deposit. The Cu content in deposits obtained from the $(hfac)Cu(I)VTMS$ and $(hfac)Cu(I)DMB$ precursors was about twice as high [41].

Transmission electron microscopy (TEM) showed that dot, square, and line deposits from $Cu(II)(hfac)_2$ on an amorphous carbon membrane were amorphous (Figure 2).

In contrast, as-deposited freestanding rods from earlier FEBID experiments with $(hfac)Cu(I)VTMS$ showed small Cu nanocrystals homogeneously dispersed in a polymeric carbonaceous matrix (see below in Figure 7 taken with a Philips EM-430 TEM at 300 keV). This matrix contains all the ligand elements: carbon, oxygen, fluorine, and silicon as well as probably some hydrogen (not detectable by EDX) [42]. The difference between amorphous and nano-composite materials obtained for the $Cu(II)(hfac)_2$ and $(hfac)Cu(I)VTMS$ precursor, respectively, can be attributed to the lower thermal stability of $(hfac)CuVTMS$ which is 63 °C compared to 250 °C for $Cu(hfac)_2$.

Electrical measurements showed that the as-deposited FEBID lines from $Cu(hfac)_2$ were highly resistive with a value of a few gigaohms being around the measurement limit of the Keithley device. This is in line with our former experiments which showed for all three copper precursors nonconductive behavior for the room temperature as-deposited material [41].
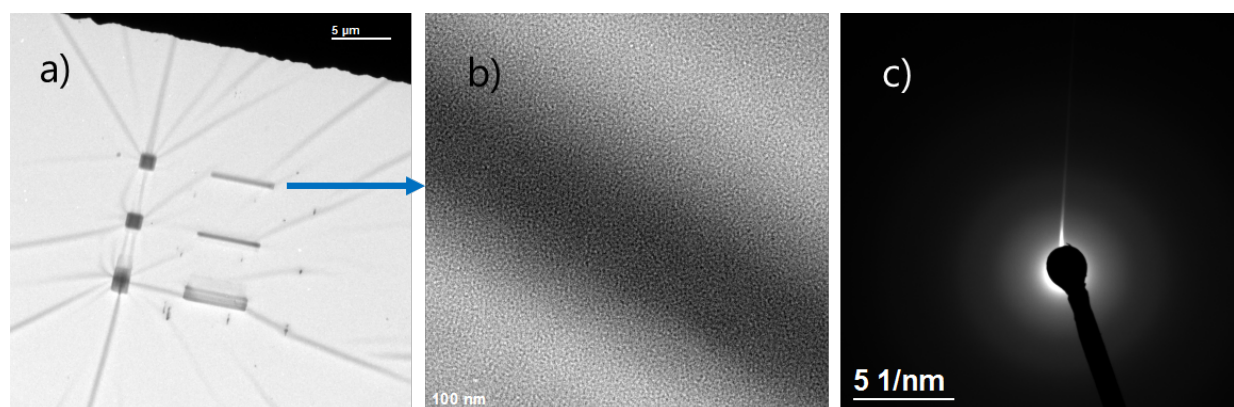
Figure 2: TEM of as-deposited lines and squares from $Cu(hfac)_2$ on an amorphous carbon membrane on a TEM grid. a) An overview of deposits, b) zoom into a line deposit, c) a SAD pattern showing amorphous nature of the deposit.

Annealed material
SEM observations

Upon annealing conventionally or with a laser the flat morphology of square, line, or tip deposits on the pre-patterned SiO_2/Si substrate changes (Figure 3 and Figure 4). While the laser allows for local heating, the conventional hotplate approach allows for more accurate temperature measurements. The visible onset of Cu nanocrystal precipitation on the deposit surface starts at around 150 °C for the $Cu(hfac)_2$ deposits on the pre-patterned SiO_2/Si substrate. Further heating to about 200 °C for 30 min did not visibly change the appearance of the Cu nanocrystal precipitation.

EDX analysis after conventional heating to 200 °C for 30 min showed an atomic ratio of approximately $Cu/C/O/F = 12:75:13:0$ with standard deviations of ± 2 atom % for Cu, ± 2 atom % for C, and ± 1 atom % for O on the same deposits. The 12 ± 2 atom % Cu content in the deposit is thus rather constant compared to the as-grown sample value of 10 ± 2 atom % Cu within the error limits and may have even been slightly overestimated systematically by the standard EDX software due to the surface-precipitated Cu nanocrystals corrected for absorption. Compared to the as-deposited material the fluorine completely disappeared and the oxygen content was halved. An estimation of the amount of precipitated copper nanocrystals that are visible in SEM gave only about 9 to 17 wt % (see Supporting Information File 1). Compared to the average Cu content in the as-grown and deposited samples of roughly 11 atom % (corresponding to an average 37 wt % Cu) this means that 20 to 28 wt % or 5 to 7 atom % of the copper dispersed in the matrix did not precipitate to be visible in SEM or segregated during the annealing. The matrix deposit volume shrunk during annealing to about 70% of its initial volume pointing to reticulation of the carbon network after release of fluorine and oxygen.
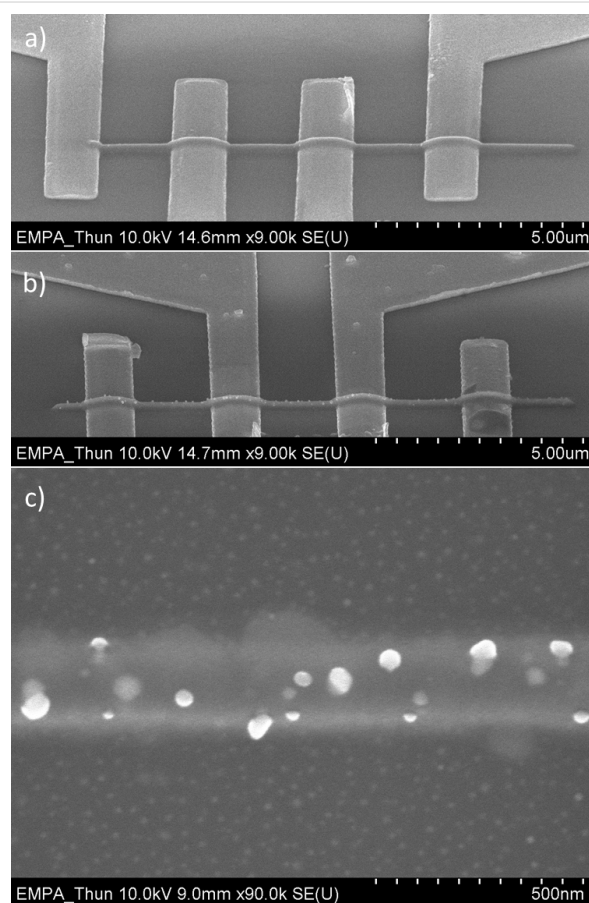
Figure 3: Post-growth annealing of FEBID line from $Cu(hfac)_2$ between four gold electrodes. SEM tilt images (60°) of a) as-deposited line, b) after annealing at 200 °C for 30 min, and c) top-view zoom into central part of the annealed line showing the Cu nanocrystals on the line deposit and inside as well as on the halo deposit.

Interestingly, the size of the nanocrystals is much smaller in the thin halo region of the deposited line, yet the nanocrystal density is much larger. This may be due to the small amount of
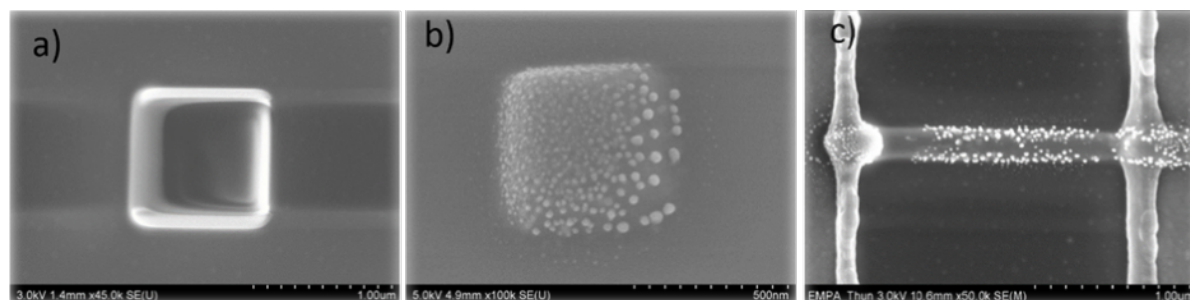
Figure 4: Post-growth laser annealing of FEBID deposits from Cu(hfac)$_2$. SEM top view images of a) as-deposited square, b) Cu nanocrystals forming due to laser annealing at a power of 13.6 W over 1 min, c) laser-annealed FEBID line between two gold electrodes.

deposit material available to form the Cu nanocrystals but could be also due to the low irradiation dose of these regions and hence a slightly less reticulated carbon network which facilitates segregation at many places.

For laser-induced heating we found the same phenomenon of surface precipitation of Cu nanocrystals although the annealing time was only one minute. Also the same trend in the variation of the atomic ratio with annealing was found. Energy dispersive X-ray measurements of the deposit shown in Figure 4a and Figure 4bgave an atomic ratio of Cu/C/O/F = 9:52:32:6 for the as-grown FEBID material which changed to Cu/C/O/F = 10:66:23:0.6 after laser annealing. Considering the error limits of 2 atom % there is no fundamental difference to the trends and absolute values for Cu stated for conventional annealing. The Cu/C = 1:6.6 ratio after laser annealing of 1 min at around 158 °C (see section Experimental) is smaller than for thermal annealing, however, time and annealing temperature were lower for the laser than for thermal annealing. Figure 4 c shows that precipitation of Cu nanocrystals is not fully uniform across the line length in contrast to the conventionally annealed lines in Figure 3b and Figure 3c (see also Figure S5 in Supporting Information File 1). At the vicinity to the gold electrodes there are fewer nanocrystals visible which might be due to a varying distribution of the laser-induced temperature.

The precipitation of Cu nanocrystals on the initial deposit surface was observed also in former experiments with the Cu(I) precursors. Figure 5 shows SEM tilt views of a periodic three dimensional line deposit obtained from (hfac)Cu(DMB). Such periodicity can arise when the vertical deposition rate is comparable to the scan speed of the focused electron beam. For the annealing experiments this is not of importance (for more details we refer to Bret et al. [43]). Upon annealing the same precipitation at deposit surfaces and at halo regions due to forward and backscattered electrons can be seen (Figure 5a–c). For a tip deposit the same features develop upon heating pointing to the fact that the dwell time per pixel during FEBID is not a very sensitive parameter for Cu nanocrystal precipitation (Figure 5d). The prolonged irradiation of a few minutes in the spot mode during FEBID with 20 keV electrons does not seem to change the reticulation of the matrix in such a way that formation of Cu nanocrystals remains contained inside the matrix. On the other hand, post-irradiation experiments with electrons energy of 5 keV were shown to be already effective to change the electron transport mechanisms in Pt–C and W–C FEBID deposits [27-29].

TEM observations
In Figure 6, the results of in situ TEM annealing experiments performed on the line and square deposit material from
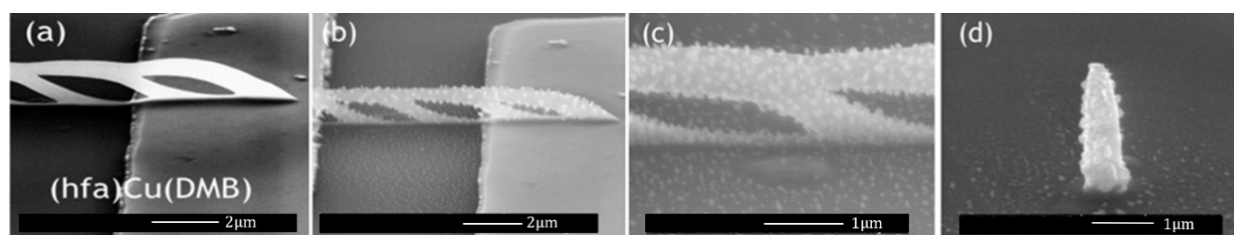
Figure 5: Periodic 3D FEBID line deposits from (hfac)Cu(DMB) between gold electrodes on SiO$_2$/Si. SEM tilt images: a) before annealing, b) after in situ vacuum annealing, c) zoom on Cu nanocrystals, d) tip deposit showing also Cu nanocrystal formation.

Cu(hfac)$_2$ FEBID (shown in Figure 2) are presented. During annealing the deposits were not observed except for one to capture the temperature of crystal formation in a video.

The formation of nanocrystals took place at a temperature of 200 °C. The time for Cu nanocrystal formation was below 500 ms – the time range of the CCD camera to take a video frame image. After this rapid transition the nanocrystal arrangement did not change anymore. We compared it to regions that were not observed in TEM and found no differences so that the given temperature for crystal formation was not subject to irradiation during the video. We have tried different annealing rates and taken TEM images at different beam currents (which can be easily done by spreading the electron beam) and the results remained the same. In Figure 6 it can be seen that the amorphous material from Cu(hfac)$_2$ turns to nano-composite with Cu nanocrystals embedded in an amorphous carbonaceous matrix. The size ranges from 2 nm to 20 nm for the face centered cubic (fcc) copper nanocrystals. This underlines that post-growth annealing has the potential to achieve one-digit-nanometer sized copper nanocrystals when using a high-resolution electron microscope for smallest dot deposition [44].

Theoretically, annealing a hemispherical FEBID deposit having a radius r_{met} and containing a given weight percentage w_{met} to pure metal would result in a metal hemisphere of radius

$$r_{met} = r_{dep} \cdot \sqrt[3]{w_{met} \frac{\rho_{dep}}{\rho_{met}}}, \qquad (1)$$

with ρ_{met} and ρ_{dep} being the densities of the metal and deposit, respectively. For our deposits from Cu(hfac)$_2$ Equation 1 yields $r_{met} = 0.46 \cdot r_{dep}$ with $w_{met} = 0.35$ (corresponding to the 10 atom % Cu in the as-grown deposit, see

section "As-deposited material"), $\rho_{dep} = 2.5$ g/cm^3 (from [45]) and $\rho_{Cu} = 8.9$ g/cm^3. This means that 1 nm Cu dots could be annealed out of a 2 nm sized hemispherical FEBID material from Cu(hfac)$_2$.

Selected results of earlier in situ TEM annealing experiments within a Philips EM-430 TEM on freestanding FEBID rods obtained from (hfac)Cu(VTMS) are shown in Fsigure 7. Interestingly, the comparison of Figure 7b and Figure 7c shows that the place of Cu nanocrystal precipitation can be controlled by post-irradiation with the high-energy electrons of a TEM in contrast to the experiments with Cu(hfac)$_2$. The Cu crystals segregate around 140 °C inside the carbonaceous matrix when the deposit was exposed to the 300 keV electrons of the TEM during the annealing experiment, probably due to an electron-triggered reticulation of the polymeric carbonaceous matrix. The stronger reticulation of the carbon matrix seems to suppress the long-range mobility of Cu atoms to diffuse to the outside surface. In contrast, irradiation with only 20 keV is not efficient in reticulating the matrix in such a way that out-diffusion is hampered as was observed for (hfac)CuDMB deposits in Figure 5 and for Cu(hfac)$_2$ deposits in Figure 3 and Figure 4.

In contrast, purification by electron beam induced heating of freestanding rods obtained from FEBID with (hfac)CuVTMS [42] gave much larger pure copper crystals (up to 150 nm in size). In comparison to the above results the differences may be explained by invoking an electron stimulated desorption effect which was suggested for FEBID by van Dorp et al. [46] which would facilitate the desorption of carbonaceous fragments and thus the formation of larger copper nanocrystals.

Electrical measurements
Figure 8 shows the typical behavior of a Cu–C FEBID line for a heating/cooling cycle. The as-deposited lines were non-conduc-
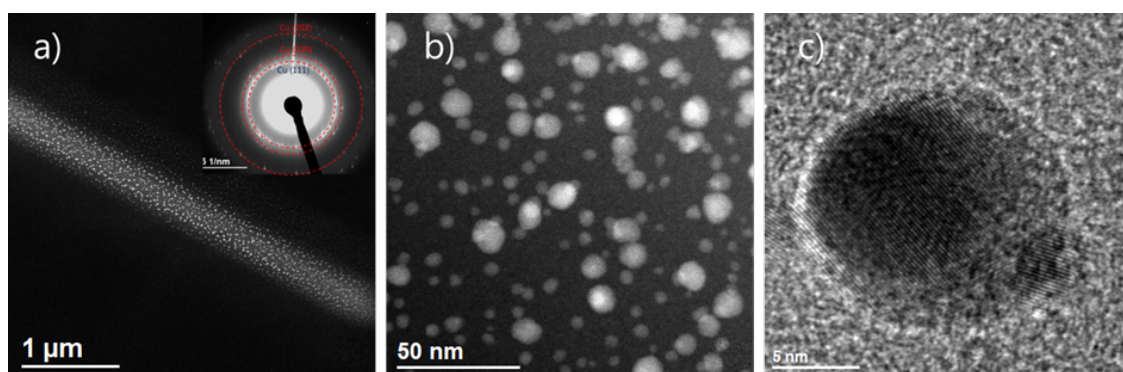
Figure 6: In situ TEM annealing for 10 min at 220 °C on a line deposit from Cu(hfac)$_2$ shown in Figure 2. a) STEM high angle annular dark field (STEM-HAADF) image of Cu nanocrystals forming from the deposit material. b) HAADF image showing distribution of Cu nanocrystals. c) High-resolution TEM (HR-TEM) image of 15 nm sized polycrystalline Cu precipitate. The inset shows the SAD pattern of Cu fcc nanocrystals.
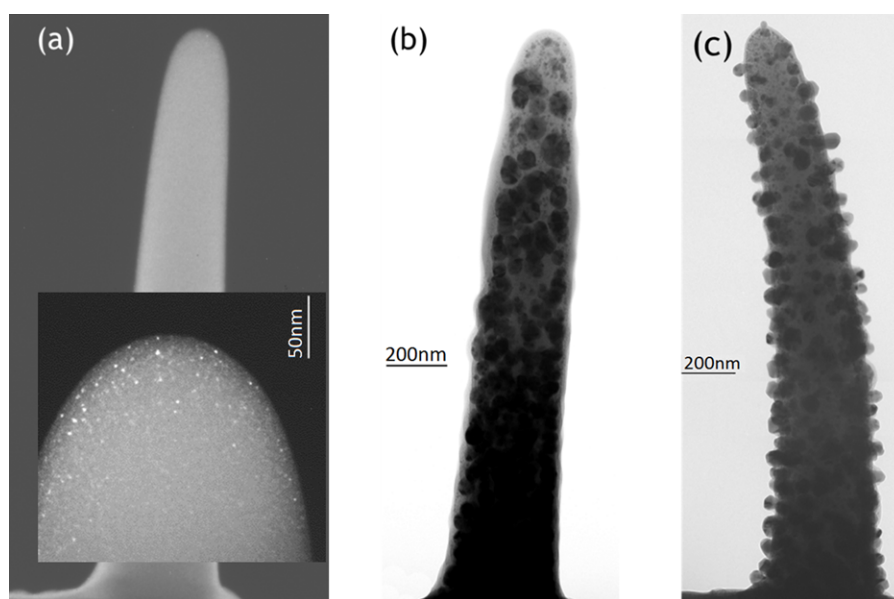
Figure 7: TEM in situ annealing of FEBID rods grown from (hfac)Cu(VTMS). a) Dark field image of an as-deposited freestanding rod. Inset: rod apex with small Cu nanocrystals in carbonaceous matrix. b) Bright-field image of same rod after 270 °C annealing and continuous TEM observation (200 keV). Large Cu nanocrystals form inside the rod. c) Bright field image of another rod not observed during the same annealing process. Cu nanocrystals form at the outside surface of the rod.
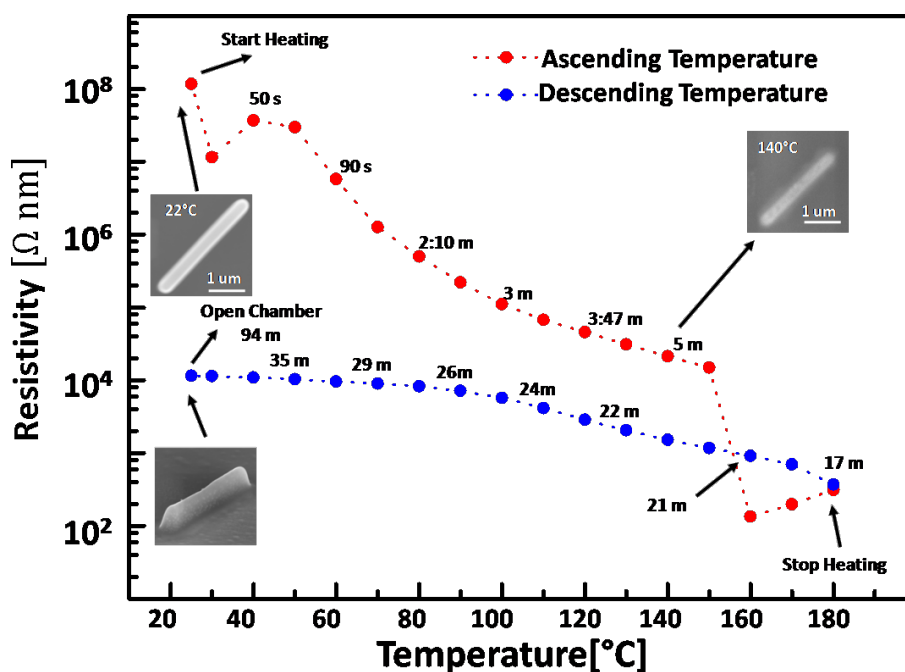
Figure 8: Calculated resistivity from the resistance measurement of a Cu–C line during in situ post-growth heating with a hot plate (red dots) and cooling down (blue dots) inside the SEM chamber. The resistance did not change when opening the chamber. The top SEM images show the morphology changes of an adjacent FEBID line which was observed simultaneously during the in situ resistance measurement.

tive, showing an electrical resistance of few gigaohms at room temperature. After thermal annealing the resistance dropped by four to five orders of magnitude to hundreds of kiloohms. At the current densities, used in the experiments (less than 0.1 MA/cm^2) the migration process of Cu atoms is rather slow. Gazzadi and Frabboni [47] reported grain formation and

electromigration in Pt–C material at current densities approaching 10 MA/cm^2 which is about a factor 100 below our maximum current densities applied. A large resistance drop was observed after nanocrystals precipitated on the surface around 150 °C.

An increase in resistivity of one order of magnitude can be observed upon the cooling cycle from 180 °C to 25 °C. The temperature coefficient for bulk Cu is 0.00386 K^{-1} and would amount to an increase of the resistance by a factor of 1.6 only for the temperature difference of 155 K. The thermally activated transport observed in this case, can be due to the variable range hopping mechanism [48], corresponding to the insulating transport regime for granular materials, as it was observed previously for various FEBID deposits, composed of metallic grains embedded in carbonaceous matrix [49]. More detailed studies are planned to characterize the electronic transport of this material including the question whether the resistance-vs-temperature behavior of the samples would be stable. Here we focused on a proof of concept study.

Conclusion

We have shown that nanostructural changes were induced in Cu–C FEBID material from Cu(I) and Cu(II) precursors upon post-growth annealing causing the segregation and precipitation of Cu nanocrystals. No fundamental differences between laser induced heating and conventional heating in the SEM and TEM with respect to trends and composition values were observed. As deposited the Cu–C FEBID deposits obtained from Cu(hfac)$_2$ were amorphous while nanocomposite deposits were obtained from (hfac)CuVTMS and (hfac)CuDMB. The as-deposited materials were non-conductive. The transition into conductive material as well as the segregation and precipitation of the copper atoms occur upon conventional or laser heating. The surface precipitation of copper nanocrystals upon annealing opens a route for depositing pure Cu nanodot patterns using highly focused electron beams.

Supporting Information

Supporting Information features additional information about the chemical mapping with electron energy loss spectroscopy, the estimation of Cu precipitation on deposit, and the distribution of Cu nanocrystals along the Cu–C lines after conventional and IR laser thermal annealing.

Supporting Information File 1

Additional experimental data.
[http://www.beilstein-journals.org/bjnano/content/supplementary/2190-4286-6-156-S1.pdf]

References

1. Utke, I.; Gölzhäuser, A. *Angew. Chem., Int. Ed.* **2010,** *49,* 9328–9330. doi:10.1002/anie.201002677
2. Utke, I.; Hoffmann, P.; Melngailis, J. *J. Vac. Sci. Technol., B* **2008,** *26,* 1197. doi:10.1116/1.2955728
3. Kolb, F.; Schmoltner, K.; Huth, M.; Hohenau, A.; Krenn, J.; Klug, A.; List, E. J. W.; Plank, H. *Nanotechnology* **2013,** *24,* 305501. doi:10.1088/0957-4484/24/30/305501
4. Huth, M.; Kolb, F.; Plank, H. *Appl. Phys. A* **2014,** *117,* 1689–1696. doi:10.1007/s00339-014-8631-9
5. Gabureac, M.; Bernau, L.; Utke, I.; Boero, G. *Nanotechnology* **2010,** *21,* 115503. doi:10.1088/0957-4484/21/11/115503
6. Gabureac, M. S.; Bernau, L.; Boero, G.; Utke, I. *IEEE Trans. Nanotechnol.* **2013,** *12,* 668–673. doi:10.1109/TNANO.2013.2266733
7. Schwalb, C. H.; Grimm, C.; Baranowski, M.; Sachser, R.; Porrati, F.; Reith, H.; Das, P.; Müller, J.; Völklein, F.; Kaya, A.; Huth, M. *Sensors* **2010,** *10,* 9847–9856. doi:10.3390/s101109847
8. Edinger, K.; Gotszalk, T.; Rangelow, I. W. *J. Vac. Sci. Technol., B* **2001,** *19,* 2856. doi:10.1116/1.1420580
9. Makise, K.; Mitsuishi, K.; Shimojo, M.; Furuya, K. *Nanotechnology* **2009,** *20,* 425305. doi:10.1088/0957-4484/20/42/425305
10. Utke, I.; Jenke, M. G.; Röling, C.; Thiesen, P. H.; Iakovlev, V.; Sirbu, A.; Mereuta, A.; Caliman, A.; Kapon, E. *Nanoscale* **2011,** *3,* 2718. doi:10.1039/C1NR10047E
11. Gavagnin, M.; Wanzenboeck, H. D.; Belić, D.; Bertagnolli, E. *ACS Nano* **2013,** *7,* 777–784. doi:10.1021/nn305079a
12. Fernández-Pacheco, A.; De Teresa, J. M.; Szkudlarek, A.; Córdoba, R.; Ibarra, M. R.; Petit, D.; O'Brien, L.; Zeng, H. T.; Lewis, E. R.; Read, D. E.; Cowburn, R. P. *Nanotechnology* **2009,** *20,* 475704. doi:10.1088/0957-4484/20/47/475704
13. Winhold, M.; Weirich, P. M.; Schwalb, C. H.; Huth, M. *Appl. Phys. Lett.* **2014,** *105,* 162603. doi:10.1063/1.4898819
14. Höflich, K.; Becker, M.; Leuchs, G.; Christiansen, S. *Nanotechnology* **2012,** *23,* 185303. doi:10.1088/0957-4484/23/18/185303
15. Brintlinger, T.; Fuhrer, M. S.; Melngailis, J.; Utke, I.; Bret, T.; Perentes, A.; Hoffmann, P.; Abourida, M.; Doppelt, P. *J. Vac. Sci. Technol., B* **2005,** *23,* 3174. doi:10.1116/1.2130355
16. Kim, S.; Kulkarni, D. D.; Rykaczewski, K.; Henry, M.; Tsukruk, V. V.; Fedorov, A. G. *IEEE Trans. Nanotechnol.* **2012,** *11,* 1223–1230. doi:10.1109/TNANO.2012.2220377
17. Utke, I.; Hoffmann, P.; Berger, R.; Scandella, L. *Appl. Phys. Lett.* **2002,** *80,* 4792. doi:10.1063/1.1489097
18. Belova, L. M.; Hellwig, O.; Dobisz, E.; Dan Dahlberg, E. *Rev. Sci. Instrum.* **2012,** *83,* 093711. doi:10.1063/1.4752225
19. Fernández-Pacheco, A.; Serrano-Ramón, L.; Michalik, J. M.; Ibarra, M. R.; De Teresa, J. M.; O'Brien, L.; Petit, D.; Lee, J.; Cowburn, R. P. *Sci. Rep.* **2013,** *3,* No. 1492. doi:10.1038/srep01492

20. Szkudlarek, A.; Szmyt, W.; Kapusta, C.; Utke, I. *Appl. Phys. A* **2014,** *117,* 1715–1726. doi:10.1007/s00339-014-8751-2

21. Winkler, R.; Szkudlarek, A.; Fowlkes, J. D.; Rack, P. D.; Utke, I.; Plank, H. *ACS Appl. Mater. Interfaces* **2015,** *7,* 3289–3297. doi:10.1021/am508052k

22. Sachser, R.; Reith, H.; Huzel, D.; Winhold, M.; Huth, M. *ACS Appl. Mater. Interfaces* **2014,** *6,* 15868–15874. doi:10.1021/am503407y

23. Stanford, M. G.; Lewis, B. B.; Noh, J. H.; Fowlkes, J. D.; Roberts, N. A.; Plank, H.; Rack, P. D. *ACS Appl. Mater. Interfaces* **2014,** *6,* 21256–21263. doi:10.1021/am506246z

24. Plank, H.; Noh, J. H.; Fowlkes, J. D.; Lester, K.; Lewis, B. B.; Rack, P. D. *ACS Appl. Mater. Interfaces* **2014,** *6,* 1018–1024. doi:10.1021/am4045458

25. Geier, B.; Gspan, C.; Winkler, R.; Schmied, R.; Fowlkes, J. D.; Fitzek, H.; Rauch, S.; Rattenberger, J.; Rack, P. D.; Plank, H. *J. Phys. Chem. C* **2014,** *118,* 14009–14016. doi:10.1021/jp503442b

26. Begun, E.; Dobrovolskiy, O. V.; Kompaniiets, M.; Sachser, R.; Gspan, C.; Plank, H.; Huth, M. *Nanotechnology* **2015,** *26,* 075301. doi:10.1088/0957-4484/26/7/075301

27. Plank, H.; Kothleitner, G.; Hofer, F.; Michelitsch, S. G.; Gspan, C.; Hohenau, A.; Krenn, J. *J. Vac. Sci. Technol., B* **2011,** *29,* 051801. doi:10.1116/1.3622314

28. Plank, H.; Haber, T.; Gspan, C.; Kothleitner, G.; Hofer, F. *Nanotechnology* **2013,** *24,* 175305. doi:10.1088/0957-4484/24/17/175305

29. Weirich, P. M.; Winhold, M.; Schwalb, C. H.; Huth, M. *Beilstein J. Nanotechnol.* **2013,** *4,* 919–926. doi:10.3762/bjnano.4.103

30. Botman, A.; Mulders, J. J. L.; Hagen, C. W. *Nanotechnology* **2009,** *20,* 372001. doi:10.1088/0957-4484/20/37/372001

31. Mulders, J. J. L.; Belova, L. M.; Riazanova, A. *Nanotechnology* **2011,** *22,* 055302. doi:10.1088/0957-4484/22/5/055302

32. Roberts, N. A.; Magel, G. A.; Hartfield, C. D.; Moore, T. M.; Fowlkes, J. D.; Rack, P. D. *J. Vac. Sci. Technol., A* **2012,** *30,* 041404. doi:10.1116/1.4731254

33. Roberts, N. A.; Gonzalez, C. M.; Fowlkes, J. D.; Rack, P. D. *Nanotechnology* **2013,** *24,* 415301. doi:10.1088/0957-4484/24/41/415301

34. Roberts, N. A.; Fowlkes, J. D.; Magel, G. A.; Rack, P. D. *Nanoscale* **2013,** *5,* 408. doi:10.1039/c2nr33014h

35. Temple, D.; Reisman, A. *J. Electrochem. Soc.* **1989,** *136,* 3525. doi:10.1149/1.2096498

36. Chiang, T. P.; Sawin, H. H.; Thompson, C. V. *J. Vac. Sci. Technol., A* **1997,** *15,* 2677. doi:10.1116/1.580942

37. Lee, W. H.; Seo, B. S.; Byun, I. J.; Ko, Y. G.; Kim, J. Y.; Lee, J. G. *J. Korean Phys. Soc.* **2002,** *33,* 107–109.

38. Rosenberg, S. G.; Barclay, M.; Fairbrother, D. H. *ACS Appl. Mater. Interfaces* **2014,** *6,* 8590–8601. doi:10.1021/am501457h

39. Miyazoe, H.; Utke, I.; Kikuchi, H.; Kiriu, S.; Friedli, V.; Michler, J.; Terashima, K. *J. Vac. Sci. Technol., B* **2010,** *28,* 744. doi:10.1116/1.3449808

40. Della Ratta, A. D.; Melngailis, J.; Thompson, C. V. *J. Vac. Sci. Technol., B* **1993,** *11,* 2195. doi:10.1116/1.586455

41. Luisier, A.; Utke, I.; Bret, T.; Cicoira, F.; Hauert, R.; Rhee, S.-W.; Doppelt, P.; Hoffmann, P. *J. Electrochem. Soc.* **2004,** *151,* C590. doi:10.1149/1.1779335

42. Utke, I.; Luisier, A.; Hoffmann, P.; Laub, D.; Buffat, P. A. *Appl. Phys. Lett.* **2002,** *81,* 3245. doi:10.1063/1.1517180

43. Bret, T.; Utke, I.; Gaillard, C.; Hoffmann, P. *J. Vac. Sci. Technol., B* **2004,** *22,* 2504. doi:10.1116/1.1800356

44. Van Dorp, W. F.; van Someren, B.; Hagen, C. W.; Kruit, P.; Crozier, P. A. *Nano Lett.* **2005,** *5,* 1303–1307. doi:10.1021/nl050522i

45. Friedli, V.; Utke, I.; Mølhave, K.; Michler, J. *Nanotechnology* **2009,** *20,* 385304. doi:10.1088/0957-4484/20/38/385304

46. Van Dorp, W. F.; Hansen, T. W.; Wagner, J. B.; De Hosson, J. T. M. *Beilstein J. Nanotechnol.* **2013,** *4,* 474–480. doi:10.3762/bjnano.4.56

47. Gazzadi, G. C.; Frabboni, C. *Appl. Phys. Lett.* **2009,** *94,* 173112. doi:10.1063/1.3119582

48. Beloborodov, I. S.; Lopatin, A. V.; Vinokur, V. M.; Efetov, K. B. *Rev. Mod. Phys.* **2007,** *79,* 469–518. doi:10.1103/RevModPhys.79.469

49. Huth, M.; Porrati, F.; Schwalb, C.; Winhold, M.; Sachser, R.; Dukic, M.; Adams, J.; Fantner, G. *Beilstein J. Nanotechnol.* **2012,** *3,* 597–619. doi:10.3762/bjnano.3.70

Continuum models of focused electron beam induced processing

Milos Toth[*1], Charlene Lobo[1], Vinzenz Friedli[2], Aleksandra Szkudlarek[2,3] and Ivo Utke[2]

Abstract

Focused electron beam induced processing (FEBIP) is a suite of direct-write, high resolution techniques that enable fabrication and editing of nanostructured materials inside scanning electron microscopes and other focused electron beam (FEB) systems. Here we detail continuum techniques that are used to model FEBIP, and release software that can be used to simulate a wide range of processes reported in the FEBIP literature. These include: (i) etching and deposition performed using precursors that interact with a surface through physisorption and activated chemisorption, (ii) gas mixtures used to perform simultaneous focused electron beam induced etching and deposition (FEBIE and FEBID), and (iii) etch processes that proceed through multiple reaction pathways and generate a number of reaction products at the substrate surface. We also review and release software for Monte Carlo modeling of the precursor gas flux which is needed as an input parameter for continuum FEBIP models.

Review
Introduction to continuum models of focused electron beam induced processing (FEBIP)

Continuum FEBIP models enable the simulation of process rates that govern focused electron beam induced etching (FEBIE), deposition (FEBID) [1-16] and surface functionalization [17] techniques. They are typically used to simulate growth rates and nanostructure geometries as a function of experimental parameters, and to help elucidate the underlying growth mechanisms. Continuum FEBIP models are comprised of differential equations for the rates of change of concentrations

of all surface-adsorbed species thought to be involved in the deposition or etch kinetics. The rate equations are functions of time and space, and require specification of the molecular properties of each adsorbate and the electron flux profile(s) at the solid–vacuum interface. Simple continuum FEBIP models can be solved analytically, yielding governing laws delineating the so-called "reaction-rate" and "mass transport" limited process regimes, and resolution scaling laws. Numerical models can account for adsorbate diffusion and enable modeling of processes such as simultaneous FEBIE and FEBID performed using a mixture of precursor gases. Here we provide software that can be used to simulate a wide range of processes reported in the FEBIP literature, and review the underlying continuum FEBIP models (recent general reviews of FEBIP can be found in [4,10,18-21]). We begin with a discussion of the reaction rate limited regime and the most common continuum model input parameters: initial adsorbate coverage, electron flux profile and the gas flux distribution produced by a capillary-style gas injection system. We then cover simple continuum models that are valid in the reaction rate limited regime (where net adsorbate transport via surface diffusion is negligible) and can be used to model FEBIP performed using continuous and pulsed electron beams, physisorbed and chemisorbed precursor molecules, gas mixtures, and multiple reaction products. Finally, we cover a number of models that account for surface diffusion and can be used to model FEBIP in both the reaction and mass transport limited regimes. Throughout, we emphasize the underlying assumptions and limitations inherent to each model.

Before beginning our discussion, we note that the terms "rate", "concentration" and "flux" are always used to describe quantities with units of reciprocal time [s^{-1}], reciprocal area [$Å^{-2}$] and their product [$Å^{-2}s^{-1}$], respectively. For example, the concentration of adsorbate species 'a', N_a, their desorption rate k_a and desorption flux $N_a k_a$ have units of [adsorbates/$Å^2$], [molecules/s] and [molecules/$Å^2$/s], respectively. Frequently used symbols in this review are defined in Table 1. The term "growth" is applied to both FEBIE and FEBID (positive and negative growth rates refer to the growth of deposits and etch pits, respectively). We limit our discussion to FEBIP performed using a stationary, continuous or pulsed, radially symmetric electron beam (i.e., models implemented in cylindrical coordinates). Examples of models of scanned beams can be found in [22-24].

Reaction rate limited growth regime

In order to reach clear conclusions it is often desirable to perform simulations and experiments under simplified conditions where one or more processes are negligible. In the case of FEBIP models, a useful simplification occurs when the net transport of adsorbates via surface diffusion is negligible. This

Table 1: Guide to commonly used symbols.

symbol	units	definition
Θ	$Å^{-2}$	adsorbate coverage
Λ	$Å^{-2}s^{-1}$	adsorption flux
Ω	$Å$ or nm	standard deviation of a Gaussian beam
δ	$Å$	molecule diameter
κ	s^{-1}	desorption attempt frequency
κ_D	$Å^{-2}s^{-1}$	diffusion coefficient pre-factor
λ	m	mean free path
σ	$Å^2$	cross-section
τ	s^{-1}	residence time
A	$Å^2$	adsorbate area
D	$Å^2s^{-1}$	diffusion coefficient
E	eV	energy
F or J	$Å^{-2}s^{-1}$	gas molecular flux
N	$Å^{-2}$	adsorbate concentration
P	Pa or mbar	gas pressure
T	K	substrate temperature
T_g	K	gas temperature
V	$Å^3$ or nm^3	volume
d	μm	GIS capillary diameter
f	$Å^{-2}s^{-1}$	electron flux
h	$Å$ or nm	height
k	s^{-1}	desorption rate
k_B	$eV·K^{-1}$	Boltzmann's constant
n_0	$Å^{-2}$	maximum (monolayer) adsorbate concentration
s	N/A	sticking probability

condition can be met by performing FEBIP in the so-called reaction rate limited growth regime (also called the electron-limited growth regime) where the extent of adsorbate depletion caused by electrons is negligible [4,10,19-21]. The strict definition of reaction rate limited growth is that the electron-induced dissociation rate is much smaller than the sum of the adsorption rate and the thermal desorption rate, i.e., using the symbols defined below and in Table 1, for adsorbate species 'a', $\sigma_\alpha f \ll s_a F_a / N_{a_0} + k_a$. Conversely, the mass transport limited growth regime (also called the adsorbate-limited growth regime) is defined as $\sigma_\alpha f \gg s_a F_a / N_{a_0} + k_a$. In the mass transport limited regime, the magnitude of the electron flux is sufficiently high to cause significant depletion of precursor adsorbates, and adsorbate diffusion into the area irradiated by electrons makes an important contribution to the growth rate.

In practice, the reaction rate limited regime can be identified simply by measuring or simulating the steady state growth rate as a function of electron flux, as illustrated in Figure 1 (in the figures, numerical values are excluded from axis labels when the plots are used to illustrate general trends that occur under a wide range of FEBIP conditions). Here, the linear portion of the

curve corresponds to the reaction rate limited growth regime. In the mass transport limited growth regime, the deposit/pit shapes can provide information on the role of diffusion in the FEBIP process. Inclusion of diffusion in continuum FEBIP models adds a layer of complexity to the modelling and to interpretation of the model outputs. It is necessary only if diffusion is a major contribution to the growth rate. We will discuss models that incorporate diffusion in a self-contained section below, but will limit the majority of our discussion to diffusion-less models.
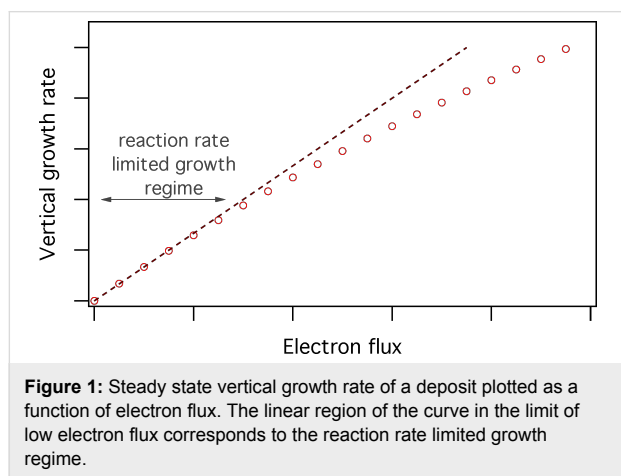
Figure 1: Steady state vertical growth rate of a deposit plotted as a function of electron flux. The linear region of the curve in the limit of low electron flux corresponds to the reaction rate limited growth regime.

Initial adsorbate coverage

FEBIP models require specification of the initial concentration of surface-adsorbed precursor molecules N_{a_0}, i.e., the steady-state concentration of adsorbates in the absence of electron irradiation. N_{a_0} can be found by solving for the difference between the flux of molecules adsorbing from and returning to the gas phase. In the gas phase, the molecule flux is given by:

$$F_a = P_a \big/ \left(2\pi m_a k_B T_g\right)^{1/2} , \qquad (1)$$

where P_a is the pressure of the precursor gas for adsorbate 'a', m_a is the mass of a gas molecule, k_B is Boltzmann's constant and T_g is the gas temperature. The simplest case of gas-molecule adsorption onto a substrate surface is that of physisorption, described by a single potential well at the surface as shown in Figure 2. The flux Λ_a of precursor molecules physisorbing to vacant surface sites is given by:

$$\Lambda_a = s_a F_a \left(1 - \Theta\right) , \qquad (2)$$

where s_a is the sticking coefficient (in the limit of zero surface coverage), and Θ is the adsorbate coverage, i.e., the fraction of surface sites occupied by physisorbed gas molecules:

$$\Theta = A_a N_a , \qquad (3)$$

where A_a is the area of a surface site occupied by adsorbate 'a', and $1/A_a$ is the maximum possible concentration of species 'a'.
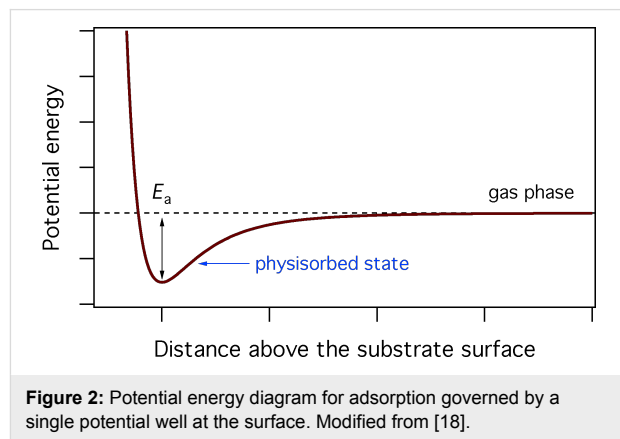
Figure 2: Potential energy diagram for adsorption governed by a single potential well at the surface. Modified from [18].

We note that Equation 2 describes non-activated Langmuir adsorption of a single molecular species 'a'. The Langmuir model limits the surface coverage to one monolayer (hence the term $(1 - \Theta)$ in Equation 2), and can be modified to account for other adsorption behavior such as multilayer adsorption and thermally activated chemisorption. We also note that most FEBIP models assume that s_a is independent of temperature.

The thermal desorption rate k_a of the physisorbed species 'a' is given by:

$$k_a = 1 / \tau_a = \kappa_a e^{-E_a/k_B T} , \qquad (4)$$

where τ_a is the adsorption time (i.e., adsorbate residence time), κ_a is the desorption attempt frequency, E_a the desorption energy, (i.e., the depth of the potential well shown in Figure 2), and T is the temperature of the substrate surface. The thermal desorption flux is given by $N_a k_a$, and the adsorbate concentration is found by solving

$$\frac{dN_a}{dt} = \Lambda_a - N_a k_a \qquad (5)$$

for $N_a(t)$:

$$N_a(t) = \frac{\left(1 - e^{-(s_a F_a A_a + k_a)t}\right) s_a F_a}{s_a F_a A_a + k_a} . \qquad (6)$$

In Equation 6, $t = 0$ represents the time at which the gas flux F_a is turned on in the model, i.e., the time at which the gas pres-

sure is changed from 0 to P_a. A typical time-evolution of N_a in the absence of electron irradiation is shown in Figure 3. As $t \to \infty$, the surface coverage reaches a steady-state equilibrium value, N_{a_0}, which is the initial value that is input into FEBIP models (in which $t = 0$ represents the time at which the electron flux is turned on):

$$N_{a_0} = \frac{s_a F_a}{s_a F_a A_a + k_a} . \tag{7}$$
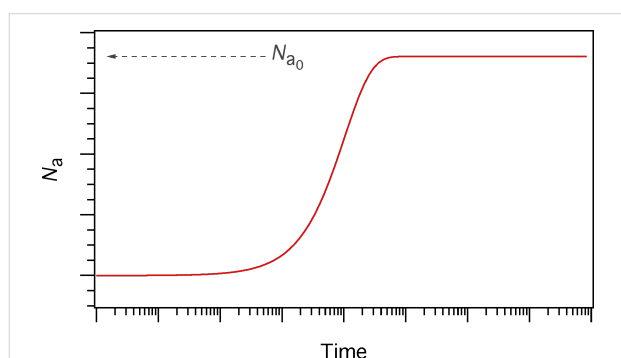
Figure 3: Adsorbate concentration (N_a) versus time in the absence of electron irradiation (here, $N_a = 0$ at $t = 0$). N_{a_0} is the steady state adsorbate concentration in the absence of electron irradiation, which is used as the initial adsorbate concentration input into FEBIP models. $N_a(t)$ and N_{a_0} are given by Equation 6 and Equation 7, respectively.

Electron flux profile

Spatially-resolved FEBIP models require specification of the electron flux profile $f(r)$. Focused electron beams are usually approximated by a Gaussian function:

$$f(r) = f_0 \exp\left(\frac{-r^2}{2\Omega^2}\right), \tag{8}$$

where Ω is the standard deviation (i.e., full width at half maximum, FWHM $= 2\sqrt{2\ln 2}\,\Omega$) of the Gaussian beam. Defocused beams typically have a tophat shape that can be approximated by:

$$f(r) = \frac{f_0}{1 + \exp\left(\beta\left(\frac{r}{\xi} - 1\right)\right)}, \tag{9}$$

where f_0 is the (maximum) flux at the beam axis ($r = 0$), β defines the abruptness of the edge of the tophat, and ξ is the beam radius. Tophat beams are useful for quantitative analyses and modeling of experimental data because they are easy to measure and control with a high degree of accuracy [2,3,6,25,26].

A Gaussian and two tophat electron flux profiles are shown in Figure 4. These profiles can be used to approximate those encountered in FEBIP. Actual flux profiles have contributions from primary, backscattered and secondary electrons, each of which has a unique spatial profile and a unique energy distribution [19].
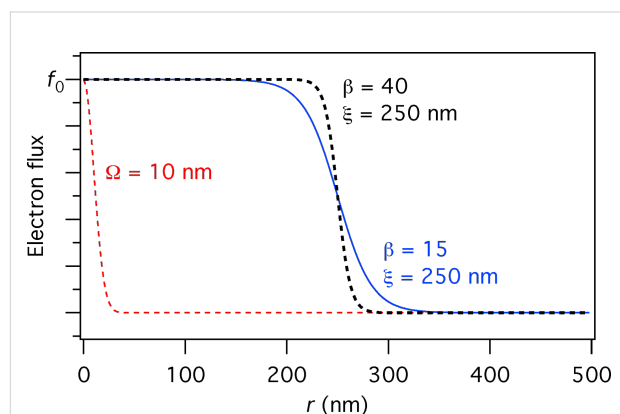
Figure 4: Gaussian electron flux profile ($\Omega = 10$ nm) and two tophat flux profiles with a radius of 250 nm ($\beta = 15$ and 40). All three profiles are normalized to f_0, the electron flux at the beam axis.

Gas flow from a capillary-style gas injection system (GIS)

FEBIP precursor gases are injected into a specimen chamber using one of two methods. In the first method, the entire vacuum chamber, or a sub-chamber [6] is filled with a precursor gas, as is done in environmental electron microscopy [27-30]. Such vacuum systems can be configured so that the gas pressure is uniform across the substrate surface, and can be measured accurately by conventional pressure gauges. However, in the vast majority of FEBIP setups, a gas injection capillary is used to inject the precursor gas into a chamber that is pumped continuously by a high-vacuum pumping system. The low conduction of the capillary makes it the element that limits the flow rate and shapes the flux profile of such gas injection systems. The capillaries are useful because they simultaneously assure a high local molecule flux at the substrate surface, and a low vacuum chamber background pressure, as required for robust operation of the vacuum system. However, a disadvantage of a capillary-style GIS is that the gas pressure varies dramatically throughout the chamber, and the gas pressure at the substrate surface cannot be measured accurately using conventional pressure gauges. Hence, in this section, we describe a Monte-Carlo simulator developed at Empa (the "GIS simulator") for calculating gas pressure distributions generated by a capillary-style GIS. The code can be used to calculate the gas molecule flux at the beam impact point on the substrate surface (which is an input parameter to all FEBIP models).

Gas molecule impingement rates on the substrate have lateral distributions that depend on the capillary nozzle geometry, the angle and distance between capillary and substrate, and the molecule flow regime. The GIS simulator code enables the selection of some pre-defined nozzle geometries, capillary inner and outer diameters, angles and distances to the substrate, and either molecular or transient flow regime. By default it maps the impingement distribution on planar substrates, the molecule flux along the tube, and the angular nozzle effusion distribution. The code was validated by capillary injection experiments for both flow regimes [31,32].

Due to the Monte Carlo code implementation, the GIS simulator does not account for gas pressure gradients inside the capillary and above the substrate. The code can be used in an executable version or an editable version (http://www.empa.ch/febipcode) to include specific shadow effects by non-planar substrate geometries (such as deposits grown by FEBID), surface gas phase collisions, or other capillary geometries.

Flow regimes

To make a correct choice of the flow regime for the simulation one needs to determine the mean free path λ between molecule–molecule collisions and the Knudsen number (the ratio of λ to the capillary diameter d):
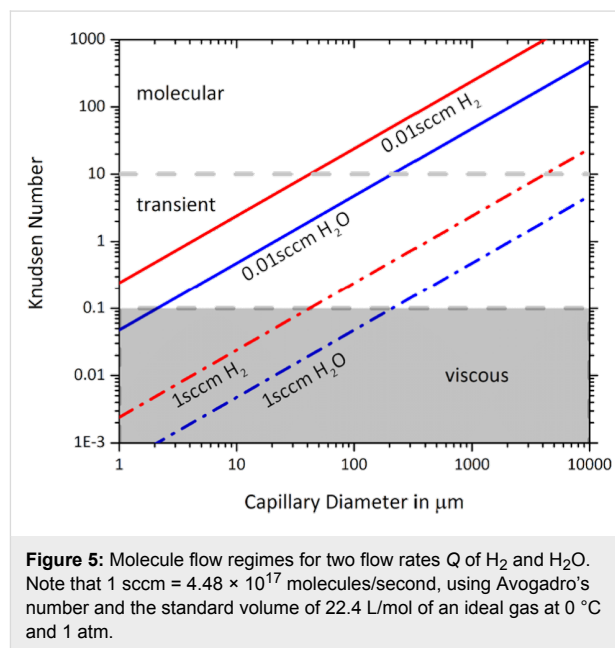
$$Kn = \frac{\lambda}{d}. \tag{10}$$

The Knudsen number specifies the ratio of wall collisions to molecule–molecule collisions. A value of $10 < Kn < \infty$ signifies rare flow conditions under which the molecule gas flow distribution is determined predominantly by tube wall collisions (molecular flow regime). In the range $0.1 < Kn < 10$ collisions between molecules become more important for shaping the flow (transient flow regime). When $Kn < 0.1$ the flow becomes viscous and can be treated by continuum models; this regime is not covered by the GIS simulator.

The calculation of the mean free path along a capillary is not trivial as the pressure P along the capillary is not constant. There will be a pressure gradient along capillaries directing net flow from the precursor reservoir ($P \approx$ vapour pressure) to the vacuum chamber ($P \leq 10^{-4}$ mbar) [33]. The commonly known relation $\lambda = kT_g \left(\sqrt{2\pi} \delta^2 P_a \right)^{-1}$, where δ is the molecule diameter and other variables are as defined in Equation 1, can only be used if the pressure close to the capillary exit is known.

Mean free paths for a given GIS can be obtained by monitoring the precursor consumption rate Q (molecules per unit time) experimentally and calculating the mean free path using

$$\lambda = \frac{1}{8} \sqrt{\frac{RT_g}{\pi M_a}} \frac{1}{\delta^2} \frac{d^2}{Q}, \tag{11}$$

where R is the ideal gas constant and M is the molar mass [33]. The Knudsen number can then be calculated by inserting Equation 11 into Equation 10. The consumption rate of the precursor can be monitored by measuring its mass or volume change due to evaporation during FEBIP. Alternatively, mass flow controllers can be used to supply a defined flow rate Q (sccm). Figure 5 shows the dependence of the Knudsen number on the pipe diameter for two flow rates of H_2 and H_2O. At a fixed flow rate and capillary diameter, the Knudsen numbers and mean free paths scale with $1/\left(\delta^2 \sqrt{M}\right)$. Values for a few molecules are given in Table 2 together with their vapour pressure and monolayer adsorbate concentration $n_0 = 1/A_a = 1.154\delta^{-2}$.

Figure 5: Molecule flow regimes for two flow rates Q of H_2 and H_2O. Note that 1 sccm = 4.48×10^{17} molecules/second, using Avogadro's number and the standard volume of 22.4 L/mol of an ideal gas at 0 °C and 1 atm.

To estimate an upper limit for the impingement rate, consider a substrate placed directly in front of a capillary with an exit area of 1 mm^2 and a flow rate of 1 sccm. This results in a molecule flux $F_a \approx 4.5 \times 10^{19}$ molecules cm^{-2}s^{-1} leaving the capillary, or $F_a \approx 5 \times 10^5$ monolayers per second (taking 10^{14} cm^{-2} as monolayer coverage). At a minimum, impingement rates of FEBIP molecules should be greater than the impingement rates of residual gases (at least one monolayer per second at a background pressure of 10^{-6} mbar). Of course, the molecule flux

Table 2: Summary of molecule diameters (δ), molar masses (M), vapour pressures P_{vap} and monolayer adsorbate concentrations n_0 of selected FEBIP precursors. The latter were calculated using $n_0 = 1.154\delta^{-2}$.

precursor	M [g/mol]	δ [Å]	n_0 [nm^{-2}]	P_{vap} [Pa/T]	P_{vap} ref.
Me$_3$PtCpMe	319.17	7.8[a]	1.9	19/31 °C	[34]
TEOS:Si(OEt)$_4$	208.33	8.1[b]	1.8	172/25 °C	[36]
XeF$_2$	169.29	4.5[b]	5.7	598/25 °C	[37]
Me$_2$Au(tfac)	310.03	3.5[a]	9.4	7.3/23 °C	[38]
W(CO)$_6$	351.90	6.8[b]	2.5	3.5/25 °C	[39]
Co$_2$(CO)$_8$	341.95	7[a]	2.4	0.6...16/20 °C[c]	[40]
Cu(hfac)$_2$	477.65	8.0[b]	1.8	0.4/25 °C[d]	[41]
(hfac)Cu(VTMS)	370.83	8.6[b]	1.6	10/23 °C	[42]
[(PF$_3$)$_2$RhCl]$_2$	628.48	5.7[a]	3.6	7.5/23 °C	[38]
O$_2$	16	3.7[e]	8.4	—	—
H$_2$	2	2.7[c]	15.8	—	—
H$_2$O	18	3.5[b]	9.4	2330/20 °C	[44]

[a]Longest dimension of molecule.
[b]The molecule size is determined from the compound density ρ according to $\delta = 1.122(M/(\rho N_A))^{1/3}$ where N_A is Avogadro's constant [35].
[c]Co$_2$(CO)$_8$ can disproportionate spontaneously in vacuum [40].
[d]Cu(hfac)$_2$ exists as dihydrate Cu(hfac)$_2$·2H$_2$O if not dried in vacuum with little effect on the vapour pressure [41].
[e]Apparent diameters from [43].

will rapidly decrease with distance between the capillary and the substrate.

Wall uptake

The GIS simulator incorporates an uptake factor for capillary wall collisions. Setting this value to zero means that all molecules colliding with the wall will immediately desorb; setting the value to 1 means that all molecules colliding with the wall will adsorb permanently (i.e., only molecules without wall collisions will exit the capillary). In most cases the uptake factor can be set to zero, as molecule condensation on capillary walls is normally avoided through the pressure gradient and keeping the reservoir at a temperature that is lower than or equal to that of the capillary walls. However, some organometallic molecules can spontaneously decompose in contact with the wall material and thus provide a surface for continuous autocatalytic decomposition through successive molecule–wall collisions. (Metal carbonyls are known for autocatalytic decomposition but data quantifying the uptake coefficients is sparse. A change in colour of the capillary points to such a mechanism). Analogous to the atomic layer deposition process [45], a more likely scenario is that at room temperature the molecules decompose partially via chemisorption upon collisions with unoccupied adsorption sites on the wall. This process is self-limiting after a short transient time during which all wall sites are occupied and the wall is passivated for further molecule decomposition.

Nozzle geometries

Two nozzle geometries are incorporated in the GIS simulator [31], and users can implement other geometries. Here we release the source code of version 1.5 containing the geometries shown in Figure 6 for straight capillaries and for bevelled capillaries with access holes. This C++ code is the base of the executable GIS simulator tool downloadable at http://www.empa.ch/febipcode. We would like to note that the code is not professionally commented nor written but has been checked against analytical solutions (for simple geometries) and against experiments. The current version of the code does not consider desorption of molecules from the substrate.

Simulation method

The physics behind the GIS simulator is described in detail in [31,33,46] and we give only a brief summary here. The code is based on the so called test-particle Monte Carlo method, which works in the molecular and transient flow regimes. The molecule flux distribution is obtained as a function of the nozzle geometry and the arrangement of nozzle and substrate. Molecule trajectories are computed consecutively for 10^6 to 10^7 molecules. This approach is strictly only valid for molecular flow conditions where molecule trajectories are independent of each other, and collisions occur only with the inner tube wall. However, it was shown experimentally [31] and by comparison with direct simulation Monte Carlo [33] that the test-particle Monte Carlo method with intermolecular collisions gives excellent results in the following way (points 3 and 4 are simplifications, which can be changed by the user if required):

1. Transient flow simulations can be performed by setting the mean free path $\lambda = d \cdot Kn$ inside the entire capillary. The mean free paths should be calculated from precursor

Figure 6: Illustration of the two capillary nozzle geometries implemented in the GIS simulator. Left: straight capillary; right: bevelled capillary. Modified from [31].
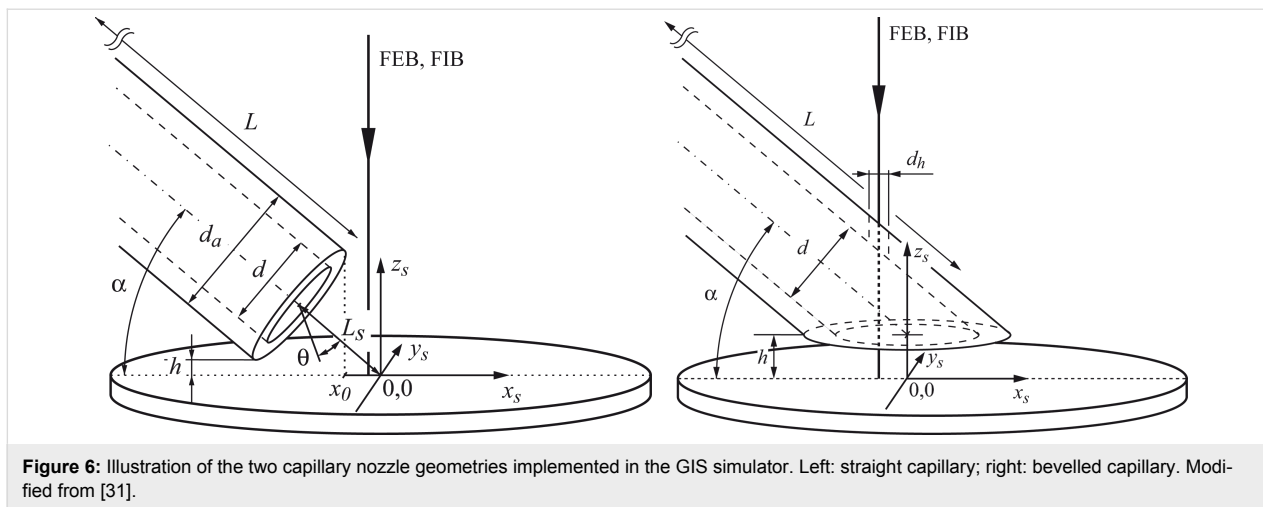
consumption measurements using Equation 11. The flow regime prevailing near the end of the capillary exit will then be entered correctly into the simulation.

2. Wall collisions are implemented such that the molecules leave the wall with a cosine distribution in space, while molecule–molecule collisions are implemented as a uniform angular distribution. The capillary entry distribution is implemented as a cosine point source. The implementation of these angular distributions of wall and molecule collisions was shown to be correct by independent experiments [31,32].

3. Outside of the nozzle the Knudsen number is set to infinity, i.e., molecules follow straight trajectories from the last collision inside the capillary until they hit the substrate (i.e., there are no molecule–molecule collisions outside the tube).

4. Consecutive trajectories inside the vacuum chamber are not taken into account (molecule desorption is neglected).

The capillary length must be entered into the simulation. For long capillaries this is an enormous computational effort. A

Figure 7: Precursor flux distributions at the substrate under molecular flow conditions for conical nozzles with cone angles, θ, varying from 0° (straight tube) to 30°. The (0,0) position denotes the upper edge of the nozzle. J_{tot} is the total molecule flow leaving the nozzle exit and the color code indicates the molecule fraction J/J_{tot}. The cone geometries are shown to illustrate which areas are covered and hence inaccessible by the electron beam.

reduced capillary length L_r can be entered instead, still giving accurate results. For molecular flow conditions, the spatial distribution of impinging molecules on the substrate is not significantly altered for lengths $L_r > 15d$. For transient flow conditions, the reduced length depends on λ with $L_r = 3\lambda$ to 5λ [31,33].

Simulation examples with the GIS simulator

It is most useful to know how the nozzle geometry and the arrangement of the capillary with respect to the substrate influences the precursor flux at the substrate. The dependence of precursor flow on nozzle geometry (straight nozzle, bevelled nozzle with FEB access hole, closed capillary with FEB access holes), capillary angle, and shadowing by 3D objects have been studied by Friedli et al. [31,33]. More recently, it was shown that certain FEBIP scan strategies also lead to shadowing effects which can cause disruptions in surface flatness [23]. A specific simulation of a gas-flow distribution on a cantilever-based mass sensor enabled the estimation of the residence time of Me$_3$PtCpMe on SiO$_2$ [47]. With the released code the reader can include new nozzle geometries or substrate morphologies, for example a conical nozzle geometry as shown in Figure 7. With respect to the straight tube geometry the conical geometries are less practical for FEBIP in the molecular flow regime: Although cones "focus" the exiting molecules, they laterally reduce the maximum impinging flux area, physically cover the maximum flux area, and reduce the maximum impinging flux value slightly as shown by the J/J_{tot} contours. This behavior can be understood from the cosine-law redistribution of molecule collisions with the inner tube wall dominating the exiting precursor distribution in the molecular flow regime in contrast to the viscous flow experienced daily in water taps. Nonetheless, keeping the inner tube geometry straight and making the outer geometry conical could solve some space restrictions in the scanning electron microscope or allow to bring the nozzle closer to the substrate to increase the molecule impingement rate.

Single gas species FEBIP model: etching or deposition

In the following sections, we outline continuum FEBIP models that can be utilized to simulate a wide range of experiments reported in the FEBIP literature. We start with the simple case of a precursor gas comprised of a single molecular species "a" (i.e., an etch or deposition precursor) that physisorbs to the substrate surface. In this case, the continuum FEBIP model is based on an expression for the rate of change of the adsorbate concentration N_a at each point r on the substrate surface. The expression for $\partial N_a/\partial t$ is obtained by extending Equation 5 to account for the dissociation of adsorbates by electrons [16,19]:

$$\frac{\partial N_a}{\partial t} = \Lambda_a - N_a k_a - \frac{\partial N_\alpha}{\partial t}. \tag{12}$$

This equation is a sum of fluxes representing gas molecule arrival at the surface through adsorption (Λ_a), adsorbate removal through thermal desorption ($-N_a k_a$), and adsorbate conversion to fragment species through electron induced dissociation ($-\partial N_\alpha/\partial t$). In Equation 12, $t = 0$ represents the time at which electron irradiation is activated in the model, and the initial adsorbate concentration N_{a_0} is given by Equation 7.

Most models of FEBIP assume that the adsorbate dissociation flux, $\partial N_\alpha/\partial t$, is proportional to the product of the electron flux f and N_a:

$$\frac{\partial N_\alpha}{\partial t} = n_\alpha \sigma_\alpha f N_a, \tag{13}$$

where n_α is the number of fragments α generated per dissociation event, and σ_α is the effective cross-section [3,18] for the generation of fragments that volatilize the substrate (in FEBIE) or deposit onto the substrate (in FEBID).

The steady state adsorbate concentration can be found by solving Equation 12 in the limit $t \rightarrow \infty$:

$$N_{a_\infty} = \frac{s_a F_a}{s_a F_a A_a + k_a + f \sigma_\alpha}. \tag{14}$$

Substituting N_{a_∞} into Equation 13 gives the steady state growth rate $\partial N_{\alpha_\infty}/\partial t$. The vertical growth rate $\partial h/\partial t$, which is easily measured experimentally, is proportional to $\partial N_{\alpha_\infty}/\partial t$:
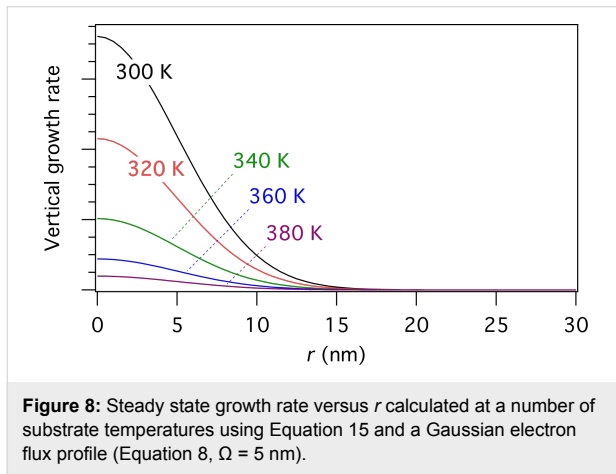
$$\frac{\partial h}{\partial t} = \iota V_D \frac{\partial N_{\alpha_\infty}}{\partial t}, \tag{15}$$

where h is the deposit height (or etch pit depth), ι is ± 1 for deposition and etching, respectively, and V_D is the volume of a single molecule removed from or added to the substrate in the etch or deposition reaction.

The electron flux f can either be fixed at f_0, or specified by an r-dependent function such as Equation 8 or Equation 9. Setting f to f_0 is justified when simulating the growth rate or the deposit height (etch pit depth) at the beam axis ($r = 0$). We emphasize that the above equations are valid only in the reaction rate limited growth regime where net transport of adsorbates through diffusion is negligible. We also note that electron-stimulated desorption (ESD) [48-51] is assumed to be negligible. This assumption is typically justified because, for most adsorbates, the ESD cross-section σ_E lies in the range from 10^{-7} to

10^{-2} Å^2 [50] (i.e., in general, $\sigma_E << \sigma_\alpha$). However, if necessary, ESD can be incorporated in the above FEBIP model simply by adding the term $(-\sigma_E f N_a)$ to Equation 12 [52].

Equation 15 can be used to calculate FEBIP growth rates as a function of experimental parameters such as the precursor gas pressure, electron flux and the substrate temperature. For example, Figure 8 shows a set of spatially resolved steady-state vertical growth rates calculated using a Gaussian electron flux profile and substrate temperatures of 300, 320, 340, 360 and 380 K. The growth rate decreases exponentially with temperature due to an increase in the thermal desorption rate k_a (given by Equation 4).

Figure 8: Steady state growth rate versus *r* calculated at a number of substrate temperatures using Equation 15 and a Gaussian electron flux profile (Equation 8, Ω = 5 nm).

Dimensionless FEBIP models

We now introduce a number of dimensionless parameters, originally employed by Utke et al. [15], which are useful for describing adsorbate kinetics in FEBIP [1] and giving concise scaling laws for the lateral resolution of the FEBIP process.

Irradiative depletion $\tilde{\tau}$ is a dimensionless parameter that quantifies the adsorbate concentration at the beam centre relative to the non-irradiated area. It is proportional to f_0 and can be expressed as [53]:

$$\tilde{\tau} = 1 + f_0 \sigma_a \tau_{out,a} . \tag{16}$$

The *effective residence* time in the absence of electron irradiation (or outside the irradiated area) $\tau_{out,a}$ is given by:

$$\tau_{out,a} = \frac{1}{1 / \tau_a + s_a F_a / n_0} , \tag{17}$$

where τ_a is given by Equation 4, and n_0 is the maximum possible adsorbate concentration (corresponding to one monolayer) in the absence of electron irradiation (i.e., $n_0 = 1/A_a$).

The steady-state concentration of adsorbates under an electron beam, given by Equation 14, and the steady-state vertical growth rate defined by Equation 15 can now be reformulated as:

$$N_{a_\infty} = \frac{N_{a_0}}{1 + \overline{f}(\tilde{\tau} - 1)} = \frac{N_{a_0}}{\tilde{k}} , \tag{18}$$

$$\frac{\partial h}{\partial t} = \imath s_a F_a V_a \frac{\tilde{k} - 1}{\tilde{k}} . \tag{19}$$

In the above, $\overline{f} = f / f_0$ is a dimensionless (normalized) version of the Gaussian or tophat electron electron flux profile given by Equation 8 or Equation 9, respectively, and $\tilde{k}$ is given by:

$$\tilde{k} = 1 + \overline{f}(\tilde{\tau} - 1) = 1 + f \sigma_a \tau_{out,a} . \tag{20}$$

The lateral resolution can be quantified by the dimensionless parameter $\tilde{\varphi}$, expressed as the ratio of the diameter of the deposit (FWHM$_D$) and the electron beam (FWHM):

$$\tilde{\varphi} = \frac{\text{FWHM}_D}{\text{FWHM}} . \tag{21}$$

In the case of negligible surface diffusion, $\tilde{\varphi}$ can be derived analytically yielding the $\tilde{\varphi}$-*vs*-$\tilde{\tau}$ *scaling law of FEBIP resolution* for stationary Gaussian [15] and tophat electron beams:

$$\tilde{\varphi}_{Gauss} = \sqrt{\log_2 (\tilde{\tau} + 1)} , \tag{22}$$

$$\tilde{\varphi}_{tophat} = \frac{\ln(2\exp(-\beta) + \tilde{\tau})}{\beta} + 1 . \tag{23}$$

The resolution scaling behavior defined by the above equations is shown in Figure 9. In the limit of very low irradiative depletion ($\tilde{\tau} \to 1$) the resolution parameter is equal to 1, giving the highest possible FEBIP resolution (i.e., the smallest possible deposit size in the case of FEBID). In other words, the reaction limited (electron-limited) regime gives better lateral resolution than the mass transport limited (adsorbate-limited) regime. Deposits generated by tophat beams exhibit a less pronounced dependency of lateral resolution on irradiative depletion than those generated by Gaussian beams, and the dependence of $\tilde{\varphi}$ on $\tilde{\tau}$ is a function of the blurring parameter β (see Equation 9). However, tophat profiles typically have a much larger beam diameter 2ξ compared to the FWHM of a Gaussian.
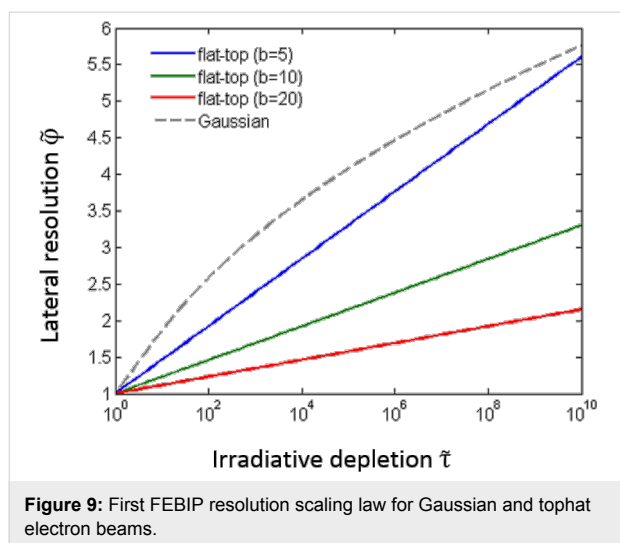
Figure 9: First FEBIP resolution scaling law for Gaussian and tophat electron beams.

Pulsed exposure: To illustrate the use of dimensionless parameters in FEBIP models, we consider the case of FEBIP performed using a pulsed, Gaussian electron beam. Specifically, we consider the adsorbate kinetics during an electron pulse, under the assumption that that the surface is replenished entirely between consecutive electron pulses. When the electron beam is turned on, the adsorbate concentration N_a initially decays with time due to electron induced dissociation. The decay rate depends on the effective residence time $\tau_{a,out}$ and the irradiative depletion parameter $\tilde{\tau}$. The resulting time-evolution of N_a is given by the solution to Equation 12, which can be expressed as:

$$N_a\left(t\right) = N_{a_0}\left[\frac{1}{\tilde{k}} + \left(1 - \frac{1}{\tilde{k}}\right)\exp\left(-\frac{\tilde{k}}{\tau_{a,out}}t\right)\right] = N_{a_0}\,\overline{n}(t). \quad (24)$$

The corresponding vertical growth rate is proportional to $N_a(t)$ and the electron flux, and is given by:

$$\frac{\partial h}{\partial t} = \iota s_a F_a V_a\left(\tilde{k} - 1\right)\overline{n}. \quad (25)$$

The lateral size of the growing structure or etch pit will evolve in time, yielding the *$\tilde{\varphi}$-vs-t law of pulsed FEBIP resolution,* expressed as the lateral resolution $\tilde{\varphi}$, (neglecting surface diffusion) versus the electron beam exposure time t [1]:

$$\tilde{\varphi}_{Gauss}\left(\tilde{\tau}, t\right) \cong \sqrt{\log_2\left(2 + \frac{\tilde{\tau} - 1}{1 + \tau_{a,out}/t}\right)}. \quad (26)$$

In the limit $t \to 0$, $\tilde{\varphi}_{Gauss}\left(\tilde{\tau}, t\right) \to 1$. In the steady state ($t \to \infty$) this converges to the scaling law given by Equation 22.

We note that Equation 8 and Equation 9 for the beam profile do not account for lateral contributions of backscattered and forward scattered electrons as well as their generated secondary electrons to the final shape of the deposit or etch pit. The above model also does not account for the change of those contributions on the developing three-dimensional pillar and etch-pit geometry. These simplifications limit the applicability of the resolution scaling laws given by Equation 22, Equation 23, and Equation 26 as well as Equation 79 and Equation 80 to aspect ratios of roughly 1 to 4 for deposits and etch pits. A more detailed discussion on the applicability range can be found in [10]. For high-aspect ratio structures either a full Monte Carlo electron trajectory approach can be chosen [54] or the continuum equations outlined in our present work need to be solved on a curvilinear reference surface, see [13] and [55].

Multiple gas species FEBIP model: Simultaneous etching and deposition

Deposition and etching arising from electron-induced dissociation of multiple adsorbed species is important in a number of experimental processes. Deliberate use of a deposition and etch precursor gas mixture, as shown in Figure 10, is often advantageous, such as in the deposition of high purity materials using a FEBID precursor and an oxygen-containing background gas [56-63], or a mixture of two FEBID precursors [4,8,64-66]. Unintentional deposition of carbonaceous films through electron-activated cross linking of hydrocarbon contaminants is a common problem in many etch processes [6,9,14].
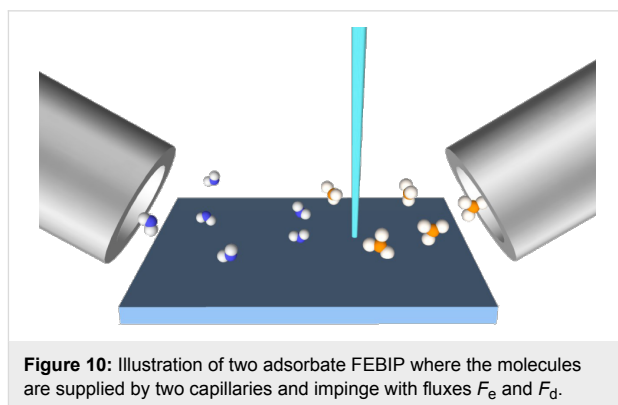
Figure 10: Illustration of two adsorbate FEBIP where the molecules are supplied by two capillaries and impinge with fluxes F_e and F_d.

Simultaneous FEBID and FEBIE can be simulated using models such as those described in [11], with adjustment to account for system-specific details such as the surface site competition behavior of the etch and deposit precursor molecules, adsorbate–adsorbate interactions, and whether the etch precursor can volatilize all or only some fraction of the deposited material. A specific example of this is H_2O-mediated FEBIE of deposits formed from organometallic precursors, where only the deposited carbon (and not the metal) is etched.

Here, we illustrate how simultaneous etching and deposition can be incorporated into a continuum FEBIP model for the case of a mixture of H_2O and $C_{10}H_{22}$ as the precursors for etching and deposition of carbon, respectively [11]. In this model, we assume that both etch and deposition precursor adsorbates (denoted by the subscripts "e" and "d", respectively) physisorb to the substrate surface (Figure 2) in a competitive process, with the total surface coverage Θ being limited to 1 ML. The fluxes and coverages of the two species are given by the following set of Equation 27–Equation 31:

$$F_e = P_e \Big/ \big(2\pi m_e k_B T_g\big)^{1/2} \ , \qquad (27)$$

$$F_d = P_d \Big/ \big(2\pi m_d k_B T_g\big)^{1/2} \ , \qquad (28)$$

$$\Lambda_e = s_e F_e \left(1 - \Theta\right), \qquad (29)$$

$$\Lambda_d = s_d F_d \left(1 - \Theta\right), \qquad (30)$$

$$\Theta = A_e N_e + A_d N_d \ , \qquad (31)$$

Here, Equation 27 and Equation 28 are directly analogous to Equation 1, Equation 29 and Equation 30 are analogous to Equation 2, and Equation 31 is equivalent to Equation 3, modified to account for the fact that the adsorbates "e" and "d" physisorb to the surface and compete for the same surface sites. Growth rates can be found by solving differential equations for the rate of change of the concentration of the species "e", "d" and "D", where the latter denotes molecules that are deposited as a result of FEBID:

$$\frac{\partial N_e}{\partial t} = \Lambda_e - N_e k_e - \frac{\partial N_\varepsilon}{\partial t} \ , \qquad (32)$$

$$\frac{\partial N_d}{\partial t} = \Lambda_d - N_d k_d - \frac{\partial N_\delta}{\partial t} - \frac{\partial N_\varepsilon}{\partial t} \sigma_r N_d \ , \qquad (33)$$

$$\frac{\partial N_D}{\partial t} = \frac{\partial N_\delta}{\partial t} - \frac{\partial N_\varepsilon}{\partial t} \left(1 - \sigma_r N_d\right) \sigma_{rD} N_D \ , \qquad (34)$$

$$\frac{\partial h}{\partial t} = V_D \frac{\partial N_D}{\partial t} \ . \qquad (35)$$

Equation 32 and Equation 33 are analogous to Equation 12, modified to account for the fact that FEBIE can volatilize the adsorbates "d" (i.e., the flux $(\partial N_\varepsilon/\partial t)\sigma_r N_d$ represents FEBIE of the deposition precursor adsorbates). Equation 34 accounts

for the simultaneous deposition of carbon through FEBID $(\partial N_\delta/\partial t)$ and volatilization of the deposit via EBIE $[(\partial N_\varepsilon/\partial t)(1 - \sigma_r N_d)\sigma_{rD} N_D]$, where $(\partial N_\varepsilon/\partial t)\sigma_r N_d$ discounts those etch precursor fragments ε that are consumed in volatilizing the deposition precursor adsorbates "d", and N_D must be capped at $1/A_d$ so that only molecules in the top monolayer of the deposit are available for volatilization by the fragments ε. The reaction cross-section σ_r (and σ_{rD}) accounts for the effectiveness of collisions between the etch precursor fragments ε and the adsorbates "d" (or deposited molecules "D") in contributing to etching [11]. Equation 35 is the vertical growth rate, and is directly analogous to Equation 15.

The fluxes $\partial N_\varepsilon/\partial t$ and $\partial N_\delta/\partial t$ represent electron-induced dissociation of the adsorbates "e" and "d", respectively, and are given by:

$$\frac{\partial N_\varepsilon}{\partial t} = n_\varepsilon \sigma_\varepsilon f N_e \ , \qquad (36)$$

$$\frac{\partial N_\delta}{\partial t} = n_\delta \sigma_\delta f N_d \ , \qquad (37)$$

where the symbols have the same meanings as in Equation 13. The thermal desorption rates k_e and k_d have the same functional form as Equation 4:

$$k_e = 1/\tau_e = \kappa_e e^{-E_e/k_B T} \ , \qquad (38)$$

$$k_d = 1/\tau_d = \kappa_d e^{-E_d/k_B T} \ . \qquad (39)$$

Initial concentrations of the species "e" and "d" (i.e., N_{e0} and N_{d0}, respectively) can be found by solving Equation 32 and Equation 33 for the case of zero electron flux. The resulting time-evolution of surface coverage is more complex than that of the single gas species model shown in Figure 3, due to the nature of the surface site competition effect implemented in Equation 29–Equation 31. This is illustrated in Figure 11a for the case where $P_e \gg P_d$ and $E_e \ll E_d$. Initially, N_e increases much more rapidly than N_d because $P_e \gg P_d$ (and hence $F_e \gg F_d$). However, at times greater than ca. 10^{-4} s the increase in N_d causes a corresponding decrease in N_e because the two species compete for the same surface sites and $E_d \gg E_e$ (and hence $\tau_d \ll \tau_e$).

The utility of the simultaneous FEBIE/FEBID model defined by Equation 32, Equation 33 and Equation 34 is illustrated in Figure 11b, which shows a number of deposits simulated using a Gaussian beam (given by Equation 8), with a maximum flux
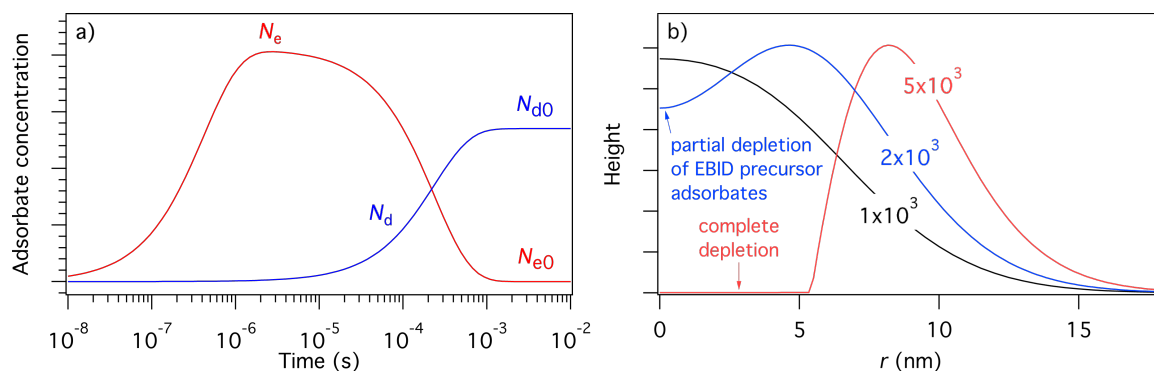
Figure 11: (a) Adsorbate concentrations N_e and N_d versus time, calculated in the absence of electron irradiation (here, $N_e = N_d = 0$ at $t = 0$). N_{e0} and N_{d0} are the steady-state adsorbate concentrations in the absence of electron irradiation, which are used as the initial adsorbate concentrations input into FEBIP models defined by Equation 27–Equation 37. (b) Deposit geometries simulated using a Gaussian electron beam with a standard deviation (Ω) of 5 nm and a maximum flux (f_0) of 1×10^3, 2×10^3 and 5×10^3 Å^{-2}s^{-1}. (Etch species = H_2O, deposition species = $C_{10}H_{22}$, $P_e = 1$ Torr, $P_d = 0.01$ Torr, $s_e = 1$, $s_d = 0.4$, $E_e = 0.56$ eV, $E_d = 1.0157$ eV, $\kappa_e = \kappa_d = 10^{16}$ s^{-1}, $\sigma_\varepsilon = \sigma_\delta = 1$ Å^2, $\sigma_r = \sigma_{rD} = A_d = 74$ Å^2, $T = T_g = 300$ K. All other model input parameters were the same as in [11].)

(f_0) of 1×10^3, 2×10^3 and 5×10^3 Å^{-2}s^{-1}. At the lowest electron flux ($f_0 = 1 \times 10^3$ Å^{-2}s^{-1}), the deposit shape is approximately Gaussian because the extent of adsorbate depletion by the beam is low. At the intermediate flux ($f_0 = 2 \times 10^3$ Å^{-2}s^{-1}), the central region of the deposit contains an indent caused by preferential depletion of the FEBID precursor adsorbates "d". At the highest electron flux ($f_0 = 5 \times 10^3$ Å^{-2}s^{-1}), FEBIE dominates in the central region of the deposit due to complete depletion of "d". The preferential depletion of species "d" is a direct consequence of the slower replenishment rate caused by the fact that $P_e >> P_d$. The difference between the replenishment rates of "e" and "d" is illustrated in Figure 11a (at times shorter than ca. 10^{-5} s).

We emphasize that the changes in deposit geometry seen in Figure 11b are caused by a competition between simultaneous FEBIE and FEBID processes, and are not caused by adsorbate diffusion (which is ignored by Equation 27–Equation 37). This competition and the resulting phenomenon of electron flux controlled switching between etching and deposition have been discussed in detail in [11,14]. The additional effects of adsorbate diffusion can be investigated using a version of the above model that incorporates diffusion (discussed below).

Multiple adsorption states: Thermally activated chemisorption

The FEBID growth rate typically decreases with increasing substrate temperature (as illustrated by Figure 8) due to thermal depopulation of the physisorbed state shown in Figure 2. However, recently it was shown that activated chemisorption can give rise to a more complex dependence of the growth rate on T due to thermal population and depopulation of chemisorbed states [5,67]. The simplest case of a system that can undergo physisorption and activated chemisorption can be described by the potential energy diagram shown in Figure 12 [68], comprised of a physisorbed state (denoted "p") and a chemisorbed state (denoted "c") separated by an activation barrier for conversion between these states. The respective physisorption and chemisorption potential wells have depths E_p and E_c, and the activation barrier has height E_{conv}.
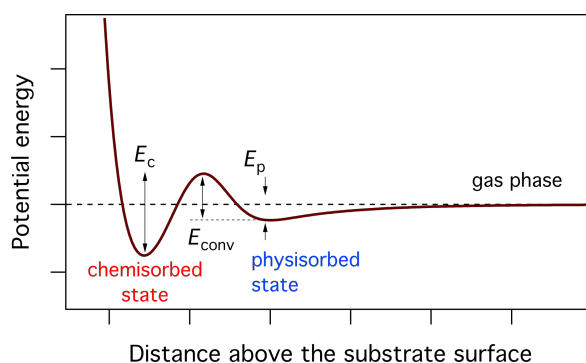
Figure 12: Potential energy diagram for the case of chemisorption governed by a potential well of depth E_c and an activation barrier of height E_{conv}. Also shown is a physisorption potential well of depth E_p. Modified from [5].

Chemisorption is typically a dissociative process in which the activation barrier represents the energy needed to fragment the precursor molecule. For example, O_2 chemisorbs onto numerous surfaces through the thermally activated reaction $O_2 \rightarrow 2O$, where O_2 is in the gas phase or in the physisorbed state, and the two O atoms are in the chemisorbed state. Similarly, XeF_2 can fluorinate many surfaces through decomposition pathways that generate chemisorbed F [17,69-71], and the FEBID precursor tetraethyl orthosilicate (TEOS, $Si(OC_2H_5)_4$)

chemisorbs onto SiO_2 as a mixture of $(SiO)_2Si(OC_2H_5)_2$ and $(SiO)Si(OC_2H_5)_3$ [72-74].

Chemisorption of gas phase precursor molecules can take place if their thermal energy is sufficiently high to surmount the barrier $E_{conv} - E_p$ (see Figure 12):

$$s_c = s_0 e^{-\left(E_{conv} - E_p\right)/k_B T_g} , \qquad (40)$$

where s_c is the sticking coefficient for activated sticking of gas molecules into the chemisorbed state (in the limit of zero surface coverage), s_0 is the preexponential factor (i.e., the sticking coefficient for the limiting case of $E_{conv} - E_p = 0$), and T_g is the temperature of the precursor gas. Similarly, molecules in the physisorbed state can surmount E_{conv} by gaining thermal energy from the substrate and populate the chemisorbed state at a rate k_{conv}:

$$k_{conv} = \kappa_{conv} e^{-E_{conv}/k_B T} . \qquad (41)$$

This pathway is more relevant to FEBID than chemisorption from the gas phase (i.e., Equation 40) because FEBID is typically implemented as a cold-wall deposition technique, whereby T_g is dominated by the temperature of the capillary used to deliver the precursor gas, and the substrate temperature T is used to control growth kinetics.

The thermal desorption rates of physisorbed (k_p) and chemisorbed species (k_c) are given by:

$$k_p = \kappa_p e^{-E_p/k_B T} , \qquad (42)$$

$$k_c = \kappa_c e^{-E_c/k_B T} . \qquad (43)$$

Activated chemisorption can be incorporated into the continuum FEBID model by accounting for the above transitions between the gas phase, physisorbed and chemisorbed states by replacing Equation 12 with a pair of equations for the rate of change of concentration of physisorbed molecules ($\partial N_p/\partial t$) and chemisorbed molecules ($\partial N_c/\partial t$) [5]:

$$\frac{\partial N_p}{\partial t} = \Lambda_p - N_p k_p - \Lambda_{conv} - N_p \sigma_p f , \qquad (44)$$

$$\frac{\partial N_c}{\partial t} = \Lambda_c - N_c k_c + \Lambda_{conv} - N_c \sigma_c f , \qquad (45)$$

and by replacing Equation 13 with:

$$\frac{\partial N_\alpha}{\partial t} = f n_p \sigma_p N_p + f n_c \sigma_c N_c , \qquad (46)$$

where n_p and n_c are the number of fragments generated per dissociation event of the physisorbed and chemisorbed molecules, respectively, assuming that both contribute to FEBID. Hence, the vertical growth rate is given by:

$$\frac{\partial h}{\partial t} = \iota V_D \frac{\partial N_\alpha}{\partial t} , \qquad (47)$$

which assumes that the volumes of molecules deposited by the dissociation of physisorbed and chemisorbed adsorbates are both equal to V_D.

The fluxes Λ_p, Λ_c and Λ_{conv} correspond to physisorption from the gas phase, chemisorption from the gas phase, and transitions from the physisorbed to chemisorbed states, respectively:

$$\Lambda_p = s_p \left(1 - s_c\right) F_a \left(1 - \Theta_p\right), \qquad (48)$$

$$\Lambda_c = s_c F_a \left(1 - \Theta_c\right), \qquad (49)$$

$$\Lambda_{conv} = N_p k_{conv} \left(1 - \Theta_c\right), \qquad (50)$$

where F_a is the flux of precursor molecules "a". The term $(1 - s_c)$ excludes gas molecules that are trapped in the physisorption potential well, and Θ_p and Θ_c are the coverages of physisorbed and chemisorbed adsorbates, each limited to 1 ML by:

$$\Theta_p = A_p N_p , \qquad (51)$$

$$\Theta_c = A_c N_c . \qquad (52)$$

We note that energetic electrons can cause partial decomposition of precursor molecules and hence induce transitions from the physisorbed to the chemisorbed state. This effect is neglected here, but can be incorporated into FEBIP models as in [17] for the case of fluorination caused by decomposition of XeF_2.

The initial concentration of physisorbed $\left(N_{p_0}\right)$ and chemisorbed $\left(N_{c_0}\right)$ species is found by solving Equation 44 and Equation 45 for the case of zero electron flux. An example of the pressure dependence of N_{p_0} and N_{c_0} is shown in Figure 13a
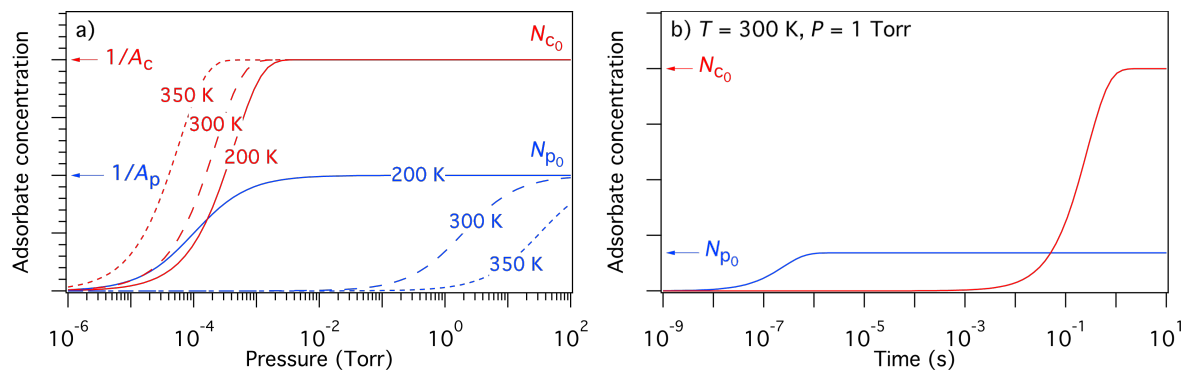
**Figure 13:** (a) Steady state concentrations of physisorbed $\left(N_{p_0}\right)$ and chemisorbed $\left(N_{c_0}\right)$ adsorbates versus pressure, calculated for the case of zero electron flux, and substrate temperatures of 200, 300 and 350 K. (b) Time-dependence of N_p and N_c calculated for a substrate temperature of 300 K and a precursor gas pressure of 1 Torr. (In all cases, gas temperature = 300 K; E_p = 510 meV, E_{conv} = 1.415 eV, E_c = 855 meV; f = 0; $A_p = 2A_c$ and n_c = 2 to represent a dissociative chemisorption process in which the precursor molecule fragments into two chemisorbed molecules. All other model input parameters were the same as in [5].)

for a particular set of the energies E_p, E_{conv} and E_c (corresponding to the chemisorption of TEOS onto SiO_2 [5]), and substrate temperatures of 200, 300 and 350 K. The residence times of physisorbed and chemisorbed adsorbates are given by k_p^{-1} and k_c^{-1}, which are governed by the depths of the chemisorption and physisorption potential wells shown in Figure 12. At a substrate temperature of 350 K, chemisorbed states are rapidly populated through the physisorbed state (Equation 41), but depopulate slowly as $E_{conv} \ll E_c$ (i.e., $k_{conv} \gg k_c$). Conversely, physisorbed states are rapidly depopulated because E_p is smaller than both E_{conv} and E_c. Consequently, N_{c_0} saturates at the monolayer limit of $1/A_c$ at a much lower pressure than N_{p_0} saturates at the monolayer limit $1/A_p$. At the lower substrate temperatures of 300 and 200 K, k_{conv}, k_p and k_c are reduced through Equation 41, Equation 42 and Equation 43, yielding the adsorption isotherms shown in Figure 13a.

It is important to note that the rate of chemisorption is always limited by the activation barrier shown in Figure 12. Hence, the rate at which physisorbed states are populated (and replenished during FEBID) is always greater than the rate at which chemisorbed states are populated. This is illustrated by the plots of $N_p(t)$ and $N_c(t)$ shown in Figure 13b where, starting with a depopulated surface, the physisorbed species take ca. 10^{-6} s to populate the surface and reach a steady state, whereas it takes the chemisorbed species ca. 1 s to reach a steady state.

Equation 47 can be used to calculate the temperature-dependence of FEBID, as shown in Figure 14 for the case of TEOS [5]. The contribution to growth rate made by physisorbed adsorbates (i.e., $f\sigma_p N_p$ in Equation 46) decreases with increasing T due to an increase in the thermal desorption rate k_p (and hence a decrease in the adsorbate coverage N_p). The chemisorption

component (i.e., $f\sigma_c N_c$ in Equation 46) is negligible at room temperature because $E_{conv} \gg k_B T_g$ and $E_c - E_p \gg k_B T$. It is characterized by a peak produced by thermal conversion of adsorbates from the physisorbed to the chemisorbed state (i.e., the low-temperature tail of the peak) and desorption from the chemisorbed state (i.e., the high-temperature tail), respectively. The general temperature dependence seen in Figure 14 (i.e., a decrease in the physisorption component followed by a peak caused by chemisorption) exists only if $k_{conv} \ll k_p \ll k_c$ [5]. A practical benefit of performing FEBID at elevated temperatures (whereby, in this case, $T \geq 350$ K) is that the deposits have much higher purity than those fabricated at room temperature [5].
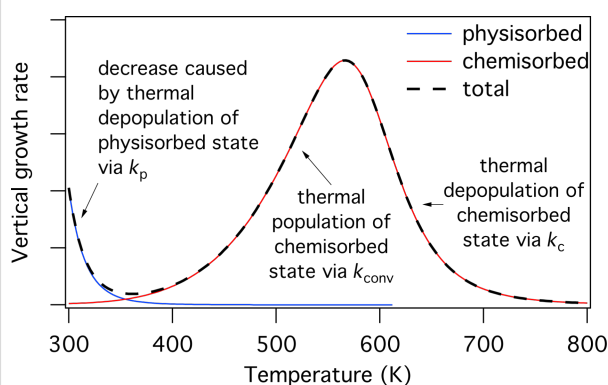

Figure 14: Steady-state vertical growth rate versus substrate temperature for a precursor that undergoes activated chemisorption described by the potential energy digram shown in Figure 12. The blue and red curves show contributions arising from electron induced dissociation of physisorbed and chemisorbed adsorbates, respectively. Modified from [5].

Role of multiple reaction products in electron beam induced etching

Etch processes such as XeF_2-mediated FEBIE of SiO_2 [12] and NF_3 FEBIE of Si [2] proceed through multiple chemical pathways that involve a number of reaction products. Here, we use the case of NF_3 FEBIE of Si [2] to illustrate how such processes can be incorporated in continuum FEBIE models.

FEBIE of Si using NF_3 as the precursor gas involves the reaction products SiF, SiF_2, SiF_3, and SiF_4, each of which can be dissociated by electrons, or can desorb from the substrate surface. For example, SiF_2 can either gain F to form SiF_3, dissociate to form SiF and F, or it can desorb (and hence give rise to etching by removing a Si atom):

$$SiF_2 + F \rightarrow SiF_3,$$
$$SiF_2 + e^- \rightarrow SiF + F + e^-,$$
$$SiF_2 \rightarrow SiF_2 \ [gas].$$
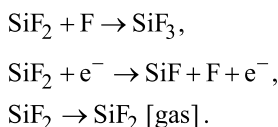
Multi-step FEBIE reactions can be modeled using a set of differential rate equations that account for each molecular species at the substrate surface, which in this case are the NF_3 precursor adsorbates (denoted by "a"), F radicals *(α)*, and the reaction products SiF, SiF_2, SiF_3, and SiF_4:

$$\frac{\partial N_a}{\partial t} = \Lambda_a - N_a k_a - \frac{\partial N_\alpha}{\partial t}, \qquad (53)$$

$$\frac{\partial N_\alpha}{\partial t} = n_\alpha \sigma_\alpha f N_a, \qquad (54)$$

The symbols in Equation 53 and Equation 54 represent the same quantities as the corresponding symbols in Equation 12 and Equation 13 (see Table 1). In Equation 55, N_n ($n = 1$–4) represents the concentration of SiF_n molecules, σ_r is the cross-section for the electron-induced scission of the Si–F bond, and k_n is the desorption rate of SiF_n:

$$k_n = \kappa_n e^{-E_n/k_B T}, \qquad (56)$$

where E_n is the binding energy of SiF_n. N_η is the concentration of surface sites at which F can bond to a Si atom, and Θ_η is the

coverage of surface sites occupied by F (see below in Figure 15):

$$N_\eta = \sum_{m=0}^{3} N_m, \qquad (57)$$

$$\Theta_\eta = \sum_{n=1}^{4} \frac{1}{n} A_{Si} N_n. \qquad (58)$$

The term $(1/n)A_{Si}$ limits the concentration of fluorinated Si atoms to one monolayer, m is an integer with lower and upper limits of 0 and 3 because an unfluorinated Si atom (designated by $m = 0$) can react with F to form SiF, whereas SiF_4 (designated by $m = 4$) cannot gain an additional fluorine atom. The integer n is bound by 1 and 4 because the total coverage of sites occupied by F must account for SiF, SiF_2, SiF_3 and SiF_4 species. N_0 (the concentration of unfluorinated Si atoms at the surface) is given by:

$$A_{Si} N_0 = 1 - A_{Si} N_{Si}, \qquad (59)$$

where A_{Si} is the area of a single Si surface site, and N_{Si} is the concentration of fluorinated Si sites:
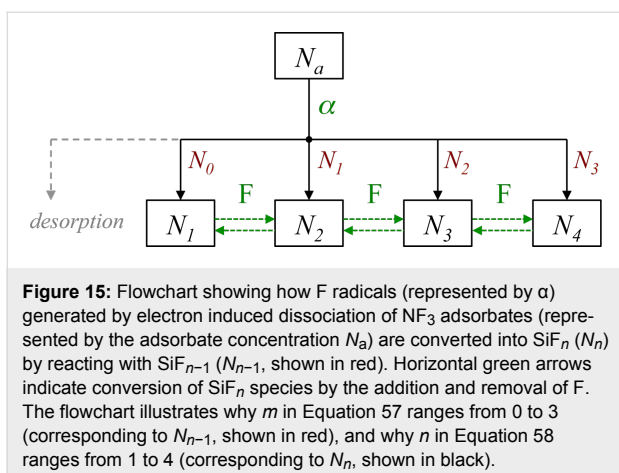
$$\frac{\partial N_{Si}}{\partial t} = \sum_{n=1}^{4} \frac{\partial N_n}{\partial t}. \qquad (60)$$

The vertical etch rate is governed by the desorption rate of SiF_n molecules:

$$\frac{\partial h}{\partial t} = -V_\gamma \sum_{n=1}^{4} N_n k_n. \qquad (61)$$

Models such as the above (Equation 53–Equation 61) are typically based on a number of simplifying assumptions in addition to those made in simple FEBID models. This particular model assumes that all available F radicals generated by electron-induced dissociation of NF_3 are converted to SiF_n by reacting with SiF_{n-1}, and that any surplus fluorine atoms desorb as shown in Figure 15 (the desorption is assumed instant, hence

$$\frac{\partial N_n}{\partial t} = \begin{cases} \dfrac{\partial N_\alpha}{\partial t} \dfrac{N_{(n-1)}}{N_\eta} \left(1 - \Theta_\eta\right) + \sigma_r f N_{(n+1)} - N_n \left(k_n + \dfrac{\partial N_\alpha}{\partial t} \dfrac{1}{N_\eta} \left(1 - \Theta_\eta\right) + \sigma_r f\right), & n = 1...3, \\[4mm] \dfrac{\partial N_\alpha}{\partial t} \dfrac{N_{(n-1)}}{N_\eta} \left(1 - \Theta_\eta\right) - N_n \left(k_n + \sigma_r f\right), & n = 4. \end{cases} \qquad (55)$$

Figure 15: Flowchart showing how F radicals (represented by α) generated by electron induced dissociation of NF_3 adsorbates (represented by the adsorbate concentration N_a) are converted into SiF_n (N_n) by reacting with SiF_{n-1} (N_{n-1}, shown in red). Horizontal green arrows indicate conversion of SiF_n species by the addition and removal of F. The flowchart illustrates why m in Equation 57 ranges from 0 to 3 (corresponding to N_{n-1}, shown in red), and why n in Equation 58 ranges from 1 to 4 (corresponding to N_n, shown in black).
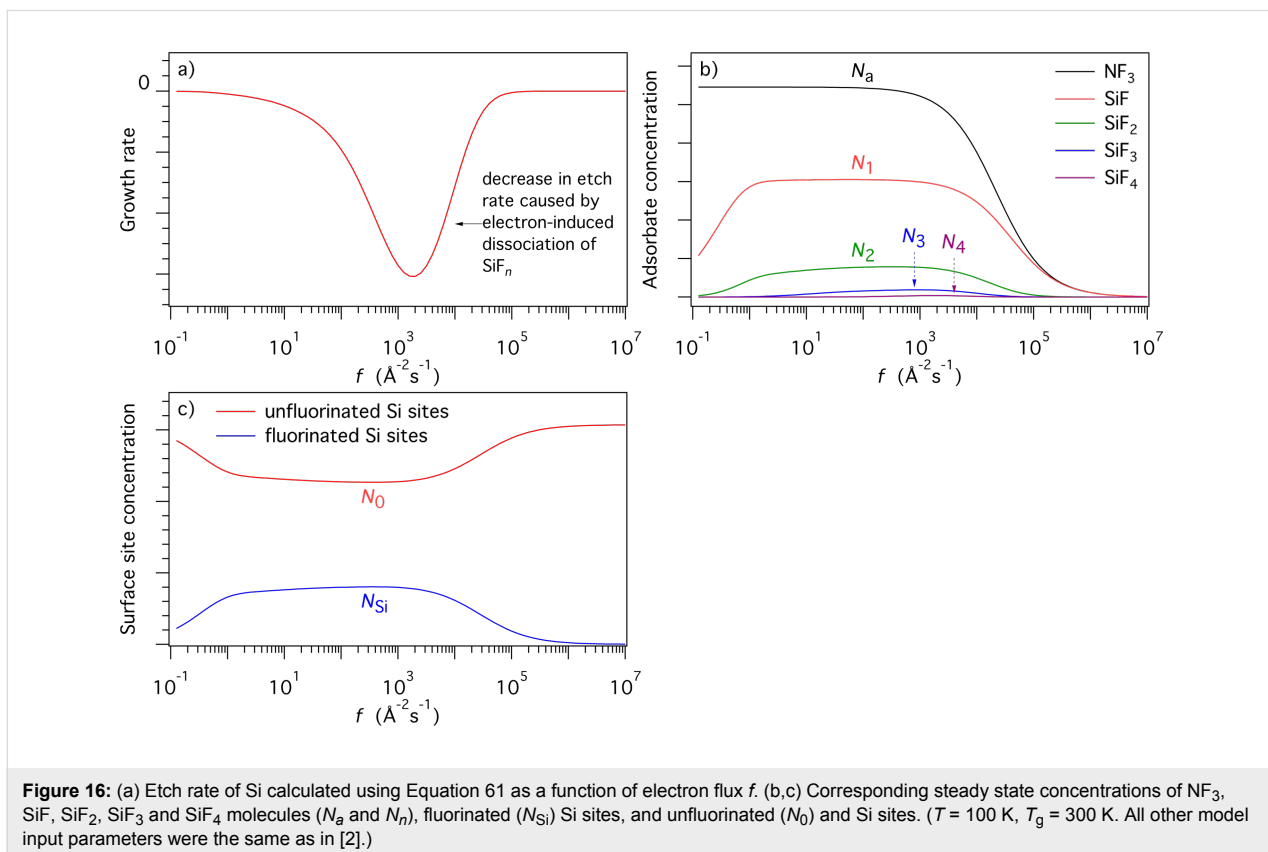
the absence of a desorption flux in Equation 54). The probability of a reaction between F and each species SiF_{n-1} is assumed equal and the total F coverage is limited to 1 ML, hence the term $(N_{n-1}/N_\eta)(1 - \Theta_\eta)$ in Equation 55 that governs the partitioning of the available F radicals illustrated by the flow chart shown in Figure 15. It is also assumed that σ_r is independent of n. Hence, the flux $\sigma_r f N_{n+1}$ represents the creation of SiF_n through electron-induced dissociation of SiF_{n+1}, and $-N_n\sigma_r f$ the consumption of SiF_n through electron-induced dissociation of SiF_n. Finally, it is assumed that electrons are not

consumed in any of the reactions, and that electron-stimulated desorption of all species is negligible.

The most significant consequence of the model defined by Equation 53–Equation 61 is that etching is inhibited at high electron fluxes, as seen in Figure 16a, due to electron-induced dissociation of SiF_n. Specifically, this effect dominates when the dissociation rate of species n is much greater greater than the corresponding thermal desorption rate (i.e., $\sigma_r f >> k_n$). The simulations presented here were performed using model input parameters appropriate for cryogenic NF_3-mediated FEBIP of Si performed at a substrate temperature of 100 K [2]. The model can be used to calculate a number of quantities such as the concentrations of NF_3, SiF, SiF_2, SiF_3 and SiF_4 molecules shown in Figure 16b, and the concentrations of unfluorinated (N_0) and fluorinated (N_{Si}) Si sites shown in Figure 16c.

Special cases
The models outlined above can be used (either directly or in modified form) to simulate most processes reported in the FEBIP literature. Here, we summarize a few special cases for which the models require modification. We include these for completeness, and refer the reader to the cited papers for detailed descriptions of the changes that must be made to the above FEBIP models.

Figure 16: (a) Etch rate of Si calculated using Equation 61 as a function of electron flux *f*. (b,c) Corresponding steady state concentrations of NF_3, SiF, SiF_2, SiF_3 and SiF_4 molecules (N_a and N_n), fluorinated (N_{Si}) Si sites, and unfluorinated (N_0) and Si sites. (T = 100 K, T_g = 300 K. All other model input parameters were the same as in [2].)

Adsorbate depletion in high aspect ratio pits [7]: The replenishment rate of precursor molecules consumed in FEBIE can be limited by the gas flow conductance of a growing etch pit. The replenishment rate affects the adsorbate concentration N which, in turn, affects the etch rate through equations such as Equation 15. Etch-pit conductance can be the most significant process limiting the FEBIE rate when fabricating high aspect ratio pits. As an etch pit grows during FEBIE, the conductance decreases, causing the etch rate to decrease with time as discussed in detail in [7].

Dynamic surface site activation during FEBIE [3]: Surface site activation caused by electron beam restructuring of the substrate (i.e., beam damage) can give rise to FEBIE of materials that can not be etched in their unmodified state. It can also alter etch kinetics, and cause the etch rate to increase with electron beam irradiation time.

Electron beam induced surface functionalization and spontaneous decomposition of precursor molecules at the substrate surface: These two processes have been modeled for the case of XeF_2 [17] which can fragment through a dissociative chemisorption pathway, leading to fluorination of many surfaces [69-71,75]. The model in [17] is a variant of the above model of thermally activated chemisorption defined by Equation 40–Equation 52.

Electron beam dwell time as a control parameter of the composition of materials deposited using a mixture of two precursor gases [8]: This situation, depicted in Figure 10, can be modeled by solving rate equations for two FEBID precursor adsorbates, denoted by "A" and "B", that compete for adsorption sites on the surface. The adsorbates are dissociated by electrons, producing non-volatile reactions products D_A and D_B (i.e., the deposit), and volatile reaction products V_A and V_B:

$$A + e^- \rightarrow D_A + V_A + e^-,$$

$$B + e^- \rightarrow D_B + V_B + e^-.$$
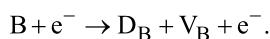
The evolution of the surface densities n_A and n_B of the two adsorbates is described by the following set of inhomogeneous first-order differential equations [8]:

$$\frac{\partial n_A}{\partial t} = s_A F_A \left(1 - \frac{n_A}{n_{ML,A}} - \frac{n_B}{n_{ML,B}}\right) - \frac{n_A}{\tau_A} - \sigma_A f n_A \ , \ (62)$$

$$\frac{\partial n_B}{\partial t} = s_B F_B \left(1 - \frac{n_A}{n_{ML,A}} - \frac{n_B}{n_{ML,B}}\right) - \frac{n_B}{\tau_B} - \sigma_B f n_B \ . \ (63)$$

The generic solution of this set as a function of electron-beam exposure (dwell time) is given by:

$$n_A(t) = n_{dA} + \exp\left(-\bar{k}_d t\right)\cdot\left[\Delta n_A \cosh(\kappa t) + N_A \sinh(\kappa t)\right], \ (64)$$

$$n_B(t) = n_{dB} + \exp\left(-\bar{k}_d t\right)\cdot\left[\Delta n_B \cosh(\kappa t) + N_B \sinh(\kappa t)\right], \ (65)$$

with the constants $n_{dA,B}$, k_d, $\Delta n_{A,B}$, κ defined in [8]. The dissociation yields $Y_{A,B}$ are then obtained by integrating over the electron beam dwell time:

$$Y_A = \sigma_A \int_0^{t_d} n_A(t)\,dt \Big/ t_d \ , \qquad (66)$$

$$Y_B = \sigma_B \int_0^{t_d} n_B(t)\,dt \Big/ t_d \ . \qquad (67)$$

A graphical representation of Equation 66 and Equation 67 is shown in Figure 17. As the molecule fluxes, residence times, and dissociation cross-sections of molecules "A" and "B" are very likely different from each other, it can be seen that the composition (given by the magnitude Z on the right hand axis) of the deposits can be tuned by changing the electron beam dwell time per pixel. Equation 64 and Equation 65 hold for micrometer-sized deposits. For small-scale deposits surface diffusion can become important and different yields and compositions are obtained as function of exposure time, see Gabureac et al. [76,77]. Including surface diffusion into the multi-adsorbate model is straightforward, however, is at the expense of having a closed analytical solution.
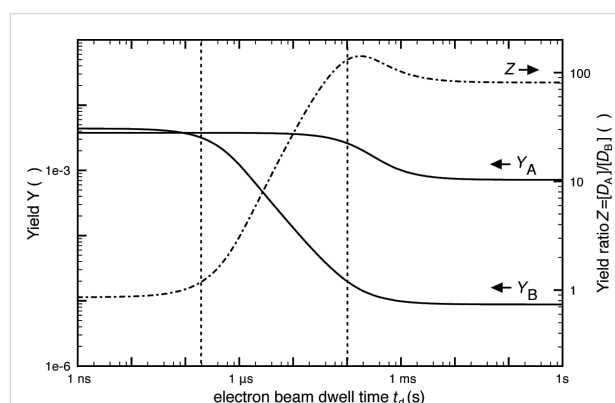
Figure 17: Calculated changes in dissociation yields Y_A and Y_B (per primary electron as defined in Equation 66 and Equation 67) and yield ratio Z versus electron beam dwell time. The example shown here was calculated for $Co_2(CO)_8$ and octanol as the deposition species "A" and "B", respectively. The yield ratio Z is a measure for the ratio of non-volatile fragments of molecule "a" and "b" incorporated into the FEBID material. Taken from [78].

Diffusion

All of the above models are, strictly speaking, valid only in the reaction rate limited growth regime. They can be used to identify conditions under which depletion becomes significant, causing the system to transition into the mass transport limited regime (e.g., under intermediate and high electron flux conditions in Figure 11b, and the high electron flux portions of the curves in Figure 16). However, when the extent of depletion is significant (or, more precisely, when the net transport of adsorbates through diffusion is significant), the models must be modified to account for the diffusion of all mobile species at the surface. In the case of FEBID or FEBIE performed using a single species of physisorbed precursor molecules "a", this is achieved simply by adding a diffusion term to Equation 12 [19]:

$$\frac{\partial N_a}{\partial t} = \Lambda_a - N_a k_a - \frac{\partial N_\alpha}{\partial t} + D_a \nabla^2 N_a \ . \qquad (68)$$

D_a is the diffusion coefficient, given by:

$$D_a = \kappa_{D_a} e^{-E_{D_a}/k_B T} \ , \qquad (69)$$

where E_{D_a} is the energy barrier for diffusion and κ_{D_a} is the preexponential factor (i.e., the diffusivity in the limit $E_{D_a} \to 0$).

The above approach for incorporating diffusion can also be applied to more complex FEBIP models, as we illustrate below. We note, however, that all of the continuum models discussed here assume a flat substrate surface. That is, the models track the time-evolution of deposits and etch pits made by FEBIP, but do not account for the effects of the resulting changes in surface geometry on adsorbate kinetics (e.g., adsorption to and diffusion along the evolving pillar sidewalls or etch pit sidewalls).

Gas mixtures

Equation 32–Equation 35 are used to model a gas mixture comprised of an etch precursor "e" and a deposition precursor "d" that simultaneously etch and deposit a material such as carbon. To account for the diffusion of the adsorbates "e" and "d" at the substrate surface, Equation 32 and Equation 33 are replaced by [11]:

$$\frac{\partial N_e}{\partial t} = \Lambda_e - N_e k_e - \frac{\partial N_\varepsilon}{\partial t} + D_e \nabla^2 N_e \ , \qquad (70)$$

$$\frac{\partial N_d}{\partial t} = \Lambda_d - N_d k_d - \frac{\partial N_\delta}{\partial t} - \frac{\partial N_\varepsilon}{\partial t} \sigma_r N_d + D_d \nabla^2 N_d \ , \quad (71)$$

where D_e and D_d are the respective diffusion coefficients which have the same functional form as Equation 69:

$$D_e = \kappa_{D_e} e^{-E_{D_e}/k_B T} \ , \qquad (72)$$

$$D_d = \kappa_{D_d} e^{-E_{D_d}/k_B T} \ . \qquad (73)$$

Equation 34 and Equation 35 remain unchanged since localized FEBIP requires the substrate temperature to be sufficiently low for diffusion of the deposited species "D" (e.g., carbon) to be negligible.

Figure 18 shows deposit geometries simulated using Equation 70 and Equation 71, a Gaussian electron-beam profile and substrate temperatures of 285, 290 and 295 K. The dip in the center of each deposit is caused by the fact that etching dominates near the beam axis where the deposition precursor is preferentially depleted, while deposition dominates in the adjacent regions of low electron flux. The deposit geometry changes with temperature because an increase in T causes: (i) a decrease in N_e and N_d through thermal desorption (Equation 38 and Equation 39), and (ii) an increase in N_e and N_d through diffusion (Equation 72 and Equation 73). The dramatic change in geometry with increasing T shown in Figure 18 is largely due to reduced depletion of adsorbates "d" near the beam axis due to an increase in the rate of diffusion (Equation 73).
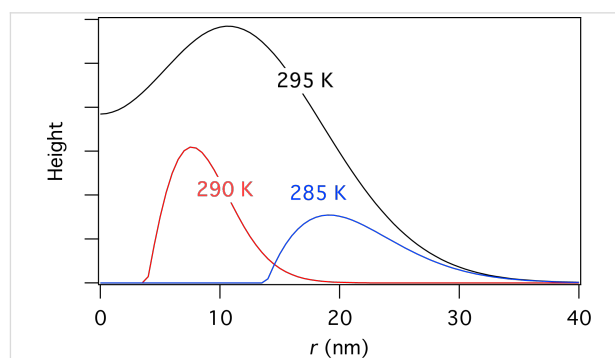
Figure 18: Deposit geometries analogous to those shown in Figure 11b, simulated using Equation 70 and Equation 71, a Gaussian electron-beam profile (Ω = 5 nm) and substrate temperatures of 285, 290 and 295 K. (Etch species "e" = H_2O, deposition species "d" = $C_{10}H_{22}$, $f_0 = 6 \times 10^4$ Å^{-2}s^{-1}, P_e = 1 Torr, P_d = 0.01 Torr, E_e = 0.56 eV, E_d = 1.0157 eV, $\sigma_\beta = \sigma_\gamma$ = 1 Å^2, T_g = 300 K. All other model input parameters were the same as in [11].)

Thermally activated chemisorption

The model of activated chemisorption described by the potential energy diagram shown in Figure 12 can be extended to account for diffusion by adding diffusion terms to Equation 44 and Equation 45:

$$\frac{\partial N_{\mathrm{p}}}{\partial t} = \Lambda_{\mathrm{p}} - N_{\mathrm{p}}k_{\mathrm{p}} - \Lambda_{\mathrm{conv}} - N_{\mathrm{p}}\sigma_{\mathrm{p}}f + D_{\mathrm{p}}\nabla^2 N_{\mathrm{p}} \; , \quad (74)$$

$$\frac{\partial N_{\mathrm{c}}}{\partial t} = n_{\mathrm{c}}\Lambda_{\mathrm{c}} - N_{\mathrm{c}}k_{\mathrm{c}} + n_{\mathrm{c}}\Lambda_{\mathrm{conv}} - N_{\mathrm{c}}\sigma_{\mathrm{c}}f + D_{\mathrm{c}}\nabla^2 N_{\mathrm{c}} \; , \quad (75)$$

$$D_{\mathrm{p}} = \kappa_{D_{\mathrm{p}}} e^{-E_{D_{\mathrm{p}}}/k_{\mathrm{B}}T} \; , \quad (76)$$

$$D_{\mathrm{c}} = \kappa_{D_{\mathrm{c}}} e^{-E_{D_{\mathrm{c}}}/k_{\mathrm{B}}T} \; , \quad (77)$$

where D_{p} and D_{c} are the diffusion coefficients for physisorbed and chemisorbed adsorbates, respectively.

Figure 19 shows FEBID rates simulated using Equation 74 and Equation 75, a Gaussian electron-beam profile and substrate temperatures of 300 K and 500 K. At 300 and 500 K, FEBID is dominated by electron-induced dissociation of physisorbed and chemisorbed gas molecules, respectively (see Figure 14), because of preferential population of the two respective states shown in Figure 12.

Dimensionless FEBIP models

In this section, we incorporate surface diffusion into the dimensionless FEBIP model, introduced above through Equation 16–Equation 26.

The magnitude of adsorbate surface diffusion with respect to the FWHM size of the beam can be correlated by introducing the *dimensionless surface diffusion replenishment* parameter:

$$\tilde{\rho}_{\mathrm{out}} = \frac{2\sqrt{D_{\mathrm{a}}\tau_{\mathrm{out,a}}}}{\mathrm{FWHM}} \; . \quad (78)$$

Substituting the irradiative depletion $\tilde{\tau}$ from Equation 16 and the surface diffusion replenishment $\tilde{\rho}_{\mathrm{out}}$ to the adsorbate rate equation, it becomes solely dependent on those two parameters and can be solved numerically [79]. Very small values of the surface diffusion replenishment parameter (e.g., $\tilde{\rho}_{\mathrm{out}} = 0.052$) have a negligible effect on the lateral growth rate, as shown by row 1 of Figure 20 and Figure 21. However, large values (e.g., $\tilde{\rho}_{\mathrm{out}} = 0.52$) can alter the deposit geometries significantly, particularly in the case of a tophat electron beam (see rows 2 and 3 of Figure 20 and Figure 21). If the contribution of surface diffusion is very high ($\tilde{\rho}_{\mathrm{out}} >> 0.1$), adsorbate replenishment through this process dominates the growth kinetics. For example, when $\tilde{\tau} = 100$, the deposit height is increased by a factor of 10 relative to the situation where adsorbate replenishment occurs only through adsorption from the gas phase.

The resolution parameter $\tilde{\varphi}$ for a stationary Gaussian beam can be obtained from the deposit shape, using a numerical solution of Equation 68, and the expression for the growth rate given by Equation 15. The numerical result is very well approximated by the $\tilde{\varphi}$-*vs*-$\tilde{\rho}_{\mathrm{out}}$ *scaling law of FEBIP resolution* formulated in [1]:
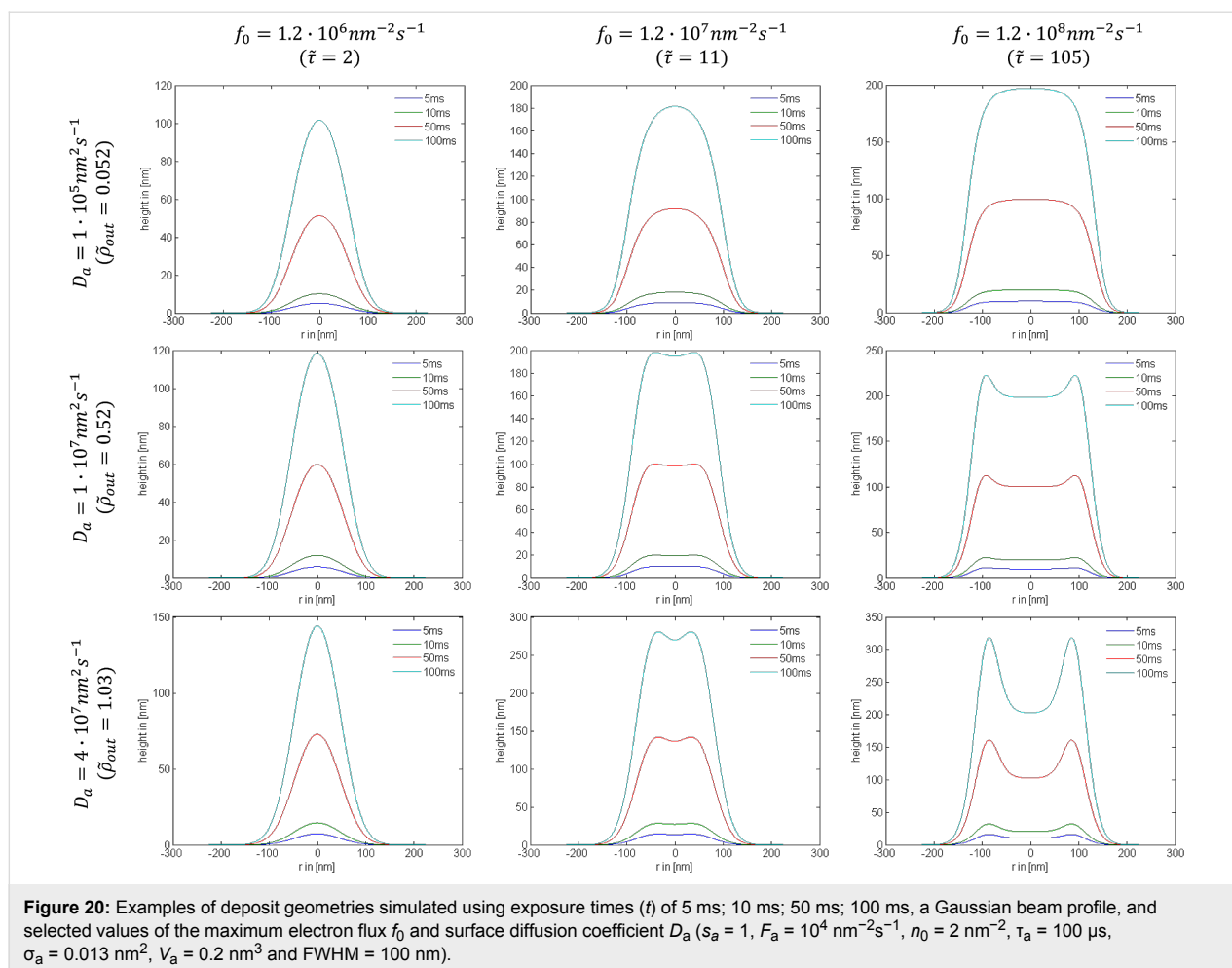
$$\tilde{\varphi}\left(\tilde{\tau},\tilde{\rho}_{\mathrm{out}}\right) \cong \left[\log_2\left(2 + \frac{\tilde{\tau}-1}{1+\tilde{\rho}_{out}^2}\right)\right]^{0.5} \; . \quad (79)$$

The above formula shows that even a relatively small surface diffusion contribution can lead to a decreasing in the deposit and etch pit size, and thus an improved lateral resolution. Once surface diffusion overcomes irradiative depletion, the deposit or etch pit diameter will approach that of the beam ($\tilde{\varphi} = 1$), as discussed in [1].

Pulsed exposure: Equation 68 can be solved numerically, and the corresponding *general scaling law of FEBIP resolution*,
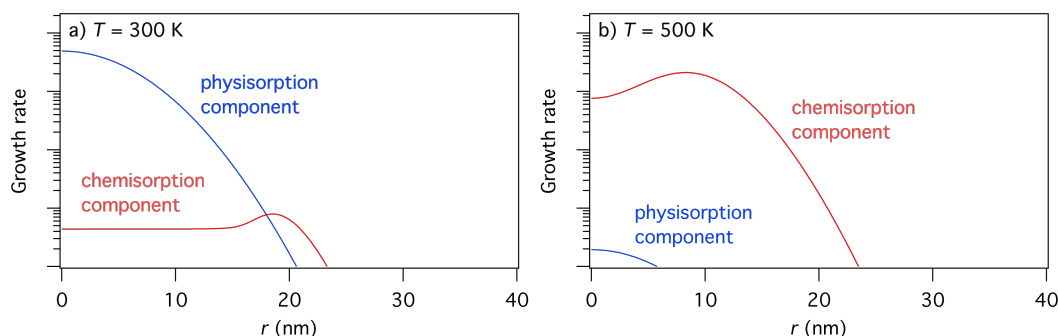
Figure 19: FEBID growth rates simulated using Equation 75 and Equation 76, a Gaussian electron-beam profile ($\Omega = 5$ nm) and substrate temperatures of (a) 300 K and (b) 500 K. (Deposition precursor = TEOS, $f_0 = 10^3$ Å^{-2}s^{-1}, $P = 0.1$ Torr, $T_{\mathrm{g}} = 300$ K, $E_{D_{\mathrm{p}}} = 0.17$ eV, $E_{D_{\mathrm{c}}} = 0.472$ eV, $\kappa_{D_{\mathrm{p}}} = \kappa_{D_{\mathrm{c}}} = 10^{11}$ Å^{-2}s^{-1} all other model input parameters were the same as in [5].)

Figure 20: Examples of deposit geometries simulated using exposure times (*t*) of 5 ms; 10 ms; 50 ms; 100 ms, a Gaussian beam profile, and selected values of the maximum electron flux f_0 and surface diffusion coefficient D_a (s_a = 1, F_a = 10^4 nm^{-2}s^{-1}, n_0 = 2 nm^{-2}, τ_a = 100 μs, σ_a = 0.013 nm^2, V_a = 0.2 nm^3 and FWHM = 100 nm).

including irradiative depletion, surface diffusion, and exposure dwell time, can be approximated by [1]:

$$\tilde{\varphi}\left(\tilde{\tau},\tilde{\rho}_{\text{out}},t\right) \cong \left[\log_2\left(2+\frac{\tilde{\tau}-1}{1+\tilde{\rho}_{\text{out}}^2+\tau_{\text{a,out}}/t}\right)\right]^{0.5} \quad . \quad (80)$$

The dependencies of deposit geometry on the electron beam exposure time *t*, irradiative depletion $\tilde{\tau}$ and surface diffusion path $\tilde{\rho}_{\text{out}}$ are shown in Figure 20 and Figure 21 for Gaussian and tophat beams, respectively. At short exposure times, depletion is negligible and the deposit shapes reflect the electron flux profiles. At long exposure times, the deposit geometry is determined by the extent of adsorbate depletion, and the relative contributions to adsorbate replenishment through diffusion and adsorption from the gas phase [1].
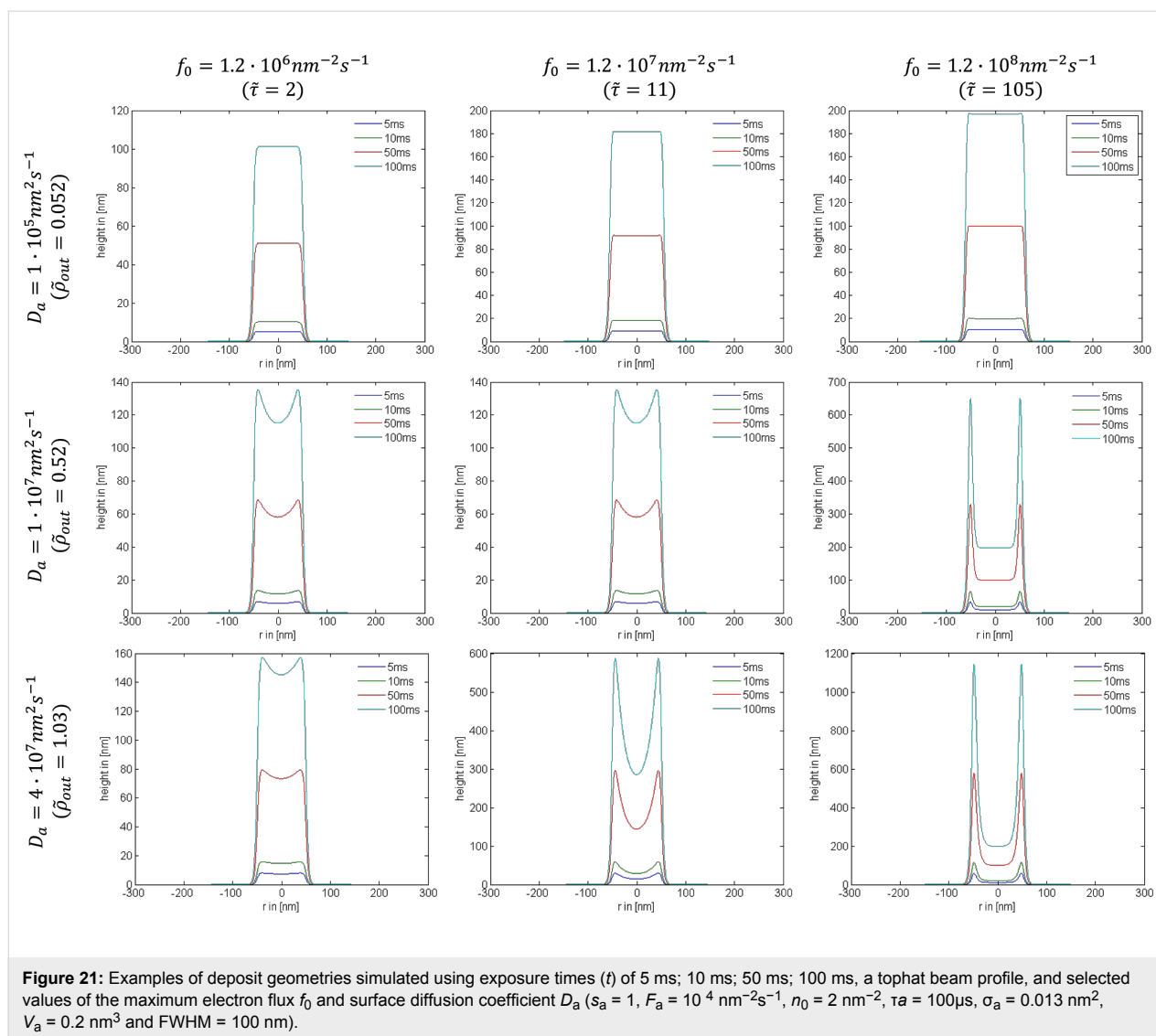
Conclusion

In summary, we have reviewed continuum modeling techniques developed by the authors that can be used to simulate most processes reported in the FEBIP literature. Accompanying this article, we have released a software implementing most of these techniques at http://www.empa.ch/febipcode.

The software release consists of the following:

- An executable binary and C++ code of the GIS simulator for simulation of impinging molecule flux from capillary nozzles on plane substrates, which can be modified to generate Figure 7.
- A MATLAB notebook for single physisorbed gas species dimensionless FEBIP model that solve Equation 68 and Equation 47 for Gaussian electron beam (Equation 8). This was used to generate Figure 20.
- A MATLAB notebook for single physisorbed gas species dimensionless FEBIP model that solve Equation 68 and Equation 47 for tophat electron beam (Equation 9). This was used to generate Figure 20.
- Eight Mathematica notebooks, detailed below, that illustrate implementation of FEBIP models of varying complexity.

Figure 21: Examples of deposit geometries simulated using exposure times (*t*) of 5 ms; 10 ms; 50 ms; 100 ms, a tophat beam profile, and selected values of the maximum electron flux f_0 and surface diffusion coefficient D_a (s_a = 1, F_a = 10^4 nm^{-2}s^{-1}, n_0 = 2 nm^{-2}, τa = 100μs, σ$_a$ = 0.013 nm^2, V_a = 0.2 nm^3 and FWHM = 100 nm).

FEBIP models implemented in Mathematica notebooks:

1. Single physisorbed gas species initial coverage calculator, used to generate Figure 3.

2. Single physisorbed gas species FEBIP model based on Equation 12. This model was used to generate Figure 8.

3. Gas mixture FEBIP model based on Equation 32–Equation 39 and used to generate Figure 11a. For this simulation, initial coverages can be calculated by setting the electron flux to zero.

4. Gas mixture FEBIP model that incorporates diffusion, based on Equation 70–Equation 73 and used to generate Figure 18 and Figure 11b (in the latter, the diffusion coefficients were made negligible).

5. Thermally activated chemisorption initial coverage calculator used to generate Figure 13.

6. Thermally activated chemisorption, based on Equation 44–Equation 52 and used to generate Figure 14.

7. Thermally activated chemisorption with diffusion, based on Equation 74–Equation 77 and used to generate Figure 19.

8. EBIE with multiple reaction products, based on Equation 53–Equation 61 and used to generate Figure 16. Initial coverages can be calculated by setting the electron flux to zero.

Gaussian (Equation 8) or tophat (Equation 9) focused electron beams can be used by selecting the appropriate equations in each notebook.

Acknowledgements

References

1. Szkudlarek, A.; Szmyt, W.; Kapusta, C.; Utke, I. *Appl. Phys. A* **2014,** *117,* 1715–1726. doi:10.1007/s00339-014-8751-2
2. Martin, A. A.; Toth, M. *ACS Appl. Mater. Interfaces* **2014,** *6,* 18457–18460. doi:10.1021/am506163w
3. Martin, A. A.; Phillips, M. R.; Toth, M. *ACS Appl. Mater. Interfaces* **2013,** *5,* 8002–8007. doi:10.1021/am402083n
4. Huth, M.; Porrati, F.; Schwalb, C.; Winhold, M.; Sachser, R.; Dukic, M.; Adams, J.; Fantner, G. *Beilstein J. Nanotechnol.* **2012,** *3,* 597–619. doi:10.3762/bjnano.3.70
5. Bishop, J.; Lobo, C. J.; Martin, A.; Ford, M.; Phillips, M. R.; Toth, M. *Phys. Rev. Lett.* **2012,** *109,* 146103. doi:10.1103/PhysRevLett.109.146103
6. Lobo, C. J.; Martin, A.; Phillips, M. R.; Toth, M. *Nanotechnology* **2012,** *23,* 375302. doi:10.1088/0957-4484/23/37/375302
7. Randolph, S.; Toth, M.; Cullen, J.; Chandler, C.; Lobo, C. *Appl. Phys. Lett.* **2011,** *99,* 213103. doi:10.1063/1.3662928
8. Bernau, L.; Gabureac, M.; Erni, R.; Utke, I. *Angew. Chem., Int. Ed.* **2010,** *49,* 8880–8884. doi:10.1002/anie.201004220
9. Toth, M.; Lobo, C. J.; Lysaght, M. J.; Vladar, A. E.; Postek, M. T. *J. Appl. Phys.* **2009,** *106,* 034306. doi:10.1063/1.3187926
10. Utke, I.; Hoffmann, P.; Melngailis, J. *J. Vac. Sci. Technol., B* **2008,** *26,* 1197–1276. doi:10.1116/1.2955728
11. Lobo, C. J.; Toth, M.; Wagner, R.; Thiel, B. L.; Lysaght, M. *Nanotechnology* **2008,** *19,* 025303. doi:10.1088/0957-4484/19/02/025303
12. Lassiter, M. G.; Rack, P. D. *Nanotechnology* **2008,** *19,* 455306. doi:10.1088/0957-4484/19/45/455306
13. Rykaczewski, K.; White, W. B.; Fedorov, A. G. *J. Appl. Phys.* **2007,** *101,* 054307. doi:10.1063/1.2437065
14. Toth, M.; Lobo, C. J.; Hartigan, G.; Knowles, W. R. *J. Appl. Phys.* **2007,** *101,* 054309. doi:10.1063/1.2437667
15. Utke, I.; Friedli, V.; Purrucker, M.; Michler, J. *J. Vac. Sci. Technol., B* **2007,** *25,* 2219. doi:10.1116/1.2789441
16. Christy, R. W. *J. Appl. Phys.* **1960,** *31,* 1680–1683. doi:10.1063/1.1735915
17. Randolph, S. J.; Botman, A.; Toth, M. *Part. Part. Syst. Charact.* **2013,** *30,* 672–677. doi:10.1002/ppsc.201300036
18. Toth, M. *Appl. Phys. A* **2014,** *117,* 1623–1629. doi:10.1007/s00339-014-8596-8
19. Utke, I.; Moshkalev, S.; Russell, P. *Nanofabrication Using Focused Ion and Electron Beams;* Oxford University Press: Oxford, United Kingdom, 2012.
20. van Dorp, W. F.; Hagen, C. W. *J. Appl. Phys.* **2008,** *104,* 081301. doi:10.1063/1.2977587
21. Randolph, S. J.; Fowlkes, J. D.; Rack, P. D. *Crit. Rev. Solid State Mater. Sci.* **2006,** *31,* 55–89. doi:10.1080/10408430600930438
22. Szkudlarek, A.; Gabureac, M.; Utke, I. *ECS Trans.* **2013,** *50,* 495–498. doi:10.1149/05012.0495ecst
23. Winkler, R.; Fowlkes, J.; Szkudlarek, A.; Utke, I.; Rack, P. D.; Plank, H. *ACS Appl. Mater. Interfaces* **2014,** *6,* 2987–2995. doi:10.1021/am405591d
24. Winkler, R.; Szkudlarek, A.; Fowlkes, J. D.; Rack, P. D.; Utke, I.; Plank, H. *ACS Appl. Mater. Interfaces* **2015,** *7,* 3289–3297. doi:10.1021/am508052k
25. Li, J. T.; Toth, M.; Dunn, K. A.; Thiel, B. L. *J. Appl. Phys.* **2010,** *107,* 103540. doi:10.1063/1.3428427
26. Li, J.; Toth, M.; Tileli, V.; Dunn, K. A.; Lobo, C. J.; Thiel, B. L. *Appl. Phys. Lett.* **2008,** *93,* 023130. doi:10.1063/1.2959112
27. Parsons, D. F. *Science* **1974,** *186,* 407. doi:10.1126/science.186.4162.407
28. Danilatos, G. D. *Adv. Electron. Electron Phys.* **1988,** *71,* 109–250.
29. Toth, M.; Knowles, W. R.; Thiel, B. L. *Appl. Phys. Lett.* **2006,** *88,* 023105. doi:10.1063/1.2161571
30. Toth, M.; Uncovsky, M.; Knowles, W. R.; Baker, F. S. *Appl. Phys. Lett.* **2007,** *91,* 053122. doi:10.1063/1.2768031
31. Friedli, V.; Utke, I. *J. Phys. D: Appl. Phys.* **2009,** *42,* 125305. doi:10.1088/0022-3727/42/12/125305
32. Wanzenboeck, H. D.; Hochleitner, G.; Mika, J.; Shawrav, M. M.; Gavagnin, M.; Bertagnolli, E. *Appl. Phys. A* **2014,** *117,* 1749–1756. doi:10.1007/s00339-014-8755-y
33. Friedli, V.; Wanzenboeck, H. D.; Utke, I. Gas Injection Systems for FEB and FIB Processing: Theory and Experiment. In *Nanofabrication using focused ion and electron beams: principles and applications;* Utke, I.; Moshkalev, S.; Russell, P., Eds.; Nanomanufacturing series; Oxford University Press: Oxford, United Kingdom, 2012.
34. Xue, Z.; Thridandam, H.; Kaesz, H. D.; Hicks, R. F. *Chem. Mater.* **1992,** *4,* 162–166. doi:10.1021/cm00019a032
35. Dayton, B. B. *Foundations of vacuum science and technology;* Wiley-VCH: New York, NY, U.S.A., 1998.
36. van der Vis, M. G. M.; Cordfunke, E. H. P. *Thermochim. Acta* **1995,** *265,* 129–134. doi:10.1016/0040-6031(95)02403-O
37. Schreiner, F.; McDonald, G. N.; Chernick, C. L. *J. Phys. Chem.* **1968,** *72,* 1162–1166. doi:10.1021/j100850a014
38. Ohta, T.; Cicoira, F.; Doppelt, P.; Beitone, L.; Hoffmann, P. *Chem. Vap. Deposition* **2001,** *7,* 33–37. doi:10.1002/1521-3862(200101)7:1<33::AID-CVDE33>3.0.CO;2-Y
39. Lander, J.; Germer, L. *Technical Publication 2259, Met.Technol.* **1948,** *14,* 1–41.
40. Chandra, D.; Lau, K.; Chien, W.-M.; Garner, M. *J. Phys. Chem. Solids* **2005,** *66,* 241–245. doi:10.1016/j.jpcs.2004.10.001
41. Widmer, M. Deposition Pyrolytique Induite par Laser de Microstructures en Cuivre a Partir de Precurseurs Volatils. Ph.D. Thesis, Ecole Polytechnique Federale de Lausanne, Lausanne, Switzerland, 1992.
42. Choi, K.-K.; Rhee, S.-W. *Thin Solid Films* **2002,** *409,* 147–152. doi:10.1016/S0040-6090(02)00118-9
43. Berman, A. *Vacuum Engineering Calculations, Formulas, and Solved Exercises;* Elsevier: Oxford, United Kingdom, 1992.
44. Wagner, W.; Pruss, A. *J. Phys. Chem. Ref. Data* **1993,** *22,* 783–787. doi:10.1063/1.555926
45. Puurunen, R. L. *Chem. Vap. Deposition* **2005,** *11,* 79–90. doi:10.1002/cvde.200400021
46. Utke, I.; Friedli, V.; Amorosi, S.; Michler, J.; Hoffmann, P. *Microelectron. Eng.* **2006,** *83,* 1499–1502. doi:10.1016/j.mee.2006.01.136
47. Friedli, V.; Santschi, C.; Michler, J.; Hoffmann, P.; Utke, I. *Appl. Phys. Lett.* **2007,** *90,* 053106. doi:10.1063/1.2435611

48. Madey, T. E.; Yates, J. T., Jr. *J. Vac. Sci. Technol. (N. Y., NY, U. S.)* **1971,** *8,* 525–555. doi:10.1116/1.1315200

49. Drinkwine, M. J.; Lichtman, D. *Prog. Surf. Sci.* **1977,** *8,* 123–142. doi:10.1016/0079-6816(77)90002-8

50. Madey, T. E.; Yates, J. T., Jr. *Surf. Sci.* **1977,** *63,* 203–231. doi:10.1016/0039-6028(77)90339-9

51. Ramsier, R. D.; Yates, J. T., Jr. *Surf. Sci. Rep.* **1991,** *12,* 246–378. doi:10.1016/0167-5729(91)90013-N

52. Cullen, J.; Bahm, A.; Lobo, C. J.; Ford, M. J.; Toth, M. *J. Phys. Chem. C* **2015**. doi:10.1021/acs.jpcc.5b00918

53. Szkudlarek, A.; Gabureac, M.; Utke, I. *J. Nanosci. Nanotechnol.* **2011,** *11,* 8074–8078. doi:10.1166/jnn.2011.5066

54. Smith, D. A.; Fowlkes, J. D.; Rack, P. D. *Small* **2008,** *4,* 1382–1389. doi:10.1002/smll.200701133

55. Fowlkes, J. D.; Rack, P. D. *ACS Nano* **2010,** *4,* 1619–1629. doi:10.1021/nn901363a

56. Perentes, A.; Hoffmann, P. *J. Vac. Sci. Technol., B* **2007,** *25,* 2233–2238. doi:10.1116/1.2798746

57. Perentes, A.; Hoffmann, P. *Chem. Vap. Deposition* **2007,** *13,* 176–184. doi:10.1002/cvde.200606583

58. Shimojo, M.; Takeguchi, M.; Furuya, K. *Nanotechnology* **2006,** *17,* 3637–3640. doi:10.1088/0957-4484/17/15/003

59. Mølhave, K.; Madsen, D. N.; Dohn, S.; Bøggild, P. *Nanotechnology* **2004,** *15,* 1047–1053. doi:10.1088/0957-4484/15/8/033

60. Wang, S.; Sun, Y.-M.; Wang, Q.; White, J. M. *J. Vac. Sci. Technol., B* **2004,** *22,* 1803–1806. doi:10.1116/1.1761266

61. Mølhave, K.; Madsen, D. N.; Rasmussen, A. M.; Carlsson, A.; Appel, C. C.; Brorson, M.; Jacobsen, C. J. H.; Bøggild, P. *Nano Lett.* **2003,** *3,* 1499–1503. doi:10.1021/nl034528o

62. Folch, A.; Servat, J.; Esteve, J.; Tejada, J.; Seco, M. *J. Vac. Sci. Technol., B* **1996,** *14,* 2609–2614. doi:10.1116/1.588994

63. Folch, A.; Tejada, J.; Peters, C. H.; Wrighton, M. S. *Appl. Phys. Lett.* **1995,** *66,* 2080–2082. doi:10.1063/1.113909

64. Porrati, F.; Kämpken, B.; Terfort, A.; Huth, M. *J. Appl. Phys.* **2013,** *113,* 053707. doi:10.1063/1.4790320

65. Winhold, M.; Schwalb, C. H.; Porrati, F.; Sachser, R.; Frangakis, A. S.; Kämpken, B.; Terfort, A.; Auner, N.; Huth, M. *ACS Nano* **2011,** *5,* 9675–9681. doi:10.1021/nn203134a

66. Che, R. C.; Takeguchi, M.; Shimojo, M.; Zhang, W.; Furuya, K. *Appl. Phys. Lett.* **2005,** *87,* 223109. doi:10.1063/1.2136071

67. Bishop, J.; Toth, M.; Phillips, M.; Lobo, C. *Appl. Phys. Lett.* **2012,** *101,* 211605. doi:10.1063/1.4767521

68. Brass, S. G.; Ehrlich, G. *Phys. Rev. Lett.* **1986,** *57,* 2532–2535. doi:10.1103/PhysRevLett.57.2532

69. Winters, H. F.; Coburn, J. W. *Appl. Phys. Lett.* **1979,** *34,* 70–73. doi:10.1063/1.90562

70. Tu, Y.-Y.; Chuang, T. J.; Winters, H. F. *Phys. Rev. B* **1981,** *23,* 823–835. doi:10.1103/PhysRevB.23.823

71. Loudiana, M. A.; Schmid, A.; Dickinson, J. T.; Ashley, E. J. *Surf. Sci.* **1984,** *141,* 409–416. doi:10.1016/0039-6028(84)90140-7

72. Tedder, L. L.; Crowell, J. E.; Logan, M. A. *J. Vac. Sci. Technol., A* **1991,** *9,* 1002–1006. doi:10.1116/1.577566

73. Tedder, L. L.; Lu, G.; Crowell, J. E. *J. Appl. Phys.* **1991,** *69,* 7037–7049. doi:10.1063/1.348932

74. Crowell, J. E.; Tedder, L. L.; Cho, H.-C.; Cascarano, F. M.; Logan, M. A. *J. Electron Spectrosc. Relat. Phenom.* **1990,** *54,* 1097–1104. doi:10.1016/0368-2048(90)80299-P

75. Hills, M. M.; Arnold, G. S. *Appl. Surf. Sci.* **1991,** *47,* 77–90. doi:10.1016/0169-4332(91)90104-R

76. Gabureac, M. S.; Bernau, L.; Utke, I. *J. Nanosci. Nanotechnol.* **2011,** *11,* 7982–7987. doi:10.1166/jnn.2011.5067

77. Gabureac, M. S.; Bernau, L.; Boero, G.; Utke, I. *IEEE Trans. Nanotechnol.* **2013,** *12,* 668–673. doi:10.1109/TNANO.2013.2266733

78. Bernau, L. Sub-Micron Nano-Composite CoC Hall Sensors by Focused Electron-Beam Induced Deposition for Microbead Detection. Ph.D. Thesis, Ecole Polytechnique Federale de Lausanne, Lausanne, Switzerland, 2011.

79. Szkudlarek, A. Surface kinetics of Focused-electron-beam-induced-deposition. Ph.D. Thesis, AGH University of Science and Technology, Kraków, Poland, 2014.

Imaging of carbon nanomembranes with helium ion microscopy

André Beyer[*1], Henning Vieker[2], Robin Klett[1], Hanno Meyer zu Theenhausen[1], Polina Angelova[2] and Armin Gölzhäuser[1]

Abstract

Carbon nanomembranes (CNMs) prepared from aromatic self-assembled monolayers constitute a recently developed class of 2D materials. They are made by a combination of self-assembly, radiation-induced cross-linking and the detachment of the cross-linked SAM from its substrate. CNMs can be deposited on arbitrary substrates, including holey and perforated ones, as well as on metallic (transmission electron microscopy) grids. Therewith, freestanding membranes with a thickness of 1 nm and macroscopic lateral dimensions can be prepared. Although free-standing CNMs cannot be imaged by light microscopy, charged particle techniques can visualize them. However, CNMs are electrically insulating, which makes them sensitive to charging. We demonstrate that the helium ion microscope (HIM) is a good candidate for imaging freestanding CNMs due to its efficient charge compensation tool. Scanning with a beam of helium ions while recording the emitted secondary electrons generates the HIM images. The advantages of HIM are high resolution, high surface sensitivity and large depth of field. The effects of sample charging, imaging of multilayer CNMs as well as imaging artefacts are discussed.

Introduction

Carbon nanomembranes (CNMs) are extremely thin and homogeneous two-dimensional objects consisting of a monolayer of laterally cross-linked molecules. They are made by exposing a self-assembled monolayer (SAM) of aromatic molecules with electron [1] or soft X-ray irradiation [2], which results in the cross-linking of neighbouring molecules into a CNM of molecular thickness. The CNM is then released from its substrate by dissolving the latter [3]. The thickness, chemical composition, and density of the original SAM determine the mechanical properties, such as elasticity and porosity, as well as the chem-

ical composition of the resulting CNM. The freely suspended CNMs are made by transferring the cross-linked SAM from its substrate to a holey structure, such as a metal grid. The resulting CNM is approximately as thick as the original SAM and can span macroscopic areas; thus far, freestanding CNMs of up to 0.5×0.5 mm^2 have been fabricated.

The electrical conductivity of the CNM can also be tailored, as pyrolysis results in a gradual transformation into graphene [4-6]. CNMs have potential for many technical applications, such as filters [7], sensors [4], resists [8], nanosieves [9], or "lab-on-a-chip" devices [10]. Many aspects regarding the fabrication, modification and functionalization of homogenous as well as patterned CNMs are compiled in a recent review [11].

Optical microscopy is suitable for imaging CNMs on SiO$_2$/Si wafers [12], but on other substrates, CNMs are not (or only barely) visible. In particular, it is not possible to directly image freestanding CNMs by regular optical microscopy. Indirect optical methods require the attachment of particles, fluorescent dyes [13], metallic nanostructures [14] or other suitable indicators that are detectable by optical microscopy. In addition, optical imaging with a Mirau interferometer allows the detection of the vibrational modes of bare CNMs with a resolution limited by the light wavelength [15].

The imaging of CNMs with higher magnification requires charged particle microscopy techniques such as scanning electron microscopy (SEM) or helium ion microscopy (HIM). As illustrated in Supporting Information File 1, Figure S1, SEM shows a low signal-to-noise-ratio for freestanding CNMs, especially at higher magnifications, due to charging issues [4,16]. This tends to be destructive for freestanding membranes. For example, an attempt at imaging perforated CNMs with SEM failed due to charging-induced rupture during the imaging process [9]. On the other hand, HIM is very well-suited to image CNMs with high signal-to-noise-ratio at high magnification. In this report, we will show examples that support this statement. We demonstrate the effect of charging on HIM images as well as the effectiveness of the HIM charge compensation mechanism. The principle of operation of HIM as well as a recent overview of HIM-related reports can be found elsewhere [17]. In short, HIM utilizes a focussed beam of He$^+$ ions that scans the sample surface. The image is usually obtained by the detection of secondary electrons. The imaging of insulating samples may lead to positive charging due to the emission of secondary electrons as well as the exposure to positive He$^+$ ions. A major advantage of HIM is its ability to compensate for sample charging by employing an electron flood gun in an alternating manner. In this way, the sample is exposed to electrons between scans of subsequent image lines or frames.

There is scarce literature on HIM imaging of ultrathin membranes. Many researchers have examined graphene, where the main focus was on the modification and production of small structures and circuits [18-22]. The thickness of graphene is comparable to CNMs, but a fundamental difference is its high conductivity, which eases charged particle imaging. Small flakes of hexagonal boron nitride (h-BN), an insulating material that shares similarities with graphene, were imaged in a comparative study [23]. Therein, it is shown that HIM is more sensitive and consistent than SEM for characterizing the number of layers and the morphology of 2D materials. It was also shown that HIM is very sensitive in characterizing supported, thin organic layers due to its high surface sensitivity [24,25].

Results and Discussion

For imaging with the HIM, the most important characteristics of CNMs are that they are ultrathin (≈ 1 nm) and electrically insulating. Due to the low thickness, the high surface sensitivity of the HIM is well suited to obtain CNM images with high signal-to-noise-ratio. It is also important to note that the helium beam easily penetrates the CNM and also strikes objects below the freestanding membrane, for example, the sample holder. Figure 1 shows an example of this effect. The images in Figure 1a,b show the same sample: a hexagonal TEM grid is mounted in a sample holder (visible in the four corners of the images) which has a mm-sized, circular opening. The CNM partly covers the TEM grid and the white arrows indicate CNM-covered regions. Although both HIM images were taken with the same ion acceleration voltage and similar ion currents, the contrast in the images appears almost inverted. This difference relates to the background: In Figure 1a, the main part of the grid is placed closely over the homogeneous metal surface of the sample holder. An edge of the sample holder surface is visible as a bright strip running from the top to the lower right of the image. These background features are visible in the HIM image as He$^+$ ions impinge upon the sample holder behind the grid and eject secondary electrons that reach the SE detector without being blocked. In Figure 1b, the sample holder background is not visible as the path of the secondary electrons emitted from the sample stage to the detector has been blocked by mounting the grid on top of a deep cavity, which acts like a Faraday cup. Thus, in Figure 1b, the uncovered openings of the grid appear dark in all parts of this image. To guide the eye, white arrows in Figure 1a,b depict the same position in the sample. Note that regardless of the CNM grid mounting, in both cases, a fast evaluation regarding the area of intact CNMs is easily obtained due to the large field of view (of more than 2 mm), high depth of view, and high contrast between bare and CNM-covered grid meshes. The recording time of such images is less than one minute.
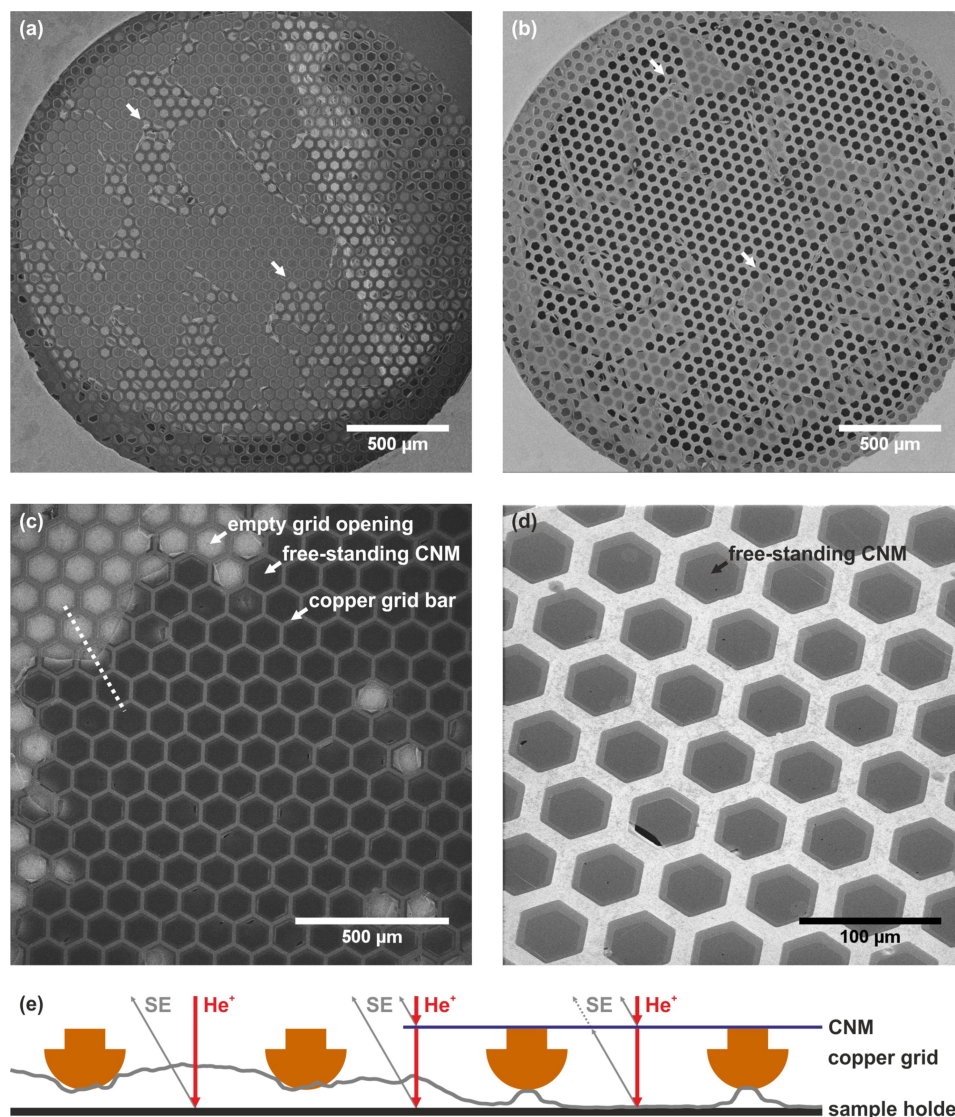
Figure 1: (a, b) HIM images of freestanding CNMs on TEM grids, illustrating the importance of the background. Both images show the same sample mounted differently. The arrows point to the same positions as a guide to the eye. (c) CNMs on a TEM grid with a bright background and substantial membrane charging. (d) CNMs are imaged on a dark background with negligible membrane charging. (e) Schematic cross-section and superimposed line profile of the image greyscale values along the dotted line in (c) with the primary He$^+$ beam and secondary electrons emitted from the CNM and the sample holder depicted at three exemplary locations. The values of the line profile (grey curve) are a measure of the amount of detected secondary electrons. Detailed information on all HIM images are given in Supporting Information File 1, Tables S1 and S2.

Another effect, which substantially changes the appearance of the CNM image, is electrostatic charging of the ultrathin, insulating membranes. In Figure 1c,d HIM images with and without charging artefacts are compared. A schematic cross-section of the sample as well as a superimposed line profile of the image greyscale values in Figure 1c corresponding to the white dotted line is given in Figure 1e. An empty grid opening on the left is followed by a partial and a fully covered opening. CNM charging due to the positively charged He$^+$ ion beam and the emission of negatively charged secondary electrons can only result in positive charging regardless of the secondary electron

yield of the CNMs. A positively charged sample will hinder the emission of secondary electrons. Therefore, positively charged CNMs will appear dark in HIM images. This is observed in Figure 1c where the freestanding regions of the membranes are dark, while the membrane regions directly in contact with the copper grid appear much brighter. In the latter, secondary electrons are also emitted from the underlying copper grid and charges in the CNM are neutralised by the metallic support. This combination of effects yields a high contrast between the CNM-covered and non-covered regions. However, the structural details of the CNMs cannot be investigated under such

imaging conditions. An interesting image feature appears in partially covered meshes: the edges of freestanding CNMs are brighter than intact CNMs, as illustrated in the area near the centre of the dotted line. This effect is explained by considering that secondary electrons are emitted from the sample support rather than from the freestanding CNMs itself, as schematically depicted in Figure 1e. The intact CNMs completely block the path of such secondary electrons to the detector while partially ruptured CNMs do not.

The reduction of the beam current, the dwell time per pixel, the use of frame averaging as well as charge compensation can reduce or completely avoid the charging of insulating membranes. These imaging parameter changes resulted in Figure 1d, which does not show any notable charging effects. Here, the sample was mounted in a way that no secondary electrons from the sample holder could reach the detector. A small rupture in the CNM reveals a high contrast between the bright CNM and

the dark background. Under these imaging conditions, fine details on the top of freestanding CNMs can be observed. For example, small pores and folds are visible.

A collection of different CNMs on hexagonal copper grids is presented in Figure 2, exhibiting the different types of features that are visible in HIM images. From these images, one intuitively obtains an impression of the detailed shape of the copper grid and the CNM on top. In Figure 2a larger folds on the upper side of the image and one rupture in the centre are visible. Figure 2b is an example of a membrane rolling up at a rupture, showing the high flexibility of CNMs. Small folds like those in Figure 2c are frequently observed, while wrinkling of the freestanding membrane (Figure 2d) is less often observed.

Examples of very large, freestanding CNMs are given in Figure 3. The ≈1 nm thin membranes are self-supporting over a distance of ≈0.5 mm, which are to date among the largest
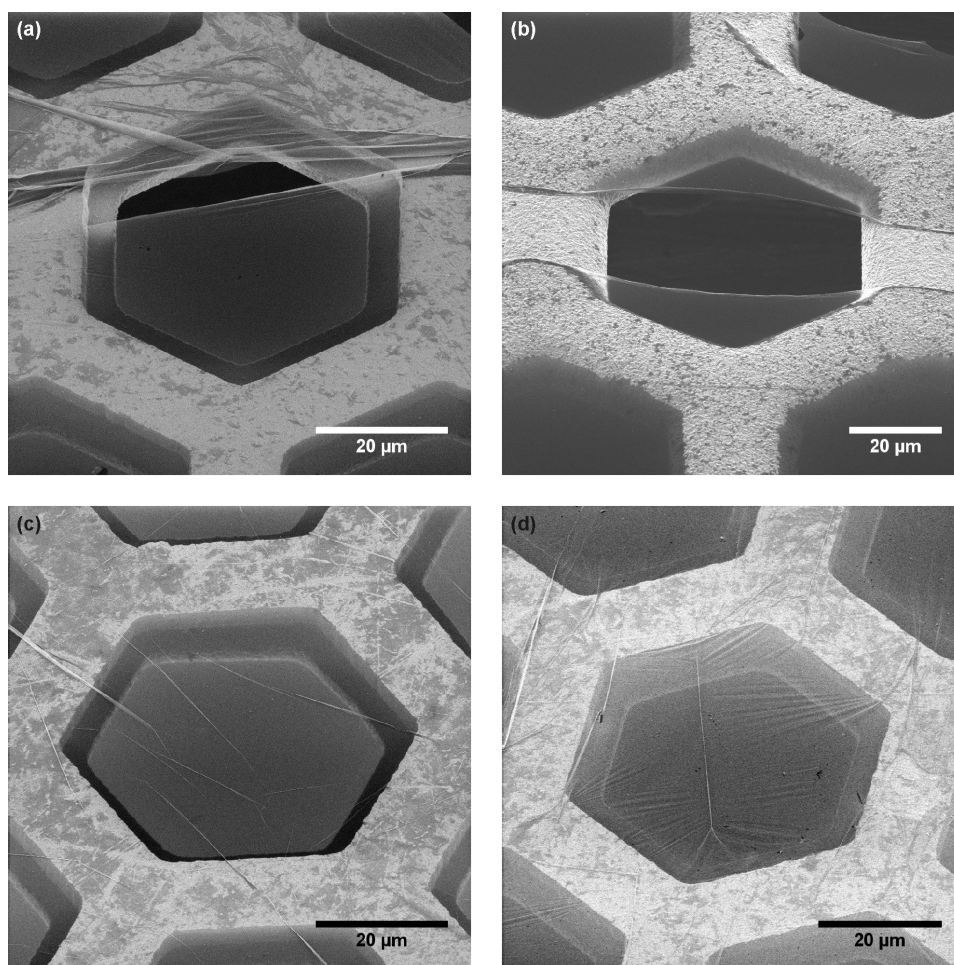
Figure 2: Examples of CNMs which were transferred onto copper grids with hexagonal openings. Different types of features are visible: (a) larger folds; (b) rolled CNM edges; (c) small folds; and (d) wrinkled CNMs. Detailed information on all HIM images is given in Supporting Information File 1, Tables S1 and S2.
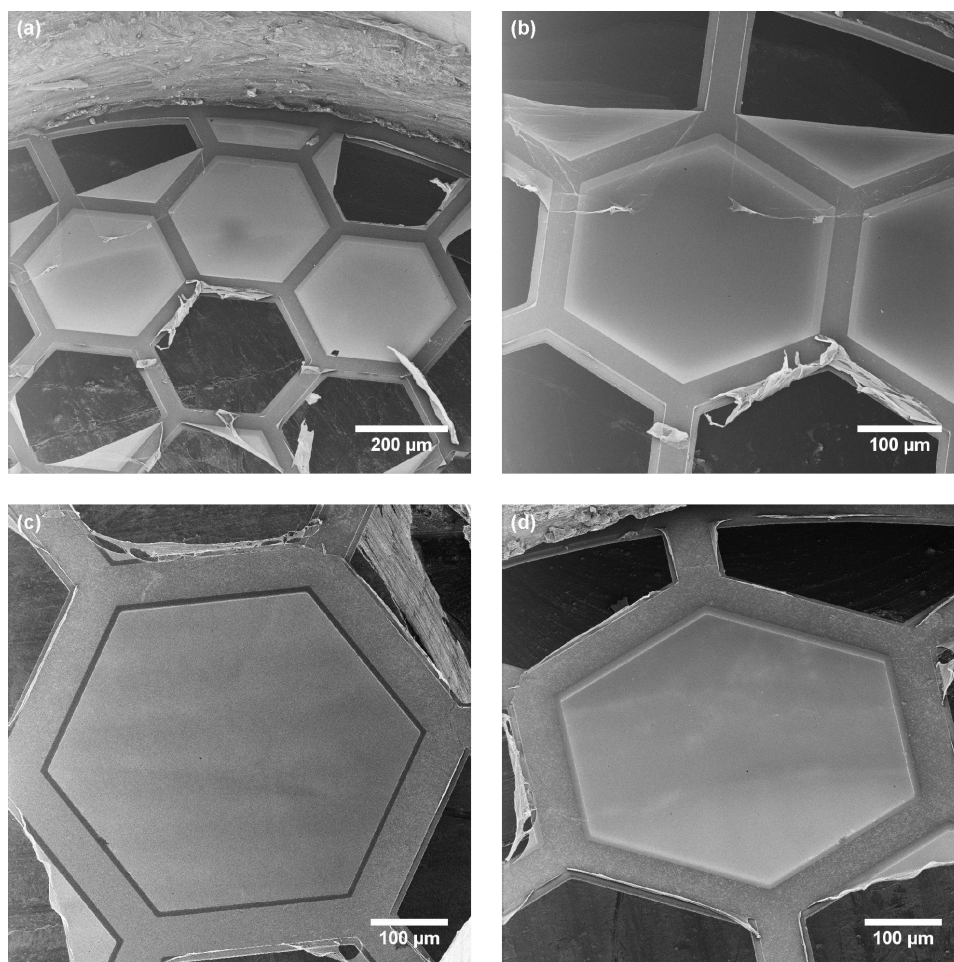
Figure 3: Examples of large freestanding CNMs. (a, b) Three intact CNMs are imaged at different magnifications. (c, d) Another intact CNM is imaged at different tilt angles. This comparison reveals that the intensity variation on the CNM surface originates mostly from secondary electrons emitted by the sample holder. Detailed information on all HIM images is given in Supporting Information File 1, Tables S1 and S2.

CNMs fabricated. The overview image in Figure 3a shows three intact freestanding CNMs, which are surrounded by ruptured membranes. In the upper part of this image, the sample holder is visible. The left membrane is shown with a higher magnification in Figure 3b. Apparently, the two ruptured membrane fragments in the upper part of the image are flipped over and cover part of the intact membrane. Another large CNM is presented in Figure 3c,d, which was imaged with different sample tilt angles. Note that the intensity variation on the CNM surface originates mostly from secondary electrons emitted by the sample holder as discussed earlier. This has been confirmed by varying the tilt angle of observation.

CNMs with different thicknesses were also imaged in this study. An increased thickness provides more secondary electrons. This can be seen in Figure 4b, where part of a membrane was folded back onto itself, creating regions with double, triple and multilayers. In the overview image in Figure 4a, this

double-layer region expands from the top left corner to the right middle of the image. The square marks the position of a magnified image (Figure 4b) where the start of the double layer region is marked with arrows. Note that the low contrast between single- and multi-layer CNMs in the overview image is related to charging. This was reduced in Figure 4b by employing the charge compensation system.

In Figure 4c,d the CNM is suspended on a copper grid with a holey carbon film some micrometres below it. A schematic cross section of both samples is depicted in Figure 4e. The CNM in Figure 4c is folded, so the lower right part is a CNM triple-layer with ≈3.3 nm thickness, where in the upper left part there is only one layer (≈1.1 nm). Figure 4d shows a CNM with 1.7 nm thickness. The structures of the holey carbon film become more blurred with increasing thickness due to an increase in scattering of the incident helium beam by the CNM before hitting the holey carbon film, as illustrated in Figure 4e.
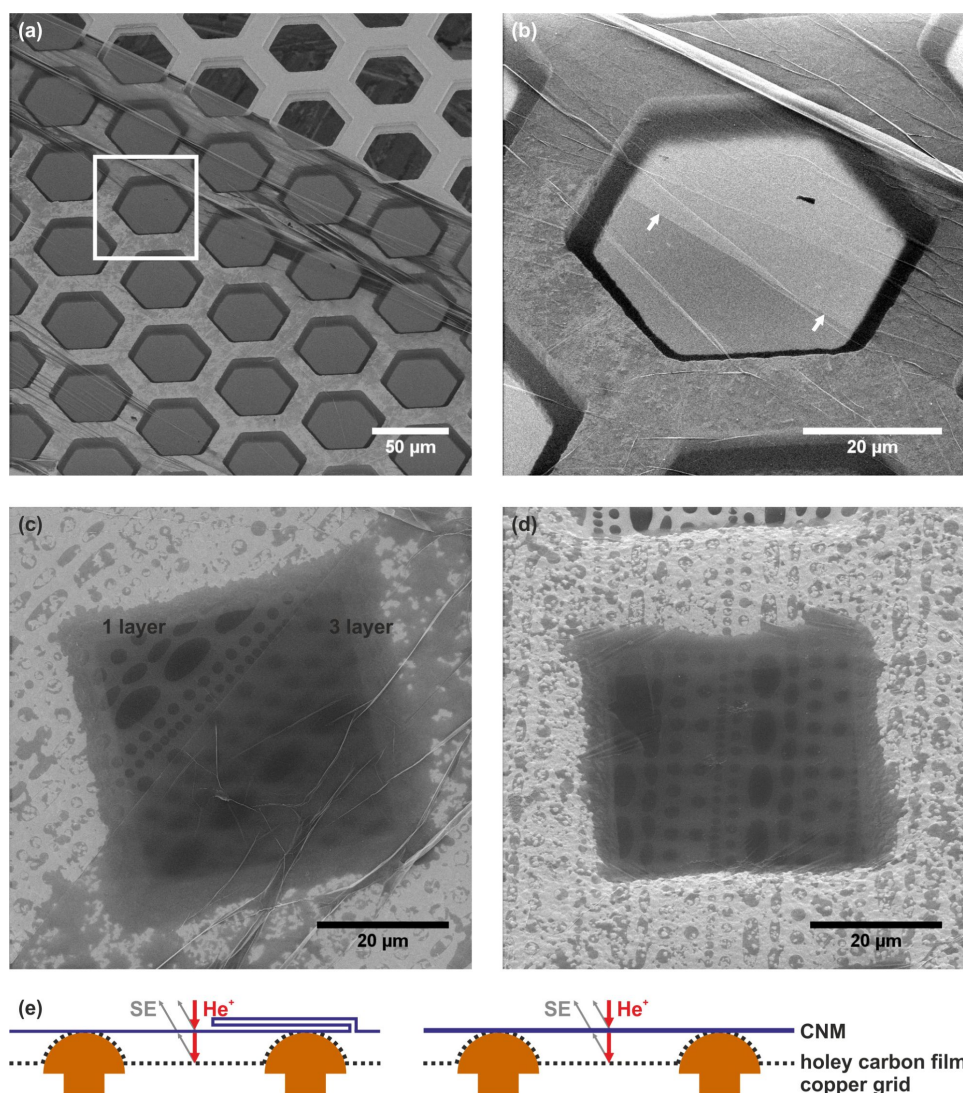
Figure 4: CNMs transferred on (a,b) bare copper TEM grids and (c,d) on grids with carbon films with regular openings (quantifoil multi-A). (b) A magnified image of the highlighted area in (a). (c,d) Increasing CNM thickness leads to more scattering of the He beam. The thickness of a single CNM layer is 1.1 nm in (c) and 1.7 nm in (d) [26]. (e) Schematic cross section of the samples in (c) and (d). The triple-layer region is folded according the scheme, which is consistent with the observed existence of a single-layer CNM on both sides of the fold. Detailed information on all HIM images is given in Supporting Information File 1, Tables S1 and S2.

Figure 5 gives an image series that demonstrates the effect of charging. All images were recorded with a very low dwell time, maximum frame averaging, but without charge compensation and with different beam currents. The contrast and brightness settings were changed for each image in order to adjust the detector to a sensitive range. Each image in this series displays the identical sample position. The images show a gold TEM grid that is covered by a CNM. The upper, square opening exhibits a tear in the membrane from the upper right to the lower left corner. Each image shows 4 features of interest: intact, freestanding CNMs, CNM-covered gold surfaces, bare gold surfaces and the background, which is visible in the uncovered opening in the grid.

In Figure 5a–e an increase in the beam current is accompanied by an increase in the signal-to-noise ratio, which can be clearly seen on the bare gold surfaces. We also observed a darkening of the freestanding CNMs with increasing beam current due an increase in electrostatic charging. From this image series, we can determine the onset of charging for a 100 µm^2 CNM under the aforementioned imaging conditions for beam currents of 0.3–0.7 pA. When imaged under the same conditions, membranes of the same size with a higher or lower conductivity should display an onset of charging at higher or lower beam currents, respectively. Thus, an imaging series such as that presented in Figure 5 might be able to give a comparative estimate about the conductivity differences between two membrane
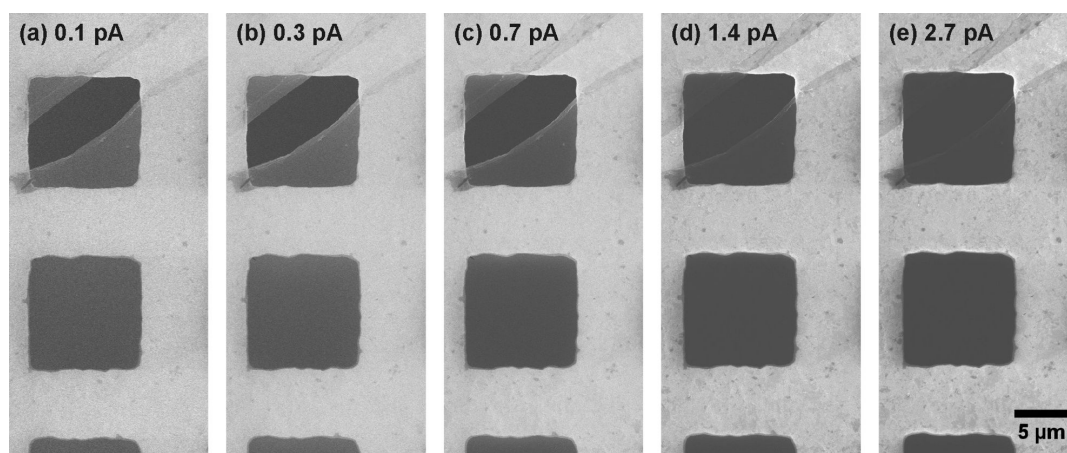
Figure 5: CNM on a gold grid. The same spot was imaged with different beam currents but under otherwise identical conditions. All images were taken without charge compensation. For a reasonable comparison of these images, the greyscale levels of the dark background of the uncovered openings as well as the surface of the bare gold areas were adjusted to be identical by means of changing the brightness and contrast of each whole image. Detailed information on all HIM images is given in Supporting Information File 1, Tables S1 and S2.

types. Note that differences in the secondary electron yield will also change the onset beam current for charging. Increasing the beam current not only leads to darker image areas for the free-standing membranes but also for CNMs on the gold support bars. Thereby, it increases the contrast between covered and bare gold surfaces.

The effectiveness of the electron flood gun for charge compensation in HIM is demonstrated by the images in Figure 6. A large area (i.e. $\approx 0.5 \times 0.5$ mm^2), freestanding CNM is imaged without and with charge compensation in Figure 6a,b, respectively. As expected, the typical charged image features are removed when the compensation is employed. That is, the free-

standing CNMs become brighter in comparison to the copper grid bars. A noteworthy observation in freestanding CNM regions close to the support structure can be made. Without charge compensation, these parts of the membrane appear darker than the central part of the CNM. This can be explained by the fact that near the support bar the CNM extents very close over the horizontal copper surface with a micron-sized gap. This is a result of the step-like shape of the supporting copper bars, which is illustrated in the grid cross section of Figure 1e. In the central part of the CNM, the He$^+$ beam penetrates the membrane and impinges upon the sample holder underneath, which is far away and emits secondary electrons that reach the detector. Near the edges of the support, the He$^+$ beam impinges
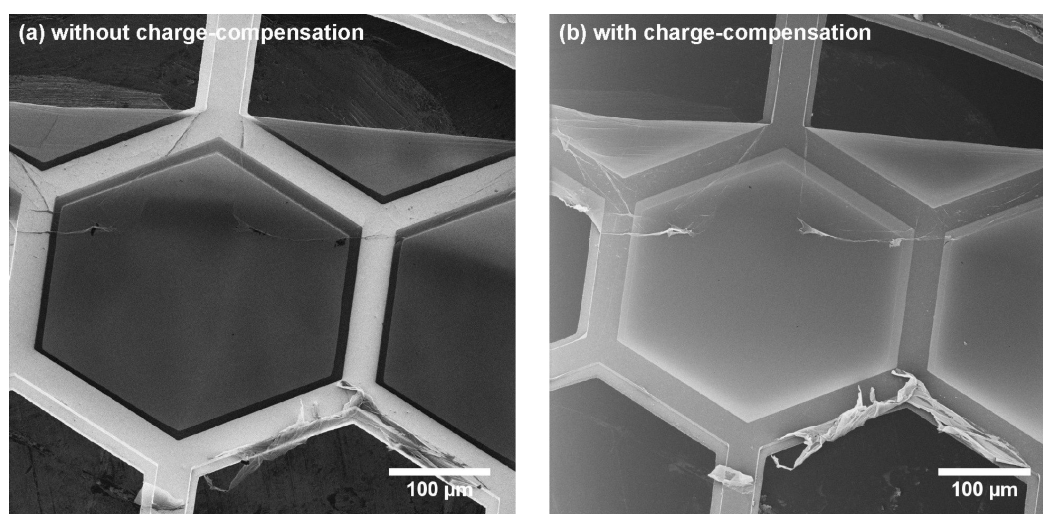
Figure 6: The same CNM is imaged (a) without and (b) with charge compensation. Detailed information on all HIM images is given in Supporting Information File 1, Tables S1 and S2.

on the step-like feature of the copper grid bar, which is very close to the CNM. Therefore, secondary electrons from this region are blocked by the CNM and do not reach the detector. Thus, in the central part of the CNM, a part of the detector signal originates from the sample holder, which is responsible for the observable inhomogeneous features in the CNM image. With charge compensation, as shown in Figure 6b, the membrane near the support structure becomes even brighter than the central part of the CNM. Again, the copper surface (some microns below the CNM) is responsible for this behaviour: Secondary electrons emitted from the copper reach the CNM and act as an additional charge compensation mechanism, leading to an increased signal at the detector. However, the charge compensation in the central part of the membrane is still sufficiently effective as the major signal originates from the CNM and not from the sample holder. This is quite obvious due to the increased image brightness as well as the more homogenous appearance of the central part of the CNM. Note that the described secondary-electron-induced partial charge compensation near the rim of CNMs also applies in Figure 6a, but in this case, the amount of secondary electrons emitted by all CNM areas is much lower than the contribution from the underlying sample holder.

HIM imaging of CNMs at higher resolution is possible in principle. However, homogenous CNMs do not possess any structures that can be imaged at the highest resolution of HIM. Such HIM images are featureless, showing only a constant grey value throughout the whole image (not shown here). This is different for CNMs with a structure imposed on the membrane. As an example, high resolution HIM images of CNMs are available where the membranes were exposed to highly charged ions [27]. This treatment induced nanopores in the size range of 10 nm, which were imaged by HIM with a reasonably high resolution [27]. Note that high resolution imaging of large free-standing CNMs requires the use of the electron flood gun for charge compensation as otherwise the membrane will easily rupture due to local charging.

Conclusion

We have shown that helium ion microscopy is a very effective technique for characterizing CNMs. Additionally, CNMs have proven to be ideal test objects for evaluating the imaging characteristics of a HIM. The large range of magnification of a HIM allows for the visualization of TEM grids by recording a single HIM image. The effects of charging as well as background features were discussed. We demonstrated that the sample holder under the CNM surface can induce image artefacts, which are avoidable by mounting the grid on top of a deep cavity that acts like a Faraday cup. The presented systematic evaluation of membrane charging might enable the electrical

conductivity of arbitrary 2D objects to be determined. The optimized HIM imaging of insulating membranes requires electron-flood-gun-based charge compensation, which was demonstrated with CNMs.

Experimental

Helium ion microscopy (HIM) was performed with a Carl Zeiss Orion Plus® microscope. The helium ion beam was operated at a current between 0.1–2.7 pA. The secondary electrons were collected by an Everhart–Thornley detector at 500 V grid voltage. For some images, the working distance was chosen to be as high as 37 mm, which allowed the acquisition of images with a very large field of view. The following imaging parameters were employed for optimized CNM imaging: a dwell time of 0.5 µs, up to 255 frame averages, and with the electron flood gun operated in line mode. The image acquisition was usually performed with fewer frame averages if the image noise level was observed to decrease to a negligible level.

The CNMs were prepared as described elsewhere [26] from the following molecules: (a) S-(pyren-1-ylmethyl) ethanethioate (MP1); (b) 1,1'-biphenyl-4-thiol (BPT); (c) S,S'-(3',4',5',6'-tetraphenyl-[1,1':2',1''-terphenyl]-4,4''-diyl) diethanethioate (HPB); (d) naphtalene-2-thiol (NPTH); (e) 2-bromo-11-(1'-[4'-(S-acetylthiomethyl)phenyl]acetyl)-5,8,14,17-tetra(3',7'-dimethyloctyl)-hexa-*peri*-hexabenzocoronene (HBC-Br). The CNMs in the presented figures were produced from the following molecules: MP1 in Figure 1a,b; HPB in Figure 1d and Figure 2a,d; NPTH in Figure 2c and Figure 4a,b; HBC-Br in Figure 4c,d; and BPT in all other figures. As shown in Figure 4c,d, different SAM structures for HBC-Br molecules led to different CNM thicknesses [26]. In Figure 4c, one HBC-Br CNM layer is 1.1 nm thick and in Figure 4d, the thickness of the HBC-Br CNM is 1.7 nm.

Supporting Information

Supporting Information File 1
Additional Experimental Information.
The supporting information provides details about the type of CNM and the employed HIM scan parameters for all presented images. Furthermore, exemplary SEM images of CNMs are shown.
[http://www.beilstein-journals.org/bjnano/content/supplementary/2190-4286-6-175-S1.pdf]

Acknowledgements

References

1. Gölzhäuser, A.; Eck, W.; Geyer, W.; Stadler, V.; Weimann, T.; Hinze, P.; Grunze, M. *Adv. Mater.* **2001,** *13,* 806–809. doi:10.1002/1521-4095(200106)13:11%3C803::AID-ADMA806%3E3.0. CO;2-W
2. Turchanin, A.; Schnietz, M.; El-Desawy, M.; Solak, H. H.; David, C.; Gölzhäuser, A. *Small* **2007,** *3,* 2114–2119. doi:10.1002/smll.200700516
3. Eck, W.; Küller, A.; Grunze, M.; Völkel, B.; Gölzhäuser, A. *Adv. Mater.* **2005,** *17,* 2583–2587. doi:10.1002/adma.200500900
4. Turchanin, A.; Beyer, A.; Nottbohm, C. T.; Zhang, X. H.; Stosch, R.; Sologubenko, A.; Mayer, J.; Hinze, P.; Weimann, T.; Gölzhäuser, A. *Adv. Mater.* **2009,** *21,* 1233–1237. doi:10.1002/adma.200803078
5. Turchanin, A.; Weber, D.; Büenfeld, M.; Kisielowski, C.; Fistul, M. V.; Efetov, K. B.; Weimann, T.; Stosch, R.; Mayer, J.; Gölzhäuser, A. *ACS Nano* **2011,** *5,* 3896–3904. doi:10.1021/nn200297n
6. Rhinow, D.; Weber, N.-E.; Turchanin, A. *J. Phys. Chem. C* **2012,** *116,* 12295–12303. doi:10.1021/jp301877p
7. Ai, M.; Shishatskiy, S.; Wind, J.; Zhang, X. H.; Nottbohm, C. T.; Mellech, N.; Winter, A.; Vieker, H.; Qiu, J.; Dietz, K. J.; Gölzhäuser, A.; Beyer, A. *Adv. Mater.* **2014,** *26,* 3421–3426. doi:10.1002/adma.201304536
8. Geyer, W.; Stadler, V.; Eck, W.; Zharnikov, M.; Gölzhäuser, A.; Grunze, M. *Appl. Phys. Lett.* **1999,** *75,* 2401–2403. doi:10.1063/1.125027
9. Schnietz, M.; Turchanin, A.; Nottbohm, C. T.; Beyer, A.; Solak, H. H.; Hinze, P.; Weimann, T.; Gölzhäuser, A. *Small* **2009,** *5,* 2651–2655. doi:10.1002/smll.200901283
10. Turchanin, A.; Tinazli, A.; El-Desawy, M.; Großmann, H.; Schnietz, M.; Solak, H. H.; Tampé, R.; Gölzhäuser, A. *Adv. Mater.* **2008,** *20,* 471–477. doi:10.1002/adma.200702189
11. Turchanin, A.; Gölzhäuser, A. *Prog. Surf. Sci.* **2012,** *87,* 108–162. doi:10.1016/j.progsurf.2012.05.001
12. Nottbohm, C. T.; Turchanin, A.; Beyer, A.; Stosch, R.; Gölzhäuser, A. *Small* **2011,** *7,* 874–883. doi:10.1002/smll.201001993
13. Zheng, Z.; Nottbohm, C. T.; Turchanin, A.; Muzik, H.; Beyer, A.; Heilemann, M.; Sauer, M.; Gölzhäuser, A. *Angew. Chem., Int. Ed.* **2010,** *49,* 8493–8497. doi:10.1002/anie.201004053
14. Beyer, A.; Turchanin, A.; Nottbohm, C. T.; Mellech, N.; Schnietz, M.; Gölzhäuser, A. *J. Vac. Sci. Technol., B* **2010,** *28,* C6D5. doi:10.1116/1.3511475
15. Zhang, X.; Waitz, R.; Yang, F.; Lutz, C.; Angelova, P.; Gölzhäuser, A.; Scheer, E. *Appl. Phys. Lett.* **2015,** *106,* 063107. doi:10.1063/1.4908058
16. Nottbohm, C. T.; Beyer, A.; Sologubenko, A. S.; Ennen, I.; Hütten, A.; Rösner, H.; Eck, W.; Mayer, J.; Gölzhäuser, A. *Ultramicroscopy* **2008,** *108,* 885–892. doi:10.1016/j.ultramic.2008.02.008
17. Hlawacek, G.; Veligura, V.; van Gastel, R.; Poelsema, B. *J. Vac. Sci. Technol., B* **2014,** *32,* 020801. doi:10.1116/1.4863676
18. Bell, D. C.; Lemme, M. C.; Stern, L. A.; Williams, J. R.; Marcus, C. M. *Nanotechnology* **2009,** *20,* 455301. doi:10.1088/0957-4484/20/45/455301
19. Lemme, M. C.; Bell, D. C.; Williams, J. R.; Stern, L. A.; Baugher, B. W. H.; Jarillo-Herrero, P.; Marcus, C. M. *ACS Nano* **2009,** *3,* 2674–2676. doi:10.1021/nn900744z
20. Fox, D.; Zhou, Y. B.; O'Neill, A.; Kumar, S.; Wang, J. J.; Coleman, J. N.; Duesberg, G. S.; Donegan, J. F.; Zhang, H. Z. *Nanotechnology* **2013,** *24,* 335702. doi:10.1088/0957-4484/24/33/335702
21. Abbas, A. N.; Liu, G.; Liu, B. L.; Zhang, L. Y.; Liu, H.; Ohlberg, D.; Wu, W.; Zhou, C. W. *ACS Nano* **2014,** *8,* 1538–1546. doi:10.1021/nn405759v
22. Archanjo, B. S.; Fragneaud, B.; Cançado, L. G.; Winston, D.; Miao, F.; Achete, C. A.; Medeiros-Ribeiro, G. *Appl. Phys. Lett.* **2014,** *104,* 193114. doi:10.1063/1.4878407
23. Guo, H.; Gao, J.; Ishida, N.; Xu, M.; Fujita, D. *Appl. Phys. Lett.* **2014,** *104,* 031607. doi:10.1063/1.4862819
24. Hlawacek, G.; Veligura, V.; Lorbek, S.; Mocking, T. F.; George, A.; van Gastel, R.; Zandvliet, H. J. W.; Poelsema, B. *Beilstein J. Nanotechnol.* **2012,** *3,* 507–512. doi:10.3762/bjnano.3.58
25. Hlawacek, G.; Ahmad, I.; Smithers, M. A.; Kooij, E. S. *Ultramicroscopy* **2013,** *135,* 89–94. doi:10.1016/j.ultramic.2013.07.010
26. Angelova, P.; Vieker, H.; Weber, N.-E.; Matei, D.; Reimer, O.; Meier, I.; Kurasch, S.; Biskupek, J.; Lorbach, D.; Wunderlich, K.; Chen, L.; Terfort, A.; Klapper, M.; Müllen, K.; Kaiser, U.; Gölzhäuser, A.; Turchanin, A. *ACS Nano* **2013,** *7,* 6489–6497. doi:10.1021/nn402652f
27. Ritter, R.; Wilhelm, R. A.; Stöger-Pollach, M.; Heller, R.; Mücklich, A.; Werner, U.; Vieker, H.; Beyer, A.; Facsko, S.; Gölzhäuser, A.; Aumayr, F. *Appl. Phys. Lett.* **2013,** *102,* 063112. doi:10.1063/1.4792511

BEILSTEIN JOURNAL OF NANOTECHNOLOGY

The role of low-energy electrons in focused electron beam induced deposition: four case studies of representative precursors

Rachel M. Thorman[1,2], Ragesh Kumar T. P.[1], D. Howard Fairbrother[2] and Oddur Ingólfsson[*1]

Review

Abstract

Focused electron beam induced deposition (FEBID) is a single-step, direct-write nanofabrication technique capable of writing three-dimensional metal-containing nanoscale structures on surfaces using electron-induced reactions of organometallic precursors. Currently FEBID is, however, limited in resolution due to deposition outside the area of the primary electron beam and in metal purity due to incomplete precursor decomposition. Both limitations are likely in part caused by reactions of precursor molecules with low-energy (<100 eV) secondary electrons generated by interactions of the primary beam with the substrate. These low-energy electrons are abundant both inside and outside the area of the primary electron beam and are associated with reactions causing incomplete ligand dissociation from FEBID precursors. As it is not possible to directly study the effects of secondary electrons in situ in FEBID, other means must be used to elucidate their role. In this context, gas phase studies can obtain well-resolved information on low-energy electron-induced reactions with FEBID precursors by studying isolated molecules interacting with single electrons of well-defined energy. In contrast, ultra-high vacuum surface studies on adsorbed precursor molecules can provide information on surface speciation and identify species desorbing from a substrate during electron irradiation under conditions more representative of FEBID. Comparing gas phase and surface science studies allows for insight into the primary deposition mechanisms for individual precursors; ideally, this information can be used to design future FEBID precursors and optimize deposition conditions. In this review, we give a summary of different low-energy electron-induced fragmentation processes that can be initiated by the secondary electrons generated in FEBID, specifically, dissociative electron attachment, dissociative ionization, neutral dissociation, and dipolar dissociation, emphasizing the different nature and energy dependence of each process. We then explore the value of studying these processes through comparative gas phase and surface studies for four commonly-used FEBID precursors:

MeCpPtMe$_3$, Pt(PF$_3$)$_4$, Co(CO)$_3$NO, and W(CO)$_6$. Through these case studies, it is evident that this combination of studies can provide valuable insight into potential mechanisms governing deposit formation in FEBID. Although further experiments and new approaches are needed, these studies are an important stepping-stone toward better understanding the fundamental physics behind the deposition process and establishing design criteria for optimized FEBID precursors.

Review
1 Introduction

Focused electron beam induced deposition (FEBID) [1-3] is a direct-write method capable of creating nanostructures with potential scientific and industrial applications. The advantages of FEBID stem from its ability to write 3D nanostructures of close to any geometry and to write on uneven surfaces. In FEBID (Figure 1), a focused high-energy electron beam impinges on a surface of a substrate that is continuously exposed to a gas stream of precursor molecules as a material source for the intended deposit. The precursor molecules are physisorbed on the surface in dynamic equilibrium with the gas feed, and ideally decompose under the electron beam to leave a well-defined deposit on the surface. The lateral dimensions of deposited structures are controlled by moving the electron beam and the vertical dimensions are controlled through variation of the dwell time.
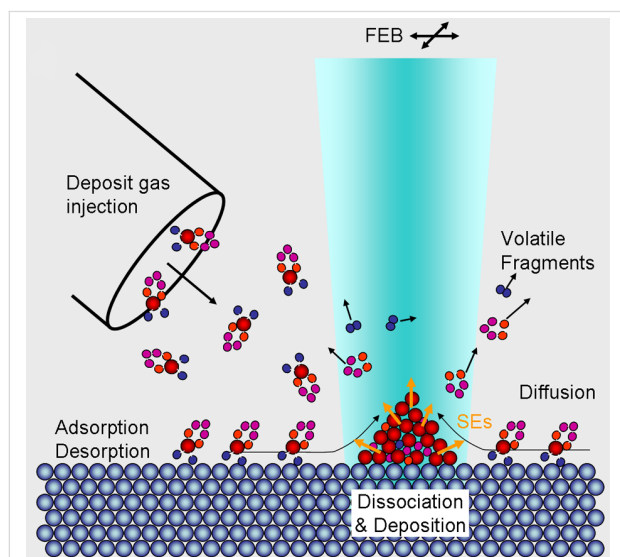
Figure 1: Schematic representation of the FEBID process (reproduced with permission from [2], Copyright (2008) American Vacuum Society): Precursor molecules are supplied through a gas injection system, shown on the left side, and are physisorbed on the surface in dynamic equilibrium with the gas feed. Ideally, the precursor molecules decompose under the electron beam (shown with turquoise shading) to leave a well-defined deposit on the surface, while volatile fragments are pumped away. Diffusion of the physisorbed molecules and the generation of secondary electrons (SEs) are also indicated with black and orange arrows, respectively.

Precursor molecules used for depositing metal-containing nanostructures are typically organometallic compounds with a central metal atom and ligand architectures that lend the compounds the following attributes: i) sufficient vapor pressure to facilitate their introduction into a vacuum chamber, ii) chemical stability under ambient conditions and iii) non-toxicity and easy handling. These criteria are the same as those that define suitable precursors for chemical vapor deposition (CVD) [4,5]. Because of this, as well as their widespread commercial availability, FEBID has to-date mainly relied on existing CVD precursors. There is, however, a fundamental difference between the physics and chemistry behind precursor decomposition and deposit formation in CVD and in FEBID. While CVD is primarily thermally driven, FEBID is initiated by electron/molecule interactions. Although thermal effects and surface-induced reactions may also play a significant role in FEBID, the initial electron-driven step will play an important role in defining the final composition of the deposits.

Because the physics and chemistry determining the spatial resolution, aspect ratio, and composition of FEBID deposits is complex, FEBID is unlikely to reach its full capacity through empirical process parameter optimization with currently available CVD precursors. Rather, a sound understanding of the chemistry and physics governing the deposit formation and the translation of such understanding to design parameters for precursor molecules tailored for FEBID is necessary.

In terms of the electron-induced processes in FEBID, it is clear that the confinement of electron/molecule interactions to the focal width of the incident high-energy electron beam is compromised by elastic and inelastic scattering processes. A portion of the high-energy electrons impinging on the surface and penetrating into the substrate will be backscattered and will exit the surface within an area defined by the scattering angle and the electron energy, rather than by the focal width of the incident beam. Unlike the primary electrons (PEs), which are confined to the focal width of the PE beam, these lower energy scattered electrons will be able to initiate electron-driven reactions outside the area of the PE beam. Moreover, the PEs lose energy as a result of inelastic, ionizing processes which, in turn, give rise to a large amount of secondary electrons (SEs) produced within the substrate. More importantly, these SEs are also produced at or close to the surface of the substrate where they may induce fragmentation of the adsorbed precursor mole-

cules (Figure 2). The reactivity of the SEs with precursor mole-
cules is thus critical in determining the spatial resolution of the
deposit. This is even more important with regard to achievable
aspect ratios of vertical structures as both backward and
forward scattered primary electrons (PEs) and SEs will reach
the surface of their sides (Figure 2b).
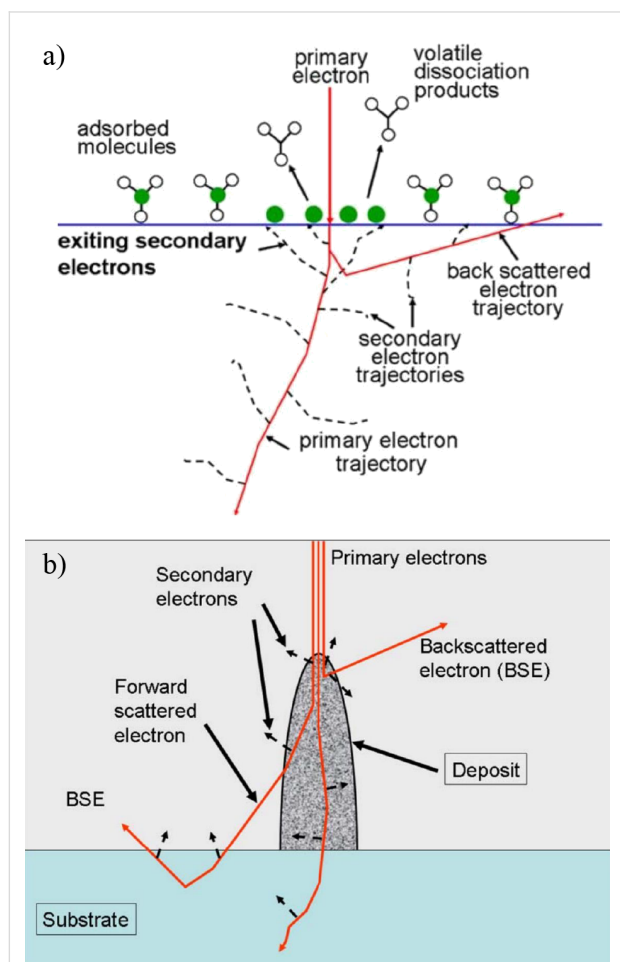
Figure 2: Schematic representation of elastic and inelastic scattering
of high-energy primary electrons impinging on a solid substrate and of
the generation of SEs through inelastic ionization processes (repro-
duced with permission from [2], Copyright (2008) American Vacuum
Society). (a) Primary electrons impinging on the surface and pene-
trating the substrate will in part be backscattered and will exit the
surface within an area defined by the scattering angle and the electron
energy. These electrons lose energy as a result of inelastic, ionizing
processes, which in turn, give rise to a large amount of secondary
electrons (SEs) produced within the substrate, and more importantly,
these SEs are also produced at or close to the surface of the sub-
strate. (b) The same process depicted for a three-dimensional struc-
ture growing under the exposure of precursor molecules to the high-
energy PE beam. In this case, forward scattered electrons can also
reach the surface and produce SEs at the sides of the structure. This
may lead to stronger restrictions on the achievable aspect ratios than
apply for the achievable resolution of thin layer deposition.

In general, the SE energy distribution extends with appreciable
intensities down to 0 eV, peaks well below 10 eV, and has a

higher-energy tail stretching well above 50 eV. The actual form
(peak position and width) of the SE *energy distribution* depends
largely on the nature of the substrate (work function, Fermi
energy, and *Z*-value (atomic number)), and to a lesser extent on
the PE energy (as long as it is above about 100 eV) [6-8].
Conversely, the SE *yield* depends significantly on both the
nature of the substrate and the PE energy. Note that the former
represents the distributions of SE energies while the latter
means the total SE yield as function of PE energy. The prin-
cipal variable determining the influence of the PE energy on the
SE yield at the surface is their penetration depth. This, in turn,
depends mainly on the *Z*-value of the substrate. In general, the
SE yield reaches a distinct maximum well below 1 keV PE
energy, before decreasing rapidly again, as is discussed in more
detail in context to the commonly used FEBID precursor
MeCpPtMe$_3$ in section 4.1.

Figure 3 shows the experimentally determined SE energy distri-
bution for 400 eV PEs impinging on a Ni(111) surface [6] and
for 1 keV electrons impinging on a Ag(100) surface [9], along
with the approximate electron energy ranges in which the prin-
cipal electron induced processes are operative, i.e., dissociative
electron attachment (DEA), neutral dissociation (ND), and
dissociative ionization (DI). While the secondary electron inten-
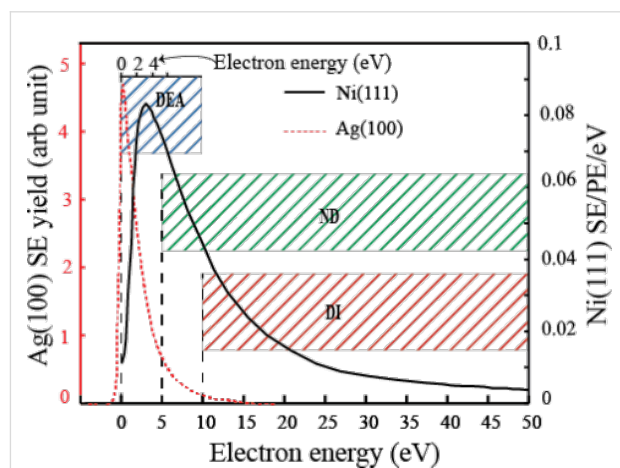
Figure 3: Experimentally measured SE spectra from Ni(111) [6] irradi-
ated by PEs with 400 eV impact energy (black solid line) and from
Ag(100) [9] subjected to PEs with 1 keV impact energy (red dotted
line). The left-hand *y*-axis shows the relative SE intensity from
Ag(100), while the right-hand *y*-axis shows the absolute SE intensity
from Ni(111) in SEs per PE per eV (SE/PE/eV). The vertical bars show
the approximate electron energy ranges in which the principal electron
induced processes are operative, i.e., dissociative electron attachment
(DEA), neutral dissociation (ND), and dissociative ionization (DI). The
relative extent of these different electron-induced fragmentation
processes will depend not only on their relative cross sections, but also
on the actual SE energy distribution. From the data shown here, for
example, high cross section DEA processes at low energies would
likely be dominating for Ag(100) while the integral efficiency of DI and
ND processes at higher energies would be more important for Ni(111)
(see also [10]).

sity from Ni(111) peaks at about 4 eV with a value close to 0.1 SEs/PE/eV (100 SEs per 1 keV electron) and is still approximately 0.02 SEs/PE/eV at 15 eV [6], the SE intensity from Ag(100) peaks below 1 eV and is already down to 1/10 of the peak intensity at 5 eV [9]. Hence, it is clear that deposit formation in FEBID will be governed by a convolution of the efficiencies of the relevant electron-stimulated processes occurring at the surface and the SE energy distribution at the surface of the substrate. In the case of three-dimensional structures this would be the surface of the growing deposit. Thus, to describe the physics and chemistry of the deposition process in FEBID, the effect of these SEs must be well understood.
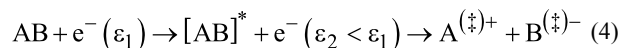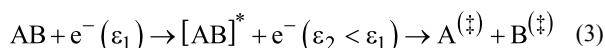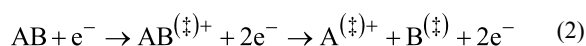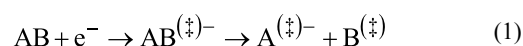
This notion that the low energy SEs produced in FEBID may play a significant and even a determining role in the deposit formation has been verified both by simulations [11] and by experiments [12]. In recent years, it has motivated a number of gas phase studies focusing on the energy dependence of the branching ratios and cross sections for various low energy (0–100 eV) electron-induced reactions with organometallic precursors such as $Pt(PF_3)_4$ [13,14], $MeCpPtMe_3$ [15], $W(CO)_6$ [16,17], $Cu(hfac)_2$ and $Pd(hfac)_2$ [18], $Co(CO)_3NO$ [10] and $Fe(CO)_5$ [19]. These processes, which are comprised of DEA, DI, ND, and dipolar dissociation (DD), cannot be distinguished in FEBID or surface experiments with high-energy PE beams, where the precursor molecules are simultaneously exposed to a distribution of low energy SEs in addition to the PEs. However, in gas phase experiments, where these precursor molecules interact with well-defined low energy electron beams, the energy dependence and extent of individual fragmentation processes may be unambiguously determined. Such data, in conjunction with surface experiments with high-energy PE beams, may in turn help to understand the mechanism and extent of action of the low energy SEs in the actual FEBID of the same precursor molecules.

In this contribution, we first give a short summary of the different low energy electron-induced fragmentation processes that can occur (DEA, DI, ND, and DD) with emphasis on the different nature and different energy dependence of these processes. We then explore the value of studying these processes through comparative gas phase and surface studies with reference to previously performed gas phase and surface studies of four organometallic FEBID precursors: trimethyl(methylcyclopentadienyl)platinum(IV) ($MeCpPtMe_3$) [15,20,21], tetrakis(trifluorophosphine)-platinum(0) ($Pt(PF_3)_4$) [13,14,22,23], cobalt tricarbonyl nitrosyl ($Co(CO)_3NO$) [10,24,25] and tungsten hexacarbonyl ($W(CO)_6$) [16,17,26]. We also discuss these results in the general context of the use of these precursors in FEBID and as part of the ongoing effort to understand the fragmentation mechanisms

behind deposit formation. Finally, future perspectives and the relevance of these studies to establishing design criteria for precursor molecules specifically tailored for FEBID will be discussed.

2 Low energy electron-induced fragmentation

In the secondary electron energy range relevant for FEBID (<100 eV), there are four distinct mechanisms by which low energy electrons may cause molecular fragmentation, and thus initiate deposition of typical organometallic precursors. These mechanisms are: dissociative electron attachment (DEA), dissociative ionization (DI), neutral dissociation (ND) and dipolar dissociation (DD) [27-32] as depicted in Equations 1–4.

$$AB + e^- \rightarrow AB^{(\ddagger)-} \rightarrow A^{(\ddagger)-} + B^{(\ddagger)} \tag{1}$$

$$AB + e^- \rightarrow AB^{(\ddagger)+} + 2e^- \rightarrow A^{(\ddagger)+} + B^{(\ddagger)} + 2e^- \tag{2}$$

$$AB + e^- (\varepsilon_1) \rightarrow [AB]^* + e^- (\varepsilon_2 < \varepsilon_1) \rightarrow A^{(\ddagger)} + B^{(\ddagger)} \tag{3}$$

$$AB + e^- (\varepsilon_1) \rightarrow [AB]^* + e^- (\varepsilon_2 < \varepsilon_1) \rightarrow A^{(\ddagger)+} + B^{(\ddagger)-} \tag{4}$$

Here; "$(\ddagger)$" denotes that the fragment(s) may be in a vibrationally and/or electronically excited state, "*" denotes the electronic excitation of the intermediate leading to ND and DD, and ε_1 and ε_2 denote the incident energy of the electron and its remaining energy after the inelastic scattering process, respectively.

Dissociative electron attachment (Equation 1) is a resonant process in which an electron is initially captured by the molecule to form a transient negative ion (TNI). This can be understood as a vertical transition from the ground state of the neutral molecule to the ground (or any accessible excited state) of the anion, as is shown in Figure 4. Consequently, the TNI formed is generally in a vibrationally and/or electronically excited state. Under collision-free conditions, it relaxes rapidly either through re-emission of the electron (autodetachment; AD) or through dissociation (DEA). Dissociative electron attachment is active below the ionization threshold of the molecule and generally most efficient at very low incidents energies. The cross section for a given DEA process is defined by the initial attachment cross section multiplied by the probability that the TNI survives nuclear relaxation beyond the crossing point of the respective potential energy curves (r_c in Figure 4). Thus, DEA is confined to narrow energy ranges defined by the Franck–Condon overlap of the wave function of neutral ground state and the respective
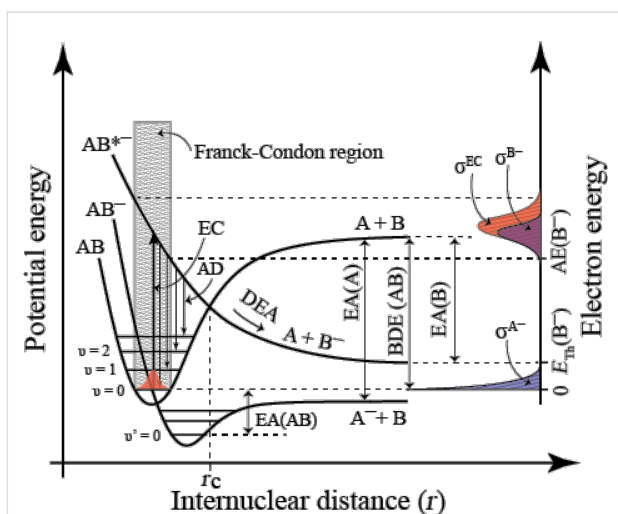
Figure 4: Simplified two-dimensional potential energy diagram for quasi-diatomic dissociation through electron attachment (DEA). The neutral ground state (AB) is depicted along with the anionic ground state (AB⁻) and an electronically excited anionic state (AB*⁻). Electron capture (EC) proceeds through a vertical transition (thick vertical arrow) within the Franck–Condon region (shaded area) and leads to the formation of a transient negative ion (TNI; AB⁻ or AB*⁻ in this case). The TNI formed can then relax through reemission of the electron (autodetachment; AD) which is depicted with thin vertical arrows from AB*⁻ to the neutral electronic ground state. In the case where this reemission process results in a transition to the ground vibrational state, the scattering process is elastic while the other arrows depict vibrationally inelastic processes. The TNI may also relax through nuclear relaxation along the respective anionic potential energy surfaces (DEA). The dissociative asymptotes are here shown to lead to A⁻/B and B⁻/A for AB⁻ and AB*⁻ respectively. For AB⁻ the potential energy curve is shown crossing the vibrational ground state of the neutral; the AB⁻ dissociative asymptote lies below this energy. Hence, the electron affinity of A (EA(A)) is larger than the bond dissociation energy of AB (BDE(AB)). Attachment of a 0 eV electron may thus lead directly to the formation of A⁻. For AB*⁻ a nuclear relaxation beyond the crossing point with the neutral ground state (r_c) must lead to dissociation, as AD is not possible for nuclear separation beyond this point. The thermochemical threshold for this process (E_{th}(B⁻)) is given by the difference between the electron affinity of B and the BDE(AB) as depicted on the right-hand y-axis. The appearance energy (AE) for the fragment B⁻, conversely, is defined by the Franck–Condon overlap and is, in this case, substantially higher than E_{th}(B⁻). This is depicted on the right-hand y-axis, in terms of the *reflection principle*, which shows the energy dependence of the electron capture cross section (σ^{EC}) as a reflection of the Franck–Condon overlap. The DEA cross section ($\sigma^{B⁻}$), which is the product of the attachment cross section and the survival probability of the TNI, i.e., the likelihood that the nuclear relaxation exceeds r_c before autodetachment is also shown.

negative ion states, and by the survival probability of the TNI with regard to AD. At very low electron energies where s-wave attachment dominates, the cross section is proportional to $E^{-1/2}$ [33] (see also [34]) and the cross section is thus highest at threshold (i.e., close to 0 eV). The survival probability is also high close to the threshold as the distance to the crossing point of the anionic ground state is short (as is depicted in Figure 4). Such a threshold process is depicted for the lower anionic potential curve in Figure 4, which is shown crossing the ground vibrational state of the neutral molecule, favoring transitions at

or close to 0 eV incident electron energy (see also the caption to Figure 4).

For FEBID, the consequence of DEA being most efficient close to 0 eV incident electron energy is that this process is only likely to contribute significantly to precursor decomposition at very low incident electron energies. Moreover, as dissociation will generally proceed along the initial anionic potential energy surface, selective single bond ruptures dominate in DEA. For such a process to be thermochemically accessible at 0 eV, the electron affinity of the neutral corresponding to the anionic fragment formed (A in Equation 1) must exceed the bond dissociation energy (BDE) of the bond being broken (A–B in Equation 1).

It should, however, be noted that the treatment here is simplified to a quasi-diatomic model and molecular rearrangement and formation of new bonds upon electron capture can in some cases lead to considerably more fragmentation with fairly high cross sections at low incident energies. Good examples of such reactions are the extensive fragmentation of tetrafluorophenol and tetrafluoroaniline [35] as well as that of the commonly used FEBID precursor ligands tri- and hexafluoroacetylacetone [36]. In each of these cases, low energy electron attachment leads to the formation of neutral HF, which in turn releases the 5.9 eV HF BDE [37] and promotes further fragmentation of the parent molecule. This is also observed for other molecules such as the amino acids glycine [38] and valine [39], and hexafluoroacetone azine [40], wherein the formation of molecular hydrogen and ethane enables the otherwise thermochemically inhibited formation of CN⁻ at low incident electron energies. With a suitable choice of ligands, such intramolecular reactions may thus also provide a new means to enhance fragmentation of potential FEBID precursors through DEA.

Perhaps more important in FEBID is the fact that interaction of precursor molecules with the surface of the substrate may alter the DEA cross sections substantially. This may be simply due to the enabled energy transfer offering a new relaxation path that competes with DEA (and AD). Conversely, in other instances polarization interactions may stabilize the TNI with respect to autodetachment and facilitate DEA [41,42].

Dissociative ionization (Equation 2) is fundamentally different from DEA. Here, energy transfer from the incident electron leads to removal of a bound electron from the target molecule and the formation of a parent cation. Similarly to DEA, this can be depicted as a vertical transition of an initially bound electron to the ionization continuum of the molecule as shown in Figure 5. However, if the incident energy in the electron/molecule collision exceeds the ionization energy of the respective
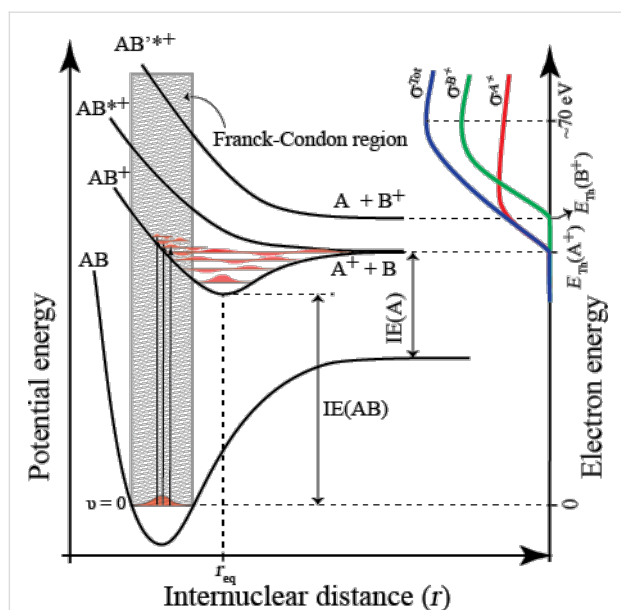
Figure 5: Simplified two-dimensional potential energy diagram for a quasi-diatomic dissociation through electron impact ionization (DI). The ionization process is depicted as a vertical transition from the neutral ground state to the cationic ground state and higher lying cationic states within the Franck–Condon region (shaded area). In this representation the cationic ground state has a considerably larger equilibrium bond length (r_{eq}) compared to the neutral, leading to a significant transition probability to vibrational states that are energetically above the dissociation limit. For simplification, the excited cationic states (AB^{+*} and $AB^{+'*}$) are shown to be purely repulsive. In this representation the parent cation is formed as long as the electron incident energy is above the ionization energy of AB (IE(AB)) but below the dissociation threshold leading to the formation of A^+ ($E_{Th}(A^+)$). The higher-lying excited cationic state ($AB^{+'*}$) is shown to lead to the formation of B^+. The threshold for this channel is given by the sum of the ionization energy of B (IE(B)) and the bond dissociation energy of AB (BDE(AB)). On the right-hand *y*-axis, the energy dependence of the relative cross section for the formation of A^+ and B^+ (σ^{A+} and σ^{B+}) are shown as red and green lines and the total DI cross section (σ^{Tot}) is shown with a solid line as the sum of the two partial cross sections. The threshold energy (E_{Th}) for the formation of the fragments A^+ and B^+ are indicated on the right-hand *y*-axis and the maximum total DI cross section is shown to be at 70 eV. In the case of a polyatomic molecule, the situation is considerably more complex and intramolecular energy re-distribution, multiple fragmentations and rearrangement reactions may dominate the ion formation at higher energies.

molecule, part of the "excess" energy can be transferred to the molecule. This will leave the parent cation in a vibrationally and/or electronically excited state, which often leads to fragmentation. In this case, the extent of the fragmentation and the branching ratios between different fragmentation channels depends on the internal energy of the ion and the thermochemical threshold (or activation energies) for the respective processes. The onset for DI in terms of electron energy is therefore generally slightly above the ionization energy of the molecule and is initially defined by a single bond rupture. With increasing incident electron energy, however, the branching ratios shift more and more to favor multiple bond ruptures, while the total cross section approaches a maximum (typically

at around 50–70 eV) before decreasing slowly again. At higher incident electron energies, the interaction time is shorter and the scattering cross section (and thus the DI cross section) decreases again (see pages 23–25 in [43]).

The consequence for FEBID is that DI is likely to contribute to more extensive fragmentation of the precursor molecules when compared to DEA, and moreover that DI will typically only contribute through precursor interaction with the high-energy tail of the SE energy distribution (above about 10 eV). Since DI is a non-resonant process, the total cross section remains fairly constant over a large energy range above the respective thresholds. This will often result in a substantial integral overlap with the SE energy distribution. Hence, while DEA can only proceed through resonances confined to narrow energy ranges below about 10 eV, DI is active from slightly above the molecule's ionization energy to well above 100 eV.

Neutral dissociation through electronic excitation (Equation 3) has characteristics of both DEA and DI. As depicted in Figure 6, it shows a threshold behavior similar to DI, as the initial electronic excitation energy defines the threshold for the process (if it is higher than the respective BDEs). The cross section for individual processes then gradually increases as the electron energy increases and more higher-lying excitation channels open up, also contributing to the total cross section. Unlike DI, the energy transfer is largely confined to the electronic excitation energy, though the resulting electronic states may generally be expected to be vibrationally excited. The available energy is thus limited by the energy characterizing the respective electronic transition in the molecule and the excess vibrational energy associated with the transition. Neutral dissociation is therefore not expected to lead to as extensive fragmentation as DI. However, as the first excited states in organometallic compounds may be as low as 3–4 eV and the ligand BDE is usually low compared to covalent bonds, ND may be active at much lower energies than DI. Similar to DI, ND may still maintain fairly high cross sections for incident electron energies, even in excess of 100 eV (depending on the energy transfer efficiency). Furthermore, electronic excitation from bonding orbitals to strongly anti-bonding orbitals can result in direct dissociation along the respective repulsive potential energy surface, similarly to DEA. In fact, recent quantum mechanical calculations on the potential energy surfaces of selected electronically excited states of $Pt(PF_3)_4$ show the repulsive nature of these states along the metal–ligand bond [44]. However, although these calculations are a considerable achievement, they do not predict whether the remaining internal energy leads to further fragmentation or is channeled into kinetic energy of the departing fragments. Also, in a recent dissociative excitation study on $Fe(CO)_5$ [19], measurements on
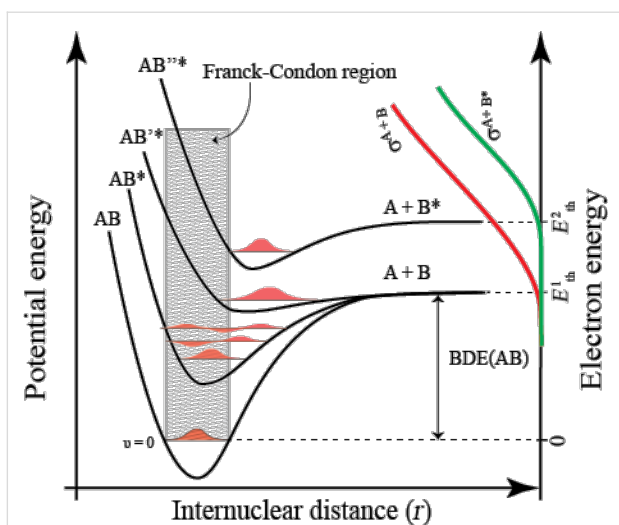
Figure 6: Simplified two-dimensional potential energy diagram for a quasi-diatomic dissociation through electronic excitation, i.e., neutral dissociation (ND). The excitation process is depicted as a vertical transition from the neutral ground state to electronically excited states accessible within the Franck–Condon region (shaded area). Here, the two lower-lying excited states AB* and AB$'^*$ are shown as bound states and dissociation can only proceed through transitions to vibrationally excited states that are energetically above the respective dissociation limit. In this representation, both AB* and AB$'^*$ dissociate to form A and B in their respective ground states. The highest-lying excited state (AB$''^*$), on the other hand, is shown to be purely repulsive and to dissociate directly to form A and B*. On the right-hand y-axis, the energy dependence of the relative cross section for the formation of A and B and A and B* (σ^{A+B} and σ^{A+B^*}) are shown as red and green lines and the total cross section for ND (σ^{Tot}) is shown with a solid line as the sum of the two partial cross sections. The threshold energy (E_{Th}) for the respective processes is indicated on the right-hand y-axis. Similarly to DI and DEA, the situation in ND is more complex in the case of a polyatomic molecule, and intramolecular energy redistribution, multiple fragmentations, and rearrangement reactions may play an important role.

the incident electron energy dependence of the induced fluorescence of the fragments formed were attributed to ND processes leading to partial and even complete CO loss up on electron impact. However, as is the case for the studies on Pt(PF$_3$)$_4$ these studies do not give measures of the efficiency of these processes.

Dipolar dissociation (Equation 4) proceeds similarly to ND, but the Coulomb interaction between the negatively and positively charged fragments must be overcome. The thermochemical threshold for this process is given by the sum of the respective BDEs and the ionization energy of the precursor of the positive ion formed less the electron affinity of the precursor of the negative ion formed. The threshold is thus generally higher than that for DEA and ND but lower than that for DI. To our knowledge there are no current gas phase studies on DD of relevant FEBID precursors and generally DD is not a very efficient process (see T. D. Märk and references therein on pages 276–277 in [27]) It is, however, worth mentioning that a recent

study on electron-stimulated negative ion desorption from Fe(CO)$_5$ films shows a significant contribution to the desorption yield from dipolar dissociation [45].

In addition to the different energy dependence of these electron-stimulated processes and the different extent of fragmentation, it should be emphasized that the fragmentation paths will also be distinctly different. While DEA predominantly leads to the formation of a closed shell anion and a neutral, radical counterpart, DI will predominantly result in a closed shell cation and neutral radical counterparts and ND in neutral radical fragments. Thus, one would expect that that the relative importance of these processes in FEBIP will not only define the initial step in the deposition process, but may also strongly influence further surface, thermal, or electron-induced chemical transformation of the deposit.

3 Gas phase vs surface studies

To study low energy electron-induced processes in the gas phase, a low energy electron beam with a resolution of about 100 meV is crossed with an effusive beam of FEBID precursor molecules and the electron energy dependence for the formation of charged fragments is monitored by mass spectrometry (MS) with sufficient resolution and dynamic range to unambiguously detect all fragments formed. For experimental detail relevant to the DEA and DI data discussed here, see [46-48]. Using this methodology, an accurate assessment of the branching ratios for individual DEA and DI fragmentation channels may be achieved and, with careful calibration, absolute cross sections may be determined. Such instruments may also be used to determine the extent of DD, but the extent of ND must currently be estimated from scattering experiments measuring the cross sections for the underlying electronic excitations. For experimental detail on the determination of the scattering cross sections discussed here, see [49]. Regardless of the experimental apparatus or the electron-stimulated processes being investigated, all of these gas phase experiments study single electron/molecule collision events for isolated species and thus do not necessarily reflect the low energy electron-induced decomposition pathways of the same molecules when adsorbed onto a substrate. This may be addressed with well-controlled UHV surface experiments where the precursors are adsorbed onto a substrate and exposed to electrons with relatively high energy (400–500 eV). In such surface experiments, the desorbing fragments are analyzed with MS and the composition of the remaining deposit can be analyzed with techniques such as X-ray photoelectron spectroscopy (XPS), reflection-absorption IR spectroscopy (RAIRS), and/or high-resolution electron energy loss spectroscopy (HREELS). For experimental details on the UHV surface experiments discussed here, see [25,50]. The shortcoming of these surface experiments is,

however, that the precursor molecules are subjected to interactions with SEs with an energy distribution (similar to that in FEBID), in contrast to the well-defined incident energies that characterize the gas phase studies. The energy dependence of the observed processes is therefore not known directly. Consequently, a comparison of the products formed in gas phase and surface science studies combined with the energy dependence of the branching ratios (i.e., the products) obtained in gas phase experiments is needed to identify the dominant processes (e.g., DEA vs DI) occurring in the surface reactions. Such comparison provides valuable insight into the dominant low energy electron-induced processes occurring with FEBID precursors adsorbed on surfaces and may eventually aid the formulation of distinct criteria defining suitable ligand structure and composition for future FEBID precursors.

4 Case studies
4.1 Trimethyl(methylcyclopentadienyl)platinum(IV); MeCpPtMe$_3$

The organometallic compound trimethyl(methylcyclopentadienyl)platinum(IV) (MeCpPtMe$_3$) was first tested as a CVD precursor by Xue et al. [51] in 1989 and was found to create high-purity platinum films, with purities greater than 99 atom % platinum when examined by XPS. Despite its high deposit purity using thermal deposition techniques, MeCpPtMe$_3$ has not been found to produce high-purity deposits in direct FEBID and such deposits do not exceed about 20 atom % Pt [52-54]. In this context, Botman et al. [54] examined FEBID-constructed platinum structures deposited at various surface power densities, calculated from the deposition beam voltage and current and the SE escape area of the substrate. The platinum purity of the unprocessed deposit was optimized to a maximum of approximately 16 atom % at power densities at and above 10 μW/μm^2, but substantially reduced platinum purities were observed at lower power densities (as low as 5.5 atom %). With thermal and electron beam-assisted in situ and post-deposition treatment with processing gases, however, considerably higher Pt content has been achieved [55,56], and resistivity only about six times that of bulk Pt may be attained [57,58]. Such approaches include exposure to atomic hydrogen [54], water [59,60] and oxygen [57,58,61,62], but also the combination of FEBID with atomic layer deposition [63] and with laser exposure [64] have proven advantageous. Despite the poor purity of Pt deposits created from MeCpPtMe$_3$ in the absence of any purification strategies, MeCpPtMe$_3$ has continued to be used as a FEBID precursor due to its stability, good vapor pressure under FEBID conditions, and commercial availability.

A 2012 study by S. Engmann et al. [15] deals with the gas phase dissociation of MeCpPtMe$_3$ upon exposure to low-energy electrons. Gas phase experiments were performed using a

crossed electron beam/effusive molecular beam apparatus and product ions were measured using mass spectrometry; the apparatus and methods have each been described in detail [46]. As previously described, electrons with incident energies below the ionization threshold of the parent molecule (7.7 eV for MeCpPtMe$_3$ [15]) can only produce ionic fragments via DEA (DD usually sets in at higher energies). Hence, negative ions collected from electron/molecule interactions at such low incident electron energies are DEA products.

Figure 7 shows the negative ion yields from DEA to MeCpPtMe$_3$ in the incident electron energy range of 0–14 eV. The highest intensity DEA fragment is at *m/z* 304 and results from a single methyl loss (CH$_3$), yielding the [MeCpPtMe$_2$]$^-$ ion. This fragment is almost exclusively produced through a low energy resonance, which the authors assigned to a single electron occupation of the LUMO of MeCpPtMe$_3$. This is anticipated to be predominantly antibonding along the Pt–CH$_3$ coordinate [65,66]. The onset of the [MeCpPtMe$_2$]$^-$ formation in the DEA ion yield curves is close to 0 eV, and the peak intensity of this fragment is close to 0.5 eV. Multiple ligand loss through DEA, on the other hand, proceeds predominantly through a higher energy resonance, which the authors assigned as a core-excited resonance (two-particle-one-hole resonance) associated with a HOMO–LUMO transition. The fragment formation through this resonance peaks close to 4.5 eV. From thermochemical considerations it is clear that multiple ligand loss through DEA is in all cases accompanied by significant
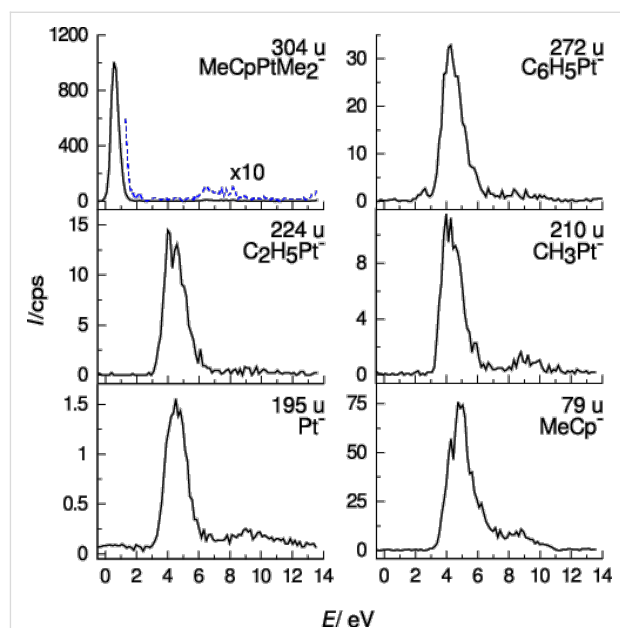
Figure 7: Energy-dependent relative cross sections (ion yields) of negative ion fragments produced by DEA to MeCpPtMe$_3$. Reproduced with permission from [15], Copyright (2012) Royal Society of Chemistry.

rearrangement and new bond formation. This can be seen particularly well in the case of the $[C_7H_{11}Pt]^-$ fragment (m/z 290), which is the only multiple ligand loss fragment formed through the low energy resonance close to 0 eV (though with very low intensity). For the formation of this fragment, the authors proposed a reaction pathway involving the elimination of an ethyl radical via the intramolecular attack of a leaving methyl radical on another methyl ligand and a H-shift from one of the methyl ligands to the central Pt, thereby reducing the central Pt(IV) to Pt(II) [15]. Such extensive rearrangement reactions have, to our knowledge, not been observed for DEA to other organometallic compounds, but have been observed for a number of covalently bonded compounds as discussed in the previous section. In addition to the resonances discussed above, all fragments observed also appear at higher energies through broad low intensity contributions.

Finally, $[C_7H_9Pt]^-$ (m/z 288) is observed through a fairly narrow contribution peaking at 2.3 eV [15] (not shown here). This fragment may be attributed to a loss of an ethyl radical and H_2 or, alternately, to the loss of an ethane molecule and a hydrogen radical, and is assigned as a single particle shape resonance. The ratio of the highest-intensity DEA fragment, $[MeCpPtMe_2]^-$ to the next highest fragment, $[MeCp]^-$ (m/z 79) (leaving a neutral fragment with a maximum C/Pt ratio of 3:1), is approximately 13:1, and all other fragments resulting from

multiple ligand loss appear with even lower intensity. Hence, single methyl loss dominates in DEA of $MeCpPtMe_3$.

Figure 8 shows the positive ion mass spectrum of $MeCpPtMe_3$ recorded at 100 eV incident electron energy, where DI dominates [15]. The principal DI channels are the loss of two or three methyl ligands and the loss of two or three methyl ligands along with one or more hydrogen. The loss of one methyl group (and one methyl group and one or more hydrogen) is about an order of magnitude less efficient, and all other fragmentation channels are even less efficient. The DI fragmentation patterns are complicated by the presence of isobaric fragments generated through hydrogen loss – specifically, through the overlap of fragments with different platinum isotopes and those with differing extent of hydrogen loss. Thus, a determination of the threshold energy for individual fragments was not possible, but it is safe to assume that the relative ratios observed at 100 eV impact energy represent fairly well the ratios over the bulk of the relevant SE energy distribution in FEBID.

From this comparison of gas phase DEA and DI data on $MeCpPtMe_3$, it is evident that the most efficient DEA channel is the loss of one methyl ligand. In contrast, the highest intensity DI channel is the loss of two methyl groups, along with the loss of two methyl groups and one or more hydrogen atoms. The second most efficient DI channel is half as intense and
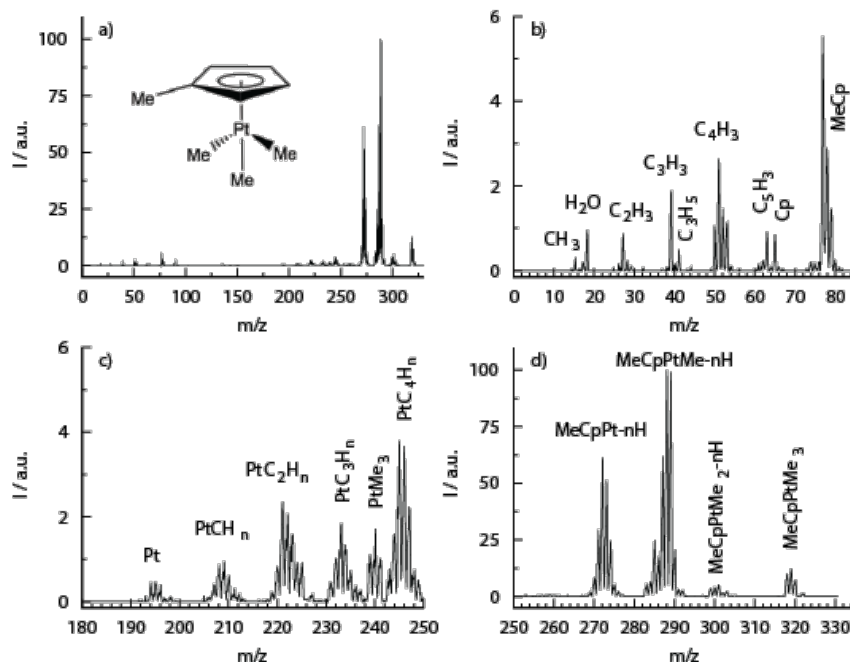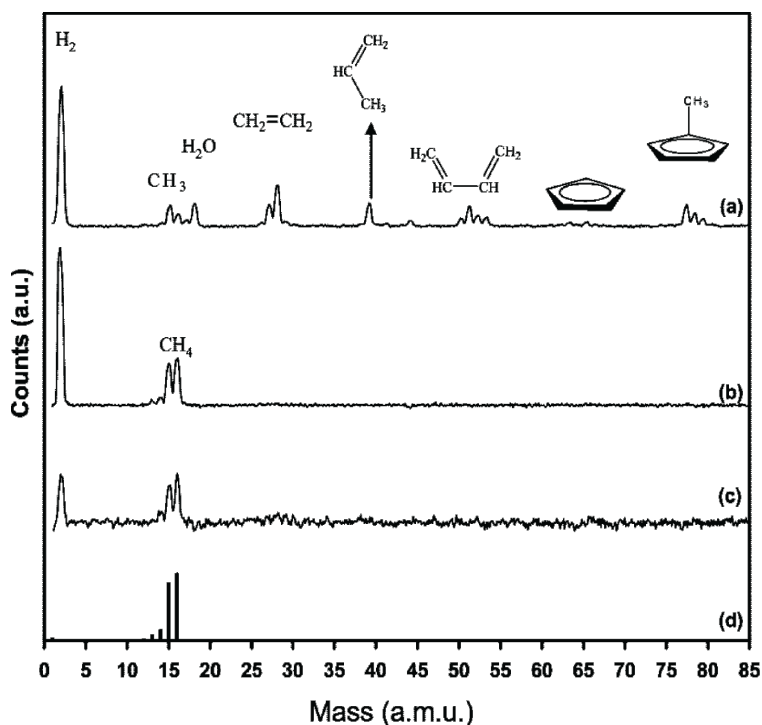

Figure 8: Positive ion mass spectrum of $MeCpPtMe_3$ recorded with electron energy of 100 eV (reproduced with permission from [15], Copyright (2012) Royal Society of Chemistry); (a) overview of the full mass range (m/z 0–330), (b), (c) and (d); expanded portion of the spectrum for m/z 0–85, m/z 180–250 and m/z 250–330, respectively.

corresponds to the loss of three methyl ligands along with the loss of three methyl ligands and one or more hydrogen.

Assuming that MeCpPtMe$_3$ adsorbed on a surface will react similarly to the gas phase, DEA to MeCpPtMe$_3$ adsorbed on a surface should lead to a reduction of the C/Pt ratio from the initial 9:1 in the intact molecule to close to 8:1, while DI of MeCpPtMe$_3$ adsorbed on a surface should lead to a deposition with C/Pt ratio between 7:1 and 6:1.

A 2009 paper by J. D. Wnuk et al. [21] describes such surface experiments performed using MeCpPtMe$_3$. These experiments were performed using UHV chambers equipped with XPS and MS, and with RAIRS, respectively, as well as commercial flood guns for use as electron sources. The MeCpPtMe$_3$ precursor was physisorbed onto gold substrates at about 180 K and irradiated with electrons with 500 eV impact energy. During electron irradiation, a MS with a 70 eV electron impact ionization source was used to monitor desorption of volatile decomposition products from the surface, while XPS and RAIRS were used to monitor the evolution of the composition of the forming deposit. Figure 9 shows the mass spectrum of species desorbing from the surface before and during electron irradiation.

The only visible species during electron irradiation are at *m/z* 15, 16, and 2. These are assigned to CH_3^+, CH_4^+, and H_2^+, with the former two appearing at the ratio observed in electron impact ionization of gas phase methane (CH_4). The initial loss of a methyl radical is likely to result from a Pt–CH$_3$ bond rupture rather than by dissociation of the methyl group from the MeCp ligand, as the BDE for the latter is expected to be more than 2 eV higher than for the former [15]. This was confirmed by Wnuk et al. [21] through a supplementary study of the analogue cyclopentadienyltrimethylplatinum(IV) (CpPtMe$_3$), which produced a similar mass spectrum during electron irradiation, despite the lack of the methyl group on the Cp ring. The conversion of the dissociated methyl radicals to the methane observed in the mass spectra is less clear as it could arise either from intra- or intermolecular reactions at the surface or from reactions of desorbed methyl radicals at the walls of the UHV chamber. While MeCpPtMe$_3$ was found to desorb from the surface when it was heated to room temperature prior to electron irradiation, no compounds were found to desorb from the surface after electron irradiation. Hence, through electron irradiation, a chemical change clearly converted the physisorbed MeCpPtMe$_3$ to a chemically bound deposit containing platinum and carbon.

Figure 9: Positive ion mass spectra of MeCpPtMe$_3$ in the *m/z* range of 0–85 (reproduced with permission from Wnuk et al. [21], Copyright (2009) American Chemical Society): (a) gas phase spectrum recorded at 70 eV impact energy; (b) positive ion mass spectrum of volatile species desorbing from a MeCpPtMe$_3$ film, adsorbed onto a gold substrate at 180 K, under irradiation with 500 eV electrons; (c) positive ion mass spectrum of volatile species desorbing from a CpPtMe$_3$ film, adsorbed onto a gold substrate at 180 K, under irradiation with 500 eV electrons; (d) reference mass spectra of gas phase CH$_4$ (adapted from NIST [67]).

In addition to the mass spectra recorded to monitor desorbing fragments, the evolution of the surface composition with increasing electron dose was monitored by XPS and RAIRS. The XPS spectra showed that the fractional Pt coverage stayed constant, but a partial reduction of Pt(IV) to a lower oxidation state took place. The C/Pt ratio decreased from the initial 9:1 of the precursor molecule to about 8:1 upon electron irradiation, as is shown in Figure 10. This ratio was found to remain the same for initial film thicknesses of 1–3 nm and for incident electron irradiation with 500 and 200 eV electron energy. Furthermore, the RAIRS data showed a systematic loss of absorbance in the $\nu(C–H)$ stretching region with increasing electron dose. The authors interpreted their findings as due to an initial electron-induced Pt–CH$_3$ bond rupture caused by DEA, which was initiated by low energy secondary electrons.
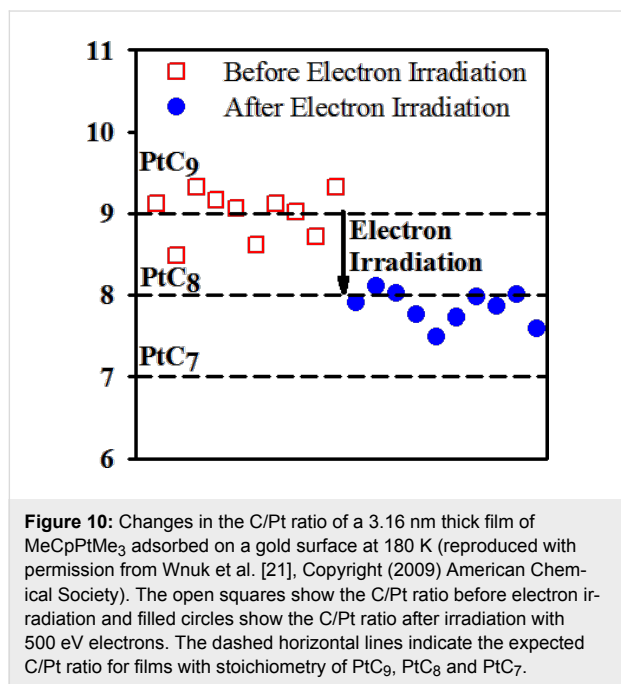
Figure 10: Changes in the C/Pt ratio of a 3.16 nm thick film of MeCpPtMe$_3$ adsorbed on a gold surface at 180 K (reproduced with permission from Wnuk et al. [21], Copyright (2009) American Chemical Society). The open squares show the C/Pt ratio before electron irradiation and filled circles show the C/Pt ratio after irradiation with 500 eV electrons. The dashed horizontal lines indicate the expected C/Pt ratio for films with stoichiometry of PtC$_9$, PtC$_8$ and PtC$_7$.

This is consistent with the expected single ligand loss through DEA, as observed in the gas phase experiments. Moreover, considering the currently available gas phase data, this implies that electron-induced decomposition of surface-adsorbed MeCpPtMe$_3$ is predominantly caused by secondary electrons with incident energy below 1 eV.

Interestingly, the cross section for methane desorption from adsorbed MeCpPtMe$_3$ exhibits a qualitatively similar PE energy dependence as that expected for the SE yield. This is also true for the MeCpPtMe$_3$ deposition yield as function of incident electron energy, and may be taken as further support for the notation that the low energy SEs are driving the deposition. To demonstrate this, Figure 11a compares a best fit to the cross

section for methane desorption from MeCpPtMe$_3$ physisorbed on a gold surface ($Z = 79$) and the calculated PE energy dependence of the SE yield from tungsten ($Z = 74$). The comparison with tungsten is chosen as its atomic number, which strongly influences the PE energy dependence of the SE yield, is close to that of gold. Further, Figure 11b compares the PE energy dependence of the MeCpPtMe$_3$ deposition yield on a silicon surface ($Z = 14$) and the calculated PE energy dependence of
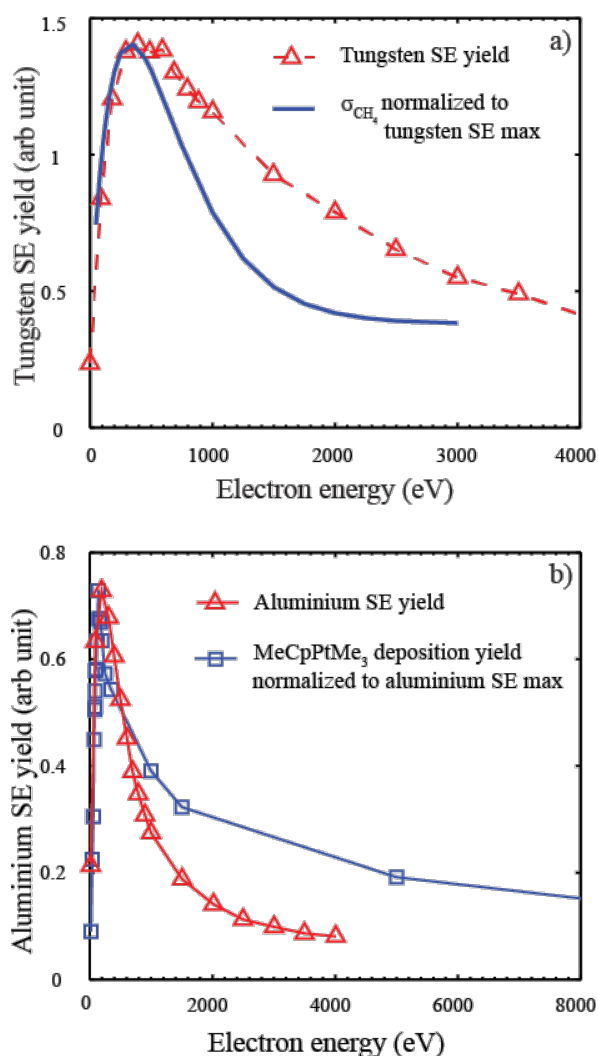
Figure 11: a) A line of best fit to the cross section for methane desorption from MeCpPtMe$_3$ adsorbed on a gold surface ($Z = 97$) and exposed to electron irradiation in the energy range from 0 to about 3000 eV (solid blue line), compared to energy dependence of the SE yield of tungsten ($Z = 94$) as a function of primary electron energy (red triangles). b) The deposition yield of MeCpPtMe$_3$ on a silicon surface ($Z = 14$) as a function of the PE beam energy in the range from about 0–5000 eV (blue squares) compared to the energy dependence of the SE yield from aluminum ($Z = 13$) as a function of primary electron energy (red triangles). The methane desorption cross sections (a) are adapted from Wnuk et al. [68] and the deposition yield (b) is adapted from Botman et al. [12]. The calculated SE yields are adapted from Ohya et al. [8] (using the partial wave expansion for the cross-section). Lines connecting the symbols are only meant to guide the eye.

the SE yield from aluminum (*Z* = 13). Here, one has to keep in mind the influence of the growing deposit on the effective *Z*-number in the measurements of the deposition yield, as this may be closer to that of carbon. In both cases (Figure 11a and Figure 11b) the calculated energy dependence is adapted from Ohya et al. [8]. The scatter in the cross section data for the methane desorption is considerable and the same is true for the errors in the deposition cross section. Furthermore, the exact peak position and the general form of the energy dependence of the calculated SE yield depend strongly on the model used and the *Z*-number of the respective substrate material, with the work function and Fermi level of the substrate also playing a role. Nevertheless, the qualitative similarities between the energy dependence of the measured cross sections and that of the calculated SE yields is evident and clearly supports the notation that the role of the SEs is dominating in the deposit formation.

4.2 Tetrakis(trifluorophosphine)platinum(0) Pt(PF₃)₄

Tetrakis (trifluorophosphine) platinum (0) ($Pt(PF_3)_4$), is a Pt-containing FEBID precursor that does no contain carbon; this has the potential advantage that unlike $MeCpPtMe_3$, it cannot create carbon-contaminated deposits. It is liquid at ambient temperatures, has a vapor pressure of 65 Torr, and is fairly stable at room temperature when stored under a PF_3 atmosphere [69,70]. It has been shown to produce pure Pt deposits using CVD [70]. In FEBID, deposits with a Pt content as high as 81 atom % have been achieved [71]. This is a considerably higher Pt content than achieved by FEBID of $MeCpPtMe_3$, where deposits typically contain less than 20% Pt [52-54]. Post-deposition procedures have also been studied and found to further improve the percent platinum content and conductivity. In this context, a platinum content of about 94 atom % has been attained through annealing in the presence of H_2O [72] and a resistance of 0.24×10^{-3} Ω·cm (only an order of magnitude higher than the bulk value for Pt) has been reached through annealing under nitrogen and a mixture of nitrogen with 5% hydrogen [73]. Tetrakis(trifluorophosphine)platinum is also one of the best-studied FEBID precursor with regards to the molecular mechanisms behind its deposition. These studies include absolute cross section measurements for DEA of $Pt(PF_3)_4$ [14] and a determination of the thermal electron attachment rate constant and the associated activation energy using a flowing-afterglow Langmuir probe [74] as well as absolute cross section measurements for elastic, vibrational, and electronic scattering [13]. Collectively, these studies provide insight into electron energy loss processes that occur through interaction with the precursor and internal excitation of the precursor, and the potential role of ND in the deposit formation. All of these gas phase studies can be compared with a UHV surface study by Landheer et al. [23], where mass spectrometry

was used to monitor desorption of volatile decomposition products and XPS and HREELS were used to monitor the evolution of the deposit during irradiation.

Figure 12 shows the energy dependence of the DEA cross sections for $Pt(PF_3)_4$ in the energy range from 0–12 eV and Figure 13 shows a positive ion FT-ICR mass spectrum of $Pt(PF_3)_4$ ionized with an axial beam of 20 eV electrons. The DEA spectra are dominated by single ligand (PF_3) loss peaking at about 0.5 eV with the very high cross section of 2×10^{-16} cm². This value is only about an order of magnitude lower than the maximum theoretical cross section for s-wave attachment at this energy [27]. All other channels are about two orders of magnitude less efficient; from these, the loss of two PF_3 ligands also proceeds through the resonance appearing close to 0.5 eV in the DEA spectra. Further fragmentation leading to the formation of $[Pt(PF_3)]^-$ and $[Pt(PF_3)F]^-$ proceeds predominantly through a higher lying resonance appearing close to 6 eV in the DEA ion yield, and F^- appears through a broad contribution close to 12 eV.
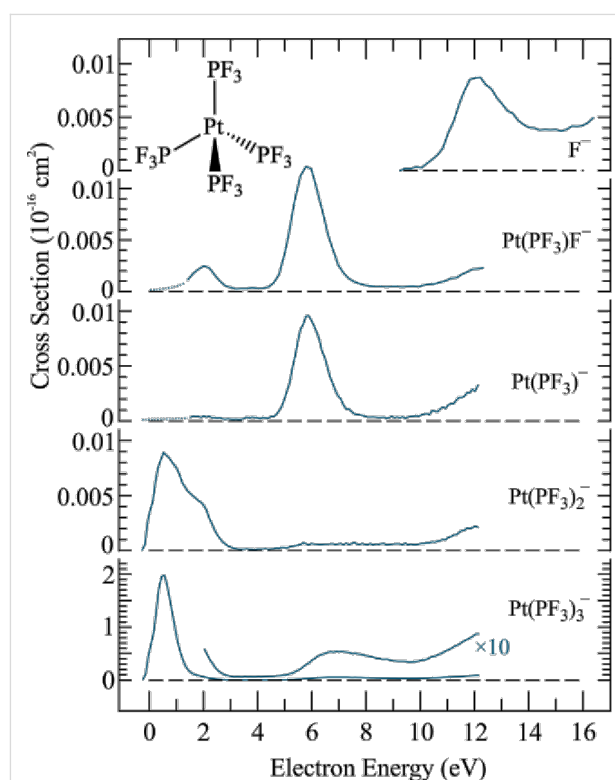
Figure 12: Energy-dependent absolute cross sections for negative ion fragments produced by DEA to $Pt(PF_3)_4$ (reproduced with permission from May et al. [14], Copyright (2012) Royal Society of Chemistry).

Unfortunately no quantitative data on the energy dependence of DI is available for $Pt(PF_3)_4$, but the FT-ICR spectrum [22] allows for qualitative comparison (see Figure 13).
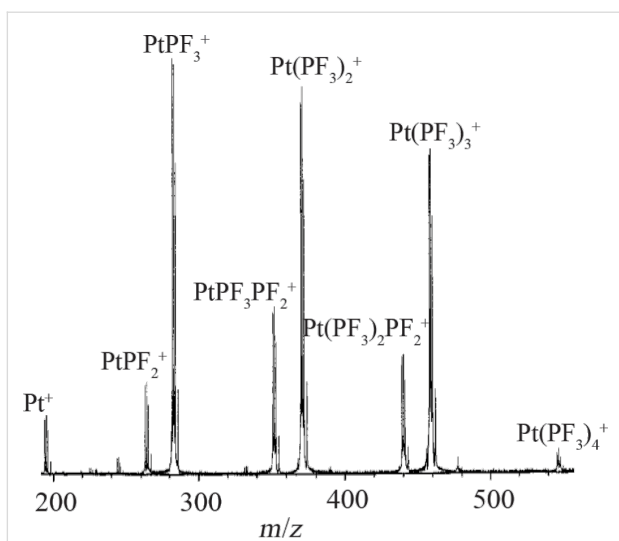
Figure 13: Electron ionization FT-ICR mass spectrum of Pt(PF$_3$)$_4$ recorded at 20 eV incident electron energy (reproduced with permission from [22], Copyright (1997) American Chemical Society).

It is clear from this spectrum that even at 20 eV electron impact energy, DI leads to considerably more extensive fragmentation than DEA. While single ligand loss is dominant in DEA, the relative cross sections for the loss of one, two, and three ligands in DI at 20 eV are all comparable. Additionally, both the loss of one fluorine atom in addition to the respective ligands (e.g., Pt(PF$_3$)$_2$PF$_2$), and the formation of the bare platinum cation contribute appreciably to the total DI yield. For higher electron impact energies, it is safe to assume that the DI branching ratios will shift further to favor more extensive fragmentation. This is a general behavior, an example of which can be seen clearly for the energy dependence of DI of W(CO)$_6$ [17] and Co(CO)$_3$NO [10], which are discussed hereafter. Thus, DEA to Pt(PF$_3$)$_4$ leads predominantly to single ligand loss while DI integrated over the energy range of the SEs generated in FEBID will predominantly lead to more extensive fragmentation.

In addition to the absolute DEA cross sections shown in Figure 12, Allan [13] has determined absolute cross sections for the angular dependence and energy dependence of elastic, vibrational, and electronic scattering of electrons from Pt(PF$_3$)$_4$ (mainly focused on the region below 20 eV incident electron energy). While elastic scattering will influence the spatial distribution of the secondary electrons and vibrational scattering will contribute to heating of the precursor molecules and substrate, electronic excitations may lead to direct ND, and therefore potentially play a significant role in the initial step in the FEBID process. Figure 14a,b compares the electron energy loss spectra for Pt(PF$_3$)$_4$ for different residual electron energies (Figure 14a) and the incident electron energy dependence of the absolute cross sections for electronic excitation (Figure 14b)
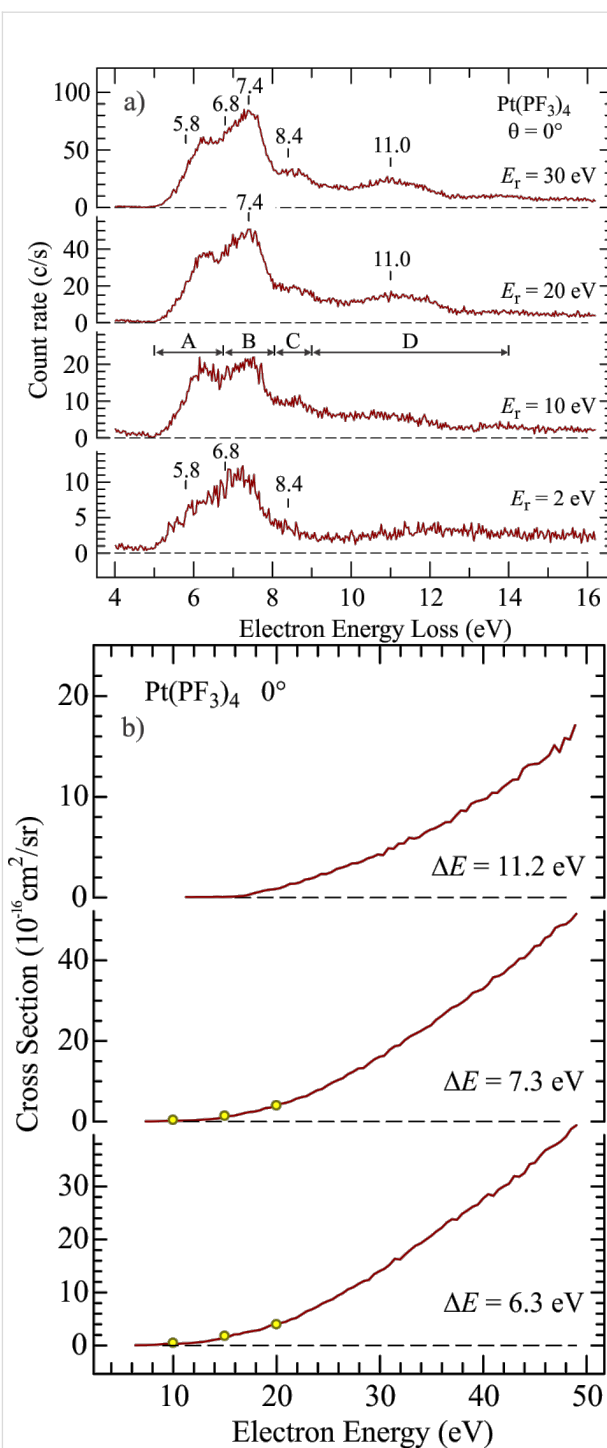

Figure 14: (a) Electron energy loss spectra of Pt(PF$_3$)$_4$ recorded at 0° angle with varying residual energies. The sections marked A–D in the third panel represent the energy ranges in which integration is performed to obtain absolute values. (b) Absolute electron excitation cross sections as a function of electron energy integrated over the energy loss ranges signified as A, B and D in Figure 14a. These cross sections are recorded at 0° angle and electron energy losses of 6.3 eV, 7.3 eV and 11.2 eV. Both figures (a) and (b) are reproduced with permission from [13], Copyright (2011) American Institute of Physics.

integrated over the energy ranges signified as A, B, and D in the third panel of Figure 14a. The data is recorded at 0° scattering angle. It is clear that the electronic excitations in $Pt(PF_3)_4$ have cross sections comparable to those measured for DEA. Unfortunately, no conclusive data exists on the extent and nature of the dissociation processes resulting from these electronic excitations. From the mass spectra reported by Hammill et al. [22] one can, however, speculate on the energetics involved and, therefore, on the possible extent of neutral fragmentation from the individual electronic excitations. It can be seen from Figure 12 that the bare Pt cation is produced from $Pt(PF_3)_4$ at 20 eV electron impact energy. Since the ionization energy of Pt is 9 eV [75], the 11 eV of residual energy must be sufficient to effect the loss of all four PF_3 ligands, indicating that the average Pt–PF_3 ligand bond dissociation energy is less than 2.75 eV. Thus the loss of two ligands may already be energetically accessible through the bulk of the excitation region marked A in Figure 14a, and three or even all four ligands may be lost through ND via the higher lying electronic excitations.

Recent quantum mechanical calculations on these states show that the potential surfaces of the four lowest electronically excited states are dissociative with respect to a single ligand loss, similarly to the DEA process [44]. However, as is apparent from the calculations above, the remaining internal energy may lead to further dissociation.

Under UHV conditions, Landheer et al. [23] have studied the decomposition of $Pt(PF_3)_4$ molecules, adsorbed at low temperatures (<170 K), upon irradiation with 500 eV electrons. In these experiments, neutral fragments desorbing from the substrate during electron irradiation were monitored by mass spectrometry, and while the chemical composition of the remaining film was probed by XPS, HREELS was used to study the change in vibrational modes of the adsorbed molecules. Figure 15 shows a time-resolved mass spectrum monitoring the PF_3 desorption during electron exposure after an initial electron dose of 0, 1.5×10^{14}, 2.5×10^{15}, and 4.2×10^{14} e^-/cm^2.

Figure 16 shows the electron dose dependence of the fractional platinum, phosphorous, and fluorine coverage determined by XPS [23]. The mass spectrum clearly shows an electron-initiated PF_3 desorption, and that this desorption comes to a halt at an electron dose slightly above 10^{15} e^-/cm^2. The loss of phosphorous and fluorine in the same electron dose range is also apparent from the XPS data, which shows that both the fractional phosphorous and fluorine contents decrease rapidly, and at the same rate as one another, to 75% of their initial 1:4 ratio. Electron exposures above 3×10^{15} e^-/cm^2 resulted in additional fluorine loss and oxygen deposition, while the fractional phosphorous content remained stable at 75% of its initial value
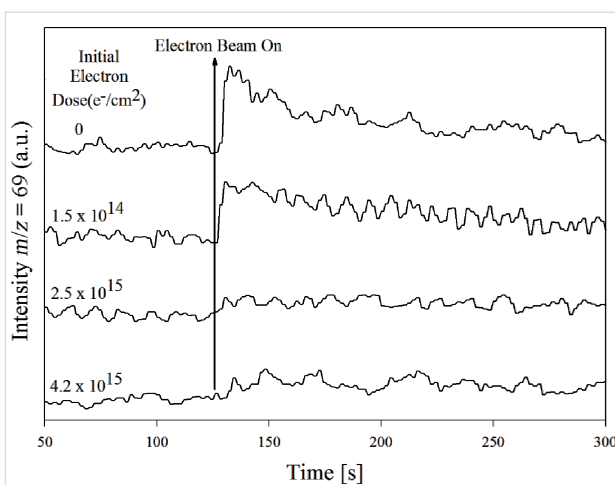
Figure 15: Time-resolved mass spectra of gas phase PF_3 (positive $[PF_2]^+$ ions produced by 70 eV electron impact are recorded) desorbing from films of $Pt(PF_3)_4$ adsorbed on an Au surface at 180 K when these are irradiated with 500 eV electrons. The time at which the electron beam is turned on is represented with a vertical line. Reproduced with permission from [23], Copyright (2011) American Chemical Society.
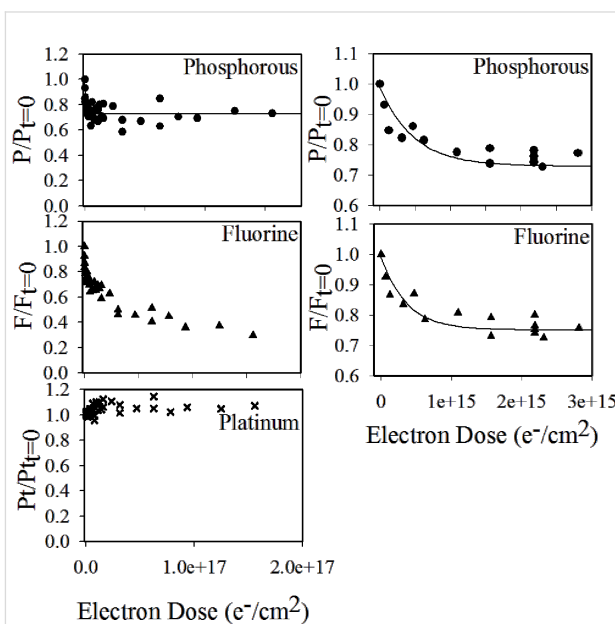
Figure 16: Electron dose dependence of the fractional coverage of Phosphorous ($P/P_{D=0}$), Fluorine ($F/F_{D=0}$) and Platinum ($Pt/Pt_{D=0}$). The left-hand side plots show the changes in fractional coverage for the full range of electron doses up to 2×10^{17} e^-/cm^2. The right-hand side plots show the phosphorous and fluorine fractional coverage for the initial period of electron exposure up to 2×10^{15} e^-/cm^2. Solid lines in the plot show a fit to experimental values based on the first order loss process. Reproduced with permission from [23], Copyright (2011) American Chemical Society.

[23]. The authors interpreted these observations as a two-step process. In the first step, electron interaction with $Pt(PF_3)_4$ leads to a single Pt−PF_3 bond rupture and transformation of the

adsorbed $Pt(PF_3)_4$ to $Pt(PF_3)_3$. This explains why the phosphorous and fluorine signals decrease at the same rate to 75% of their initial values while the P/F ratio remains constant. In the second step, further electron exposure nearly exclusively leads to P–F bond rupture and the coordinately unsaturated phosphorous reacts with residual water to form phosphorous oxides.

If we compare the evidence of single PF_3 ligand loss as the initial step in the deposit formation (as shown by the XPS data) with the existing experimental gas phase data, the observed single ligand loss points strongly towards DEA, rather than DI, as the initiator of deposition. This is not conclusive, however, as the role of ND is not certain without further information on the relaxation of the respective electronically excited states. Interestingly, if DEA is in fact the dominating process, the electron-induced deposition of $Pt(PF_3)_4$ is initiated by SEs with an incident electron energy of less than 1 eV, and the rest of the SE energy distribution as well as the primary electrons play an insignificant part in this primary step. Conversely, if ND in fact plays an important role in the initial single ligand loss, then energies above about 10 eV will also be important as is apparent in Figure 14. This notion, however, presumes that the processes observed in the gas phase remain similar with regards to the fragmentation, when $Pt(PF_3)_4$ molecules are adsorbed on surfaces.

4.3 Cobalt tricarbonyl nitrosyl; [Co(CO)₃NO] and tungsten hexacarbonyl [W(CO)₆]

Cobalt tricarbonyl nitrosyl [$Co(CO)_3NO$] was initially introduced in CVD as a liquid, easy-to-handle Co source. [76-78]. In CVD, Crawford et al. [78] reported an average composition of $CoN_{0.5}O_{0.9}$ with only traces of carbon when using Ar or N_2 as carrier a gas at deposition temperatures below 380 °C. Above 400 °C, the authors found the deposits to consist of a mixture of CoO and Co metal. Deposition under hydrogen atmosphere, on the other hand, was found to result in pure cobalt deposits already at 350 °C [76,77]. Cobalt tricarbonyl nitrosyl has a normal boiling point of 78.6 °C, a vapor pressure of 91 Torr at 20 °C [79], and a thermal decomposition temperature of about 130–140 °C measured on SiO_2 [80]. It is also commercially available and relatively nontoxic. Furthermore, the commonly used Co precursor $Co_2(CO)_8$ is unstable under vacuum and tends to polymerize, releasing CO. This, in turn, may lead to pressure buildup in precursor reservoirs, complicating the protocol for its use [81]. Consequently, a number of FEBID studies and an electron beam-induced surface activation (EBISA) study have been conducted on $Co(CO)_3NO$ [80-83]. In these studies, at room temperature, the Co content of the deposits was found to be about 40–50 atom %, independent of beam energy and current. The Co/N and Co/C ratios are similar in these deposits (about 3.5:1), while the initial ratios in the

precursor molecule are 1:1 and 1:3, respectively. Hence, carbon loss is clearly much more pronounced than nitrogen loss. Furthermore, EDX and TEM studies along with resistivity measurements indicate that the deposit consists of Co nanograins embedded in an insulating CoO matrix [82]. The chemical speciation of the nitrogen and carbon in the deposits remains an open question in these studies. However, as the bulk of the oxygen is bound as CoO, the nitrogen is likely bound as the respective cobalt nitride.

Focused electron beam induced deposition of $Co(CO)_3NO$ at elevated substrate temperatures [80] leads to a substantial decrease in the carbon content (by about a factor of three). At 50 °C, the oxygen content decreases fairly abruptly to about 50% of its initial value (from 15 to about 7.5 atom %); at 100 °C, the nitrogen content increases by approximately the same atomic percentage. The cobalt content, gradually increases from about 40 atom % at room temperature to about 50 atom % at 200 °C. This results in a composition of approximately $CoC_{0.15}O_{0.45}N_{0.45}$. We are not aware of studies on post-deposition or in situ purification of the deposits formed with $Co(CO)_3NO$, but in a recent study, the combination of annealing, H_2 exposure, and electron irradiation of deposits formed with $Co_2(CO)_8$ was found to result in compact, carbon and oxygen free Co layers [84].

In a 2011 gas phase study, Engmann et al. [24] published absolute cross section values for DEA to $Co(CO)_3NO$. These were the first absolute cross section values published for DEA to any potential FEBID precursor. The energy dependence of these cross sections is shown in Figure 17.

Similar to $MeCpPtMe_3$ and $Pt(PF_3)_4$, the most efficient channel in DEA to $Co(CO)_3NO$ is a single ligand loss close to 0 eV. Moreover, the absolute cross section for single ligand loss through DEA is very high. For $Co(CO)_3NO$, the loss of one CO ligand was assigned to the formation of a single particle resonance resulting in a maximum $[Co(CO)_2NO]^-$ yield close to 1 eV incident energy, while hot band transitions associated with the same resonance result in another maximum close to 0 eV. The maximum cross section for $[Co(CO)_2NO]^-$ formation was found to be about 4×10^{-16} cm² and, although the uncertainty associated with these measurements is considerably larger than these associated with the measurements by May et al. for $Pt(PF_3)_4$ [14], these cross sections are clearly very high. The loss of the NO ligand is also observed but is confined to the energy range from about 1–3 eV with a peak intensity close to 2 eV and a maximum cross-section that is an order of magnitude lower than that for the single CO loss. This NO loss channel was assigned as a low-lying two-particle-one-hole resonance associated with a HOMO–LUMO transition. The loss of
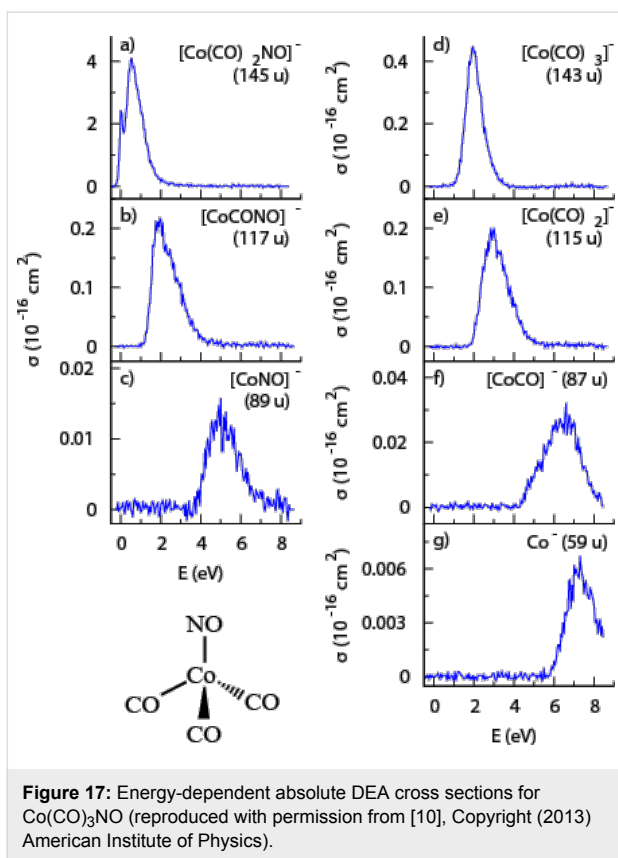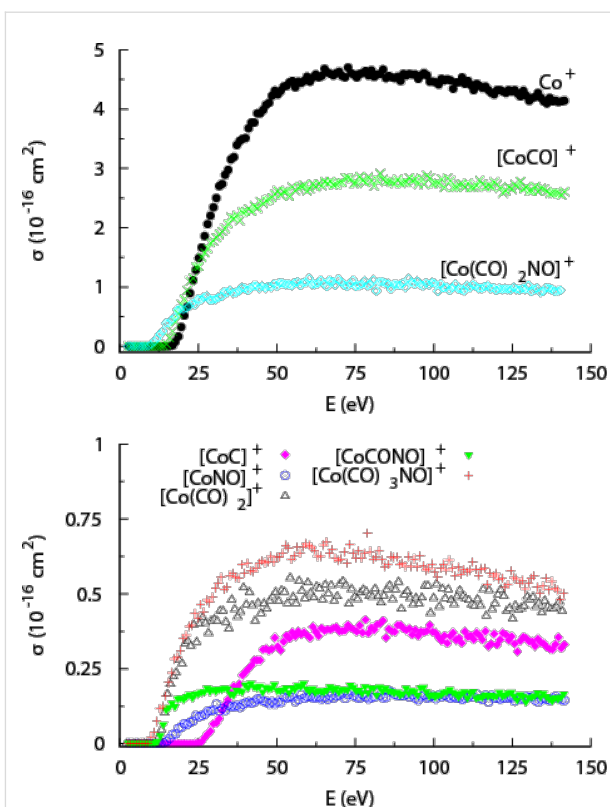
Figure 17: Energy-dependent absolute DEA cross sections for Co(CO)$_3$NO (reproduced with permission from [10], Copyright (2013) American Institute of Physics).
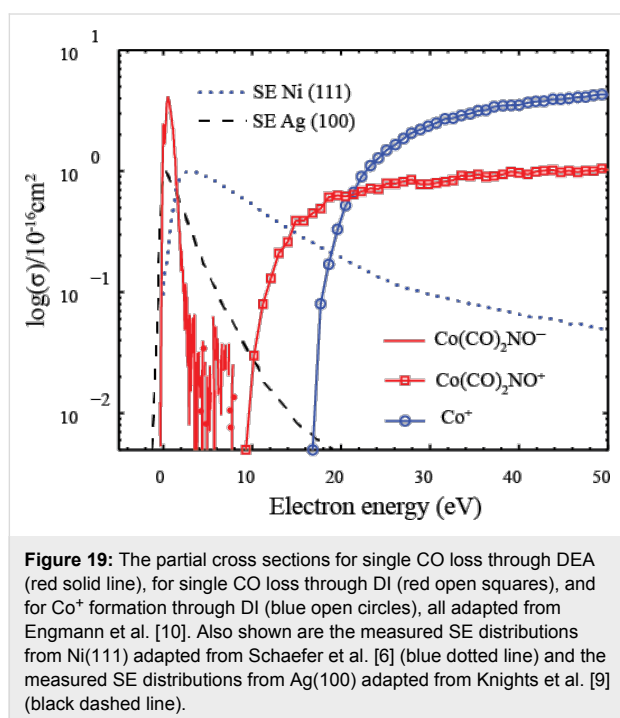

Figure 18: Energy dependence of the partial cross sections for positive ion fragments formed from Co(CO)$_3$NO (reproduced with permission from [10], Copyright (2013) American Institute of Physics).

two or more ligands, i.e., the formation of [Co(CO)NO]⁻, [Co(CO)$_2$]⁻, [CoNO]⁻, and [CoCO]⁻, is observed in the range from about 2 eV to about 6 eV and is attributed to further decomposition of [Co(CO)$_2$NO]⁻ and [Co(CO)$_3$]⁻ at the high energy tail of the respective resonances, where there is sufficient energy to induce further fragmentation. However, the maximum cross section for the formation of these fragments in this energy range is only about 5% of the cross section for single CO loss for [Co(CO)NO]⁻ and [Co(CO)$_2$]⁻, and about 0.5% for [CoNO]⁻ and [CoCO]⁻. [Co(CO)]⁻ is also formed through a higher-lying core-excited resonance but with a maximum cross section close to 0.5% of that for single CO loss, while the bare Co⁻ ion is also formed through the same resonance with a cross section that is close to 0.2% of that for single CO loss.

Figure 18 shows the absolute cross sections for the various fragments produced through DI of Co(CO)$_3$NO as a function of the incident electron energy. At the maximum of the total cross section, around 50 eV, the most intense DI fragment is the bare cobalt cation (Co⁺) with a maximum absolute cross section of about 4.6 × 10⁻¹⁶ cm², i.e., similar to that for a single CO loss through DEA. The second most efficient channel at this energy is the formation of [CoCO]⁺, with an absolute cross section of about 2.8 × 10⁻¹⁶ cm². Hence, DI of Co(CO)$_3$NO, unlike DEA,

results largely in complete or almost complete dissociation of the precursor molecule. The relative cross sections for the loss of a single CO ligand or the NO group are nonetheless still appreciable, and at about 50 eV they amount to about 25% and 12.5% of that for the Co⁺ formation, respectively. Interestingly, the formation of [CoC]⁺ is also observed with a fairly high cross section above its formation threshold – about 3 × 10⁻¹⁶ cm². All cross sections mentioned here are for incident energies of about 50 eV, where all channels have reached their maximum cross sections (Figure 18). At higher energies the cross-sections remain fairly constant. Conversely, the threshold for the individual channels is very different; for example, while the appearance energy for single CO loss is at about 8.47 ± 0.15 eV, that for Co⁺ formation is about 14.90 ± 0.15 eV [85]. The energy-dependent cross sections for these processes cross at about 25 eV and the single CO loss is thus the more efficient channel in the energy range from 8.47 ± 0.15 eV to about 25 eV (Figure 18).

As discussed previously, to properly evaluate the efficiency of individual DEA and DI channels determined in gas phase studies in the context of FEBID, it is important to consider not only the energy-dependent reaction cross sections (as shown in

Figure 17 and Figure 18), but also the energy distribution of the secondary electrons produced from the substrate and their overlap with the respective cross sections for each dissociation channel. This is a reflection of the fact that the overall efficiency of a given reaction pathway mediated by DEA, DI, or ND will be a convolution of the energy-dependent reaction cross section and the secondary electron yield at each energy. To demonstrate this, Figure 19 shows the partial cross section for single CO loss from Co(CO)₃NO through both DEA and DI along with the cross section for the formation of Co⁺ through DI. On the same plot the measured SE distributions from Ni(111) and Ag(100) are also shown.

Figure 19: The partial cross sections for single CO loss through DEA (red solid line), for single CO loss through DI (red open squares), and for Co⁺ formation through DI (blue open circles), all adapted from Engmann et al. [10]. Also shown are the measured SE distributions from Ni(111) adapted from Schaefer et al. [6] (blue dotted line) and the measured SE distributions from Ag(100) adapted from Knights et al. [9] (black dashed line).

Figure 20: Predicted relative effective damage yield for single CO loss through DEA (red solid line), for single CO loss through DI (red open squares) and for the formation of Co⁺ through DI (blue open circles). Damage yields are derived from the product of the respective partial cross sections and the normalized measured SE yields for (a) Ni(111) and (b) Ag(100). The cross sections are adapted from [10] and the SE yields for Ni(111) and Ag(100) from [6] and [9], respectively.

Using the information contained in Figure 19, Figure 20a and Figure 20b show the predicted relative effective damage yield for each channel, derived from the product of the respective ion yields and the normalized measured SE yields for Ni(111) and Ag(100), respectively. It is clear from this comparison that the SE energy distribution will influence not only the relative importance of DEA compared to ND and DI, but may also cause the relative efficiency of individual DI channels to differ significantly from their relative cross sections in the gas phase. We recognize that the energy distribution of the SEs from the single crystal Ni(111) and Ag(100) surfaces is not likely to accurately reflect the SE energy distribution in a FEBID experiment where the substrate is polycrystalline or, as deposition proceeds, the deposit surface itself. The physisorbed precursor molecule and the background gas also play a role. Nevertheless, it is obvious from Figure 20b that a SE energy distribution
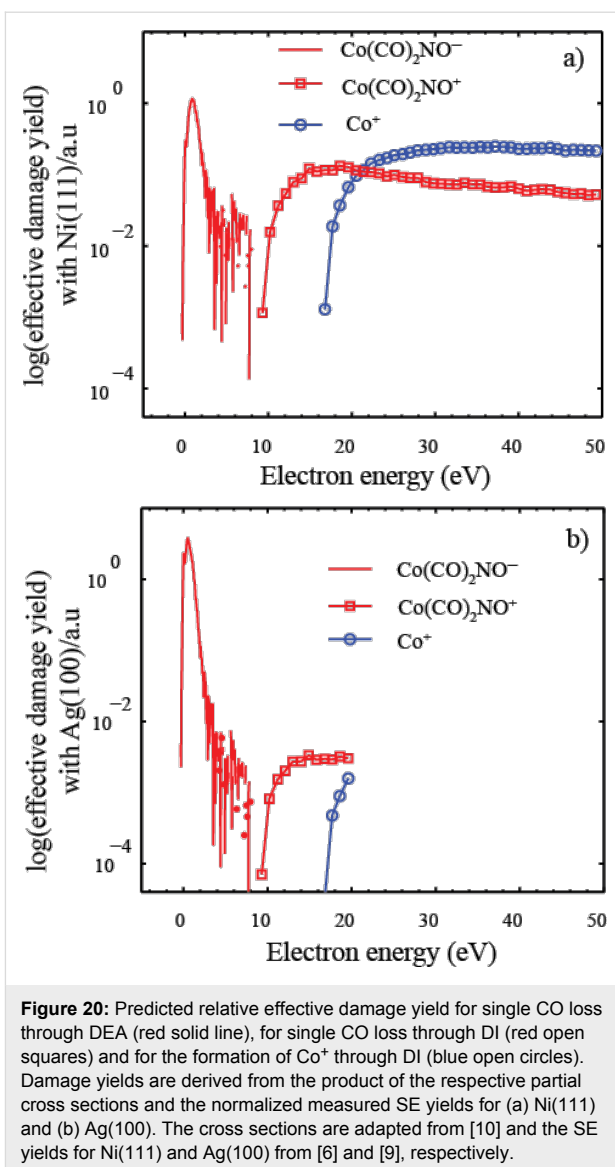
similar to that for Ag(100) would strongly favor DEA over DI, and from the observed DI channels those with the lowest threshold energies would dominate, yielding a single CO loss rather than leading to Co⁺ formation. For the SE energy distribution measured for Ni(111) (Figure 20a), on the other hand, the integral damage yields through DEA and DI are comparable with Co⁺ formation being favored over single CO loss in DI.

Judging from the gas phase data alone, one would expect that if the decomposition of adsorbed Co(CO)₃NO molecules is driven solely by DEA, it would mainly occur through CO desorption (see Figure 17) and would lead to a reduction of the relative Co/C/O ratio from 1:3:4 to about 1:2:3. The loss of nitrogen should be insignificant. In contrast, for a DI-driven decomposition process, NO desorption would be significant based on the integral cross sections (Figure 18) and the expected Co/N ratio

remaining on the surface should be reduced from the initial 1:1 to about 1:0.25.

This can be compared with a UHV surface study of adsorbed $Co(CO)_3NO$ by Rosenberg et al. [25]. In this study the authors used XPS, MS, and RAIRS to examine metal–ligand bond dissociation caused by irradiation of the adsorbed precursor molecules with 500 eV primary electrons. Figure 21 shows mass spectra of (a) gas phase $Co(CO)_3NO$ and (b) the fragments desorbing during the electron irradiation of approximately 8–10 monolayers of $Co(CO)_3NO$ adsorbed on a polycrystalline Au surface. In the gas phase mass spectrum, the ratio of CO (*m/z* 28) to NO (*m/z* 30) is close to the stoichiometric composition of $Co(CO)_3NO$. Conversely, the mass spectrum recorded during electron exposure of adsorbed $Co(CO)_3NO$ shows dominating CO desorption while the NO contribution is insignificant. This is observed for electron doses up to about 5×10^{16} e^-/cm^2, above which the CO desorption comes to a halt.
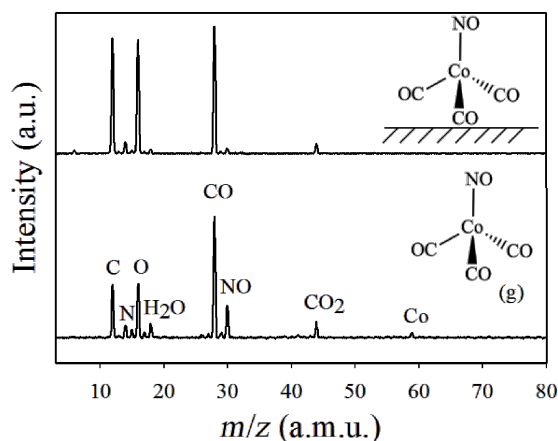
Figure 21: Positive ion (DI) mass spectra of (a) gas phase $Co(CO)_3NO$, (b) volatile species desorbing from a 2.5 nm thick $Co(CO)_3NO$ film, adsorbed onto a gold substrate at 105 K, during irradiation with an electron dose of 5×10^{16} e^-/cm^2 at an electron energy of 500 eV (reproduced with permission from [25], Copyright (2013) American Chemical Society).

The dominance of CO desorption from adsorbed $Co(CO)_3NO$ molecules exposed to electron irradiation is also reflected in the composition of the remaining deposit as measured with XPS [25]. Figure 22 shows the evolution of the fractional carbon, nitrogen, and oxygen content on the surface, referenced to the composition of the precursor prior to electron irradiation. While the fractional nitrogen content stays constant during the whole exposure time, the fractional oxygen and carbon contents fall to about 50% of their initial value by an electron dose of 5×10^{16} e^-/cm^2. Above 5×10^{16} e^-/cm^2, however, the frac-
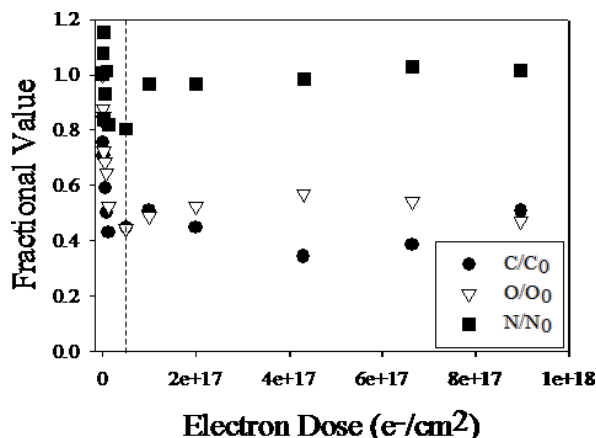
Figure 22: Electron dose dependence of the fractional coverage of carbon, oxygen and nitrogen from $Co(CO)_3NO$ adsorbed onto a gold substrate at 105 K and exposed to 500 eV electrons. The vertical dotted line represents an electron dose of 5×10^{16} e^-/cm^2 (reproduced with permission from [25], Copyright (2013) American Chemical Society).

tional oxygen and carbon contents stay constant up to electron doses as high as 10^{18} e^-/cm^2. Although the fractional nitrogen content stays constant throughout the electron doses studied, it is reduced from the initial nitrosyl to a nitride species [25]. Reduction of the carbonyl carbon to graphitic carbon and concurrent conversion of the carbonyl and nitrosyl oxygen to an oxide species is also observed. While the nitride speciation change occurs at electron doses below 5×10^{16} e^-/cm^2 and is coincident with CO ejection, the carbon and oxygen changes primarily take place at higher electron doses. Furthermore, as a result of electron irradiation, changes in the cobalt region suggest the formation of a cobalt oxide and/or cobalt nitride.

The authors interpreted their data as a two-step process governing the electron-induced deposition of adsorbed $Co(CO)_3NO$. The first (deposition) step occurs at low electron dose. In this step, one or more (an average of 1.5) CO ligands dissociate from the parent molecule and the NO ligand decomposes, producing a nitride species. The lack of NO desorption is also evident in the MS, which shows significant CO desorption from the surface. During this period, the cobalt is slightly oxidized and shows a peak broadening to a higher binding energy, likely resultant from oxide and/or nitride formation. This step is complete at an electron dose of about 5×10^{16} e^-/cm^2.

After this point, the second (decomposition) step can be observed. The partially decarbonylated species remaining; $[(CO)_xOCoN]$, undergoes an electron-stimulated decomposition of the remaining CO ligand(s) and adsorbed carbon is

formed. More cobalt oxide is formed; likely due to reactions between reactive oxygen species released from the decomposition of the remaining CO ligands and Co atoms. The chemical composition of the final product formed due to electron irradiation of the physisorbed $Co(CO)_3NO$ film is a mixture of metallic cobalt, cobalt oxide and nitride, and adsorbed carbon. A similar evolution was observed when adsorbed $Co(CO)_3NO$ was exposed to X-ray radiation, indicating that the bulk of the decomposition is induced by SEs, rather than the 500 eV PEs [25].

Returning to the gas phase measurements of $Co(CO)_3NO$, a decomposition process dominated by DEA would be expected to proceed through loss of a single CO ligand while DI would occur via a much more complete fragmentation. For an electron energy of 50 eV where the DI cross-sections reach their maximum values, a weighted average loss of slightly above 2 CO ligands is predicted for a DI process. The weighted average is estimated as the sum of the partial cross sections for the individual dissociation channels at 50 eV, multiplied by the number of CO ligands lost in each channel and divided by the total DI cross section at 50 eV. The average CO loss of about 1.5 observed in the surface experiments is therefore intermediate to what would be expected from a DEA- and DI-driven decomposition when considering the existing gas phase data alone. Cleavage of the N=O bond is neither observed in gas phase DEA, nor in DI. This is not surprising, as the BDE of nitric oxide is about 6.5 eV [37] and the activation barrier for the electron-induced formation of a nitride species from gaseous $Co(CO)_3NO$ is likely to be considerable. From comparison of surface and gas phase data it is thus likely that the decomposition observed at surfaces is initiated by a CO loss as proposed by Rosenberg et al. [25], though the gas phase experiments do not allow any clear conjecture on the underlying process (i.e., if the initial CO loss is through DEA or DI). The surface science studies, however, indicate that the decomposition of the unstable intermediate left after the initial CO loss proceeds through a surface-catalyzed conversion of the nitrogen from the nitrosyl group to the nitride species observed, which is consistent with CVD and FEBID from $Co(CO)_3NO$ showing the persistence of nitrogen in the deposits.

In summary for $Co(CO)_3NO$, comparisons of currently available gas phase and surface science studies do not provide a definitive clear-cut answer as to the initial dissociation mechanism, although a combination from both DEA and DI channels seems most likely. However, even this assertion is speculative in the absence of any information on potential ND channels and a detailed analysis of the overlap between the individual DI and DEA channels and the actual SE energy distribution from the surface (which is currently not available).

Finally, it is worthwhile to take a brief look at gas phase and surface studies on the metal carbonyl compound $W(CO)_6$. A recent DEA study of this compound by Wnorowski et al. [16] shows that, again, single CO loss is the most efficient channel and is confined to a fairly narrow energy region below 1 eV incident electron energy. Both the loss of two and three CO units, however, are fairly efficient through DEA and the integral ion yields for these channels are about 50% and 25% of that for a single CO loss, respectively. The loss of four CO units is also observed in DEA, but at higher energies (7–12 eV) and with low intensities (about 2.5% of that for single CO loss). No further fragmentation is observed in DEA to $W(CO)_6$. Dissociative ionization of $W(CO)_6$ is considerably more complex [17]. The loss of one CO (formation of $[W(CO)_5]^+$) has an appearance energy of about 10 eV and the appearance energy for the formation of W^+ (loss of all ligands) is at about 20 eV. The intermediate fragments, $[W(CO)_n]^+$ ($n = 1–4$), appear at energies between these two fragments. Above 20 eV, the relative cross section for the formation of these cations stays fairly constant, with the formation of W^+ ($n = 0$) as the most efficient channel and the relative cross section for the loss of one CO at about 50% of that for the W^+ formation. The relative cross sections for the formation of other $[W(CO)_n]^+$ ($n = 1–4$) are, again, intermediate to these two. Above 20 eV, however, the formation of $[(CO)_nWC]^+$ ($n = 0–3$) appears, and at about 40 eV the efficiency of these channels is on the same order of magnitude as the respective $[W(CO)_n]^+$ channels. Further, both the doubly charged $[W(CO)_n]^{2+}$ and $[(CO)_nWC]^{2+}$ are also formed above 40 eV, though with efficiencies about an order of magnitude less than for their respective singly-charged species.

Despite the complexity of the DI fragmentation, a rough estimate of the DI average weighted CO loss of approximately 4 can be deduced from these ion yield curves at about 40 eV, where all single ionization channels are close to their maximum. This can be compared to an estimated DEA weighted average CO loss of 2. Thus, for a direct translation of the gas phase data to the surface experiments, considerably less CO loss would be expected for DEA-initiated deposition than for DI-initiated deposition; one would also expect considerable carbide formation via DI.

Similar surface experiments to those described in previous sections (500 eV PEs and Au surface at 160 K) have been conducted by Rosenberg et al. for $W(CO)_6$ [26]. As expected, the mass spectrum of desorbed species upon electron irradiation shows CO as the dominating species. Further, the CO desorption decreases rapidly with increasing electron dose and above a dose of about 1×10^{17} e$^-$/cm^2 the CO desorption becomes insignificant. Consistent with these findings, XPS data reveals an average loss of 2 CO units for an electron dose of

about 7×10^{16} e$^-$/cm^2. Above about 7×10^{16} e$^-$/cm^2, the dominant pathway becomes CO ligand decomposition rather than desorption, and the remaining W(CO)$_n$ is converted to graphitic carbon and a W(VI) oxide. The final deposits were found to consist of tungsten oxides encrusted in a carbonaceous matrix and no signs of carbide formation were observed.

In summary, the surface study revealed a deposition process for W(CO)$_6$ that is similar to the other compounds examined here: a two-step process wherein the first is an electron-induced ligand loss and the second is characterized by decomposition of the remaining ligands. The number of ligands lost in the initial step is close to that observed in DEA rather than in DI and the absence of any carbide formation also favors DEA over DI. However, we stress again that ND is not included in these considerations, and the actual energy distribution of the secondary electrons is not taken into account when comparing the weighted average CO loss in the gas phase experiments.

Conclusion

Here we have compared gas phase and surface data on low energy electron interaction with the common FEBID precursors MeCpPtMe$_3$, Pt(PF$_3$)$_4$, Co(CO)$_3$NO, and W(CO)$_6$. For Pt(PF$_3$)$_4$ and MeCpPtMe$_3$, single ligand loss dominates the initial step in their electron-induced decomposition at surfaces. This is also the most efficient DEA fragmentation channel in the gas phase, while DI predominantly leads to more complete fragmentation. Furthermore, in both cases single ligand loss through DEA in the gas phase is essentially exclusively confined to the electron energy range below 1 eV. Hence, an uncritical comparison between the current gas phase and surface data, as discussed here, indicates that the initial electron-induced fragmentation of these precursors is principally through DEA, and is primarily effected through secondary electrons with incident energies below 1 eV.

For the carbonylated precursors Co(CO)$_3$NO and W(CO)$_6$, deposition is somewhat different. For Co(CO)$_3$NO, the surface studies show an initial average CO loss of about 1.5 ligands upon electron irradiation and essentially no NO loss. In gas phase DEA, the main channel is a single CO loss and the second most efficient channel is the loss of NO, with an absolute cross section that is about 10% of that for the single CO loss. The DEA-induced loss of two CO ligands has an absolute cross section that is about 5% of that for single CO loss. In gas phase DI above 50 eV, the loss of all ligands (formation of Co$^+$) dominates and the weighted average CO loss above 50 eV is about 2. The weighted average NO loss in gas phase DI is about 0.7. It is therefore clear that, for Co(CO)$_3$NO, neither the gas phase DEA nor the DI results correlate directly with the observed surface results. This is especially true in

terms of accounting for the lack of nitrogen loss and the chemical transformation of the nitrogen species in the surface experiments. Indeed, the results obtained for Co(CO)$_3$NO highlight the potentially important role that the surface can play in modifying the nature of the electron stimulated decomposition step.

For W(CO)$_6$, the surface experiments show an initial CO ligand loss corresponding to an average of about 2. In gas phase DEA, single CO loss dominates below 1 eV, but the integral ion yield for the loss of two CO ligands is significant in the range of 2.5–4.5 eV and the loss of three CO ligands is also appreciable in the energy range of 3–6 eV. The weighted average CO loss through DEA in the gas phase estimated from the ion yield curves is about 2. Similarly to the other compounds, gas phase DI leads to much more extended fragmentation and an estimated average CO loss above about 40 eV is close to 4. Here, we find that the CO loss in the initial deposition step for W(CO)$_6$ suggests DEA as the likely candidate; however, this is not conclusive. It is possible that for Co(CO)$_3$NO and W(CO)$_6$, deposition is a reflection of both DEA and DI processes.

It is unsurprising that low energy electron-induced decomposition of these organometallic compounds manifests differently when isolated in the gas phase and adsorbed on a surface. As previously mentioned, different relaxation processes are available at the surface and the lifetime of DEA resonances can be affected by polarization interactions with the surface. Furthermore, orientation effects may play a large role when molecules are adsorbed on surfaces – an effect that might explain the lack of NO desorption from Co(CO)$_3$NO in the surface experiments. Additionally, the electron-induced loss of a single ligand from a precursor molecule may promote further ligand loss through surface interactions and/or chemical conversion of ligands (e.g., NO ligand in Co(CO)$_3$NO), as is evident for all compounds compared here. This may be true even if such destabilization is not observed in the gas phase.

Furthermore, the current comparison is solely based on DEA and DI data from gas phase experiments and no systematic studies on ND cross sections and branching ratios exist. As has been demonstrated for Pt(PF$_3$)$_4$, the electronically inelastic cross sections can be very high and, in the gas phase, these are likely to relax predominantly through dissociation. Considerable progress is currently being made through quantum mechanical calculations on Pt(PF$_3$)$_4$, describing the potential energy surfaces for such electronically excited states [44]. These confirm the repulsive nature of the calculated states along a Pt–PF$_3$ bond, indicating at least an initial single ligand loss. The resulting Pt(PF$_3$)$_3$ fragment may nevertheless contain enough internal energy for more extensive fragmentation, and thus,

without further information on the branching ratios and cross sections for ND, a comparison between gas phase and surface data at this time remains incomplete.

Another major issue is that in the current surface experiments the adsorbed precursor molecules are exposed to electrons with fairly high energy, around 500 eV. The precursor molecules are thereby subjected to interaction with secondary electrons with a broad energy distribution and the energy dependence of individual processes are not manifested on the surface. Rather, these experiments reflect the cross sections for all processes (at the surface) convoluted with the SE energy distribution. This significantly complicates the direct comparison between gas phase and surface science studies.

To address these points, new experimental approaches are needed, most noticeably: a) ones that allow for the exploration of branching ratios and absolute cross sections for ND channels, which are perhaps achievable through a combination of the current crossed electron/molecule beam experiment with post-ionization sources; b) more detailed information on the secondary electron yield from surfaces exposed to electrons, including the surfaces that form as FEBID structures begin to grow; and c) experiments that allow electron energy-dependent studies on deposit formation and ligand desorption from adsorbed precursor molecules at lower energies, that includes the regime from about 0–15 eV (there are already a few laboratories with such setups, but to date their focus has been on other research topics). Moreover, the energy resolution of these electron sources must be sufficient to allow individual DEA resonances to be resolved, while the energy range must also be sufficient to scan through the onset region of DI and ND up to the maximum efficiency of these processes (typically in the regime between 50–70 eV). Our current inability to predict which precursors will react through which dissociation channels also highlights the need for a better theoretical understanding of electron/molecule interactions.

Despite the uncertainties associated with the current comparison, the comparison of gas phase and surface experiments on potential FEBID precursors is clearly an important step on the way to better understanding their initial decomposition mechanisms, illuminating the first step in the deposit formation in FEBID. For example, comparison between gas phase and surface studies has clearly implicated DEA rather than DI as the mechanism responsible for the initial decomposition of two of the precursors studied (MeCpPtMe$_3$ and Pt(PF$_3$)$_4$). This is the kind of information which in turn may aid the targeted design of precursors, whose initial decomposition step promotes further decomposition, and the control of which may thus be essential to optimize their performance.

References
1. Chattopadhyay, S.; Chen, L.-C.; Chen, K.-H. *Crit. Rev. Solid State Mater. Sci.* **2006,** *31,* 15–53. doi:10.1080/10408430600689299
2. Utke, I.; Hoffmann, P.; Melngailis, J. *J. Vac. Sci. Technol., B* **2008,** *26,* 1197. doi:10.1116/1.2955728
3. van Dorp, W. F.; Hagen, C. W. *J. Appl. Phys.* **2008,** *104,* 081301. doi:10.1063/1.2977587
4. Jasinski, J. M.; Meyerson, B. S.; Scott, B. A. *Annu. Rev. Phys. Chem.* **1987,** *38,* 109–140. doi:10.1146/annurev.pc.38.100187.000545
5. Choy, K. L. *Prog. Mater. Sci.* **2003,** *48,* 57–170. doi:10.1016/S0079-6425(01)00009-3
6. Schaefer, J.; Hoelzl, J. *Thin Solid Films* **1972,** *13,* 81–86. doi:10.1016/0040-6090(72)90158-7
7. Schou, J. *Scanning Microsc.* **1988,** *2,* 607.
8. Ohya, K.; Harada, A.; Kawata, J.; Nishimura, K. *Jpn. J. Appl. Phys.* **1996,** *35,* 6226–6232. doi:10.1143/JJAP.35.6226
9. Knights, A. P.; Coleman, P. G. *Appl. Surf. Sci.* **1995,** *85,* 43–48. doi:10.1016/0169-4332(94)00306-8
10. Engmann, S.; Stano, M.; Papp, P.; Brunger, M. J.; Matejčík, Š.; Ingólfsson, O. *J. Chem. Phys.* **2013,** *138,* 044305. doi:10.1063/1.4776756
11. Silvis-Cividjian, N.; Hagen, C. W.; Leunissen, L. H. A.; Kruit, P. *Microelectron. Eng.* **2002,** *61–62,* 693–699. doi:10.1016/S0167-9317(02)00515-4
12. Botman, A.; de Winter, D. A. M.; Mulders, J. J. L. *J. Vac. Sci. Technol., B* **2008,** *26,* 2460–2463. doi:10.1116/1.2976576
13. Allan, M. *J. Chem. Phys.* **2011,** *134,* 204309. doi:10.1063/1.3594206
14. May, O.; Kubala, D.; Allan, M. *Phys. Chem. Chem. Phys.* **2012,** *14,* 2979–2982. doi:10.1039/C2CP23268E
15. Engmann, S.; Stano, M.; Matejčík, Š.; Ingólfsson, O. *Phys. Chem. Chem. Phys.* **2012,** *14,* 14611–14618. doi:10.1039/c2cp42637d
16. Wnorowski, K.; Stano, M.; Matias, C.; Denifl, S.; Barszczewska, W.; Matejčíka, Š. *Rapid Commun. Mass Spectrom.* **2012,** *26,* 2093–2098. doi:10.1002/rcm.6324
17. Wnorowski, K.; Stano, M.; Barszczewska, W.; Jówko, A.; Matejčík, Š. *Int. J. Mass Spectrom.* **2012,** *314,* 42–48. doi:10.1016/j.ijms.2012.02.002
18. Engmann, S.; Ómarsson, B.; Lacko, M.; Stano, M.; Matejčík, Š.; Ingólfsson, O. *J. Chem. Phys.* **2013,** *138,* 234309. doi:10.1063/1.4810877
19. Lacko, M.; Papp, P.; Wnorowski, K.; Matejíčk, Š. *Eur. Phys. J. D* **2015,** *69,* 1–9. doi:10.1140/epjd/e2015-50721-8

20. van Dorp, W. F.; Wnuk, J. D.; Gorham, J. M.; Fairbrother, D. H.; Madey, T. E.; Hagen, C. W. *J. Appl. Phys.* **2009,** *106,* 074903. doi:10.1063/1.3225091

21. Wnuk, J. D.; Gorham, J. M.; Rosenberg, S. G.; van Dorp, W. F.; Madey, T. E.; Hagen, C. W.; Fairbrother, D. H. *J. Phys. Chem. C* **2009,** *113,* 2487–2496. doi:10.1021/jp807824c

22. Hammill, C. L.; Clark, R. J.; Ross, C. W.; Marshall, A. G., III; Schmutz, J. *Inorg. Chem.* **1997,** *36,* 5973–5977. doi:10.1021/ic970590a

23. Landheer, K.; Rosenberg, S. G.; Bernau, L.; Swiderek, P.; Utke, I.; Hagen, C. W.; Fairbrother, D. H. *J. Phys. Chem. C* **2011,** *115,* 17452–17463. doi:10.1021/jp204189k

24. Engmann, S.; Stano, M.; Matejčík, Š.; Ingólfsson, O. *Angew. Chem., Int. Ed.* **2011,** *50,* 9475–9477. doi:10.1002/anie.201103234

25. Rosenberg, S. G.; Barclay, M.; Fairbrother, D. H. *J. Phys. Chem. C* **2013,** *117,* 16053–16064. doi:10.1021/jp404905t

26. Rosenberg, S. G.; Barclay, M.; Fairbrother, D. H. *Phys. Chem. Chem. Phys.* **2013,** *15,* 4002–4015. doi:10.1039/c3cp43902j

27. Christophoru, L. G. *Electron-Molecule Interactions and their Applications;* Academic Press: Orlando, FL. U.S.A., 1984; Vol. 1.

28. McConkey, J. W.; Malone, C.; Johnson, P.; Winstead, C.; McKoy, V.; Kanik, I. *Phys. Rep.* **2008,** *466,* 1–103. doi:10.1016/j.physrep.2008.05.001

29. Hotop, H.; Ruf, M.-W.; Allan, M.; Fabrikant, I. I. *Adv. At., Mol., Opt. Phys.* **2003,** *49,* 85–216. doi:10.1016/S1049-250X(03)80004-6

30. Bald, I.; Langer, J.; Tegeder, P.; Ingólfsson, O. *Int. J. Mass Spectrom.* **2008,** *277,* 4–25. doi:10.1016/j.ijms.2008.06.013

31. Arumainayagam, C. R.; Lee, H.-L.; Nelson, R. B.; Haines, D. R.; Gunawardane, R. P. *Surf. Sci. Rep.* **2010,** *65,* 1–44. doi:10.1016/j.surfrep.2009.09.001

32. Böhler, E.; Warneke, J.; Swiderek, P. *Chem. Soc. Rev.* **2013,** *42,* 9219–9231. doi:10.1039/c3cs60180c

33. Wigner, E. P. *Phys. Rev.* **1948,** *73,* 1002. doi:10.1103/PhysRev.73.1002

34. Schramm, A.; Weber, J. M.; Kreil, J.; Klar, D.; Ruf, M.-W.; Hotop, H. *Phys. Rev. Lett.* **1998,** *81,* 778. doi:10.1103/PhysRevLett.81.778

35. Ómarsson, B.; Bjarnason, E. H.; Ingólfsson, O.; Haughey, S.; Field, T. A. *Chem. Phys. Lett.* **2012,** *539–540,* 7–10. doi:10.1016/j.cplett.2012.04.059

36. Ómarsson, B.; Engmann, S.; Ingólfsson, O. *RSC Adv.* **2014,** *4,* 33222. doi:10.1039/C4RA04451G

37. Luo, Y.-R. *Comprehensive handbook of chemical bond energies;* CRC Press: Boca Raton, FL, U.S.A., 2007. doi:10.1201/9781420007282

38. Mauracher, A.; Denifl, S.; Aleem, A.; Wendt, N.; Zappa, F.; Cicman, P.; Probst, M.; Märk, T.; Scheier, P.; Flosadóttir, H.; Ingólfsson, O.; Illenberger, E. *Phys. Chem. Chem. Phys.* **2007,** *9,* 5680–5685. doi:10.1039/b709140k

39. Papp, P.; Urban, J.; Matejčík, Š.; Stano, M.; Ingolfsson, O. *J. Chem. Phys.* **2006,** *125,* 204301. doi:10.1063/1.2400236

40. Bald, I.; Dabkowska, I.; Illenberger, E.; Ingólfsson, O. *Phys. Chem. Chem. Phys.* **2007,** *9,* 2983–2990. doi:10.1039/b702482g

41. Ingólfsson, O.; Weik, F.; Illenberger, E. *Int. Rev. Phys. Chem.* **1996,** *15,* 133–151. doi:10.1080/01442359609353178

42. Tegeder, P.; Lehmann, L.; Ingólfsson, O.; Illenberger, E. *Z. Phys. Chem.* **1996,** *195,* 217–236. doi:10.1524/zpch.1996.195.Part_1_2.217

43. Franz, G. *Low pressure plasmas and microstructuring technology;* Springer: Berlin, Germany, 2009. doi:10.1007/978-3-540-85849-2

44. Zlatar, M. *JAMA, J. Am. Med. Assoc.* **2015,** in press.

45. Massey, S.; Bass, A. D.; Sanche, L. *J. Phys. Chem. C* **2015,** *119,* 12708–12719. doi:10.1021/acs.jpcc.5b02684

46. Matejčık, Š.; Foltin, V.; Stano, M.; Skalný, J. D. *Int. J. Mass Spectrom.* **2003,** *223–224,* 9–19. doi:10.1016/S1387-3806(02)00776-5

47. Dressler, R.; Allan, M. *Chem. Phys.* **1985,** *92,* 449–455. doi:10.1016/0301-0104(85)85038-2

48. Bjarnason, E. H.; Ómarsson, B.; Engmann, S.; Ómarsson, F. H.; Ingólfsson, O. *Eur. Phys. J. D* **2014,** *68,* 1–8. doi:10.1140/epjd/e2014-50091-9

49. Allan, M. *J. Phys. B: At., Mol. Opt. Phys.* **1992,** *25,* 1559. doi:10.1088/0953-4075/25/7/025

50. Ipolyi, I.; Michaelis, W.; Swiderek, P. *Phys. Chem. Chem. Phys.* **2007,** *9,* 180–191. doi:10.1039/B612261B

51. Xue, Z.; Strouse, M. J.; Shuh, D. K.; Knobler, C. B.; Kaesz, H. D.; Hicks, R. F.; Williams, R. S. *J. Am. Chem. Soc.* **1989,** *111,* 8779–8784. doi:10.1021/ja00206a002

52. Yavas, O.; Ochiai, C.; Takai, M.; Hosono, A.; Okuda, S. *Appl. Phys. Lett.* **2000,** *76,* 3319–3321. doi:10.1063/1.126638

53. Yavas, O.; Ochiai, C.; Takai, M.; Park, Y. K.; Lehrer, C.; Lipp, S.; Frey, L.; Ryssel, H.; Hosono, A.; Okuda, S. *J. Vac. Sci. Technol., B* **2000,** *18,* 976–979. doi:10.1116/1.591310

54. Botman, A.; Hesselberth, M.; Mulders, J. J. L. *Microelectron. Eng.* **2008,** *85,* 1139–1142. doi:10.1016/j.mee.2007.12.036

55. Botman, A. P. J. M. Towards high purity nanostructures from electron beam induced deposition of platinum. Ph.D. Thesis, Delft University of Technology, Delft, Netherlands, 2009.

56. Botman, A.; Mulders, J. J. L.; Hagen, C. W. *Nanotechnology* **2009,** *20,* 372001. doi:10.1088/0957-4484/20/37/372001

57. Mehendale, S.; Mulders, J. J. L.; Trompenaars, P. H. F. *Nanotechnology* **2013,** *24,* 145303. doi:10.1088/0957-4484/24/14/145303

58. Villamor, E.; Casanova, F.; Trompenaars, P. H. F.; Mulders, J. J. L. *Nanotechnology* **2015,** *26,* 095303. doi:10.1088/0957-4484/26/9/095303

59. Langford, R. M.; Ozkaya, D.; Sheridan, J.; Chater, R. *Microsc. Microanal.* **2004,** *10,* 1122–1123. doi:10.1017/S1431927604883417

60. Geier, B.; Gspan, C.; Winkler, R.; Schmied, R.; Fowlkes, J. D.; Fitzek, H.; Rauch, S.; Rattenberger, J.; Rack, P. D.; Plank, H. *J. Phys. Chem. C* **2014,** *118,* 14009–14016. doi:10.1021/jp503442b

61. Plank, H.; Noh, J. H.; Fowlkes, J. D.; Lester, K.; Lewis, B. B.; Rack, P. D. *ACS Appl. Mater. Interfaces* **2014,** *6,* 1018–1024. doi:10.1021/am4045458

62. Botman, A.; Mulders, J. J. L.; Weemaes, R.; Mentink, S. *Nanotechnology* **2006,** *17,* 3779. doi:10.1088/0957-4484/17/15/028

63. Mackus, A. J. M.; Mulders, J. J. L.; van de Sanden, M. C. M.; Kessels, W. M. M. *J. Appl. Phys.* **2010,** *107,* 116102. doi:10.1063/1.3431351

64. Stanford, M. G.; Lewis, B. B.; Noh, J. H.; Fowlkes, J. D.; Roberts, N. A.; Plank, H.; Rack, P. D. *ACS Appl. Mater. Interfaces* **2014,** *6,* 21256–21263. doi:10.1021/am506246z

65. Yang, D. S.; Bancroft, G. M.; Puddephatt, R. J.; Tan, K. H.; Cutler, J. N.; Bozek, J. D. *Inorg. Chem.* **1990,** *29,* 4956–4960. doi:10.1021/ic00349a025

66. Shen, J.; Muthukumar, K.; Jeschke, H. O.; Valentí, R. *New J. Phys.* **2012,** *14,* 073040. doi:10.1088/1367-2630/14/7/073040

67. Stein, S. E. Mass Spectra. In *NIST Chemistry WebBook, NIST Standard Reference Database Number 69;* Linstrom, P. J.; Mallard, W. G., Eds.; National Institute of Standards and Technology: Gaithersburg, MD, U.S.A..
http://webbook.nist.gov (accessed on May 18, 2015).

68. Wnuk, J. D.; Rosenberg, S. G.; Gorham, J. M.; van Dorp, W. F.; Hagen, C. W.; Fairbrother, D. H. *Surf. Sci.* **2011,** *605,* 257–266. doi:10.1016/j.susc.2010.10.035

69. Kruck, T.; Baur, K. *Angew. Chem., Int. Ed. Engl.* **1965,** *4,* 521. doi:10.1002/anie.196505211

70. Rand, M. J. *J. Electrochem. Soc.* **1973,** *120,* 686–693. doi:10.1149/1.2403534

71. Barry, J. D.; Ervin, M.; Molstad, J.; Wickenden, A.; Brintlinger, T.; Hoffman, P.; Meingailis, J. *J. Vac. Sci. Technol., B* **2006,** *24,* 3165–3168. doi:10.1116/1.2395962

72. Elbadawi, C.; Toth, M.; Lobo, C. J. *ACS Appl. Mater. Interfaces* **2013,** *5,* 9372–9376. doi:10.1021/am403167d

73. O'Regan, C.; Lee, A.; Holmes, J. D.; Petkov, N.; Trompenaars, P.; Mulders, H. *J. Vac. Sci. Technol., B* **2013,** *31,* 021807. doi:10.1116/1.4794343

74. Friedman, J. F.; Miller, T. M.; Friedman-Schaffer, J. K.; Viggiano, A. A.; Rekha, G. K.; Stevens, A. E. *J. Chem. Phys.* **2008,** *128,* 104303. doi:10.1063/1.2831391

75. Lias, S. G.; Liebman, J. F. Ion Energetics Data. In *NIST Chemistry WebBook, NIST Standard Reference Database Number 69;* Lindstrom, P. J.; Mallard, W. G., Eds.; National Institute of Standards and Technology: Gaithersburg, MD, U.S.A..
http://webbook.nist.gov (accessed on May 19, 2015).

76. Ivanova, A. R.; Nuesca, G.; Chen, X.; Goldberg, C.; Kaloyeros, A. E.; Arkles, B.; Sullivan, J. J. *J. Electrochem. Soc.* **1999,** *146,* 2139–2145. doi:10.1149/1.1391904

77. Lane, P. A.; Oliver, P. E.; Wright, P. J.; Reeves, C. L.; Pitt, A. D.; Cockayne, B. *Chem. Vap. Deposition* **1998,** *4,* 183–186. doi:10.1002/(SICI)1521-3862(199810)04:05<183::AID-CVDE183>3.0. CO;2-M

78. Crawford, N. R. M.; Knutsen, J. S.; Yang, K.-A.; Haugstad, G.; McKernan, S.; McCormick, F. B.; Gladfelter, W. L. *Chem. Vap. Deposition* **1998,** *4,* 181–183. doi:10.1002/(SICI)1521-3862(199810)04:05<181::AID-CVDE181>3.0. CO;2-U

79. Gilmont, P.; Blanchard, A. A.; Mason, C. M.; Barnard, R. L. Dicobalt Octacarbonyl, Cobalt Nitrosyl Tricarbonyl, and Cobalt Tetracarbomyl Hydride. In *Inorganic Syntheses;* Fernelius, W. C., Ed.; John Wiley & Sons: Hoboken, NJ, U.S.A., 1946; Vol. 2, pp 240 ff. doi:10.1002/9780470132333.ch76

80. Mulders, J. J. L.; Belova, L. M.; Riazanova, A. *Nanotechnology* **2011,** *22,* 055302. doi:10.1088/0957-4484/22/5/055302

81. Gazzadi, G. C.; Mulders, J. J. L.; Trompenaars, P.; Ghirri, A.; Rota, A.; Affronte, M.; Frabboni, S. *Microelectron. Eng.* **2011,** *88,* 1955–1958. doi:10.1016/j.mee.2010.12.031

82. Gazzadi, G. C.; Mulders, H.; Trompenaars, P.; Ghirri, A.; Affronte, M.; Grillo, V.; Frabboni, S. *J. Phys. Chem. C* **2011,** *115,* 19606–19611. doi:10.1021/jp206562h

83. Vollnhals, F.; Drost, M.; Tu, F.; Carrasco, E.; Späth, A.; Fink, R. H.; Steinrück, H.-P.; Marbach, H. *Beilstein J. Nanotechnol.* **2014,** *5,* 1175–1185. doi:10.3762/bjnano.5.129

84. Begun, E.; Dobrovolskiy, O. V.; Kompaniiets, M.; Sachser, R.; Gspan, C.; Plank, H.; Huth, M. *Nanotechnology* **2015,** *26,* 075301. doi:10.1088/0957-4484/26/7/075301

85. Papp, P.; Engmann, S.; Kučera, M.; Stano, M.; Matejčík, Š.; Ingólfsson, O. *Int. J. Mass Spectrom.* **2013,** *356,* 24–32. doi:10.1016/j.ijms.2013.09.011

License and Terms

Correction: Formation of pure Cu nanocrystals upon post-growth annealing of Cu–C material obtained from focused electron beam induced deposition: comparison of different methods

Aleksandra Szkudlarek[1,2], Alfredo Rodrigues Vaz[1,3], Yucheng Zhang[4], Andrzej Rudkowski[5], Czesław Kapusta[5], Rolf Erni[4], Stanislav Moshkalev[3] and Ivo Utke[*1]

Correction

Address:
[1]Empa, Swiss Federal Laboratories for Materials Science and Technology, Laboratory for Mechanics of Materials and Nanostructures, Feuerwerkerstrasse 39, 3602 Thun, Switzerland, [2]AGH University of Science and Technology, Academic Centre for Materials and Nanotechnology, al. A. Mickiewicza 30, 30-059 Krakow, Poland, [3]Center for Semiconductor Components, State University of Campinas, 13083-870, Campinas, SP, Brazil, [4]Empa, Swiss Federal Laboratories for Materials Science and Technology, Electron Microscopy Center, Überlandstrasse 129, 8600 Dübendorf, Switzerland and [5]AGH University of Science and Technology, Faculty of Physics and Applied Computer Science, Department of Solid State Physics, al. A. Mickiewicza 30, 30-059 Krakow, Poland

Email:
Ivo Utke[*] - ivo.utke@empa.ch

* Corresponding author

Keywords:
Cu(hfac)$_2$; Cu nanocrystals; focused electron beam induced deposition (FEBID); post-growth annealing of Cu–C material

This correction refers to *Beilstein J. Nanotechnol.* **2015**, *6*, 1508–1517. doi:10.3762/bjnano.6.156

In Figure 8 of the original article, the scale of the ordinate was wrong. The correct figure looks as follows:
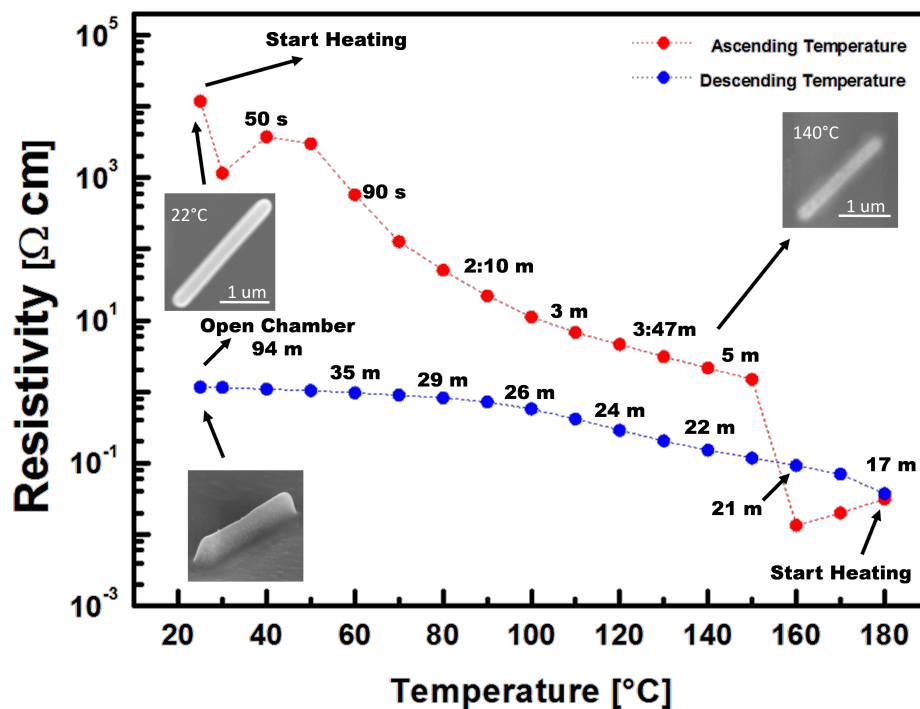
Figure 1: Figure 8 in the original article: Calculated resistivity from the resistance measurement of a Cu–C line during in situ post-growth heating with a hot plate (red dots) and cooling down (blue dots) inside the SEM chamber. The resistance did not change when opening the chamber. The top SEM images show the morphology changes of an adjacent FEBID line which was observed simultaneously during the in situ resistance measurement.